Variable-Stiffness Protective Material

by

Caleb Jordan Petersen

A thesis submitted to the Graduate Faculty of
Auburn University
in partial fulfillment of the
requirements for the Degree of
Master of Science

Auburn, Alabama
May 7, 2016

Keywords: Nonlinear Bending Stiffness 3D-Printed Arrays

Approved by

Royall M. Broughton, Professor Emeritus of Polymer and Fiber Engineering
David Beale, Professor of Mechanical Engineering
Peter Schwartz, Professor of Polymer and Fiber Engineering

Abstract

The focus of this research is to develop a system for limiting the motion of a mechanical joint to prevent damage to the joint. One obvious application is enhancing the safety of human joints during athletic events. For maximum reliability, the designer should eschew electronic sensors or actuators. The system also must provide minimum mechanical inhibition or altered stiffness (even if elastic) inside the safe zone of motion, but significant strength as well as stiffness on the border of the joint's safe zone. To this end, several domains were investigated, starting with an adaptation of Auburn's patented "open structures" with a weave that gives some bending compliance, layup-varying approaches (just as aeroelastic tailoring uses special layup directions to produce deflection coupling for altered aerodynamic properties), and new chainmail weaves. These approaches were all unsuccessful, but later research found planar compliant mechanisms and fabric arrays of teeth stiffen sufficiently in simple bending through self-contact. The former were rejected because of their discrete, unconforming nature, but the latter proved successful in restricting a test fixture's motion when wrapped into a cylindrical shape. Finally, the fabric arrays of teeth were successfully adapted into pre-curved arrays that can be worn around a human ankle and limit its motion; however, an attempt to generalize the compliant planar comb idea by revolving its shape about an offset axis produced insufficient stiffening up (even when special backbone geometries that stiffen in tension were used), indicating that fabric backbones are a key component of the material. Further research is needed into how to generate tooth geometries for the fabric-backed arrays that will conform to a complicated shape (like the lower leg) and lock up at a specific desired angle.

Acknowledgements

Thanks to my parents for all their support during my education.

This research was made possible by a generous grant from the Gackstatter Foundation.

Table of Contents

List of Tables

List of Figures

Chapter 1. Problem Statement and Review of Protection Strategies.

Introduction.

Athletes, especially at the most elite levels, must push their bodies to the limit in terms of force developed versus maximum safe joint force and in terms of rate of movement and acceleration versus the nervous system's minimum response time. As such, athletes often risk debilitating (if hardly life-threatening) injuries from forcible overextension of joints given the low "safety factor" under which they operate. The most common embodiment of such an injury is when an athlete tries to change direction dynamically with parts of the body in an improper position, thereby risking a tear in cartilage or ligaments of the ankle, knee, or hip. Given the short timescale and high inertia of the event, even if the athlete realizes the danger of his movement early on in its execution, he probably will be unable to ameliorate its effects.

Athletes already employ protective strategies, but they are of limited utility and are fraught with performance-reducing characteristics. For instance, basketball players are known to bind their ankles with a moderate-stiffness polymer fabric; unfortunately, this restricts the athlete's feasible range of ankle motions (and may thereby impact running performance). Similarly, this practice also adds unnatural stiffness: specifically, this can increase the time required to move the foot, and it adds restoring stiffness that might cause the foot to overshoot its rest position when a load is removed. Plus, sources of energy dissipation (from viscoelasticity in the band, to sliding friction, to fibers sliding relative to each other) waste some energy (even if the elastic force is desirable), although this may be relatively insignificant. More to the point,

because the stiffening of the ankle joint is relatively constant with respect to deflection, without practically immobilizing the joint, little real protection can be achieved, and thus only player vigilance and inherent bodily strength can prevent injuries.

Ironically, a protective device that allows a maximum of freedom of movement (just barely under the threshold for injury) could reduce injury incidence relative even to that of the stiffest ankle binding because the free protective device would allow recruitment (thus strengthening) of the peroneal muscles while the ankle is inside the safe range. These muscles stabilize ankle eversion, and ankle binding has come under fire from sport enthusiasts for the way in which it limits peroneal muscle usage during non-mission-critical practice[1] strengthening them (and entraining their reactions) would add to joint strength in play and prevent a strength deficit that would be problematic when the device is not being worn. If it were possible to develop a solution that is superior both to an unprotected joint and the unnatural, restrictive, and ineffective ankle-binding strategy, it would significantly reduce player downtime, which one presumes can cost teams significant amounts of money that could justify even an expensive, effective protection strategy.

That said, assuming an unlimited acceptable price is folly. While the popularity of high-end Nike shoes shows that people will pay a premium for footwear (even though air soles appear to increase the likelihood of injury relative to higher-quality shoes[2]), the price must be limited as much as possible to broaden the available market. In particular, children will likely especially benefit from this device as they're still growing and injuries sustained in sports could

---

[1] Smith, Jimmy. "The Ankle Paradox." *The Ankle Paradox*. T-Nation, 12 Feb. 2008. Web. 22 Feb. 2015.

[2] Mckay, G. D. "Ankle Injuries in Basketball: Injury Rate and Risk Factors." *British Journal of Sports Medicine* 35.2 (2001): 103-08.

permanently hamper development (even if comparable adult injuries could easily be recovered from); however, as there's no money to be made from children's sports, families would have to buy the device out-of-pocket.

Of course, the issue of clothing costs raises a related question of the importance of the item's appearance. Given the importance of competitive symbolism to an athlete's psyche (however irrelevant to the physical considerations of athletic performance), the device should not advertise the wearer's concern for his joint safety, although if it could be recast as a significant advantage allowing risk with impunity, its adoption would be faster as wearers could hope to intimidate their opponents just by wearing it.

Sponsor's Requirements.

The most important of the sponsor's requirements is that the device have the strength and stiffness to prevent deflection of the ankle (or other human or even mechanical) joint past certain safe limits, or, failing this, to absorb as much energy as possible so that the excursion outside the safe limit is as non-dynamic as possible and can be resisted by the body's tendons and ligaments well. It is similarly quite important that the device have very low or even true zero static stiffness within a certain range. Likewise, dissipative forces should be minimum within the safe regime. Common sense also suggests that there should be a limit on the rate at which stiffness ramps up as one gets close to the edge of the safe envelope. Also, clearly the solution needs to be lightweight, and it should always conform to the leg and ankle rather than taking up significant real estate outside the limb – this sort of geometry would not only increase the inertia of movement of the leg in certain directions, but it would also likely collide with other limbs in movement.

Mechanics and Mechanisms of Injury of the Human Ankle.

The ankle complex actually consists of two separate joints, although the bones associated with one are both hidden and coupled with the other such that to casual observation it appears there is only one. The true ankle joint, known more technically as the talocrural joint, is generally modelled as a hinge with only one degree of freedom[3]: this is the most obvious motion of the ankle complex. Special names are assigned to this mode depending upon direction: dorsiflexion (sometimes called "foot extension") is said to entail bringing one's forefoot upwards, plantarflexion (sometimes referred to simply as "foot flexion") the opposite. Figure 1 illustrates connects the nomenclature with joint direction.

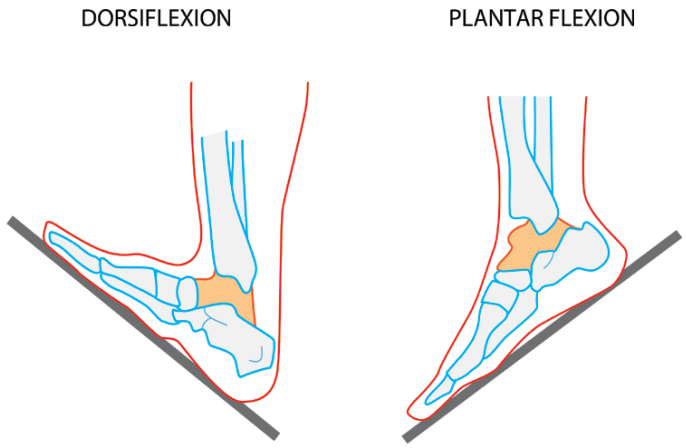

Figure 1: Showing plantarflexion and dorsiflexion deflection modes from neutral in a human foot[4].

The axis around which the true ankle joint *initially* rotates is somewhat rotated from "even" horizontal and vertical angles, as Figure 2 shows. (There are significant variations in the

[3] Levangie, Pamela K., Cynthia C. Norkin, and Pamela K. Levangie. *Joint Structure and Function: A Comprehensive Analysis*. Philadelphia: F.A. Davis, 2011. Print. p.440

[4] Image source: http://garrettmclaughlin.com/2014/02/04/self-evaluationtreatment-strategies-for-the-ankle/

literature as to the reported neutral values of these angles, with Figure 2's taken from [5]. They may vary significantly enough to require personalization). Moreover, minor changes in the orientation of this rotational axis occur with respect to joint rotation, for it is not a perfect revolute joint—however, the ankle-complex motions of inversion and eversion see much greater changes in the orientations of their rotary axis. Plus, there is of course no such thing as a perfect constraint, and the true ankle joint has some freedom in the coronal plane (the plane perpendicular to the initial "main" axis of joint rotation) and even in the transverse plane (the plane roughly perpendicular to the leg's axis), especially at significant rotation from neutral[6]. The plane in which the main rotation occurs is known as the sagittal.

[5] Levangie, Pamela K., Cynthia C. Norkin, and Pamela K. Levangie. *Joint Structure and Function: A Comprehensive Analysis*. Philadelphia: F.A. Davis, 2011. Print. *p.444*

[6] *Modeling and Simulation of the Foot and Ankle to Predict Ankle and Subtalar Joint Motion*, citing Lundberg, A., Svensson, O.K., Nemeth, G., Selvik, G., "The Axis of Rotation of the Ankle Joint", J. Bone J Surg., v71B, 1989, 94-99 and Lundberg A., Goldie I., Kalin B., Selvik G., "Kinematics of the ankle/foot complex: plantarflexion and dorsiflexion", Foot & Ankle, v9, n4, 1989, 194-200

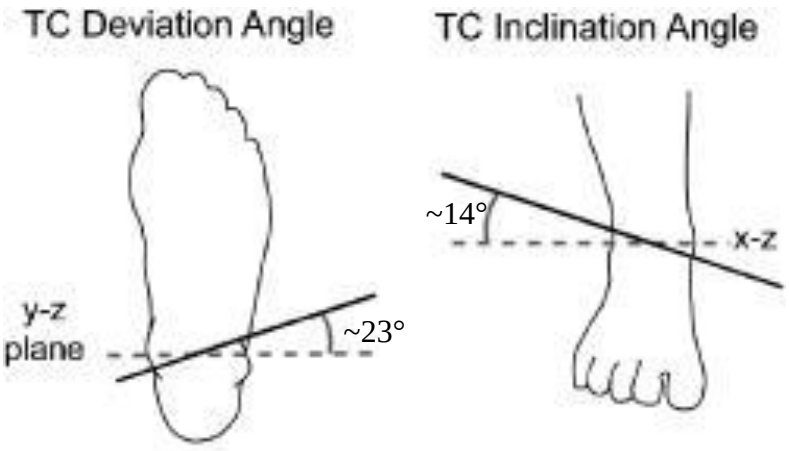

Figure 2: Average angles of the initial axis of the ankle joint. Note that the axis rotates somewhat throughout plantar/dorsiflexion.

Dorsiflexion and plantarflexion comprise the most important of the ankle's three modes, at least as concerns gross human mobility; hence, most human foot prosthetics currently on the market consist of flexible beams that bend around the "coronal" axis (i.e. that associated with dorsiflexion/plantarflexion in a natural foot) yet are stiff in torsion and about the "longitudinal axis" (i.e. that associated with inversion/eversion). Figure 3 shows one such prosthesis.

Figure 3: Carbon-fiber foot prosthesis. Note its relative compliance in bending about the coronal axis.

The free range of motion customarily given for the ankle joint in dorsiflexion is around 10° to 20°, and that for plantarflexion ranges from 20° to 50°[7]; strictly speaking, these values are for the entire foot (including the freedom in this direction added by the subtalar and transverse tarsal joints to that of the true ankle joint), and when the ankle joint is isolated, its freedom affords 10° of dorsiflexion and 20° of plantarflexion[8]. A minimum functional range of 10° of dorsiflexion (from all joints) is required for ambulation without significant gait problems or injury[9]. Interestingly, the range of motion for dorsiflexion is slightly reduced when the knee is in

[7] Levangie, Pamela K., Cynthia C. Norkin, and Pamela K. Levangie. *Joint Structure and Function: A Comprehensive Analysis*. Philadelphia: F.A. Davis, 2011. Print, p. 464

[8] Levangie, Pamela K., Cynthia C. Norkin, and Pamela K. Levangie. *Joint Structure and Function: A Comprehensive Analysis*. Philadelphia: F.A. Davis, 2011. Print, p. 465

[9] Levangie, Pamela K., Cynthia C. Norkin, and Pamela K. Levangie. *Joint Structure and Function: A Comprehensive Analysis*. Philadelphia: F.A. Davis, 2011. Print, p. 465

extension (i.e. leg straightened) as compared with that when the knee is in flexion (i.e. leg bent)[10].

Despite the importance of sagittal rotation to general ambulation, ankle injuries rarely occur in excessive pure dorsiflexion or plantarflexion: pure-plantarflexion injuries are rare (anecdotally, their main cause is when one kicks a solid object with toes pointing downwards, mistaking it for a ball that is to be kicked with a precise soccer kick[11]—however, if one kicked a movable object like a soccer ball in this position, no injury would result, and constraining plantarflexion before this position could be reached would inhibit kicking accuracy; whether or not to attempt to constrain it likely depends on how close it is to the envelope of injury), and pure-dorsiflexion injuries seem likely only in falls from great height, being likewise unreferenced in the literature. Indeed, some dorsiflexion actually increases the ankle's vertical-load-bearing capacity[12]. However, when rotation in the sagittal plane is coupled with another rotation (principally inversion, as discussed below), injury becomes more likely than when rotation in the sagittal plane is neutral. It is then not immediately apparent whether constraints should exist in the range encompassing pure dorsiflexion and plantarflexion, or whether constraint should exist only when another joint motion (inversion/eversion or transverse rotation) is added. Given anecdotes of injury from a kick to a , it may be preferable to prevent high plantarflexion/dorsiflexion than merely to guard against any subsequent excessive

[10] Levangie, Pamela K., Cynthia C. Norkin, and Pamela K. Levangie. *Joint Structure and Function: A Comprehensive Analysis*. Philadelphia: F.A. Davis, 2011. Print, p. 467

[11] "Rupture of the Joint-capsule at the Front of the Ankle Joint." SportNetDoc.DK. Web. 22 Aug. 2015. <http://www.sportnetdoc.com/foot-ankle/rupture-of-the-joint-capsule-at-the-front-of-the-ankle-joint>.

[12] Levangie, Pamela K., Cynthia C. Norkin, and Pamela K. Levangie. *Joint Structure and Function: A Comprehensive Analysis*. Philadelphia: F.A. Davis, 2011. Print, p. 465

inversion/eversion, even though it is the latter that will do the damage, due to constraints in the rate or precision of lockup.

This brings the study of the ankle's constraints to the salient joint mode as concerns protection: inversion and eversion, which are rotations involving the subtalar joint. Strictly speaking, these gross, highly-coupled motions are known as supination and pronation: supination contains the inversion component of rotation in the frontal plane, plus other components, and pronation likewise consists of the eversion component plus other rotations. However, these motions are more commonly referenced by their frontal-plane components (i.e. as inversion/eversion) than as supination and pronation; the lack of consistent nomenclature is an irritant to some commentators[13]. Figure 4 illustrates these two modes.

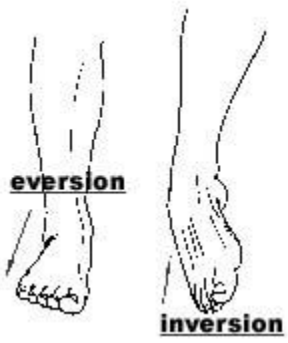

Figure 4: Inversion entails rotating the outer edge of the foot down; eversion is the opposite. Image source:[14]

The foot complex also sees a modicum of rotation in the transverse plane. Figure 5 depicts this mode, using the nomenclature assigned to it: as resolved into the transverse plane,

[13] Levangie, Pamela K., Cynthia C. Norkin, and Pamela K. Levangie. *Joint Structure and Function: A Comprehensive Analysis*. Philadelphia: F.A. Davis, 2011. Print, p. 449

[14] Image source: http://www.courses.vcu.edu/DANC291-003/ankle_moinev_copy.jpg

abduction (sometimes called lateral axial rotation) is the outward rotation component, adduction (sometimes called medial axial rotation) the inward.

The kinematics of foot pronation and supination are vastly more complicated than those of dorsiflexion and plantarflexion, for the former two are strongly coupled with transverse rotation (as well as some dorsiflexion or plantarflexion), whereas frank dorsiflexion and plantarflexion can occur with very little coupling. Herein lies the inherent kinematic complexity of the ankle joint. The complexity only intensifies when one considers that the ankle has somewhat different coupling when it is weight-bearing compared with when it is not[15].

Figure 5: Abduction (outward rotation) and adduction (inward rotation) of the ankle complex relative to a stationary leg.

[15] Levangie, Pamela K., Cynthia C. Norkin, and Pamela K. Levangie. *Joint Structure and Function: A Comprehensive Analysis*. Philadelphia: F.A. Davis, 2011. Print, p. 448

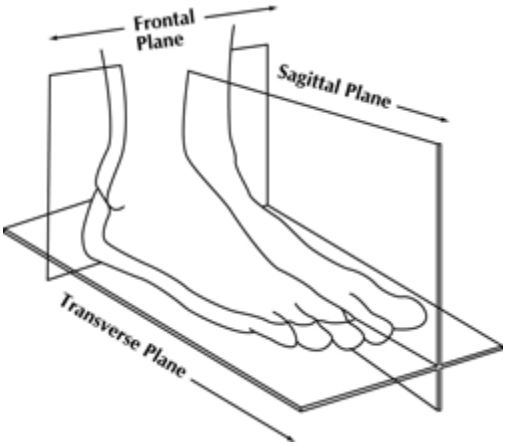

Figure 6: Nomenclature of initial planes for the freedoms of the human ankle complex. Note that rotation in one mode is never perfectly confined to the plane therewith associated (especially for inversion/eversion).[16]

While it is important to note that this motion-limiting device could be adapted to many other joints, advising experts commend the ankle-subtalar complex to the writer for its current vulnerability, comparable only to that of the knee joint. Additionally, the knee both possesses a greater range of motion and experiences greater moment loadings than does the ankle, both of which are likely to render the development of a protective strategy for it more difficult than for the ankle. Finally, players often rest upon one knee (or frequently land thereon); hence, a protective device for the knee must also be comfortable in this position and capable of bearing a significant fraction of the player's weight in the form of a localized compression.

Basic Angular Limits.

Treating the above-described modes of ankle rotation as uncoupled and the axes of rotation as non-rotating during throughout the range of motion of the ankle, average ranges for safe movement without injury and needed freedom for most athletic endeavors have been calculated. Even the average values vary from one source to another, and ideally at least the safe

[16] Image source: http://www.insolepro.co.uk/biomechanics.html

range for each relevant degree of freedom would be calculated for each individual athlete (then, the designer would extrapolate from this to calculate the angle at which lockup should begin, i.e. where the end of the needed freedom for athletic performance would be reached). Note that a rotation from neutral along one axis can change the angle of onset of danger for another rotational mode.

Individualization Concerns.

A manufacturing technique that allows interchanging parts (for instance, the force regulator, the shoe, and the connection to the upper leg) would be useful as it could accommodate natural variations not only in leg and foot sizes but also safe range of motion for athletes (which might be a highly-individualized function of previous injury history, limb shapes, stretching regimes, etc.).

The sponsor also rightly distrusts electronic system elements (sensors, processors, and force actuators) as they may not be reliable. Also, no conveniently-portable actuator could produce enough force to itself resist an adult male's inertia developed when landing improperly in a run; however, it's conceivable that a lock engaging a stiffening property of a segment could be engaged even with a very light servomotor. If the approach outlined in this thesis fails, future researchers could investigate this 'electronic locking' approach instead.

Current Protection Devices.

The simplest protection strategy consists of binding the ankle. However, as discussed above, it is often insufficient to protect against injury, and may be counterproductive to an extent since it weakens the muscles that stabilize the ankle against injury. Plus, its linear response yields unnecessary restriction inside the safe zone.

Orthotics, largely intended to assist or protect the joints of already-injured patients, also deserve attention. Some interest in orthotics that can be customized to the individual has prompted CRP Technology[17] to research ankle orthotics that can be custom-printed for each individual by the expensive but precise 3D printing technology of Selective Laser Sintering (SLS). SLS technology traditionally utilizes nylon powder, but for greater strength in orthoses, CRP Technology also has developed relatively strong and stiff materials for SLS printing that use chopped, unaligned carbon fiber and polyamide. While this reinforcement is somewhat of an improvement over unreinforced nylon, the resulting mechanical properties are still vastly inferior to those of composite parts made by traditional layup techniques because the process cannot use sufficiently-long fibers to maximize matrix-fiber adhesion, and the fibers cannot be aligned in load directions. Ultimately, the orthosis is presumably intended to have high constant stiffness to enable rehabilitation of an injured joint, not variable stiffness to promote safety and high performance in a healthy joint. Figure 7 shows a sample ankle orthosis developed by CRP.

[17] "The New Frontier in Generative Orthotics." *CRP Technology 3D Printing and Additive Manufacturing Company RSS2*. CRP Technology, 16 July 2014. Web. 18 Aug. 2015.

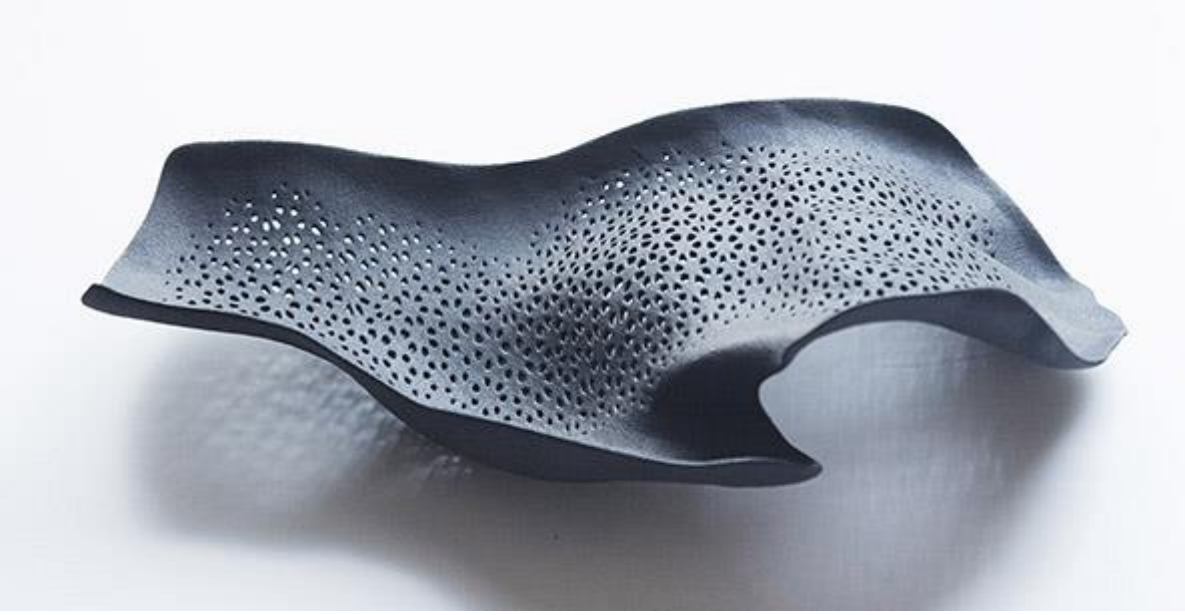

Figure 7: CRP Technology's ankle orthosis, custom-sized for each individual and then manufactured with carbon-fiber-reinforced polyamide by selective laser sintering 3D printing technology, from [18].

One concern with protection devices in general is the possibility of simply shifting injury locus throughout the body: for instance, a very stiff protection device at the ankle might completely shield it from injury during a fall in which the ankle is subjected to moments to which it is unsuited, but these moments could then be transferred to the knee and injure it instead. Indeed, this particular outcome would probably be worse than the ankle injury that was prevented since the knee is so complex and so crucial to basic walking. In defense of the concept, however, if knee injury would have been avoided by the ankle's failure, this would be the result of energy dissipated in tearing associated ankle ligaments (or even fracturing bones, as occasionally occurs in ankle injury), and this energy-dissipation mechanism could be replicated in an artificial protection device by engineering material yielding, much as emergency bungee cords experience significant plastic strain

[18] Image source: http://www.crptechnology.eu/2201-new-frontier-generative-orthotics.html

Derived Mechanical Requirements.

Ignoring shearing, axial compressive, and axial tensile loads (none of which athletes are likely to encounter), there are three modes of joint movement whose allotted safe operating ranges could be exceeded: inversion/eversion, plantarflexion/dorsiflexion, and transverse rotation. Figure 1, Figure 4, and Figure 5 show these modes, and Table 1 shows some common safe ranges of motion (in quasi-static loading) for the ankle joint. Inversion is by far the most common source of injury, although the safe operating range for inversion tends to decrease with other joint displacement (i.e. dorsiflexion/plantarflexion and/or transverse rotation). This coupling of joint motions dictates an important requirement: the system must either limit deflections in one direction differently depending upon the instantaneous deflection in another direction During normal walking, no joint direction is constant over any portion of the stroke, and the axis of rotation for inversion/eversion changes with respect to the amount of inversion/eversion; this complicates analysis of the joint motion, although rigid-body dynamics programs have been produced that can use force and motion capture data from real people to produce curves of joint forces, motions, instantaneous rotation centers, etc.

Table 1: Average safe and working ranges for several joint modes for the human ankle.

Joint Mode	**Max. Average Safe Angle (Uncoupled!)**
Dorsiflexion	10-20°[19]

[19] Levangie, Pamela K., Cynthia C. Norkin, and Pamela K. Levangie. *Joint Structure and Function: A Comprehensive Analysis*. Philadelphia: F.A. Davis, 2011. Print, p.444, citing numerous

Plantarflexion	20-50°[20]
Inversion	20-30°[21]
Eversion	5-10°[22]
Transverse Rotation	~10°[23]

In order to control the ankle joint, a sturdy connection must be established between the device, the foot, and the lower leg (this assumes that the device is not directly connected to the bone immediately surrounding the ankle, which is a reasonable assumption since it would be very difficult to exert an effective torque this close to the ankle). Thus, the sleeve that goes on the lower leg should not slide or rotate relative to the leg, or it will not be able to adequately capture the joint rotation or inhibit it.

[20] Levangie, Pamela K., Cynthia C. Norkin, and Pamela K. Levangie. *Joint Structure and Function: A Comprehensive Analysis*. Philadelphia: F.A. Davis, 2011. Print, p.444, citing numerous

[21] Levangie, Pamela K., Cynthia C. Norkin, and Pamela K. Levangie. *Joint Structure and Function: A Comprehensive Analysis*. Philadelphia: F.A. Davis, 2011. Print, p.450, citing numerous

[22] Levangie, Pamela K., Cynthia C. Norkin, and Pamela K. Levangie. *Joint Structure and Function: A Comprehensive Analysis*. Philadelphia: F.A. Davis, 2011. Print, p.450, citing numerous

[23] Levangie, Pamela K., Cynthia C. Norkin, and Pamela K. Levangie. *Joint Structure and Function: A Comprehensive Analysis*. Philadelphia: F.A. Davis, 2011. Print, p.451, citing numerous

Chapter 2. Preliminary Research into Stiffening-up Materials and Systems

Abstract.

A survey of material science literature found no known materials that experience sharp but elastic stiffening after a fixed amount of tensile strain. Most materials become less stiff with strain (particularly as they enter a plastic region, if applicable). Some foams are known to become stiffer in large-strain, plastic compression due to increasing self-contact of cells, and some polymers have a J-shaped tensile stress-strain curve (some experience stiffening up only in plastic deformation; others are elastomers whose stiffening up is indeed elastic but requires high strain and is of modest magnitude, which would necessitate undesirably-high thickness in the protective device); however, highly-crosslinked elastomers do not even feature J-cure-style stiffening. Various weaves of chainmail, both extant and unique to this team, were also investigated, but the chainmail idea was deemed impractical due to manufacturing and computational difficulties. Microstructures that experience stiffening in one-dimensional tension were evaluated for stiffening in bending, but with little success. Finally, a variation on Auburn University's classic tubular 'open structures' of braided composite yarns[24] was investigated for stiffening in bending. While it might be feasible to create such structures with very low initial bending stiffness, most tested here showed mild stiffening up at best and was not very consistent from test to test. Thus, these investigations were put on hold.

Introduction.

[24] Austin Gurley, "Design and Analysis of Optimal Braided Composite Lattice Structures"

It is easy to think of materials that get softer after a significant amount of strain, usually at their yield points—ductile metals display this phenomenon, as do ductile thermoplastics. However, any increase in material stiffness (let alone one significant enough for this application) is far rarer. Many foams exhibit gradual stiffening in crushing; for instance, Figure 8 shows plots of stress vs. compressive strain for a certain well-understood industrial foam. However, foam crushing is not an ideal mode of protection for this assignment, mainly because it is highly plastic even within the safe region, thus not only wasting energy but causing the protective device to quickly deteriorate even absent any excursions outside the safe zone.

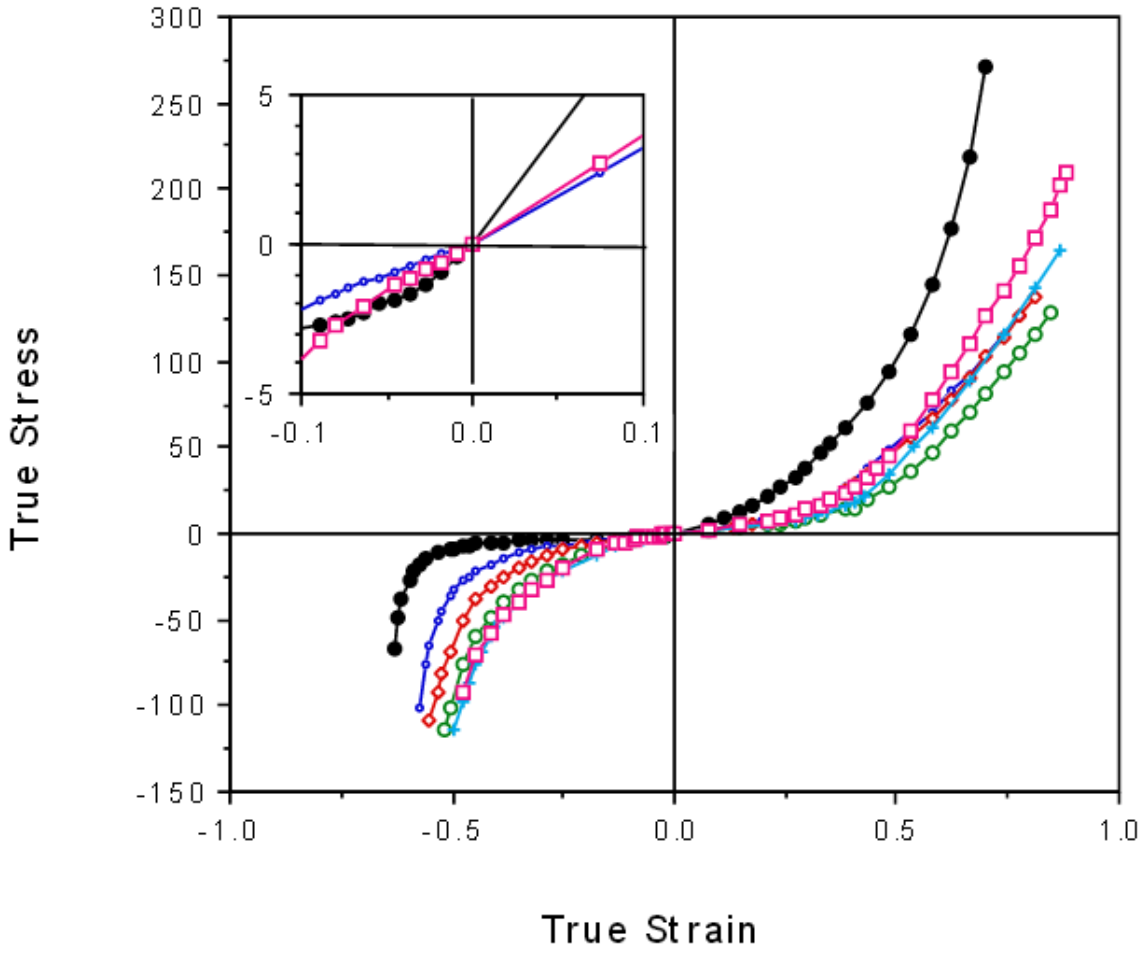

Figure 8: Compressive nonlinearity of conventional, non-auxetic foams, taken from [25].

Hyperelastic Materials and Stiffening Behavior.

Many elastomers evince significant stiffening in tension at high strains, often on the order of 1 or greater. However, not only is the magnitude of final to initial stiffness ratios for elastomers unlikely to be sufficient for this application, but the transition is broad and takes place over much larger strains than could easily be accomplished with a conceivable protective

[25] Choi, J. B. and Lakes, R. S., "Nonlinear properties of polymer cellular materials with a negative Poisson's ratio", J. Materials Science, 27, 4678-4684 (1992

geometry. Figure 9 shows an example stress-strain curve for an elastomer that stiffens. Such behavior is often referred to colloquially as a "J-curve".

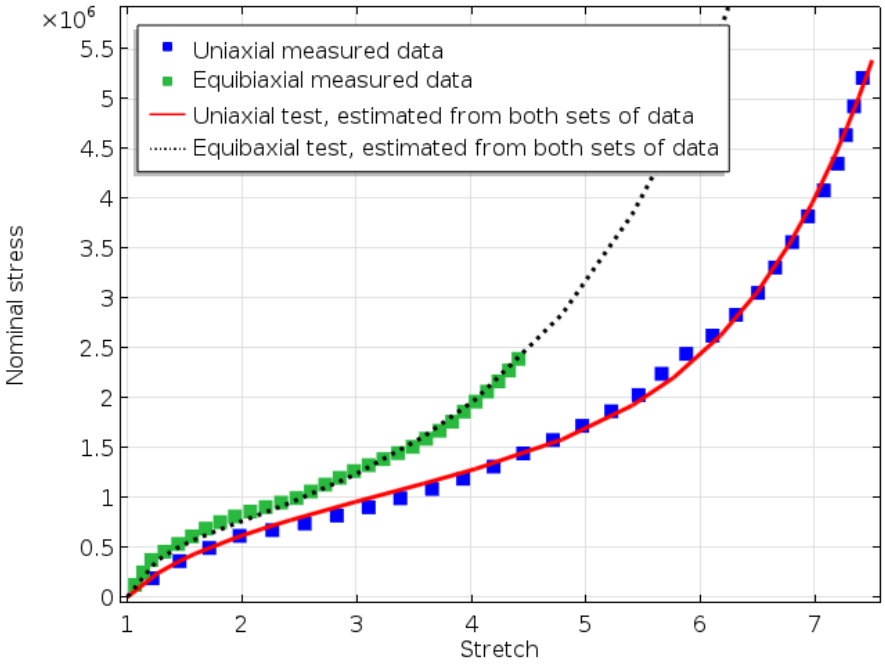

Figure 9: Hyperelastic materials sometimes stiffen greatly in tension. Taken from[26].

Flexible biological materials, such as blood vessels, also often have J-curve stress responses in tension, giving them great toughness and low energy release upon cracking for their modest initial stiffnesses[27]. For instance, Figure 10 shows the tension-response of human lung tissue.

[26] "Obtaining Material Data for Structural Mechanics from Measurements." *COMSOL Blog*. 2015. Web. 03 Aug. 2015. <https://www.comsol.com/blogs/obtaining-material-data-for-structural-mechanics-from-measurements/>.

[27] "J-Shaped Curves." *TLP Library Elasticity in Biological Materials*. University of Cambridge. Web. 03 Apr. 2015. <http://www.doitpoms.ac.uk/tlplib/bioelasticity/j-shaped-curves.php>.

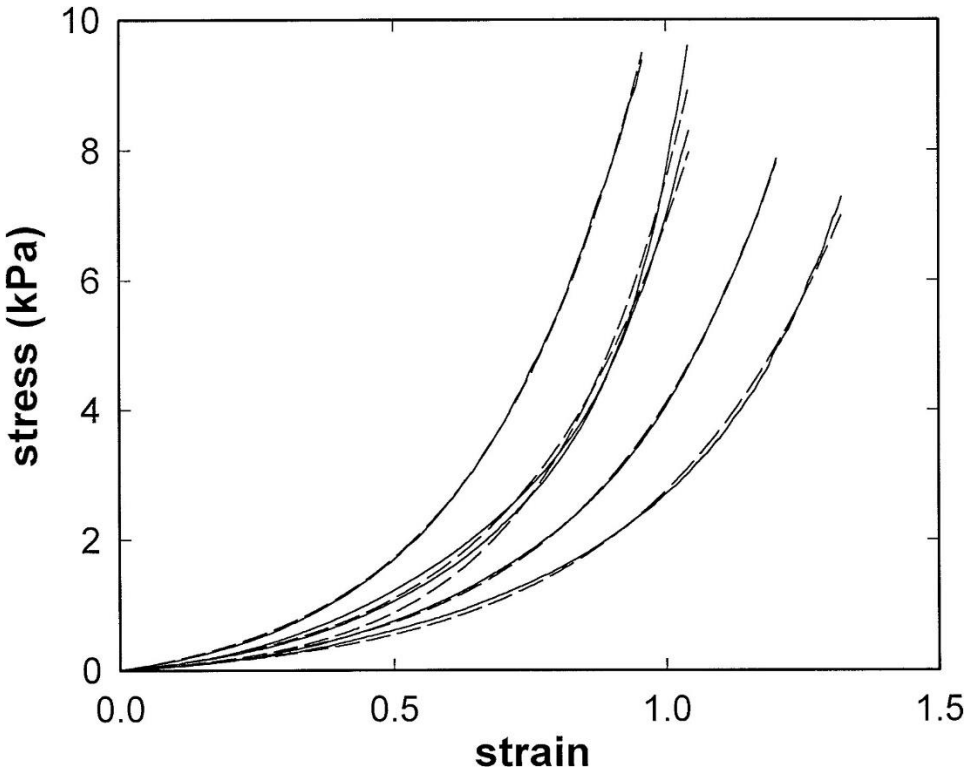

Figure 10: Tension-stiffening behavior of lung tissue samples at moderate strains. This is reminiscent of the behavior of synthetic elastomers. Taken from[28]

Also, many elastomers stiffen in compression after a modicum of deformation due to their high Poisson's ratios and corresponding near incompressibility. Figure 11 shows a Yeoh model of a specific elastomer's mechanical behavior reflecting this stiffening behavior.

[28] "A distributed nonlinear model of lung tissue elasticity" Geoffrey N. Maksym, Jason H. T. Bates. *Journal of Applied Physiology* Published 1 January 1997 Vol. 82 no. 1, 32-41

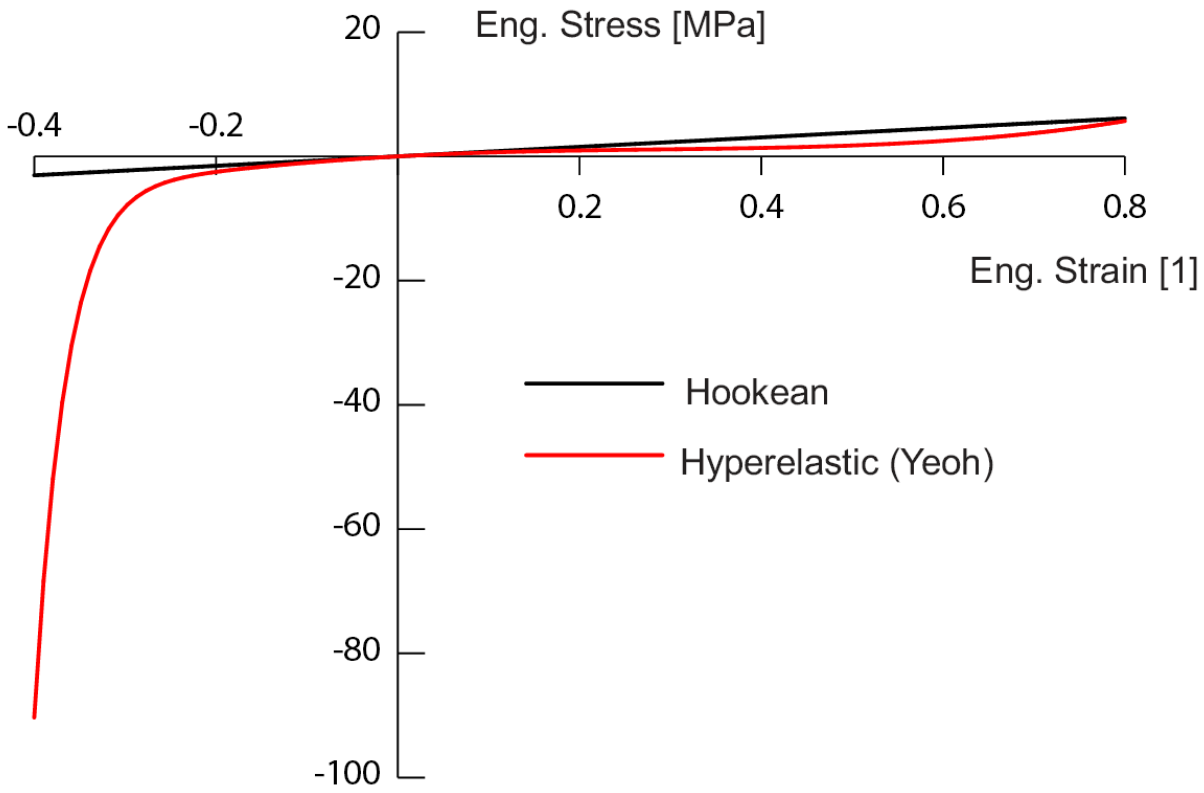

Figure 11: Yeoh model for an elastomer showing rapid stiffening after around 0.3 strain in compression. Taken from [29]

Elastomers exhibit other complexities besides mere tension-stiffening and plasticity, including viscoelastic effects and the Mullins Effect, whereby the material is dramatically more compliant the second and subsequent times it enters a stress region (i.e. in cyclic loading and unloading), although this effect does not really apply to thoroughly-crosslinked elastomers[30]. These effects do not necessarily render them unsuitable for the protective application, but they might complicate design.

Solid Rubber "Sock" Tested for Stiffening-Up.

[29] "MSC.Software: Whitepaper - Nonlinear Finite Element Analysis of Elastomers." http://www.mscsoftware.com/Submitted-Content/Resources/WP_Nonlinear_FEA-Elastomers.pdf
[30] "MSC.Software: Whitepaper - Nonlinear Finite Element Analysis of Elastomers." http://www.mscsoftware.com/Submitted-Content/Resources/WP_Nonlinear_FEA-Elastomers.pdf

A quick FEA of an elastomer having some stiffening behavior after compressional and tensile strain was conducted to determine if these material properties alone (absent any special geometry) could confer stiffening up. A "leg" was modelled as a basic rigid cylinder rotating about an axis enclosed by a cylinder of elastomer. The analysis was quasi-static, with viscoelasticity of the rubber and friction in the contact ignored; the material model used was the 3rd-order Yeoh model, with certain coefficients that conferred stiffening up in tension and compression. Graph 1 shows the material response of the 3rd-order Yeoh model with the specific coefficients used in this study.

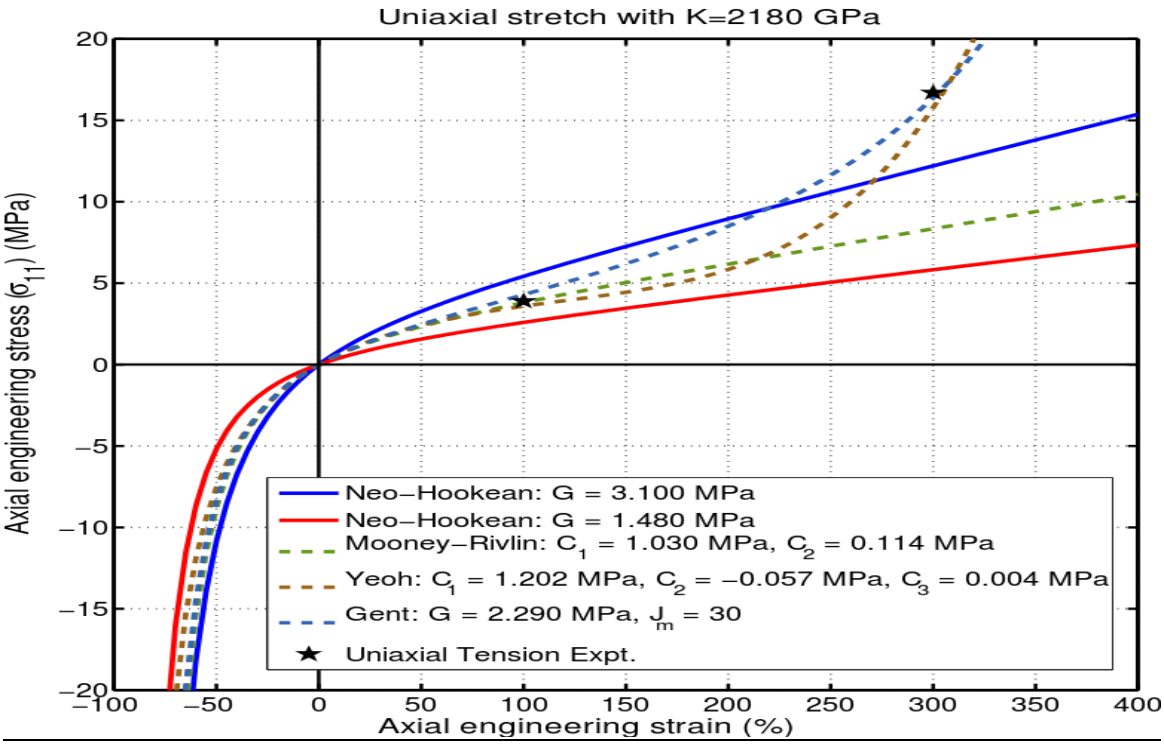

Graph 1: 3rd-order Yeoh material model's response to uniaxial tension and compression plotted with the coefficients used in this study (along with several other potential elastomeric material models with similar behavior).

Also, rubber self contact along the outer edge was to be checked for (in case complicated buckling brought the outer surface into contact with itself). Figure 12 shows the geometry, mesh

(consisting of 2nd-order, mixed u-P formulation, hexahedral elements), and "leg" rotation direction of this simple simulation.

Initially, using the incompressibility parameters D1, D2, and D3 of the Yeoh model all equal to zero (as most literature shows them), the study failed to converge after the slightest leg rotation, despite viscoelastic-mimicking stabilization, repeated bisection, loosened convergence tolerances, aggressively-updated contact stiffness (especially important given the huge disparity in stiffness between "leg" and the rubber "sock"). This may be due to difficulties with those regions of the mesh in compression (which could be nearly hydrostatic, given the constraints of the symmetry region, leg, and vertical compression effects). However, setting the incompressibility parameters all to 1.2e-11 allowed relatively easy convergence. As shown in Graph 2, there was indeed some stiffening-up behavior in the moment reaction required of the leg to rotate (although the data was surprisingly noisy, with a consistent tendency for individual points to jump towards zero moment reaction); however, it was not nearly as sudden as desired, nor indeed as sudden as the elastomer modelled stiffens in either uniaxial compression or tension. Despite the near incompressibility of the elastomer, its very low shear stiffness likely allowed stresses to spread to areas of the sock not directly contacting the leg, thereby reducing the concentration of uniaxial tensile and compressive stresses that could provoke stiffening; a contour plot of von Mises stress is shown in Figure 13.

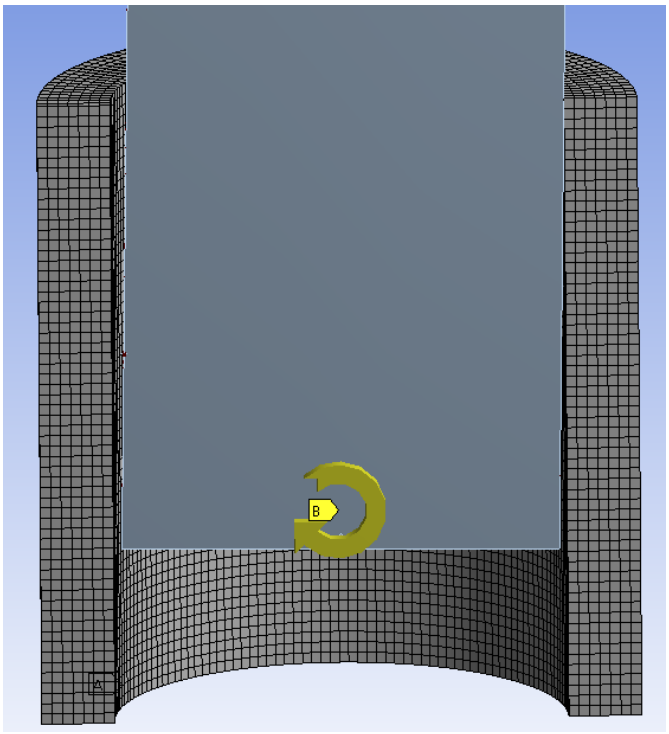

Figure 12: Thick rubber sleeve to be tested in FEA for gross stiffening in bending.

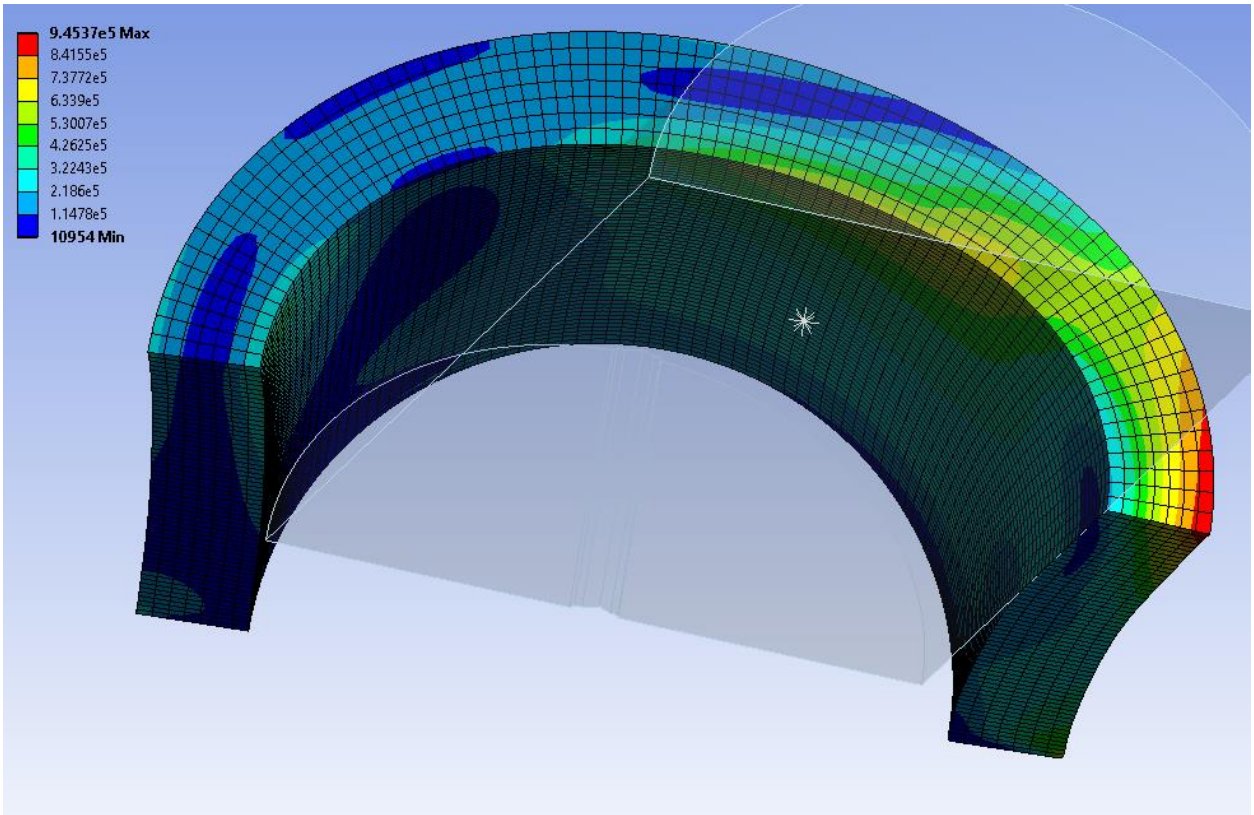

Figure 13: Plots of von Mises stress for the rubber sock, after 12.5° of leg rotation.

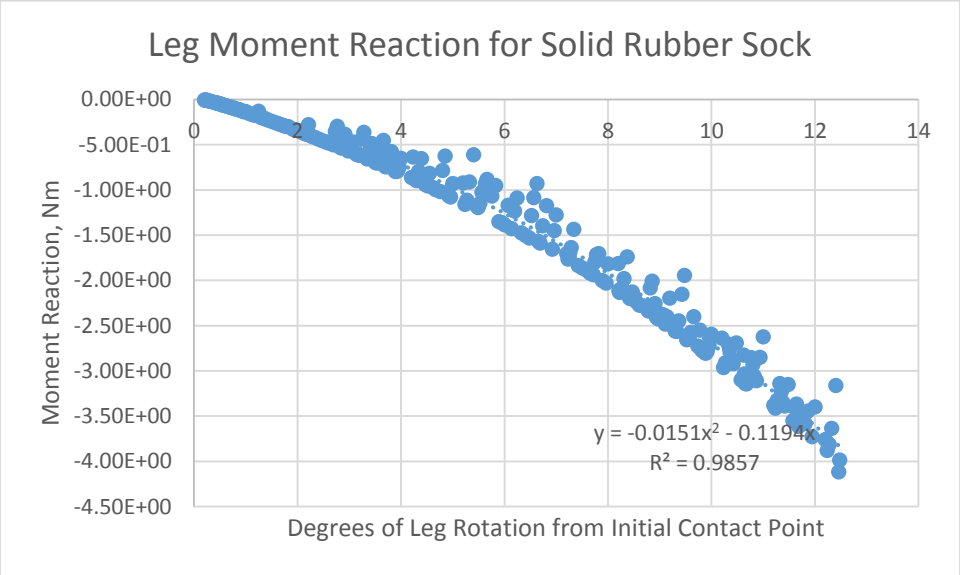

Graph 2: Moment reaction for solid rubber sock. Note that the scatter in the data appears biased consistently towards zero, and thus the boundary of the data (which can easily be fit with a separate polynomial) may be the most accurate relationship between moment and angular rotation.

Though this geometry was unsatisfactory, it may be that a more-complicated geometry containing rubber could prove an answer to this question; an interested reader may want to skip to Chapter 4 on the "annular comb" concept.

Chainmail Weaves.

Chainmail is a textile traditionally constructed of interlocking metallic links. In medieval times, it was used for relatively-flexible armor, and it is still employed as a glove material by butchers who work with very sharp knives. Due to the axial and bending stiffness of chainmail links, most chainmail weaves possess features rarely seen in textiles: significant compressive stiffness, resistance to buckling, and, most appealing of all, bending stiffness that begins after a zero-stiffness regime. At the level of individual links, this behavior results from contacts between links that can be interrupted (and, when most contacts are open, the links have enough kinematic freedom to give the overall weave low or zero stiffness), or that can stably hold links (inhibiting global buckling).

While the geometric complexity of chainmail poses obvious difficulties for both design and manufacture of weaves, the mechanism-like, low-initial-stiffness behavior combined with the potential for high post-lockup stiffness made chainmail initially appear an attractive domain of research. Unfortunately, no existing research into the mechanics of chainmail that treat the contacts between individual links is known; the only mention of it in literature treats the fabric largely as a network array of linked joints, which of course has no initial kinematic freedom. However, a modicum of research [31] exists into the computational techniques required to produce a chainmail mesh that conforms to complex geometry (for instance, the human body).

[31] *Efficient Three Dimensional Modelling of Additive Manufactured Textile Structures*
G. A. Bingham

In a related vein, a company has developed a process for designing "fabrics" based on jointed rigid bodies by modelling the fabric elements with real-time rigid-body dynamics and then printing them with SLS. However, the joints are more-traditional revolute joints rather than the arbitrary and interruptible contacts to be established between solid maille rings[32].

These weaves are manufactured by plastically bending circular, metal links open and closed, a time-consuming process that has yet to be mechanized. Open links have much lower stiffness against radial loads than links that have been welded closed, but steel links can subsequently be welded closed by laser to improve link radial and bending stiffness by a semi-automatic process[33]. Given their unfavorable stiffness-to-weight ratios relative to composites, metals are not the ideal material for this application, but perhaps a gluing process could be substituted for bending and welding metal links to allow chainmail links to be made of carbon-fiber-reinforced polymer.

To this end, existing chainmail weaves sourced from hobbyists were first inspected, with most being two-dimensional sheets (that is, while they might have multiple rings through their thicknesses, the weave can be extended in only two dimensions, not three), but a couple being solely one-dimensional chains. Nearly all weaves showed some freedom in uniaxial tension and (unlike traditional fabrics) compression, followed by stiffening as contact between links engaged the radial and bending stiffness of the rings; planar weaves also saw some limited freedom in in-plane shear. Intriguingly, one linear weave saw a clear transition in bending stiffness, going from kinematic behavior in which links experienced almost no elastic strain, to elastic behavior

[32] http://n-e-r-v-o-u-s.com/blog/?p=6644&utm_source=feedburner&utm_medium=feed&utm_campaign=Feed%3A+NervousSystem+%28Nervous+System+-+explorations+in+generative+design+and+natural+phenomena%29
[33] http://theringlord.com/cart/shopdisplayproducts.asp?id=164&

as contacts restricted link freedom and transferred loads to them. Since the links were made of metal, the overall structure would then become quite stiff. However, none of the planar weaves exhibited the desired stiffening behavior in bending. Since this might have been due to excessively-large clearances between cylindrical rings, unlinked rings of various ratios of inner to outer diameters were ordered, and some basic weaves attempted with rings of thicker sweep-cross-section relative to the diameter of the sweeping circle, but unfortunately these too failed to produce the desired bending lockup.

The failure of these basic weaves was thought to be due to the lack of constraint on rings sliding past each other due to their simple toroidal shapes. Link geometries with curves of changing curvature could allow links to slide in-plane inside a certain window, then forbid further sliding (or direct it in another direction); in turn, since gross bending of the structure should require rotation of individual links, gross bending could translate to local link sliding, which would need to be constrained by appropriate link geometry. Thus, link geometries were generated in CAD by sweeping circular profiles not along simple circular paths, but along regular curves generated with parametric equations containing mainly sinusoidal terms; note that the curves also had to interlock to prevent the fabric from falling apart (this made geometry generation somewhat more difficult). As for the rule for patterning links, it was initially deemed preferable to use a simple geometric tessellation (such as close-packed rectangular or hexagonal patterns) rather than an arbitrary one that might demand a multiplicity of link designs for fabric stability. Granted, in the final product, each link might need a different initial geometry from its neighbors to produce the proper conformation to the leg and lockup properties for the ankle joint; however, this might still be accomplished with a relatively simple tessellation, and, at any rate, it was necessary to first prove that the chainmail concept could stiffen in gross bending.

The first chainmail pattern generated is rendered in Figure 14; a single link geometry was patterned in a square packing. As shown in Figure 15, the structure had some initial freedom in both biaxial compression and biaxial tension before it locked up. Moreover, as illustrated in Figure 16, the entire structure could bend virtually freely until link geometry produced lockup at a constant curvature. As might be expected from the fourfold rotational symmetry of the weave, the radii of curvature for lockup at 0° and 90° angles seemed the same.

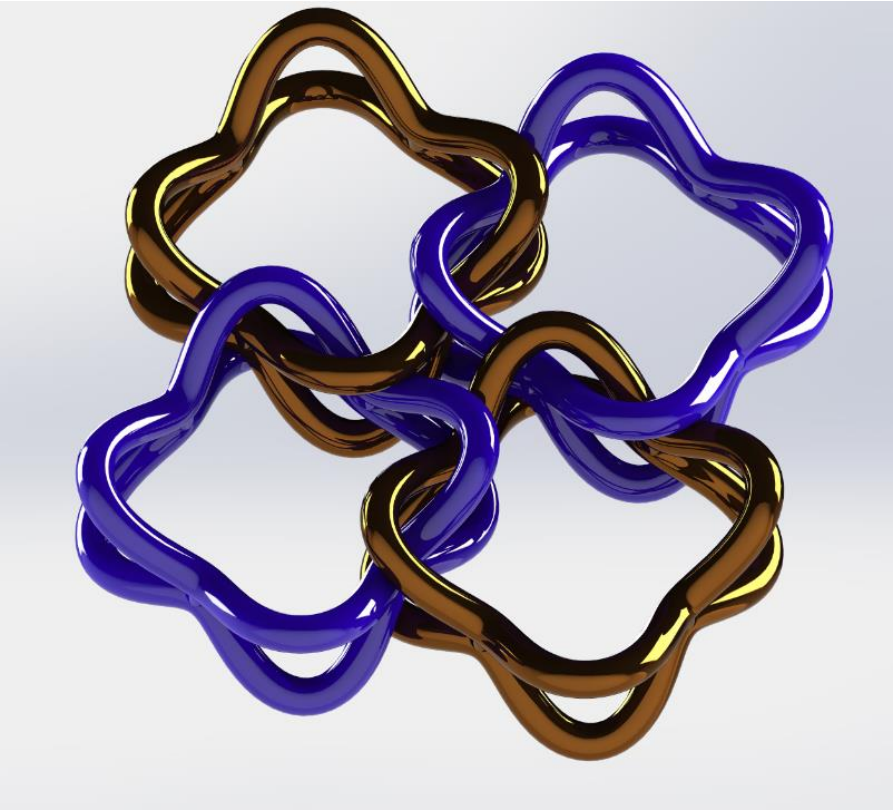

Figure 14: Rendering of square chainmail pattern developed by this researcher.

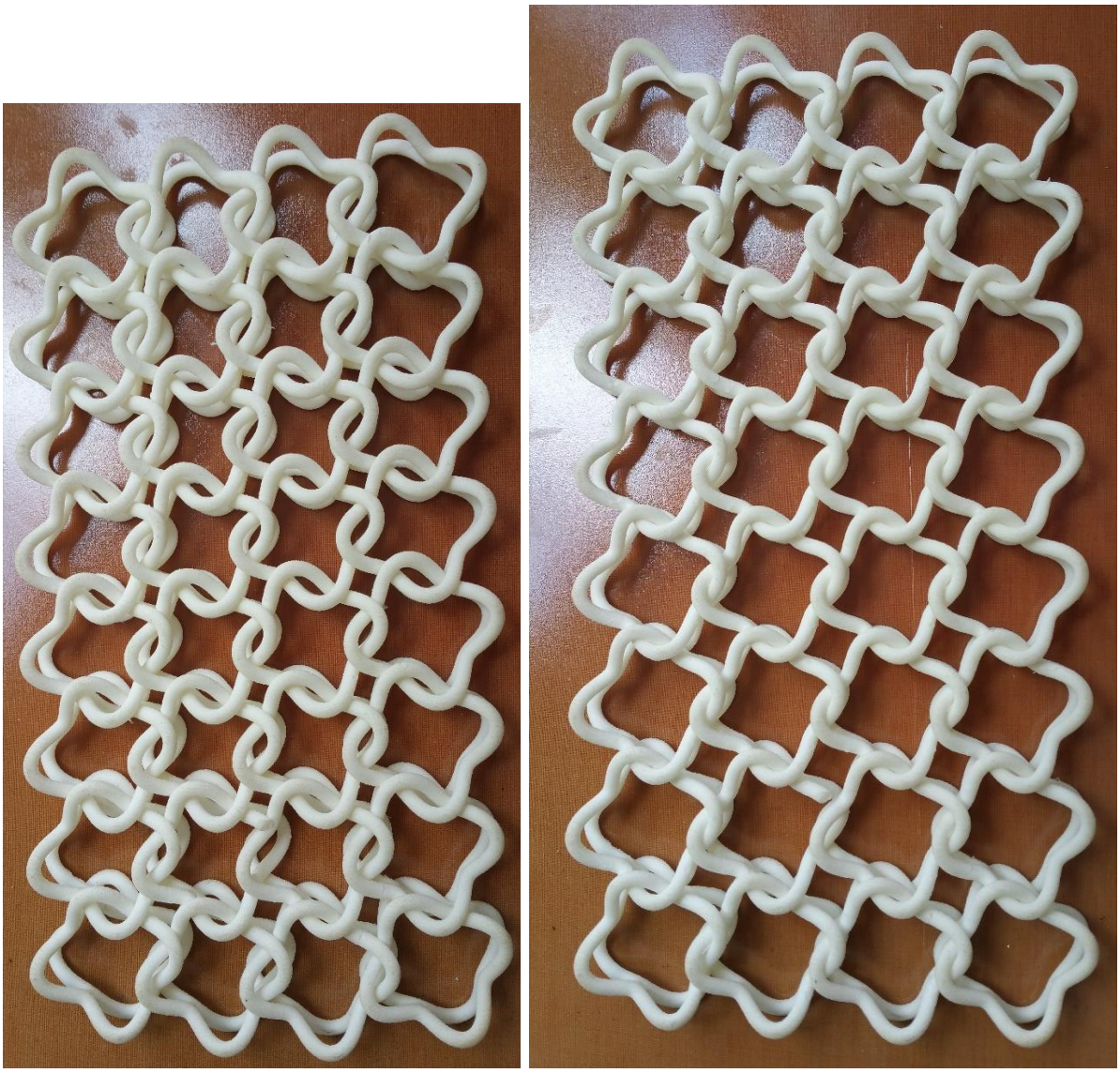

Figure 15: One chainmail weave produced by SLS in planar, biaxial compression (left) and tension (right) until stiffness is encountered (whereupon the structure still has some compliance).

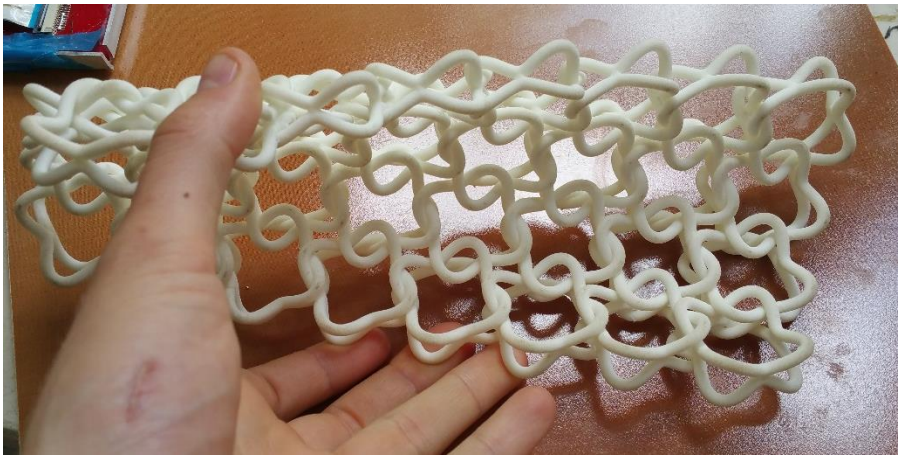

Figure 16: Bending the fabric until resistance ("lock-up") is encountered.

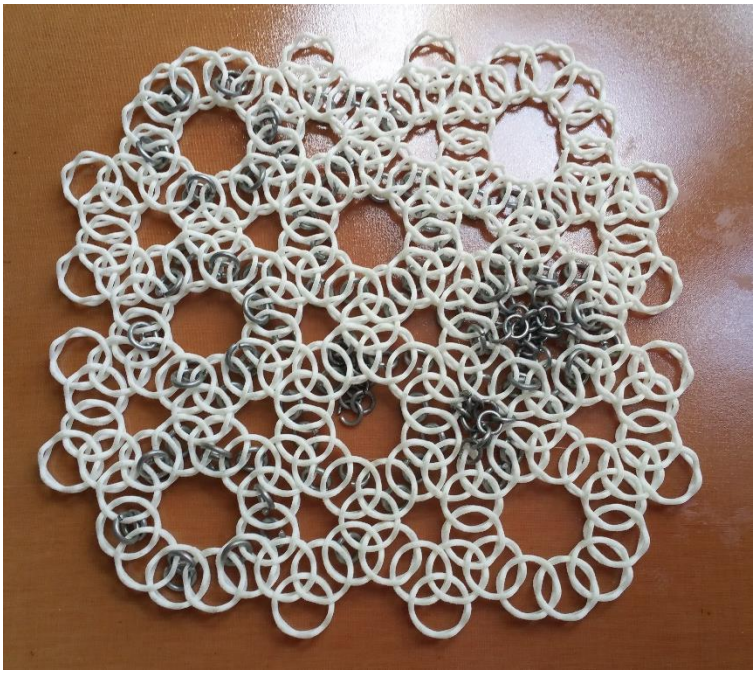

Figure 17: Another chainmail weave (with metal rings manually added in an attempt to decrease bending freedom before lockup). The weave has been compressed biaxially in-plane to the maximum extent of the rings' kinematic freedoms.

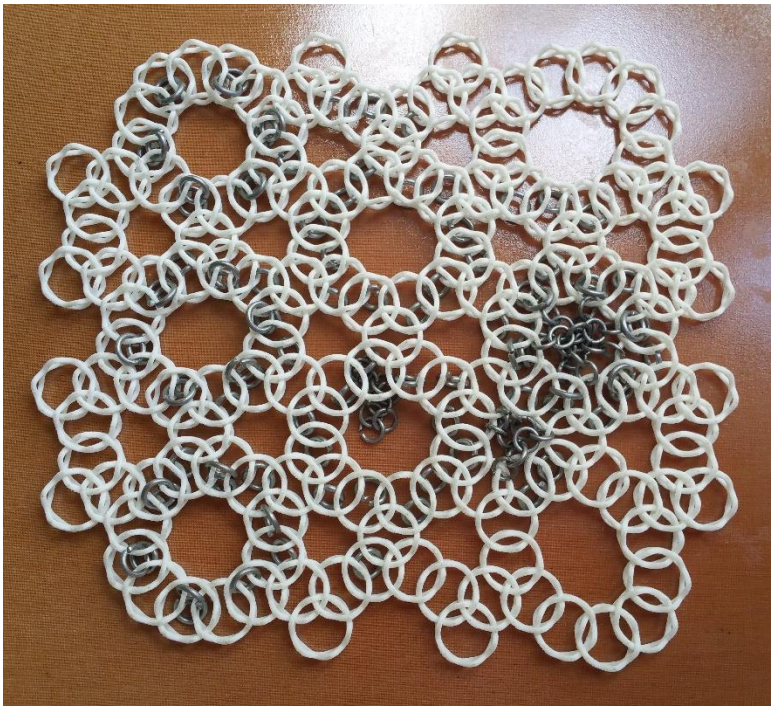

Figure 18: The same chainmail weave as above, but expanded biaxially in-plane to the maximum kinematic extent.

Figure 19: Same chainmail weave as above, bent to the maximum kinematic extent about an axis parallel to the horizontal.

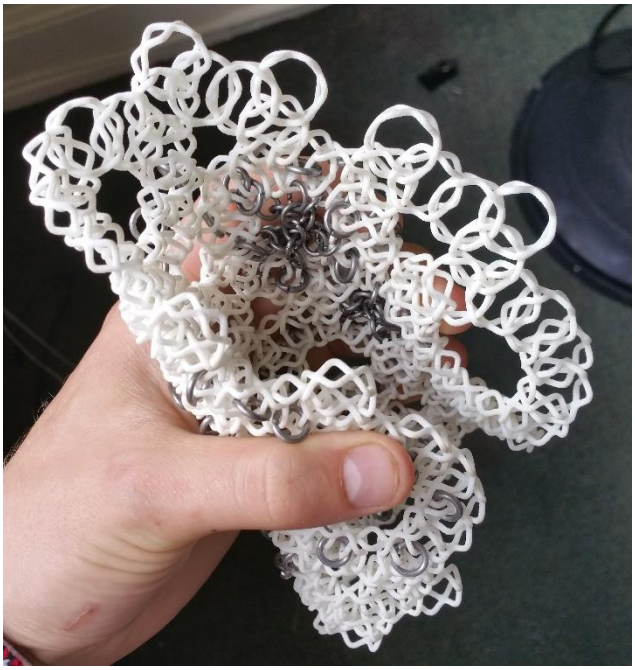

Figure 20: Same weave as above, bent to maximum kinematic extent about a diagonal axis (this direction gave more freedom before kinematic lockup).

While these chainmail weaves did indeed stiffen up from nearly-zero bending stiffness, they were far from the solution to the problem posed by the sponsor, mainly because the individual links were themselves fairly compliant and thus could not precipitate a high final stiffness. Beyond this, both weaves experienced far more bending before lockup than the ankle-protection problem could allow. Consequently, the individual links needed to be given much more radial stiffness and see modifications to the main curves that control link sliding to ensure faster lockup. To this end, the square array was given truss-like members for added radial stiffness; of note, those on the top had to be curved into a swastika-like shape to avoid interfering with the freedom of the sliding faces of the rings. Figure 21 shows a rendering of this second iteration of the chainmail design, with the sliding portion of the rings painted red and the reinforcing members painted blue (these would be 3D printed as one single part, however, with no material differences indicated by render color).

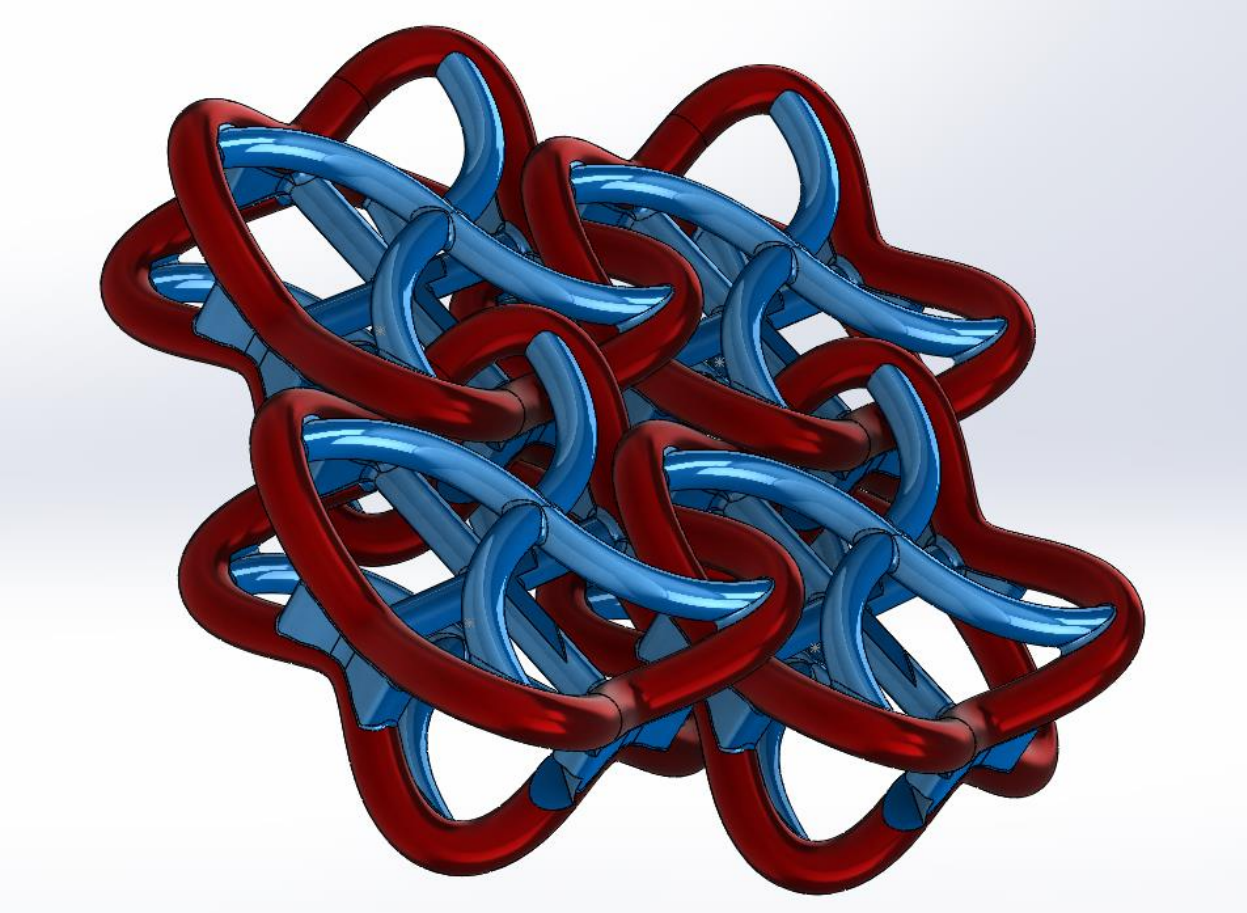

Figure 21: Proposed alteration to a chainmail weave, with added curved beams in blue for increased link stiffness without altering kinematic compatibility much.

Some highly-outlandish designs involving cams on the beam-like features defining the link that could not only restrict sliding to within a definite range but even cause sympathetic deformations (that were anticipated to be incompatible with surrounding links, thereby causing lockup that might even be intensified in stiffness by auxetic-like local densification) were also generated before it was realized that these would be difficult to fabricate even by SLS and were time-consuming to generate. These geometries were modifications of a structural mechanism based on the 4R Bennett spatial mechanism that could expand from a sheet into a cylinder that

was developed in [34], but with some joints removed and an interlocking structure generated instead that should give the structure initial freedom in multiple modes, including tension and compression; renderings of this geometry are shown in Figure 22. Figure 23 shows a modified version of this geometry with special cams that should further restrict motion.

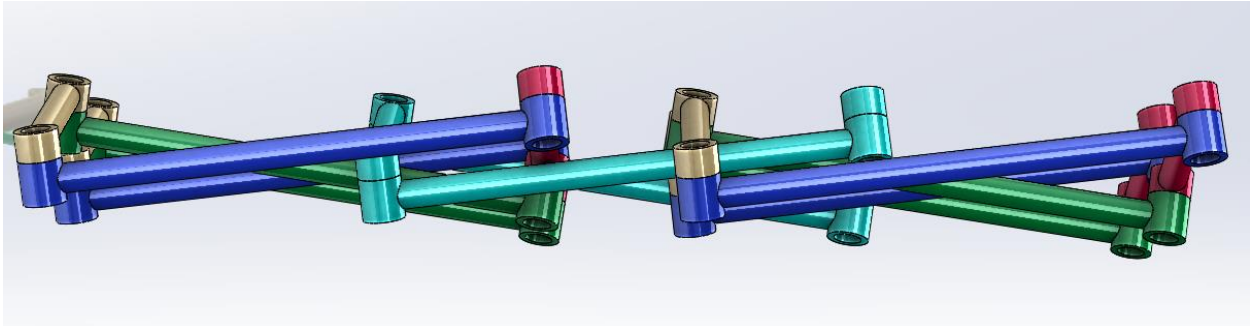

[34] "Design of Structural Mechanisms" by Yan Chen

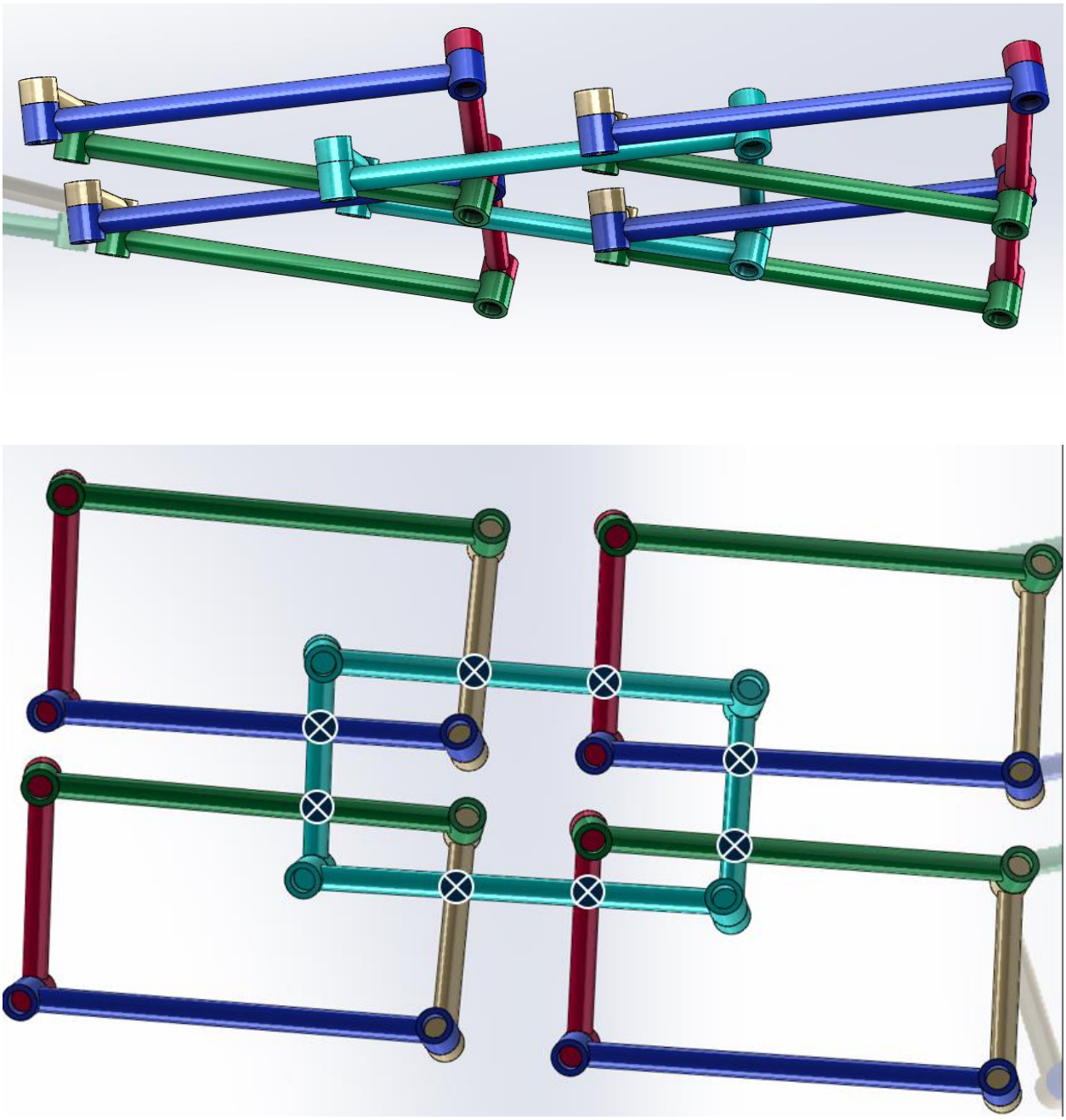

Figure 22: "Structural-mechanism chainmail" based on removing joints from the

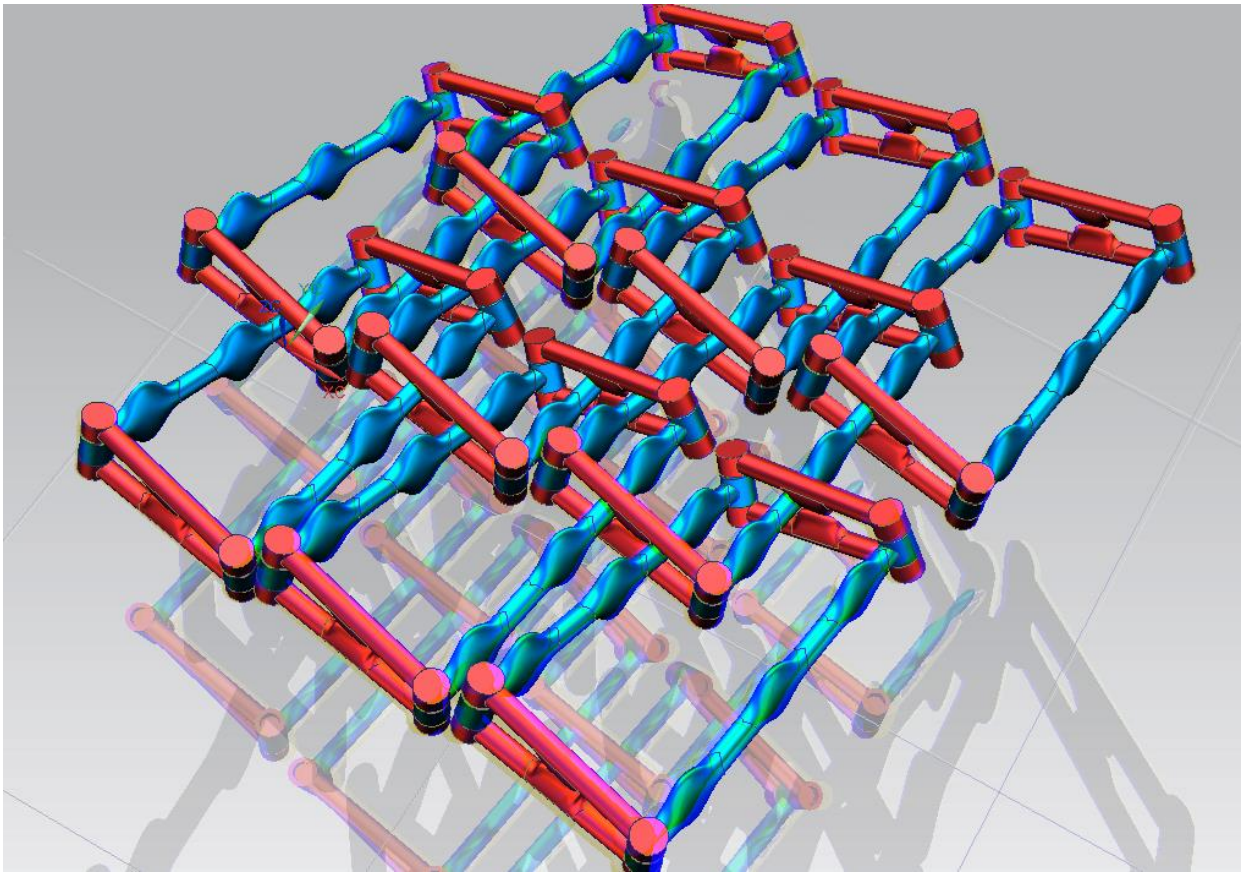

Figure 23: Yellow-blue anaglyph stereoscopic rendering of "structural-mechanism chainmail" with added restrictive features.

Ultimately, the concept of the linear comb (described in Chapter 3) seemed much more promising than chainmail for its relative ease of manufacture and design, and thus the chainmail concept was abandoned without being fully investigated. That said, the expense of designing and manufacturing even simple chainmail weaves, let alone those that lock up under the complicated cylindrical boundary conditions of the leg-protection problem, will probably prevent this idea from being applied to the problem.

Layup-Varying Approaches.

It is well known that the anisotropy of high-strength fibers can be exploited to produce coupled deformations with an input deformation; the primary application of this property is to

aircraft wings that are given a sympathetic counter-twist in response to vibratory excitement in a bending mode in order to alter their shape in an orthogonal direction after bending (which in turn gives different aerodynamic properties)[35]. Coupled deformations can also be achieved through complex networks of beams of isotropic materials having cross-sections biased towards higher bending stiffness in one direction than in another (e.g. with an I-cross section)[36] However, this sympathetic force has not been stated to produce nonlinearity in the force-deflection relationship of the main bending mode; thus, it was interesting to see if nonlinearity could indeed be produced thus.

To this end, a cylindrical tube was modelled in FEA as a composite layup having fiber orientations that varied according to a power law (producing significant differences over the radius of the tube, without the randomness of orientation that would actually approximate isotropy). The overall geometry, with fiber orientation superimposed, is shown in Figure 24. Of note, actual aircraft wings tailored thus also tend to have significant variations in fiber angles over their geometries, just as the solution to the ankle protection problem might require significant variation in some property over the geometric domain (however, this hardly proves that the aeroelastic concept can be adapted to this application). Some examples of complicated layup orientation variations in the geometric domain can be found in reference 37.

[35] "Aeroelastic Tailoring-Theory, Practice, and Promise", M.H. Shirk, T.J. Hertz, and T.A. Weisshaar, 1986.
[36] "Aeroelastic Tailoring of the NASA Common Research Model via Novel Material and Structural Configurations"
[37] "Aeroelastic Tailoring-Theory, Practice, and Promise", M.H. Shirk, T.J. Hertz, and T.A. Weisshaar, 1986.

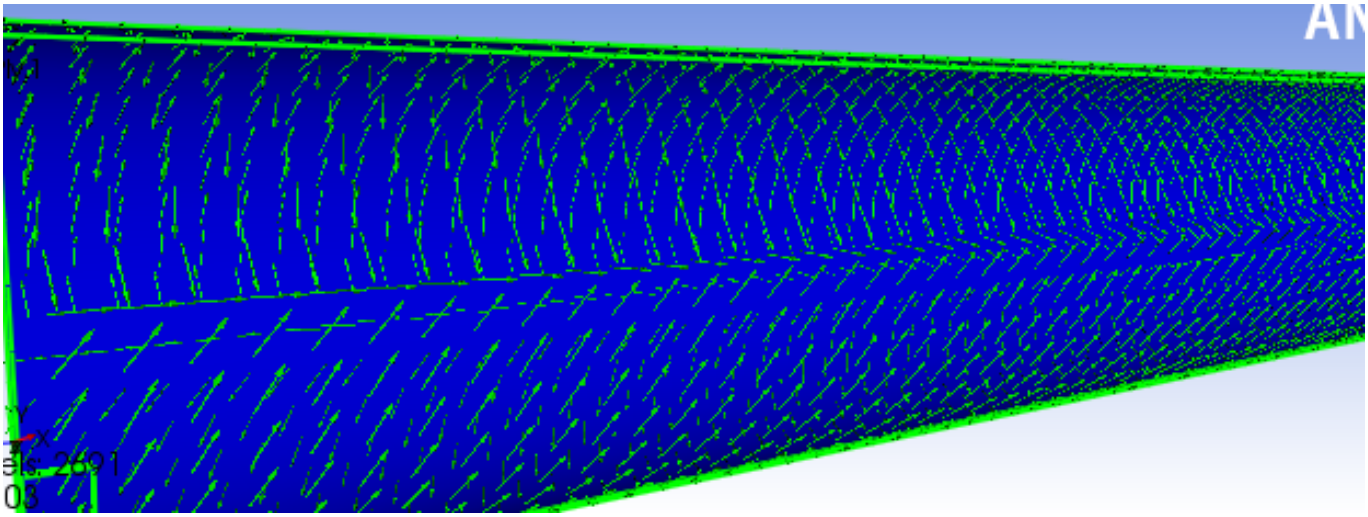

Figure 24: FEA model of a cylindrical tube (the body of which is shaded deep blue) with meaningful angular fiber angle variation, shown with short green arrows.

When the above-shown composite tube was cantilevered at one end and subjected to a bending force in one plane in the other (with no constraint on out of plane motion, nor any force out of plane) and analyzed in a large-deflection static analysis, the beam accordingly experienced coupled deformation, resulting in a sympathetic out-of-plane bending moment as shown in Figure 25. Unfortunately, the relationship between applied force and deflection in the *y* direction (i.e. that of the applied force, not the coupled direction) was highly linear. This suggests that it is difficult if not impossible to obtain nonlinear stiffness behavior from anisotropic but linearly elastic materials, even with concerted orientations. Thus, research into this subject was dropped.

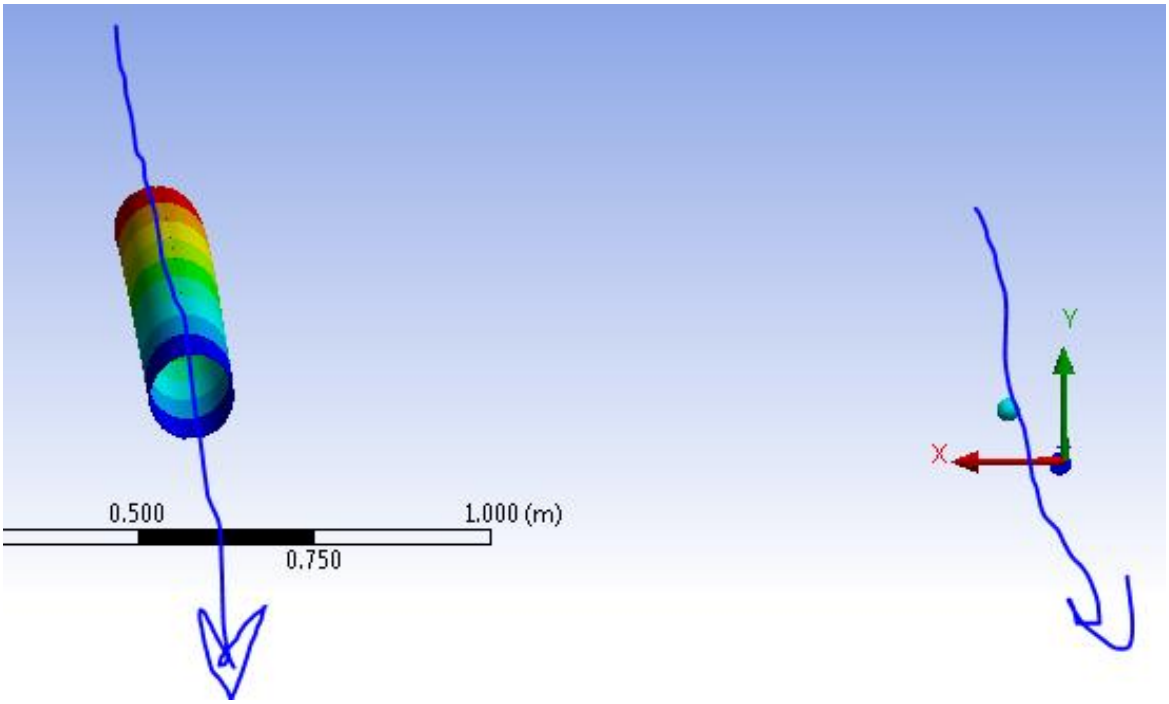

Figure 25: Sympathetic bending behavior of the composite tube with a complex layup. Note that the only bending force applied was vertically oriented in the y *direction; the* x *displacement is solely the result of deflection coupling.*

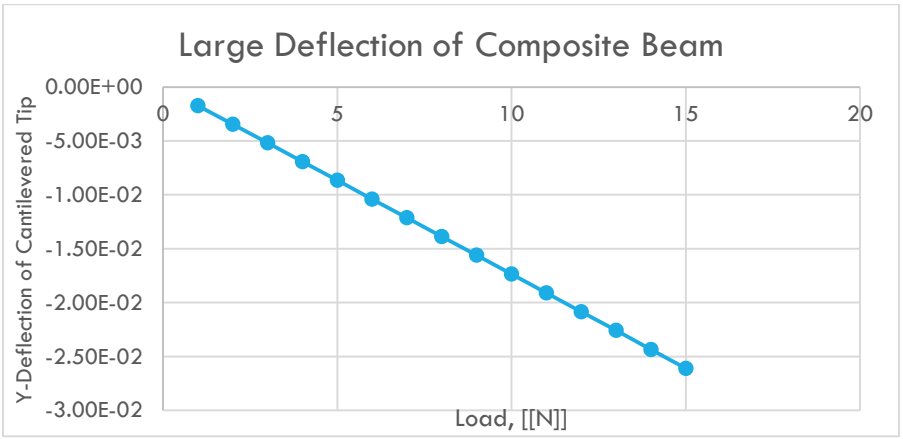

Graph 3: Force-deflection (resolved in y *axis, as shown in the previous figure) response for the composite tube. Despite the deformation coupling, the overall response was linear in magnitude.*

Auburn University Composite Open Structures.

Researchers at Auburn University have pioneered an inexpensive method of manufacturing composite beams with superior stiffness-to-mass ratios compared with solid-

cross-section (or even honeycomb-cored) beams, in which prepreg and carbon-fiber yarns are braided around a mandrel and then cured, solidifying not only the matrix around the carbon fibers, but also bonding yarns to each other. A modification to the braiding regime instead produces a compliant, springy structure that has limited stiffness in bending and (to a lesser extent, given the proper weave) axial compression/tension: this configuration is known as a biaxial braid (in which all axial members are removed from the "true triaxial" braid, also developed at Auburn). Figure 26 shows an example biaxial braid that has moderate bending compliance, and Figure 27 shows a much-stiffer "true-triaxial" braid for comparison (note its numerous axial fibers that strongly inhibit bending). Figure 28 and Figure 29 show the high axial and bending compliance of one particularly compliant 8x8 weave (note that biaxial weaves produced on our machinery must have carriers in a multiple of 12 for even coverage).

Figure 26: Generic biaxial braid of cured carbon-fiber prepreg. This particular braid was formed over a mandrel with rectangular cross-section, although most studied had circular cross-sections.

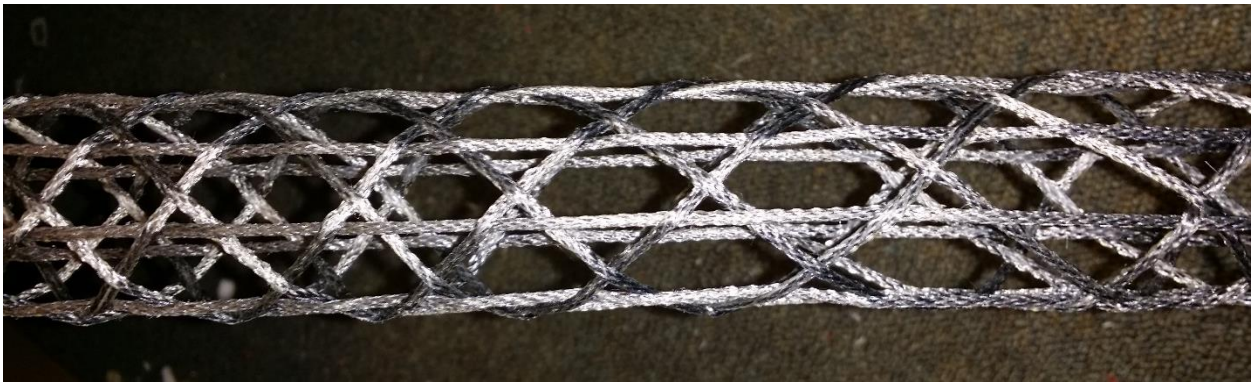

Figure 27: A true-triaxial weave that is quite stiff in bending thanks to its axial yarns.

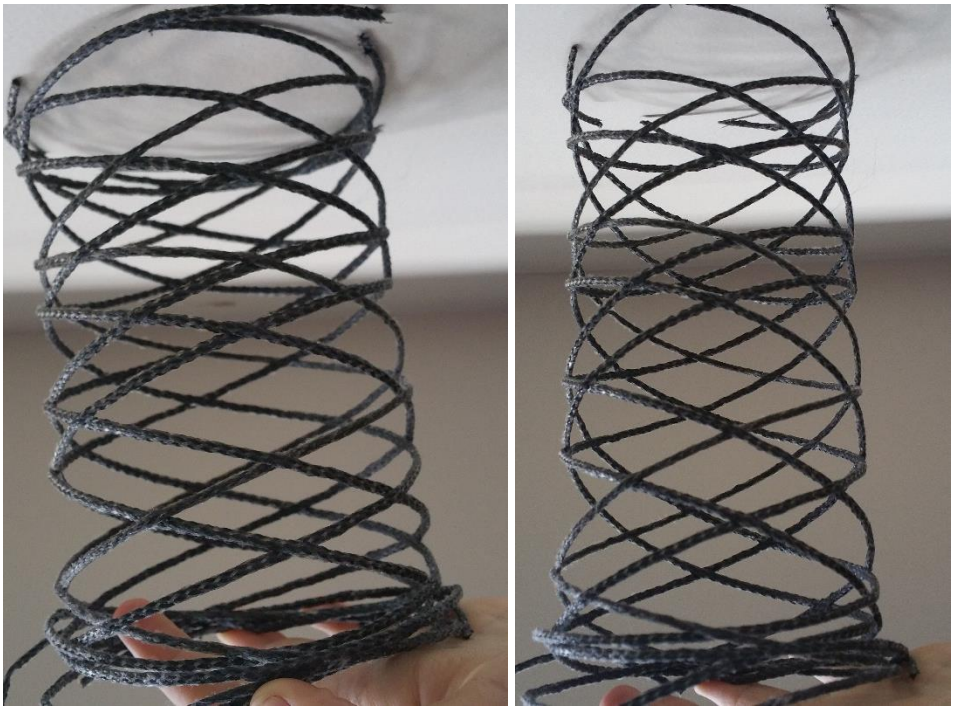

Figure 28: These braids have significant axial compliance, much like a spring. Left: compressed axially, right: original, undeformed. Below, find this braid in bending.

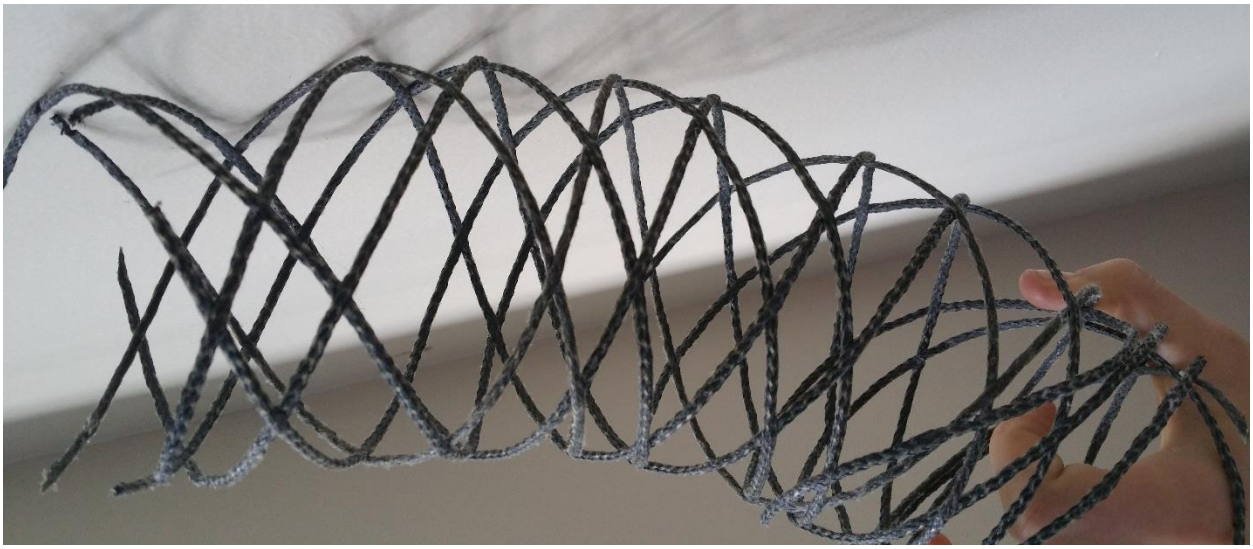

Figure 29: Open-structure braids also have significant bending compliance.

Given Auburn's expertise concerning open structures, it was deemed worthwhile to investigate whether any braiding configuration could produce a significant and rapid stiffening effect. Some structures indeed saw modest stiffening in bending (albeit only when bent to much greater curvature than would be needed for protecting human joints), but no structure appeared to rapidly and strongly lock up. Plus, repeatability (between tests and between sections of the same braid) was poor. The precise cause of the moderate stiffening effect seen in some braids is unknown: potential causes include effects from reorientation of the highly-anisotropic carbon fiber yarns such that the bending load path is better aligned with the stiff direction of the fiber, and also perhaps warp and weft yarns having limited freedom to rotate relative to each other. This latter phenomenon would specifically cause the braids to stiffen in gross compression, and might be expected to cause stiffening in gross bending since some regions of the braid will be in effective axial compression. Graph 4 and Graph 5 show axial compression tests of two braids, the former of which did not appear to stiffen in compression, the latter of which did. Indeed, in a subsequent four-point bending test, this braid also had some stiffening in bending (at least at first, before softening precipitously), as shown in Graph 6. Graph 7 and Graph 8 show force-deflection curves for three- and four-point bending of two other open structure braids and corresponding regressions that show a mild stiffening effect, at least for part of the deformation range. Note that plenty of braids tested showed softening effects from the onset, and their deflection curves were not included as they were not interesting.

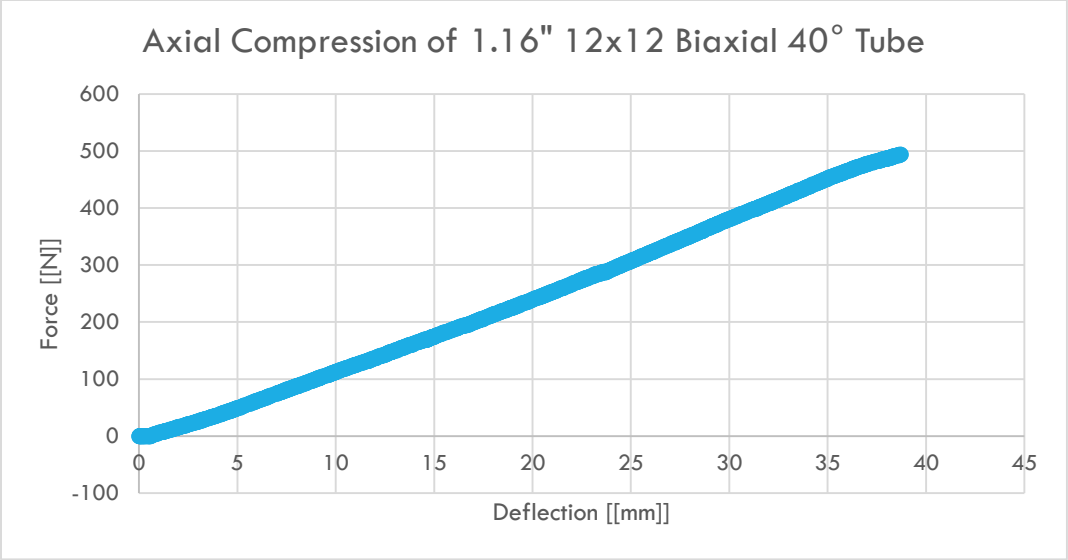

Graph 4: Force-displacement curve for axial compression of a short section of a 40° biaxial-weave tube. Note that the relation is highly linear.

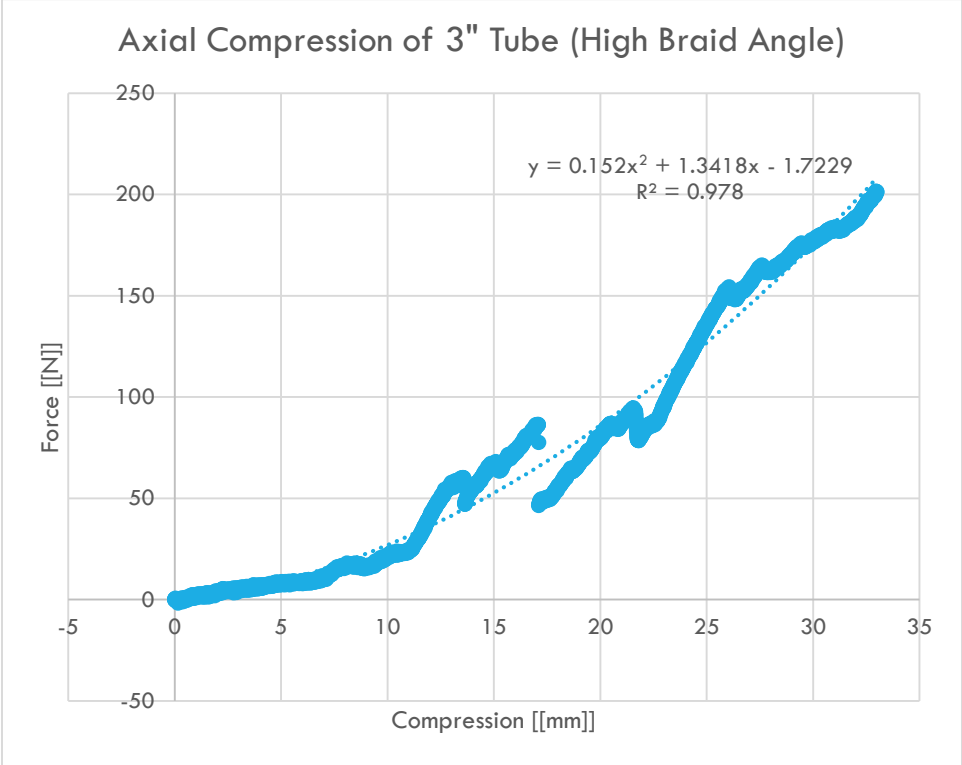

Graph 5: Axial compression of high-braid-angle tube. It stiffened by 8.75x over the entire range, although simple bending is not likely to entail so much compression, and anyways the data were quite noisy.

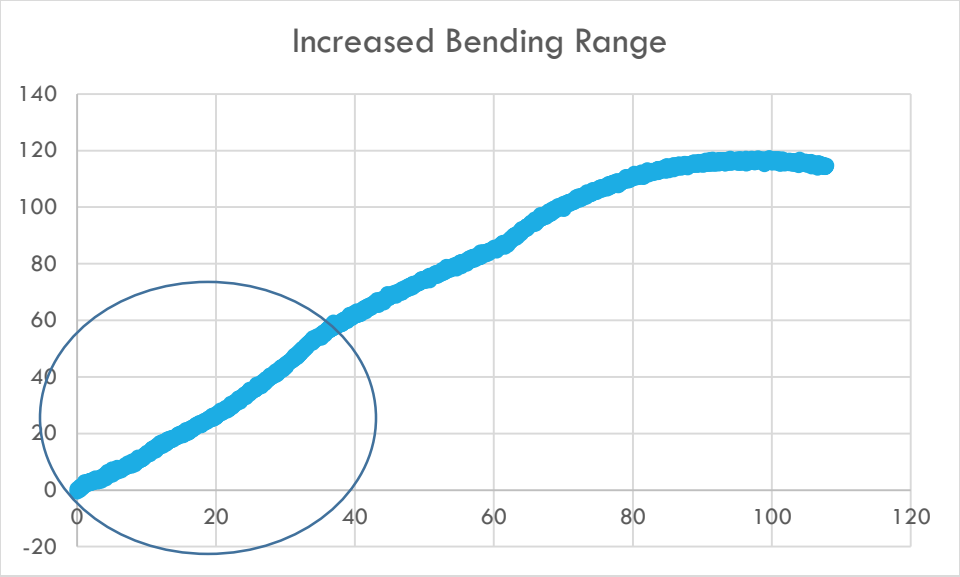

Graph 6: Four-point-bending test results from the 3" high-braid-angle tube (whose response to axial compression is shown in the previous figure). The bending stiffness of the tube increased by 109% over the range circled, although it promptly reversed this behavior afterwards and began to soften.

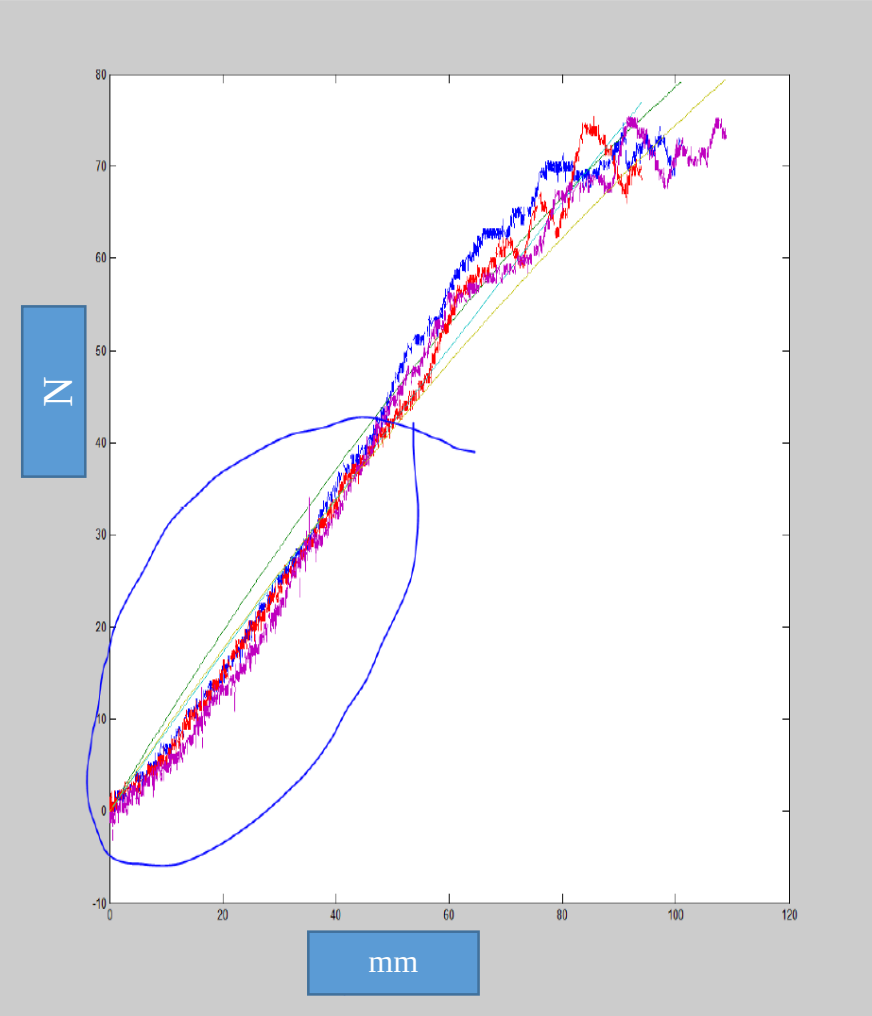

Graph 7: Four-point-bending test of 1.16" inner diameter 12x12 40° tube. In the circled region, there was a stiffness increase ranging from 16% to 90% across the four tests, although overall there was a decline in stiffness over the full test range.

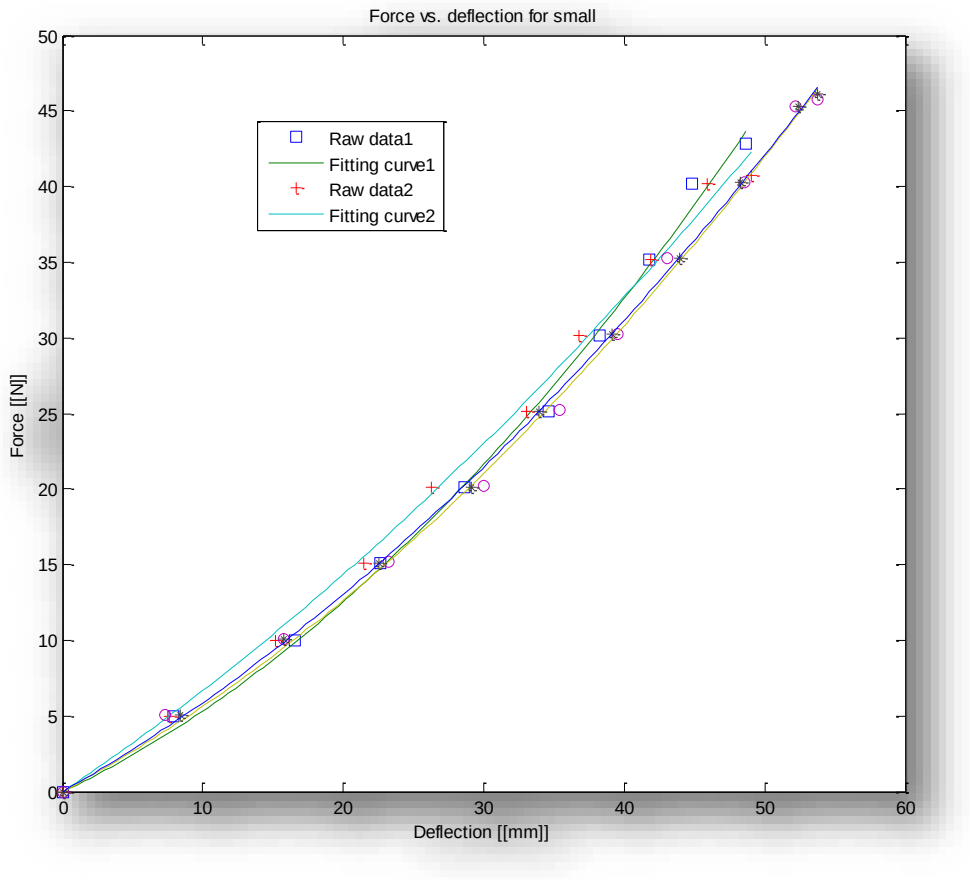

Graph 8: Force-deflection curve for four-point-bending test of open structure biaxial tube with a high braid angle and 3" diameter. The test was repeated four times, with the first seeing a stiffness increase of 206%, the second a 79% increase, the third a 149% increase, and the fourth a 129% increase (after smoothing with fitting parabolas).

Two sandwiches of braids were also investigated in bending. Both had inner cores with high braid angles to give high radial stiffness, preventing the outer braid (which had a low braid angle) from experiencing shell buckling (which was otherwise a common occurrence, even in bending, for biaxial braids with low braid angles). The inner braid was first braided on a mandrel, then the outer braid produced on top of the inner braid, and then the structure was cured and removed from the mandrel. Graph 9 shows the bending response of the two-part sandwich, and Graph 10 the response of the three-component sandwich.

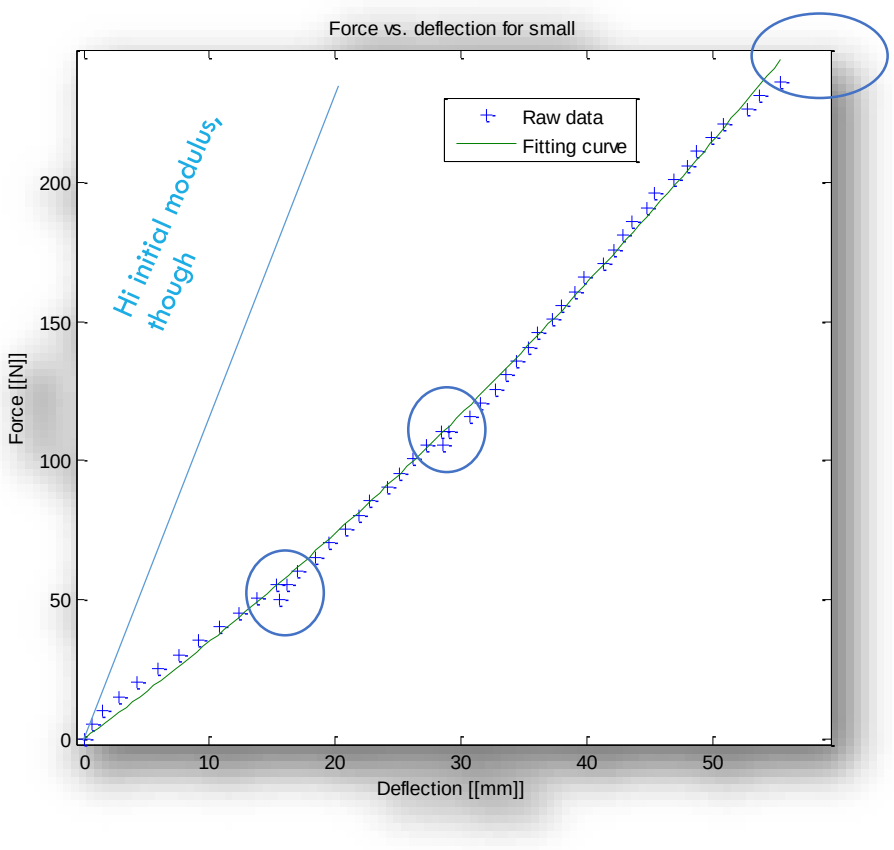

Graph 9: Four-point bending test of a sandwich consisting of a core with a high braid angle and a jacket with a low braid angle. Areas of apparent yielding (or perhaps sudden slippage in the test fixture) are circled in green. The fitting parabola's stiffness saw an increase of 68.9% over the entire range.

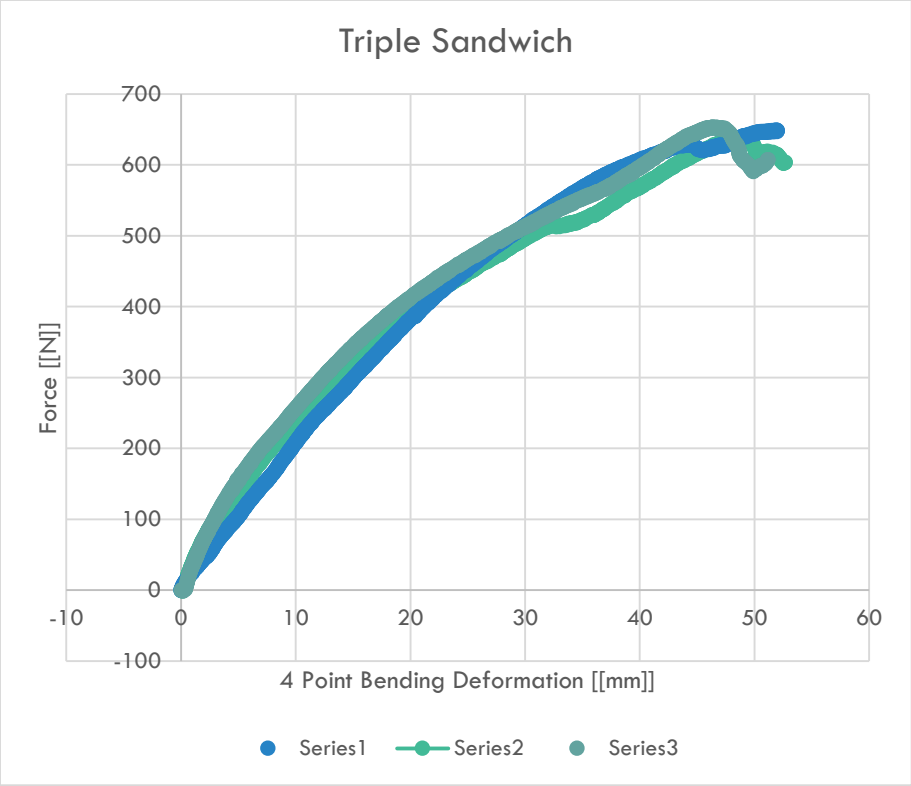

Graph 10: Four-point-bending test of sandwich consisting of low-braid-angle inner and outer braids and high-braid-angle central braid. The test was performed three times.

Many of the braids also showed unusual mechanical behavior: bending about one axis often produced a "sympathetic", coupled torsion or bending about a different axis. The most common coupled behavior was "sympathetic" distortion into a shape resembling the arctangent function, as shown in Figure 30 (although this greatly exaggerates the magnitude of the coupled deformation). This same phenomenon is exploited in "aeroelastic tailoring" as described in the previous section in this chapter, in which deformation-coupling is employed to control flutter in aircraft wings. However, there is no obvious way to exploit this phenomenon to produce any change in bending stiffness, let alone a suitably-sharp one.

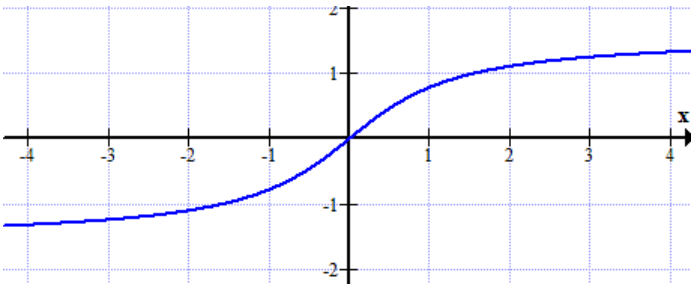

Figure 30: General shape of sympathetic bending in biaxial tubes.

Given the high initial stiffness of these braids and the moderate magnitude of the stiffening effect that even the best showed, this approach was abandoned. However, this researcher observed that, unlike "true triaxial" braids, traditional triaxial braids also showed significant bending compliance when joints between yarns were unglued: this behavior appeared principally to be the result of sliding between yarns, which gave a mechanism-like quality to the braid (although some axial yarns also appeared to experience elastic bending). Previous braids were primarily jacketed with tufted nylon to improve bonding between yarns (which correspondingly increased sliding friction and stiction coefficients between the yarns), so, to promote this sliding, the jacket was replaced with Teflon® fibers, and experimentation with weaves that would allow sliding to an extent and then lock up was undertaken.

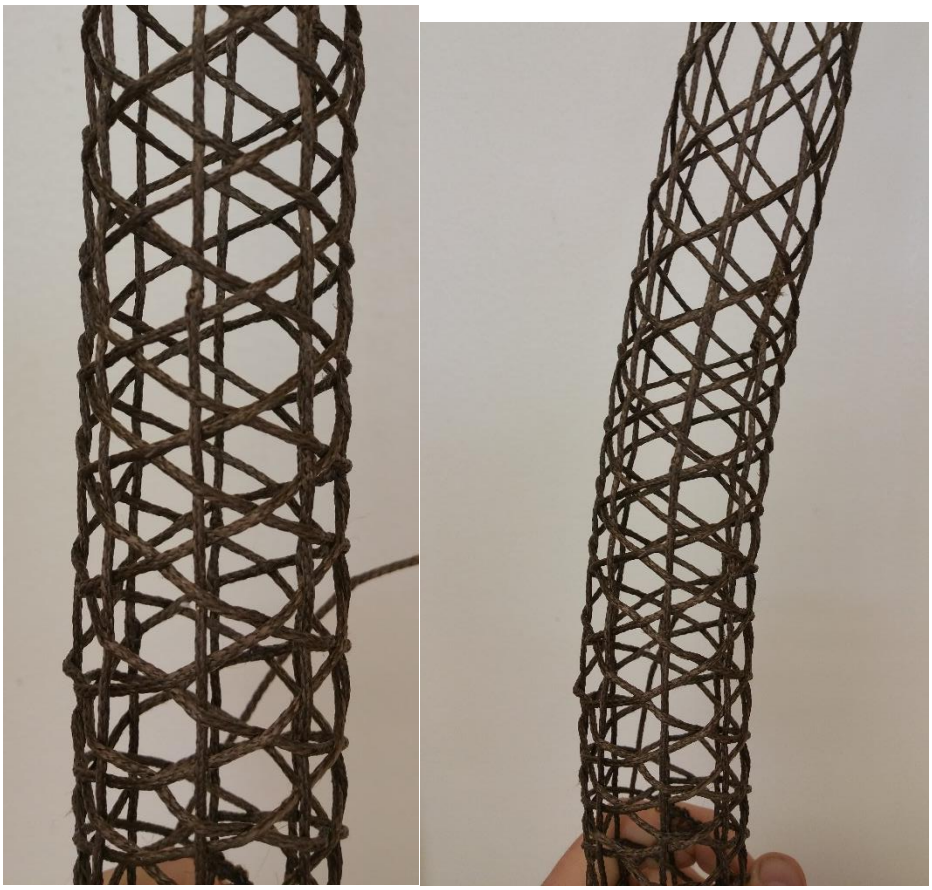

Figure 31: Teflon-coated true-triaxial braid. Left: braid in neutral position, right: mechanism-like behavior--to get to this position from neutral, it takes almost no force. Subsequently, the braid has more bending stiffness.

The compliant triaxial structure also experienced sympathetic, coupled deformation: bending along a single neutral axis produced a complicated curve that is sketched in Figure 32.

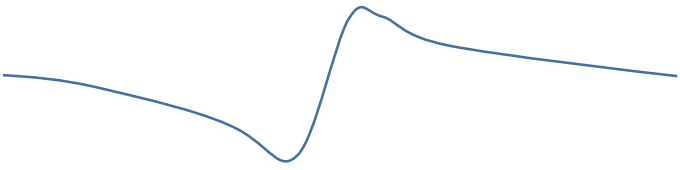

Figure 32:Rough shape of coupled deformation of triaxial tube in bending.

"Microtruss" Structure.

Some closely-guarded research appears to be occurring into the use of very small compliant mechanisms oriented into arrays that give special macromechanical properties, called "mechanical metamaterials". For instance, a 3D network of reentrant hexagons has been designed to produce a material having auxetic properties in all 3 dimensions[38], much as 2D networks of reentrant hexagons produce a structure with auxeticity in the plane. Similarly, a so-called "pentamode" metamaterial having a very low initial shear modulus relative to its bulk modulus has been developed from conical beams with compliant joints[39]. So far, there is no known research into producing the specific property of stiffening with respect to deformation (especially bending deformation), but it was thought that a material geometry that stiffens up when the overall material is in bending could be developed by first creating a truss-like network (as in the metamaterials above) and then introducing interrupted contacts that only engage after sufficient leg movement, which would probably entail stiffening the individual members in tension or compression rather than bending. This would in significantly stiffen the overall structure by limiting force paths. If interrupted contacts in truss elements proved successful in producing stiffening up in bending, the structure could be optimized with one of several well-understood optimization methods. Figure 33 shows a rendering of the overall concept, although the beams have not been given the precise geometry that would allow them to stiffen in compression and/or tension.

[38] "Tailored 3D Mechanical Metamaterials Made by Dip-in Direct-Laser-Writing Optical Lithography"
[39] http://arxiv.org/ftp/arxiv/papers/1203/1203.1481.pdf

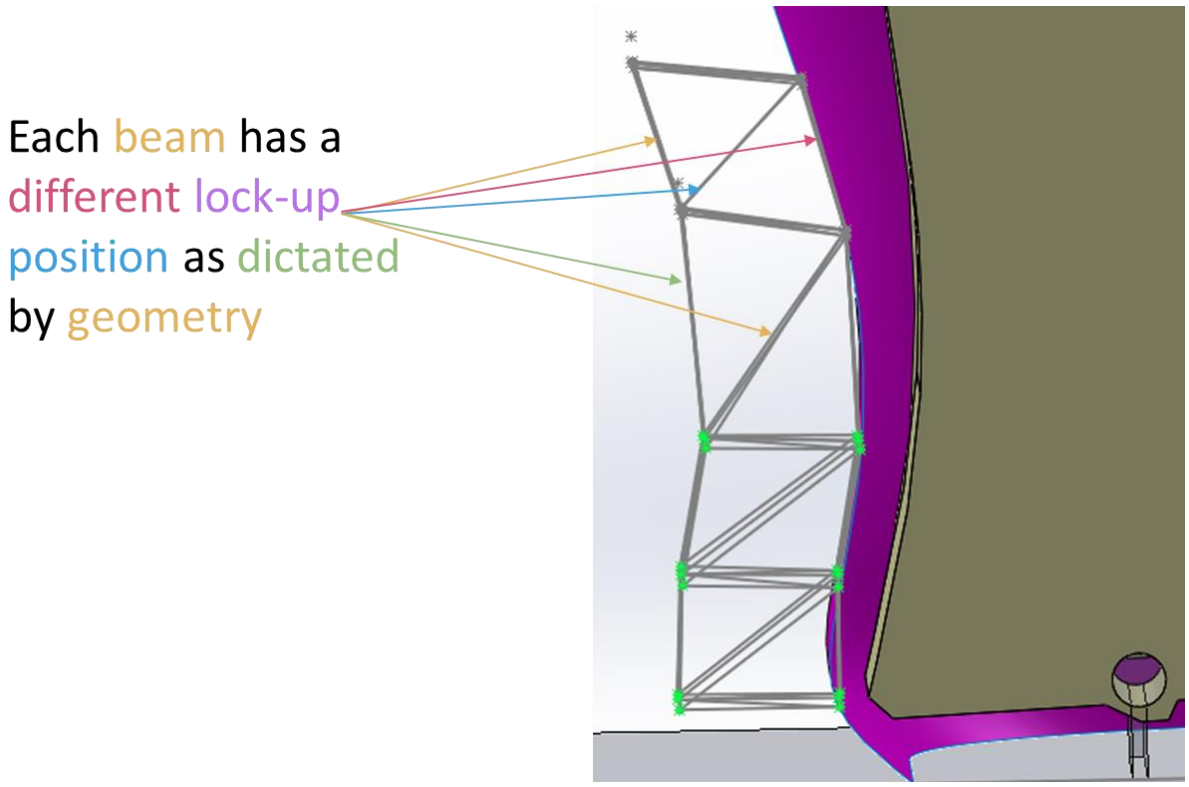

Figure 33: Rendering of the 'microtruss' concept, with the envelope of conformity shown in pink and lines of force shown in grey. The precise geometry that would produce lockup

Geometrically speaking, the simplest modification to a basic truss-based metamaterial (for instance, modifying the metamaterial in Figure 34, which is the trivial case of the idea and does not have any special properties) would be to replace some or all of the links with two links joined by cylindrical or translational joints whose axis would lie on the line between their two endpoints, as sketched in Figure 35. Stops (governed by the lengths of the translating members) would cause the joint to stiffen instantly in compression or tension after a set amount of displacement, which might have to vary with respect to some geometrical parameters over the volume of the metamaterial. If enough joints locked up in this way, it would eliminate the kinematic freedom of the structure; however, given its low volumetric density and the fact that it would probably have to be 3D printed out of plastic, the locked-up structure might still have

insufficient stiffness. Admittedly, if the beams enter a large-deformation bending regime, the constraint afforded by simple translational joints could become incompatible (even before lockup was desired), so the joint geometry might need to be modified with tangentially-contacting followers instead. As for the ideal joints at link intersections, it may be that they should be connected with spherical joints in 3D or revolute joints in 2D (as in a true truss), or it may be that they should be cantilevered together (as in a framework pseudo-truss).

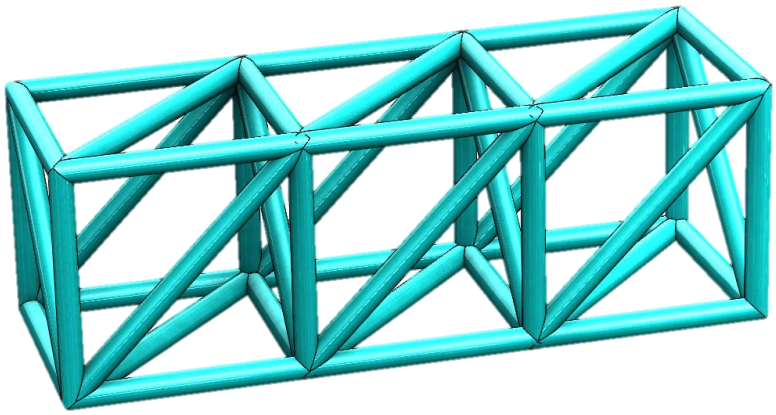

Figure 34: A basic metamaterial with no special properties (trivial case). It is to be modified into a metamaterial that stiffens after some bending.

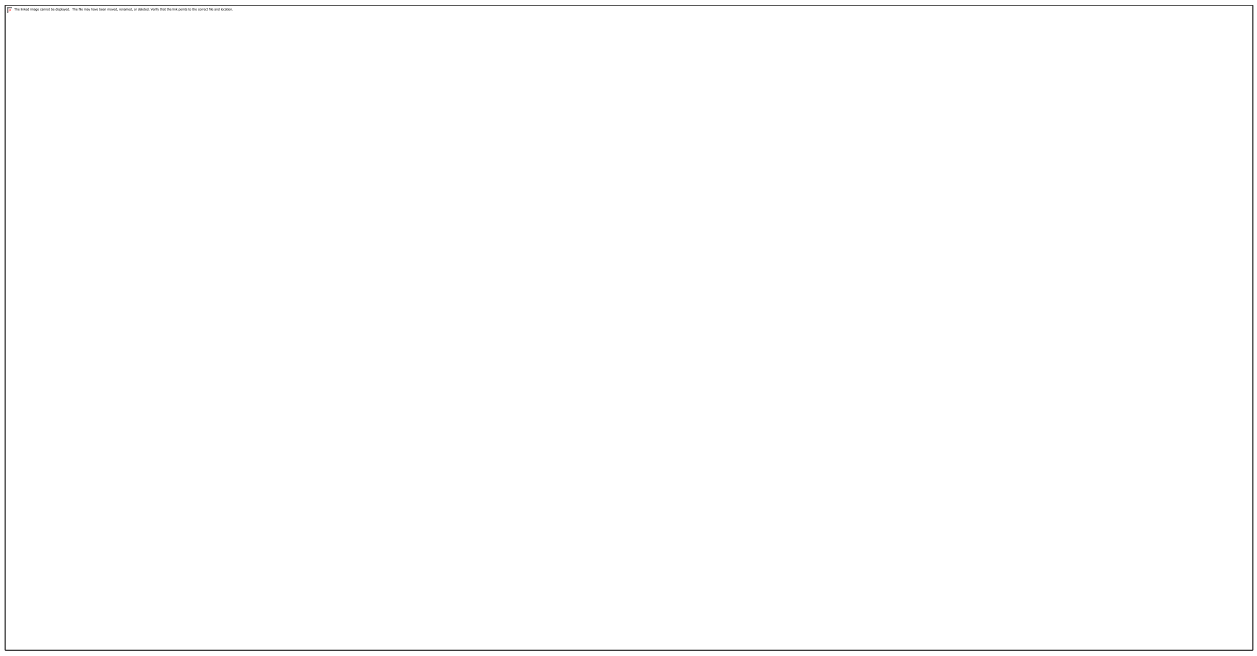

Figure 35: A drawing illustrating how one link of the metamaterial might be separated into two separate links connected by a cylindrical (or translational) joint, the two halves of which are drawn in red and black. Replacing many to all of the links with such translational joints (with maximum and minimum stops set independently depending on the stiffening-up point desired) would be one implementation of the microtruss idea.

To calculate the translational clearances that should be "programmed" into the material by setting maximum and minimum stop positions for the translational joints, a simple FEA study of a truss system having a square base and two levels was conducted. The joints were pinned, not cantilevered, and the truss was not overconstrained (in fact, there might be some advantage in overconstraining the microtruss with extra members). The initially-flat structure was given an arbitrary displacement boundary condition of parabolic shape on the bottom edge, and the axial strains in the members were plotted. It was this researcher's idea that, to produce instantaneous lockup at this shape, the beams in this microtruss would be replaced with translational joints, each having one stop set to correspond to the amount of strain the elastic beams saw in the model at this point (the other stop could be set to produce the same shape in lockup in the opposite

direction, or a different shape if desired). Figure 36 shows contours of stress, visually separated between compression and tension.

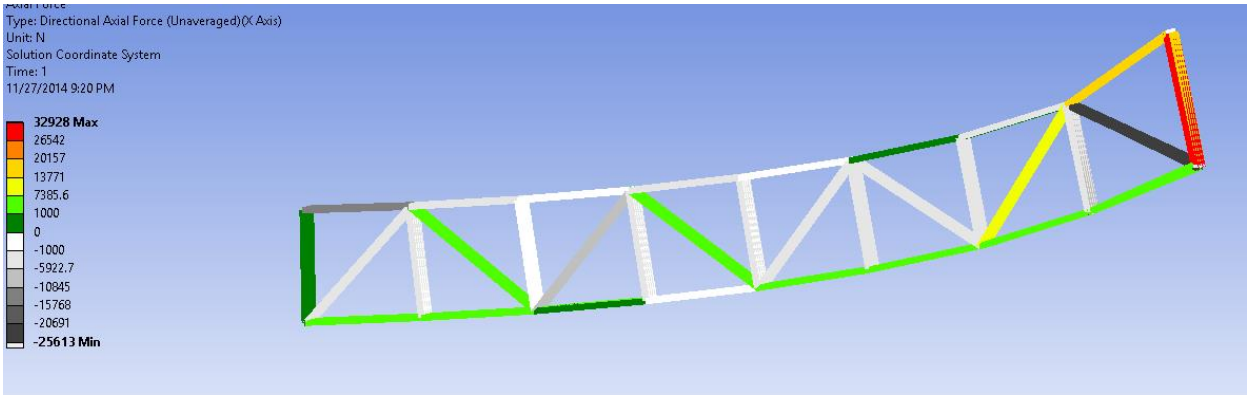

Figure 36: Deformed microtruss (with bottom subjected to a parabolic displacement boundary condition), with deformation as shown (not scaled). Note that colored shading indicates the member is in tension, greyscale compression. Note the slight instability at the very tip that puts the members in tension instead of the expected compression.

Unfortunately, the clearances required to successfully manufacture translational joints between already-small links would be very small indeed and not likely feasible even with SLS, at least if the material is to be printed in one piece (adopting manual assembly might allow much smaller tolerances, but this would cause a cost explosion). Consequently, it was thought beneficial to replace the kinematic translational joints with compliant translational joints: while they have more geometric features, they do not require as much geometrical resolution to produce. Lockup would need to be accomplished by interrupted facial contacts between halves of the joint; while it is easy to envisage how to accomplish lockup by this mechanism in compression, to produce lockup in tension requires more-complex geometry. However, these joints do not have zero initial stiffness and tend to have more out-of-plane compliance than a comparable kinematic translational joint, so they may decrease the feasible stiffening-up ratio that can be obtained. Beyond this, as shown in Figure 37, they tend to consume significant

physical real estate (in order to accommodate long beams that will be compliant in bending about one axis).

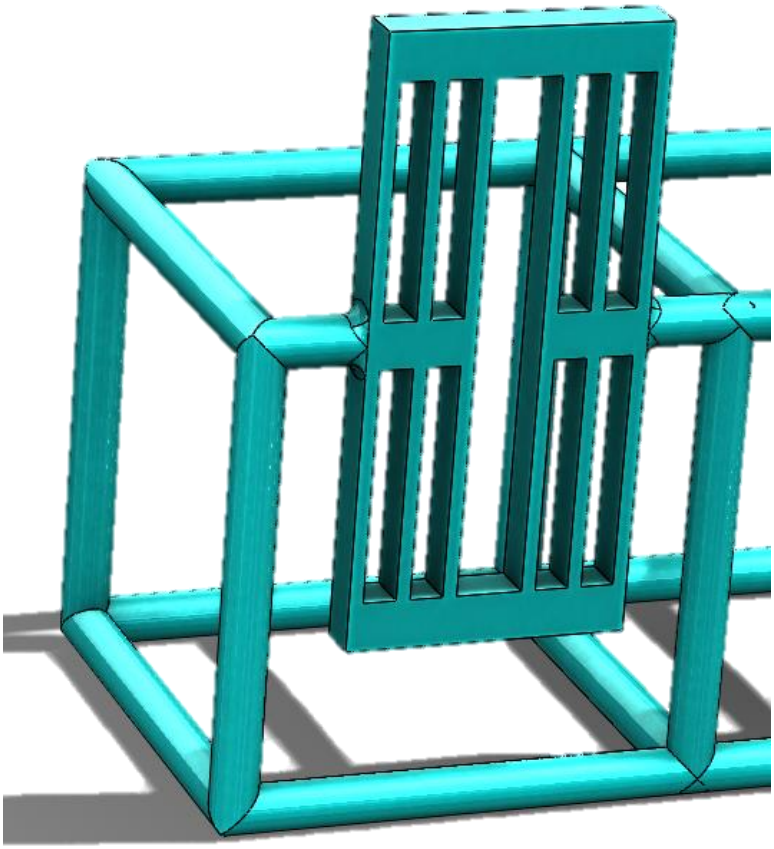

Figure 37: Instead of using kinematic joints (which require small clearances that would be difficult to manufacture and might jam easily), translational freedom could be approximated with a compliant translational joint such as this one, shown in the context of a microtruss. The joint is naturally limited in its compressive freedom by faces that will contact each other after a set amount of compression. However, it must be noted that the small beams making up the joint have been made long to give the joint low initial stiffness; if these are shortened (as they must be to accommodate many of them in a truss structure), the joint will naturally become stiffer.

One other potential stiffening-up mechanisms conceived of was to produce very small tooth-like appendages normal to the length of the constituent beams of the metamaterial; they should have a small initial gap between them, and as the beam curves in bending (which, of note,

it would do only if the beam joints were cantilevered fairly firmly as in a frame, rather than free to rotate as in a true truss), the teeth would be brought into contact with each other, transferring moment to the beam and stiffening the beam (ergo, hopefully, the entire structure) significantly. The proposed geometry is rendered in Figure 38; note that the absence of translational joints here is not intended to imply that the concept could not employ selective translational freedom (as suggested above) in addition to the self-contacting principle outlined in this paragraph. While the entire microtruss concept was soon dropped for its extreme complexity of manufacture and design, this interrupted tooth concept was carried over with interest into the next chapter, where it became the "comb" concept, the first concept to date that demonstrated significant stiffening-up in bending.

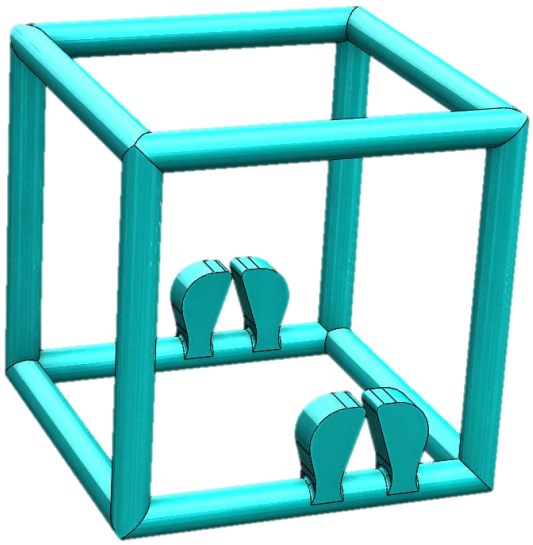

Figure 38: A single frame from the microtruss concept modified with teeth to stiffen it suddenly when the beams to which teeth are attached curve in bending.

As an aside, a similar concept to the one above, a 2D microstructured material that stiffens in tension through the action of numerous small compliant mechanisms, was developed in Chapter 5 and applied to the "annular comb" concept in the hopes it would stiffen a leg-like

spherical joint. Unfortunately, despite the 10x magnitude of tensile stiffness increase obtained for the metamaterial itself (plus the addition of interrupted self contact between teeth like those shown in the above figure), the overall structure had poor performance overall and was dropped from investigation.

Chapter 3. Interrupted-Contact, 1D, “Comb”-based Systems.

Abstract.

A relatively-simple geometry is disclosed featuring a backbone that may be straight or curved with perpendicular protrusions. In bending, when these “teeth” are not touching, the system is initially relatively compliant; after a certain amount of deflection, the backbone brings the teeth into contact, producing greatly-increased bending stiffness. A system of mechanical joints to engage the comb’s bending with actual leg movement has also been developed. The effects of basic comb parameters, including tooth length, the gap between teeth, and the shape of the backbone (linear vs. curved—which imposes constraints on tooth shape as a function of backbone curvature) on mechanical properties before and after the onset of stiffening are also investigated. Finally, efforts to optimize post-lockup stiffness with respect to weight (via composite reinforcement) are discussed.

Introduction.

The comb approach is a sort of compliant mechanism (as the backbone experiences moderate deflection, usually in a regime similar to that of a simple beam in Eulerian bending) that also incorporates the geometrically-interrupted contact of chainmail to produce increases in stiffness. Unlike chainmail, however, the geometry is much simpler to model and analyze/optimize under load, and manufacturing prototypes is vastly easier than producing the intricate chainmail link shapes.

Geometry of a Linear Comb.

Figure 39shows an early finite-element model of a simple, linear-backbone comb, with the nomenclature used in this thesis highlighted.

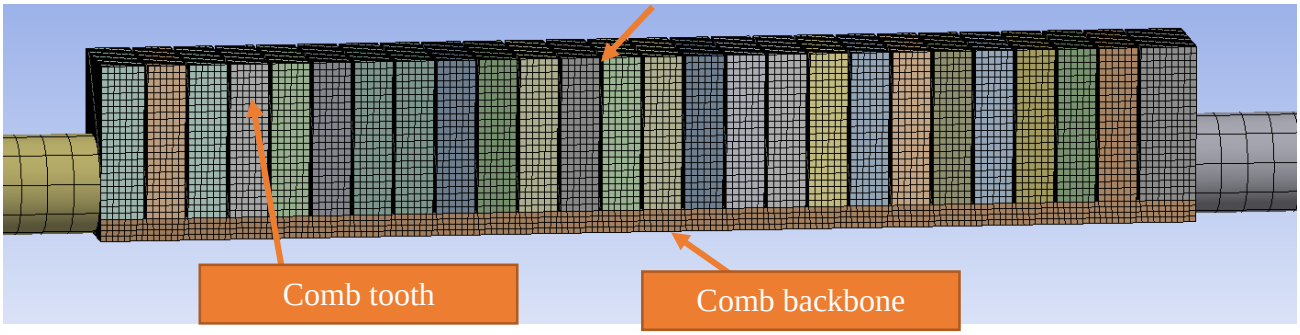

Figure 39: Nomenclature used to describe geometry of a linear comb.

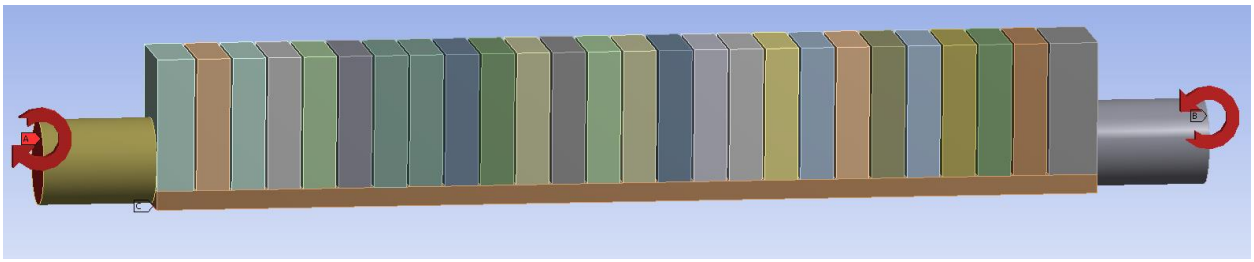

Figure 40: 4-point bending boundary conditions for quasistatic FEA.

In pure, 4-point bending (with boundary conditions shown in Figure 40), Figure 41 shows the von Mises stress contours immediately before and after the deflection at which the teeth lock up—note the constant radius of curvature of the backbone (ergo all teeth lock up at exactly the same point), and note how contours of stress slowly enter the teeth even before lockup.

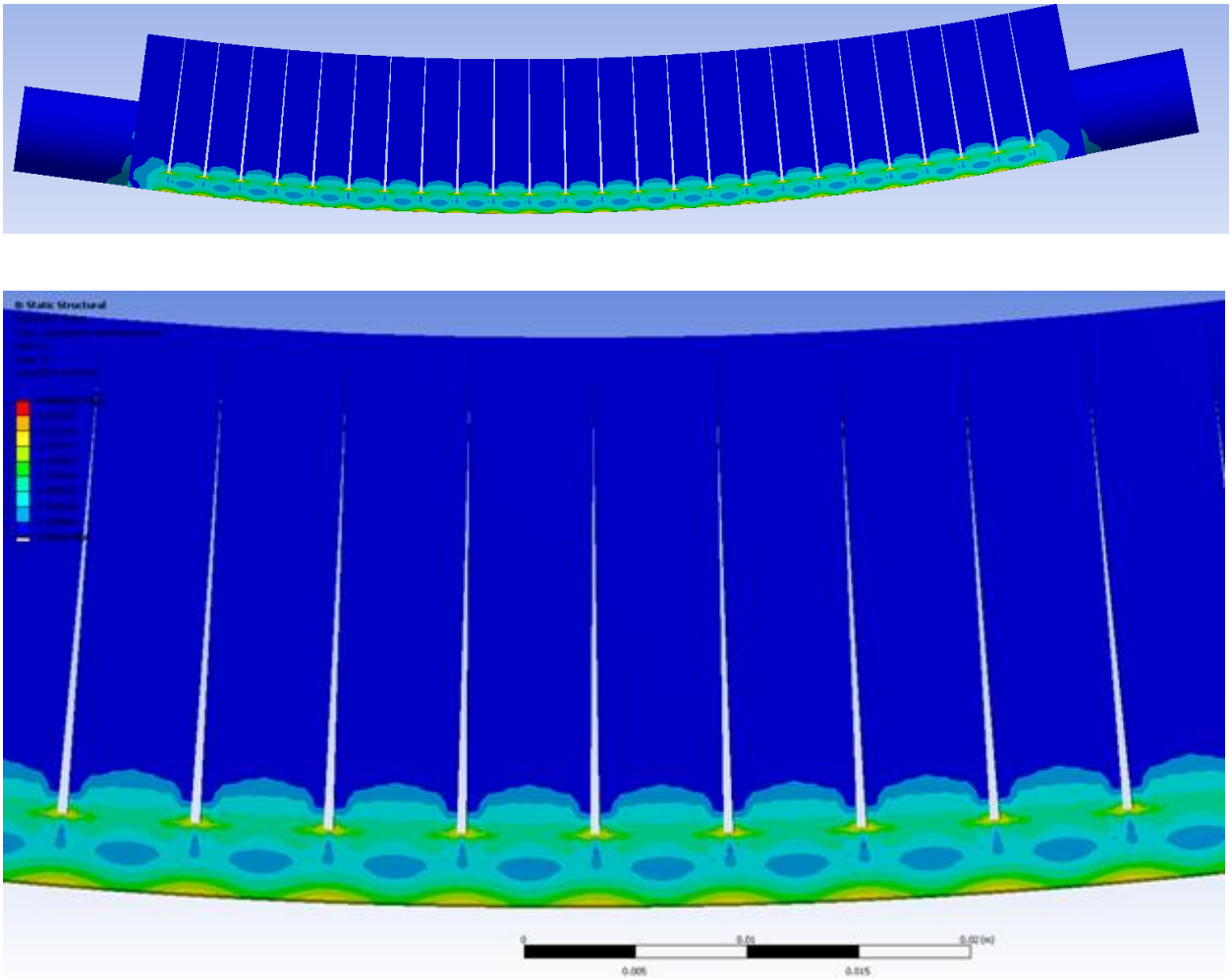

Figure 41: FEA on a simple, linear comb immediately before (above) and after (below) tooth lockup.

Preliminary FEA easily confirms that the comb structure sees a sharp increase in overall bending stiffness once enough bending is achieved to produce tooth contact, with the above comb's bending stiffness illustrated in Graph 11; note that the stiffness post lockup stiffness increases quite sharply to attain 51x the original stiffness.

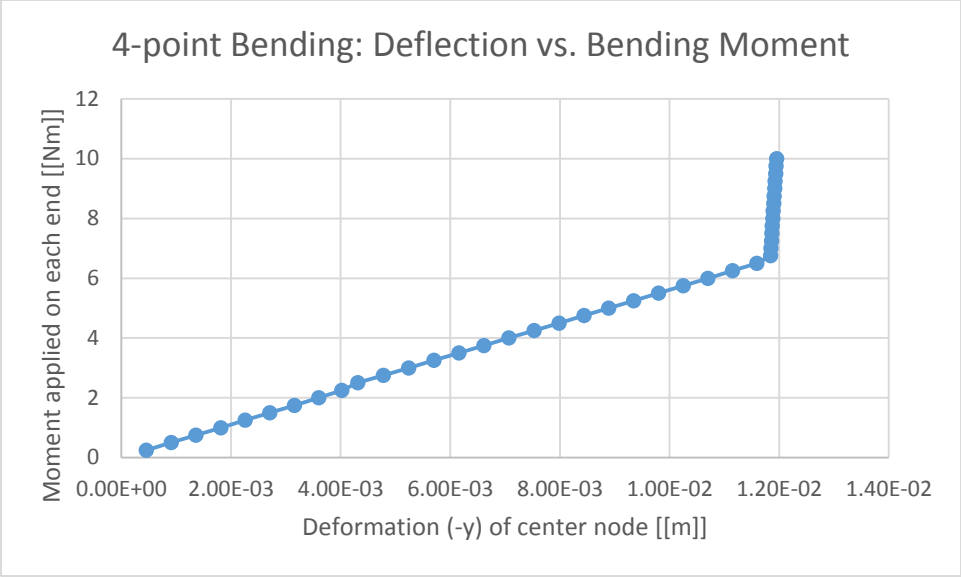

Graph 11: The first FEA comb model in 4-point bending.

Graph 12 and Figure 42 show an FEA investigation of a different tooth profile. At this time, it was believed that tooth shape, particularly as regards attachment to the backbone, would have a significant impact on pre-lockup and post-lockup comb stiffness in our final design. FEA does indicate that tooth shape has some effects on the stiffening-up ratio. However, the constraints on the width of protrusion off from the leg, the low angle at lockup (i.e. high radius of curvature of the locked-up comb), and limited 3D printing precision appear to render the fine details of tooth shape irrelevant to this project, even though they are mechanically significant.

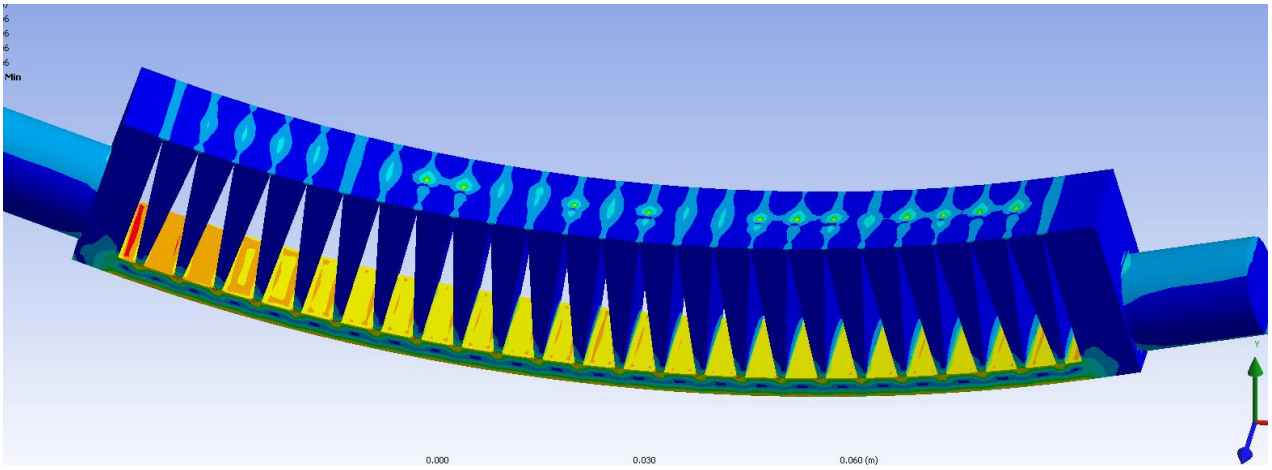

Figure 42: Contours of von Mises stress of a comb with a trapezoidal tooth profile immediately after tooth lockup

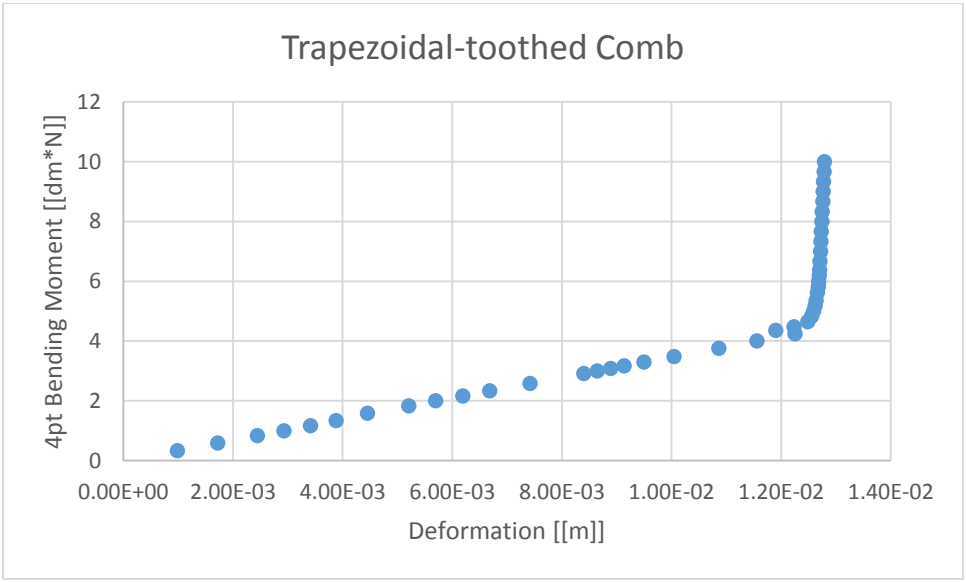

Graph 12: Bending moment of a trapezoidal-toothed comb before and after lockup, at which point stiffness increases to 119x pre-lockup stiffness. Pre-lockup stiffness is in turn 38% lower than that of the rectangular-toothed comb, even though both have the same backbone thickness.

Convinced of the stiffening-up effect of a linear comb, this author began to produce combs in a nylon copolymer called Taulman 618 on a fused freeform fabrication (FFF) 3D printer. As discussed in the chapter on 3D printing techniques, this is an economical yet versatile

setup that seems well-suited to printing moderately-complex geometries in flexible yet tough nylon.

First Test Fixture.

It would be useful to quantify the bending stiffness per angle of joint rotation of a particular comb in a given mounting arrangement before and after lockup. As discussed above, every motion common to the healthy ankle joint—plantarflexion, dorsiflexion, transverse rotation, inversion, and inversion—entails rotation about an axis that is itself constantly rotating in space. Thus, after some inversion, for instance, the new axis of rotation effectively entails a component of rotation about the original plantarflexion-dorsiflexion axis. While this phenomenon will almost certainly need to be taken into account to develop the final product, for simple, proof-of-concept structures, it is vastly preferable to work with a simple spherical joint representing the ankle-joint complex.

A part was designed to mount a spherical joint that could join two parts, one representing the leg above the ankle, the other the foot. To further simplify the problem, the leg was treated as a simple cylinder, the only important parameter of which was a radial offset from the axis running through the center of the sphere of the joint's constraint (this axis is shown in Figure 43). Given that the most attractive point at which to mount the base of the comb might very well be in the sole of the athlete's shoe (given the significant thickness it would provide for attachment of whatever fastening system would be required), the test fixture should position the base of the comb a corresponding distance below the ankle joint. For ease of production, the parts were 3D printed, but, for maximum stiffness and strength attainable without resort to metal cutting, instead of being produced in solid ABS, they were printed as hollow shells and then filled with polyester resin (by hand pouring) after glass fibers were laid up by hand therein. The test system

allows easy alteration in the distance between the fixed base of the comb and the ankle joint center (as this was considered a possible variable of optimization)—during a test, it is to be fixed, of course. Figure 43 shows a rendering of this test fixture.

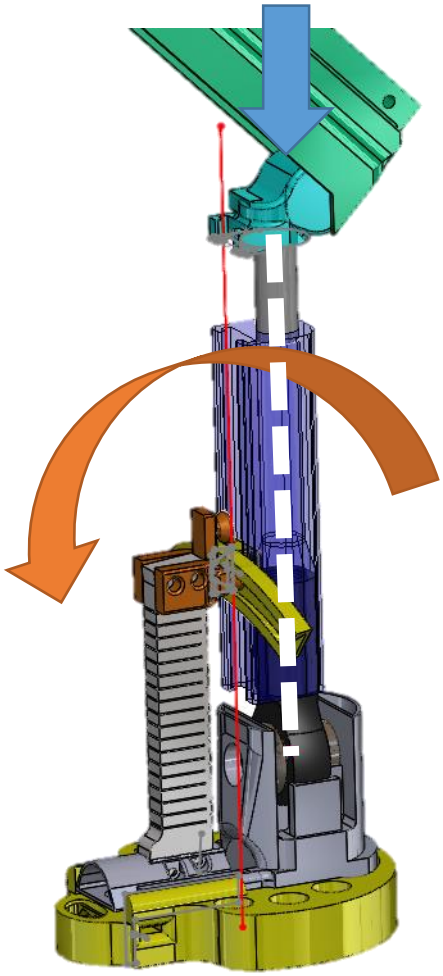

Figure 43: Test fixture for Instron measurement machine; the blue arrow shows the direction of displacement applied by the Instron machine, and the orange arrow shows the rotation of the "leg" that results from the cam interaction. The central axis referenced in the above paragraph is shown with a thick, white dashed line.

Boundary Conditions for Linear Comb.

For the simplest case of joint motion (i.e. only in one direction at once—given the higher probability of injury from excessive inversion/eversion rather than from plantarflexion / dorsiflexion, it makes sense to prefer angular constraints appropriate for inversion/eversion at first), there are several conceivable boundary conditions to apply to the comb. Clearly, the base should be cantilevered (i.e. position and angle fixed)—but how should the rest of the comb interact with the upper leg?

Pinning and cantilevering the comb to a position on the leg was found to produce high initial stiffness (regardless of the horizontal distance away from the leg, comb angle relative to leg, or vertical distance of attachment point on leg away from the center of ankle rotation with respect to comb length), presumably because the comb was being compressed axially (and, depending upon the orientation of the axial load, often cannot even buckle). While intuitive, this is quite unfortunate as this is would be the easiest and most reliable boundary condition to enforce on the leg.

In contrast, a T-slot joint running parallel to one of the joint axes along the length of the leg seems an excellent boundary condition. As shown in Figure 44, a rotation of approximately 15° about the main axis of interest for now suffices to bring the comb teeth into contact for the chosen tooth shape and length; the slider slides around 1cm in the T-slot over this period. With the base of the comb stiffly cantilevered to the foot, cursory inspection shows the joint experiences a sudden and significant increase in bending stiffness when the teeth lock up. The slight downward angle from perpendicular given to the T-slot slider was selected to ensure that all teeth, even the topmost two, lock up nearly at once. Note that the backbone of the comb takes on an almost constant curvature along its entire length. Figure 45 shows a computer rendering of the comb tooth geometry that was printed; note that the gap between teeth was constrained to be quite small to ensure lockup after only around 15° of rotation, much smaller than was intuitively expected; fortunately, it was within the capabilities of our printer to produce a gap of this size.

Figure 45: Close-up of successful comb tooth geometry.

In a final product, it would be ideal to minimize the length of T-slot required to allow free bending to minimize the footprint of the attachment system: note that the bending direction 180° opposite the one that engages comb teeth also adds to the required T-slot length. If a very long T-slot were required (for instance, for the comb that protects against excessive plantarflexion/dorsiflexion), it might need to conform to the contours of the leg instead of being purely linear (as is the one shown above). This is because a straight-line T slot would protrude from the leg significantly in some areas, and such protrusion is subjectively felt to reduce the comfort afforded by the system and increase the chance of the system catching accidentally on foreign objects. This consideration applies mainly to the T-slot that would run along the rear of the calf, as this part of the leg has significant curvature and would need a lot of sliding length to accommodate the large safe amounts of dorsiflexion and plantarflexion that athletes experience.

While this solution ultimately seems quite promising for its sharp ramp up in stiffness and simple geometry, it has a glaring defect: the comb currently must bend along an axis perpendicular to that along which it stiffens up when the joint simulates plantarflexion/dorsiflexion. While this does not engage the teeth (which might make the joint so stiff as to be immobilized), it will obviously waste the athlete's energy through dissipative forces and add undesired elastic stiffness that would greatly alter his biodynamics. Figure 46 shows how the comb stiffens the joint undesirably when bent perpendicular to the direction in which the teeth can stiffen up.

Figure 46: Simulated plantar/dorsiflexion sees greatly-increased bending stiffness throughout the entire range as the comb's backbone is quite thick in this direction. Obviously, this is unsatisfactory.

One option, although unsatisfying for its complexity (and the subjective sense that sliding joints are prone to jamming) is to add a curved slot that will free the joint in plantarflexion/dorsiflexion, only engaging the comb in inversion/eversion; this interrupter would then be fitted to the main leg T-slot. Presumably such a slot should be curved with its center of curvature and radius roughly corresponding to the distance between the ankle center and the attachment point on the comb; however, the radius of curvature will obviously change with the main deformation (inversion/eversion in this case)—it is unclear what the optimum geometry

would be, given this fact, but it is likely that the interrupter's ability to slide up and down along the leg's main T-slot renders this more a question of limiting friction (from interrupter-slot normals that are oriented in such a way as to be likely to catch the interrupter's slider from non-zero friction in this joint) than preventing joint locking or added stiffness when friction is ignored. Figure 47 and Figure 48 show the function of the interrupter. Figure 49 shows CAD geometry of one possible interrupter configuration. (Note that it is an open question whether the two or more points of contact along the slider required for an extra degree of constraint are ideal or whether just one point, which would give two degrees of freedom, would be preferred).

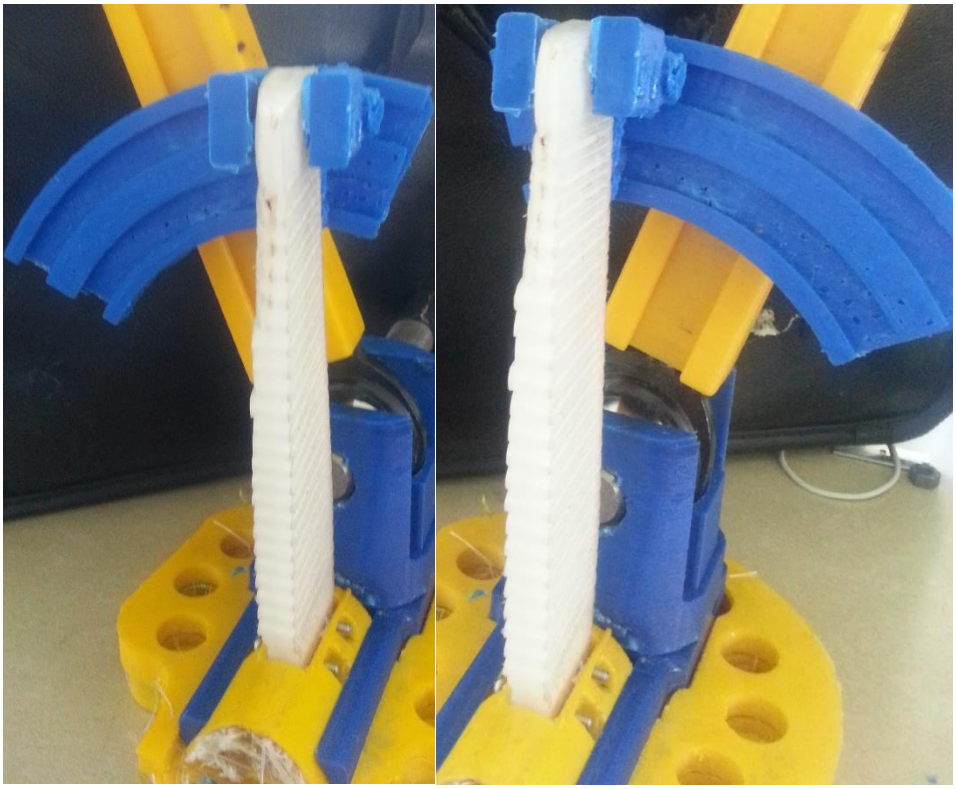

Figure 47: The interrupter allows for free (neglecting friction) plantarflexion/dorsiflexion. Note that the interrupter can suddenly engage at the end if desired.

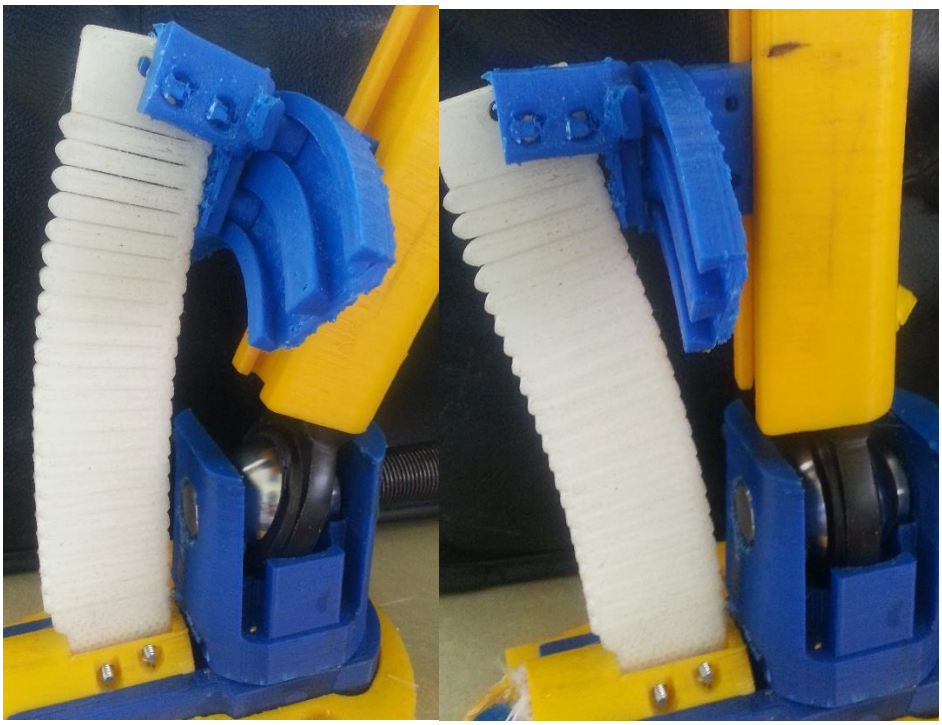

Figure 48: The interrupter still engages the comb teeth in inversion.

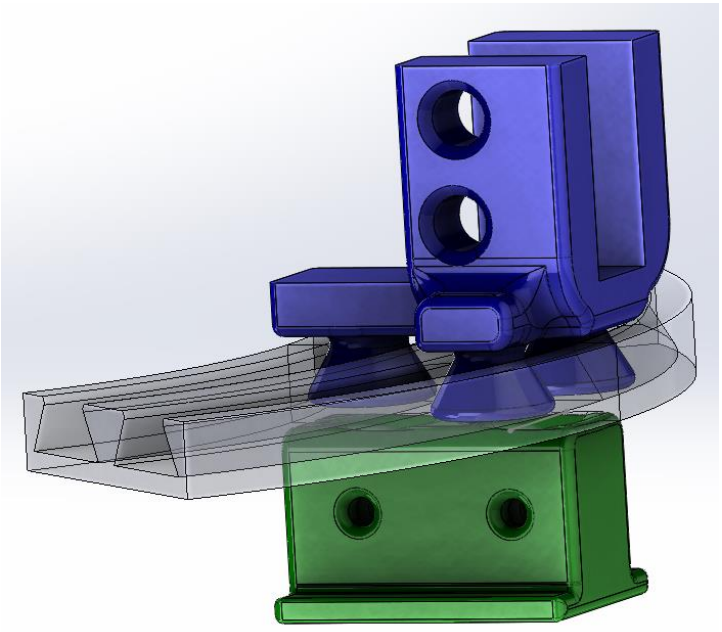

Figure 49: Slot-based interrupter slides in main T-slot in leg.

It may seem a fair question why a joint directly connecting the comb to the leg is required in the first place. After all, the comb's backbone obviously supports its weight when it is not in contact with the leg, and once the leg has contacted it, the comb initially has very low bending stiffness, until the teeth lock up. As Figure 50 demonstrates, the deformation of the comb is quite as one would expect, with the structure assuming roughly constant curvature (technically, the contact stiffness between leg and comb could become important in a human model, with the soft tissue of the leg conforming) when the leg contacts it.

Figure 50: Deformation of comb when sole attachment to leg is low-friction contact. Right: unattached comb stands up roughly straight under its own weight.

Indeed, this approach nearly eliminates one minor problem of the constantly-attached comb approach: even when a given motion will never engage the teeth in one of the combs, the backbone component of the unneeded comb adds a little bit of unwanted stiffness (and presumably dissipation through hysteresis of the deforming nylon) for every leg motion, whereas with the unattached approach, a considerable subset of motions would see no interaction whatsoever with the comb. Unfortunately, this approach is practically vulnerable: the protruding comb ends could catch on something—another athlete's body, the opposite leg of the wearer, etc., potentially tripping the player. Plus, attaching the comb to the leg allows the mass-moment of inertia of the protection system about the leg axis to be minimized—although how practically important this reduction would be to athletic performance is uncertain. Finally, a foreign object would be marginally more likely to come between leg and comb with the top open (also a possibility with other mounting regimes), possibly causing premature lockup (which is at least conservative, still preventing overextension injury). If these problems could be surmounted, the top of the comb would need to be rounded (and probably made of a soft, albeit low-friction, material) to cam gently with the contacting leg instead of catching and "stabbing" it.

Curved-Backbone Comb Concept.

This setup might also benefit from the use of curved backbones (i.e. before deformation is begun) with combs oriented towards the leg to ensure that they are usually in contact. Such a setup would be especially useful for preventing the top of the comb from catching on the leg muscle. Unfortunately, these setups seem to require a significant offset distance between comb and foot, which is potentially even less desirable than an equal offset distance between comb and leg (as it would require substantial modifications to shoes, which would should be avoided at all cost). Figure 51 shows a comb with an initially-curved backbone, corresponding potential tooth geometry, and predicted lockup backbone shape (which was used to generate the tooth shape). This geometry was produced intuitively, based on the idea that the desired tooth shape for instantaneous lockup is a (complex) function of instantaneous backbone curvature at lockup, instantaneous backbone curvature when free, and tooth length.

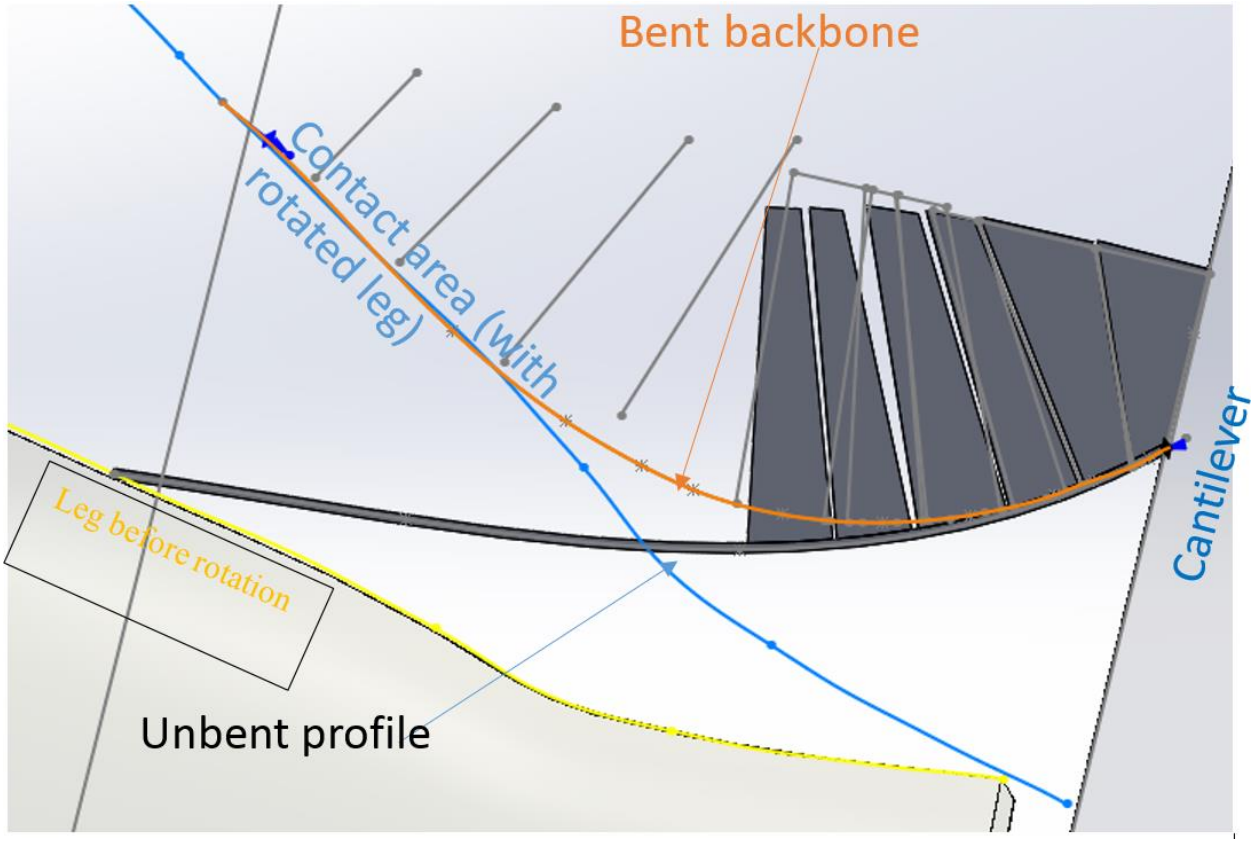

Figure 51: Proposed curved-backbone comb (unbent geometry generated based on predicted bend profile). Note significant offset from leg. Also, this comb is to engage with the leg in pure sliding, although a T-slot might be superior.

Improving Comb Mechanical Properties.

While the simplest comb structure seems promising and mechanically sufficient for the task, we have thus far been dissatisfied with its large form factor, the complexity of leg-comb connections, and the necessity of employing numerous combs (at least 8) to capture the changing safe zone when joint movements in multiple dimensions occur simultaneously. Consequently, reducing the thickness of the overall structure is paramount, and such reductions will presumably come primarily from shortening teeth (since the backbone is subjectively felt to be compliant enough already, reductions in its thickness do not immediately seem necessary, and in any event it is so thin that thinning it further will be of little use in reducing overall size).

Reinforcing Teeth to Increase Stiffening-Up Ratio.

As the teeth become shorter, it seems advisable to somehow stiffen them along their length in bending (provided this added stiffness is only minimally imparted to the backbone when the teeth are not touching) to maintain a high stiffening-up ratio. FEA on the linear comb in bending shows that stress intensity is concentrated in the comb's backbone even upon tooth lockup, with only moderate diffusion into the teeth, which might mean that stiffening-up could be intensified by pulling force paths deeper into the teeth after lockup, though it might also indicate that tooth bending simply does not play a major role in post-lockup stiffness (at least with small tooth gaps as used in these combs). The author of this paper thus chose to investigate the effects of installing spars or sheets of a stiff material (carbon-fiber-reinforced polymer or metal, to be glued to the surrounding nylon with a special chemical suited to the bonding task) inside the comb teeth, jutting slightly into the backbone proper, to distribute some of this load further into the teeth a verbal description of this is insufficient. It is hoped that this will occur only at tooth lockup, however, otherwise it would prove counter-productive. Figure 52 shows contours of von Mises stress in a simple linear comb at lockup, with stress barely travelling into the teeth, and Figure 53 shows potential geometries of reinforcement for the teeth of such a linear comb.

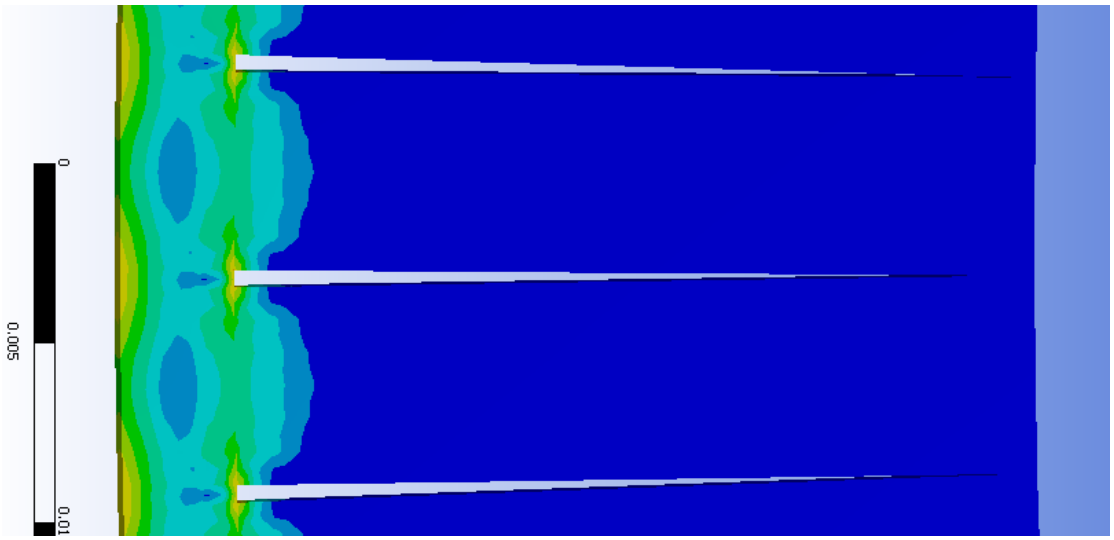

Figure 52: Contours of von Mises stress in FEA of a linear comb that has locked up in bending. Note that stress is concentrated in the backbone even at lockup.

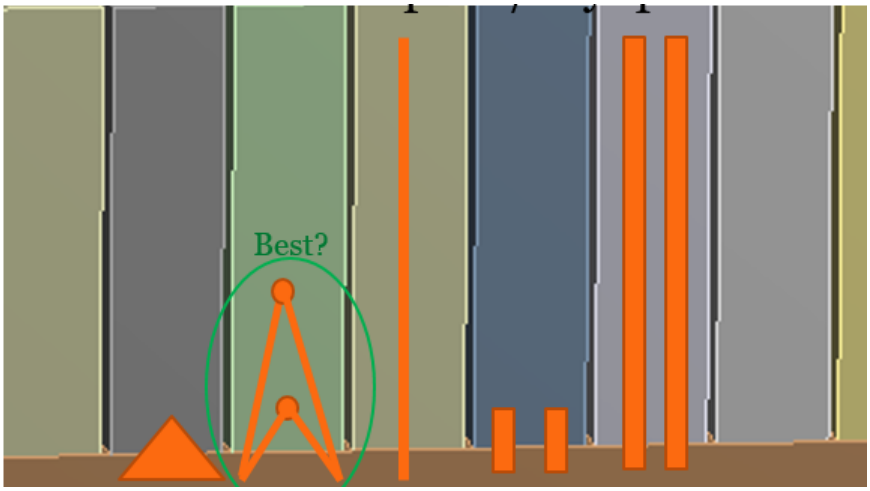

Figure 53: Proposed inserts of stiff material (carbon fiber or metal) that extend a short distance into the backbone and thence deep into the teeth to produce greater stiffness at lockup with minimal effects on stiffness before lockup.

Testing the Reinforced Comb Concept.

For simplicity, the first reinforcing concept investigated was that of a long, thin spar. The spars were assumed to fill the depth of the comb teeth, which, being basically two-dimensional, would not likely see qualitatively-different lockup behavior if the spar depth were shortened (i.e.

the stiffness parameters would likely change, but only proportionally to the depth, without introducing new stiffening/softening behavior).

For constant tooth and backbone envelope shapes and backbone/reinforcement material properties, three variables stand out as most likely to influence pre- and post-lockup stiffness: overall length of the reinforcing spar, the length of protrusion of the spar into the backbone, and spar width. These variables are all illustrated in Figure 54. (Note that other comb parameters, mainly tooth length, width, and backbone thickness, could also be manipulated).

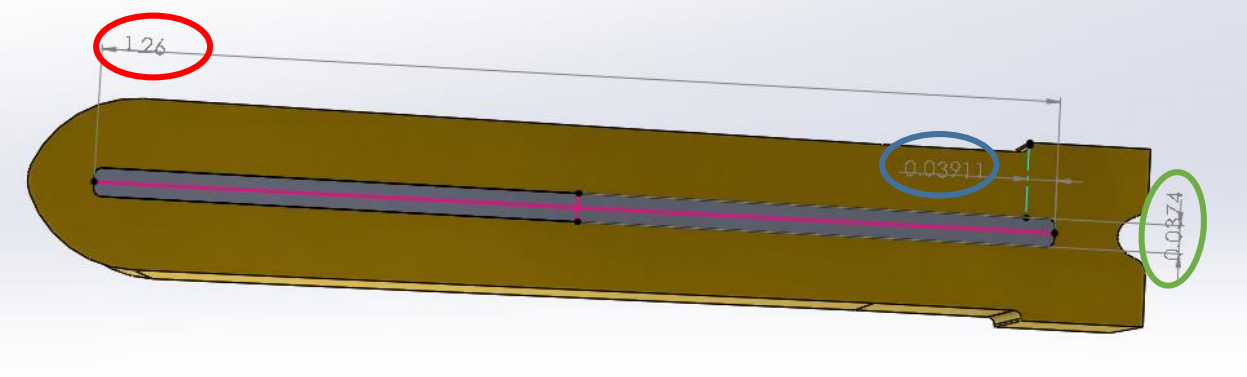

Figure 54: Relevant variables for single-spar reinforced comb. Overall spar length is circled in red, spar width in green, and depth into backbone in blue.

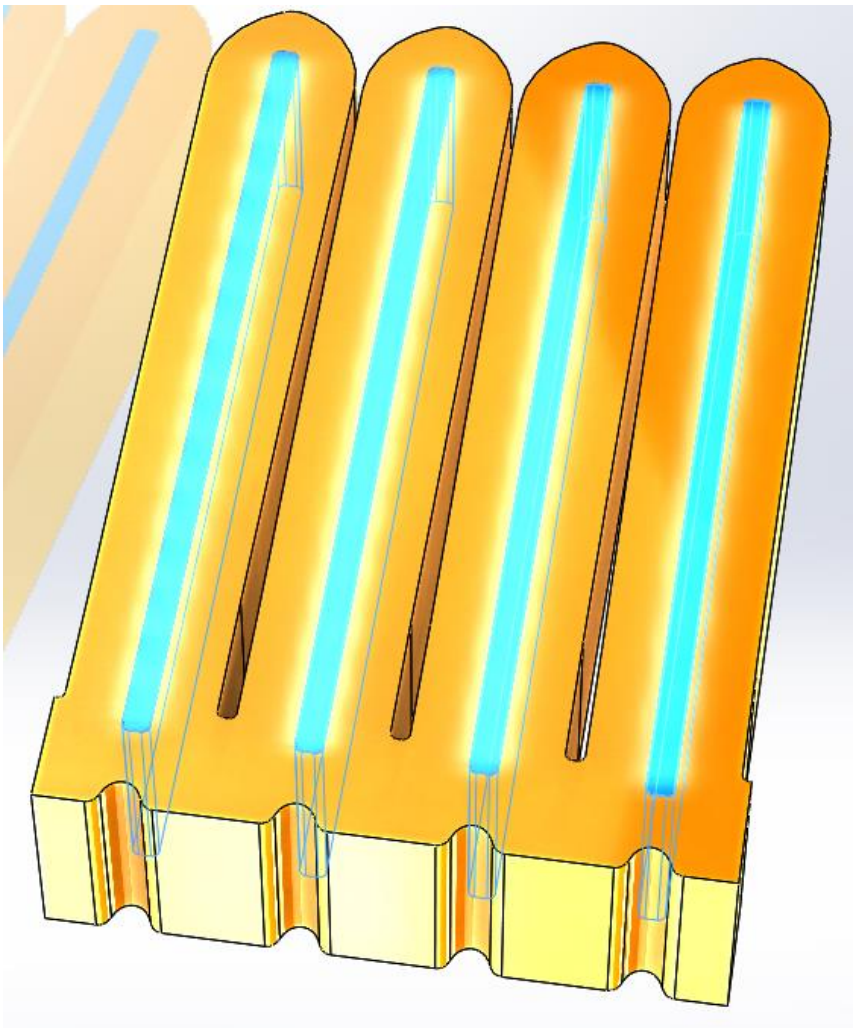

Figure 55: CAD geometry for first FEA simulation of reinforcing the comb. The bodies highlighted in blue are to be treated as unidirectional carbon-fiber laminates, the body highlighted in yellow is to be made of flexible nylon.

The first simulation of a reinforced annular comb was conducted with unidirectional 70% 395GPa-modulus carbon fiber (30% epoxy) laminates as the reinforcement, and 250Mpa-modulus nylon as the surrounding material. Only four teeth were simulated; while any comb in service would be significantly longer with far more teeth, just four should be enough to compare stiffening-up effects between reinforced and unreinforced teeth with the same perimeter shapes. Thus, the model shown in Figure 55 was subjected to four-point bending from moments on rigid, dummy teeth added left and right of the actual, compliant teeth, and the vertical displacement of

the center of the comb was plotted against moment applied to get a measure of the structure's bending stiffness.

While the combs did indeed stiffen up to a moderate degree, the replacement of tooth centers with carbon fiber laminates did not appear to produce mechanical improvements significant enough to justify the increased manufacturing cost that would likely result from such a modification. Table 2 summarizes stiffness parameters before and after lockup (which occurred at roughly the same amount of vertical deformation), and Graph 13 and Graph 14 show the moment vs. vertical displacement profile for both combs.

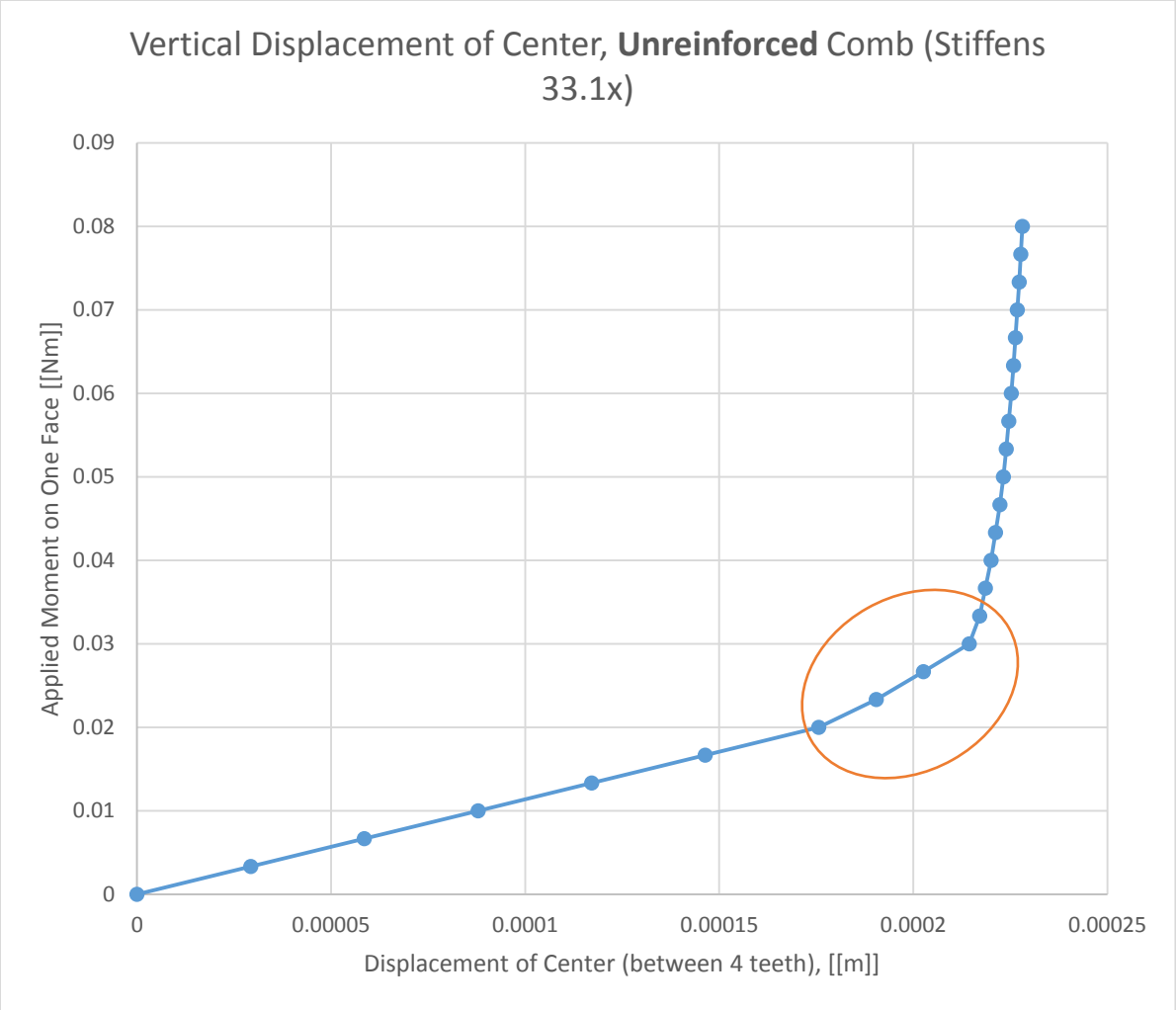

Graph 13: Vertical displacement of center vs. moment applied for the unreinforced, solid-nylon comb. Using linear regressions before and after obvious visual stiffening, and ignoring the transition zone (circled in orange), the stiffening-up ratio was calculated to be 33.1.

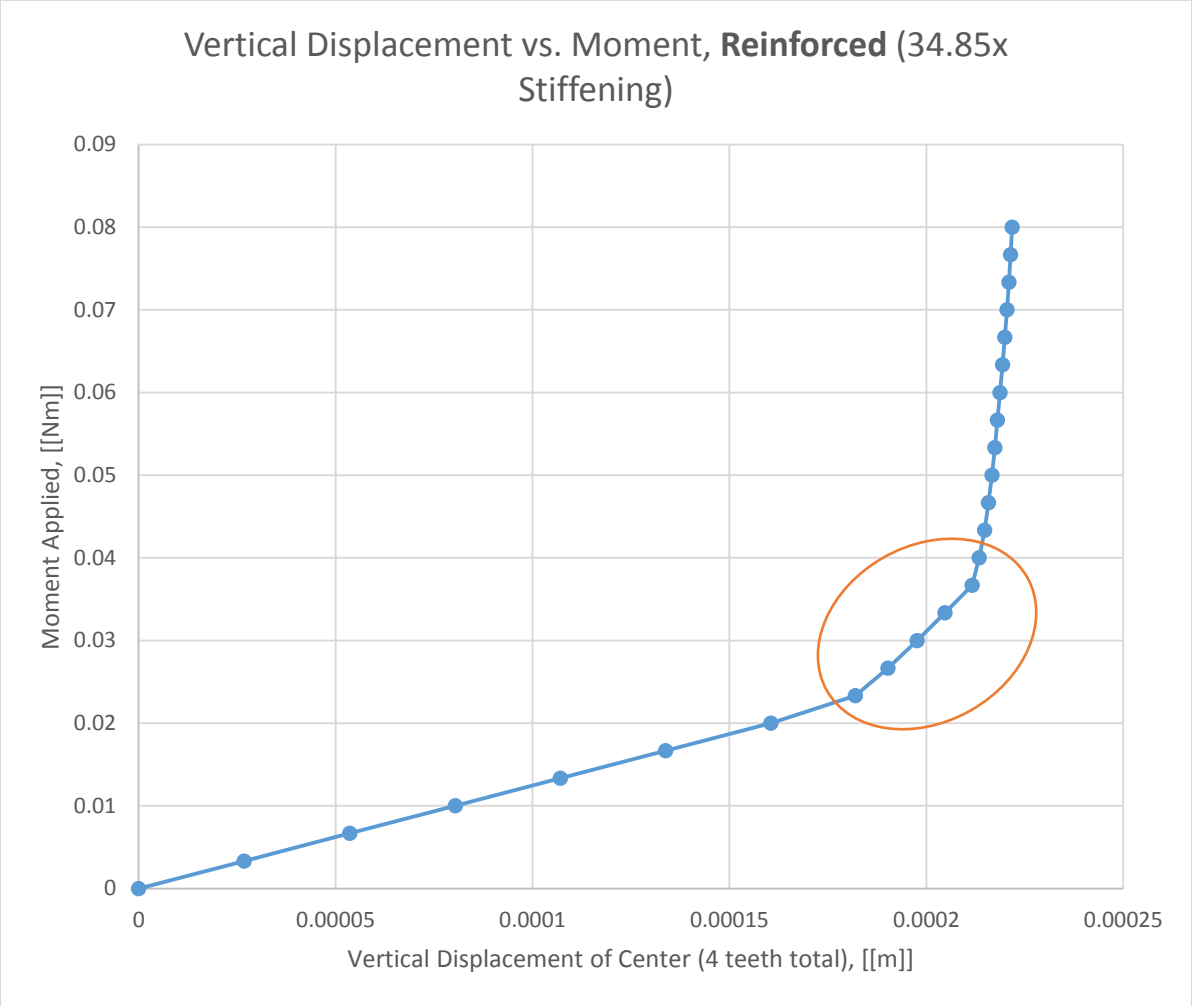

Graph 14: Vertical displacement of center vs. moment applied for the carbon-fiber-reinforced nylon comb. Using linear regressions before and after obvious visual stiffening, and ignoring the transition zone (circled in orange), the stiffening-up ratio was calculated to be slightly higher than that of the unreinforced comb at 34.85 instead of 33.1.

Table 2:Pertinent statistics comparing the stiffnesses of the unreinforced and reinforced combs, before and after lockup.

Reinforced comb is __% stiffer **after** lockup:	16.3%
Reinforced comb is __% stiffer **before** lockup:	10.5%
Reinforced comb has __% higher lockup ratio:	5.3%

Finally, the mechanically-interrupted comb concept should be investigated further: attempts should be made to drastically reduce its footprint (which seems possible), and internal cams should be corrected, first simply conceptually, then with precise data on the ratios of axial compression to bending required for a given leg in a given direction of deformation.

For any linear comb idea to become the preferred focus of research, it should be compatible with an anthropomorphically-correct leg model that features soft and hard tissues, realistic limb shapes, and (perhaps most important) coupled deflections/changing axes of rotation for all joint movement modes. The current test fixture is understood to be a gross approximation lacking all three of these features.

Wavy-Backbone Comb.

Another attempt to increase the stiffening-up ratio of the linear comb entailed altering the backbone design to make it more compliant. This was accomplished with two modifications: one, introducing waviness that would greatly increase the backbone's compliance in both local tension and local bending; and two, decreasing the area of tooth contact with backbone, giving more backbone length between teeth (which should increase local bending compliance as beams become less stiff in bending as they lengthen). This comb was also printed in an alloy containing both nylon and thermoplastic elastomer, having a mean bulk tensile modulus of 76MPa as printed[40]. Figure 56 shows the undeformed comb as printed; while the significant stringing evident in the print is not evocative of high quality, it did not connect teeth enough to exert any mechanical effects.

[40] http://taulman3d.com/pctpe-features.html

Figure 56:Undeformed comb with wavy backbone printed in elastomer-nylon alloy.

Before the teeth contacted, this structure had remarkable compliance in bending, making it far superior in this respect to the simpler, straight-backbone combs discussed above. Of note, it also had moderate compliance in axial tension and compression, although in the latter mode it was highly prone to buckling, both in plane (in which teeth would spontaneously separate, especially in the center of the comb) and out of plane (in which the backbone would curve roughly into an 'S' shape). However, post-lockup stiffening was very poor; it was easy to produce nearly 360° of curvature with a single hand, as shown in Figure 58 (as might be expected, the backbone witnessed little tension before lockup, as illustrated in Figure 57). Of note, after tooth contact began, the backbone experienced significant tension, in which mode it was unfortunately all too compliant. The failure of this comb to stiffen much in bending indicates that high tensile stiffness is an essential property for the backbone; at the same time, it seems clear that the segments of the backbone between the teeth must have low bending stiffness to produce low overall stiffness before the structure's teeth have contacted each other. Basic beam mechanics indicates that this combination of properties is best obtained through very thin geometries made in high-stiffness materials.

Figure 57:Wavy-backbone linear comb bent just until teeth touched lightly. Note that the wavy backbone is not significantly, visibly *elongated.*

Figure 58: Subjecting the comb to significant bending moment after *initial tooth touching brings significant tensile stretching of the backbone, which, thanks both to its wavy geometry and the low bulk stiffness of the elastomer-nylon alloy in which it was*

printed, was not very stiff in tension. Note that if the backbone had been stretched much further, it might have stiffened moderately once the wavy features of the backbone were straightened.

Cable-Based Linear-Backbone Stiffener.

Instead of relying on interrupted tooth contacts to provoke stiffening of the structure in bending, slack cables could be run between teeth. As the structure experiences global bending, the backbone will curve (or, if already curved, the curvature will change), and the tooth normals will generally track those of the nearby backbone areas without teeth. If the teeth are spread apart sufficiently, the slack cables will become taut and thereby add significantly to the structure's stiffness (prior to this, however, they will contribute negligibly, since such cables are like very thin and long beams). Figure 59 shows a drawing of a potential such stiffener, with initially-slack cables added. Note that such a stiffener may require the teeth to face the leg (which would likely be quite uncomfortable for the wearer), or for teeth facing away from the leg but on the opposite side of the direction of deformation to engage. Finally, note that this concept could be combined with that of the traditional comb, in that teeth could either close in self-contact or only open to a degree limited by cable length.

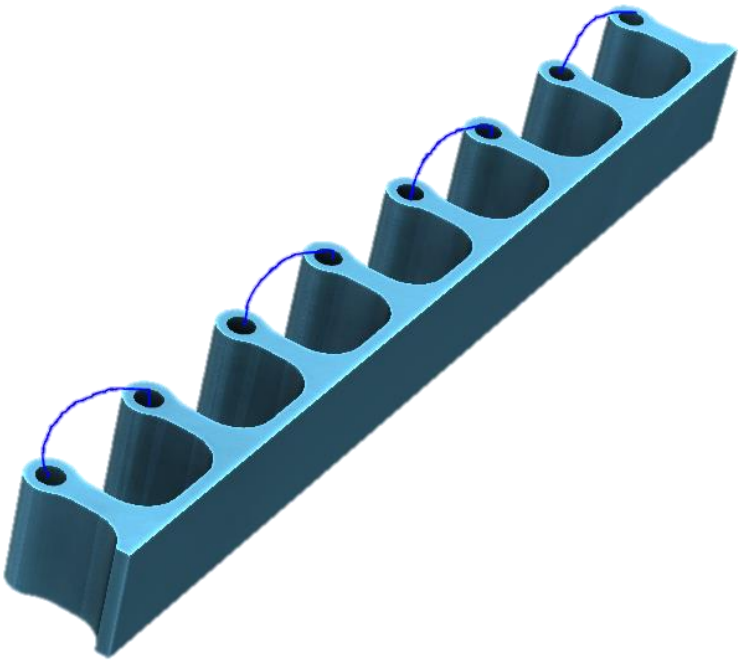

Figure 59: Artist's impression of potential stiffening device. Cables that will be slack at neutral deformation are drawn in blue (note that they thread along the cylinder length, so only half are visible here); they should have negligible bending stiffness and thus not affect the overall structure's bending stiffness until they are made taut.

Apart from the problem of uncomfortable, complex contacts arising from teeth facing the leg, this idea generally suffers also from difficulty in precisely manufacturing such combs, principally because precisely setting cable lengths and then securing them to the teeth with knots is difficult to do by hand. However, cutting cables to length and then gluing them to the teeth might be much weaker than knotting the cables.

When the backbone sees a significant curvature change, it may become vulnerable to local buckling once the cables are engaged, making it softer in bending until teeth contact each other (which is not the intended mode of stiffening for this structure); this mode is shown in Figure 60. This may recommend a backbone design that is less vulnerable to buckling for the cable-stiffened principle.

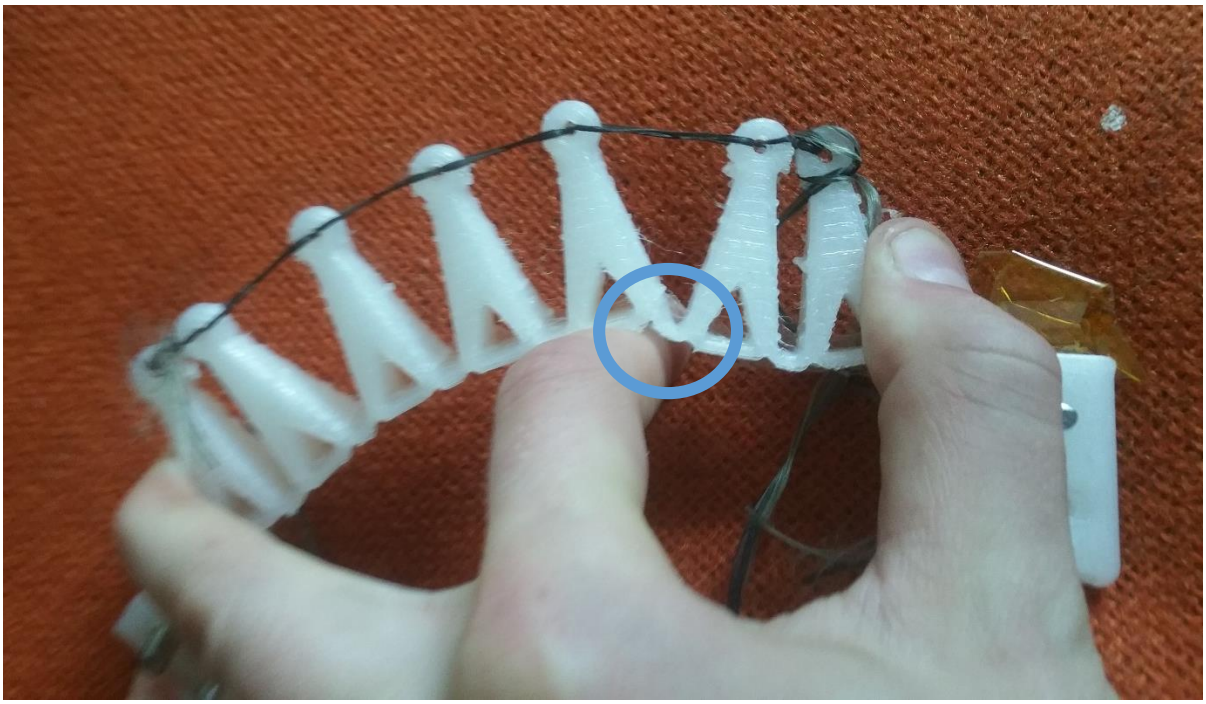

Figure 60:Local buckling of the backbone of the cable-based stiffener (circled in blue) after most cables have become taut. The backbone may have been especially vulnerable to buckling at this point because of local damage it sustained. The backbone also saw some deformation in shear normal to its curvature.

Mechanically-Decoupled Comb.

A novel departure from the traditional compliant-mechanism comb entails connecting the teeth through mechanical joints rather than an elastic backbone. Not only could this modification give zero initial bending stiffness, it could also give some initial axial freedom. This latter modification would allow a simple tied connection to the top of the leg, obviating the complicated T-slot mechanism shown above. Recall that Figure 44 shows how little travel is required in the T-slot for a comb of incompressible backbone, at least for simulated inversion/eversion. Admittedly, this modification would increase the system's geometric complexity, but at least it would be better contained, being completely inside the overall comb structure. Also, there is in fact likely to be little increased stiffening up effect from long teeth as

compared with that from short teeth, especially when the teeth are made of a stiff material (as would be feasible for a structure that got its initial freedom not from elastic deformation of the structure but from kinematic freedoms of jointed parts), allowing for a smaller footprint: as material compliance is not the driver of low pre-lockup stiffness, materials far stiffer than nylon could conceivably be used, which would give the same structural stiffness for a lower second moment of area in bending. That said, (although the first prototype was created with long teeth whose profile was drawn from a successful compliant comb.

A preliminary design was printed in relatively-rigid ABS (but scaled up 3x from its intended final size to better capture details with a 3D printer that gave poor print quality) to capture details and found to have some promise with mechanical freedom as predicted; however, it was evident that the internal cams needed to be redesigned just for basic function (for various reasons, including jamming from mild geometric incompatibility, low strength, and uncertainty if there was any forward bending freedom before lockup), from which further tailoring to the precise lockup conditions would also be necessary. Figure 62 shows the CAD

Teeth touch

model of the first prototype mechanically-disjoint comb and the degrees of freedom its cams and clearances afford it, and Figure 61 shows the behavior of the first 3D-printed prototype.

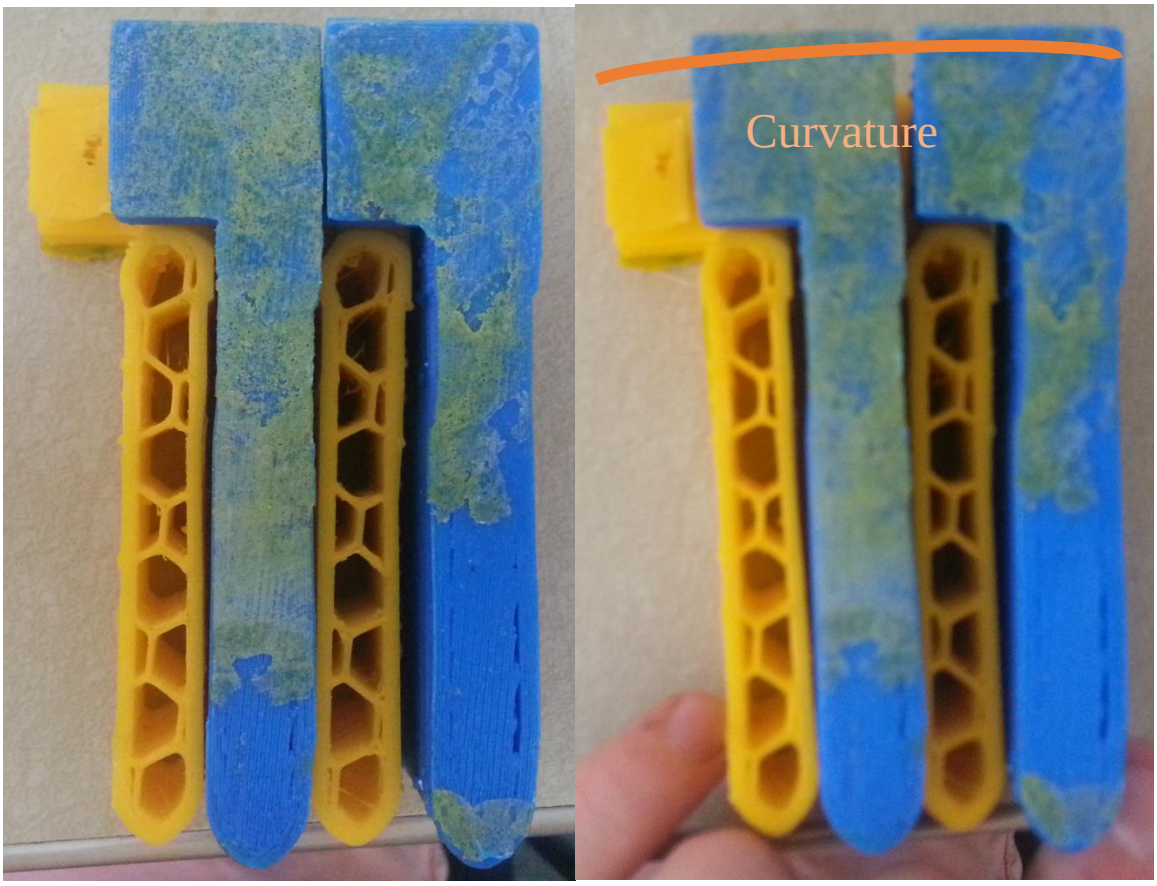

Figure 61: Left: teeth are parallel ("neutral position"). Right: comb bends slightly, teeth touch at tips, and curvature develops at backbone.

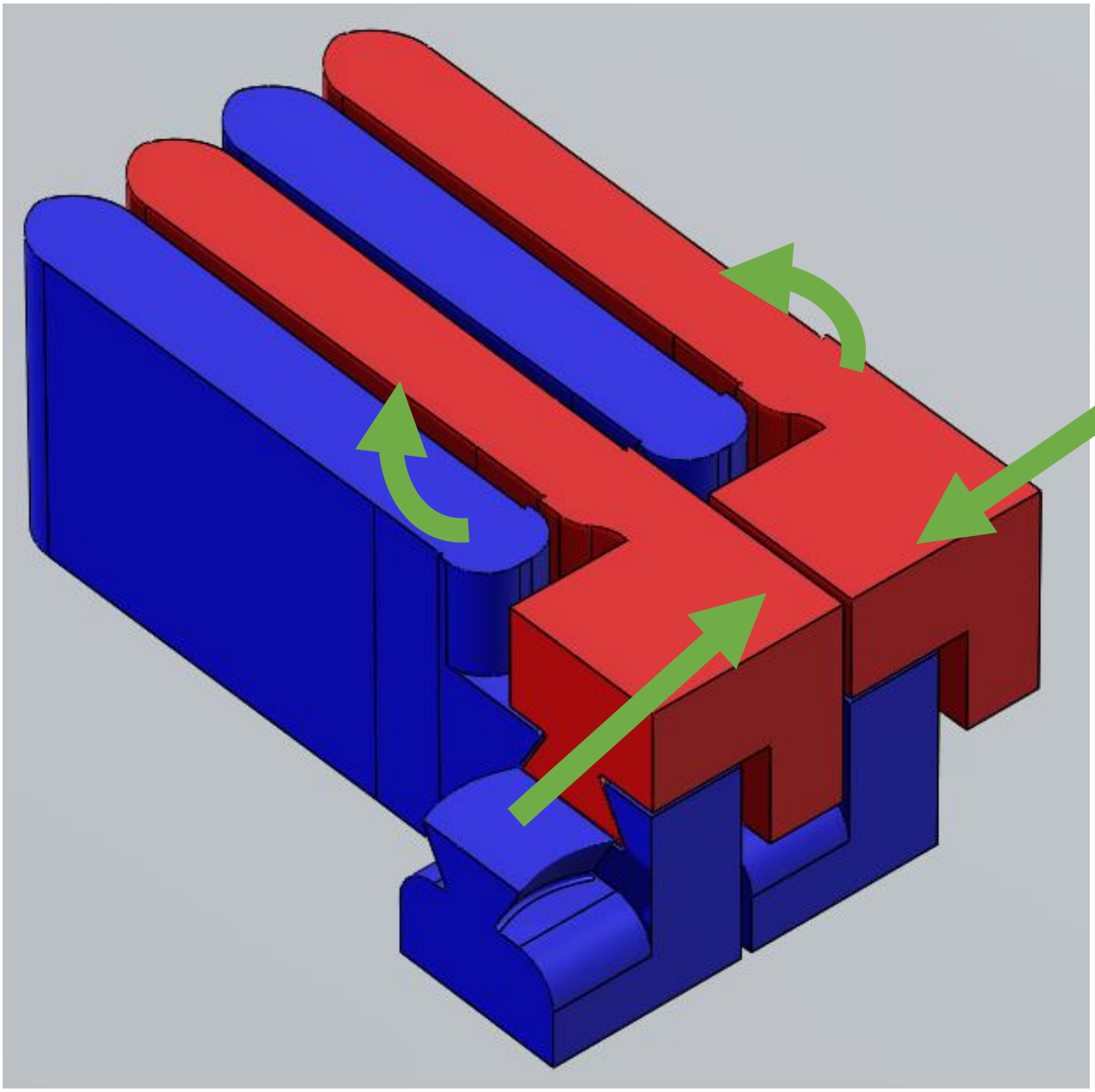

Figure 62: Multiple deformation degrees of freedom of the mechanically-decoupled comb, thanks to clearances.

One potential variable of interest with this mechanically-interrupted comb concept was the shape of the swept, trapezoidal-cross-section cams, particularly the locations of the centers of

curvature of the cams' edges. Having the edges share a center of curvature, and having this center lie on the centerline of the adjacent tooth, seemed a logical configuration, and

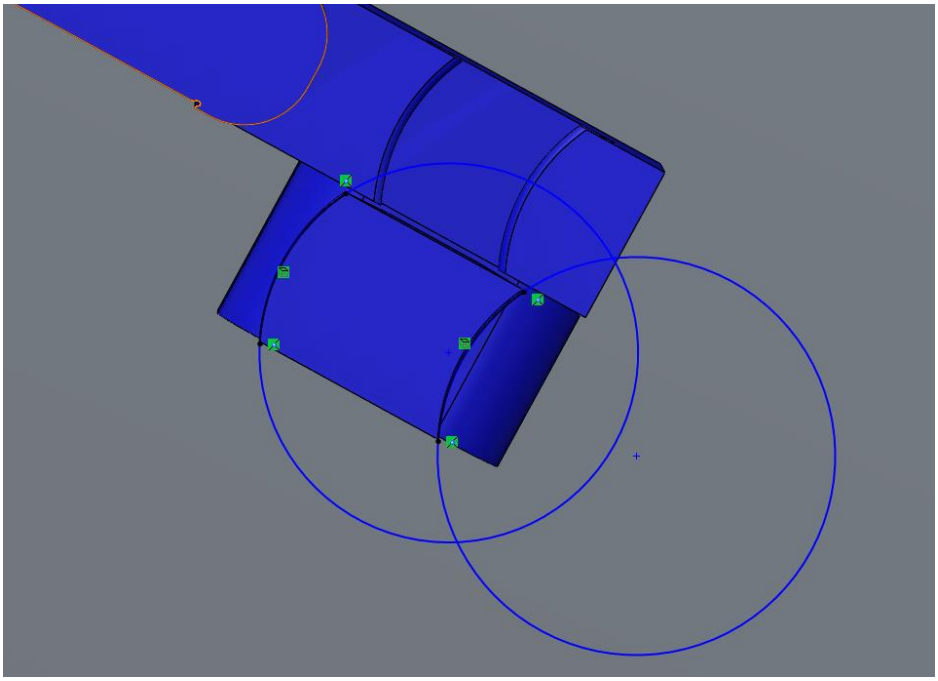

Figure 64: Cam's edges' centers of curvature for initial embodiment of the mechanically-decoupled comb idea.

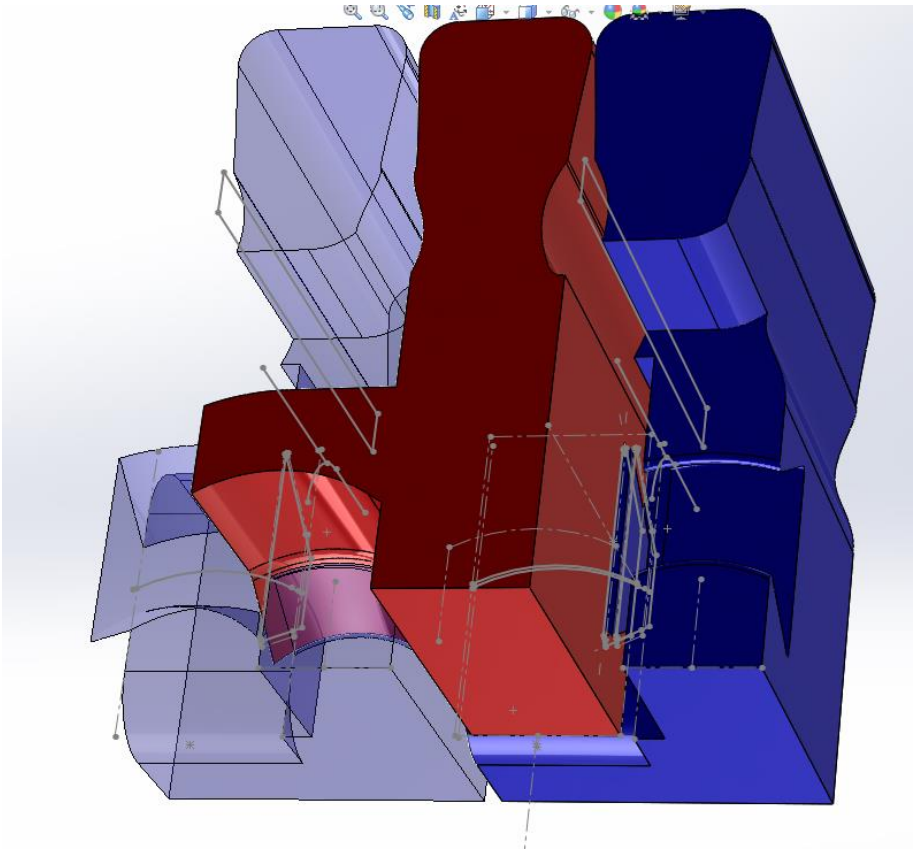

Figure 65: New embodiment of mechanically-decoupled comb idea having cam edges that share a center of curvature.

Simpler Mechanism Linear Comb.

Another potential embodiment of the principle of a kinematically-decoupled comb is much simpler, resembling the initial (compliant) comb: it features teeth joined by revolute joints that will contact each other and stiffen the structure after some global bending causes moderate amounts of rotation around the joints. Figure 66 shows such a comb in the neutral position, Figure 67 when it is locked up.

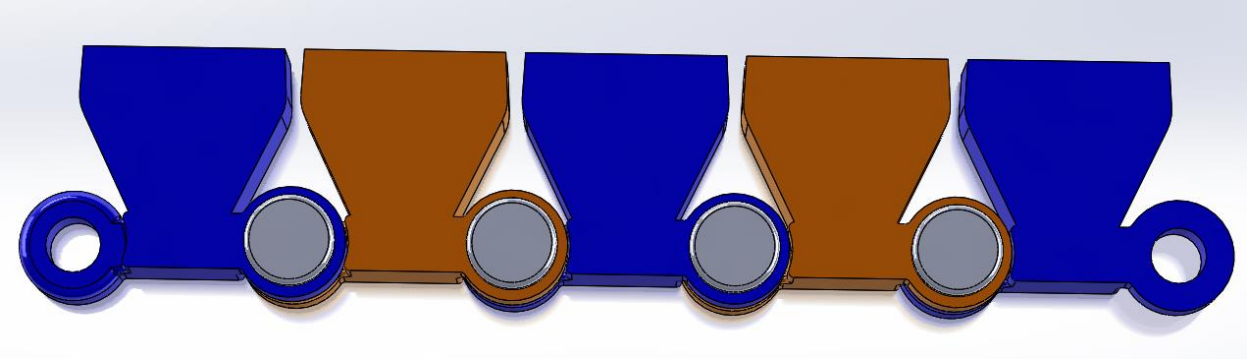

Figure 66: Proposed linear mechanism comb, neutral position.

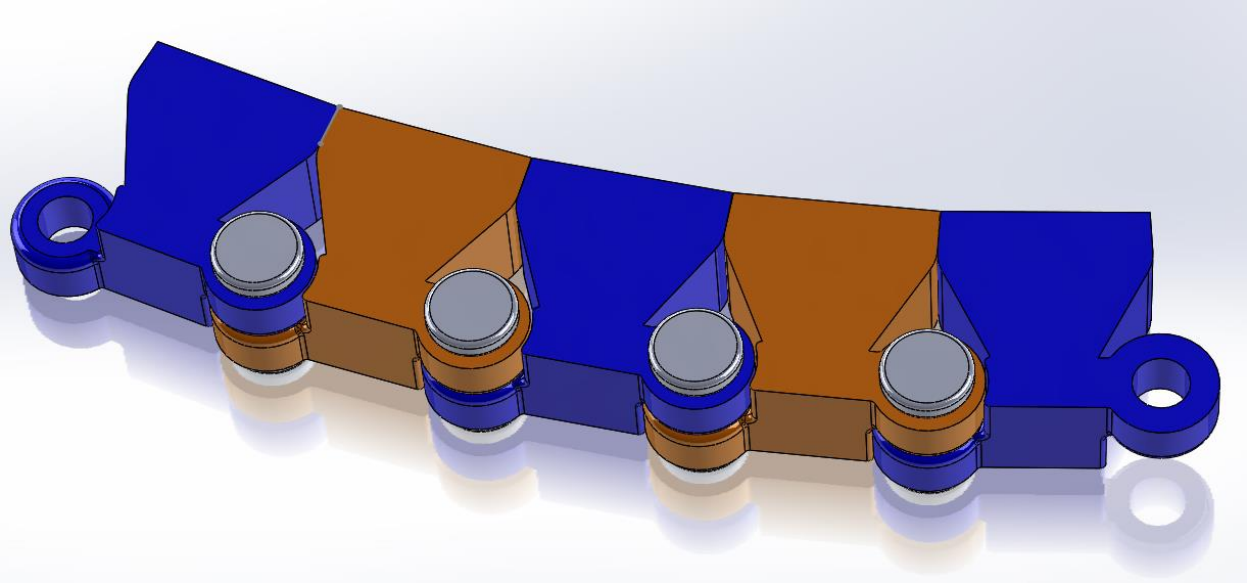

Figure 67: Proposed mechanism comb, subjected to enough gross curvature to produce lockup.

However, if there are teeth only on one side, the mechanism would be even more vulnerable to buckling than would most of the compliant combs studied thus far: having zero theoretical stiffness, the structure could easily enter a buckling mode, and then it would conceivably jam open (see Figure 68 for a visualization of this mode). As such, it would be wise to add teeth on the other side of the centerline as well (shown in Figure 69), and perhaps these teeth would augment the stiffening effects of the comb, too.

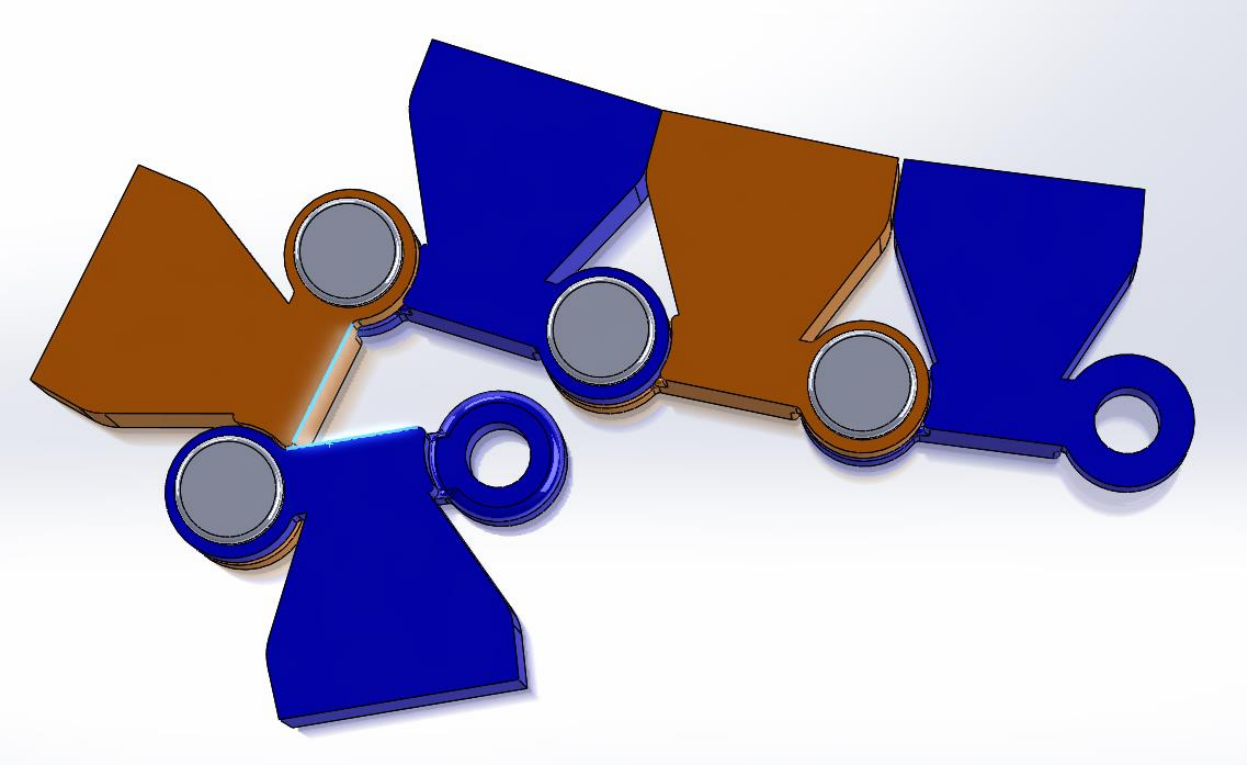

Figure 68: Gross "buckling" on the part of the two leftmost links. The angle between the edges highlighted in light blue (beyond which, thanks to features on the links, the links cannot rotate) should be maximized to prevent buckling.

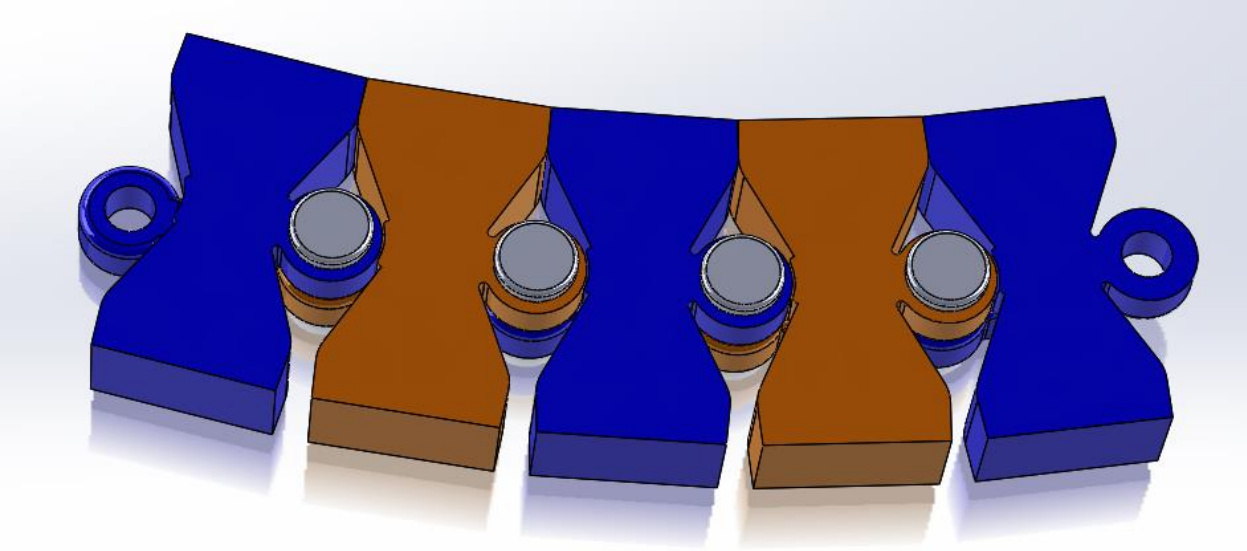

Figure 69: Making the teeth double sided protects against buckling, but at the cost of increased thickness. (However, it may also be beneficial because it protects against deformation in the opposite direction)

The simple revolute joints here could be modified with complicated guide cams to allow the structure to compress (to a limited extent!) along its main axis as well as have limited bending freedom. This cam modification would allow one end of the structure to be tied to the leg and the other to the base of the foot without having high initial axial stiffness. Of note, the structure could also be given universal joints instead of revolute joints, and each individual link given another set of teeth perpendicular to the first (or created by revolution instead); this would allow the structure to bend in 3D and lock up accordingly. Finally, the slack-cable-stiffener principle discussed in the previous section could be applied to the mechanism-based comb, both to prevent buckling and to add an extra stiffening mode.

Chapter 4. Interrupted-Contact, “Annular-Comb” Systems.

Abstract.

The ‘comb’ design detailed in the last chapter is revolved about the leg axis to produce a single part that can surround the leg like a sock and constrain its motion by stiffening up in bending after a certain amount of deflection. Furthermore, the cross-sectional gap distance between the teeth can be varied with the angle of revolution around the leg axis to produce different bending angles before lockup, corresponding to the different constraints imposed on the ankle joint by pure dorsiflexion, pure plantarflexion, pure eversion, pure inversion, and combined loading. Special backbone geometries reminiscent of compliant mechanisms can even be utilized in an attempt to reduce pre-lockup stiffness. However, FEA studies reveal that these structures do not stiffen up rapidly or significantly enough to be useful in their intended application, and tooth contacts are not the primary drivers of what moderate stiffening-up does occur. This principle would require further design to allow donning and removal past the human foot and conformity to the complex geometry of the human leg, although it is not promising enough to warrant such research.

Introduction.

While the simple, one-dimensional (linear or curved backbone of small thickness) comb design shows promise in limiting a joint’s rotation by selectively stiffening up in bending, it is not optimally suited to protecting the ankle: for instance, if a comb is employed to protect against

pure ankle inversion, if the user experiences inversion coupled with dorsiflexion, the safe amount of inversion will decrease, and with a protection scheme guarding solely against excessive inversion, the user could still sustain injury. By varying the gap width between teeth with respect to rotation angle, the designer should be able to produce a continuously-variate lockup position for varying proportions of inversion/eversion and plantarflexion/dorsiflexion. The annular comb approach has the added advantage of also protecting against pure dorsiflexion and plantarflexion, both of which occasionally (although rarely) produce injury. (Theoretically, one could also protect against these regimes with added, separate linear combs). Figure 70 shows a basic annular-comb structure (for mechanical testing—the final, human-wearable structure will require additional geometric features). Figure 71 and Figure 72 show added views of the part, highlighting the varying tooth gap.

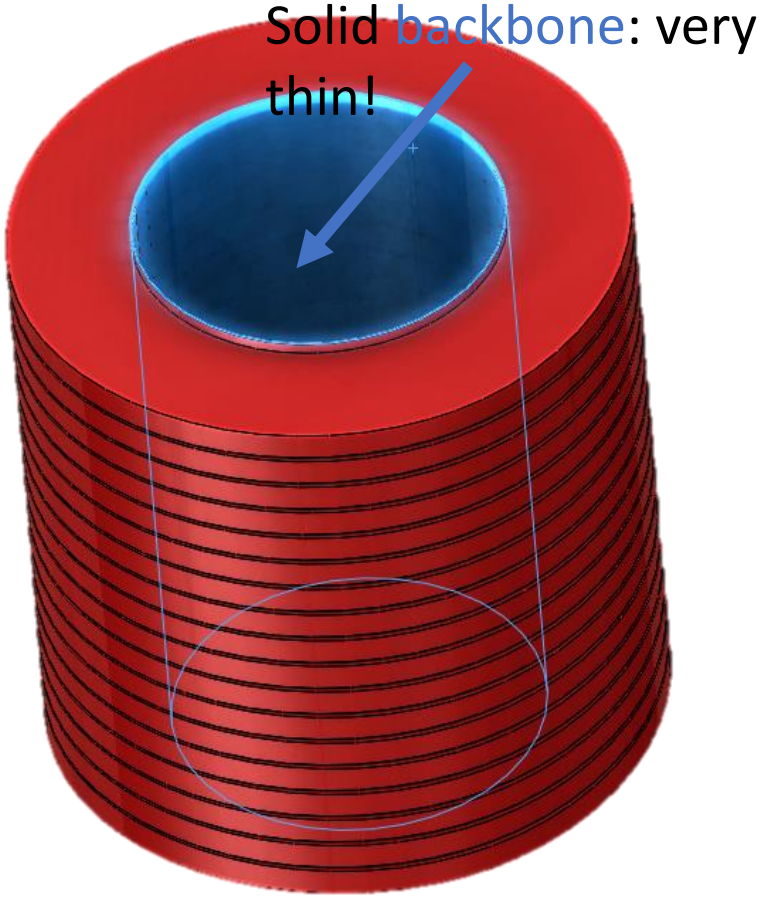

Figure 70: Annular comb, perspective view. Note backbone, 'teeth' with gaps

Figure 71: Tooth gap width varies with respect to angle according to a chosen profile.

Figure 72: Sectioned view of annular comb, showing solid backbone and interrupted, annular teeth. (The green cylinder in the middle is a placeholder for the human leg)

Of note, this basic embodiment of the annular-comb concept uses a perfectly-right-cylindrical backbone. While a backbone shape that conforms to the human leg contours (albeit with a slight offset) might intuitively seem preferable, not only would corresponding annular-tooth geometry become significantly more difficult to model (an unwise investment of time to undertake before the suitability of the basic annular comb is proved), but also the sliding nature of the leg-backbone contact could cause the leg to catch against the backbone unless the offset was so great as to make the geometry practically indistinguishable from that of a right-cylinder backbone.

FEA of First Annular Comb.

To investigate the practicality of the basic concept, finite element analysis of an annular comb in sliding contact with a right cylinder of somewhat smaller diameter rotating about a point representing the ankle was performed. The geometry of the 'leg' was obtained by creating an ellipsoidal cylinder (roughly representative of a human leg when the calf muscle is ignored—although since this muscle is only somewhat compressible this is not a terribly realistic assumption) with a moderate initial gap between leg and annular-comb backbone; then, the leg was rotated to touch the very top of the annular comb lightly (as theoretically the annular comb

will add no stiffness to the leg before contact). Self-contact-checking was established between comb teeth, and large-deflection geometrical nonlinearity was considered by the solver. The "leg" stand-in was treated as perfectly rigid for computational efficiency, the annular comb modeled with linear approximations of nylon's mechanical properties, although accuracy in modelling these properties was of little importance: the purpose of the analysis was mainly to see what shape the deformed structure would take on and how it would interact with the leg. Figure 73 shows the mesh and boundary conditions applied in the first analysis of the annular comb.

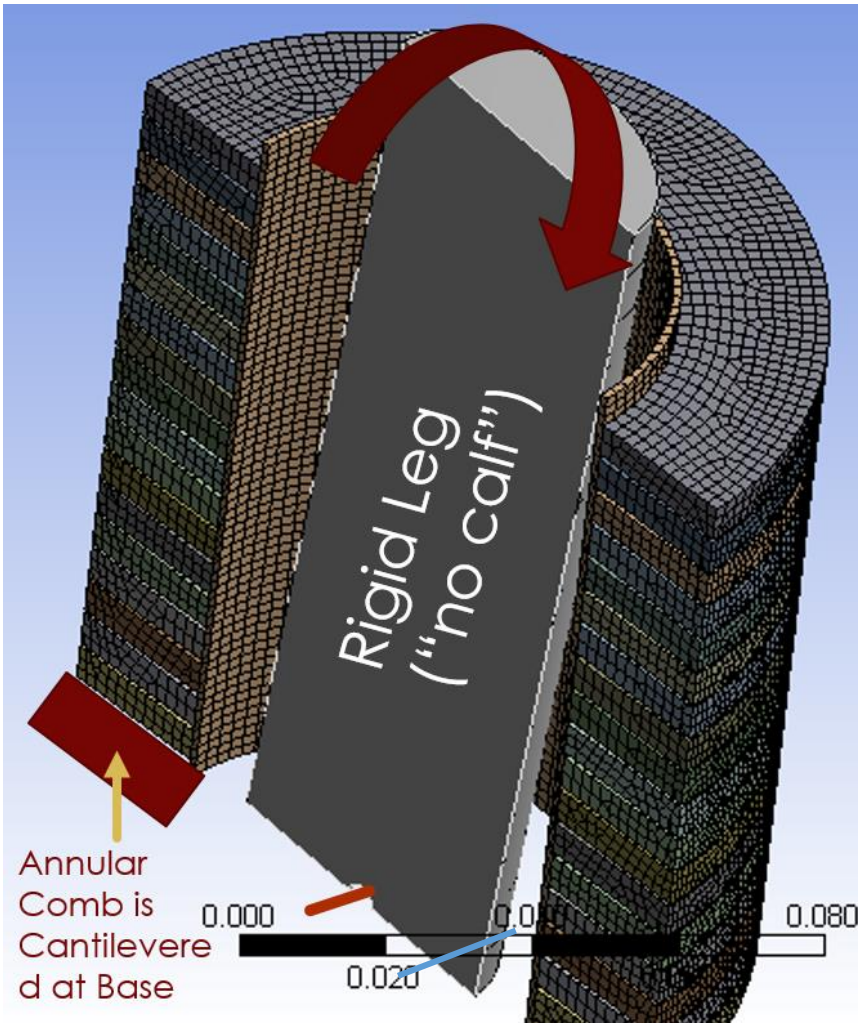

Figure 73: Mesh and boundary conditions for preliminary FEA of annular comb.

Just as the material properties, leg geometry, and leg-backbone contact stiffness were not terribly accurate, the mesh was not likely refined enough to yield precise measures of stiffness before and after lockup; however, the main point of this preliminary analysis was to understand the deformation patterns, amount of sliding, and distribution of stress throughout the structure. The strain profile should yield answers to two key preliminary questions: 1) how many teeth are needed or even capable of engaging during sliding contact between leg and backbone, and 2) whether the sliding leg-backbone interface is suitable, or whether the backbone should be in some way connected to the leg (just as the comb could be attached to the leg with a translational

joint or allowed to freely contact the leg, although in the 1D case tying the comb to a specific point on the leg was found to be unsuitable).

The FEA on this initial configuration yielded surprising insights and show that serious modification of the concept is required to produce a usable, let alone effective, device. After simulating rotation of 19.85° from the vertical (equal to 15° degrees of rotation from the point of first contact between leg and annular comb), many of the teeth were touching on the side of leg-comb contact. As shown in Figure 76, tooth contact was concentrated well below the area of contact between leg and comb backbone, since the leg enforced minimal curvature on the top part of the comb with which it was in contact (preventing teeth from locking up there). Note that Figure 75 explores the cross-sectional view of the backbone's curvature quasi-mathematically by producing curvature "combs" showing direction and magnitude of curvature along a trace of the comb backbone, confirming that the curvature is dominated by the leg contact where it exists (which enforces a very broad, nearly linear, curvature) and by the cantilevered boundary condition where leg-backbone contact is not present (which produces a much sharper curvature). However, Figure 76 also reveals that a region of contact was developing with its locus in the upper-left; presumably, this contact would have become mechanically significant after another degree or two of rotation. Of note, while the model employed several approximations (namely coarse mesh and linear elastic material model for nylon) that would impair accurate computation of stresses, Figure 74 depicts von Mises stresses nearly everywhere (not just in the highly-stressed backbone, but even in teeth in regions far away from contact) stressed at over 70MPa, which is in any event a very optimistic yield strength for nylon that would be achieved only by injection molding or machining, not by 3D printing.

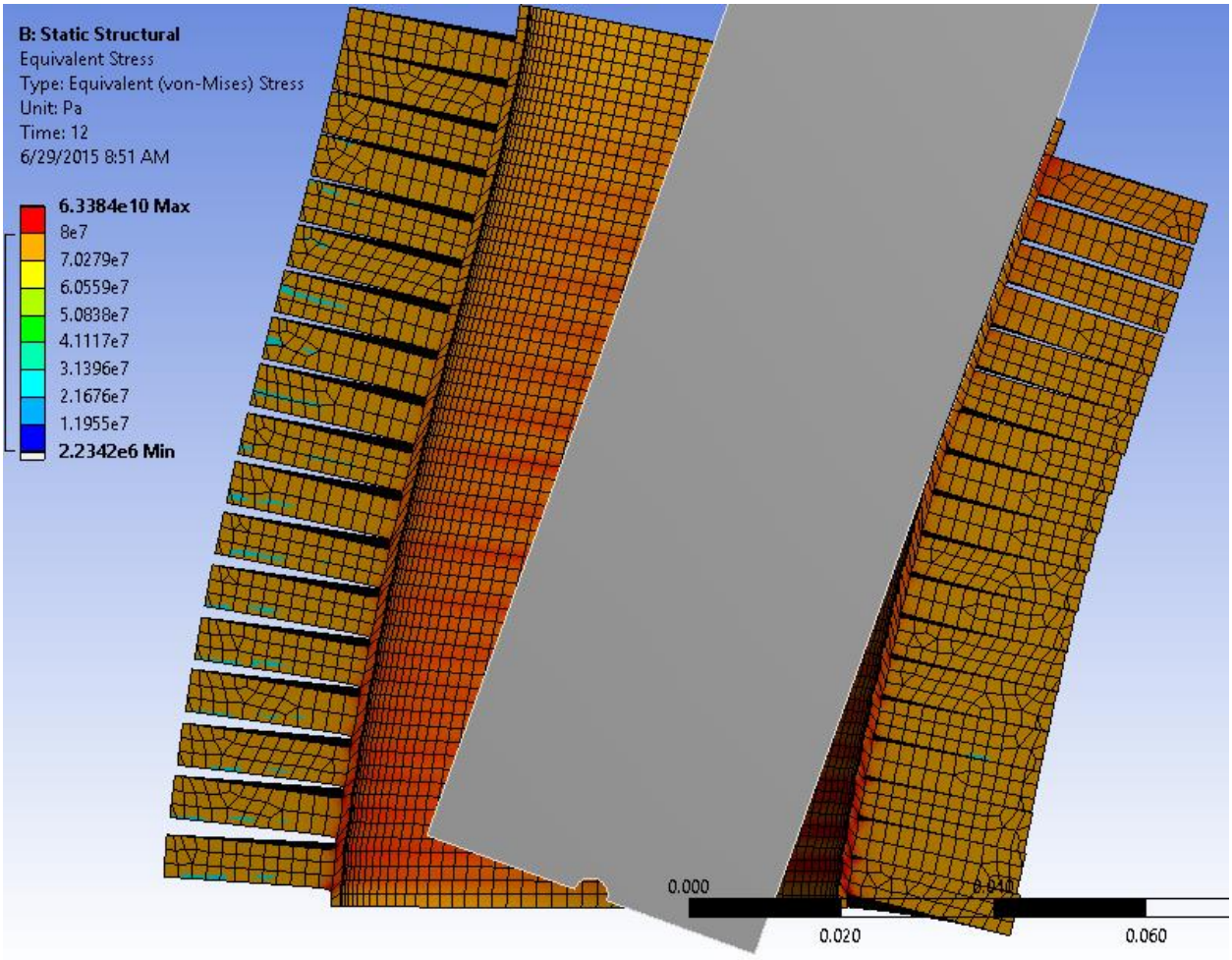

Figure 74: von Mises stress contours for 15° of rotation from first touching point (19.85° from vertical).

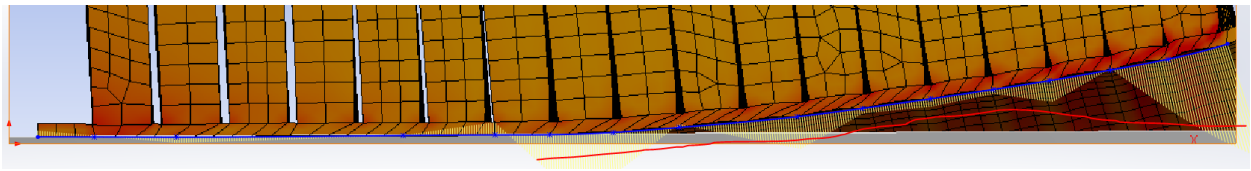

Figure 75: Curvature of one cross-section of annular comb divided into two distinct regions: nearly-straight region of leg-comb contact, and curved region dominated by boundary condition. Yellow lines show curvature magnitude and direction off from blue line, a manual tracing of the overall pattern of the backbone (ignoring the waves in it imposed by the teeth).

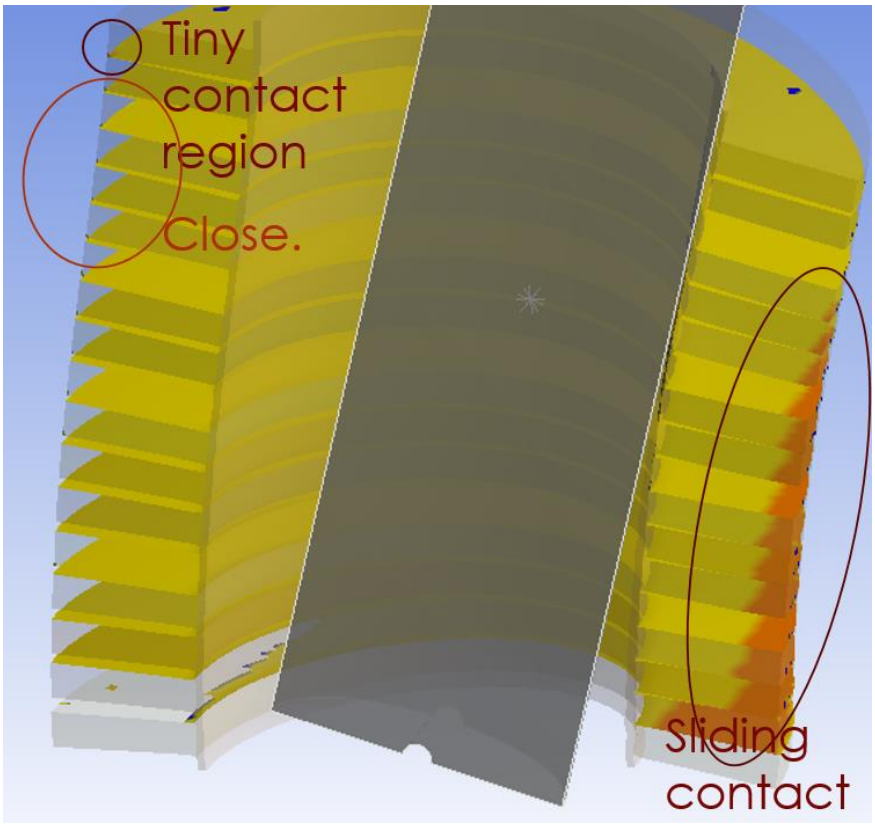

Figure 76: Areas of annular-tooth contact after 19.85° rotation from vertical.

In principle, the contacting deformed geometry of the first annular comb appears serviceable, although it might benefit from changes in tooth thickness or gap distance along its length to produce better tooth utilization. Unfortunately, a quick examination of the reaction moment required to rotate the leg reveals that the structure is extremely stiff throughout the leg's interaction with it and that its stiffness ramps up only mildly (and well before it should). Graph 15 shows the reaction moment for this simulation.

This excessive stiffness may be due to the behavior of the teeth (which, as continuous, thick, large-diameter rings have formidable bending stiffness in their own right) and to the backbone, which may be seeing a significant amount of z-theta shear and a moderate amount of

z-axis compression in some places. Figure 77 and Figure 78 attempt to determine the locations of areas of axial compression: the former shows stresses in the annular comb resolved along the vertical (that is, normal to the base boundary condition, or along the comb's undeformed cylindrical axis), and the latter resolves stresses along the leg's axis after rotation by 19.85° from vertical (i.e. along the segment of the inner backbone edge that is tangent to the leg). Strictly speaking, neither one is a perfect measure of the axial compression (as distinct from bending) stresses: a perfect measure would resolve continuously along the backbone by using a function of its instantaneous direction and radius of curvature, but this would be quite difficult to implement.

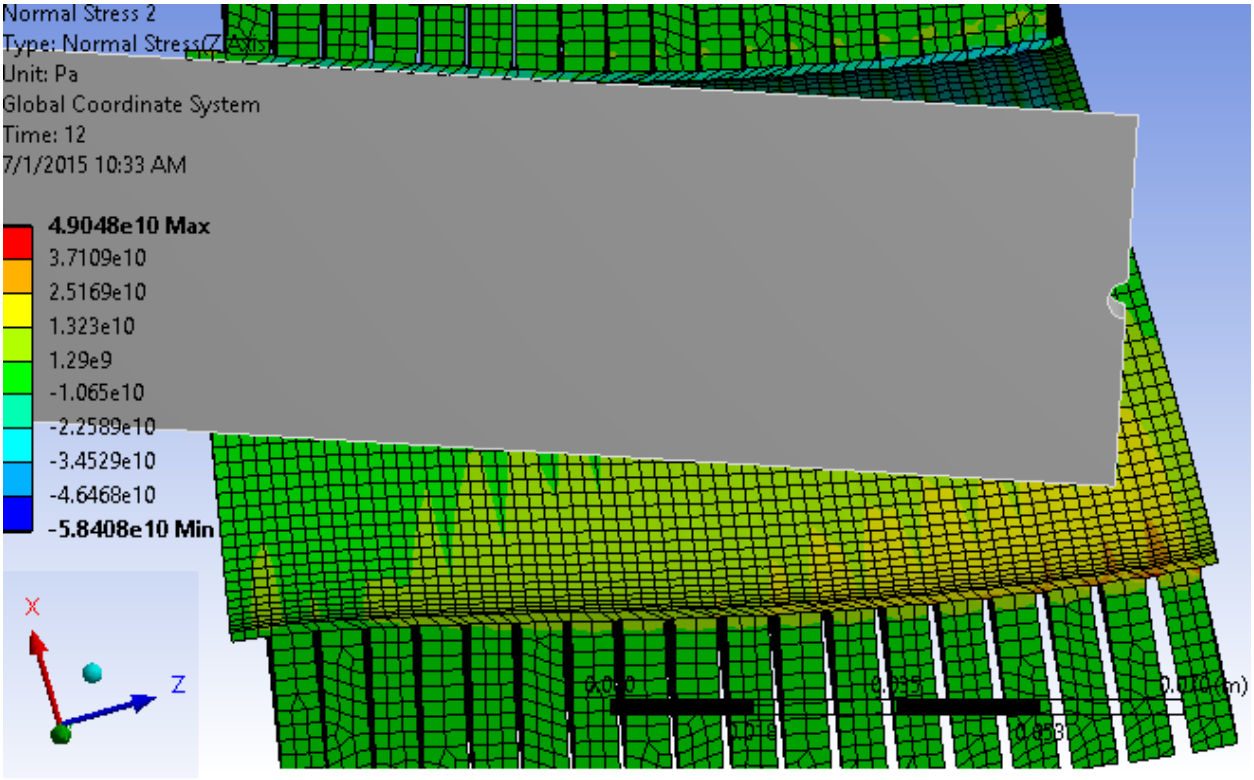

Figure 77: Stress resolved along 'z' axis (shown in blue in lower left). Note that compression is indicated by light or dark blue shading. The side of the backbone contacted by the leg has notable areas of compression; the opposite side features tension. This resolving is most accurate near the base of the comb.

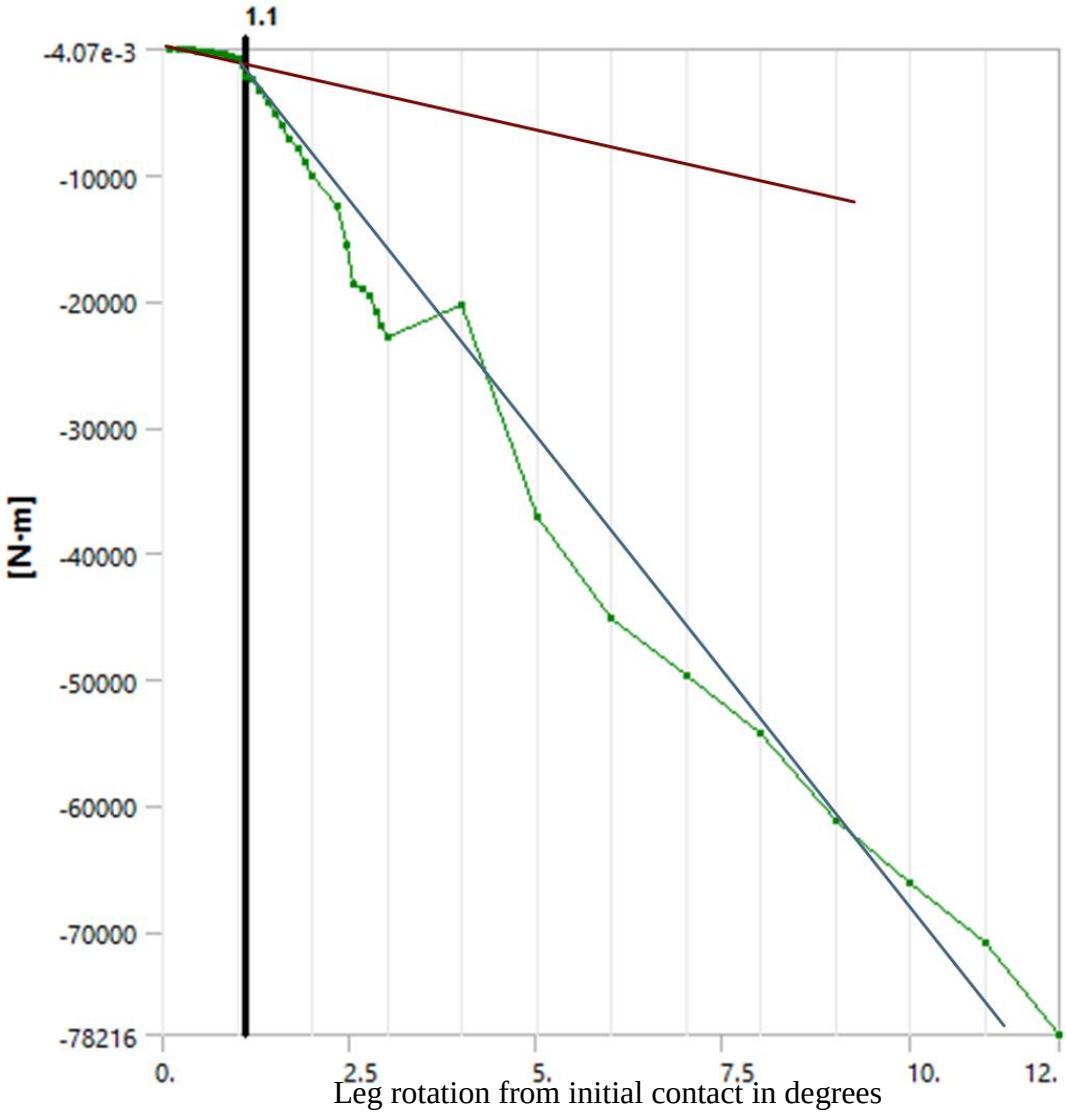

Graph 15: Reaction moment for first annular comb rotated by 12° from the point of initial contact (i.e. to an angle 19.85° from vertical). Note the ridiculously-high moment, and that there is a modicum of lockup, but long before many teeth touch, let alone before the angle that was desired for lockup (pre-stiffening slope is traced in brown, post stiffening traced in blue).

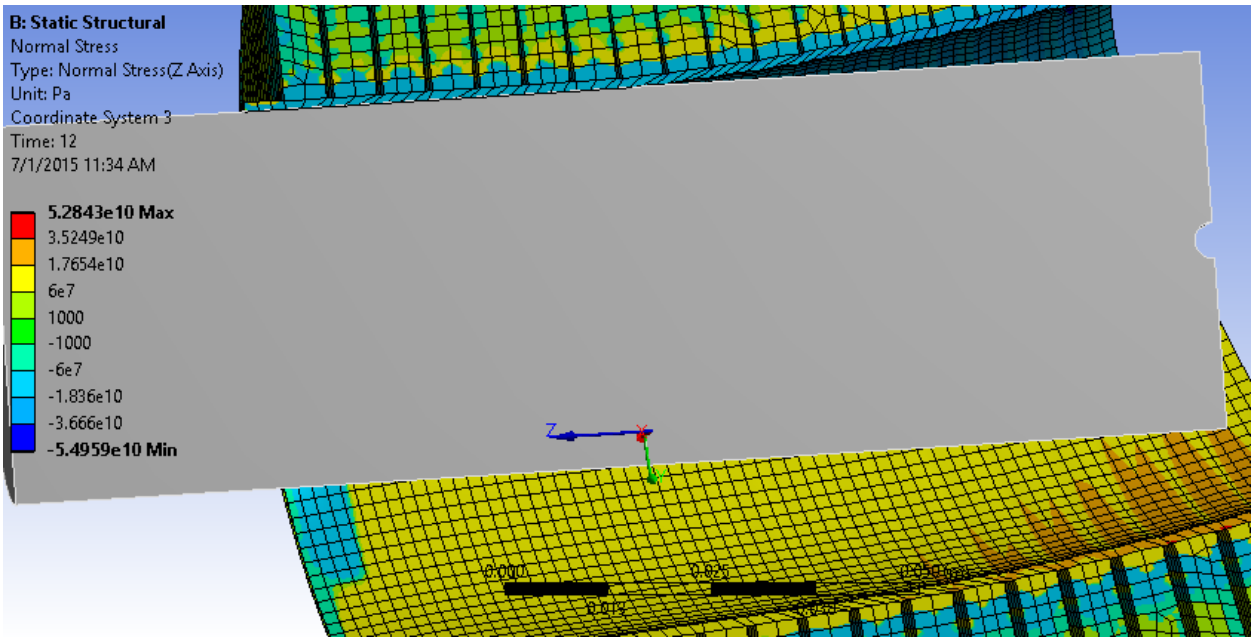

Figure 78: Stress resolved along a different 'z' axis (shown superimposed on top of leg). Stresses resolved in this direction most closely correspond to compressive-axial stresses close to the region of leg-comb contact.

Note that the backbone of this FEA model was assigned a thickness of 1.15mm, about the thinnest value that could be reliably printed solid on our FDM 3D printer (and then only with a special 0.35mm nozzle, smaller in diameter than the typical 0.5mm nozzle: it is the author's experience that wall thicknesses below three nozzle diameters can easily produce random gaps during the print). That said, gaps in the print may be tolerable, in which case smaller wall thicknesses would be feasible. In fact, below this author proposes studying the effects of conscious inclusion of gaps in targeted backbone areas to reduce the contribution of pre-lockup backbone stiffness.

While it adds to print complexity (necessitating dissolvable support material in FDM printing, or alternatively the use of SLS nylon printing), producing interruptions in the annular teeth may prove advantageous towards the goal of minimizing pre-lockup stiffness for a given post-lockup stiffness, for this modification would eliminate the stiffness imparted by a

continuous annular tooth against relatively-localized backbone deformation (which tends to try to expand the tooth along a radial line, which while a bending/shearing deformation of the tooth sees a high bending second moment of area). Figure 79 illustrates this stiffening mode caused by a continuous annular tooth (note the high stresses resolved along one Cartesian axis that correspond to this bending mode—do not confuse this bending mode with a radial stress that would be expressed in cylindrical coordinates), and Figure 80 illustrates an annular comb with radial interruptions in the teeth at a frequency deemed to be a good starting point to interrupt this stiffening mode.

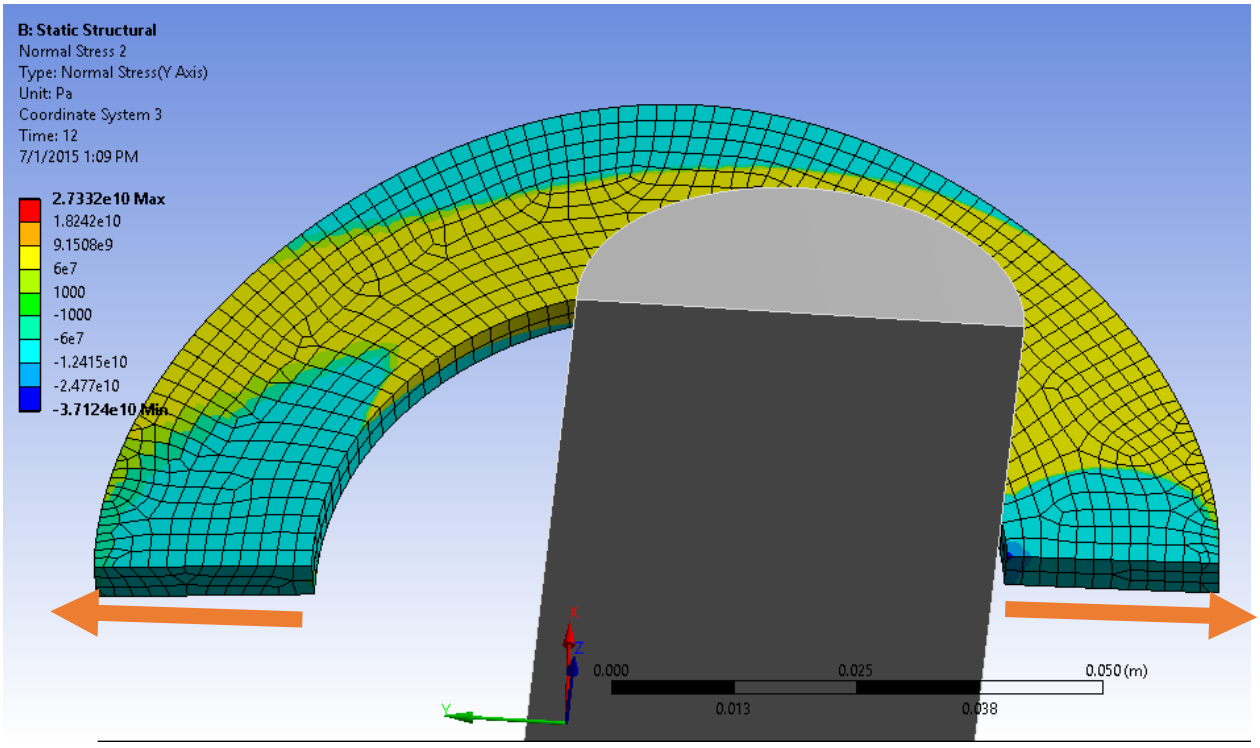

Figure 79: Stress contours as resolved along the 'y' axis, indicated in green (note how high they are). This corresponds to the bending mode of the tooth shown by the large orange arrows. Clearly, this is a stiff mode aligned with a large second moment of area.

Figure 80: Reducing the pre-lockup bending stiffness of the annular comb teeth by radial interruptions.

Another way of reducing pre-lockup stiffness relies upon reducing backbone stiffness by selective material cutouts in the backbone. Incorporating the above idea of radial separations between annular teeth, Figure 81 adds circular holes 'drilled' (strictly speaking these features are to be 3D printed) between the teeth into the backbone. Admittedly, these holes entail only modest material removal and might reduce stiffness to a correspondingly-limited degree; unfortunately, it seems unwise to expand them to the point that they extend into that part of the backbone that formerly contacted a radially-interrupted tooth, for this would be a crack locus and allow the tooth to peel away. Figure 82 illustrates a hole in the backbone of excessive diameter for the chosen radially-interrupted annular tooth size. To further reduce backbone area without facilitating tooth-backbone debonding, making radial cuts into the very centers of the teeth in

one direction and through the backbone in the opposite direction might suffice. Later in this section, backbones of much lower areal density (than that achieved by the inclusion of these modest holes) are considered.

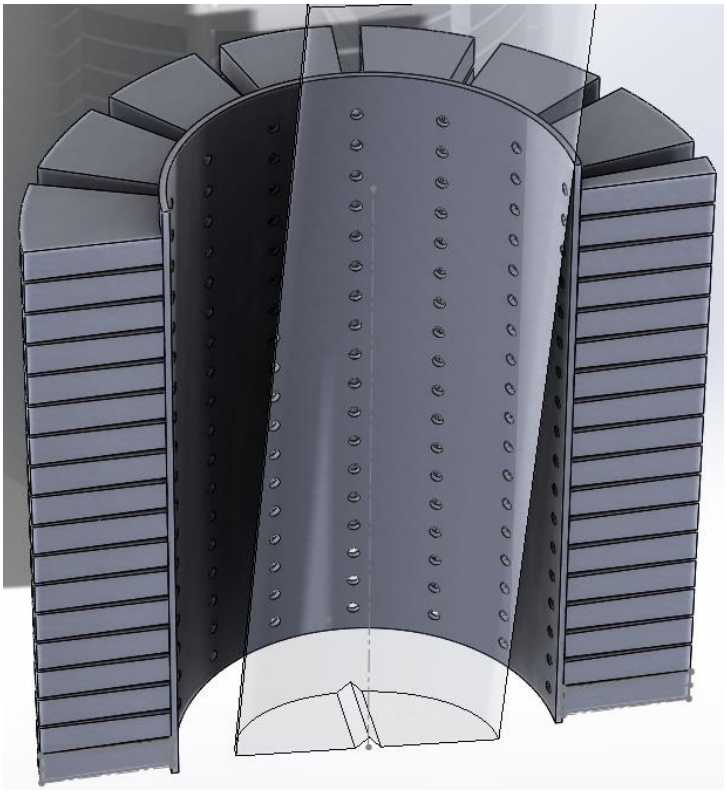

Figure 81: Annular comb with radial interruptions to teeth plus circular holes cut into the backbone at intervals for reduced backbone stiffness.

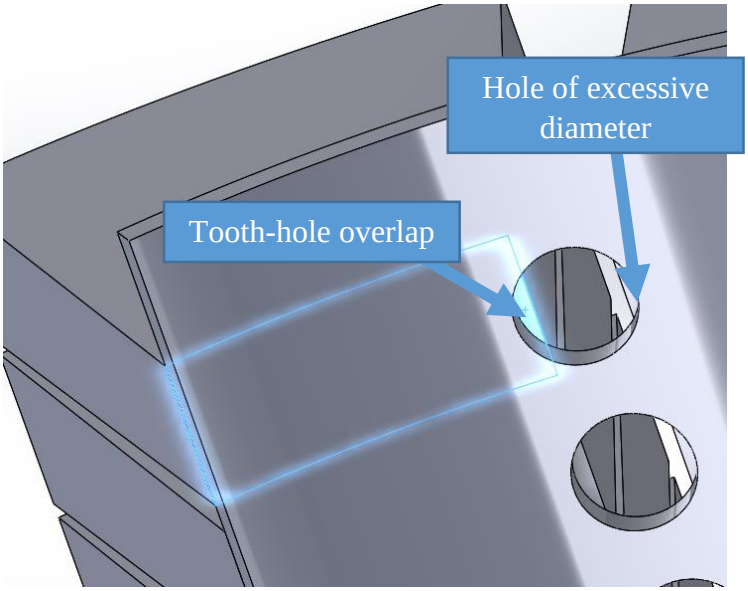

Figure 82: The inadvisability of tooth-hole overlap limits the maximum amount of material that can conceivably be removed from the backbone.

FEA of Basic, Radially-Interrupted Annular Comb.

The radial interruptions appeared to have a largely salutary effect on the comb's mechanical properties, reducing its moment reaction from when few teeth were touching from the massive quantity of tens of thousands of Newton-meters to a couple hundred Newton-meters, as seen in Graph 16. Strangely, the stiffening-up ratio of the original annular comb was far higher and more sudden than the angularly-interrupted comb, although it occurred very early in the deformation and saw massive pre-lockup stiffness, so this second iteration is only an improvement over the first in some respects.

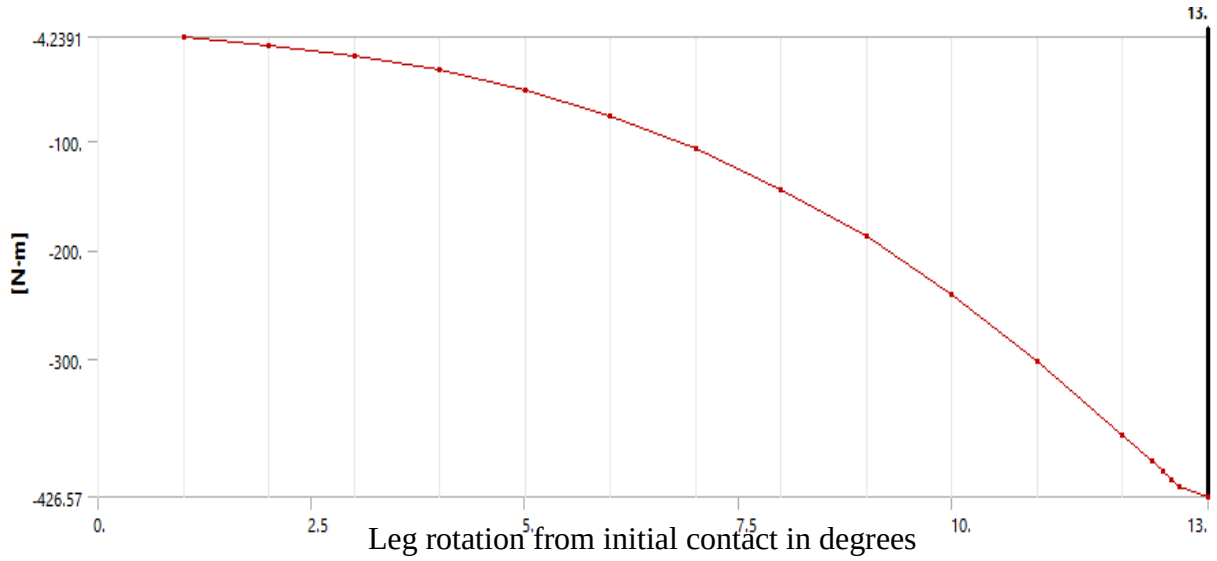

Graph 16: Reaction moment for the first radially-interrupted annular comb. Note that the stiffening is quite gradual, although it does occur. This behavior is far removed from the true lockup behavior that the researcher seeks.

Close-Conforming Annular Comb.

The annular comb embodiment simulated possesses a practical defect in addition to the above mechanical problem: it has a significant offset from the leg that would make it unwieldy and likely to contact something when worn by an athlete. It is thus worthwhile to simulate or construct an annular comb that adheres to the leg much more closely to determine if it will have any freedom *before* tooth lockup, or whether the backbone itself will produce significant stiffness even before tooth lockup due to a high degree of axial compression thereof by the leg. Given the massive stiffness of the first annular comb even before any teeth were in contact (let alone before they all were, the point at which stiffness was desired to instantly ramp up), modifications to the backbone and possibly teeth to reduce pre-lockup stiffness will be extra important for an annular comb that closely adheres to the leg, although frankly a well-offset comb still would be non-functional without them.

To this end, the ellipsoid-cross-section leg was expanded to fit much more closely inside the annular comb, while the annular comb's own geometry was left unchanged. Graph 17 shows the reaction moment for this simulation; Figure 83 and Figure 84 show different views of the geometry.

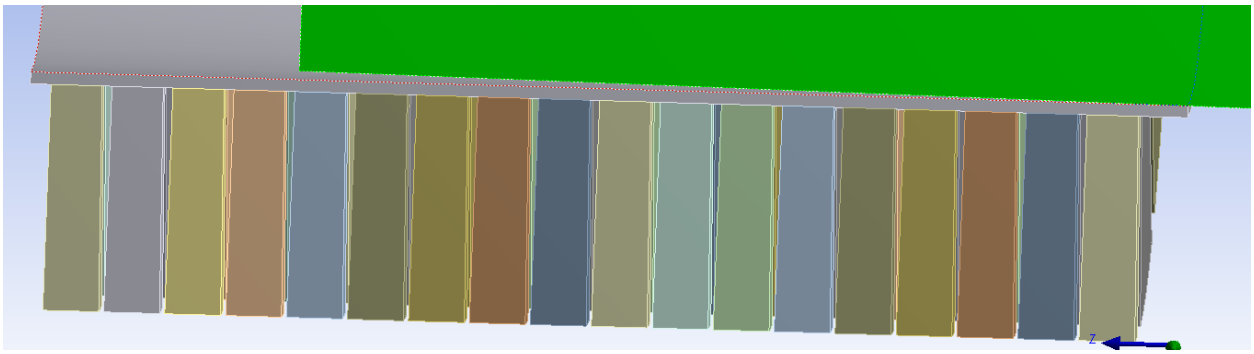

Figure 83: Side view for radially-interrupted annular comb that conforms closely to the leg. The leg is highlighted in lime green.

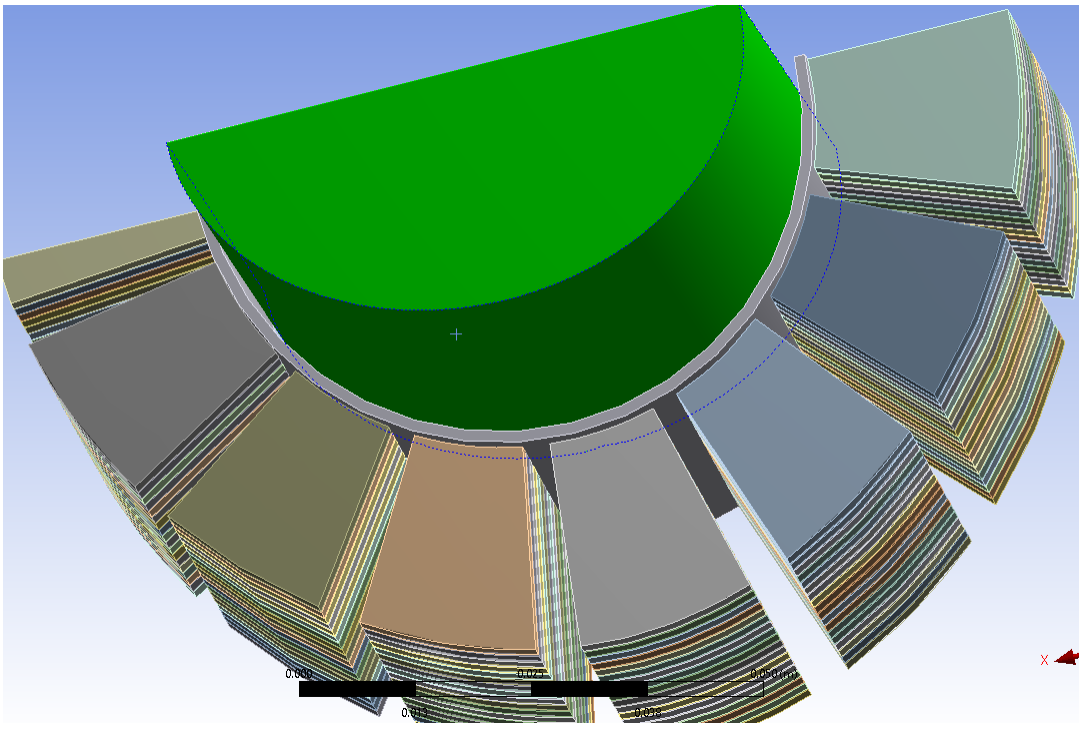

Figure 84: Top view for radially-interrupted annular comb that conforms closely to the leg. The leg is highlighted in lime green.

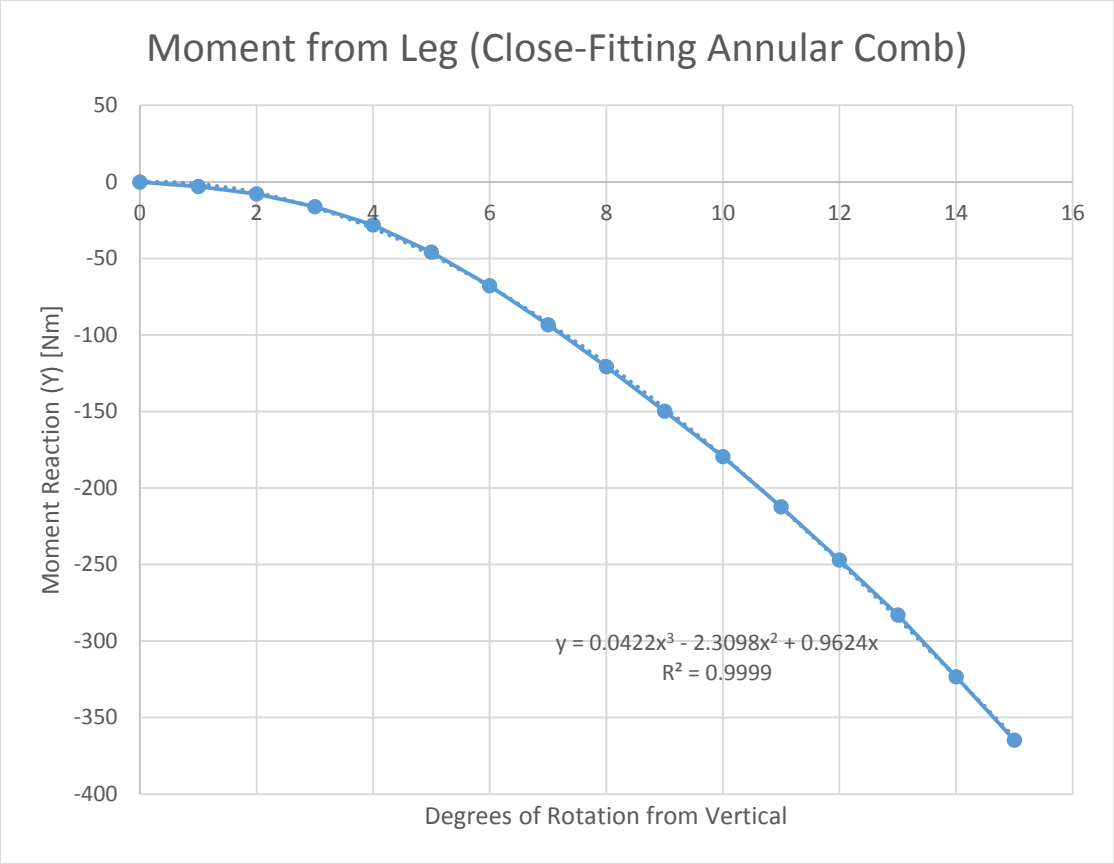

Graph 17:Reaction moment for close-fitting, radially-interrupted annular comb.

Small-Radius, Close-Fitting Annular Comb and Leg Model.

Out of curiosity, the annular comb and leg were both significantly reduced in diameter (while maintaining the structure's height, backbone thickness, tooth lengths, etc.). Potential benefits of this study included improving understanding of how much offset (if any) was required from the "leg", how much vertical (i.e. along the *z* axis) compression would occur in this limiting case, and testing the concept for application to protection of machinery joints (which might have much smaller radii as normalized to arm lengths). The analysis solved successfully, unlike one in which there was no offset distance at all between leg and backbone

(which failed to converge on a single step, despite the absence of friction in the leg-backbone contact).

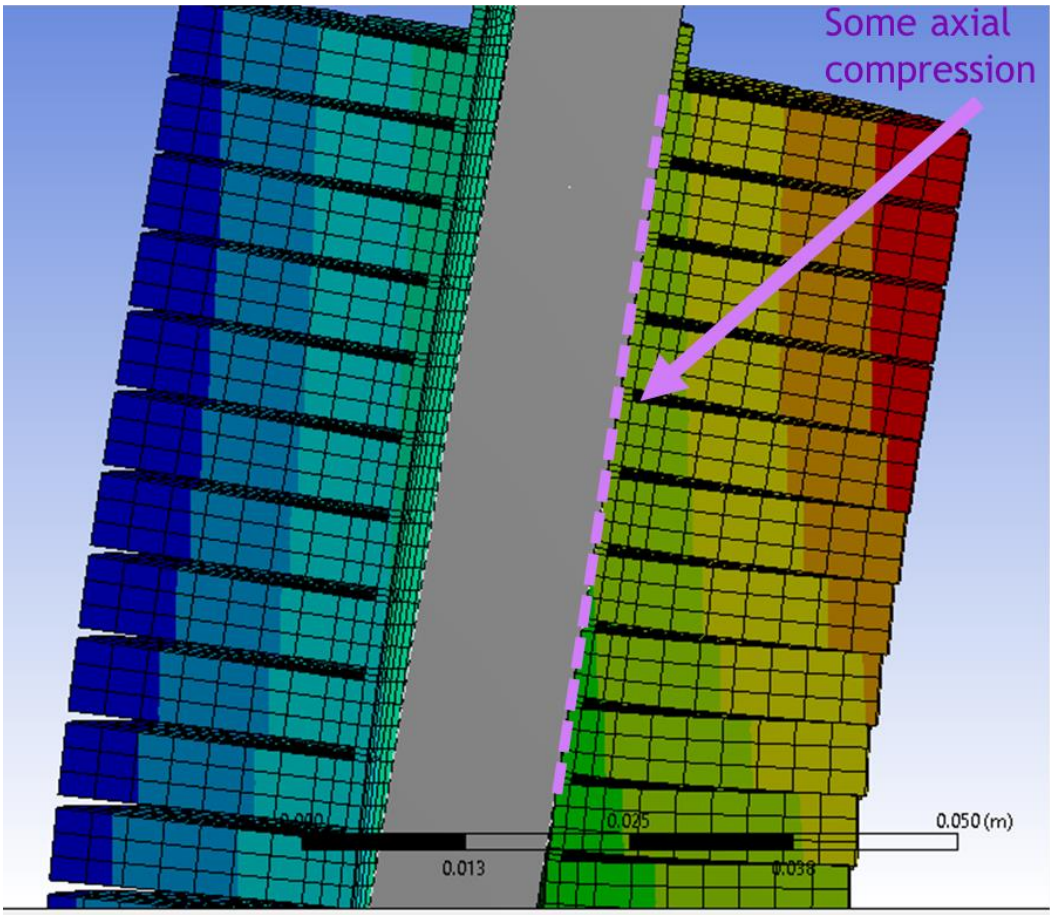

Figure 85: Net vertical displacement from undeformed position of the small-diameter annular comb. Note that green, lime green, yellow, orange, and red indicate negative net displacement (i.e. downwards), and teal is roughly zero. Cyan, light blue, and deep blue are positive. This indicates that, when the structure is in gross bending, there are some areas in vertical compression.

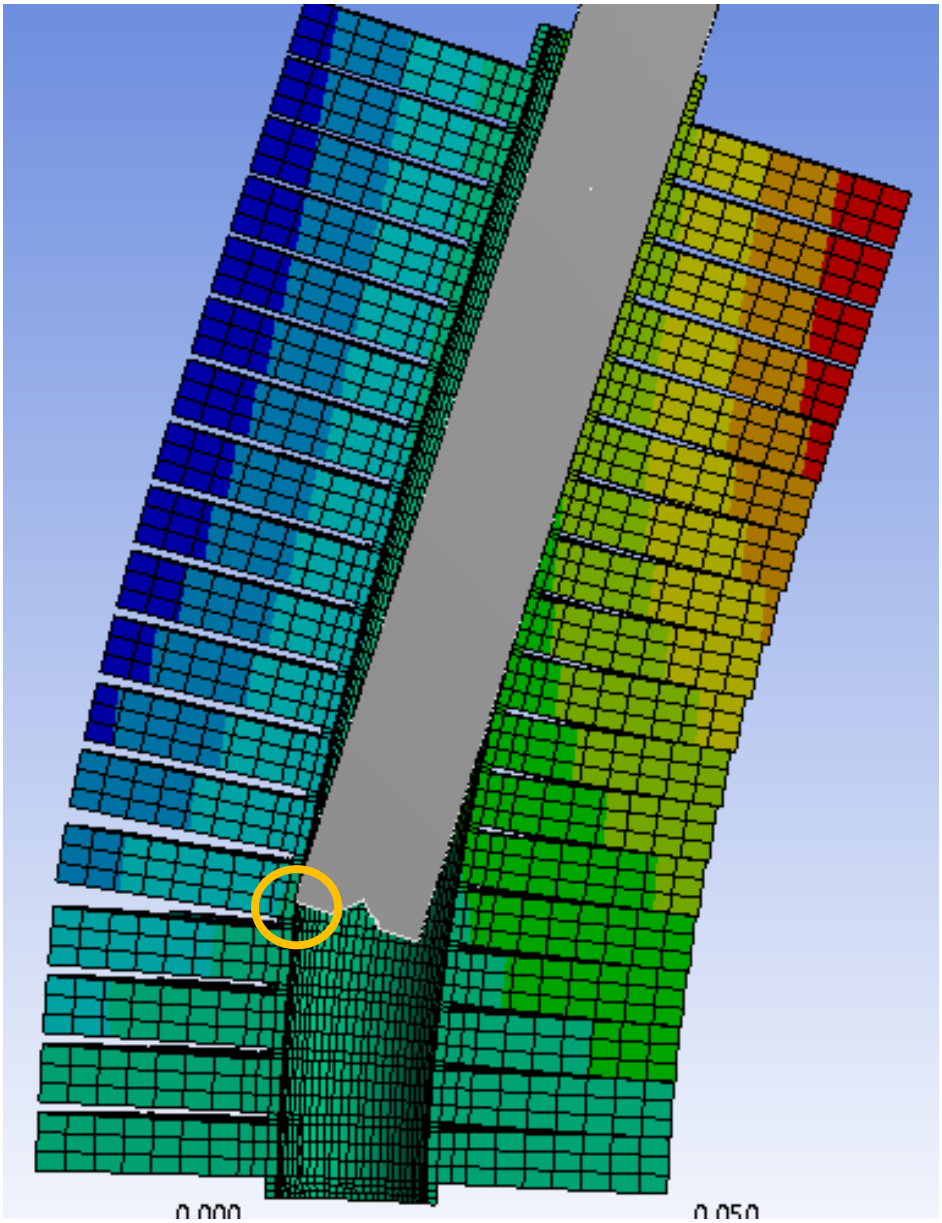

Figure 86: Contour plot of net vertical displacement, overall view. Note that the "leg" contacts the comb at an additional region (to the left, circled in this symmetry view), a phenomenon not observed in the previous close-fitting annular comb study. It may be due to higher curvature in the part of the backbone in contact with the main leg surface (although the circled contact produces a sharp bend in the left portion of the backbone once this contact begins).

As shown in Figure 85 and Figure 86, there is a substantial area of vertical negative deformation from backbone compression (highlighted in Figure 85 with a purple line), and, in particular, this compression allows teeth that are well above the onset of leg-backbone contact to

still contact with each other (note that only the last three teeth in the cross-section are not touching, even though the contact between leg and backbone begins five teeth below the third tooth from the top!).

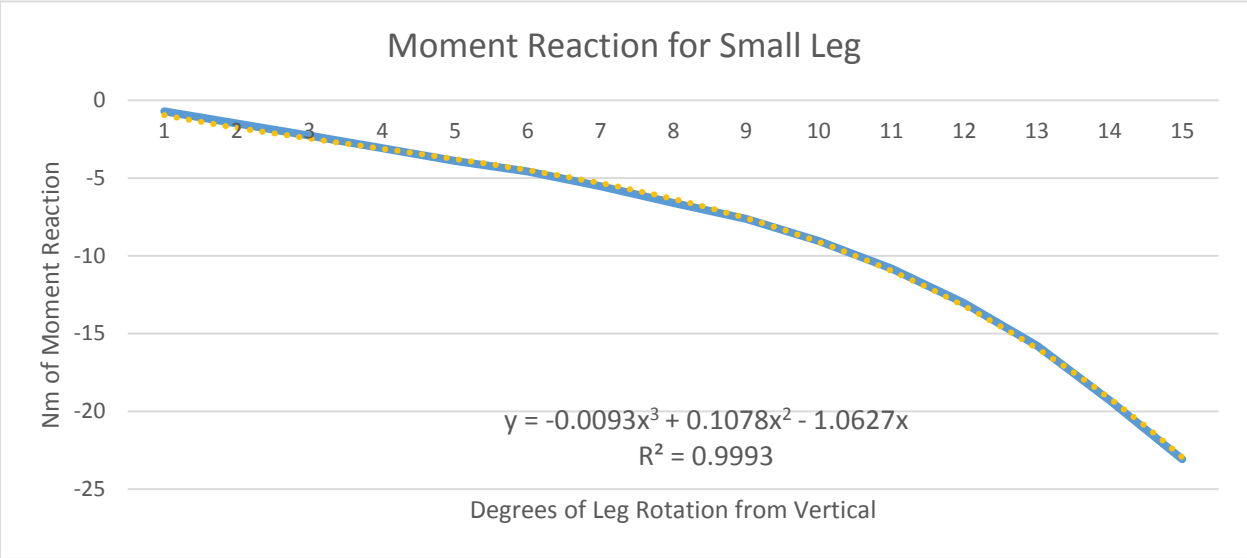

Graph 18: Moment reaction for small-radius, radially-interrupted annular comb. Note that the stiffening effect occurs notably later than in the previous annular comb.

Effects of Tooth Stiffness on Lockup.

After the teeth begin to contact each other, they can produce stiffening in two ways. The first, the most common in these analyses, is when the normals of the contact patches between locked teeth and backbone would intersect if the teeth did not contact and begin to bend along axes radial to the comb's backbone. Next, if the leg rotates significantly before lockup, when teeth finally do lock up, much of the load will be transferred vertically through the teeth, with the backbone playing a minor role; as a result, the bending stiffness (i.e. along a neutral axis radiating from the center of the cylindrical coordinate system defining the annular comb) of the

teeth is of limited importance, but the compressive stiffness of the teeth at their edges is quite important. The first mode dominates when the tooth gaps are small (normalized relative to tooth length, that is) because then the leg rotates only a moderate distance before lockup begins; the second mode dominates when tooth gaps are very large. However, the second mode will presumably still have an impact (however minor) on post-lockup stiffness as long as there is a nonzero component of vertical compression (i.e. the leg has rotated past vertical before lockup begins). Note that elastomer teeth would have relatively low bending stiffness but, if properly constrained to take advantage of their near incompressibility, could have very high vertical-compressive stiffness (i.e. in the second mode)—this would require an extra fixture to prevent radial expansion of elastomer material.

Also note that, in either mode, the teeth stiffen the backbone even when they are not contacting because the backbone cannot bend much at the contact patch with a tooth.

For the application of protecting the ankle and the correspondingly moderate-sized gaps used so far, tooth bending appears significant. For instance, in Figure 85 and Figure 86 in the previous section, despite the presence of some vertical compression of the backbone, the teeth are visibly subjected to bending. As the gaps are made smaller, it is expected that vertical tooth compression will become more influential. Moreover, tooth bending is more relevant where the backbone experiences high curvature—in this case, below the onset of contact with the leg, and above the region whose curvature is reduced thanks to the cantilevered base boundary condition. A rigid top tooth or similar projection might be expected to further promote tooth compression over bending. Finally, note that a couple of teeth *even above* the onset of the contact patch sometimes still come to contact each other (for instance, in Figure 85), although the contact seems compression-dominant, not bending-dominant. In fact, it is the vertical compressive

compliance of the backbone that allows teeth to contact each (although this mode is clearly quite stiff in the foregoing annular combs thanks to their solid backbones; later combs that feature compliant-mechanism-based backbones have even greater compressibility).

The question of the dominance of bending vs. compressive tooth modes is not purely an academic one: answering it would permit the designer to reinforce the teeth in bending or vertical compression with anisotropic composite reinforcement, oriented either along the axis of bending or vertically, between contact points (or both, depending on the load that particular tooth experiences at lockup). However, before such outlandish reinforcement schemes are studied, it makes sense to quantify how much overall post-lockup stiffening can be achieved for a given backbone if the teeth are stiffened significantly. If increased tooth bending stiffness reliably translates into increased post-lockup stiffness, the current problem of low stiffening-up ratio could be corrected simply by somewhat increasing tooth bending stiffness, for instance by using metal or composite inserts (or perhaps reducing tooth length or increasing the second moment of area of the cross-section). On the other hand, if increasing tooth stiffness has moderate to no effect on post-lockup stiffness, some backbone modification would remain the only possible way to make the annular-comb concept viable, and no effort should be wasted on stiffening teeth with composite inserts (no doubt this would massively increase manufacturing costs). Finally, it is conceivable that tooth material could also affect pre-lockup stiffness (more from constraining the backbone at the contact patch, which is a function of the tooth's vertical compressive stiffness, than from the its stiffness in bending); this effect should be evaluated for rough magnitude, for if stiffening the teeth increases the structure's post-lockup stiffness significantly but also increases its pre-lockup stiffness by a similar magnitude, it will be useless.

An easy way to gauge the rough magnitude of tooth stiffness (both bending and bulk compressive) effects on lockup behavior was to simulate the radially-interrupted annular comb with the teeth modelled with linear elastic 'steel' but the backbone still modelled as a stiff (still linear-elastic) nylon; steel is around 100x stiffer than the stiff nylon material model used in these simulations. (Clearly, this model does not accurately simulate bonds between steel and nylon at the tooth-backbone interface, which would likely be weak even with the best-available adhesives. If steel were to figure in an annular comb's teeth, it would probably be surrounded by a nylon body for many reasons including bonding to the backbone, but generating this geometry would be a significant amount of work and not likely to show qualitatively-different behavior). The geometries employed in these two comparison simulations were identical. Figure 87 shows a side view of the teeth directly facing the leg; note that the steel teeth all bend very little even long after lockup, whereas the curvature of most nylon teeth is easily visible at the same amount of leg rotation. Also, as shown in the close-up Figure 88, the lack of bending in the steel teeth caused increased distortion in the backbone at the gaps between teeth.

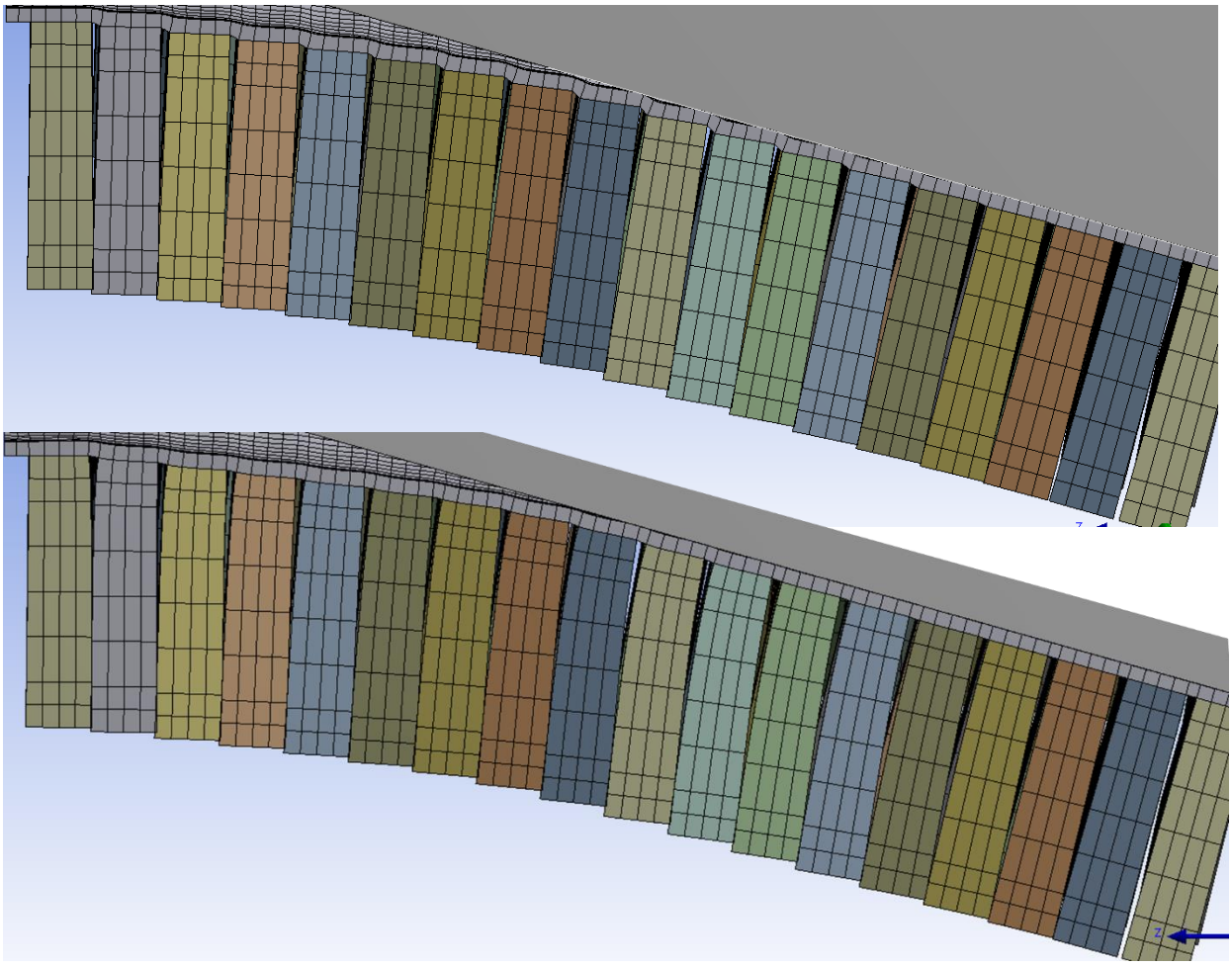

Figure 87: Symmetry view of the nylon-backed annular comb, with teeth modelled as steel (above) instead of nylon as well (below). 15° of leg rotation from initial contact.

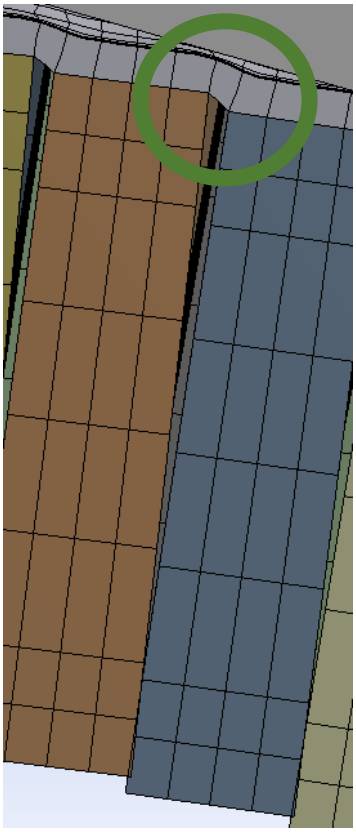

Figure 88: Simulation with steel teeth showing significant backbone straining and shearing where the backbone does not contact the tooth bases.

When the moment reactions for the two simulations are plotted (see Graph 19), it becomes evident that the steel teeth did not massively increase the structure's post-lockup stiffness; the 10,000% increase in tooth stiffness produced only a 100% increase in final reaction moment. Interestingly, stiffening the teeth increased the structure's stiffness even before any teeth were contacting, presumably due to extra constraint of the backbone at the contact patches.

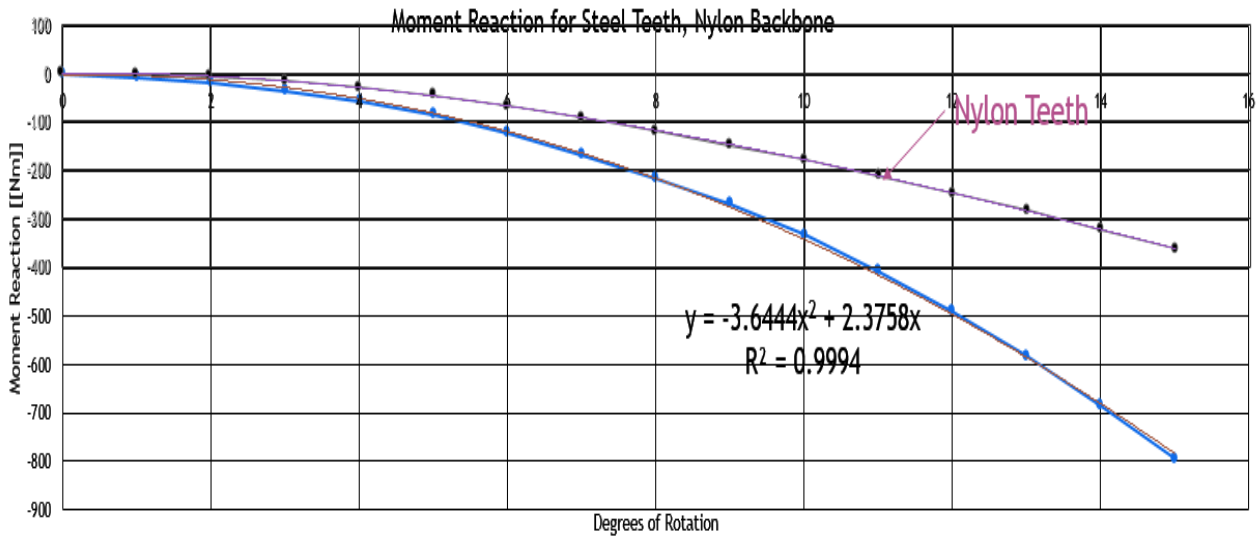

Graph 19: Superimposed plots of moment reaction for nylon-backbone annular combs with either nylon or steel teeth. Note that the nylon-toothed comb is less stiff even when no teeth are touching.

Admittedly, this simple analysis does not resolve the effect of bending vs. vertical compression stiffness. To estimate the magnitude of this differential, it might be expedient to treat the teeth as being unidirectional carbon-fiber laminates, with fibers oriented either in the radial direction (thus maximizing bending stiffness relative to compressive stiffness), or alternatively in the vertical direction. This approach will be employed in the event that the distinction proves important.

Finally, given that stiffness for the steel-toothed, nylon-backed comb was higher even before any teeth were touching, perhaps the contact patch area between backbone and teeth should be reduced in order to limit pre-lockup stiffness. Indeed, larger contact patches seem protective against backbone buckling (which both results from low bending stiffness and further decreases the overall structure's bending stiffness once buckling is begun).

Effects of Solid Backbone (Constrained by Contact Patches) Only.

While radial interruptions were a significant improvement in reducing pre-lockup stiffness, it was still far too high after this modification. To estimate the backbone's contribution to pre-lockup stiffness in isolation (i.e. absent the contacting effects of the teeth, a few of which, as noted above, contacted each other prematurely, long before the desired lockup at 15° of "leg" motion), an FEA study was conducted in which tooth self-contact was ignored. However, because the teeth were still modelled as bonded to the backbone, they could still exert a significant effect on the result by forcing the backbone to conform to their geometry at the points of bonded contact between backbone and teeth. Much to this researcher's dismay, it was found that the contacting teeth only added moderately to stiffness—the nylon backbone was itself far too stiff for this application (for instance, without tooth contacts, the backbone produced 204.5Nm of reaction moment, and the same analysis with tooth contacts enabled saw only a modest increase to a reaction moment of 350Nm!). Indeed, the high recorded reaction moment before lockup occurred *after* some localized post-buckling softening—without this buckling (i.e. if tooth contacts had been active to prevent it, or, less plausibly, if some unbucklable backbone geometry could be devised), the pre-lockup moment would have been even higher! Graph 20 shows the reaction moment over the course of this study, and Figure 89 shows an image of the buckled backbone at the end of the simulation. Note that shell buckling began at around 8° of rotation, precisely when the backbone's stiffness declines somewhat.

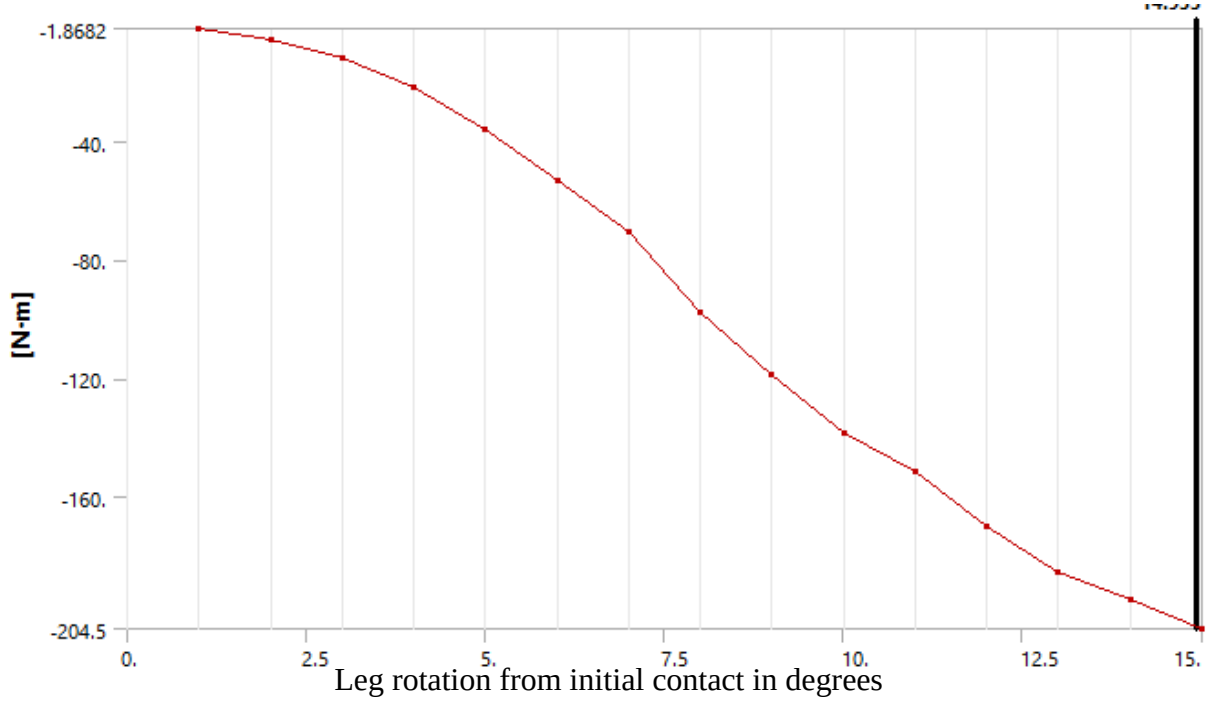

Graph 20: Moment reaction (required at leg) for FEA study in which teeth-self-contacts were ignored, and all stiffness came from the backbone. Plots Nm of reaction vs. ° of leg rotation. Note that this analysis also shows a stiffening-up effect (howbeit one that is much too mild for the intended application).

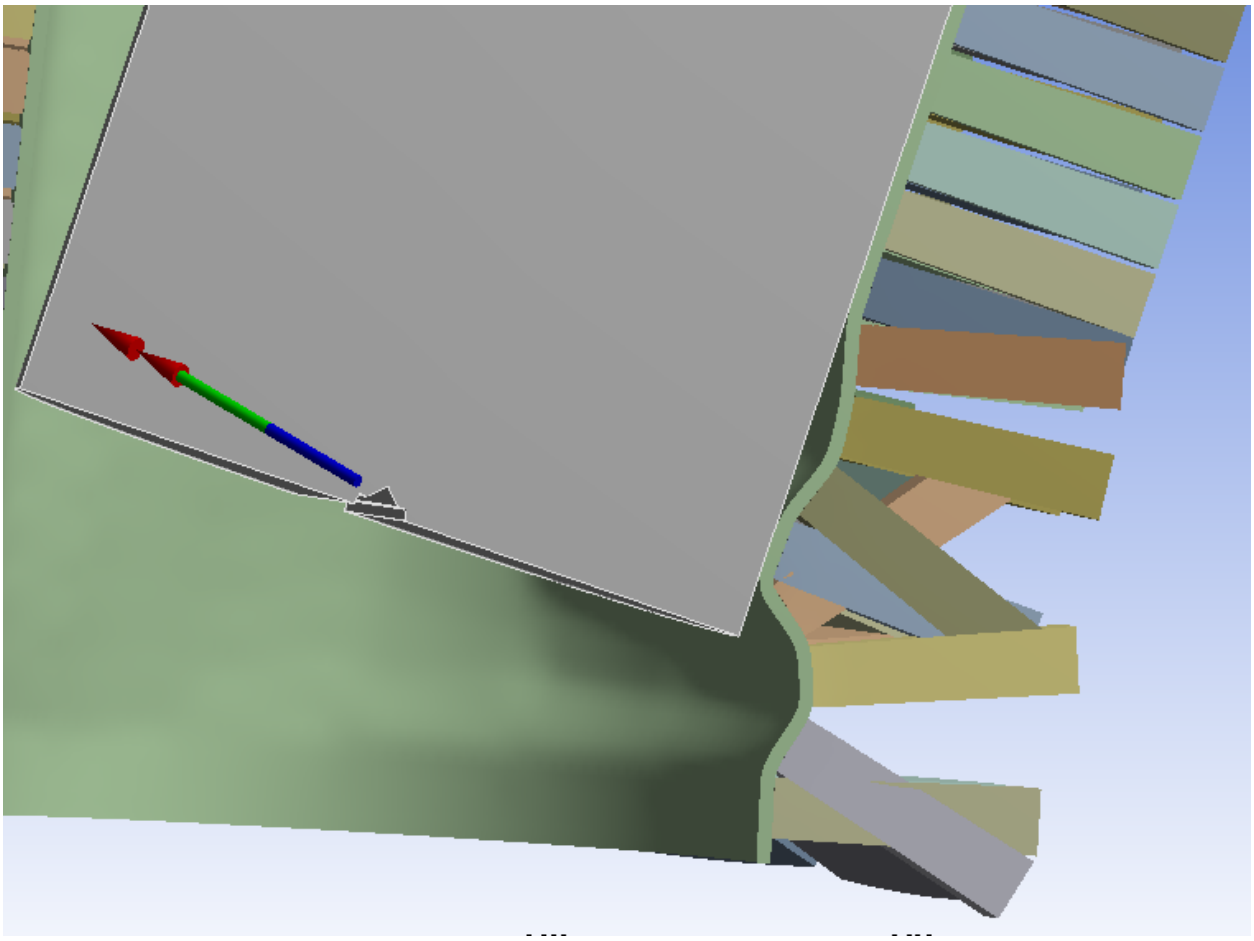

Figure 89: Post-buckling behavior of the backbone that the teeth would have inhibited had their contacts been active. This behavior probably softened the backbone somewhat! This image is from 15° degrees of rotation, but buckling visibly began at 9°.

In the case that these cutouts approach a greater area than that which remains of the backbone, a honeycomb-like low-density structure would be obtained, and this too might be a viable low-stiffness backbone. Specifically, a honeycomb-based backbone could use a geometry that produced either synclastic or anticlastic curvature: note that all known synclastic-curvature materials and mesomaterials are auxetic (although not all auxetic materials have synclastic curvature). Figure 90 explains the difference in curvature, showing two mesomaterials produced by this author with 3D printing: one has synclastic curvature, the other anticlastic. Figure 91

shows an annular comb with a mesostructured, synclastic-curvature backbone; plus, the teeth have been given radial interruptions as considered above. While synclastic metamaterials have special shell and global buckling properties when made into tubes

Figure 90: Honeycomb-like chiral mesomaterials produced by 3D printing, one exhibiting synclastic curvature, the other anticlastic

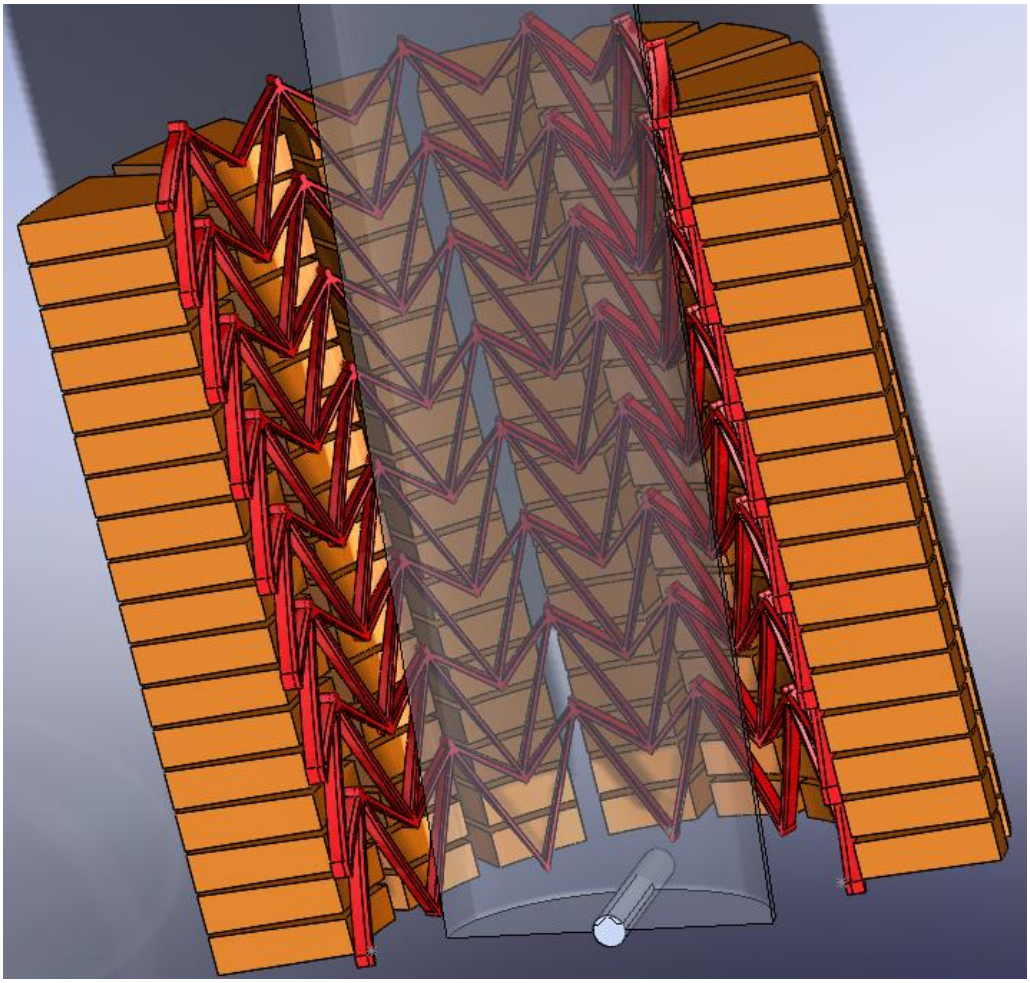

Figure 91: Annular comb with honeycomb-like low-density synclastic-curvature backbone and interrupted annular teeth. Note that the backbone is colored differently from the teeth only for clarity: they need not be made of different materials (although this might prove advantageous—in which case they would be welded or glued together)

Another option to reduce initial structural stiffness is to give the backbone sinusoidal or saw-wave striations, much like a straw designed to bend without buckling in a certain region has such striations in the joint, or as a wire theoretically becomes less stiff when it goes from a straight rod to a coiled, helical spring (i.e. when buckling is ignored!). Of course, the wave amplitude should be carefully controlled to protect against gross buckling. Figure 92 shows a rendering of an annular comb with waves introduced in one direction in the backbone to promote bending without buckling. Note that the contact area between teeth and backbone is very small

in this model; the peaks of the revolved waves in contact with the teeth (but not the opposing troughs!) should be widened to produce larger contact with the teeth, and the teeth could be made more trapezoidal if necessary to maintain a small tip gap distance, even with wider troughs. However, this idea seemed suspect because the backbone would have very low tensile stiffness (much as a spring has lower tensile stiffness than the straightened wire of which it is made), and work on the linear comb showed this is essential, so it was not simulated. Finally, the backbone could be replaced with a piece of tough cloth that (like all fabrics) intentionally buckles in compression, but to which teeth (true annuli or otherwise) could be welded/riveted/glued; this idea is developed in detail in Chapters 6 and 7.

Figure 92: Rendering of annular comb with striated backbone.

Tooth Length Varied with respect to Angle.

One notable problem with even the radially-interrupted combs is that their teeth project out much too far away from the ankle and leg: while the sponsor indicates that prototypes should have a maximum thickness of 0.5cm, tooth lengths approaching 0.9in have been utilized thus far. It was deemed useful to generate and analyze a preliminary annular comb with shorter teeth, at least in the area to the sides of the foot (which would have the most limited real estate); teeth might be kept longer in the front and back (or perhaps solely the front), where more space can be used without increasing the likelihood of hitting one's leg on something. Benefits of maintaining tooth length where feasible include increased lockup stiffness in this direction (although, unfortunately, the plantarflexion/dorsiflexion direction is not the principal direction to protect), and the possibility of also increasing lockup effects from inversion/eversion when the front teeth contact each other tangentially. (That said, even aside from the possibility of a large, protruding device catching on something, there are additional reasons to wish to reduce real estate space taken up, including weight reduction and mass-moment of inertia reduction. Consequently, if tangential lockup did not prove to be very useful, the front teeth might need to be shortened to save weight). Figure 93 shows a top-down view of a preliminary model to study lockup behavior and estimate a good tooth gap for lockup around 15°.

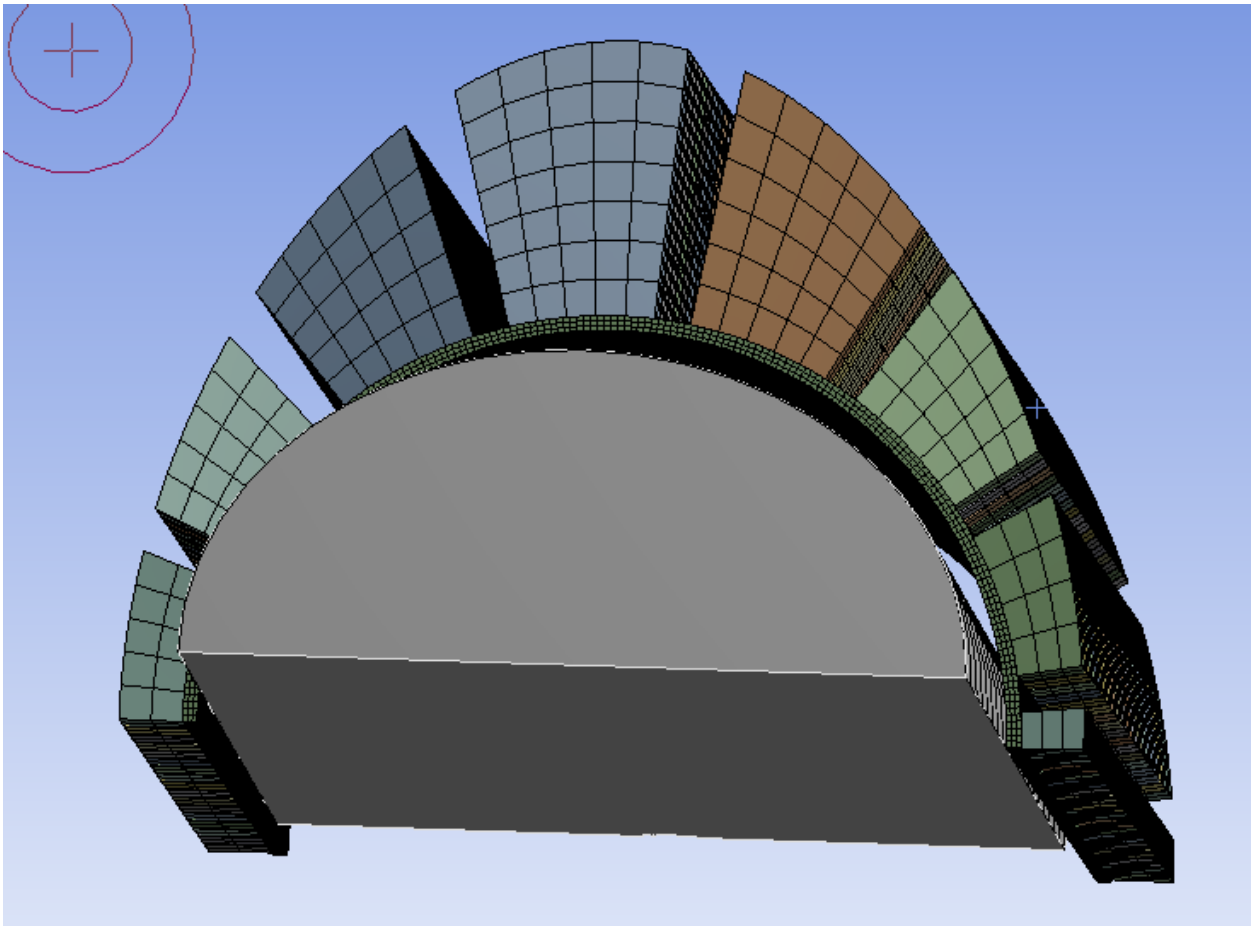

Figure 93: Preliminary annular comb with tooth length varied over cylindrical angle.

A standard static FEA was then performed, yielding the results shown in the following figures. Note that several of the teeth were indeed in contact by the end, indicating that the tooth gap was at least within an order of magnitude correct, though it should be optimized later for faster and more-complete lockup. Also note buckling of the backbone near the gap between third and fourth teeth, and that very little tooth movement occurred above the onset of contact between leg and backbone. Also, as Figure 95 displays, many of the teeth that were around 90° away from the area of leg contact still contacted each other tangentially. Finally, the moment reaction (shown in Graph 21) shows notable instability due to post-buckling behavior (that was corrected for numerically with ANSYS's energy-reduction stabilization feature)

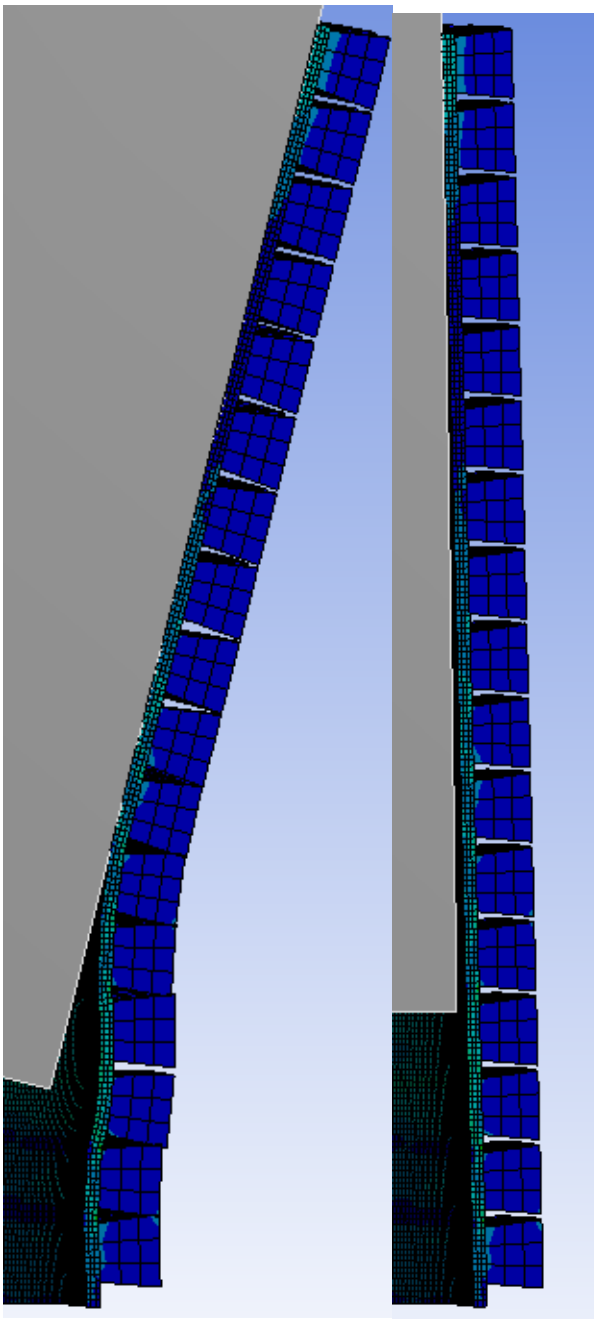

Figure 94: Symmetry view of annular comb with tooth length varied over cylindrical ankle, deformed (by 15° of leg rotation about an axis normal to the page) and undeformed.

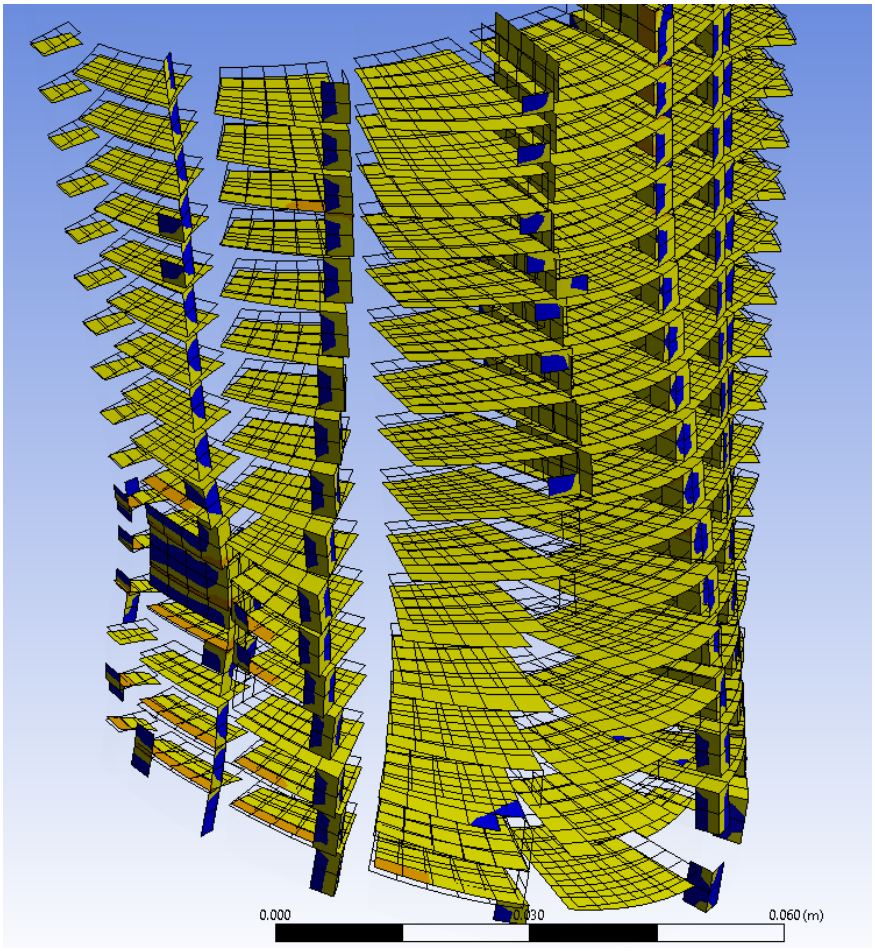

Figure 95: Areas of contact between teeth (for the annular comb with varied tooth thickness as a function of cylindrical angle) are shown in orange.

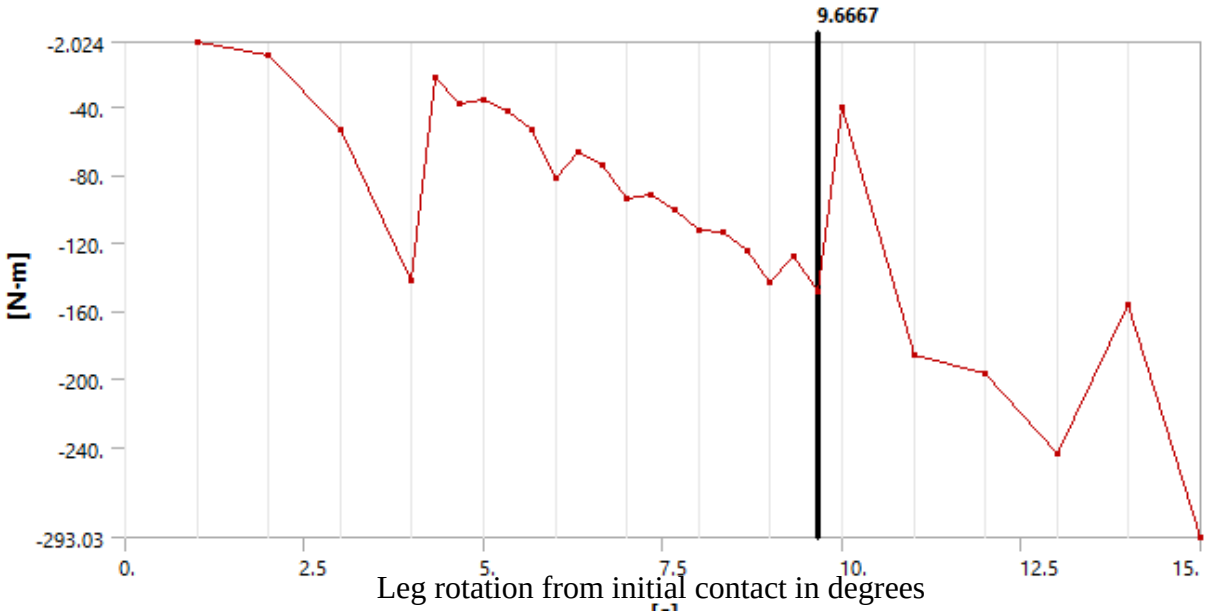

Graph 21: Moment reaction for annular comb with tooth length varied by cylindrical angle. Despite the noise in the data, overall it appears quite linear, indicating that the short teeth had a negligible stiffening-up effect.

Optimizing Lockup of the Basic Cylindrical Leg and Annular Comb System.

Although the real human leg has many mechanical features that distinguish it from the model used thus far – principally the coupled motions of the subtalar and talocalcaneal joints, and the flared shape imparted by the calf muscle – it was deemed advisable to continue using this highly-simplified model to produce a proof of concept in which lockup was significant and rapid. Up to this point, even with the radial interruptions in teeth, lockup magnitude had been quite moderate and gradual, and, in particular, pre-lockup stiffness has been far too high, resulting in wasted energy and changed joint feel inside the safe zone.

The first attempt to make lockup occur more rapidly entailed increasing or decreasing the vertical gaps between two teeth proportionate to the angle at which they originally came in contact, with the goal of producing lockup as close to 15° as possible (for instance, if the gap between teeth X and Y closed at 10°, the gap would be increased in size by 50% in an attempt to

cause it to close at 15°). In addition, the radial gaps were generally increased since radial contact originally occurred too early. With these changes, simulations were re-run (maintaining backbone geometry, etc.). It was understood that nonlinearities (mainly the sudden local stiffness from teeth locking up, as well as potential softening, postbuckling behavior) would necessitate running this optimization process many times before an optimum rate of lockup could be achieved. Since the goal was to optimize a stiffening-up ratio (instead of more common FEA optimization objectives like maximizing stiffness vs. weight) and an algorithm appropriate to this goal was unknown in ANSYS, the process was done manually (i.e. tooth gaps were updated based on the results of the previous iteration, then the model was remeshed and analyzed again).

Despite the known limitations of a solid backbone (i.e. excessive pre-lockup stiffness), it was determined to attempt this process first with this most basic of backbones (due to the simplicity of meshing), and if the process proved effective by producing significant and rapid lockup, then it could be used to produce a similar magnitude of lockup with a backbone that is less stiff. While some "metastructured" backbones (e.g. those with special bulk, shear, or auxetic macromechanical properties in accordance with the concepts mentioned in Chapter 2) might experience qualitatively-different behavior and thus require different tooth gaps for optimal stiffening up, the process of optimization itself should be transferrable.

First Iteration.

Figure 96 and Figure 97 show various views of the undeformed geometry of the annular comb produced by the first iteration of the above optimizing process; note the increased vertical tooth gaps at the base and reduced vertical tooth gaps at the top. Also note the increased radial tooth gaps.

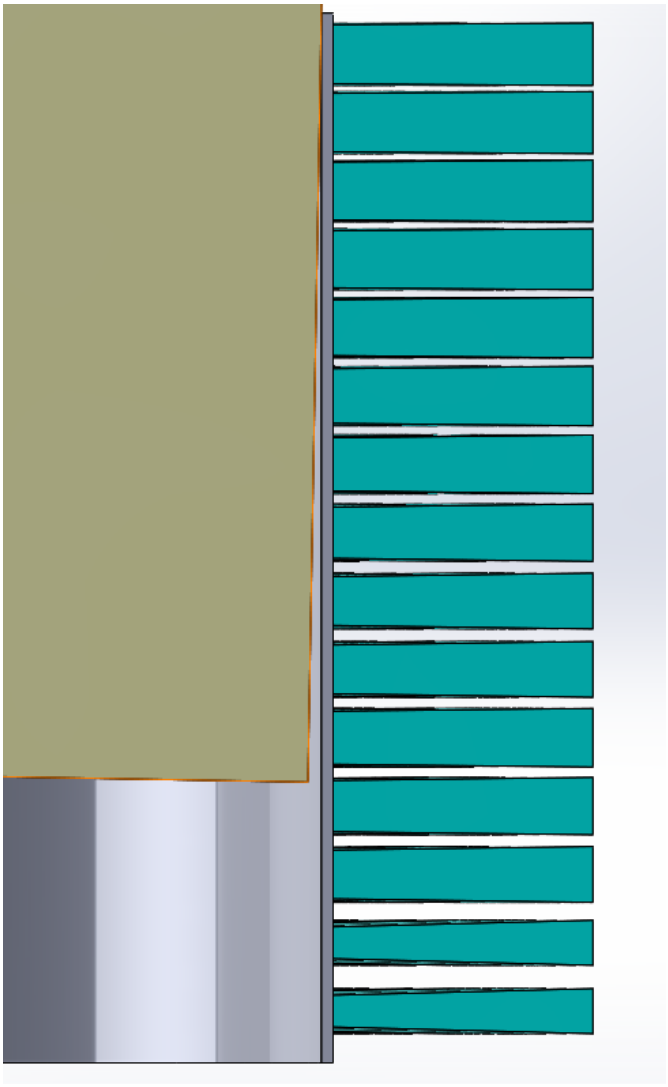

Figure 96: First iteration of increasing/decreasing tooth gaps selectively to make lockup more sudden. Symmetry view.

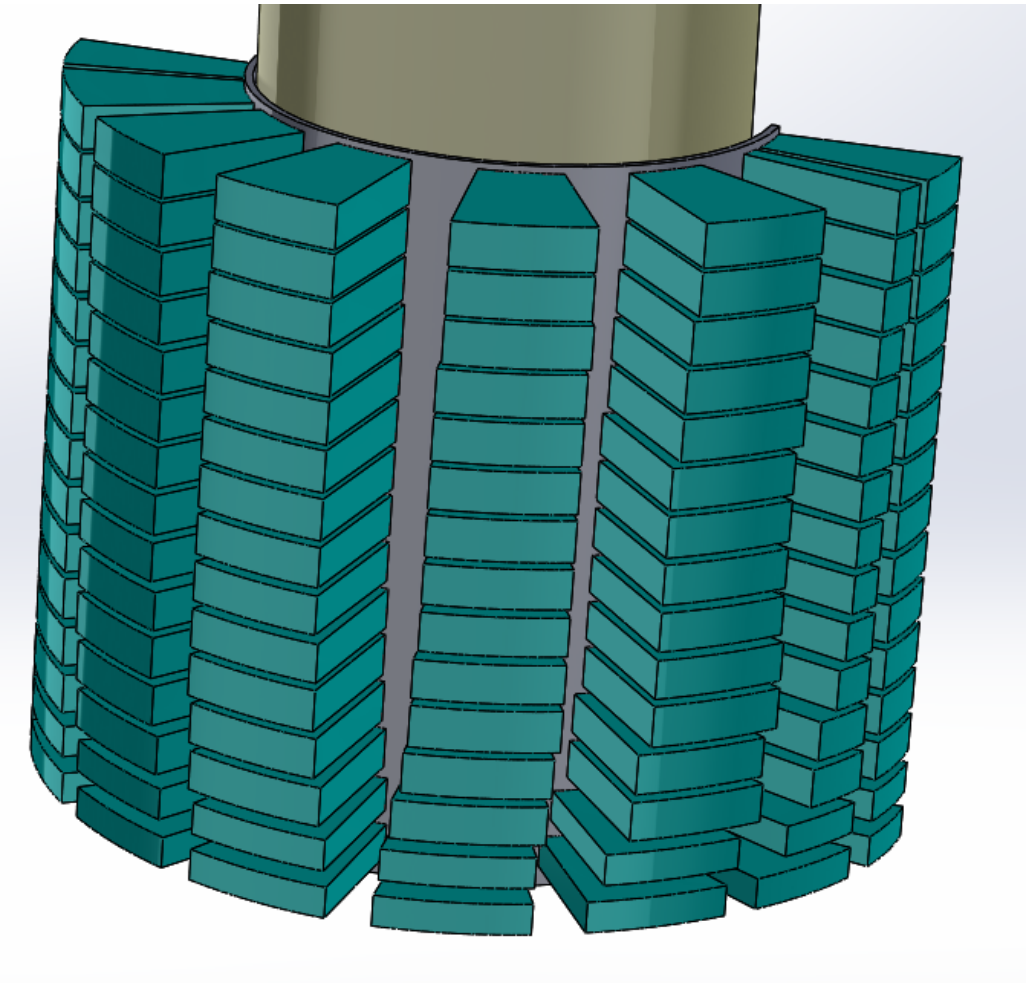

Figure 97: First iteration of altered tooth gaps, oblique view (see also: previous figure). Note that radial gaps were also increased nearly everywhere.

However, as shown in Graph 22, the first iteration of the process produced results that were far from perfect, with stiffening up of limited magnitude, slow, and starting earlier than desired. As visible in Figure 98, many but not all of the teeth in the set lying in the symmetry plane (i.e. those directly facing the leg motion) were touching by 15° of leg rotation, although the backbone had buckled inwards slightly around the second annular row from the bottom.

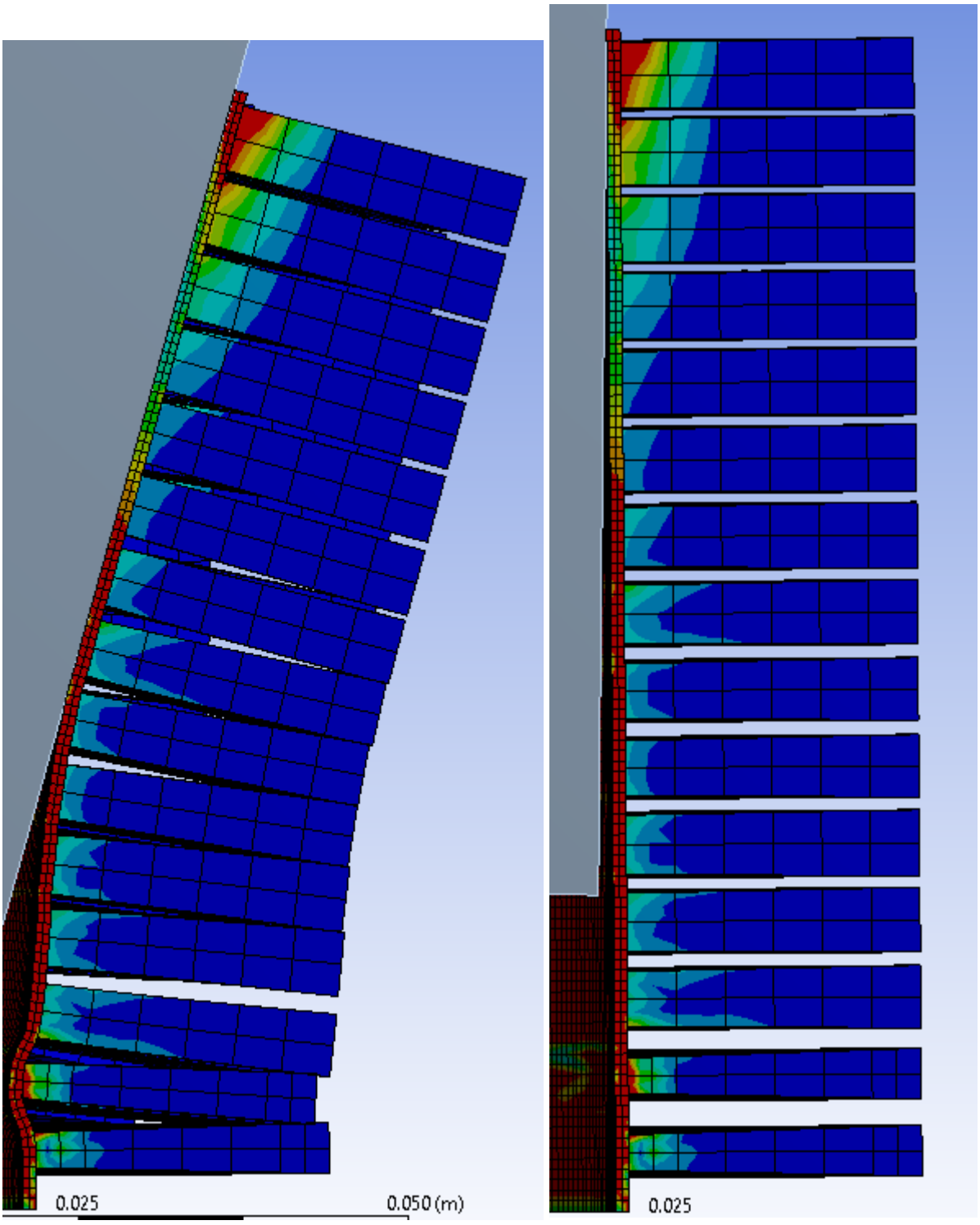

Figure 98: Side, sectioned view of annular comb after 1st iteration of the optimization process, deformed (left) and undeformed (right) for comparison, with contours of von Mises stress plotted.

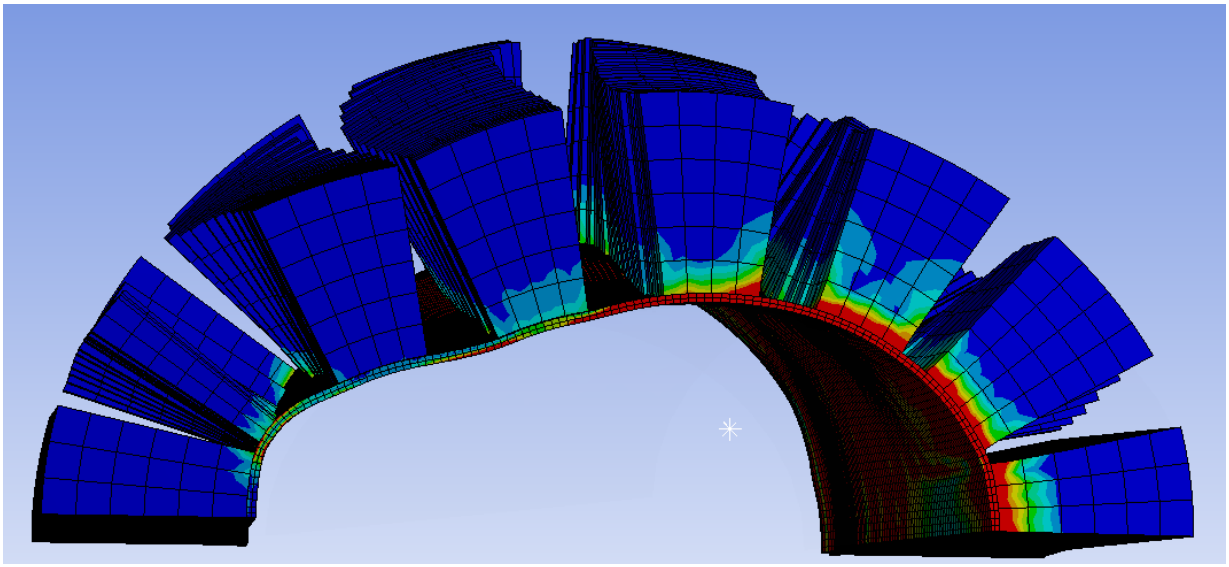

Figure 99: Top view of annular comb after 1st iteration of optimization process, deformed after 15° of leg rotation from initial contact, with contours of von Mises stress colored.

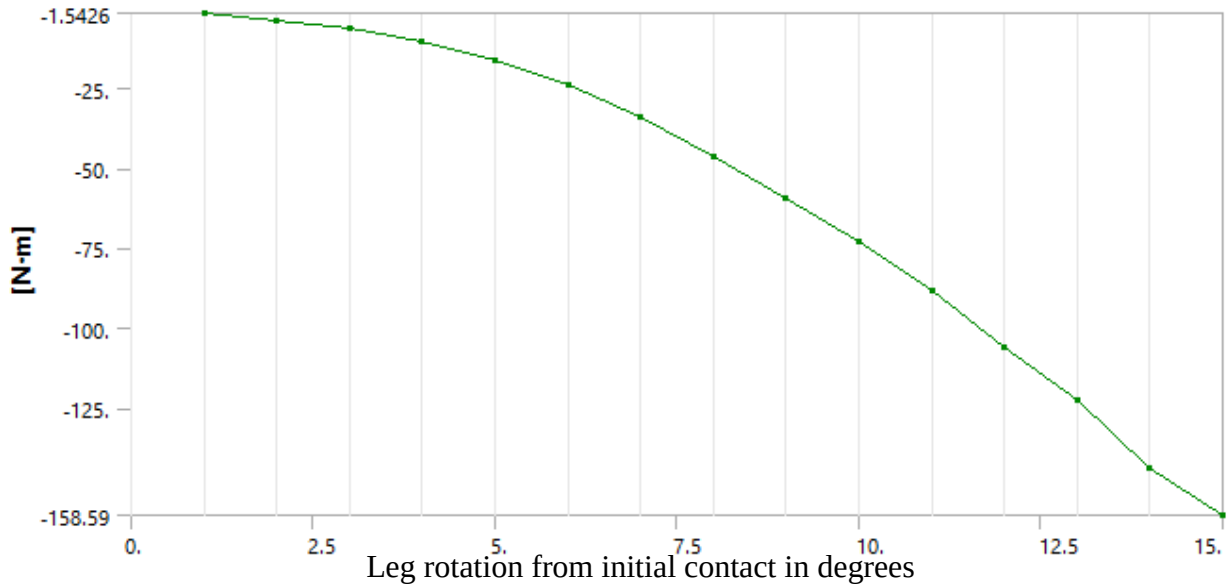

Graph 22: Moment reaction for annular comb after iteration 1 of the optimization process.

Iteration 2.

Given the imperfect behavior of the annular comb after the first iteration, the process was repeated, generating the geometry shown in Figure 100; the process again resulted in reductions

in vertical tooth gaps above the contact patch and increases in the gaps below it. However, it did not succeed in bringing all of the teeth into lockup at 15°, and in particular, the process seems to be biased in favor of excessive gap distance for teeth at the very base of the annular comb. Also, in an attempt to eliminate backbone buckling, the base areas of the teeth were increased; while this was indeed successful in preventing backbone buckling (at least at 15° of leg rotation) it likely also accounts for the increased stiffness (both pre-lockup and post-lockup) that this annular comb saw, as the moment reaction curve (shown in Graph 23) illustrates.

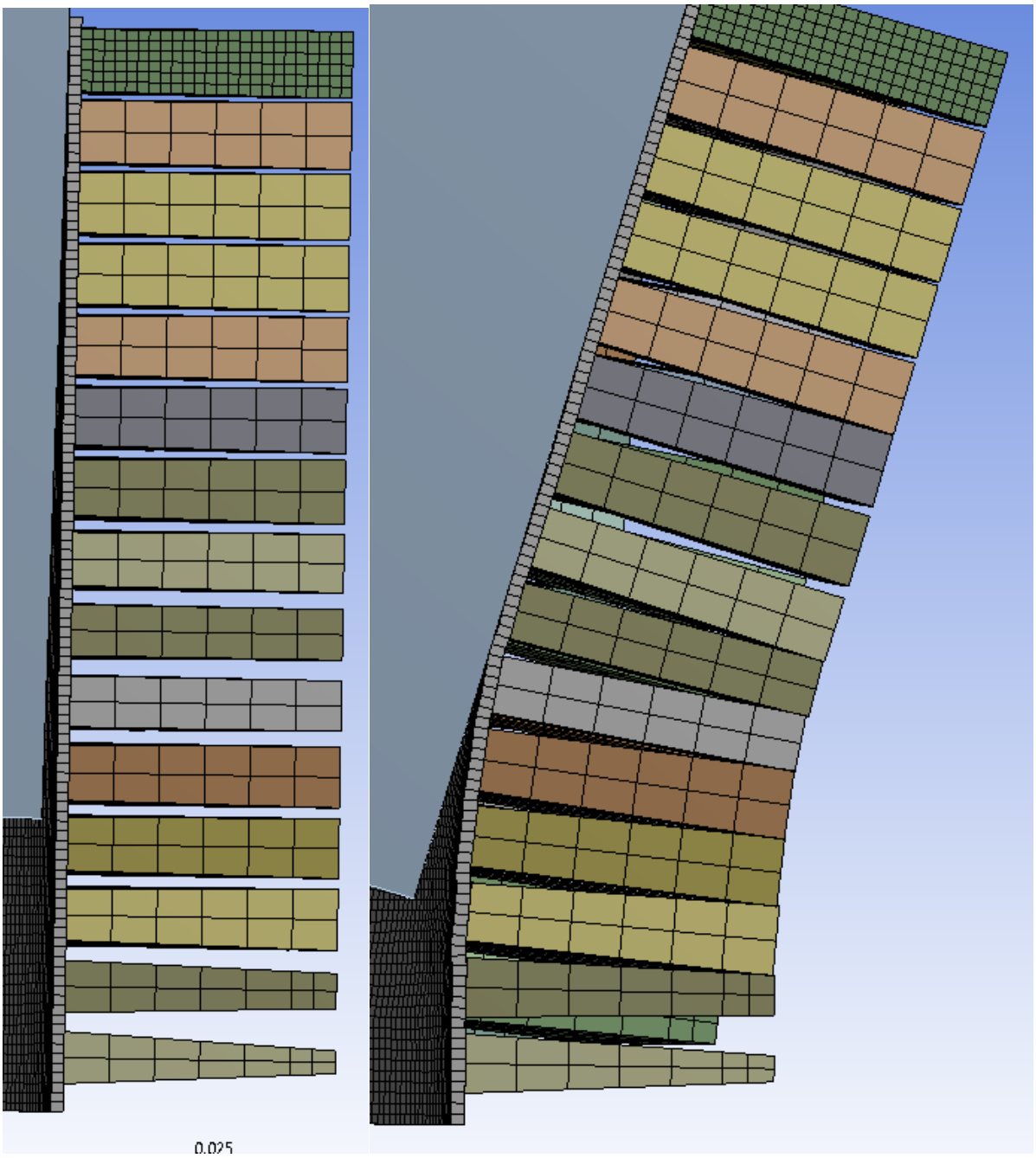

Figure 100: Second iteration of process attempting to produce instantaneous lockup, undeformed (left) and deformed (right) in the symmetry plane.

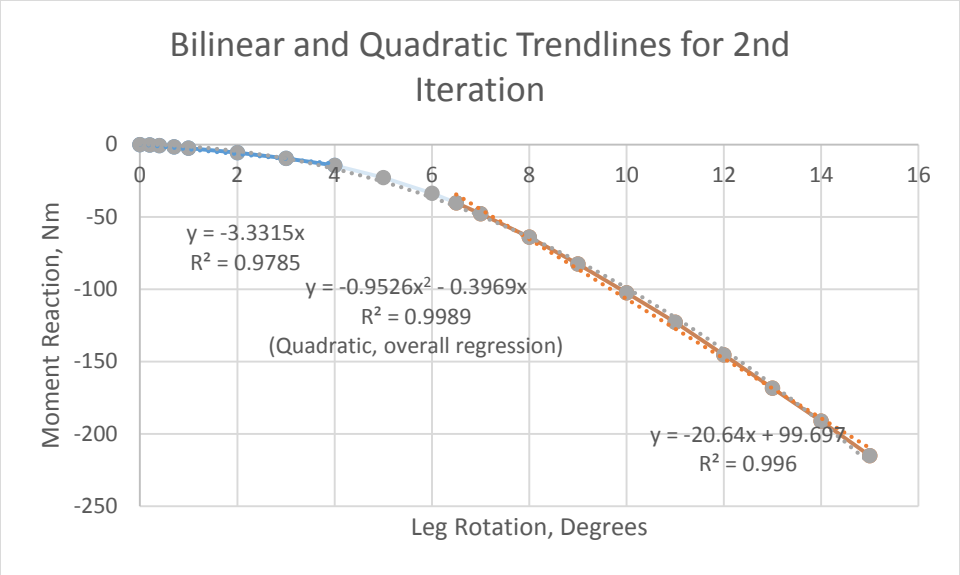

Graph 23: Moment reaction for annular comb after 2nd iteration of optimization process with bilinear trend lines with a slope ratio of 6.2x, centered around 5°. Quadratic regression for the entire range may be more accurate (though less accessible to the reader); it shows stiffness at 15° is 49% higher than that at 10°.

Third Iteration.

Despite some reservations about the effectiveness of the iterative process, it was decided to continue it for a couple more iterations. Deformed and undeformed views of the geometry for this third iteration are shown in the symmetry plane are shown in Figure 101; note the continued tendency towards decreasing tooth gaps above the onset of leg contact. The considerable noise in the moment reaction (plotted in Graph 24) near the end of the simulation is likely due to the shell buckling of the backbone that can easily be observed in the deformed results. Unfortunately, the stiffening up ratio in this iteration was only 5.45x, smaller even than that of the previous iteration (6.2x), and still occurred far too early (with onset near 5°, about the same onset value as in the second iteration); presumably, shell buckling of the backbone reduced post-lockup stiffness somewhat, doubly so since the buckling tendency was to open teeth rather than close them.

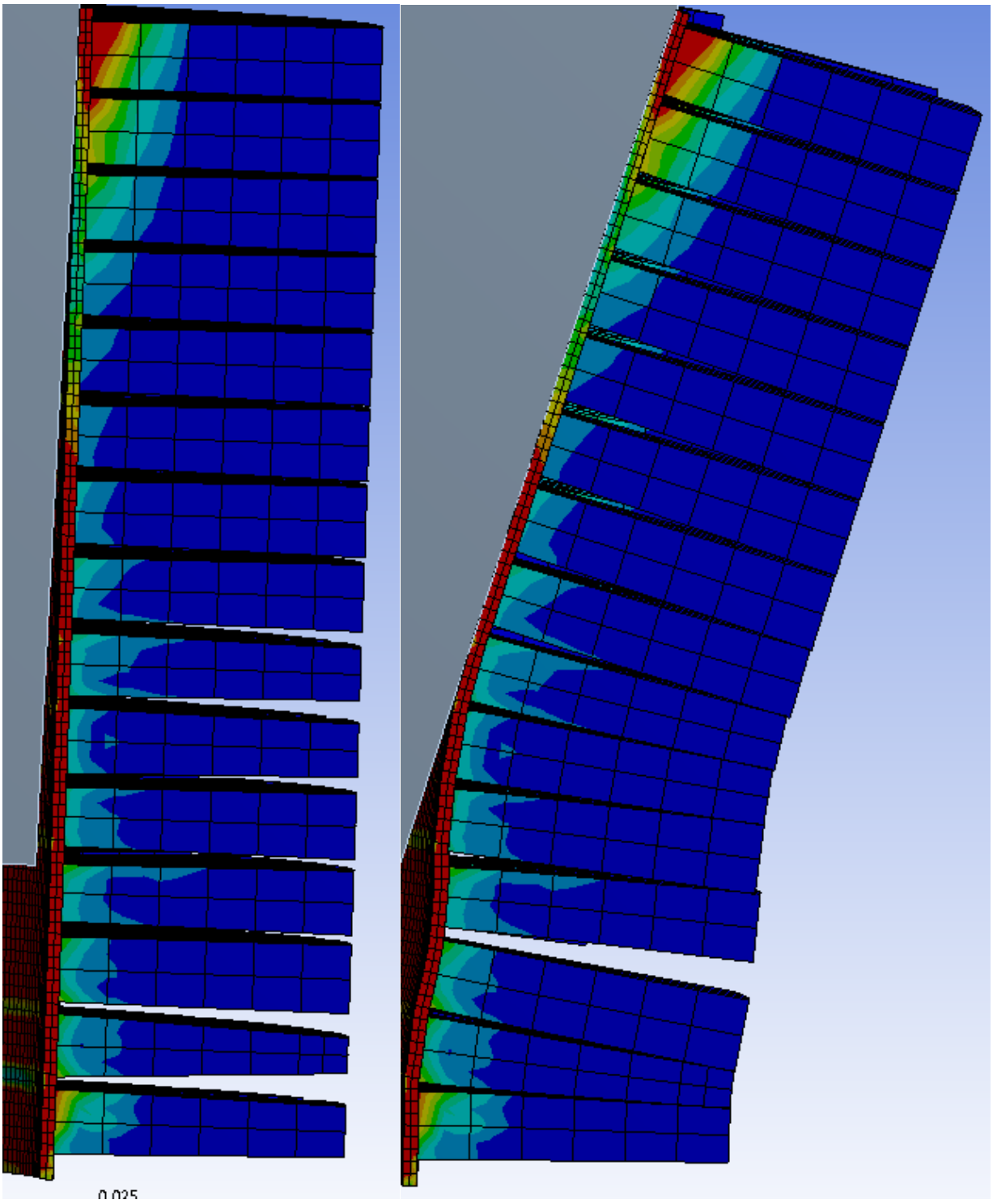

Figure 101:Undeformed (left) and deformed (right) geometry after 3rd iteration of the optimizing process. Note the significant buckling, outwards this time (instead of inwards as in the annular comb generated by the 1st iteration).

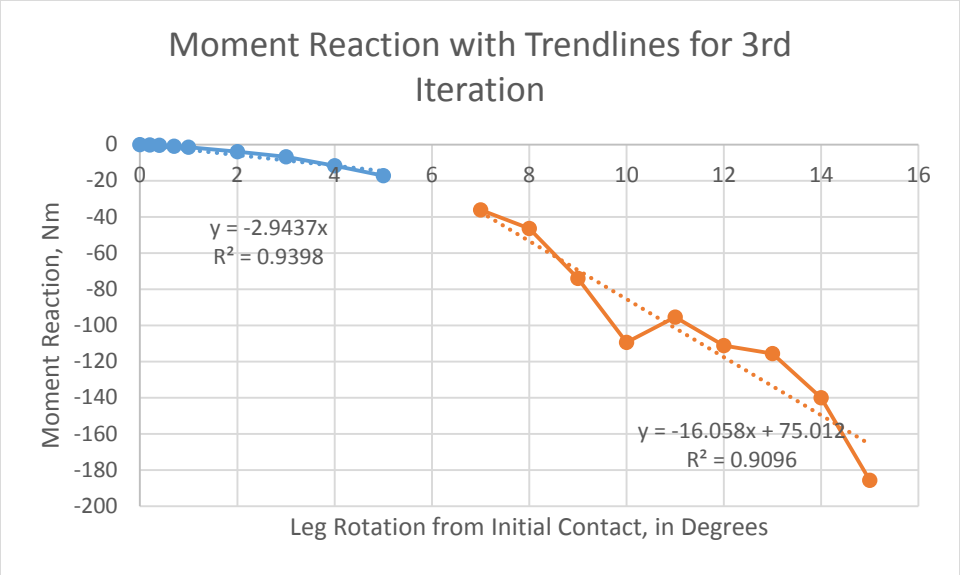

Graph 24: Moment reaction for annular comb after 3rd iteration of optimization process. Note the significant noise near the end of the simulation (and correspondingly-low correlation coefficient in the fitting line) thanks to shell buckling of the backbone. The orange area was 5.46x stiffer than the blue area on average.

Fourth Iteration.

In an attempt to preclude buckling, the tooth gaps used in the previous iteration were maintained, but the area of the teeth in contact with the backbone was increased in the hope that this would inhibit backbone buckling (later research shows that this is indeed the case, but at the cost of higher pre-lockup stiffness). Figure 102 shows the symmetry view of these teeth, before deformation started and at 15° of rotation; as in the previous iteration, some outwards buckling is evident between teeth 3 and 4 from the bottom, although this time it does not result in instability (as shown in the moment reaction curve in Graph 25). Then, out of curiosity, a further 5° of leg rotation was analyzed; interestingly, the buckled region snapped back into a configuration that brought teeth 3 and 4 into lockup (Figure 104 shows a side view so the behavior of other sets of teeth can be observed, particularly in tangential contact). However, the moment-response curve did not show a significant acceleration of moment (i.e. corresponding to a significant stiffness

increase) in the last 5° of rotation, so finally obtaining complete lockup was of little utility. Indeed, using a bilinear least-squares regression (as shown in Graph 25), the structure is about 6.75x stiffer from 7° to 20° than it initially was; however, as shown in Figure 105, not one pair of teeth is in contact (vertical or tangential) even at 7°, so this mild stiffening-up effect must be due to the backbone alone (although it is constrained to some extent by the teeth because its curvature is constrained locally at the bonding faces between teeth and backbone).

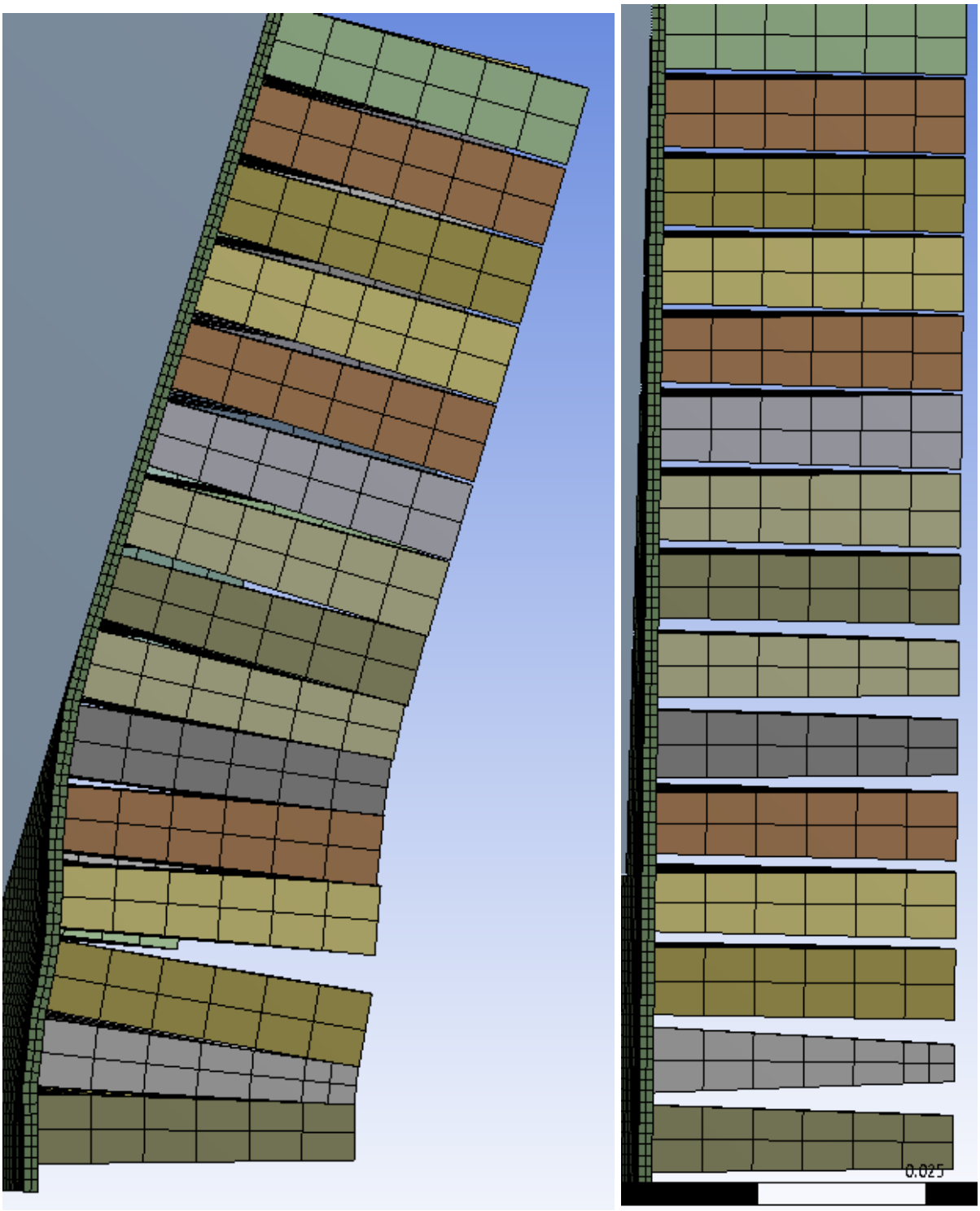

Figure 102: Fourth iteration, view at symmetry plane (right: 15° of rotation, left: undeformed).

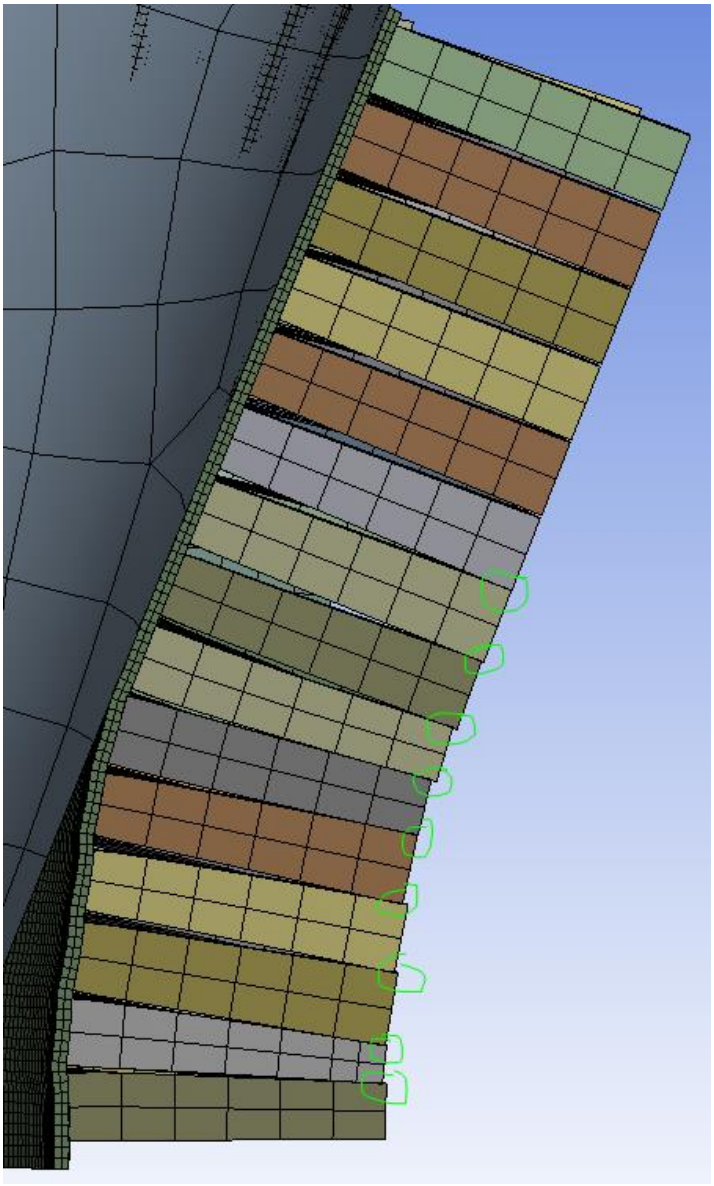

Figure 103: Fourth iteration, simulation extended to 20°. Contacting teeth circled in green. Note that the snapthrough reversed.

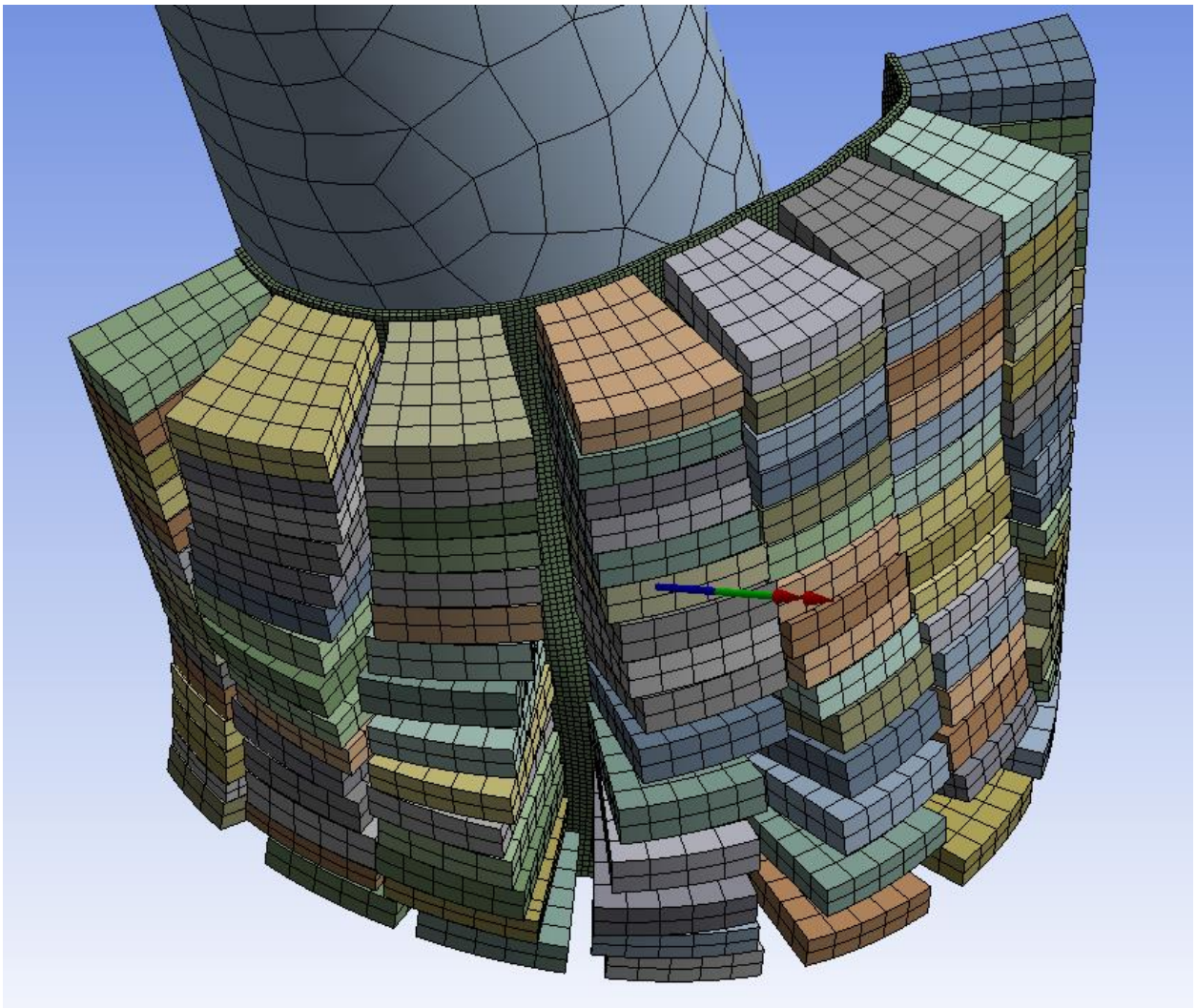

Figure 104: Side view of fourth iteration showing modest recruitment of other teeth in tangential and vertical contacts (leg rotated 20°).

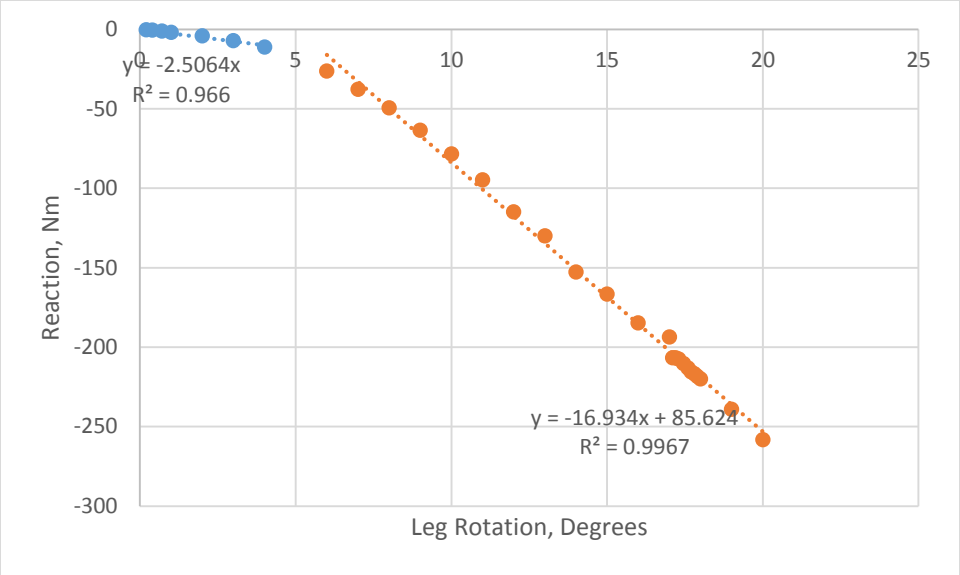

Graph 25: Two linear trend lines for the moment reaction curve, separated into pre-stiffening and post-stiffening areas. Note that the stiffening is mild at around 6.75x

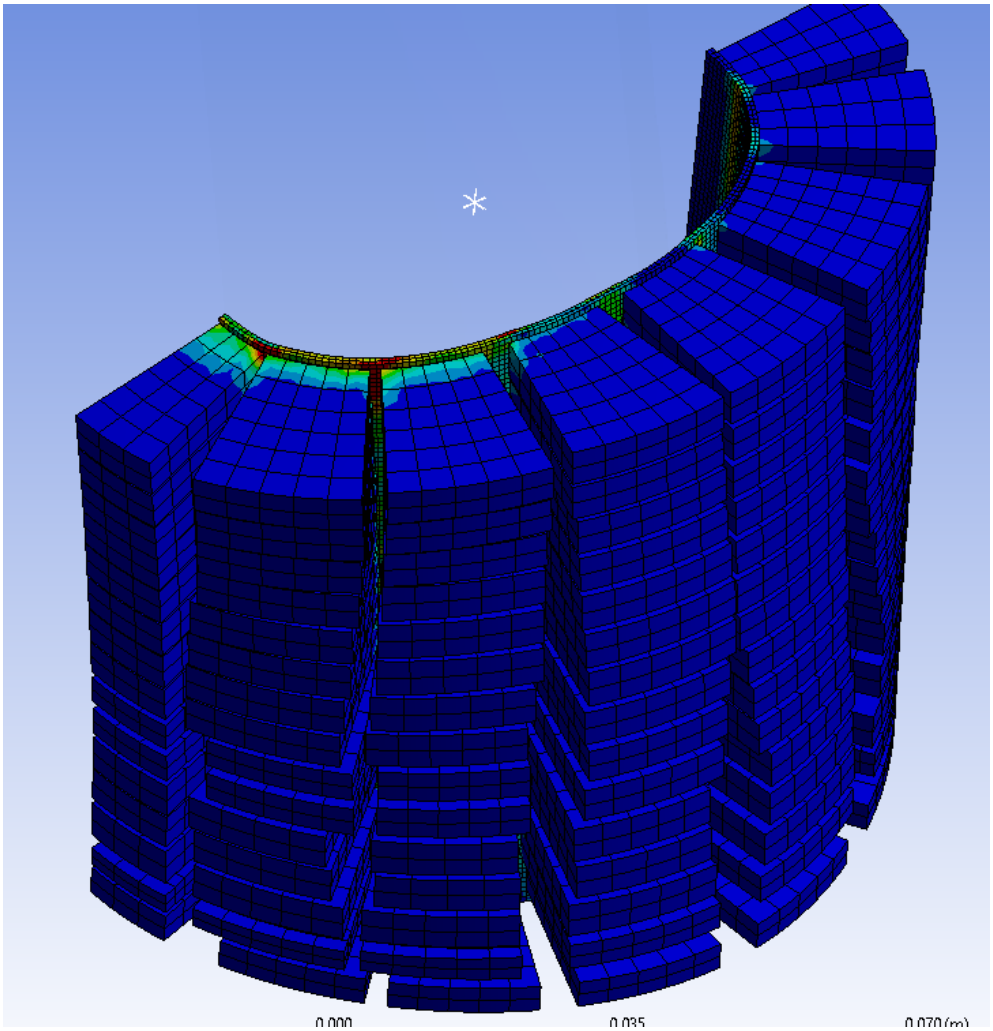

Figure 105: No teeth are contacting at 7°, so it is unclear why the moment-reaction curve shows that stiffening up has ended well before this position.

Special Backbone Geometries.

Given the lack of success in producing the desired mechanical behavior solely by altering teeth geometry, it was determined to investigate the effects of backbone modifications, perhaps in conjunction with tooth modifications.

First, geometries with limited density were investigated in the particular hope of decreasing pre-lockup stiffness (both generically by removing material, and particularly by

introducing bending-dominated rather than shear-dominated or tensile-dominated local modes when the structure is globally in bending). Note that these geometries often use principles from compliant mechanisms, and indeed, individual complaint mechanisms are sometimes tessellated in this way to form "mesomaterials".

Reentrant-Honeycomb Backbone.

The reentrant-honeycomb geometry (that is, a hexagon with concavity from four angles with measures under 90° and only two obtuse angles; note that these 'reentrant' hexagons tessellate) is remarkable for two reasons: one, it produces auxetic macromechanical behavior (which may yield novel and perhaps even useful buckling properties, although it is not expected that merely negative Poisson ratio will cause stiffening; however, geometries that tend towards infinitely-negative Poisson's ratio after some deformation are known[41], and these might be more promising due to the magnitude of this transition), and two, it seems like it should stiffen in tension after moderate deflection as the members that are initially angled inwards (in which position they give the structure compliance when it is in overall tension, because gross tension translates to local bending, in which they should be more compliant than when in tension) are reoriented vertically (putting them in local tension, in which they should be stiffer). A 2D projection of the geometry is shown in Figure 106; one of the principle parameters that control how much strain is required before tensile stiffening is the 'reentrant angle' (80° in the sample geometry shown). The closer to 90° this angle is, the less tensile strain required before the tensile stiffness of the structure should increase when the beams are reoriented to be purely in tension.

[41] "Deformations of Skeletal Structures: Finite Auxetic Mechanisms in Periodic Tessellations," Holger Mitschke

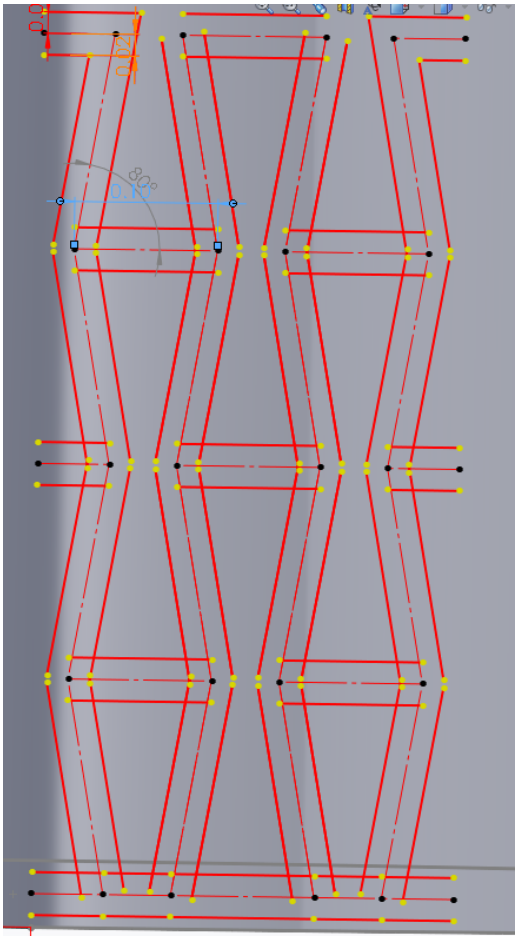

Figure 106: The 80°/150° reentrant hexagon flat geometry was projected onto a cylindrical backbone to produce the reentrant-honeycomb-backbone annular comb. Note that the 80° angles are fairly large (i.e. close to 90°, to which they should stretch when the geometry is in tension).

It was hoped that this stiffening property in particular could combine with interrupted tooth contact to produce significant stiffening-up behavior in global bending. The tooth profiles from the fourth iteration of the study that attempted (unsuccessfully) to optimize lockup behavior with a solid backbone were used for convenience. Figure 107 shows the overall geometry of the reentrant-backbone annular comb, and Figure 108 shows a closeup of the cylindrically-projected reentrant backbone.

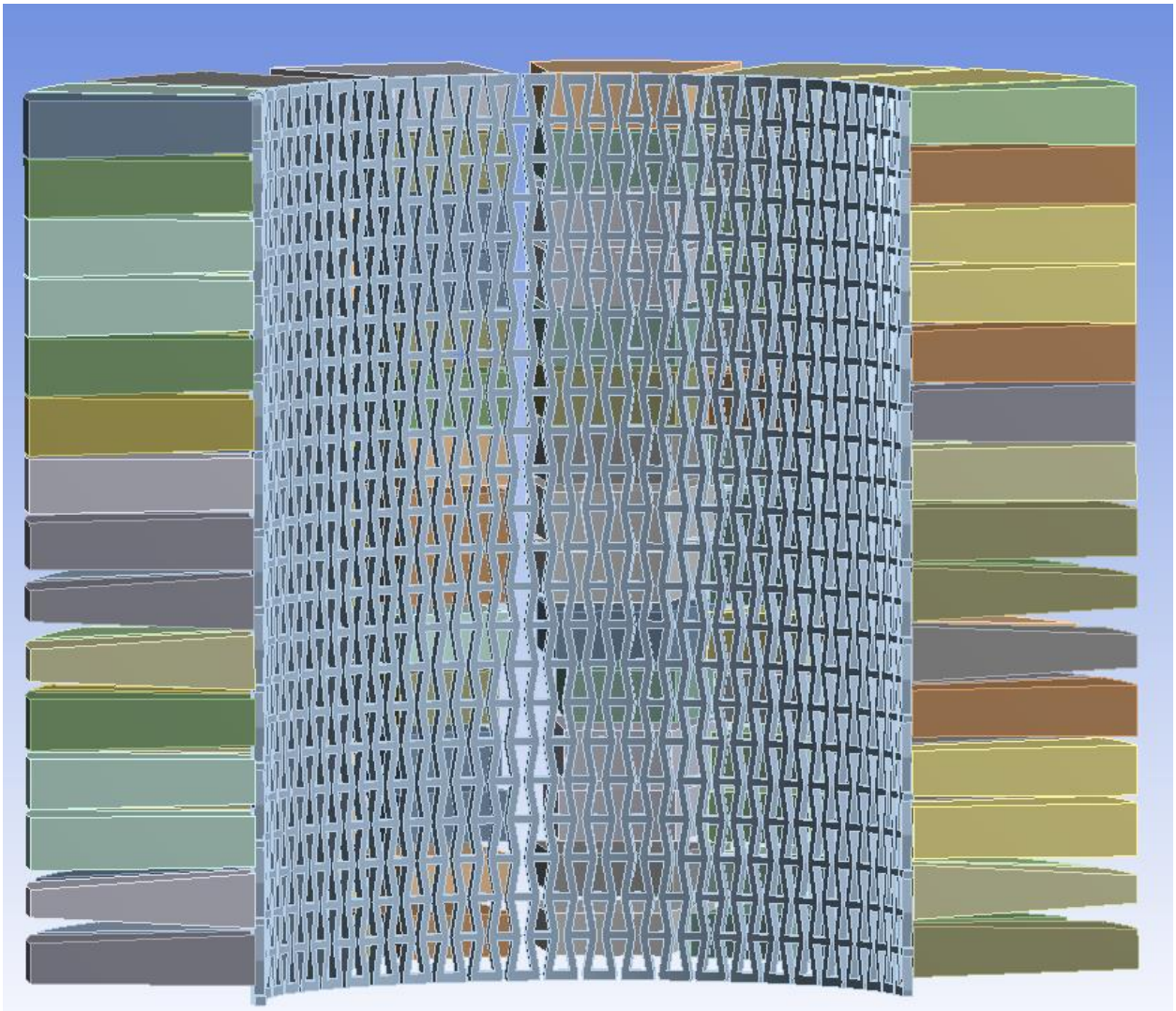

Figure 107: Overall geometry of reentrant-honeycomb backbone.

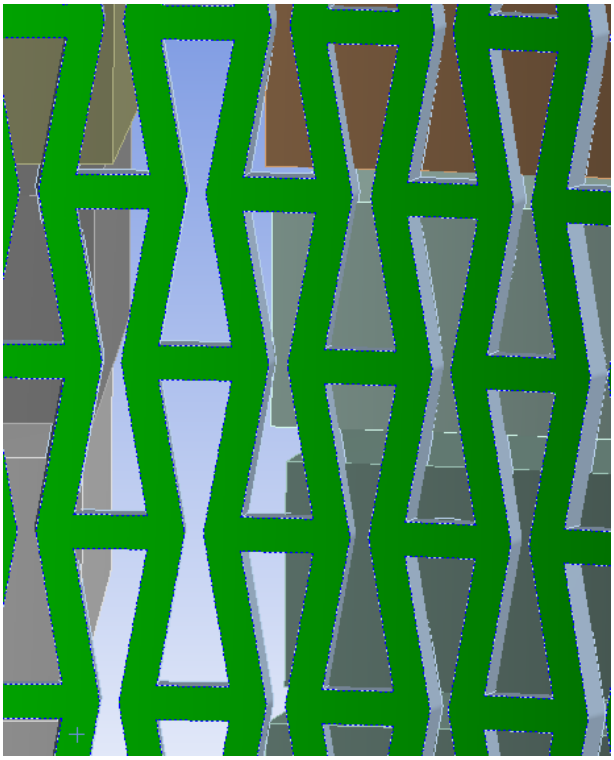

Figure 108: Closeup view of reentrant-honeycomb backbone and a few attached teeth.

The tooth profile of the latest iteration of the process attempting to produce rapid lockup at 15° with the solid backbone was employed (with full cognizance that this tooth profile would likely be even less successful in this reentrant-backbone comb than it was in the solid-backbone comb). Then, as usual, the rigid leg was rotated 15° in a quasi-static simulation. Figure 109 shows the deformed mesh at the end of the simulation. The auxetic properties of the backbone produced several anomalous deformation modes. The most obvious of these is bowing inwards of the backbone under the "leg" (which would be stopped by the lower portion of the foot, had that been modeled), which likely results from the auxetic property of lattice densification and inward contraction in compression; if so, this would seem to indicate that the backbone does not experience tension, at least before enough teeth have locked up, but on the contrary sees compression. In addition, a few reentrant cells experienced significant radial stretching, to the

point that the walls that were formerly angled inward actually experienced snap-through local post-buckling behavior and became angled outward (as in a traditional hexagon). Figure 110 shows a close-up of this mode. Finally, as shown in Figure 111, some cells (particularly at radial gaps between teeth) also showed significant shearing in the *z-theta* direction (which is in-plane shearing when projected onto the page), again mainly at the radial gaps between teeth.

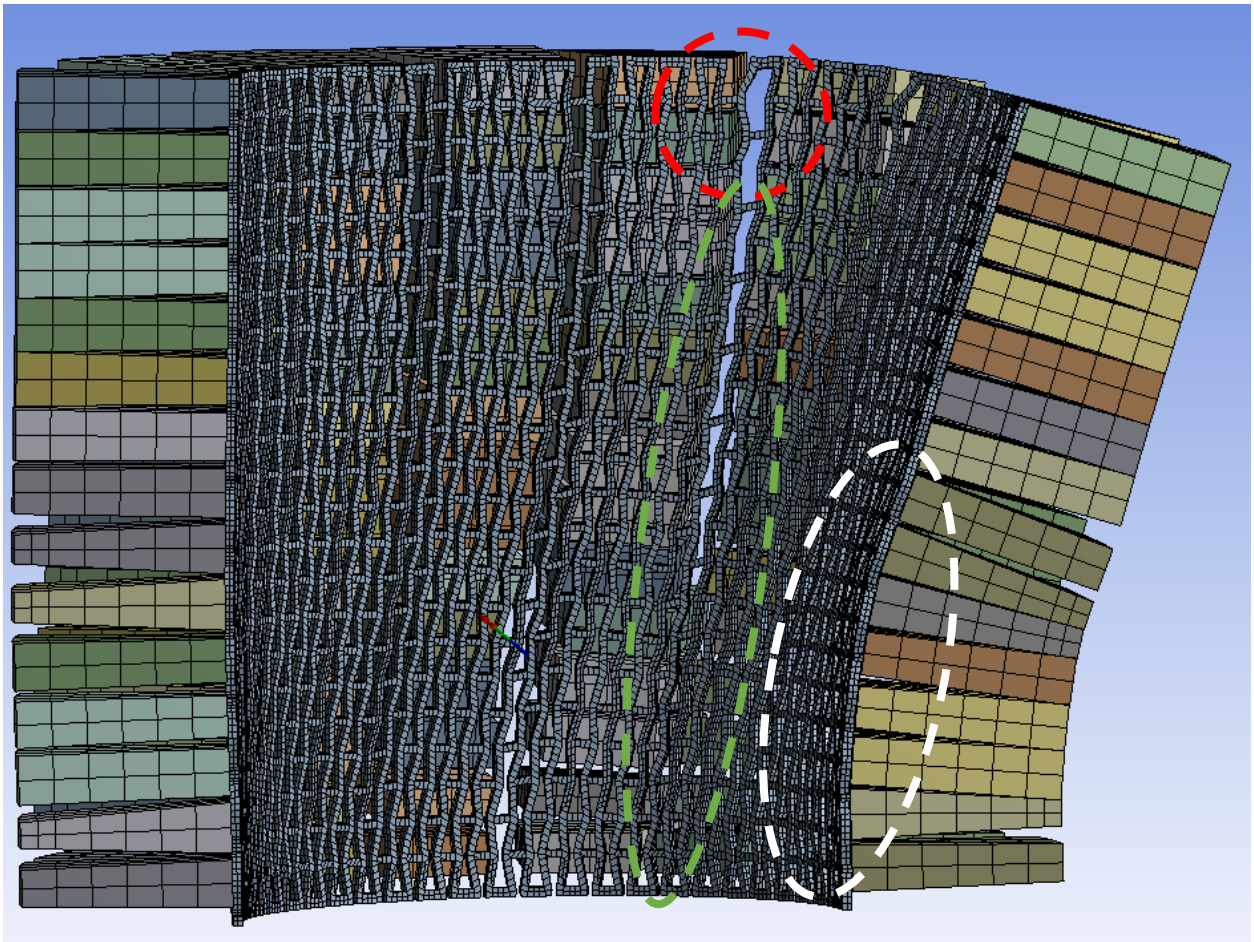

Figure 109: Overall symmetry view of deformation of annular comb with reentrant backbone. Bowing inward under leg is circled in white, radial snap-through circled in red, and large z-theta shearing of reentrant hexagons circled in green.

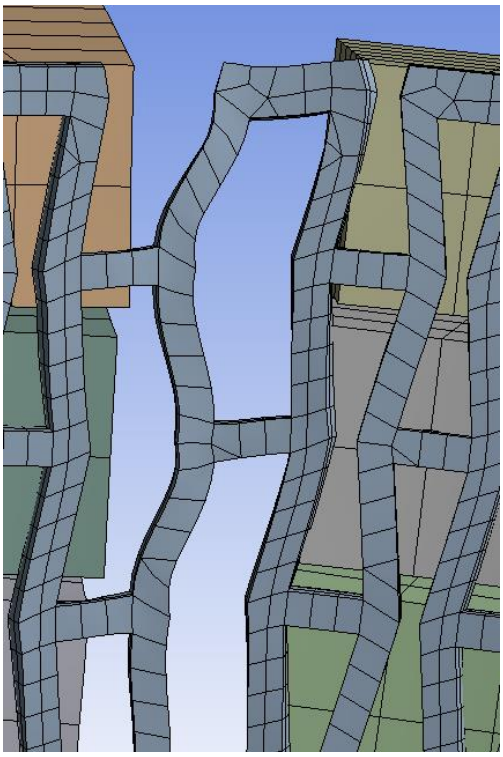

Figure 110: Closeup of reentrant cells showing radial snap-out behavior.

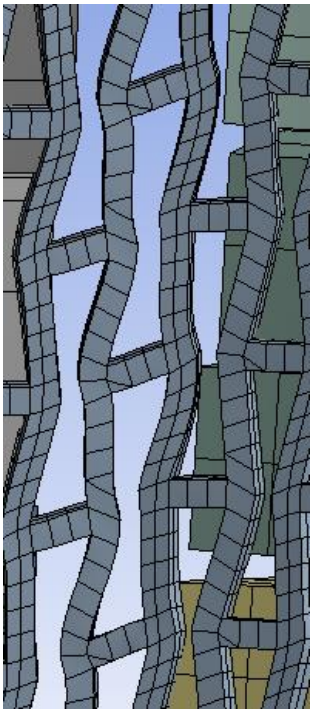

Figure 111: Closeup of reentrant cells showing z-theta shearing behavior.

Testing the Reentrant-Hexagon ("Bowtie") Backbone only in Tension.

Given the lackluster performance of the overall structure in bending, it was deemed important to test whether the backbone itself stiffened up in pure tension; if so, then it would seem that backbone stiffening properties were of little use in producing stiffening up in global bending. However, if the backbone in fact did not stiffen, the reentrant-backbone annular comb's poor performance would not be sufficient justification to stop investigating tensile-stiffening backbone geometries.

To this end, the teeth were entirely disabled (ensuring that their contact patches would not locally stiffen the structure and prevent the reentrant hexagons from expanding until their initially-angled members had been reoriented vertically, which was anticipated to cause stiffening), and the cylindrical backbone was pulled vertically in tension. The top and bottom were unconstrained radially, but were constrained against relative angular rotation.

As shown in Figure 112, the reentrant hexagon cells were straightened into near-rectangles mostly as anticipated (and then, as expected, they stopped rotating and did not, say, keep rotating to turn into non-reentrant hexagons). However, they did not completely lose their bowtie shape, suggesting that the joints between the individual segments were too stiff and exerted somewhat of a cantilevering effect on the joints. Of note, it was later discovered that only after the cantilevering effect of the joints was nearly eliminated by significant cutouts did reorientation of hexagonal elements cause tensile stiffening (more on which in the next chapter); the main effect of this cutout modification was to reduce initial stiffness much more than final stiffness (rather than, say, increasing final stiffness). Thus, as Graph 26 shows, the tensile reaction force showed no stiffening, but on the contrary a modicum of softening (coming only from geometric effects; the material model was purely linear).

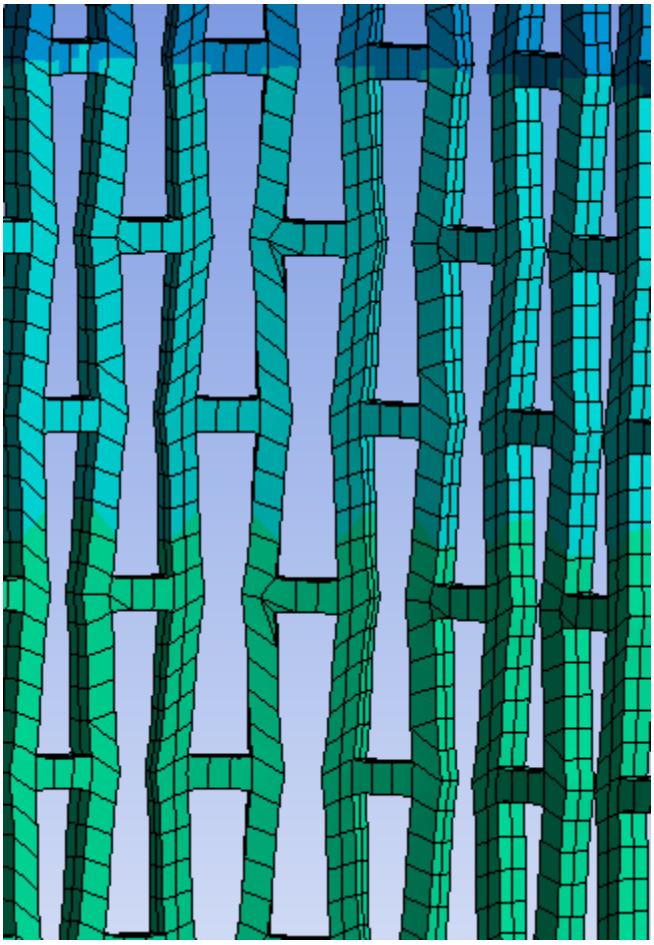

Figure 112: The maximum stretch achieved by the simulation. Subjecting the reentrant backbone alone to vertical tension did indeed straighten out the reentrant hexagon cells into near-rectangular shape as anticipated. However, there was some vestigial bowtie-like shape to the cells even after significant tension, suggesting that some aspect of the cantilevered joints between cells was behaving improperly.

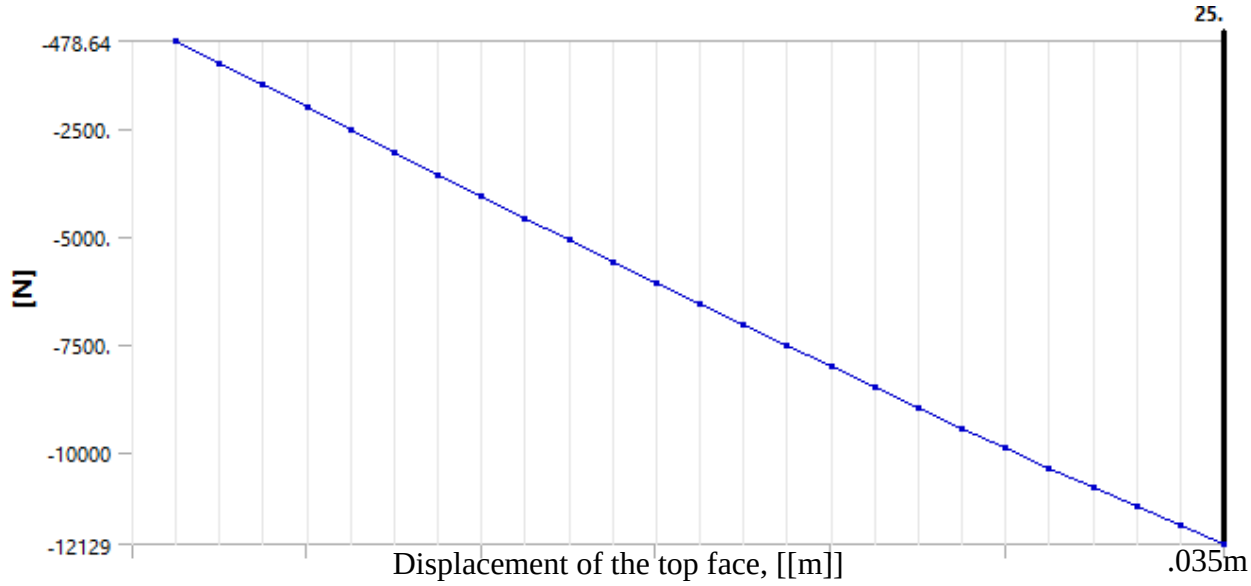

Graph 26: A graph of reaction force vs. tensile displacement for the reentrant-hexagon backbone shows no stiffening-up behavior, surprisingly, even after the reentrant cells are straightened out.

Interestingly, the curved backbone developed an unexpected pattern of radial waviness when subjected to tension, as shown in the top-down view of Figure 113. While this behavior does not have any conceivable benefit to the application at hand, it is a mode of deformation that could potentially cause strange tooth lockup behaviors (especially as regards tangential contact). It is probably the result of the auxetic property of the backbone geometry (although note that 2D sheets do not evince such dimpling in tension).

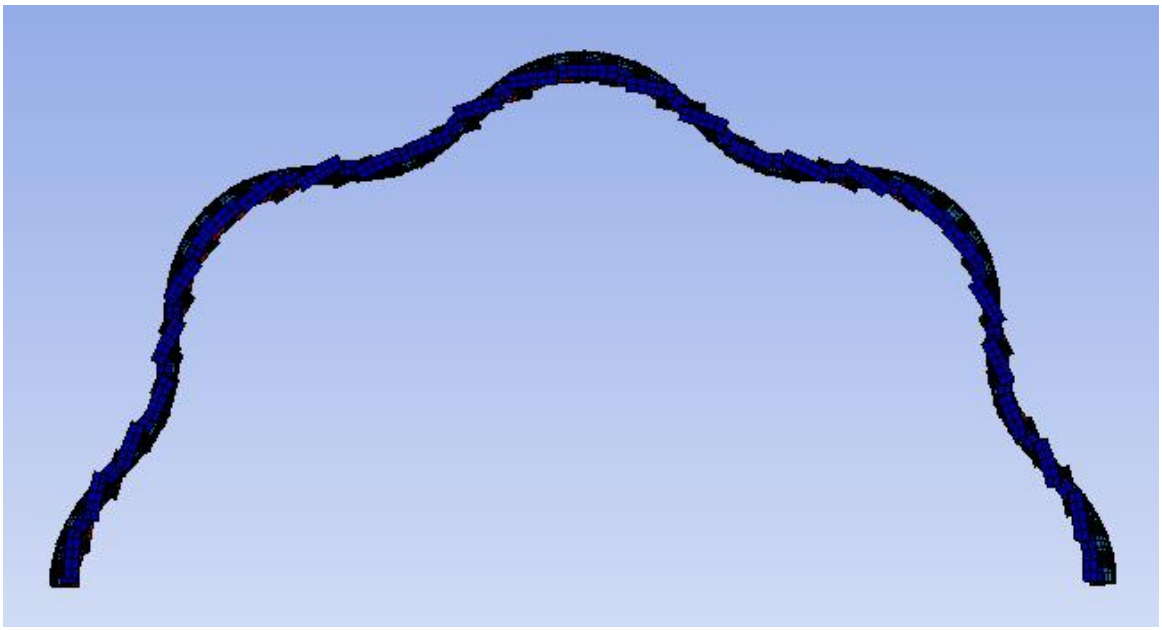

Figure 113: Top-down view of reentrant backbone in tension; note the wavy radial pattern.

Even if the backbone alone showed excellent tensile stiffening, it is an open question whether the portions of the backbone having contact patches with the teeth backs would still be free to experience this deformation. It might prove necessary to make those portions of the backbone in contact with the teeth solid, and add reentrant elements in the gaps between teeth (which might necessitate greatly increasing the size of the gaps).

Square Lattice—Vertically and Tangentially Oriented.

Square lattice structures might be expected to show very similar gross behavior to the solid backbone, just having reduced stiffness (probably both pre-lockup and post-lockup). However, this is an incorrect assumption, as each unit cell can act like a four-bar mechanism when the joints between them are at least as compliant as the beams themselves. Indeed, in large deflection, the backbone might even be anticipated to have an effective Poisson's ratio in excess of the hydrostatic limit of 0.5 locally in the ±45° direction, just as carbon-fiber laminates

oriented at ±45° relative to the load see an effective Poisson's ratio of 0.8 when fibers are free to rotate[42]. Likewise, woven fabrics can see local Poisson's ratios greater than 0.5 on the bias[43].

However, more important than interesting Poisson effects, such a structure should have increased shear compliance relative to tensile stiffness, which might prove especially useful for the annular comb given the way the portions of the backbone that are roughly 90° off from the contact area are put into shear.

Also, they might easily be modified into a rectangular array in which the elements running tangentially could be made thinner, and thus more compliant, than those running vertically, in order to give the backbone enough tensile stiffness to lock up when enough teeth were contacting vertically, while keeping the shear work done on the backbone to a minimum. Finally, as discussed in the "microtruss" concept (see Chapter 2), joints allowing selective self-contact between beams might be added here (in order to make the backbone compliant when the joints were not contacting), although this would further increase geometric complexity.

Thus, a preliminary lattice-based structure was tested in FEA. Figure 114 shows the overall geometry for the setup, and Figure 115 shows the backbone in isolation. Figure 116 shows a symmetry view of the deformed structure, plotting contours of von Mises stress: note that many of the teeth in the symmetry plane facing the area of leg contact have locked up by this point (specifically, all of the teeth below the onset of leg-backbone contact). As Graph 27 illustrates, the structure is more compliant than solid-backbone annular combs, thanks

[42] http://www.compositesworld.com/columns/doing-the-impossible-with-poissons-ratio
[43] *Structures: Or Why Things Don't Fall Down*, by Dr. J.E. Gordon, p.253

presumably to the lower areal density of the lattice backbone, although lockup behavior is, as usual, too slow and insignificant for this application.

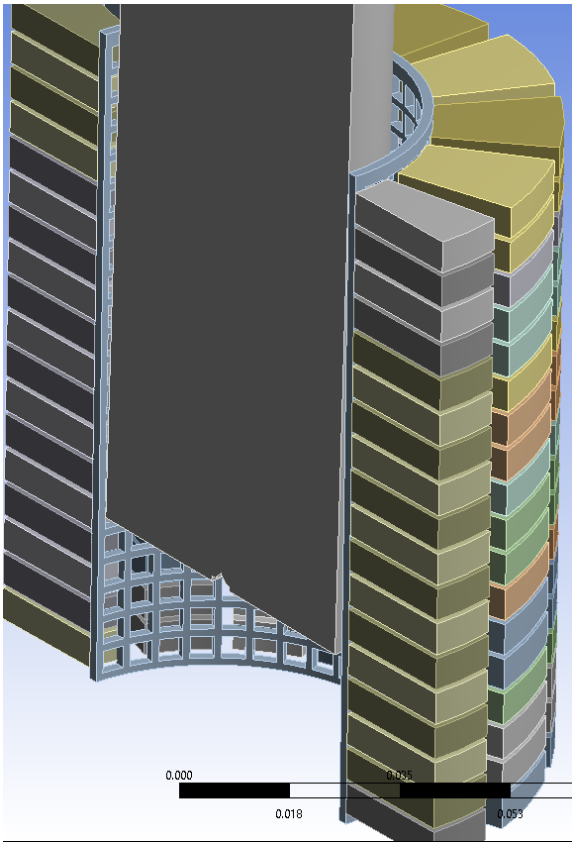

Figure 114: Undeformed view of 0/90° lattice annular comb with teeth and rigid "leg". Note that the annular comb conforms closely to the leg, unlike in initial annular comb models.

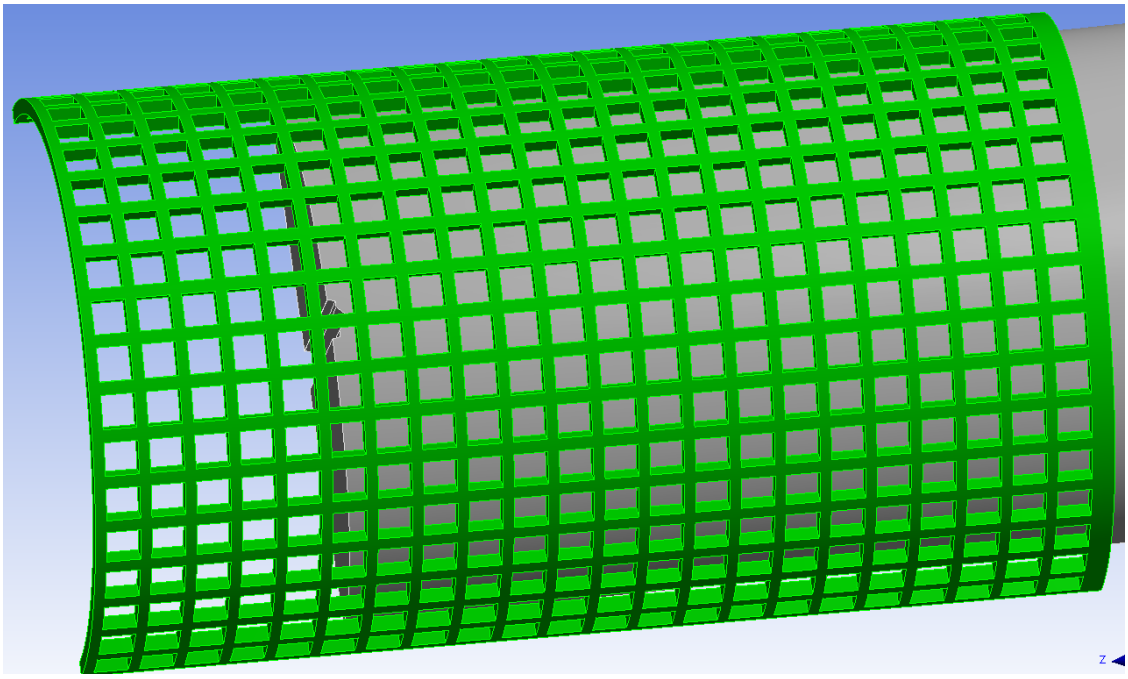

Figure 115: Backbone of 0/90° square lattice annular comb, teeth hidden to show backbone features. Note that the square cuts in the backbone are made radial to the central axis of the backbone cylinder.

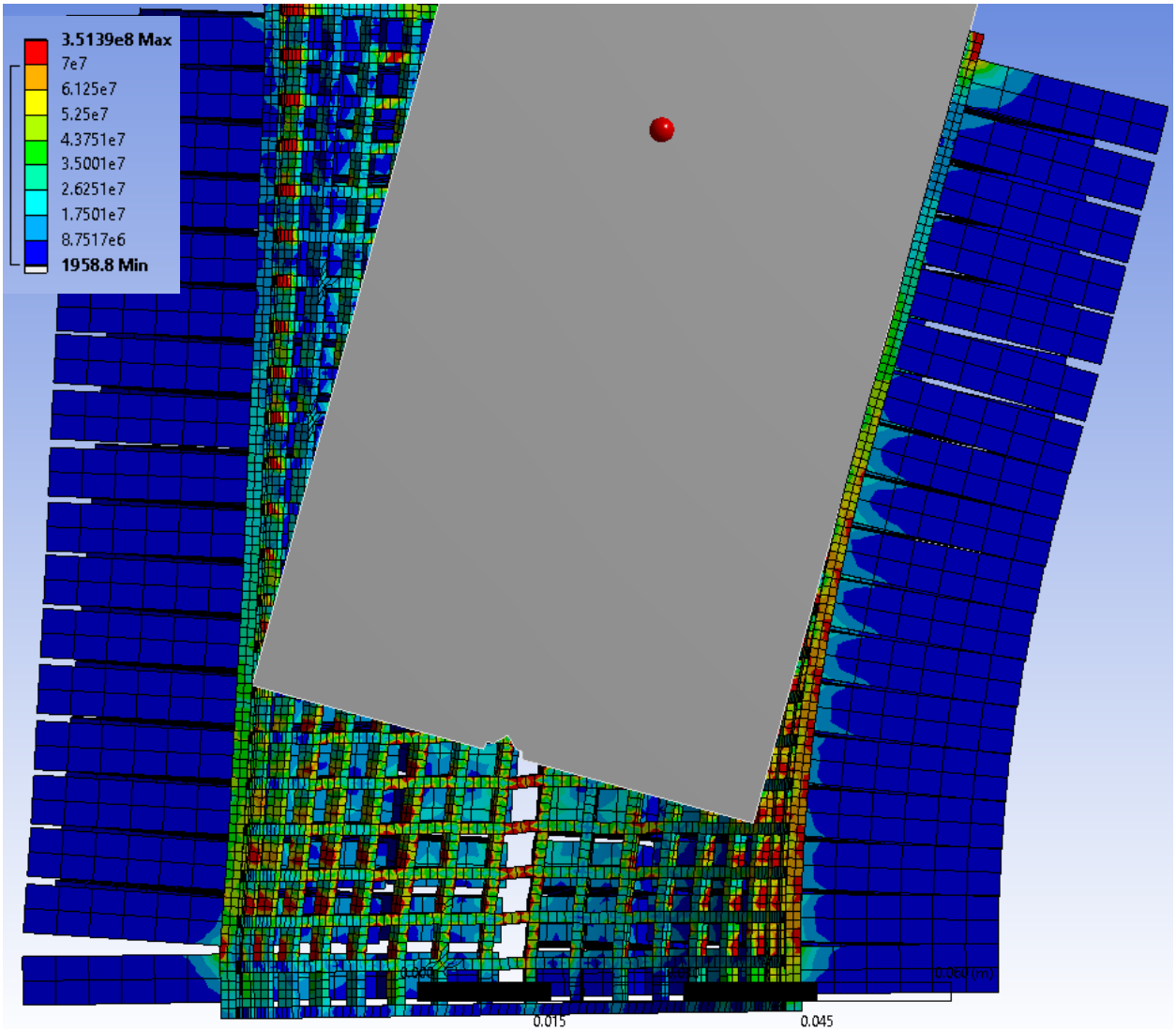

Figure 116: Contours of von Mises stress after 15° of leg rotation from the point of initial contact. Note the visible shearing of initially-square backbone holes into rhomboid shapes (which is probably a good thing as it indicates good shear compliance).

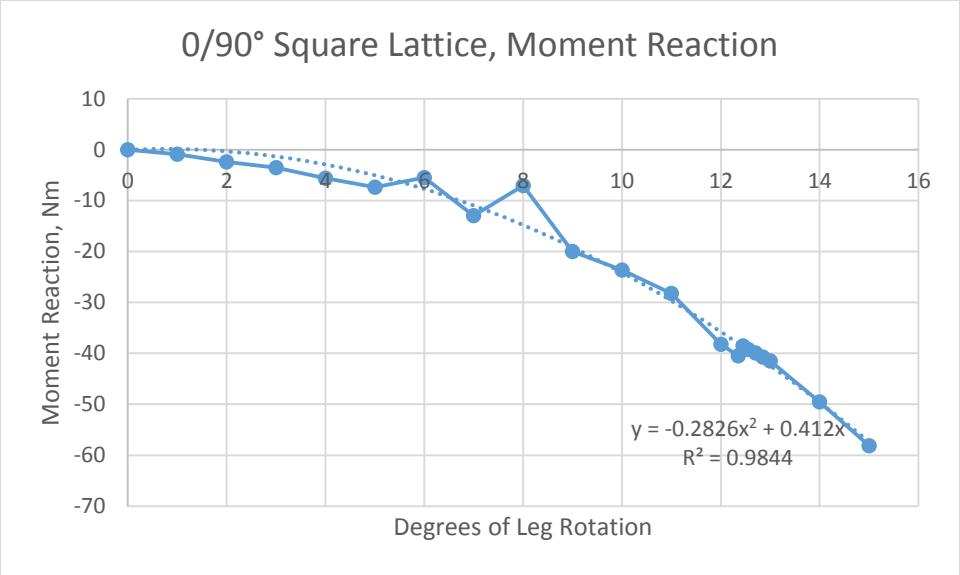

Graph 27: Moment reaction for 0/90°-oriented square lattice backbone and fitting parabola. Note the moderate noise in the data around the point of stiffness transition. The fitting parabola shows a nearly-zero slope (actually, a negative stiffness) initially, thanks in large part to distortion from this noise, and anyways, this does not continue for long.

Square Lattice—Oriented at 45°.

Holes of the same shape as those in the 0/90° lattice were cut in a backbone with the same thickness as that used in previous studies, with the only modification being the reorientation of the holes. This was thought to be of potential interest because of the high local Poisson's ratio at 45° to a square lattice (although this might give too much compliance to the backbone in tension while doing little to relieve shear stiffness, so it was far from certain to be a beneficial modification). Figure 117: Geometry of the 45°-oriented lattice-backbone annular comb. shows the geometry used in this simulation; its backbone geometry is reminiscent of the biaxial braids used in Auburn University's patented open structures, which were unsuccessfully investigated for good stiffening-up properties in Chapter 2 (although this geometry lacks the waviness where warp and weft yarns cross over each other in a true braid).

Unfortunately, this geometry also showed little promise. Figure 118: Side view of the deformed 45°-oriented lattice-backbone annular comb after 15° of leg rotation. Note some minor shell buckling outward between the third and fourth rows of teeth from the bottom. The structure is colored by von Mises stress, with red indicating stress above 70MPa., Figure 119: Close-up view of part of the deformed 45°-oriented lattice-backbone annular comb after 15° of leg rotation. This view shows many of the diamonds in the backbone being slightly compressed vertically. The structure is colored by von Mises stress, with red indicating stress above 70MPa., and Figure 120: Top view of the deformed 45°-oriented lattice-backbone annular comb after 15° of leg rotation. Unusually, tangential contacts between teeth are most active here at a higher angle than the usual 90° counterclockwise from the contact area. The structure is colored by von Mises stress, with red indicating stress above 70MPa show different views of the deformed result, with Figure 118: Side view of the deformed 45°-oriented lattice-backbone annular comb after 15° of leg rotation. Note some minor shell buckling outward between the third and fourth rows of teeth from the bottom. The structure is colored by von Mises stress, with red indicating stress above 70MPa. focusing on vertical contacts between the row of teeth immediately facing the leg (showing that tooth activation was poor, although this is not surprising as the tooth gaps were intended for a solid backbone, not a lattice backbone). Figure 119: Close-up view of part of the deformed 45°-oriented lattice-backbone annular comb after 15° of leg rotation. This view shows many of the diamonds in the backbone being slightly compressed vertically. The structure is colored by von Mises stress, with red indicating stress above 70MPa. shows a closeup view of some lattice elements in the backbone that saw significant distortion (which should be accompanied by fairly strong Poisson effects); note that the distortion was compressive, not tensile as expected. Figure 120 shows a top-down view of the deformed

structure to illustrate the fact that tangential contact between teeth, usually most prominent at a 90° counterclockwise offset from the point of leg contact (at least when the radial gaps between teeth are of the same width), was concentrated further to the left in this study, though this does not appear particularly significant.

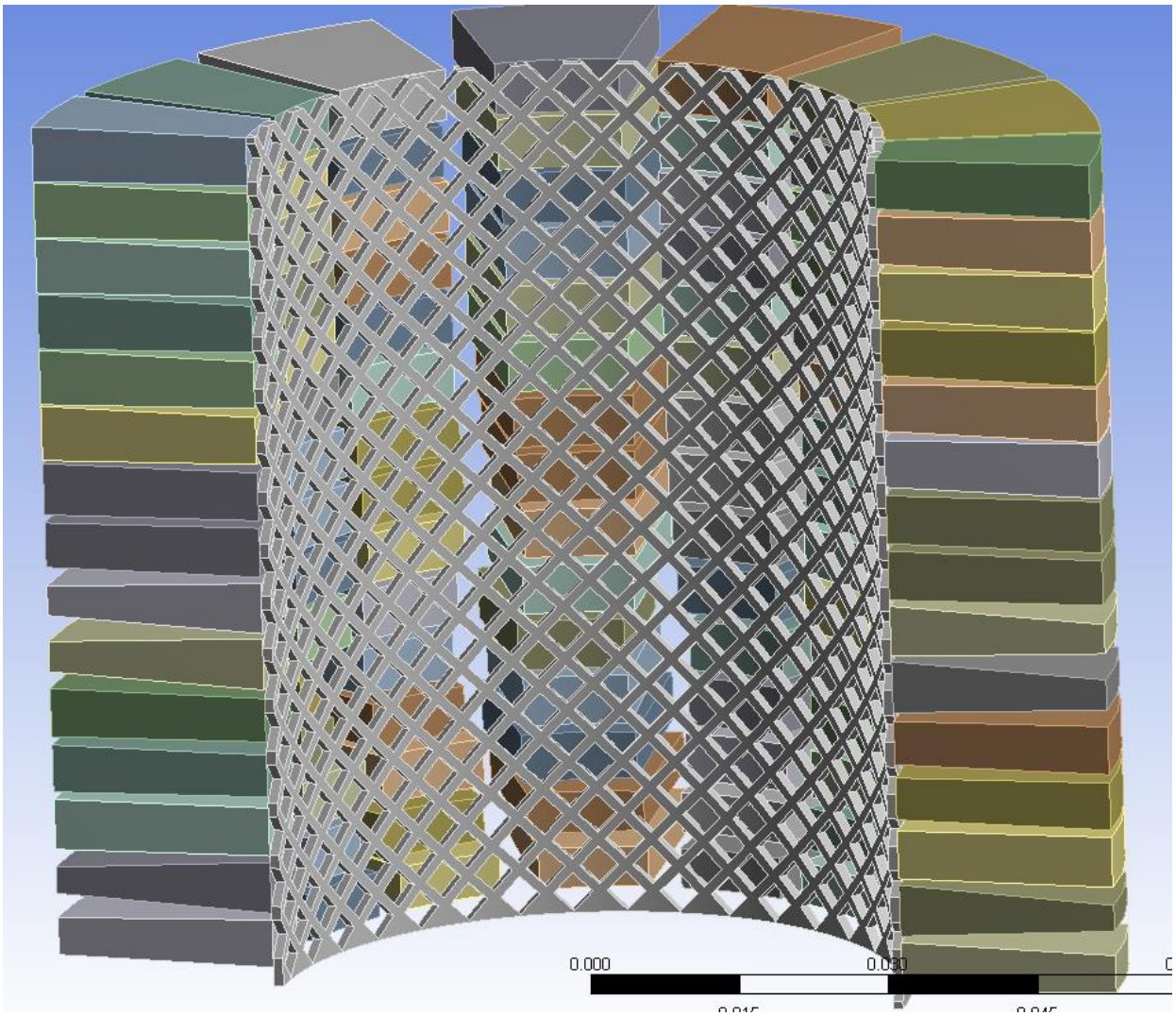

Figure 117: Geometry of the 45°-oriented lattice-backbone annular comb.

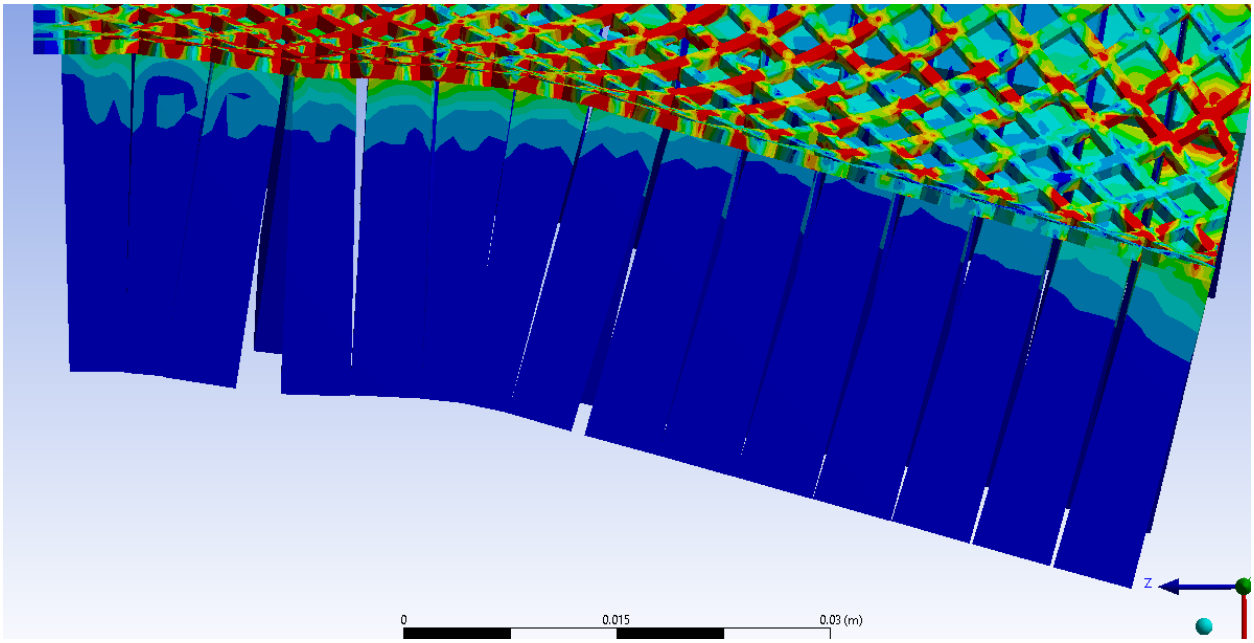

Figure 118: Side view of the deformed 45°-oriented lattice-backbone annular comb after 15° of leg rotation. Note some minor shell buckling outward between the third and fourth rows of teeth from the bottom. The structure is colored by von Mises stress, with red indicating stress above 70MPa.

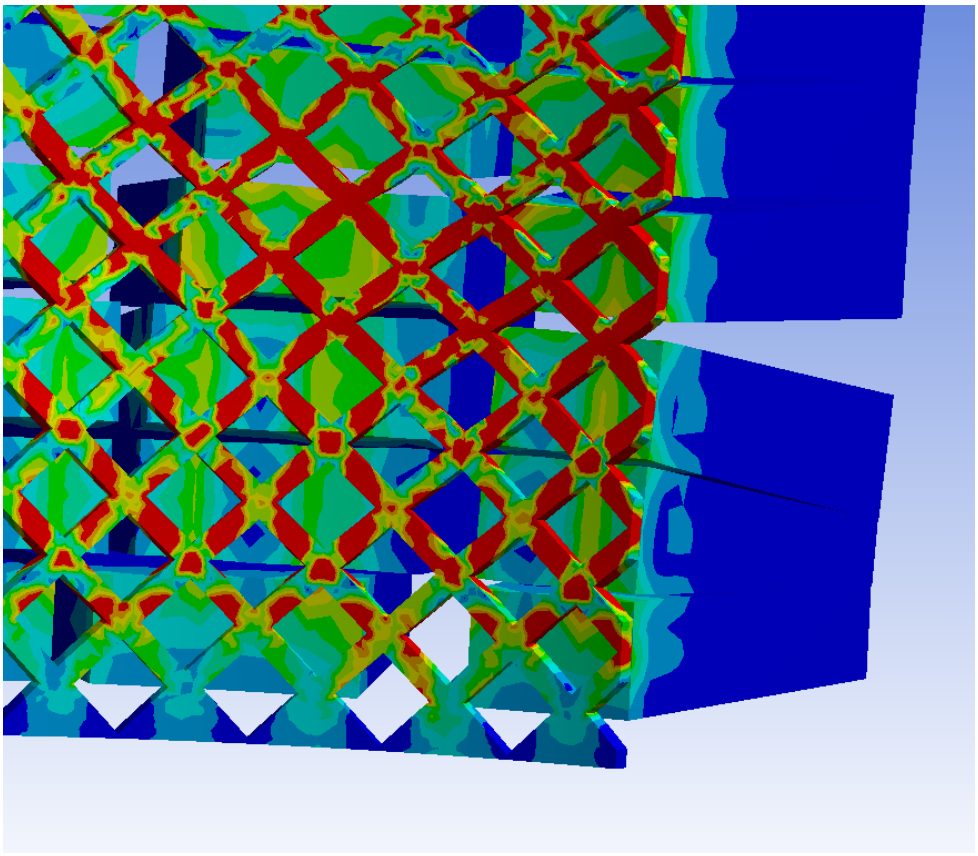

Figure 119: Close-up view of part of the deformed 45°-oriented lattice-backbone annular comb after 15° of leg rotation. This view shows many of the diamonds in the backbone being slightly compressed vertically. The structure is colored by von Mises stress, with red indicating stress above 70MPa.

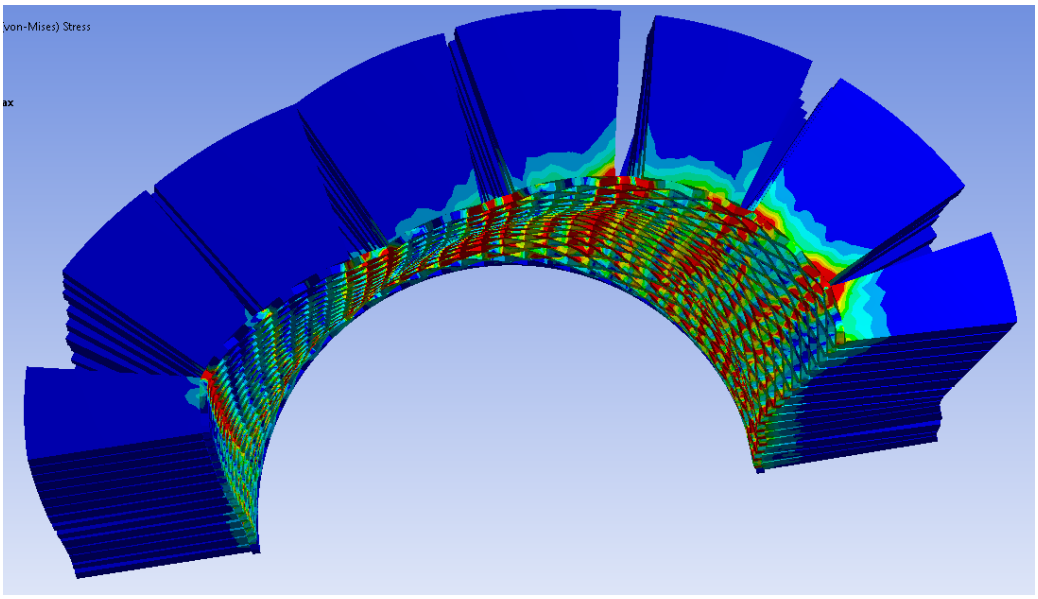

Figure 120: Top view of the deformed 45°-oriented lattice-backbone annular comb after 15° of leg rotation. Unusually, tangential contacts between teeth are most active here at a higher angle than the usual 90° counterclockwise from the contact area. The structure is colored by von Mises stress, with red indicating stress above 70MPa

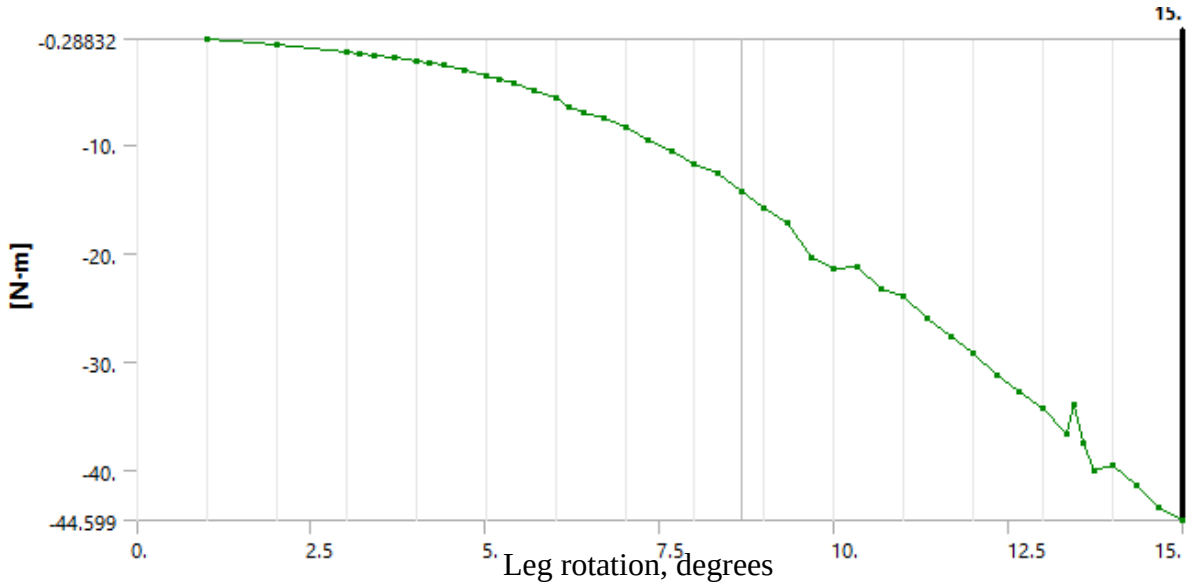

Graph 28: Moment reaction for 45°-oriented square-lattice annular comb.

<u>For Comparison: 45°-Oriented Square-Lattice-Backbone Annular Comb with Tooth Contacts Disabled</u>.

Out of curiosity, the influence of the backbone's stiffness in bending was again to be quantified (as done earlier in this chapter for solid backbones) by disabling tooth contacts with each other while maintaining their contacts with the backbone (which become doubly important for accuracy to maintain when the backbone could see mechanism-like geometric reorientation behavior absent the bonded teeth that the teeth would restrain from their bonded contact). As expected, the backbone experienced significant shell buckling without tooth contacts to stop it, as can be seen in Figure 121. Finally, as Graph 29 shows, the moment reaction from this analysis was very close to that from the teeth-enabled analysis until the backbone began to buckle later in this one, whereupon this analysis's structure became less stiff than it had been previously and than the previous structure was. After all, even after some teeth contacts where active in the previous analysis, the moment reaction was not detectably higher than at the same angle in this analysis! This may indicate that the primary contribution (such as it is) of the teeth to the mediocre stiffening-up performance of the annular comb is not from directly exerting significant moments on the backbone, but simply from preventing it from buckling (which results in a stiffness reduction) very late in the deformation regime, with the backbone geometry itself providing the modest stiffening-up of around 5x after 5° of leg rotation seen in most of these analyses.

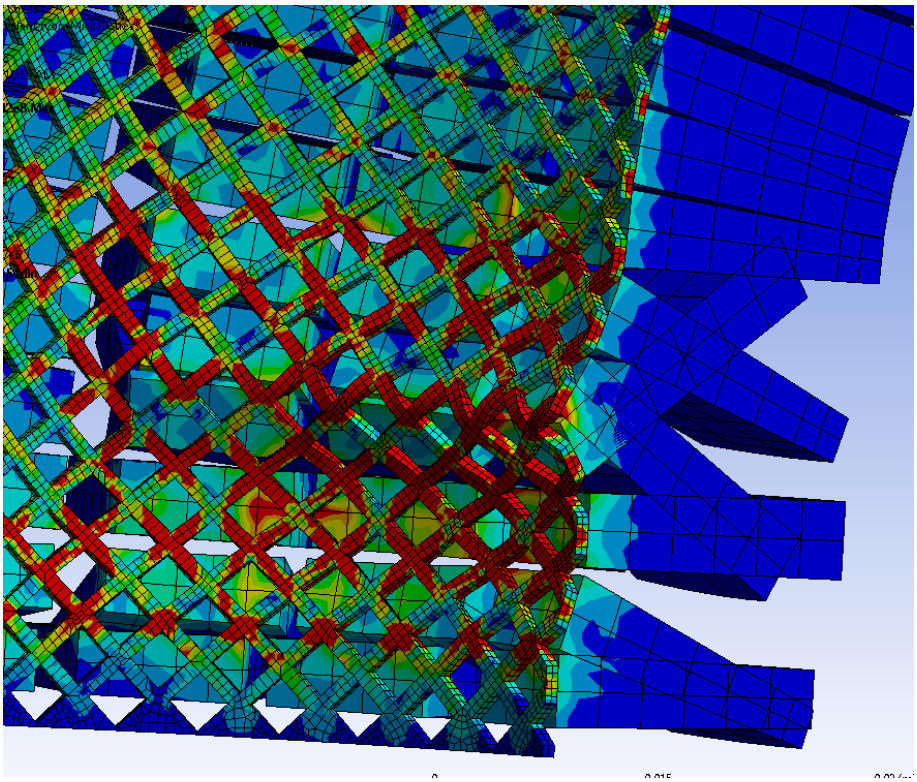

Figure 121: Deformed result after 15° of leg rotation (colored by von Mises stress, with red indicating over 70MPa of stress), when contacts between teeth are disabled (but contacts with the backbone maintained). Note the significant shell buckling the backbone experiences when teeth cannot prevent it.

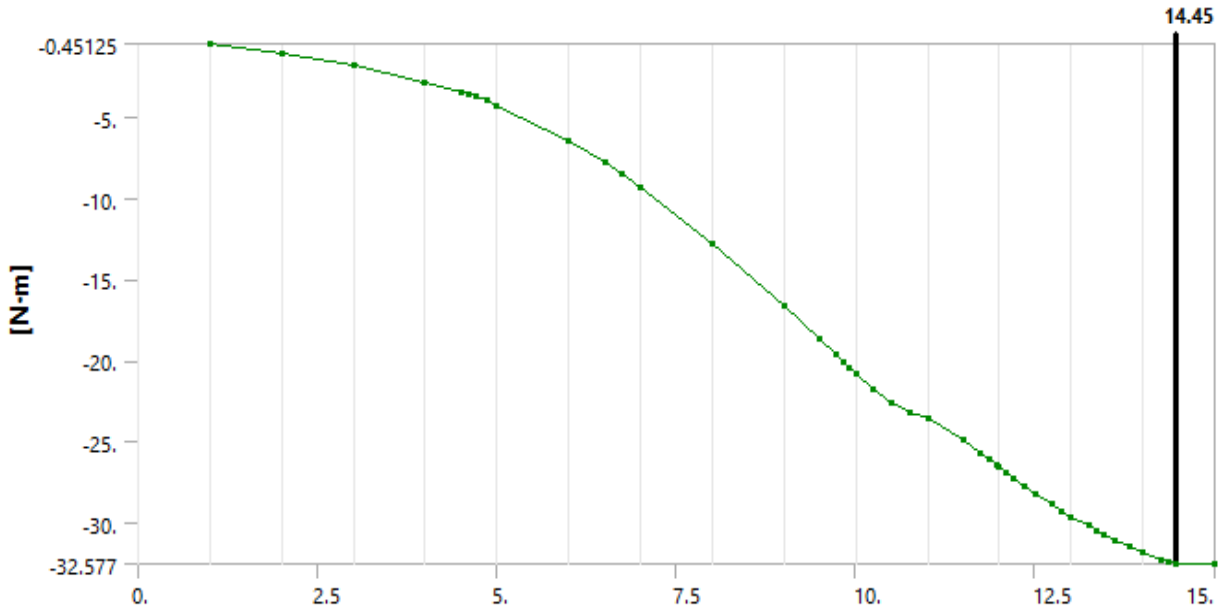

Graph 29: Moment reaction for 45°-oriented square-lattice-backbone annular comb after 15° of leg rotation), when contacts between teeth are disabled (but contacts with the backbone maintained). Note that this shows that the backbone here is responsible for most of the structure's stiffness, including its modest stiffening-up properties after 5° of leg rotation.

Kite-Based Auxetic, Synclastic-Curvature Lattice.

One more "metamaterial" backbone was investigated for the annular comb. Like the reentrant hexagon backbone investigated earlier, this design also has auxetic bulk and synclastic curvature properties. However, this backbone uses a kite pattern, and, in 2D, the kite pattern's auxetic properties are somewhat different from those of the reentrant-hexagon array: while the reentrant hexagon's Poisson ratio varies over a deformation region from around -2.5 to 1.0[44], the kite array features a Poisson's ratio that varies from -0.5 to -7[45]. Also, this geometry is not expected to be as vulnerable to snap-through (as the reentrant-hexagon-backbone annular comb saw in the tangential direction—see Figure 110). The backbone geometry, created by extruding

[44] "Deformations of Skeletal Structures," P.56
[45] "Deformations of Skeletal Structures," P.58

radial cuts from the 2D kite profile projected to a cylindrical face, is shown in Figure 122, with a close-up of the cells rendered in Figure 123.

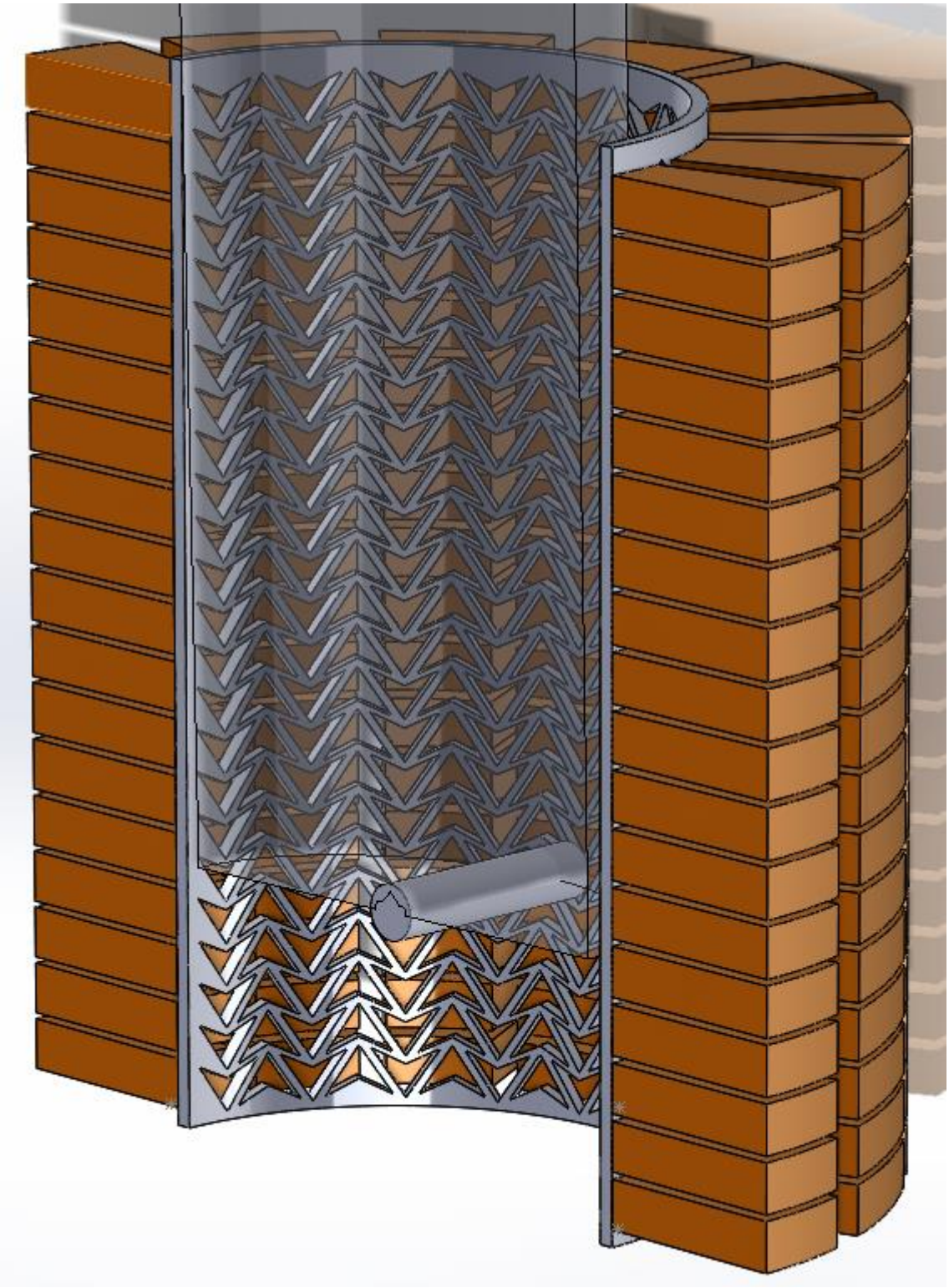

Figure 122: Overall view of reentrant-kite backbone annular comb (leg rendered transparent). Note that the comb closely conforms to the "leg".

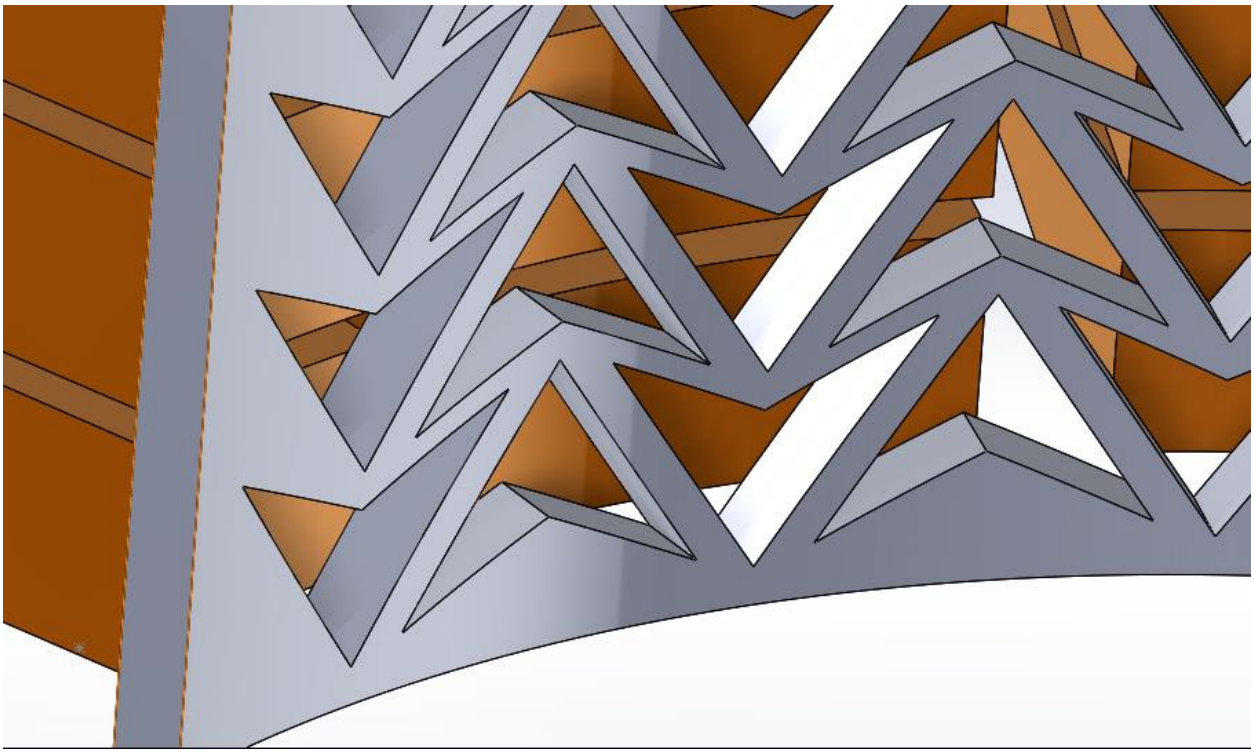

Figure 123: Close-up view of reentrant kite cells in backbone.

Accidental Treatment of Model as Steel Produces Auxetic Densification.

In the initial solution of the problem, this researcher forgot to change the material model for the entire annular comb structure (teeth and backbone) from the steel linear elastic model (to which ANSYS defaults) to the linear-elastic model with coefficients suitable for nylon. While the 1000x stiffness differential between the two materials should give different moment reaction values, at first one might expect the same moment reaction profile over rotation and deformation profile over the geometry of the annular comb. However, this ignores the different Poisson's ratios for steel (around 0.3) and nylon (around 0.4). Indeed, when one compares the deformed model when treated as steel (pictured in Figure 124, Figure 125, and Figure 126) with the nylon model (pictured in Figure 127 and Figure 128), one notices significant differences in the shapes the two annular combs take on after the same 15° of leg rotation. The principal difference is that

the steel backbone shows classic auxetic densification and withdraws inward when the leg does not constrain it (see the circled area in Figure 124), whereas this behavior is not evident in the nylon annular comb (the same area still sees separation from the backbone—look at the circled area in Figure 127). Perhaps the reason for this significant difference in behavior is that nylon's higher Poisson ratio inhibits the auxetic behavior of the metastructured backbone to a greater degree than does steel's more moderate Poisson's ratio. (It was later discovered that the shape of joints between beams in metastructured materials has a significant effect on some properties, such as tensile stiffening, as documented in the following chapter. Perhaps joint shape also affects auxetic properties, and perhaps the sculpted joint shapes developed in the next chapter would give this auxetic metamaterial more independence from the Poisson's ratio of its base material).

The backbone contraction that occurred in the steel model also affected the nature of contacts between teeth in this region. As shown in Figure 125, vertical tooth contacts occurred on an unusually high proportion of the total length of the teeth, and some teeth that were bonded to parts of the backbone also saw significant bending and sliding past each other. In this case, it was not clear how tooth bending curvature was related (if at all) to backbone curvature. Also, as shown in Figure 126, the auxetic contraction of the backbone tended to be localized enough to precipitously separate some tangential contacts between teeth (while enforcing others).

As might be expected from their fundamentally-different deformation behaviors, the two combs saw moment reaction curves with different shapes (if the Poisson ratios of the underlying materials had not effected the analyses, one would have expected the two curves to be directly proportional to each other, probably proportional by the ratio of the elastic stiffnesses of the two materials). The curves are presented in Graph 30 (for the steel annular comb) and Graph 31 (for

the nylon annular comb). Note the softening near the very end of the analysis for the steel comb and relatively linear behavior after 5° but before 12°; in contrast, the nylon comb saw a very parabolic relation between moment reaction and leg rotation. Frankly, the softening that occurred with auxetic contraction of the backbone is quite counterintuitive; one would expect local densification nearest the leg to boost the structure's stiffness there and then expect that region to play the biggest role in producing the overall moment reaction. Ultimately, neither analysis shows the desired moment reaction behavior of rapid and significant stiffening up.

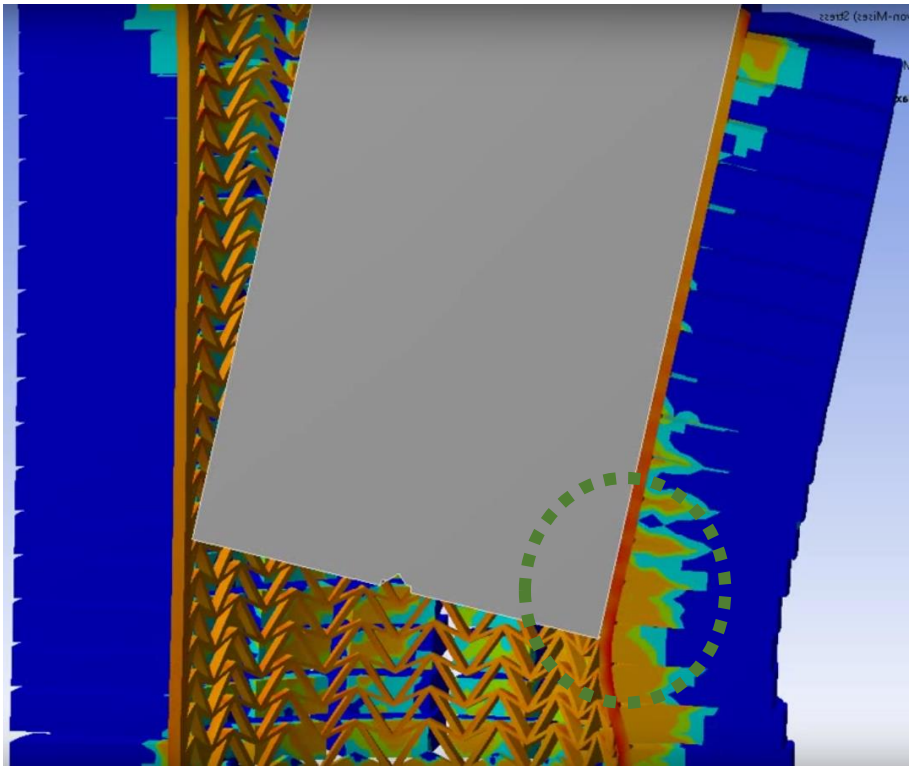

Figure 124: Symmetry-plane view of kite-backbone annular comb (modelled here, accidentally, as steel, not nylon), showing auxetic contraction that brings the backbone into contact with the leg near the bottom of the leg (circled in green)—compare this with the behavior of the nylon-modelled annular comb of the same geometry shown in Figure 127, in which no such densification is evident and in which there is thus less area in contact with the leg. The deformed structure is colored according to contours of von Mises stress, with red contours indicating a stress over 70MPa.

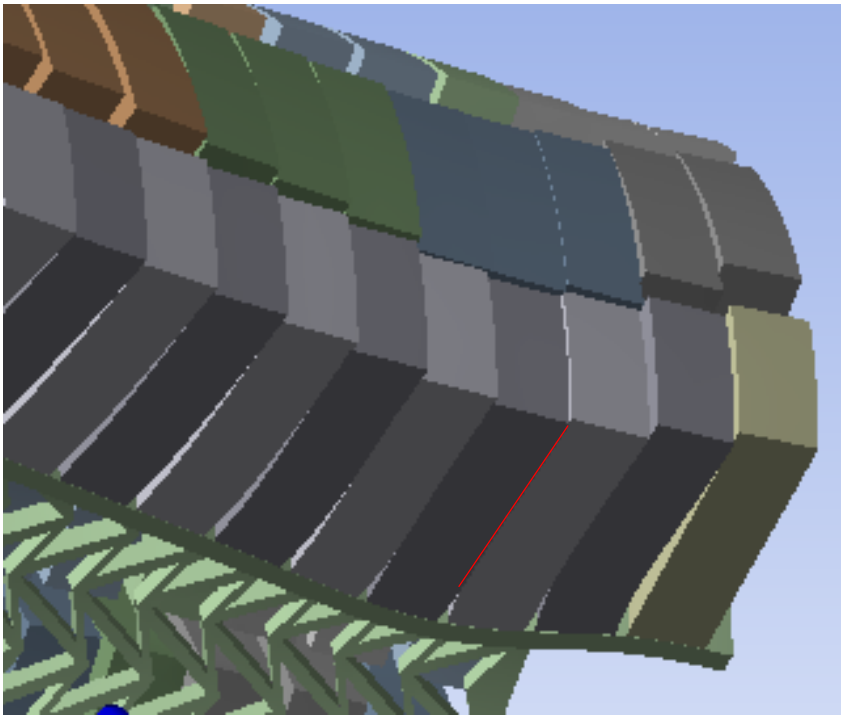

Figure 125: In this close-up view of the annular comb (looking at the base on the side facing the direction of leg rotation), the tendency of those teeth found in the area of backbone auxetic densification to contact along a significant proportion of their length is illustrated (for instance, one contact pair is highlighted in red).

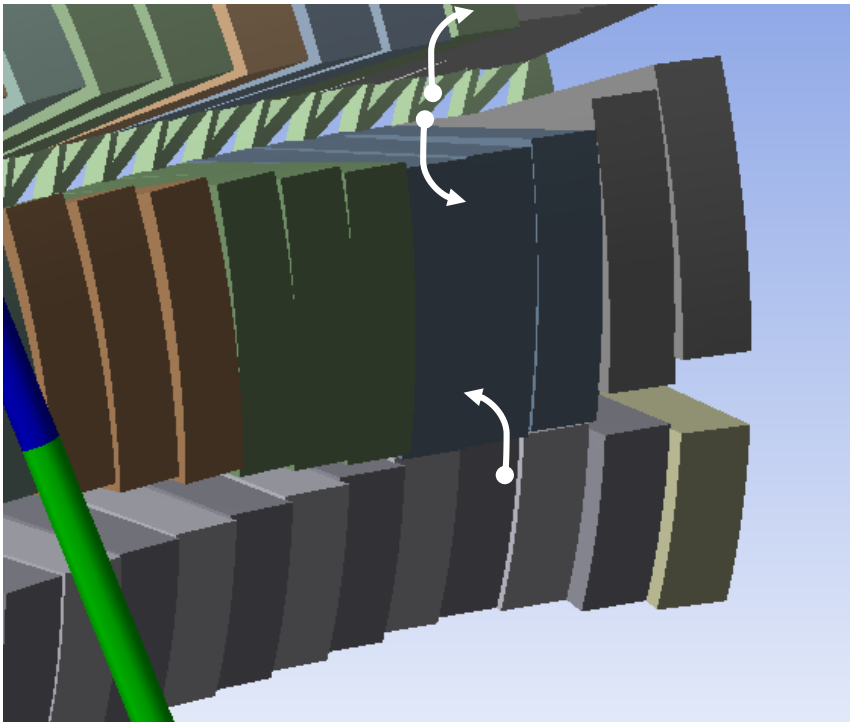

Figure 126: In this close-up view of the annular comb (looking at the base on the side facing the direction of leg rotation), the tendency of some teeth to spread apart when the backbone saw auxetic densification is illustrated in white arrows.

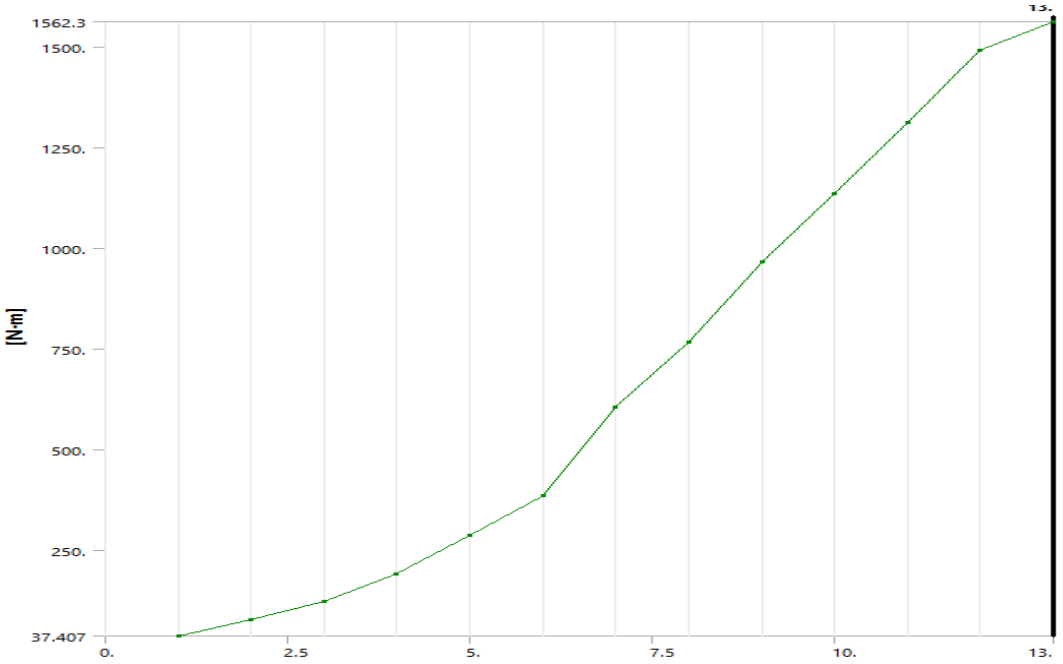

Graph 30: Moment reaction for the annular comb that was accidentally simulated as being made of steel (which gave it the significant backbone auxetic densification behavior shown in the previous two pictures), hence the higher moment reaction values than those for the same geometry simulated as nylon (shown in Graph 31: Reaction moment for reentrant-kite-backbone annular comb, with material correctly simulated as nylon with a corresponding Poisson's ratio of 0.4.).

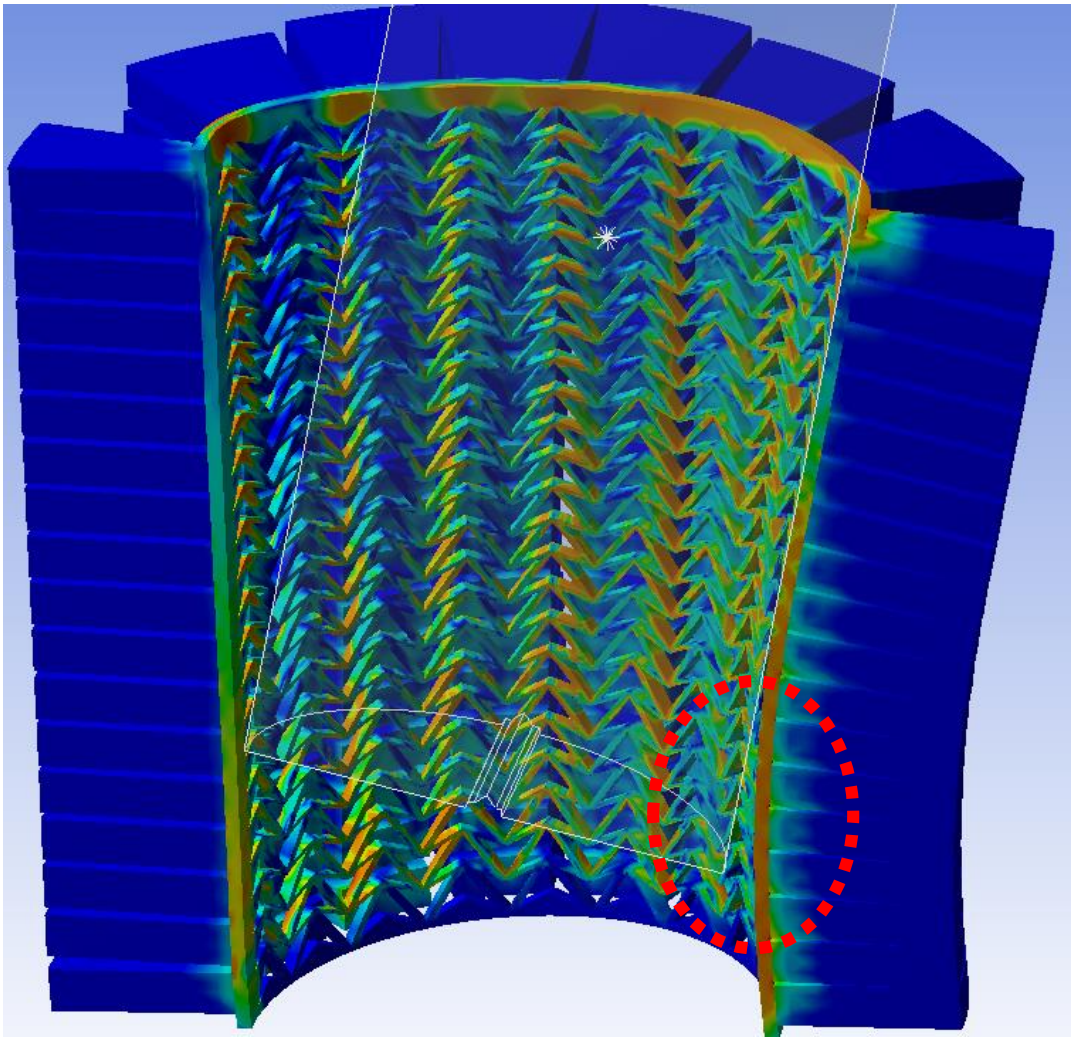

Figure 127: Deformed result after 15° of leg rotation, with contours of von Mises stress (with red indicating stress over 70MPa). Note that overall the auxetic property of the backbone did not have any significant effects here. (This simulation should not be confused with the one shown in Figure 124, which was accidentally performed with all parts treated as being of linear steel, with its corresponding Poisson ratio of 0.3 instead of nylon's 0.4). The red circle highlights the separation between the backbone and leg that did not remain in the steel annular comb in the same area (see the green circle in Figure 124).

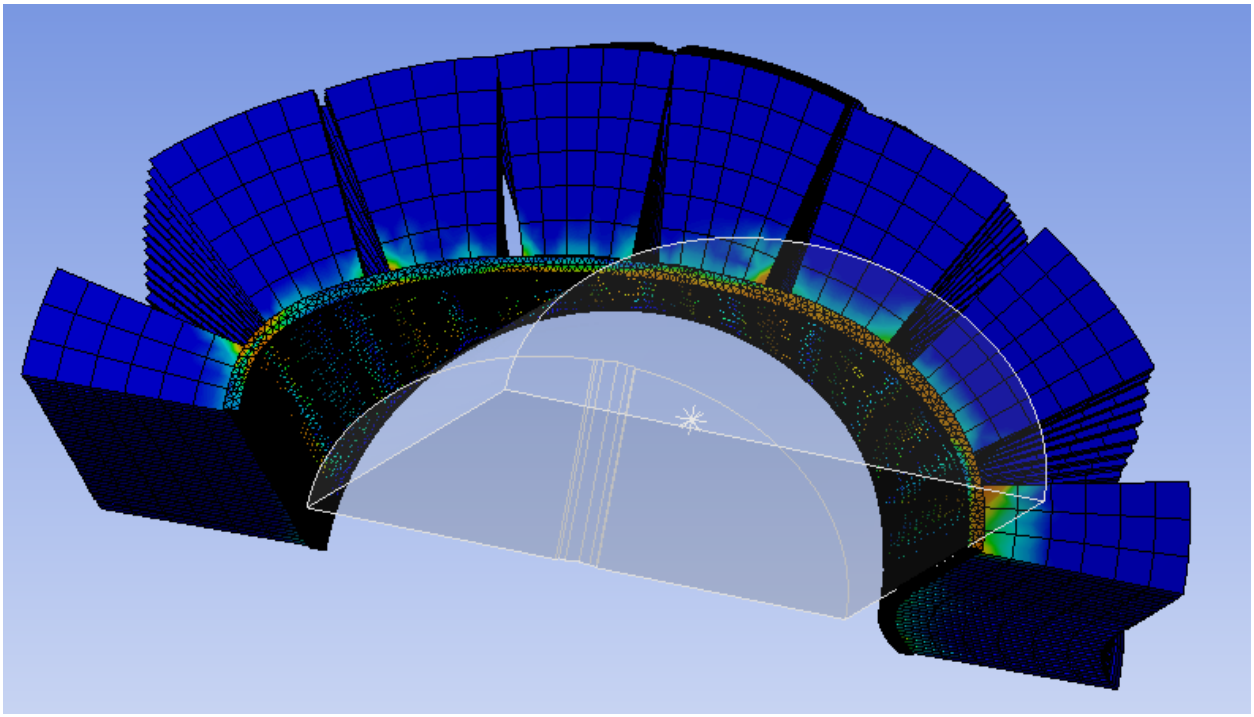

Figure 128: Top view of kite-backbone annular comb after 15° of leg rotation, colored by von Mises stress (with red indicating a stress in excess of 70MPa).

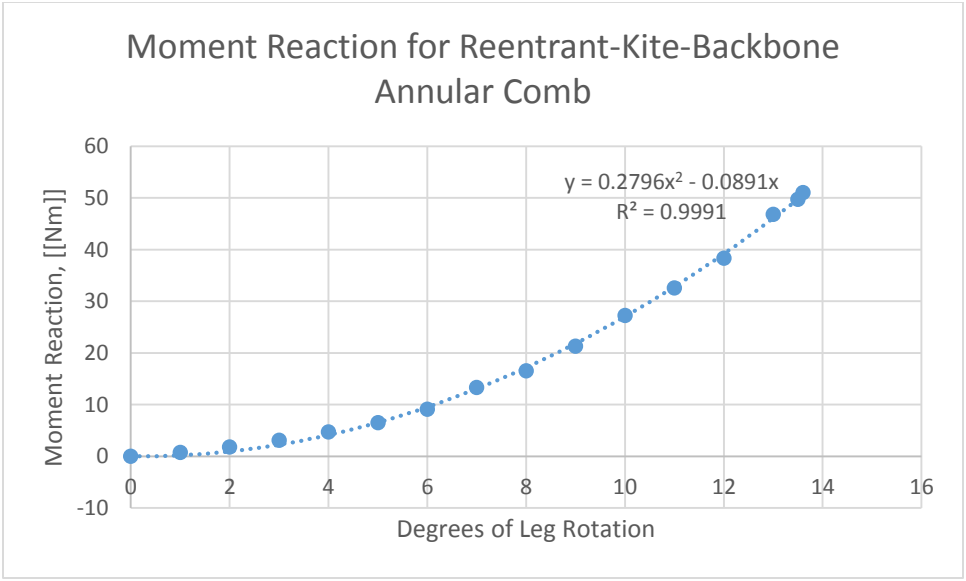

Graph 31: Reaction moment for reentrant-kite-backbone annular comb, with material correctly simulated as nylon with a corresponding Poisson's ratio of 0.4.

Triangular Lattice.

It is anticipated that this geometry will produce the most similar behavior to that of the solid backbone (as regards Poisson effects or other micromaterial effects, since three links joined into a triangle do not have any mechanism freedom), just be less stiff for a given thickness due to lower effective density. Given this, no obvious reason to go to the trouble of generating and analyzing this model was seen, since the annular comb concept has thus far proven ineffective.

Rethinking Lattice Geometry: Focus on Joints.

While the above lattices did indeed reduce pre-lockup moment reaction (by virtue of reducing backbone density without increasing its thickness, plus perhaps adding bending-dominated modes of deformation), their results were far from satisfactory, especially for geometries that should have stiffening-up potential on their own (namely the reentrant hexagon) but yet showed no such behavior. It occurred to this author that this subpar performance might be due to the nature of the joints between the lattice beams; borrowing from the domain of compliant mechanisms, the joints should perhaps instead consist of relatively-thin beams (connected to each other by much-thicker, ergo stiffer, beams). When the joints are as thick as the beams are elsewhere, this condition more closely resembles a cantilevered condition, which is no way to provide freedom. As such, the beams were thinned in the vicinity of their joints, and an annular comb backbone based off this was developed. Please see the next chapter for an exploration of the concept.

Controlling Backbone Buckling with Bends.

In order to maximize stiffness at the lockup point, avoiding shell buckling in the backbone seems essential for two reasons: first, the bending stiffness of a shell (or beam) is reduced in post-buckling bending, so presumably this would reduce the bending stiffness of a

shell-and-beam complex such as the annular comb. In addition, it is the backbone shape that determines when teeth will be angled appropriately in order to contact each other: specifically, depending on the direction of buckling, it may bring teeth into contact faster than they should, or it may spread teeth away from each other, thus preventing them from ever contacting (at least unless the buckling is reversed). Presumably, it suffices to control buckling before teeth touch, as once they are touching, the bending stiffness of the structure should locally be large enough to prevent buckling.

For instance, FEA of an annular comb structure with a backbone with square cutouts (with sides oriented 45° from vertical/horizontal) was first analyzed and found to have local buckling between the third and fourth teeth in the symmetry plane (presumably, this set of teeth is most important to lockup since they directly oppose the rotating leg); in these simulations, post-buckling behavior showed the backbone bowing outward and separating these teeth, although it is likely that a slightly-different perturbation or loading condition could result in the

opposite behavior (which would bring the teeth into contact and short-circuit the buckling). Figure 129 and Figure 130 show this behavior.

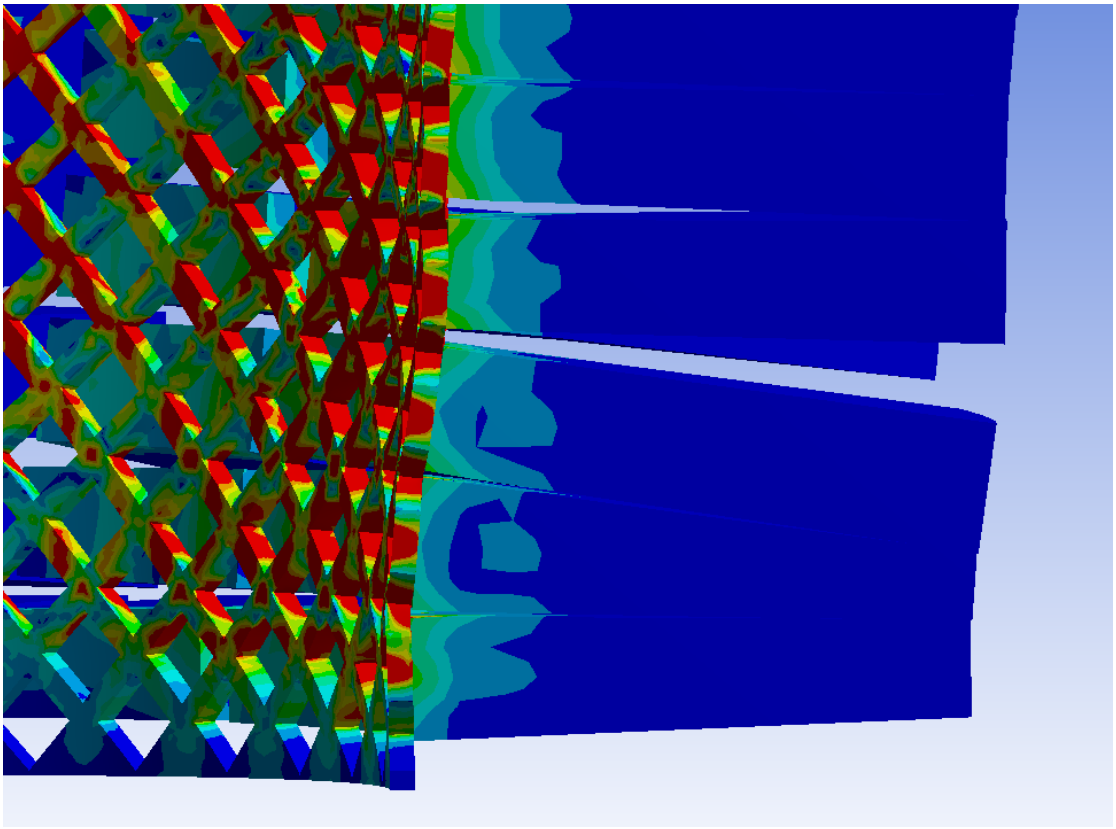

Figure 129: Close-up view of rotated-square lattice structure with some shell buckling between third- and fourth-from-bottom teeth.

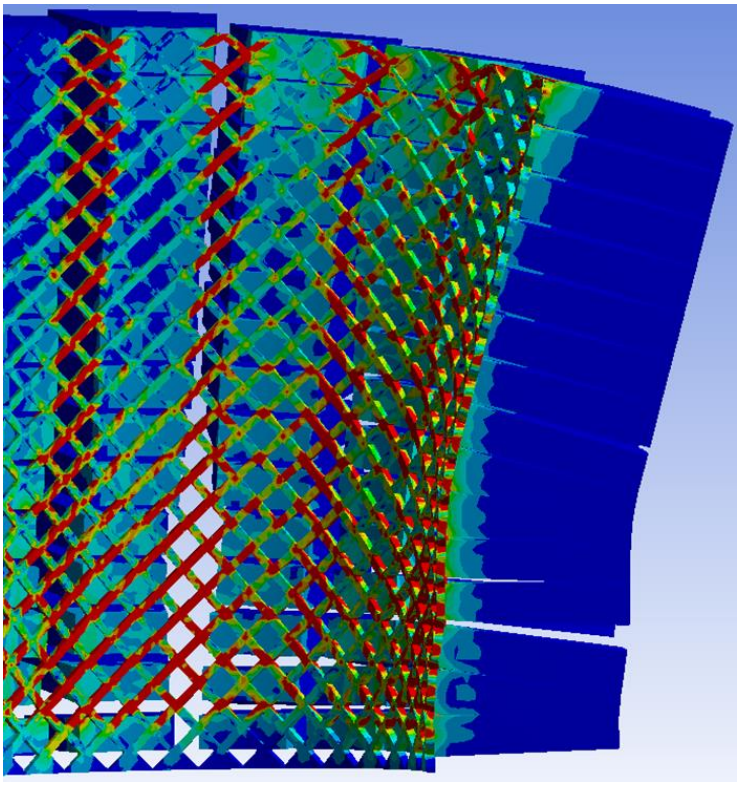

Figure 130: Overall view of rotated-square lattice structure with some shell buckling between third- and fourth-from-bottom teeth.

To counter this buckling, material thickness was selectively added (roughly doubling the lattice thickness at the most buckling-prone point) while maintaining the diamond shape of the cutouts. Figure 131 and Figure 132 show the backbone geometry after thickening. Unfortunately, the change simply shifted the locus of buckling upwards to areas that were not thickened against buckling, as shown in Figure 133.

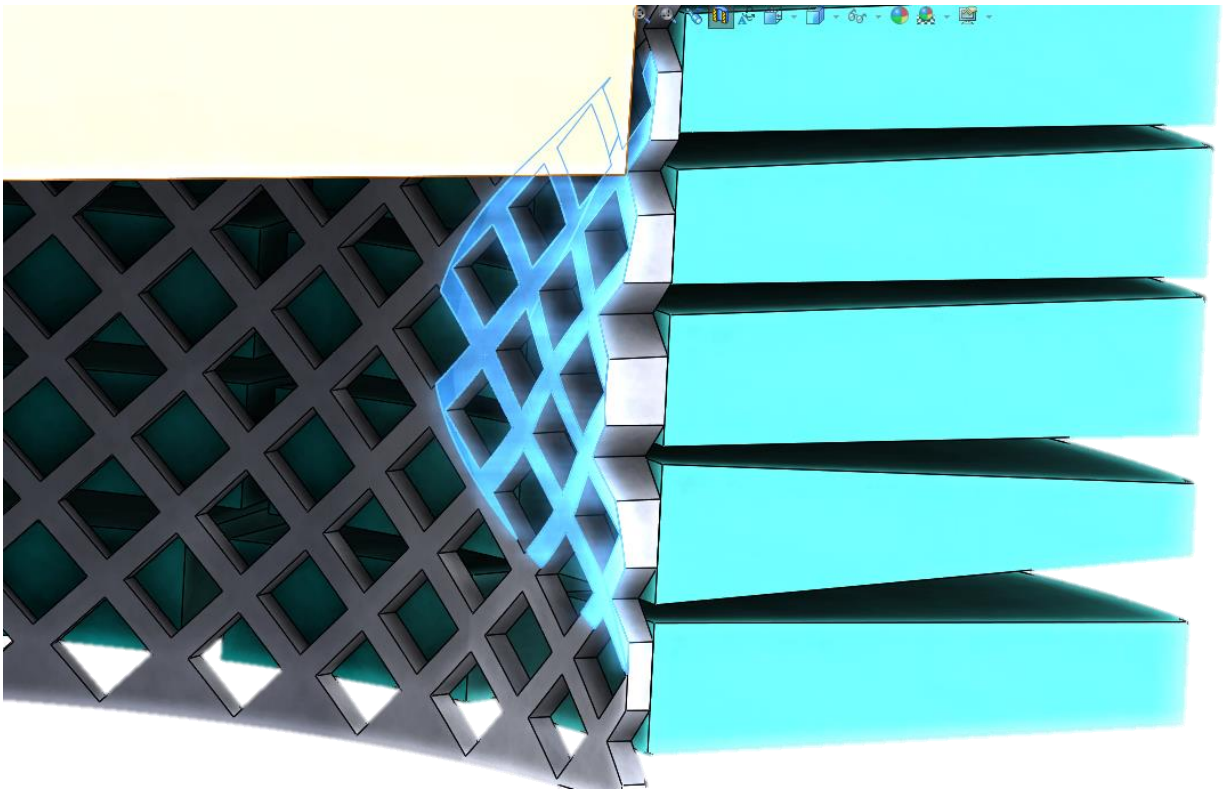

Figure 131: Selective thickening of diamond-lattice-backbone annular comb against local buckling, view 1. The thickened area is highlighted in blue.

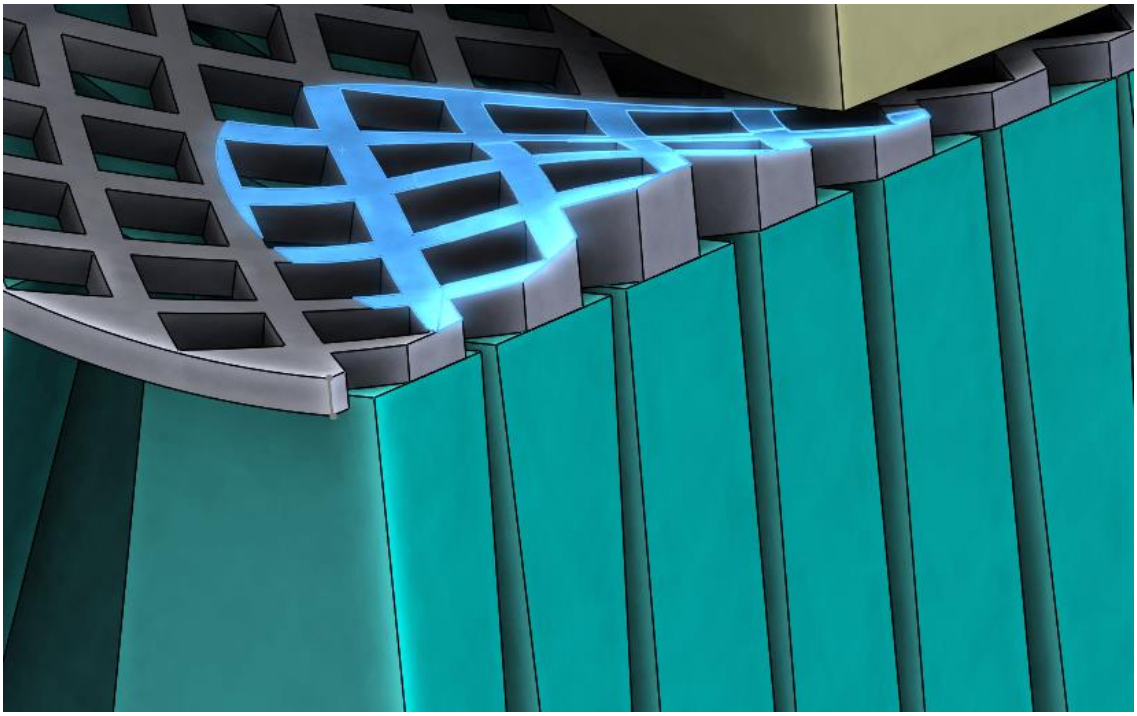

Figure 132: Selective thickening of diamond-lattice-backbone annular comb against local buckling, view 2.

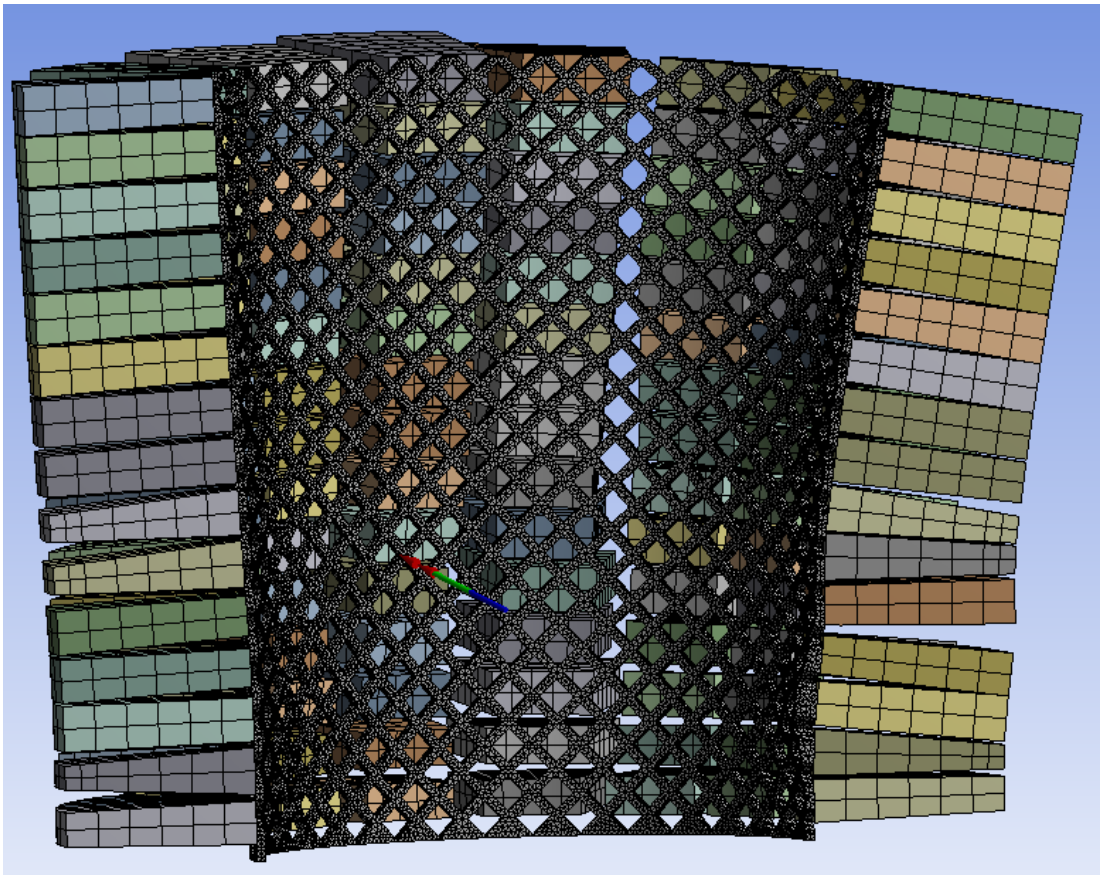

Figure 133: New buckling locus between teeth 4 and 5 (in the symmetry plane and facing the leg's rotation) after thickening the backbone between teeth 3 and 4.

Flaring Backbone against Buckling.

It may also be feasible to prevent deleterious backbone buckling by angling it outward at the base. However, this modification may increase the overall pre-lockup stiffness of the joint (for the same backbone thickness), and it would also increase the footprint of the protective device. Indeed, this flare would likely need to extend for several tooth-thicknesses from the base of the annular comb, for that is how far the buckling locus is from the base in the constant-diameter annular combs.

Combination of Cable-Based Stiffener and Annular Comb.

If backbone buckling cannot be controlled and made to be "well-behaved", then it may instead make sense to connect slightly-slack cables to those teeth that will separate further instead of getting close together near the lockup point. Note that in the chapter on the linear comb, such a stiffener was proposed and attempted in 1D, and some drawbacks (such as the necessity of hand manufacture and difficulty in getting a precise cable length) were observed, although little effort was expended to overcome them, so the principle may still be valid. Figure 134 shows a sketch of an annular comb with recommended addition of an initially-slack cable that will be stretched to its full length and then become quite stiff (if made of high-tensile fibers like Kevlar, Vectran, etc.). Note that special features might need to be added to the teeth to facilitate cable attachment. Also, it might be ideal to anticipate post-buckling backbone bending in either direction, either away from or towards the leg, all depending on the vagaries of the precise loading conditions. This would dictate that the designer allow both for tooth contact and cable tightening to occur between certain teeth (i.e. rather than adding features for cable tightening that would not offer the appropriate contact stiffening if the backbone buckled the opposite way that the post-buckling behavior predicted).

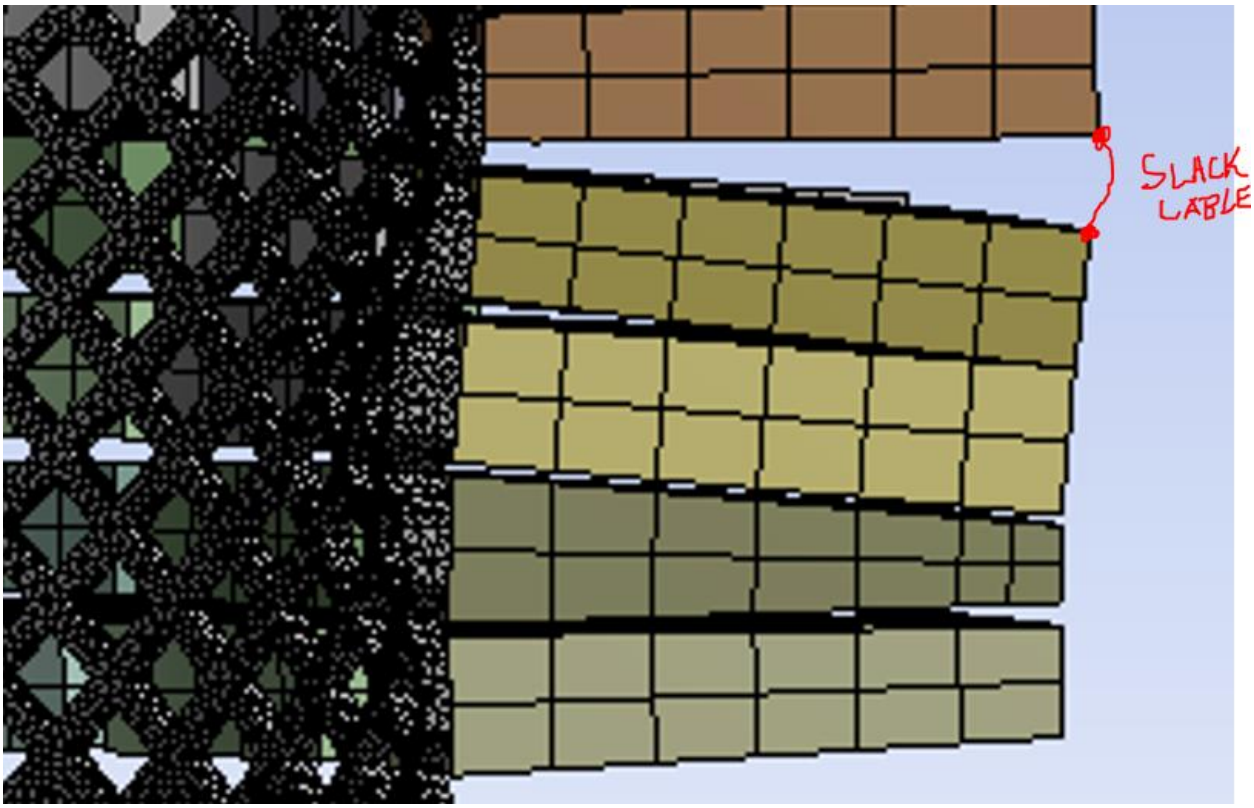

Figure 134: Proposed addition of initially-slack cable that will go taut when teeth separate by a prescribed amount.

Angled-Fiber Backbone.

White, Hafner, and Whatley discovered[46] (incidentally, during development of artificial tendons for a prosthetic ankle that would mimic human ankle tendon properties) that a composite of an elastomeric matrix and high-stiffness anisotropic fibers added in one direction with a wave-like pattern can experience stiffening-up on the order of 25x with 5% strain. This stiffening occurs from two factors: one, when the high-stiffness fibers experience large-deflection reorientation from a wavy/springy geometry that experiences local bending when the ends of the overall structure are in tension (and is thus not terribly stiff) to a straight geometry dominated by tension; and two, when the highly-anisotropic fibers are reoriented in the large-deflection regime

[46] "Development of an Advanced Biofidelic Lower Extremity Prosthesis", Moreno White, Brian Hafner, Walter Whatley

such that their stiff axes are closer to parallel to the overall load path. Figure 135 shows the original concept developed by the above researchers, both unloaded and loaded, and Figure 136 shows load-strain curves for some bands that the same researchers developed. Note that the researchers did not attempt to optimize their bands for the absolute maximum tensile stiffness increase, but rather towards biofidelity.

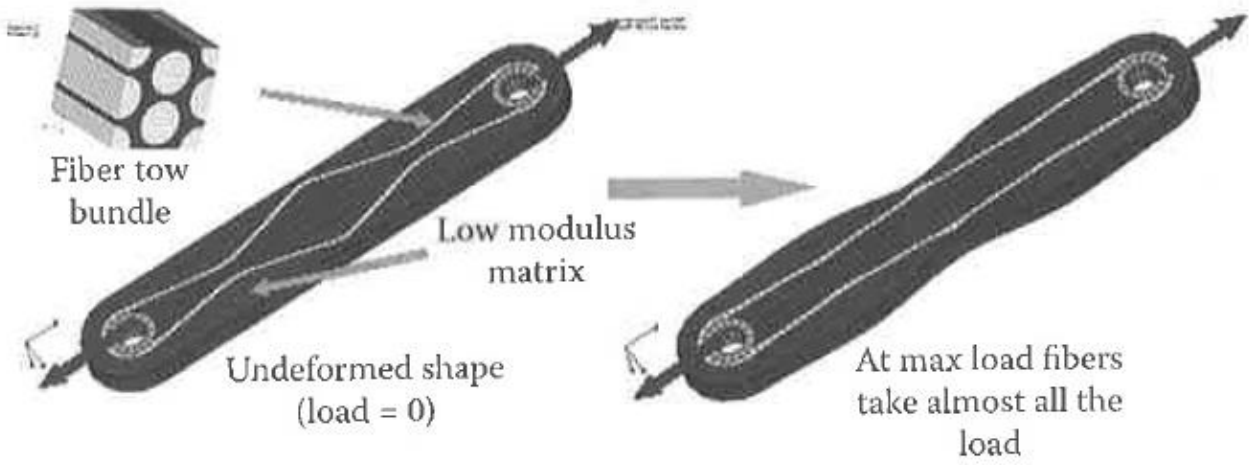

Figure 135: FEA simulation of elastomer-fiber composite stiffening up in large deflection showing reorientation of wavy fiber bundle, taken from [47].

[47] "Development of an Advanced Biofidelic Lower Extremity Prosthesis", Moreno White, Brian Hafner, Walter Whatley

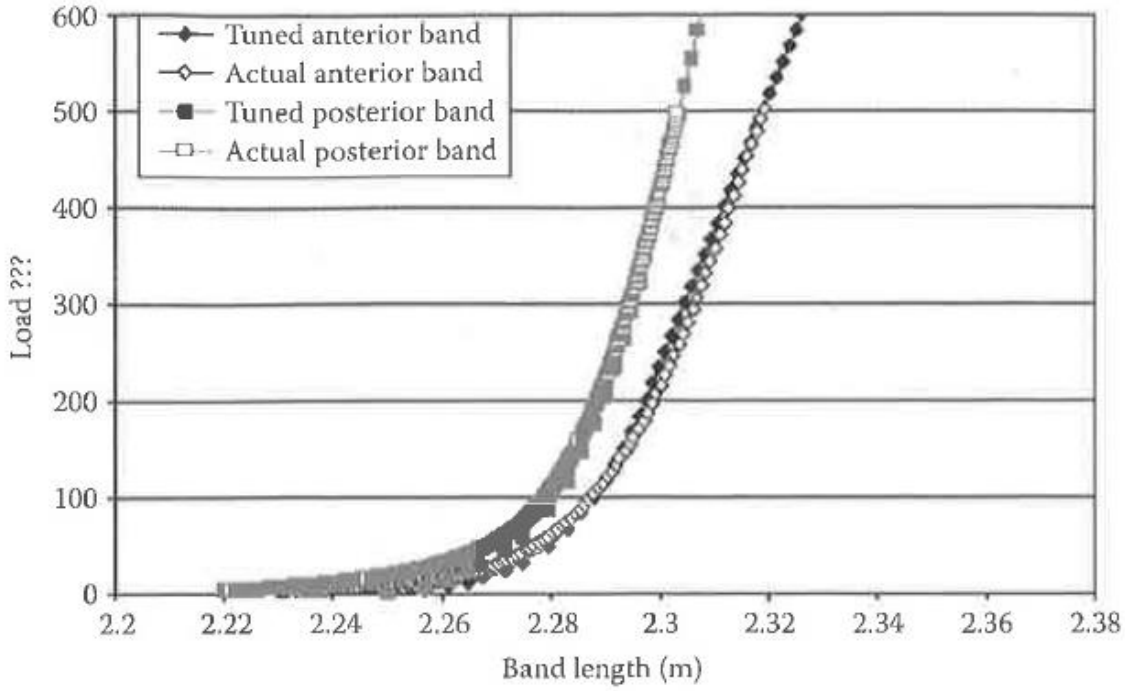

Figure 136: Test results for elastomer-fiber composite showing remarkable stiffening after a moderate amount of strain, taken from [48].

In the annular comb, the part of the backbone contacted by the leg should experience local tension from backbone bending, just as elements in a beam in bending experience tension when far from the neutral axis and on the convex side. In addition, after teeth in the annular comb contact, the effective neutral axis of the structure should be moved well outside the backbone, such that further bending of the overall annular comb should increase tension throughout the area of the backbone near the contact patch with the leg (where teeth are locked up vertically).

For comparison, recall the linear comb from the previous chapter (pictured in Figure 56) – its wavy backbone gave it more compliance for the same backbone thickness than would a

[48] "Development of an Advanced Biofidelic Lower Extremity Prosthesis", Moreno White, Brian Hafner, Walter Whatley

linear backbone (in the same way that the helix shape of a spring gives it tensile compliance). When bending the comb before the teeth have locked up, the tensile-strain distribution in the backbone is no doubt complex, and presumably some areas are in compression instead of tension. However, once the teeth have contacted, the neutral axis of bending moves towards the teeth tips, and the whole backbone is stretched with further bending. Indeed, the wavy geometry makes the overall tensile displacement of the backbone easy to recognize, as it is accompanied by changes in the wave angles, as shown in Figure 58 in the case of the wavy-backbone linear comb. (Note that this springy geometry is used here only to make the tensile strain of the backbone post-lockup visible. This wavy structure would almost certainly make a poor backbone for the annular comb because it would be too compliant in tension—after all, the linear comb with springy backbone did not gain sufficiently in bending stiffness after tooth lockup since the springy backbone was so compliant in tension).

Unfortunately, this principle did not seem to apply to the annular comb, and FEA results of multiple embodiments of the principle showed poor performance, as will be documented below.

Rubber-Matrix Wavy-Fiber Backbone Annular Comb.

The first logical embodiment of the above-described principle for stiffening up in tension was to also use an elastomer "matrix" for most of the backbone but add some quantity of wavy fiber bundles (it was unknown what exact proportion of the entire backbone the fiber bundles should compose to keep pre-lockup stiffness sufficiently low but post-lockup stiffness sufficiently high). Even absent the effects of wavy fiber bundles being straightened, some elastomers show stiffening behavior after some strain (in both uniaxial tension and compression), although the amount of strain required to realize the stiffening is high, and the stiffening is not of

sufficient magnitude on its own to solve the mechanical problem of this thesis. However, given a choice of elastomeric matricies (and assuming all other mechanical and chemical properties, such as bonding to the fiber bundles, are within desired ranges), it seems preferable to use a matrix that stiffens up even moderately!

Such an elastomer has been modelled with the Yeoh 3rd-order material model, and this was selected for use in the simulations, representing roughly a best-case scenario. Uniaxial tensile and compressive properties dictated by this elastomeric material model are shown in Graph 32.

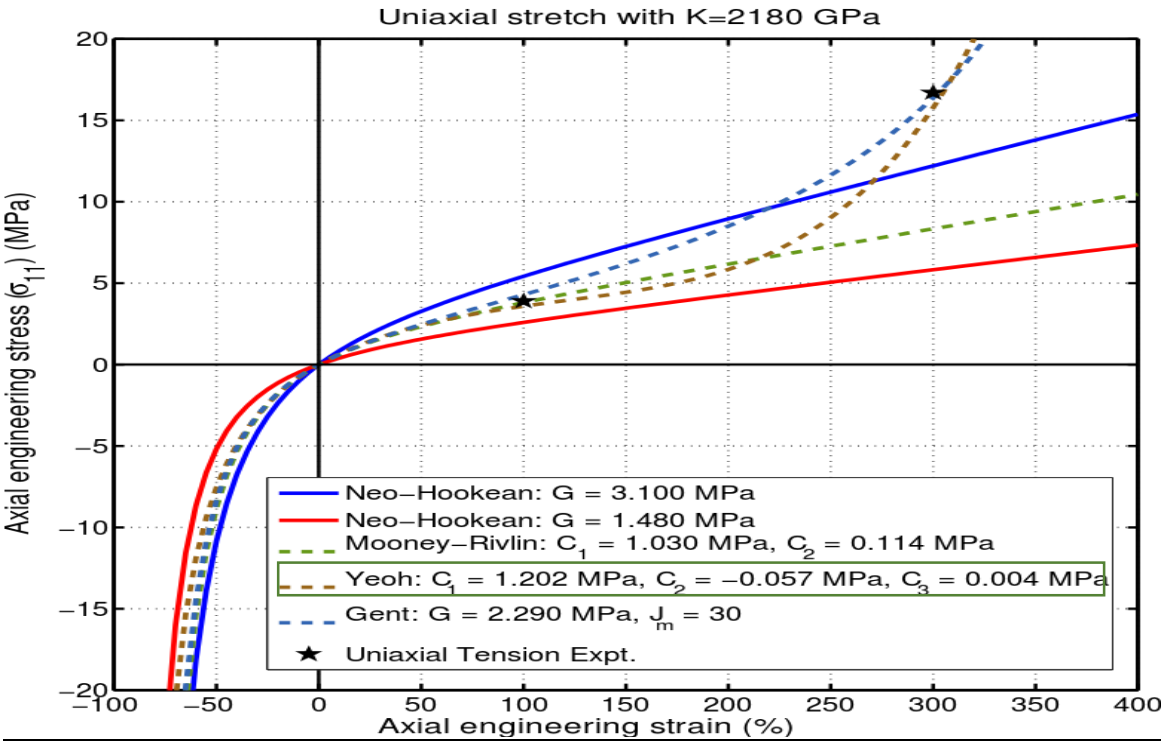

Graph 32: Uniaxial tensile and compressive response for several hyperelastic models, including Yeoh 3rd-order.

The fiber bundles themselves were treated as unidirectional carbon-fiber (70%) and epoxy (30%) laminates (strictly speaking, it would have been more accurate to use the Rule of Mixtures with elastomeric properties for the matrix instead of epoxy properties, but since the

matrix contributes fairly little to the stiffness, this was neglected. That said, epoxies obviously have lower Poisson's ratio than do elastomers, so if bulk compression effects dominated, the fiber tows might have inaccurate properties in this mode). Elements were oriented along the edges of the bundles to ensure proper direction of the anisotropy.

There were numerous geometric variables to consider when generating the preliminary fiber-elastomer backbone annular combs. The salient variable, judging from the work of White et. al. cited above, is the angle at which the fiber initially (before tensile strain) deviates from vertical orientation. It is anticipated that the higher the angle, the lower the initial stiffness of the overall geometry in tension (remember the two modes by which the structure stiffens that were explored above—fiber anisotropy and local fiber bending from global tension), and the greater the strain required until the fiber is nearly vertically aligned and thus providing significant stiffness. Unfortunately, there will probably be a trade-off between rapidity of stiffening up and magnitude stiffness increase from beginning to end (the former can be achieved by giving a small deviation from vertical, the latter a large deviation). Figure 137 shows the overall annular comb geometry that was generated as the first proof of concept, with fibers surrounded by elastomer on both sides; Figure 138 shows a 2D projection of a fiber tow, with the angle of declination from vertical illustrated.

The teeth were treated as being of nylon, as in previous analyses, in anticipation that they would need to be 3D printed for real manufacture.

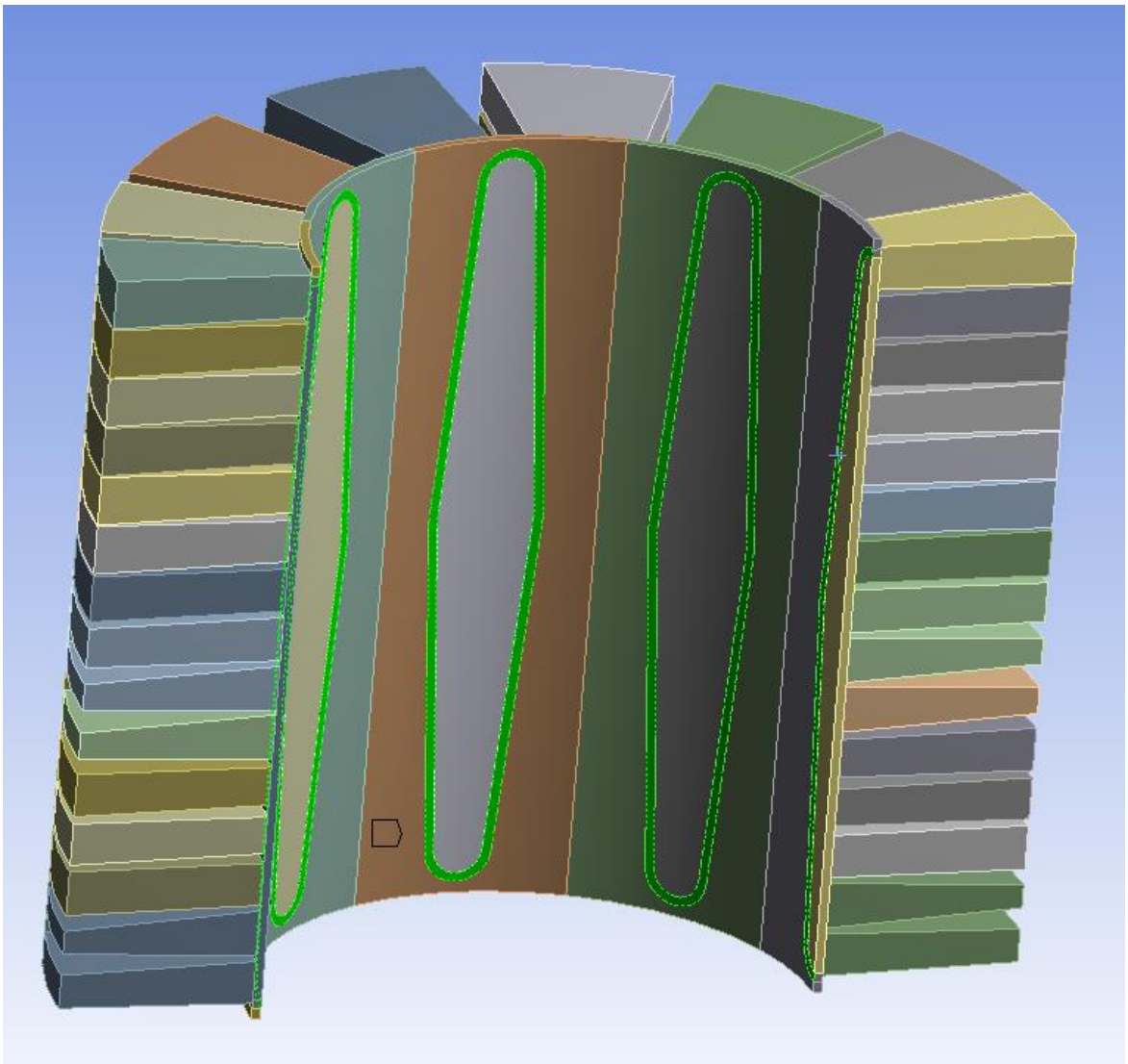

Figure 137: Elastomer-fiber annular comb geometry. The high-stiffness fiber tows have been highlighted in lime green.

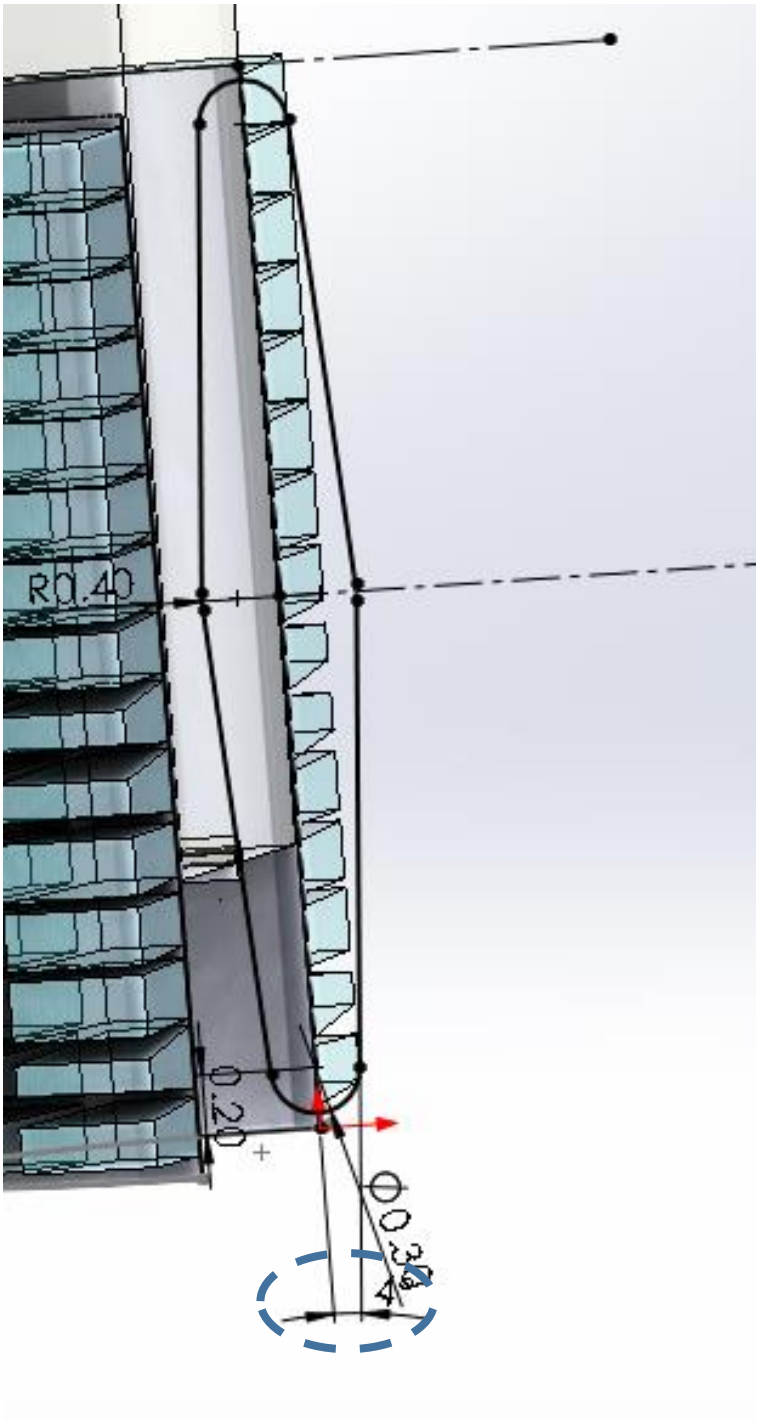

Figure 138: Basic tow outline that was projected onto the cylindrical face of the backbone to produce the tow geometry. Here, the angle of deviation from the vertical is shown to be 4°, a relatively shallow angle.

Other potential variables of interest include the ratio of fiber tow volume to overall backbone volume (here quite small, as the four whole tows used in the half-section were quite

thin). To increase the fiber content of the whole backbone, the fiber tows could simply be thickened, the distance between them could be decreased, and smaller tows could even be nested inside one another.

A note about FEA parameters is in order: due to the low stiffness of the rubber portion of the backbone, some elements would experience significantly-greater strain than would elements in most previous simulations (which used stiffer nylon) since other areas would be more constrained by the stiff carbon fiber tows. Consequently, it proved necessary to employ adaptive remeshing in the analysis, which has been implemented in the version of ANSYS available to us only for linear, tetrahedral elements. Ordinarily, these elements are quite inferior to 2^{nd}-order hexahedral elements (although a mesh containing the latter cannot always be generated by the meshing algorithm), but in this case there was no other way to implement remeshing. Owing to the imprecision of the linear, tetrahedral element, a much finer global element size had to be employed; Figure 139 shows a closeup view of the elastomer portion of the mesh.

Also, because using the automatic remeshing feature activates partial pivoting, the solver cannot automatically detect self-contact, and instead must be given manual contact pairs (generating which is a tedious process). Finally, partial pivoting unfortunately is incompatible with the use of GPU acceleration from devices like the Quadro 6000; all of these combined to raise the time required to both prepare and run the analysis. Initially, the solution was attempted assuming complete incompressibility of the rubber, but this resulted in severe convergence difficulties (even when using mixed u-P-formulation elements), so Yeoh incompressibility factors (D1, D2, and D3) were all chosen to be 1.2e-11Pa^{-1} instead of exactly zero, whereupon it became possible to obtain a solution, at least for some quantity of leg rotation.

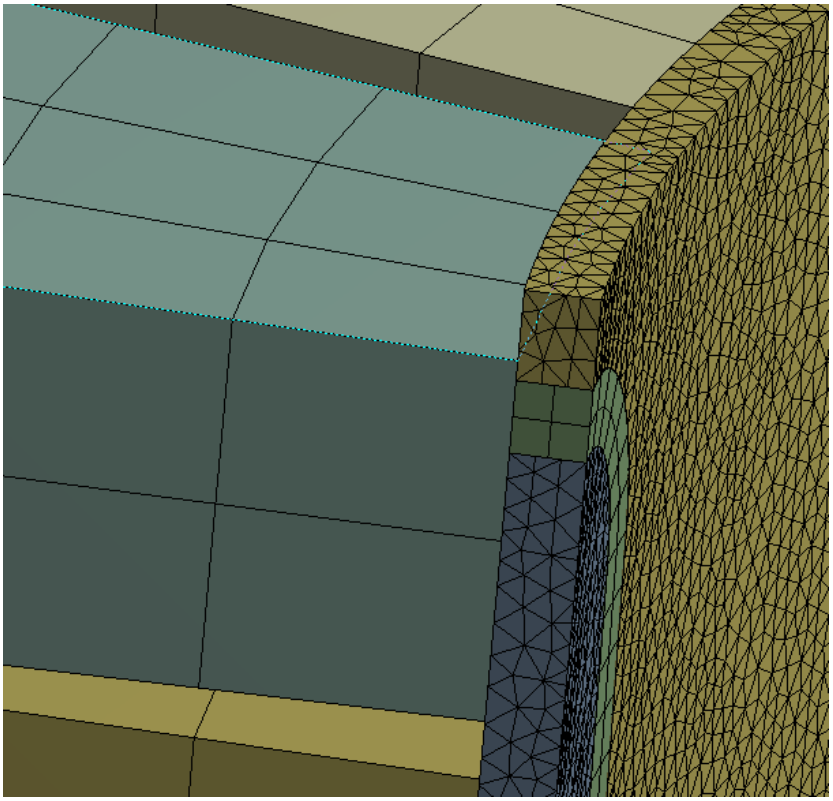

Figure 139: Mesh for elastomer-fiber backbone. Note the higher density of elements than in the backbones of previous combs (which were meshed with hexahedral elements), and their tetrahedral shape.

The FEA results for this structure did show very low pre-lockup stiffness, which is presumably attributable to the high compliance of the rubber component of the backbone. Unfortunately, the magnitude of stiffening was even less dramatic than for the previous annular combs simulated, as shown in Graph 33 (while occurring even earlier than in the homogenous annular combs, at 3.5° instead of the former's 5-6°, neither of which was anywhere near the 15° towards which optimization had vainly been conducted). The analysis quickly ran into trouble from strain concentrations in the rubber backbone near the bond sites with corners, perhaps because of ill-conditioning from the large stiffness differences between the nylon teeth and rubber backbone; contours of the resulting strain concentrations are visible in Figure 141. . (Note that remeshing occurred once in the simulation, probably in an attempt to alleviate the

stress concentrations; the entire history of convergence is shown in Graph 34: History of force convergence for the FEA of the basic reinforced-rubber annular comb, showing). While this may seem like a non-physical, numerical error, note that in real life the stiffer nylon teeth might actually pierce the rubber at these sharp points, leading to catastrophic tearing of the backbone and thus failure of the annular comb. There was also some minor strain concentration at the interface between one fiber bundle and the rubber backbone, with a moderate tendency towards radial separation along the interface, as shown in Figure 140, although this phenomenon was not likely responsible for the convergence difficulties.

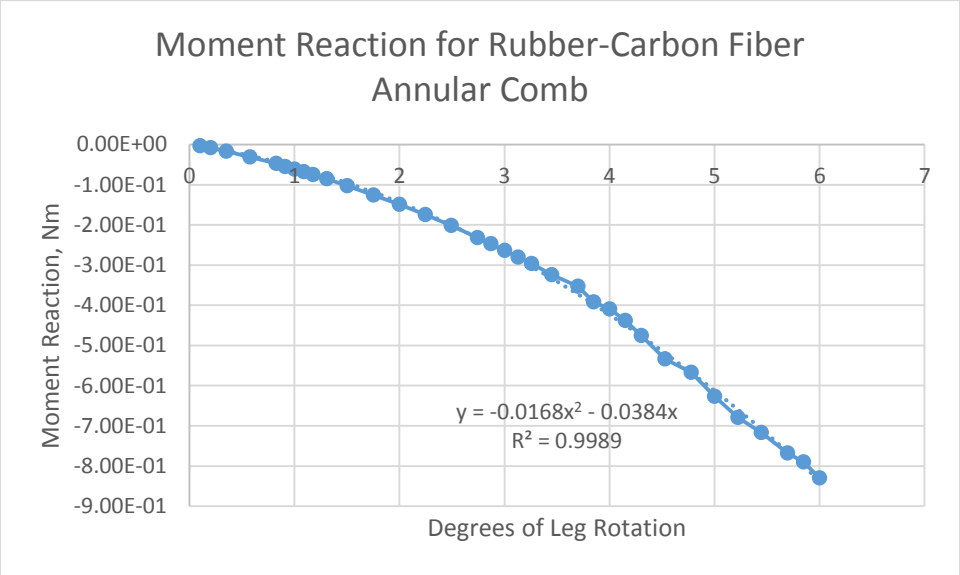

Graph 33: Moment reaction for solid rubber/carbon fiber backbone annular comb. Note that the analysis would not converge beyond around 6° of leg rotation.

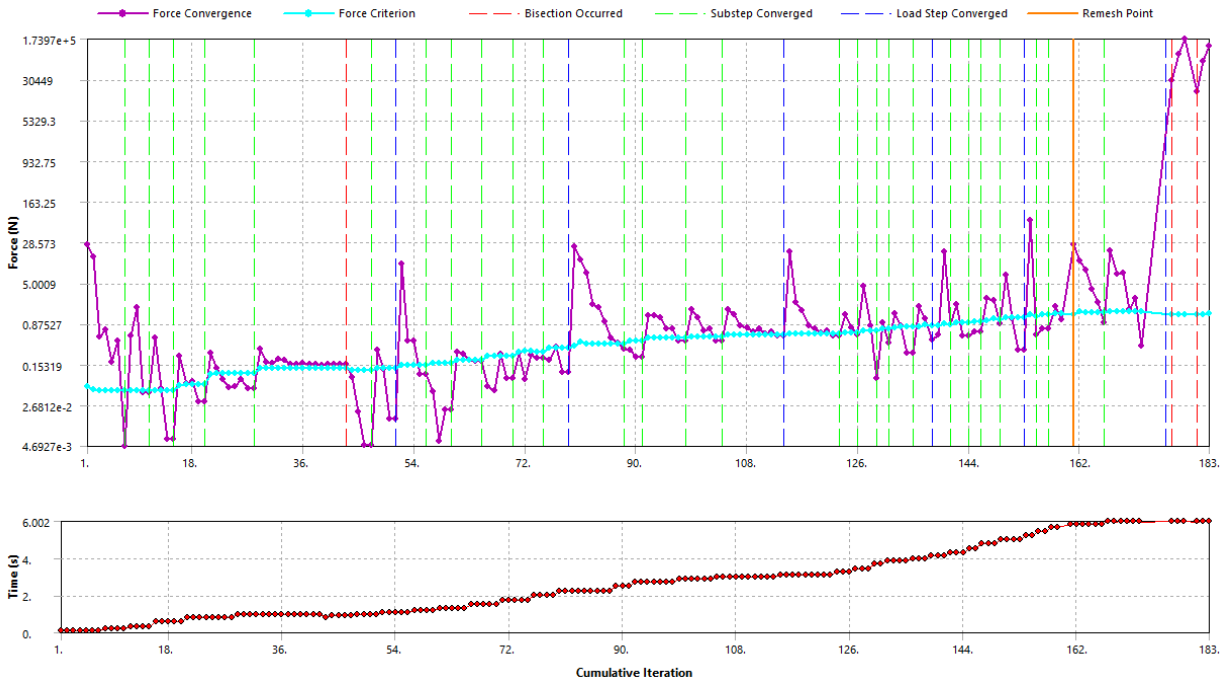

Graph 34: History of force convergence for the FEA of the basic reinforced-rubber annular comb, showing the instance of remeshing and final 'blowing up' of the solution.

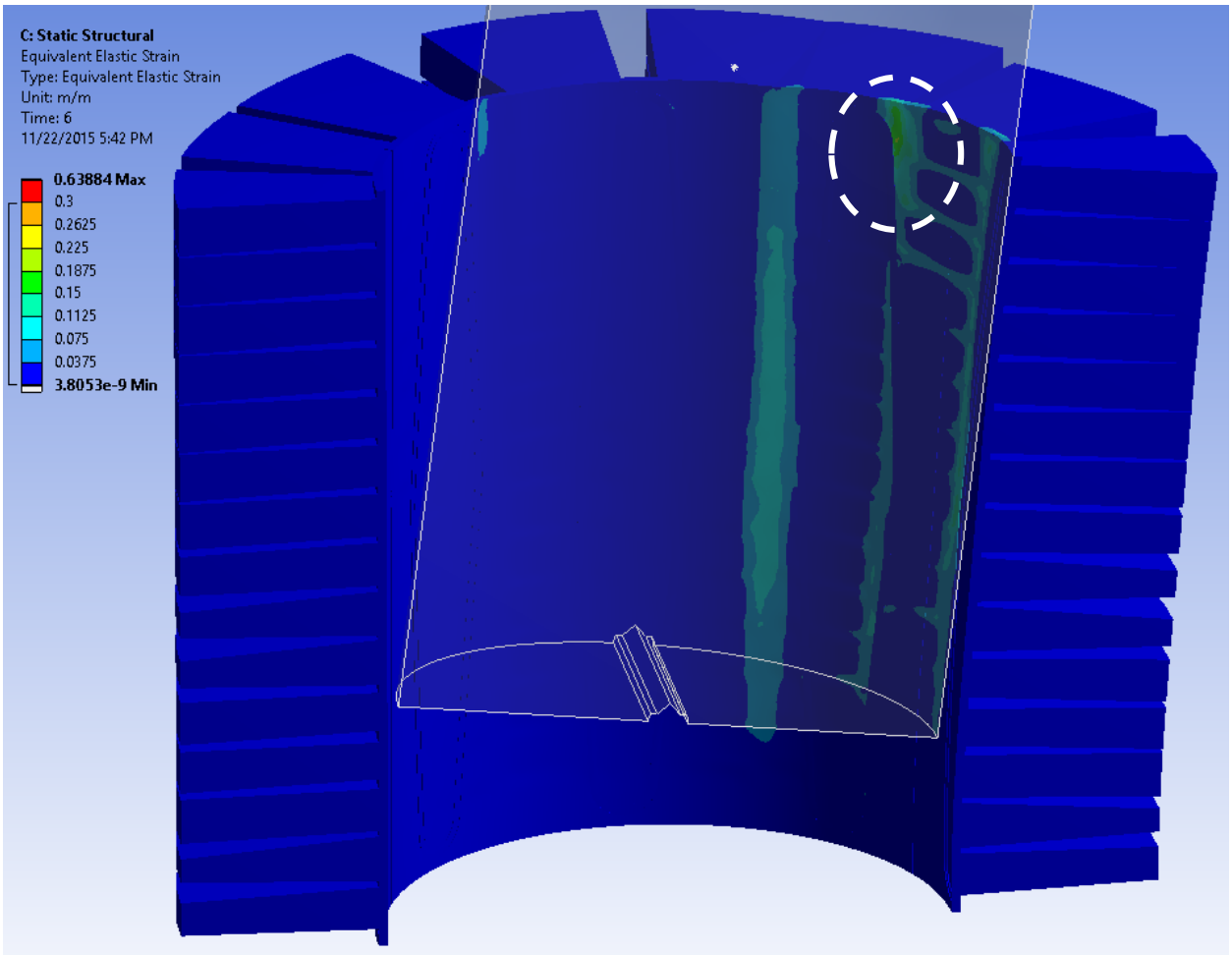

Figure 140: Von Mises strain profile for the reinforced-rubber annular comb. Note that there is a minor strain concentration at the interface between one fiber bundle and the rubber backbone (circled above in white), although it pales in intensity when compared with the strain concentrations shown in the following figure.

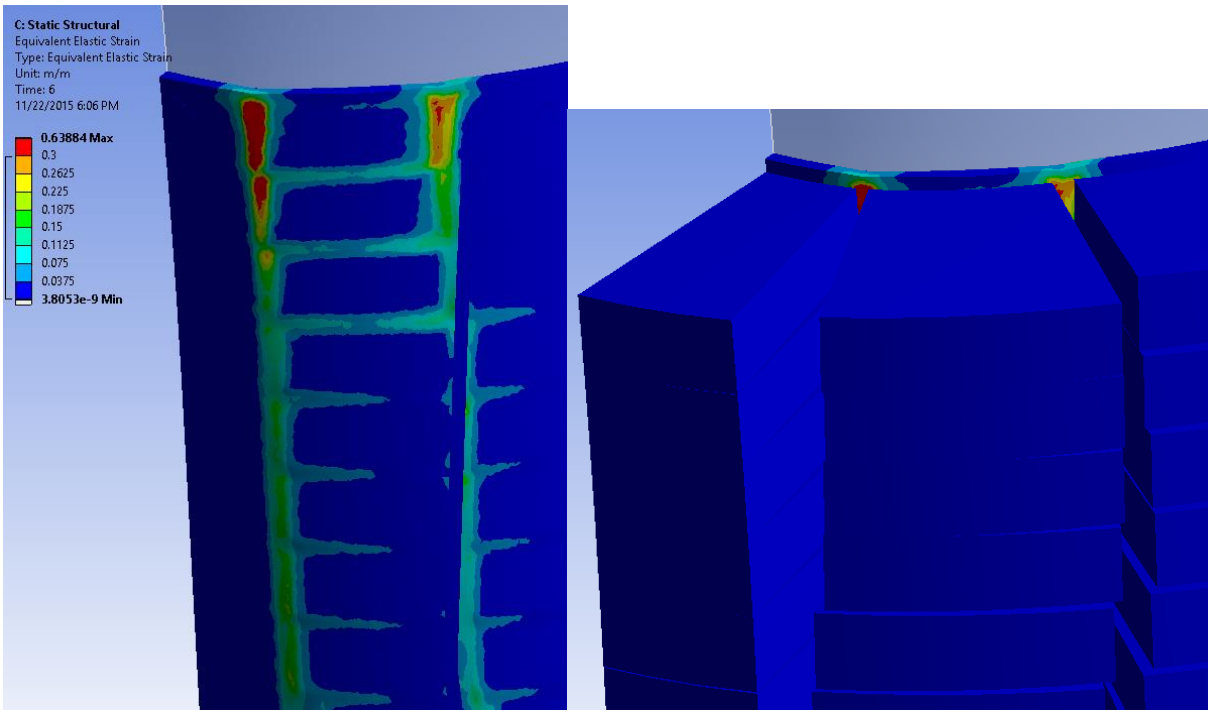

Figure 141: Closeup of strain concentrations near corners of the bond areas between teeth and backbone (in the left view, the teeth are hidden so reveal the full extent of the strain concentrations).

Since convergence ceased when only four teeth in the symmetry plane had engaged in vertical contact, there may still be a small chance that the structure can stiffen in gross bending thanks to the tensioning of the fiber bundles (which should only occur after many more teeth are engaged); however, significant stiffening absent the effects of the fiber bundles would not be expected from the further engagement of teeth because none of the previous nylon-backed FEA studies show significant stiffening after the change in stiffness that occurs fairly consistently after around 5° of leg rotation (here at around 3.8°).

Nylon-Carbon Fiber Annular Comb—Unsupported Centers of Bundles.

The next FEA experiment considered an annular comb with the same fiber shape, but with the material inside the areas enclosed by the fiber bundles removed in the hopes that this would facilitate fiber realignment with backbone tension. Of note, these new gaps roughly

coincided with radial gaps in the teeth (giving the backbone extra compliance there, which had the unpleasant potential to produce strange buckling patterns but might also give the backbone extra shear compliance before teeth locked up). Figure 142 shows this geometry.

Also, the remaining plastic in the backbone was switched to nylon from elastomer as the high tensile compliance of the elastomer was thought to be unable to adequately transfer any increase in stiffness from the deformed fiber bundles. Plus, FEA with nylon was easier to solve.

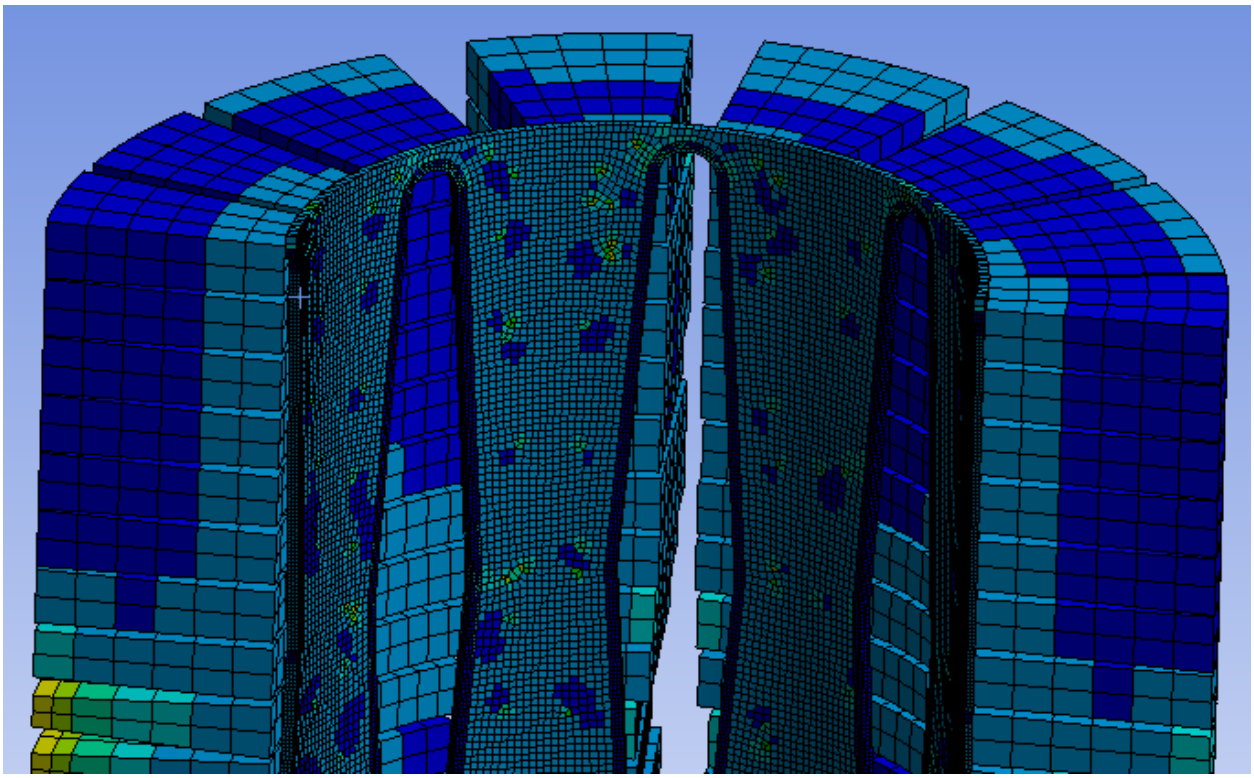

Figure 142: Geometry of annular comb with nylon instead of elastomer backbone, and plastic enclosed by fibers removed (to facilitate mechanism-like behavior).

Unfortunately, this geometry was quite unsuccessful. As shown in Graph 35, the acceleration in moment reaction was as gradual as with most previous backbone geometries (most of which would be far easier to manufacture, too!), and the stiffening up again seemed to occur long before any teeth had begun to touch.

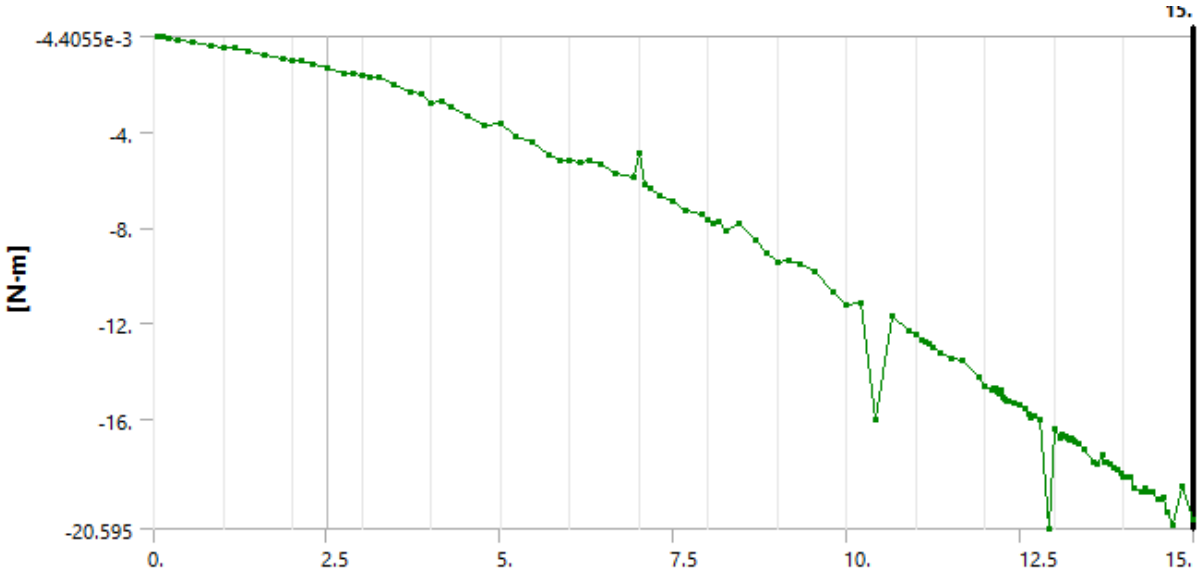

Graph 35: Moment reaction for nylon/carbon-fiber, unsupported-centers annular comb.

Furthermore, the deformed mesh (one view of which is shown in Figure 143) showed no indication that the fiber bundles were undergoing any kind of mechanistic stretching that would see them straighten and thus become stiffer in tension. (Granted, vertical tooth lockup was not optimized, and perhaps backbone stretching could only begin once the neutral axis of bending was altered by tooth lockup). Figure 144 shows a closeup view with no visible reorientation of the fiber bundle.

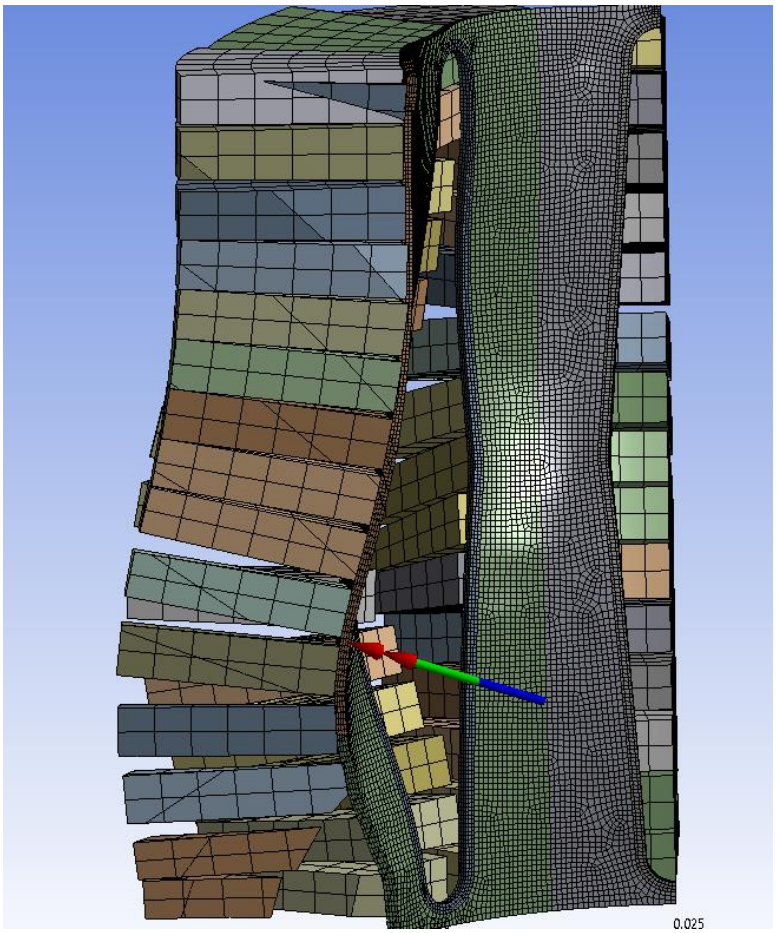

Figure 143: Double-sectioned view of the annular comb after leg rotation of 15°.

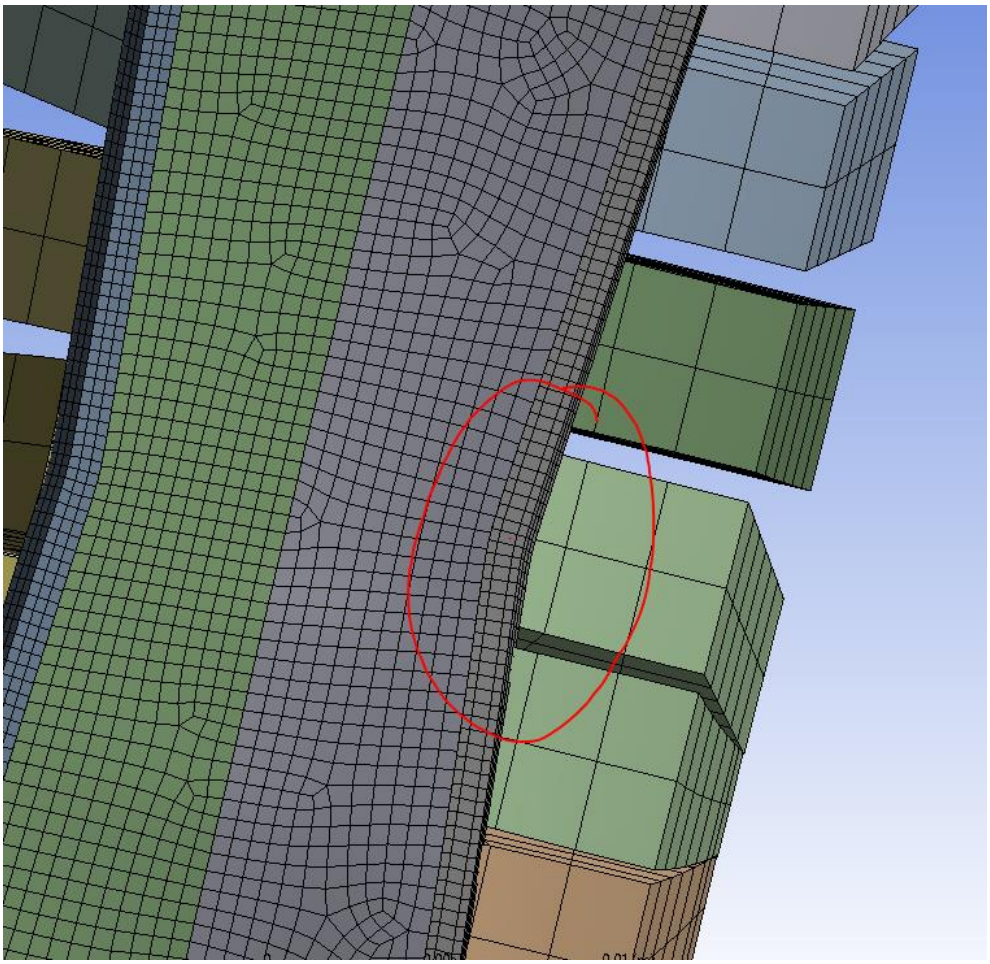

Figure 144: Fiber bundles not visibly reoriented from tension.

A plot of vertical stresses (with respect to the undeformed coordinate system) did show significant vertical stress in the fiber bundles (indeed, enough to exceed the strength of the fiber-epoxy laminates in both compression and tension), but this was mainly from vertical stress components from laminate bending, not vertical tension. Figure 145 shows a fiber bundle with such stresses.

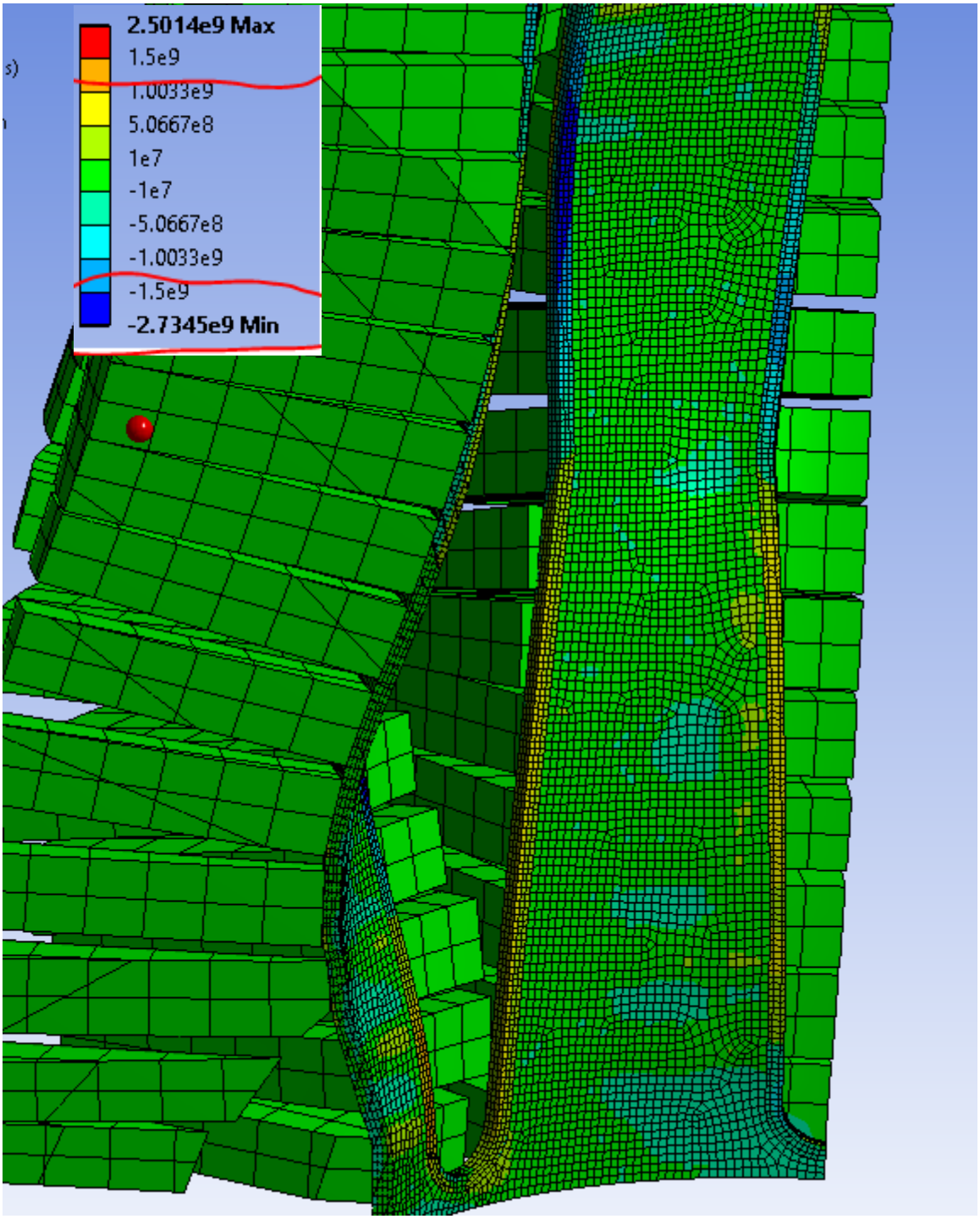

Figure 145: Vertical component of stress in fibers (and nylon backbone). The deepest blue shows compressive stresses that should cause failure of the bundles (and likewise, red regions should see failure from tension).

Modified Nylon-Carbon Fiber Annular Comb.

Removing all material inside the area enclosed by the fiber bundles seemed responsible for the significant shell buckling the backbone experienced (which presumably reduced post-tooth-lockup stiffness). As such, it was deemed advisable to try a compromise between the completely-solid-inner-volume and completely-empty-inner-volume combs. Thus, some ellipses were cut into the inner volumes enclosed by the fiber bundles; also, slightly-smaller ellipses were cut into the backbone around the outermost points of the bundles (where, without these cuts, the backbone might inhibit the fibers from pulling inwards and thus lengthening to stiffen the backbone in tension). Figure 146 shows this geometry.

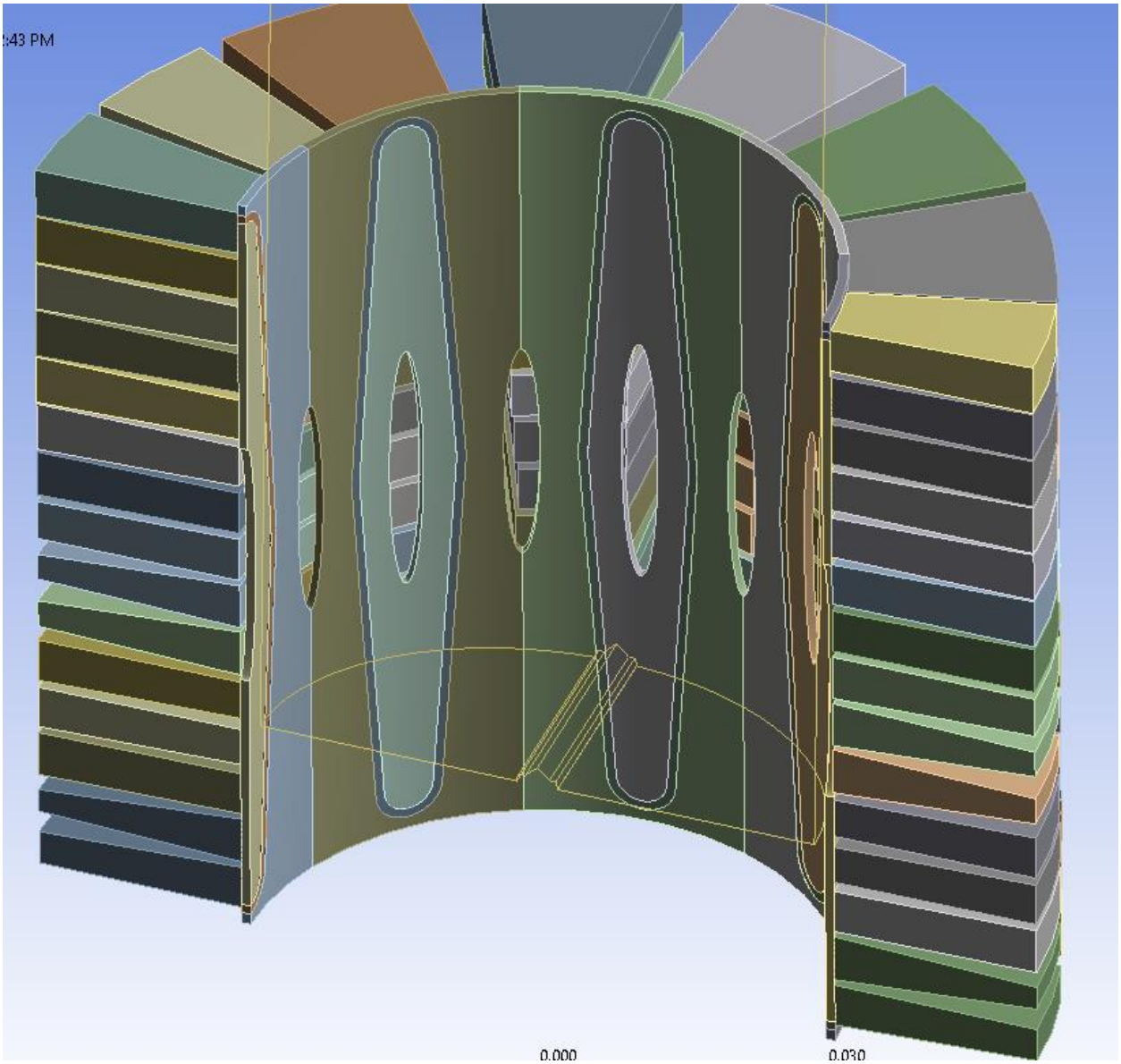

Figure 146:CAD geometry of annular comb with some cutouts inside and between the areas enclosed by the looped fiber bundles.

Unfortunately, the simulation suggested that this model, like all the others before it, was unsuccessful. As shown in Graph 36, the moment reaction increased only moderately, at the wrong time, independent of tooth lockup (few teeth were locked up by the end of the simulation, and strangely, it was the teeth *above* the onset of leg-backbone contact that were touching—usually these are the last to contact!) as shown in Figure 147, and, as shown in Figure 148, the

fiber bundles did not see significant tension (perhaps because the teeth did not lock up and change the instantaneous neutral axis of radial-segment bending). For better or worse, the elliptical cuts seemed to increase the backbone's shearing compliance, resulting in shear distortion of backbone and fibers.

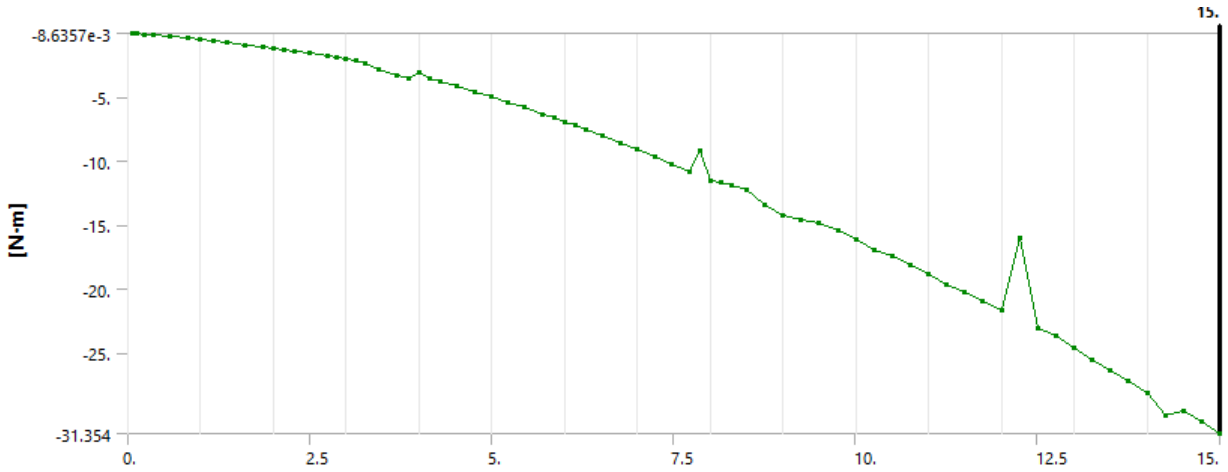

Graph 36: Moment reaction for annular comb with ellipsoidal cuts. Note that very limited tooth contact had occurred by the end of this simulation; as usual, the modest stiffening that did occur happened before 5° of leg rotation.

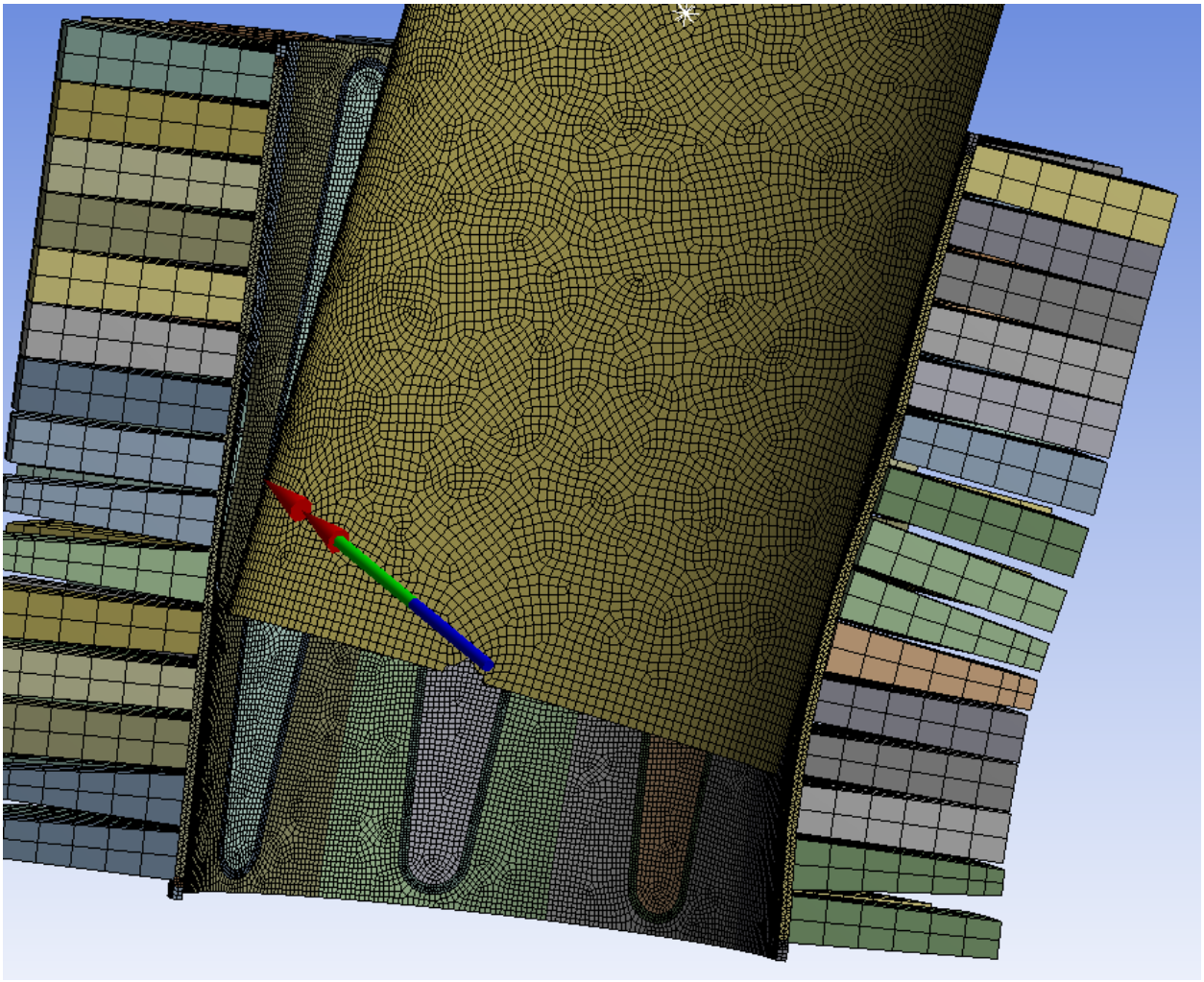

Figure 147:Deformation of structure after 15° of leg rotation from initial contact point. Note that most teeth were not contacting at this point; surprisingly, those that were contacting were the ones above *the leg-backbone contact patch.*

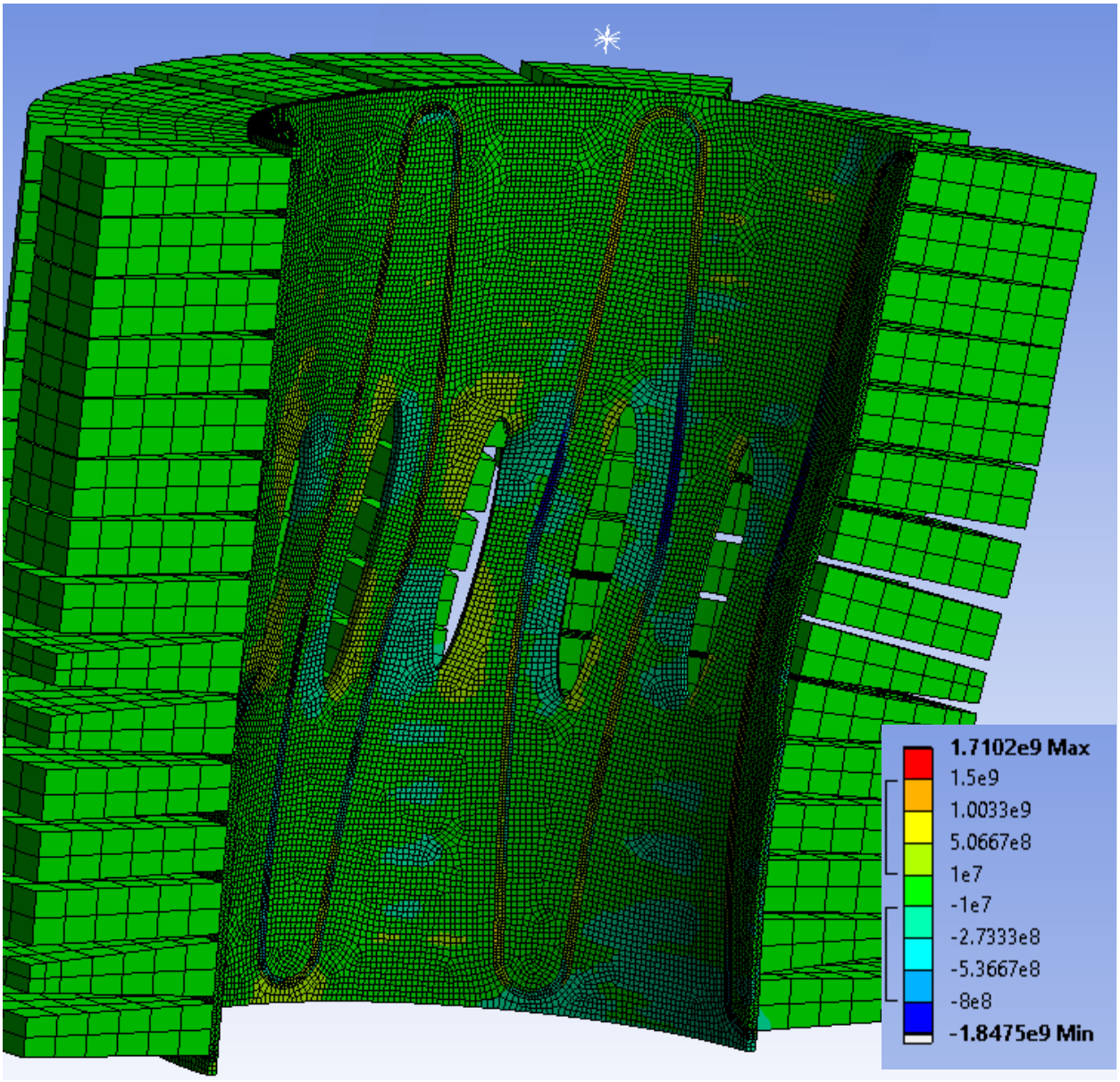

Figure 148: Contours of vertical (z) stress, blue indicating compression, lime green roughly zero stress.

Thus, the wavy-fiber concept has not proven to assist stiffening up in the annular comb. It might be worthwhile to investigate using wavy fiber bundles in the backbones of linear combs, but FEA models of the concept do not show any promise in the annular comb.

Conclusions on the Annular Comb Concept.

Unfortunately, these finite-element analyses suggest that development of the annular comb concept is not worth continuing, since we were unable to produce high lockup ratios even with the significant simplifications of a cylindrical leg and simple joint motion.

In fact, the concept seems to promise so little success that it may not be worthwhile to even 3D print a prototype of one of the models analyzed in FEA. However, if we wished to print a prototype of one of the simulated annuli, it should be possible with our FFF, moderate-resolution 3D printer. In this case, there would be a couple possible approaches. The easiest would be to print the actual comb in one or more materials, and add a supporting material between teeth (and also under any holes in the backbone, in the case of complex backbone geometry). While water-soluble polyvinyl alcohol (PVA) interfaces strongly enough with nylon to allow its use as a dissolvable support material for nylon, even with significant amounts of retraction, the PVA filament tended to ooze out when the printer extruded in nylon, thereby interfering with interlayer bonding in the nylon portion. Fortunately, other flexible materials are available for 3D printing instead of nylon, in particular ones that can interface with other dissolvable support materials than ooze-prone PVA. For instance, the Bendlay filament (an alloy of thermoplastic elastomer and ABS) has roughly the flexibility of thermoplastic-elastomer-alloyed nylons, and it bonds to HIPS (which can be selectively dissolved with D-limonene) as well as unalloyed ABS.

If support material did not properly interface with flexible backbone materials, it might be possible to print the annular comb structure without support material by printing it in two pieces and "bridging" horizontal gaps with fast print head motion. Projected modifications for this include orienting the object on its side, comb teeth tangential to the plate (the object could not have been printed with the cylinder axis oriented normal to the glass plate without support

for overhanging comb teeth), it was necessary to increase the contact area between teeth and plate, for one-point tangential contact often results in significant warping (which can ruin the print if the head is thrown off upon impacting areas that have warped up by even a few hundred microns).

Of course, the part would be easiest to produce on a Selective Laser Sintering (SLS) printer, as such printers provide automatic support to overhanging features and gaps against gravity with unsintered powder (and are also capable of providing much higher print quality, with smaller minimum detail sizes and no oozing effects); however, the cost to produce one moderate-sized annular comb was in excess of $350, which seemed unacceptable given the lack of success shown by the concept so far.

Chapter 5. Mechanism-Based Annular Combs.

Abstract.

The annular comb concept from the last chapter is updated with the discovery that lattices can be made to stiffen up in tension thanks to compliant-mechanism-like geometry (using either kinematic joints or compliant-mechanism-inspired easily-bended beams). Teeth of various designs, including very-small teeth that should not interfere with this mechanism behavior, were generated and the resulting structures simulated in global bending, with a variety of boundary conditions. The simulations saw only modest increases in bending stiffness, although only some of the hexagonal cells saw the tensile strain needed to cause stiffening. Thus, although the concept remains unproven, it is possible that adding vertical-compressive-stiffening properties to some cells would allow the concept to work. Also, another type of mechanism, also using the interrupted-contact principles of the comb, but connecting discrete links with revolute and/or spherical joints, was also studied briefly, but the idea was abandoned because it failed to show any initial kinematic freedom.

Basic Hexagonal Stiffening Array.

In the previous chapter, recall that a basic reentrant hexagonal array geometry was devised (see Figure 108) that was expected to stiffen at least modestly in tension but unfortunately did not. This was quite confusing, as a rigid-body model of a hexagon connected by revolute joints will confirm that the geometry should stiffen up from theoretically-zero static

stiffness (neglecting friction and inertial effects) to very high stiffness (limited only by the tensile stiffness of the rods and shear stiffness of the joints) once the lateral members are oriented parallel to the load. The only explanation for the lack of stiffening up seen in that reentrant geometry (presumably excessively-high initial stiffness, rather than excessively-low post-stiffening stiffness) would be some difference in the nature of cell joints. Indeed, most compliant mechanisms seem to have their joint areas notably reduced in cross-sectional area and cross-sectional second moment of area for local compliance at the joint; however, the geometries initially tried used constant-thickness beams, which might see excessive moments at the joints (as if the joints were cantilevered, although imperfectly, beams, instead of beams with unconstrained end rotations). The joints in the following complaint mechanism engineered by the author as a derivative of the 4-to-1 mechanism optimized by [49] are much more typical of compliant mechanisms:

[49] "Design and Fabrication of Compliant Micromechanisms and Structures with Negative Poisson's Ratio", Ulrik Darling Larsen, Ole Sigmund, and Siebe Bouwstra

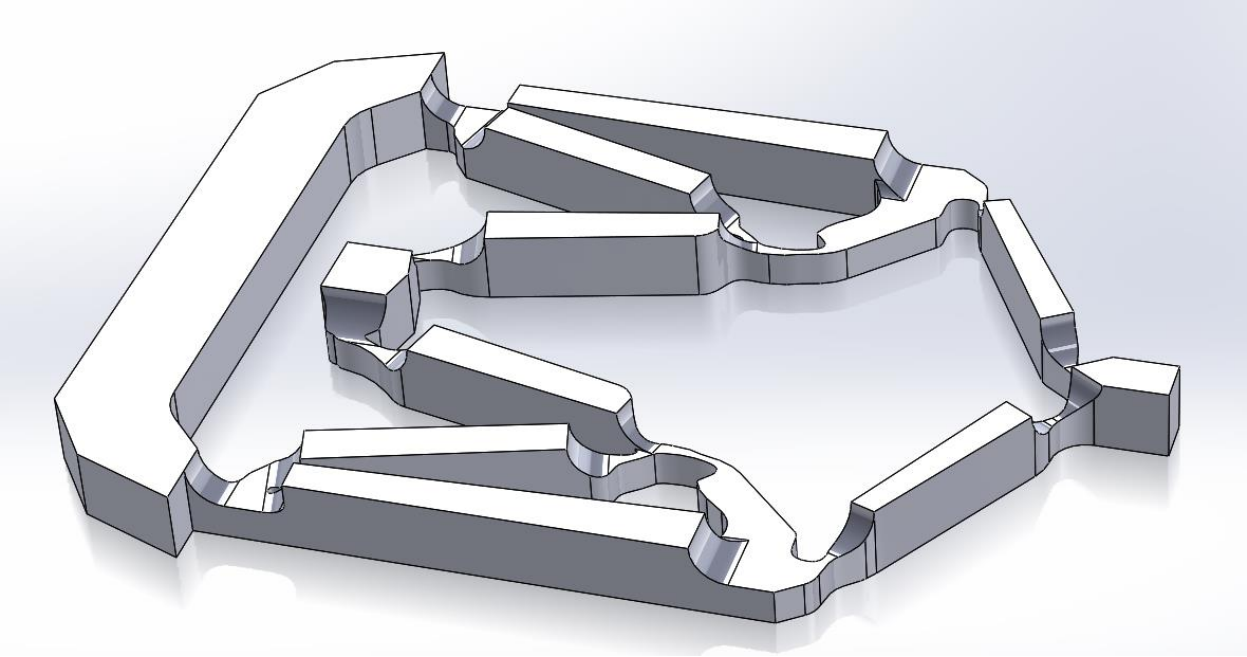

Figure 149: Compliant mechanism with 4-to-1 force ratio and carefully-sculpted compliant joints.

To this end, a simple hexagonal array was generated with such compliant joints. A non-reentrant geometry (which would give a positive gross Poisson's ratio) was chosen for simplicity, although a reentrant, negative-Poisson material should still stiffen in uniaxial tension by the same principle. Joints were sculpted moderately, without any attempt at optimization based on stiffness increase, etc.; the resulting cell is shown in Figure 150.

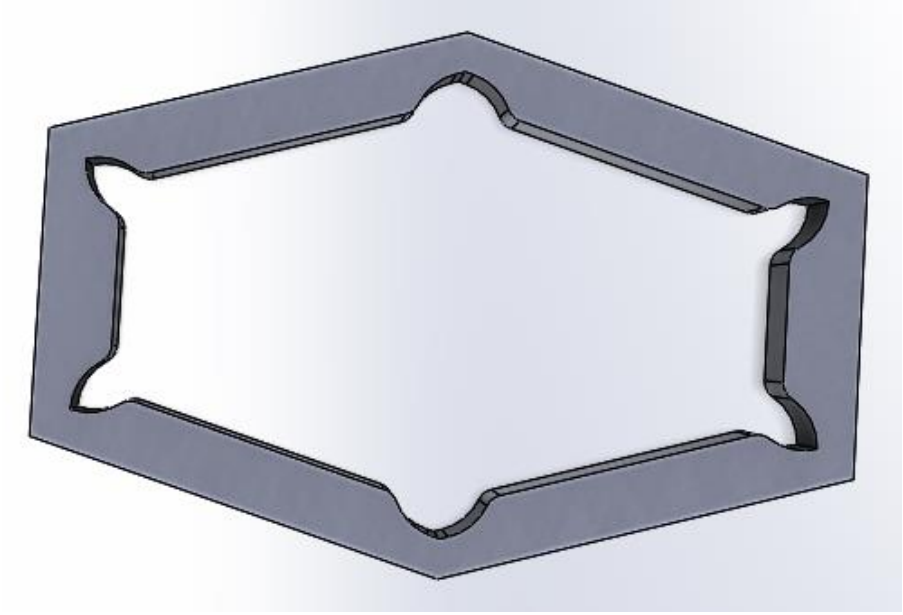

Figure 150: Hexagonal unit showing compliant-mechanism-inspired joint design. Note that this cell is not a reentrant design, but, like the previously-proposed reentrant hexagon, it too should *stiffen up in tension after some displacement.*

The above hexagonal unit was combined with a few others into an array, which was then subjected in FEA to a basic tensile test to verify that it experiences reasonable tensile stiffening. Figure 151 shows the geometry of the array and boundary conditions of the simulation, and Graph 37 shows the force reaction for constant displacement, with the derivative of force (i.e. instantaneous tensile stiffness) shown in Graph 38. Clearly, stiffness ramps up fairly rapidly to around 700% of its initial value (reaching a maximum after a mere 0.003m displacement before symmetry, which amounts to a gross strain of 8%); however, it declines moderately after the maximum value is reached (on the order of a 16% decline). Perhaps this slight tensile softening is due to necking at the joint cutouts—as Poisson effects narrow the joints in tension, their reduced cross-sectional area gives them less tensile stiffness.

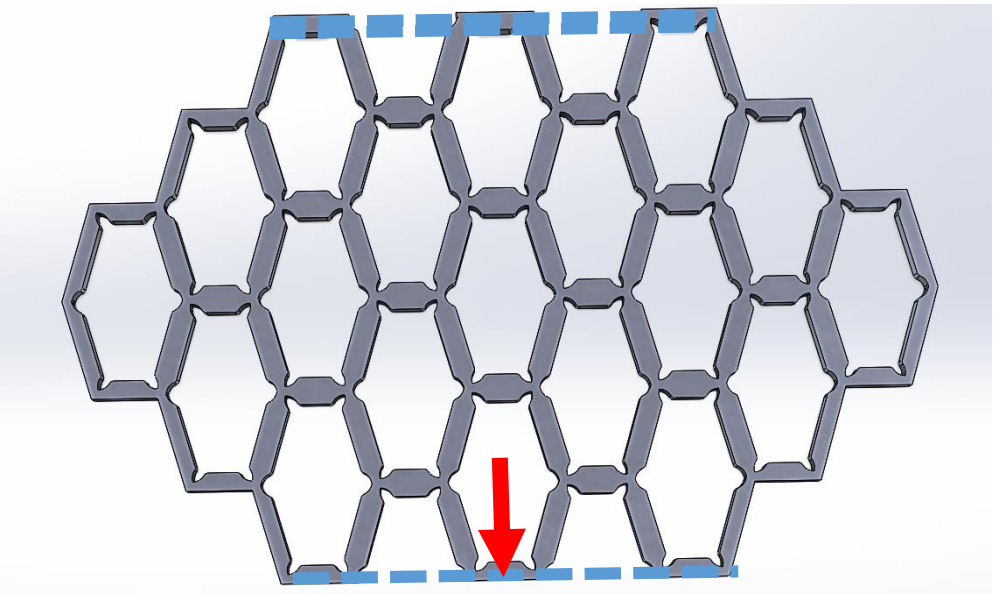

Figure 151: Hexagonal array subjected to vertical tension. The top was fixed vertically (but free to contract horizontally), the bottom pulled downwards and likewise free to contract horizontally. Note that the FEA model that was actually computed had double symmetry.

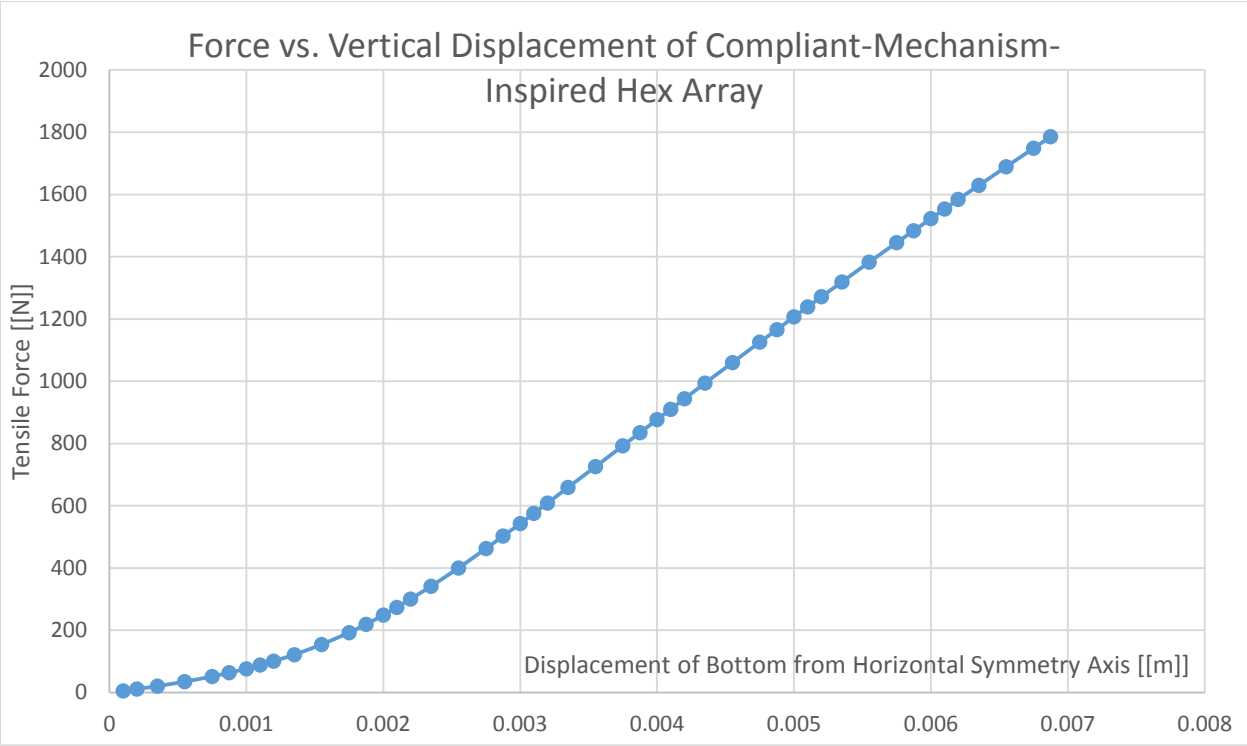

Graph 37: Force reaction for vertical displacement of hex array. Note stiffening up behavior!

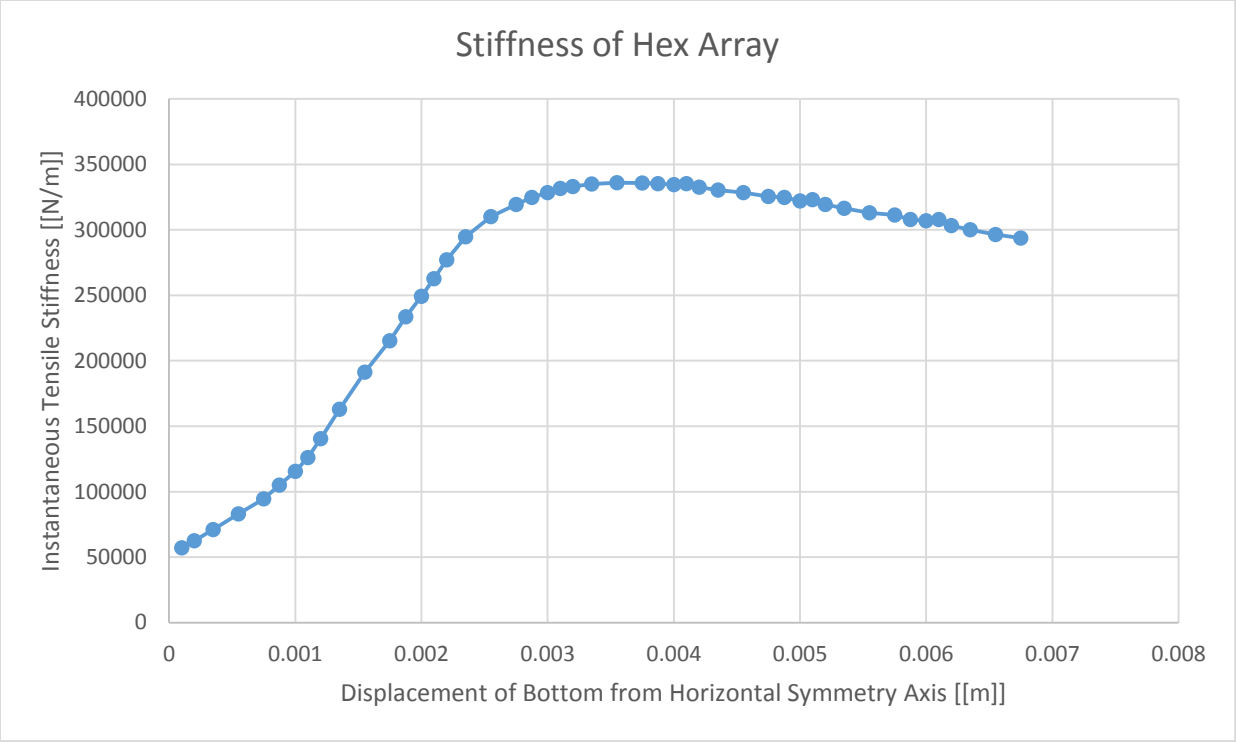

Graph 38: Instantaneous stiffness of hex array in tension, estimated by backward difference 1st-order numerical formula.

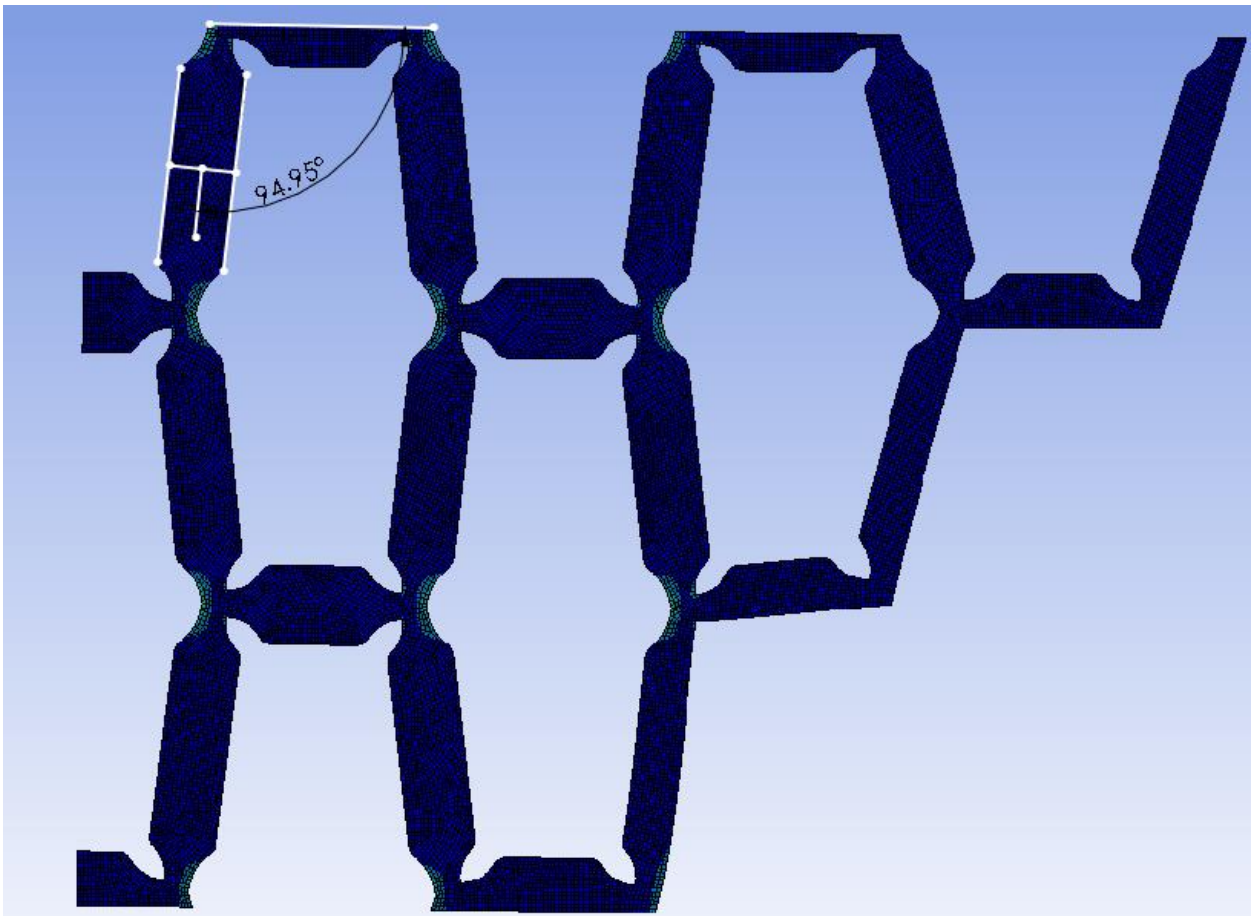

Figure 152: After .002m displacement (from symmetry), the point at which lockup seems nearly complete.

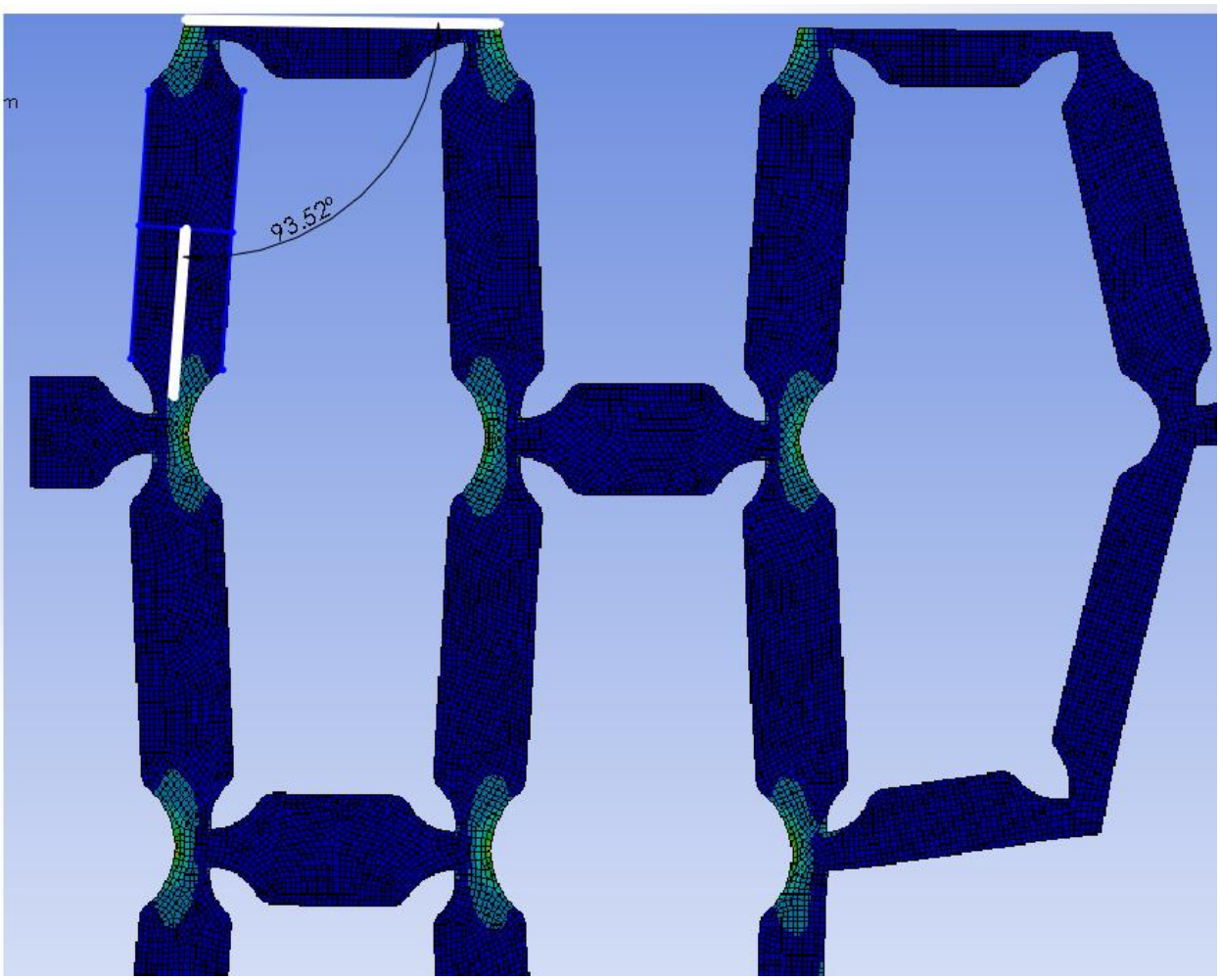

Figure 153: Deformed shape after .003m of tensile stretch, roughly where stiffness peaks.

The tensile stiffening could be further increased printing high-strength fibers in the very center of each beam (the further they are from the neutral axis, the greater their local bending stiffness [which is undesirable], but their tensile stiffness [which is desirable] will remain unchanged), avoiding the strain contours that form before the structure is completely straightened out—thus, they should be engaged in tension only once the beams have straightened, hopefully seeing little to no local bending prior to this global straightening (in which they would stiffen the structure *before* desired).

While such a modification to the backbone might produce better performance, it would raise several problems. First, to simulate it accurately, mesh complexity would explode exponentially in order to accommodate the complex curved-cutout geometry (and meshing with hexahedrons might not be feasible, requiring the use of tetrahedral elements instead, which are less computationally efficient). Also, once the hexagons are elongated in tension, the thinned-out joints might see stress concentrations (i.e. in real life) or high tensile stresses. Such fine details might simply be difficult to manufacture even by the most precise fabrication technology (presently SLS) unless the whole unit cell size was increased.

However, a factor suggesting against increasing cell size to accommodate fine details like fibers is the fact that tooth contact patches completely restrain the unit cells in tangential, vertical, *and* radial modes (with only *r*-*z* shearing unconstrained!); thus, cells should probably exist only at the gaps between teeth (and the gaps could only be increased in size to a limited extent before shear forces could tear teeth off, leaving relatively small gaps for the lattice cells).

That said, given the ability to manufacture sufficiently strong and precise details, it might even prove worthwhile to replace the compliant joints with actual revolute, etc. joints that (absent friction and stiction) would give the joint zero stiffness within a certain range; teeth could be attached between lattice sections.

Semi-Reentrant Octagonal Array, 2D.

Another potential array that was briefly tested offered tensile lockup in two dimensions, plus alternating reentrant geometries that give a virtually zero gross Poisson's ratio. (This

geometry was inspired by the work cited in reference 50, although those researchers did not use compliant-mechanism-inspired joints as done here). As with the hexagon-based geometries (reentrant and non-reentrant), there are lines of links slightly angled away from a full 180° angle to each other, leading to straightening after a modicum of tensile deformation. Figure 154 shows a 2D version of this geometry, with the unit cell highlighted.

[50] Virk, K., A. Monti, T. Trehard, M. Marsh, K. Hazra, K. Boba, C. D L Remillat, F. Scarpa, and I. R. Farrow. "SILICOMB PEEK Kirigami Cellular Structures: Mechanical Response and Energy Dissipation through Zero and Negative Stiffness." *Smart Mater. Struct. Smart Materials and Structures* 22.8 (2013): 084014. Web.

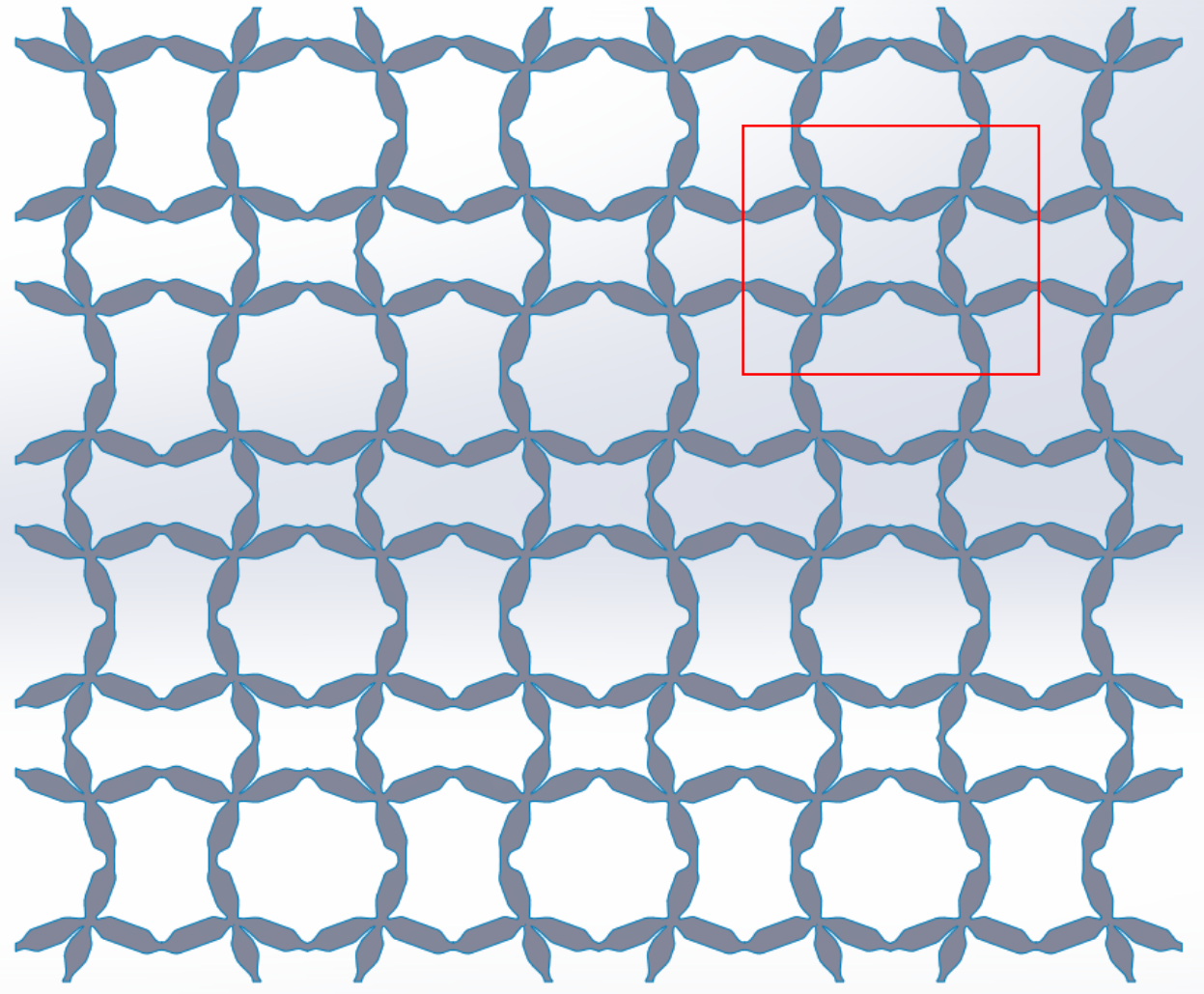

Figure 154: Another potential 2D lattice with tensile stiffening behavior thanks to reorientation of beams facilitated by compliant-mechanism-inspired joints. The unit cell is shown in red; note that there are four distinct shapes, three of which have some reentrant geometry.

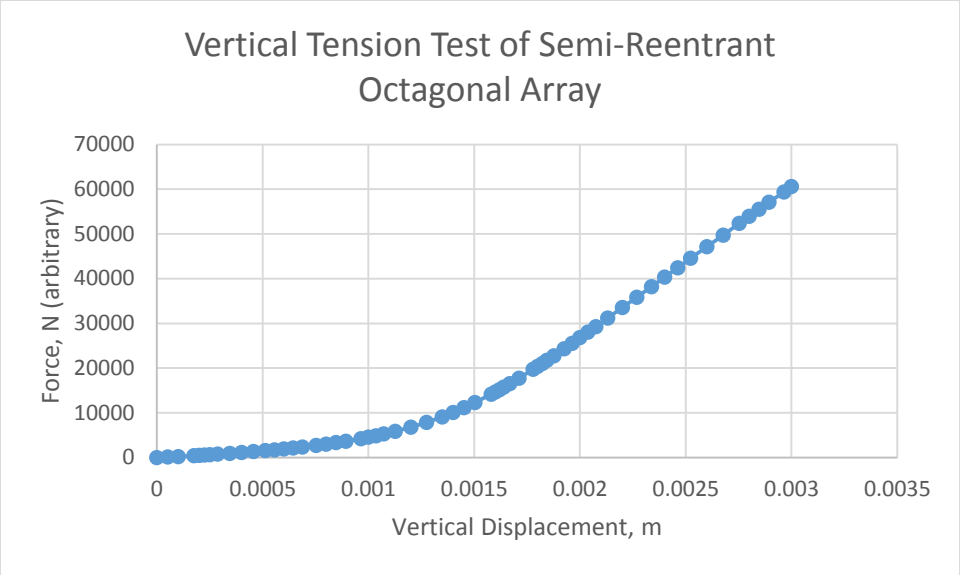

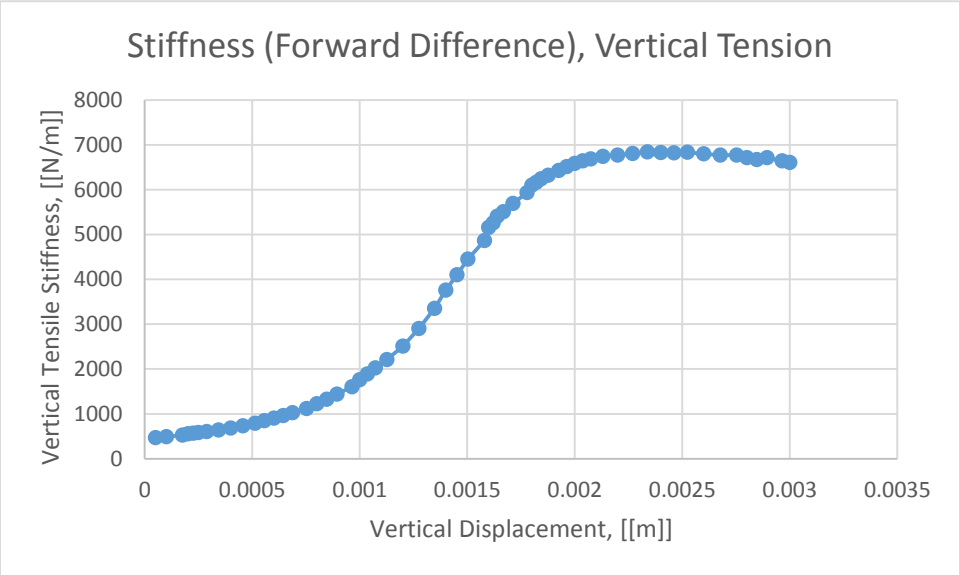

Graph 39: Stiffness for array over displacement range. Note that stiffness appears to peak at around .002m, of displacement, which is roughly 10% gross strain. Peak stiffness was about 1400% of initial stiffness.

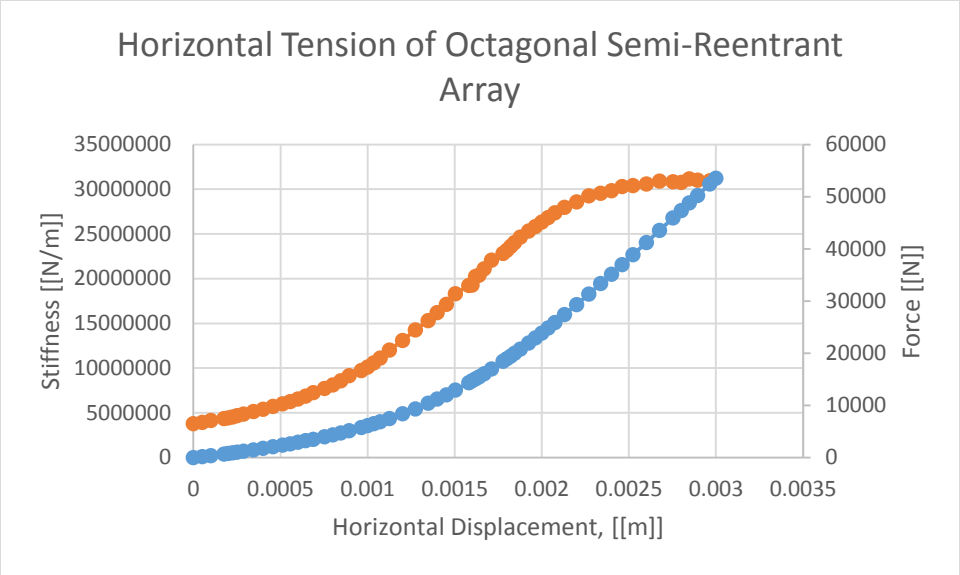

Graph 40: Horizontal tension only. Note that stiffness appears to peak at around .0025m, of displacement, which is roughly 10% gross strain. Stiffness increased to around 600% of original.

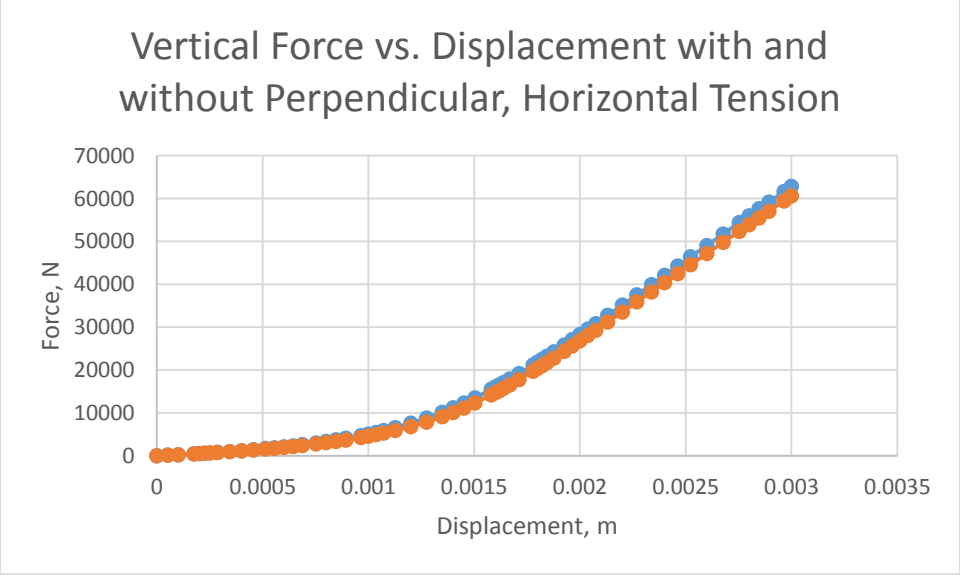

Insights Available from Pure Hex Backbone.

<u>Pure-Hex Backbone, Free, Sliding Leg Contact Only</u>.

Out of curiosity (particularly in search of insight into where, if ever, the backbone would see the tension that can stiffen it up when installed around the leg), the tensile-stiffening

backbone was simulated without any sort of teeth. The first boundary condition used was free sliding contact with the leg; predictably, there was almost no tensioning of the backbone to speak of, save directly above where the backbone buckled (which was indeed unexpected) as shown in the view of Figure 155. Additionally, while no cells directly opposite the direction of the leg's rotation were tensioned, some in a plane nearly perpendicular to the direction of leg movement did indeed see tension, which might have been due to Poisson contraction of the backbone, as shown in Figure 156.

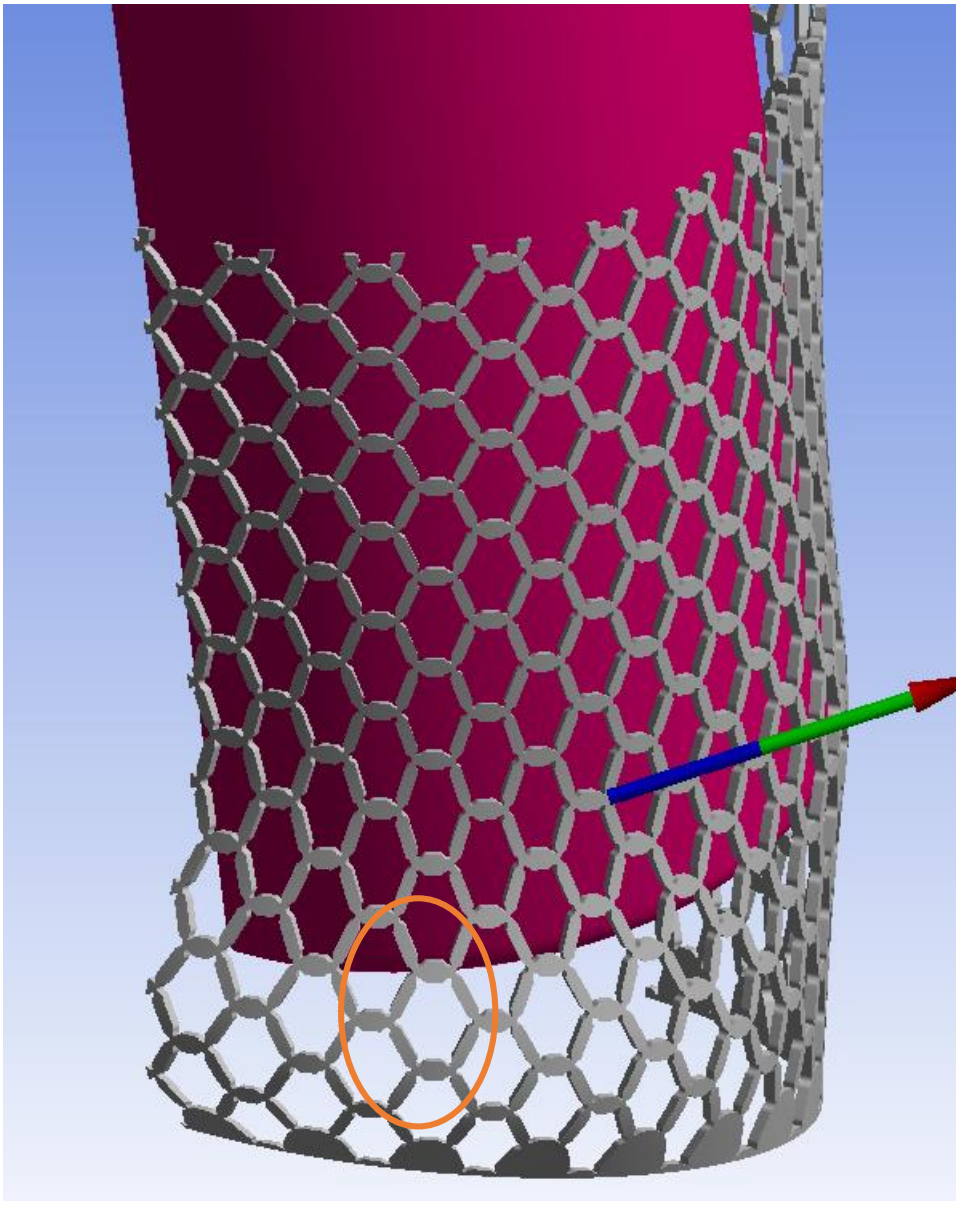

Figure 155: Deformed result after 20° of rotation from first point of contact (which was nearly at vertical). Note that those cells that saw enough tension to somewhat elongate (a mode of deformation known to cause stiffening up) have been circled. As might be expected, most cells on this side saw more compression.

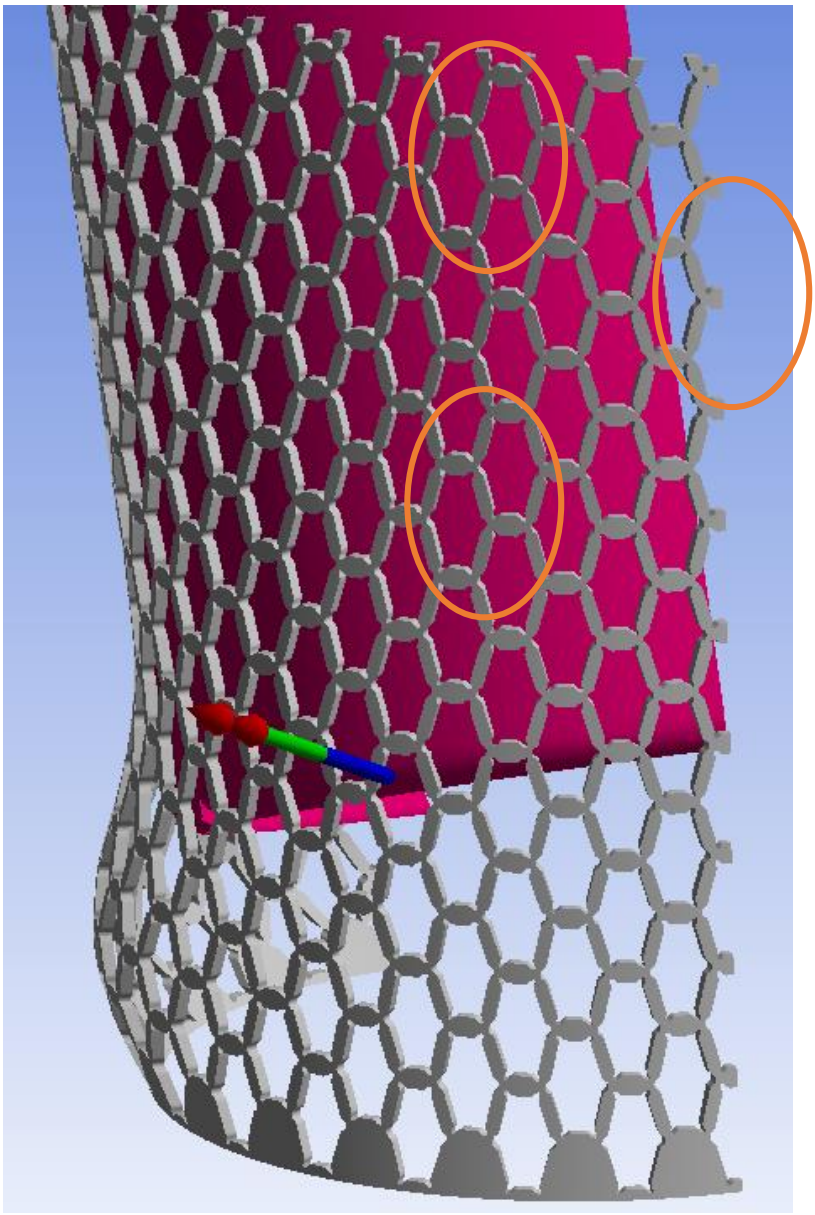

Figure 156: 20° of rotation without teeth, other view. Note that those cells that saw enough tension to somewhat elongate (a mode of deformation known to cause stiffening up) have been circled.

As was expected, not only did the untoothed backbone not stiffen up, it actually lost stiffness due to shell buckling, as the moment reaction shows in Graph 41.

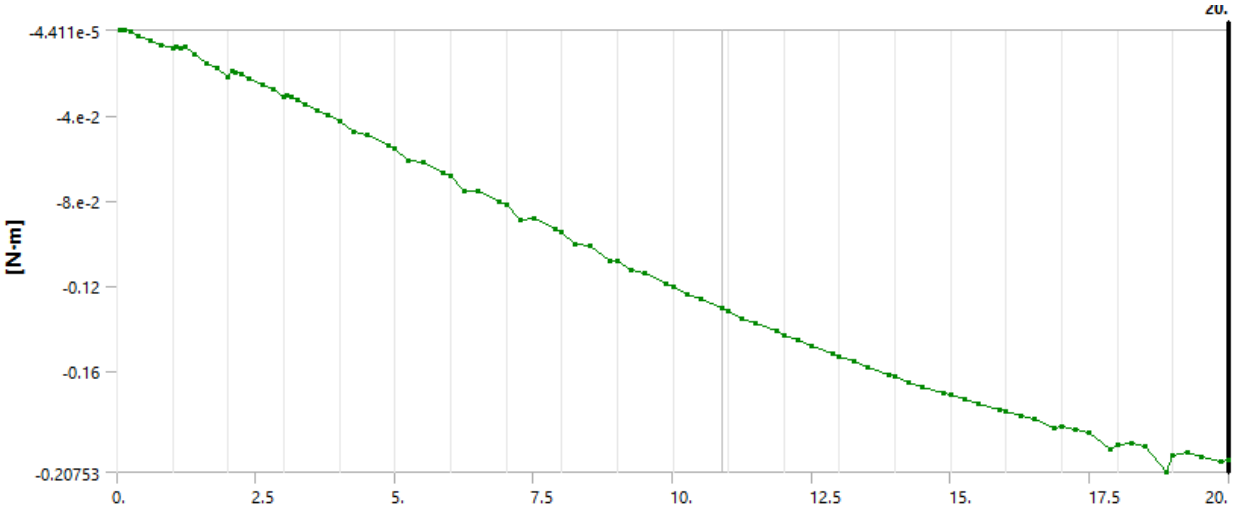

Graph 41: Moment reaction for toothless, hex-only backbone.

Pure Hex Backbone, Sliding Contact and Tied Contact at Top.

This model was expected to fare somewhat better and perhaps even experience some modest stiffening thanks to one side of the backbone being in significant tension. Unfortunately, the opposite side saw enough buckling (more severe than in the previous simulation) that whatever stiffening some cells experienced was largely negated; the deformed result is shown in Figure 157. Correspondingly, the moment reaction was on average fairly linear, as shown in Graph 42; apparently, the tensile stiffening effects of the geometry balanced out the buckling effects nearly perfectly. That said, this boundary condition was at least an improvement over the softening seen in the previous analysis.

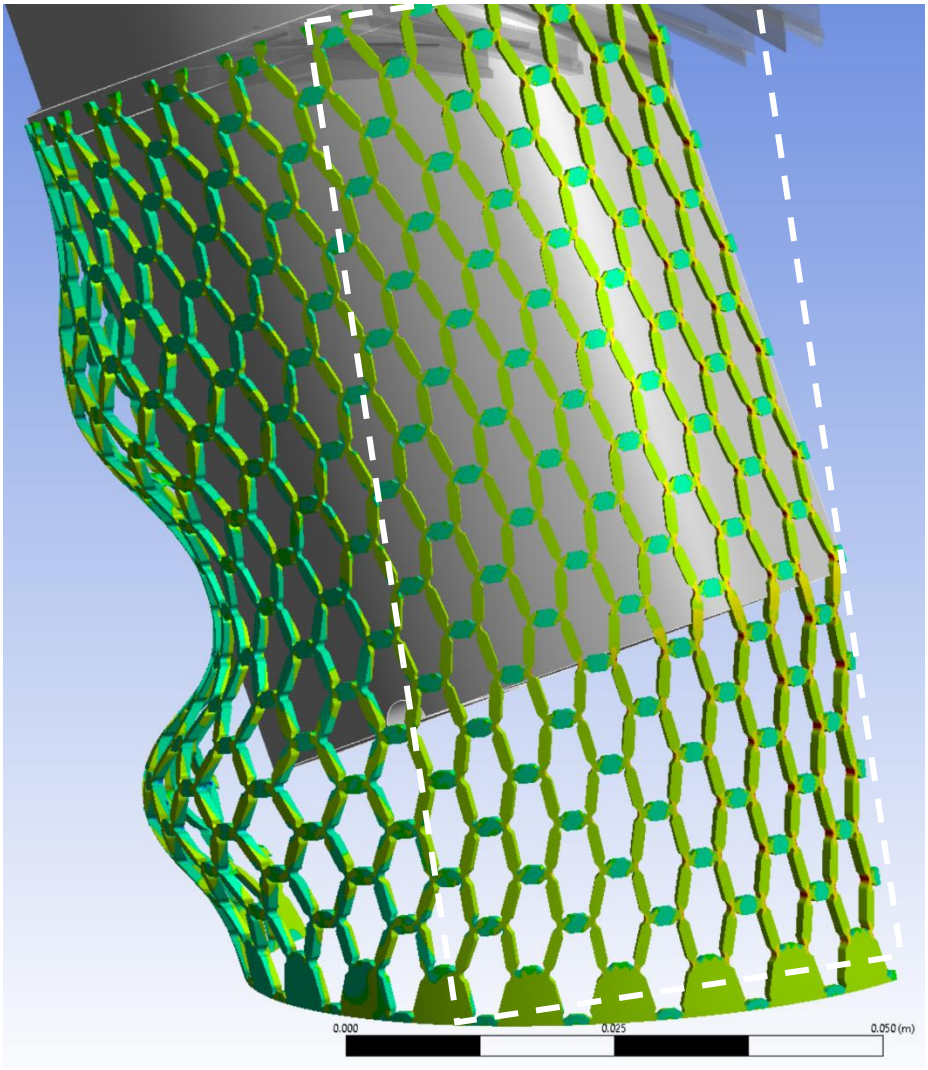

Figure 157: Simulation of closely-conforming untoothed hex backbone tied to leg at top and with sliding contact, leg rotated 20° from initial contact position. Note that there are two loci of extreme shell buckling in this case, although the opposite region sees some tensioning of hex cells (with the rough area in which this occurs indicated with dashed lines).

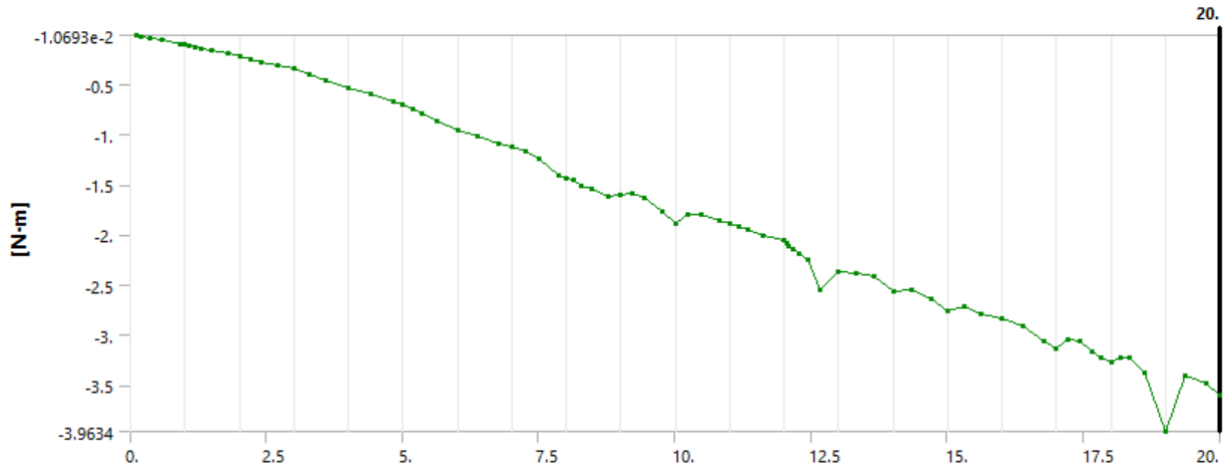

Graph 42: Moment reaction for closely-conforming untoothed hex backbone tied to leg at top and with sliding contact, leg rotated 20° from initial contact position.

Insights from Toothless Simulations.

These simulations might suggest varying the hex shape over the geometry (i.e. in terms of r, θ, and z in a simple cylindrical geometry such as those used in these preliminary simulations) to perfectly time the lockup of as many cells as feasible in tension. However, given that hexagons of different angles are unlikely to properly tessellate, this might require strangely-shaped beams to be generated; moreover, it would be a labor-intensive process, and so far no research has been done into the effects of stiffening-up ratio (or stiffening-up speed) on initial angles of the cells; it is conceivable that a smaller initial divergence from the rectangular shape would also result in a smaller stiffening-up ratio (and slower stiffening-up speed) for a given cell, so it might not produce much better results.

Beyond this, it is clear that shell buckling must be prevented for any hope of stiffening up; even tensioning a significant proportion of other cells cannot really compensate for its softening effects. Ideally, teeth or initially-slack cables should stiffen the backbone locally to prevent shell buckling.

Annular Combs with Tensile-Stiffening, Compliant-Mechanism Backbone

Reduced-Contact-Patch Annular Comb with Compliant-Mechanism-Based Joints.

Combining the above principles of improved joints at lattice segments and reduced tooth interference with lattice mechanism behavior yielded the geometry shown in Figure 158. Note this geometry uses notably altered tooth shapes (to free the backbone from the influence of the tooth-backbone contact patch at the portions containing lattice elements but still contact each other and produce lockup). It theoretically should still be feasible to print by existing commercial SLS processes (e.g. in nylon), since all details are over .01mm in thickness, although ensuring reliable strength here is another matter that cannot really be investigated without several test prints.

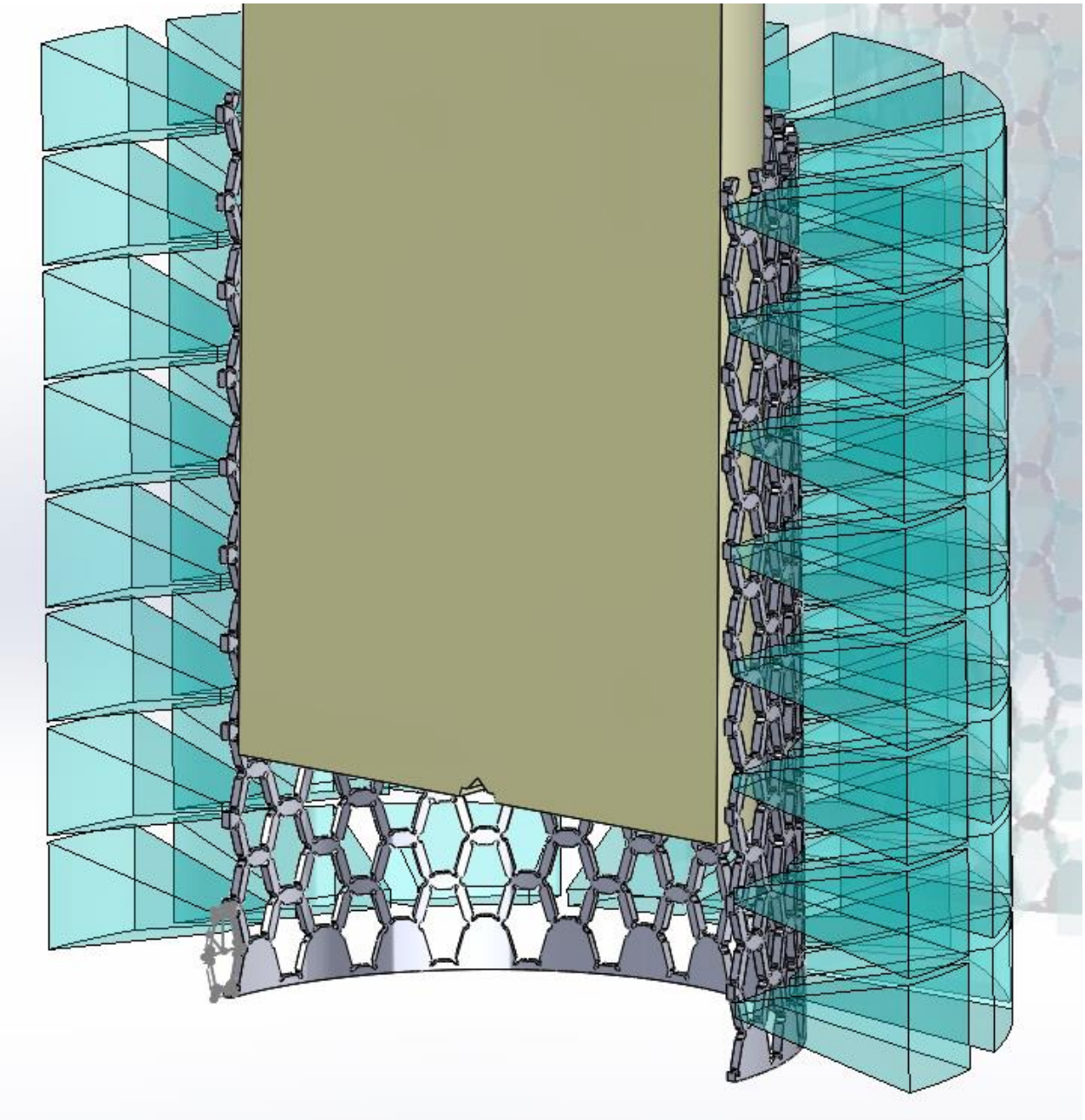

Figure 158: CAD model of annular comb featuring non-reentrant hexagonal backbone with joints cut away as in compliant mechanisms, plus comb teeth with reduced base contact area.

In order to simulate this complex geometry, it was deemed necessary to model the hexagonal-compliant-mechanism backbone with shell elements (thus neglecting through-membrane stresses); this produced a mesh with 90% fewer elements than could be generated

from tetrahedron meshing at the same characteristic element length (and the shell mesh was dominated by quadrilaterals, not triangles, which is good because quadrilaterals are more computationally efficient than triangles just as hexahedrons are more computationally efficient than tetrahedrons, and meshing a full 3D version of the backbone could not be accomplished with hexahedrons). However, to give accurate moment reaction values, a shell thickness of 1mm traditionally used in analyses of the previous chapter was also used for the backbone elements.

Basic Compliant-Mechanism-Backbone Annular Comb.

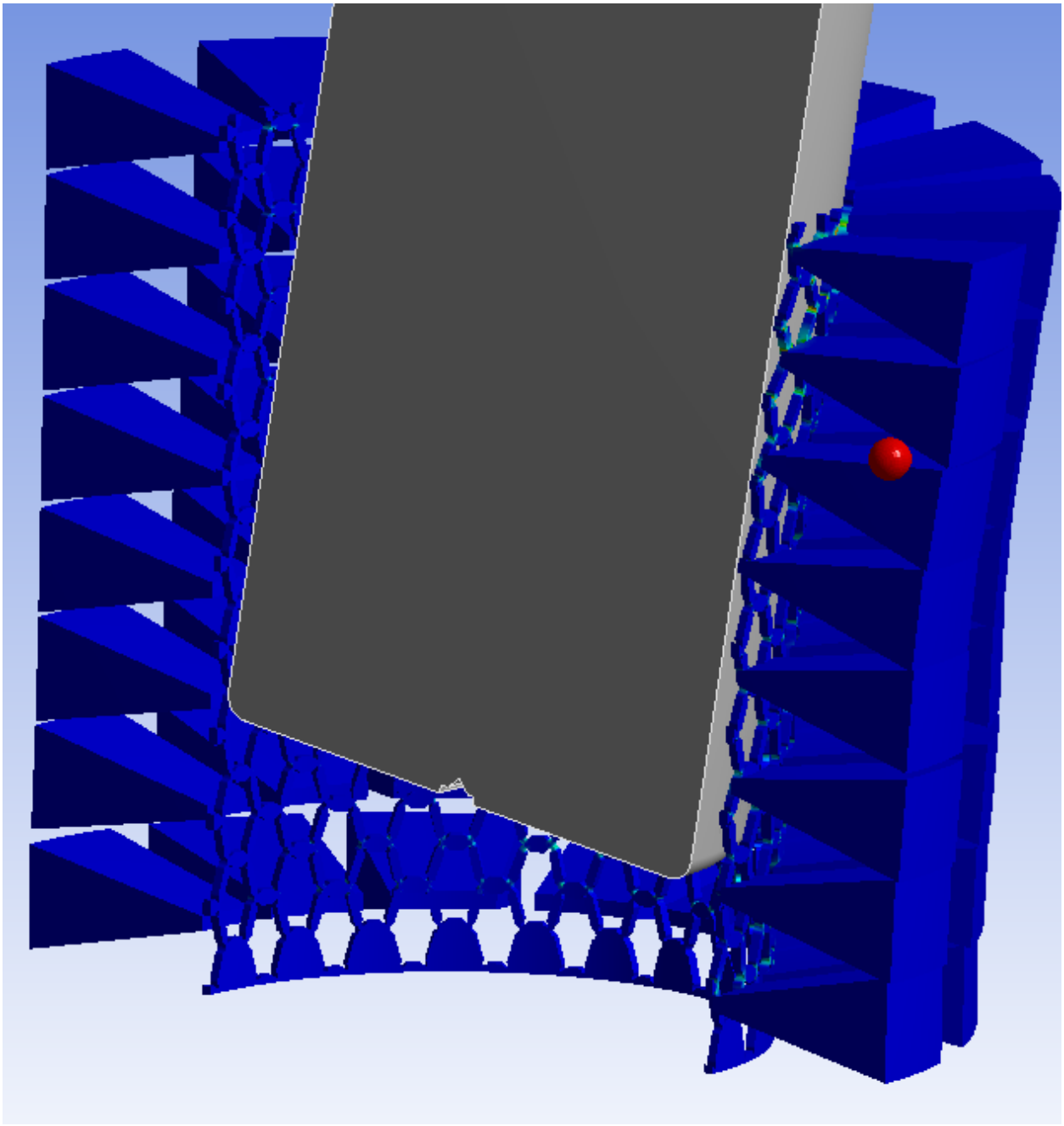

Figure 159: Analysis after 8.5° of leg rotation from point of first contact. Note that most of the teeth in the symmetry plane opposite the leg's rotation direction have locked up (although their trapezoidal shape, which gives small tooth contact area, has caused some to slip radially relative to each other).

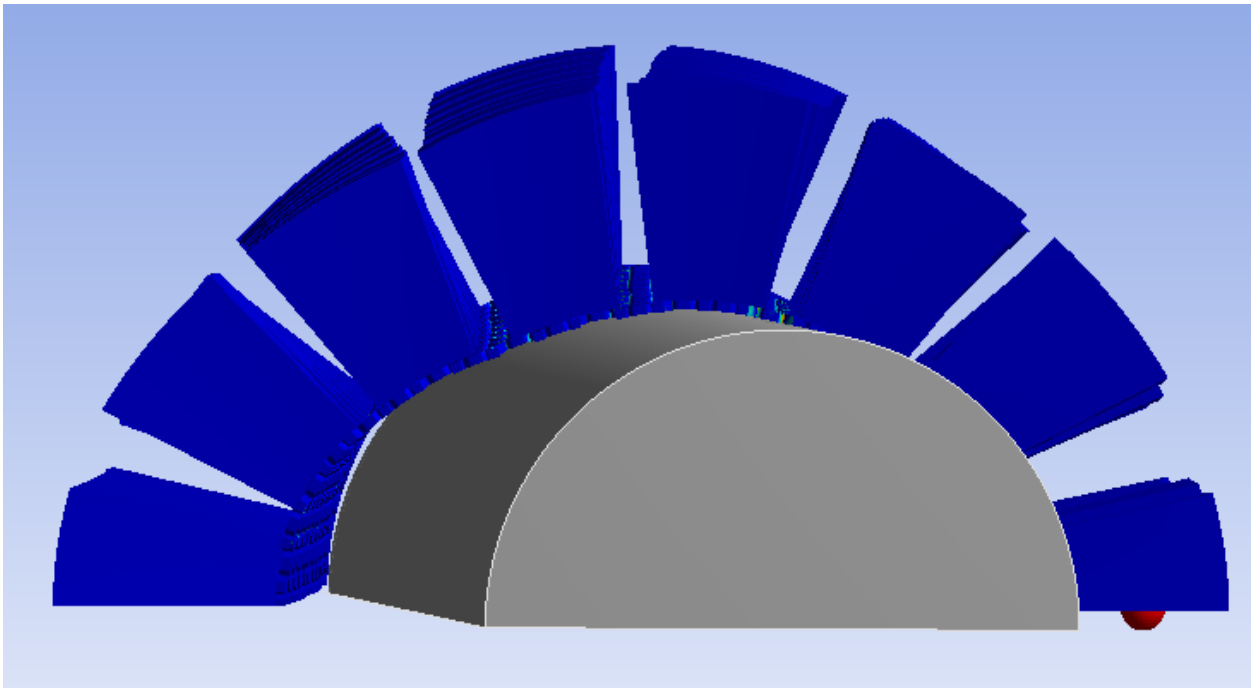

Figure 160: Top view of analysis after 8.5° of rotation. Note that the teeth shapes are such that no tangential contact occurs. (Better stiffening-up properties might be obtained by reshaping them to provoke tangential contact at the desired time).

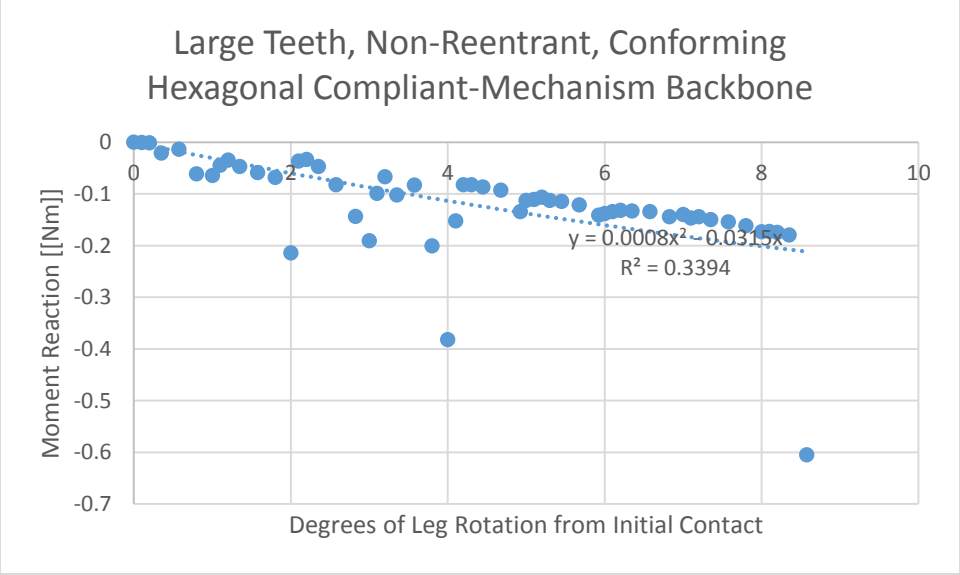

Tiny-Tooth Compliant-Mechanism-Backbone Annular Comb.

Finally, mechanism behavior in the backbone might be facilitated by making the teeth very small, with contact patches no thicker than the lattice 'beams' making up the backbone. While this would require very fine detail (yielding difficulty in model generation, analysis, and manufacturing), it would give the backbone nearly complete freedom when teeth were not touching. Figure 161 through Figure 165 show a proposed comb based on this principle, with compliant-mechanism-inspired joints to the lattice and very fine, very numerous teeth to correspond with it. Note that the gaps between teeth and the lattice dimensions are both large enough to be manufactured using SLS of nylon, should this concept prove its worth.

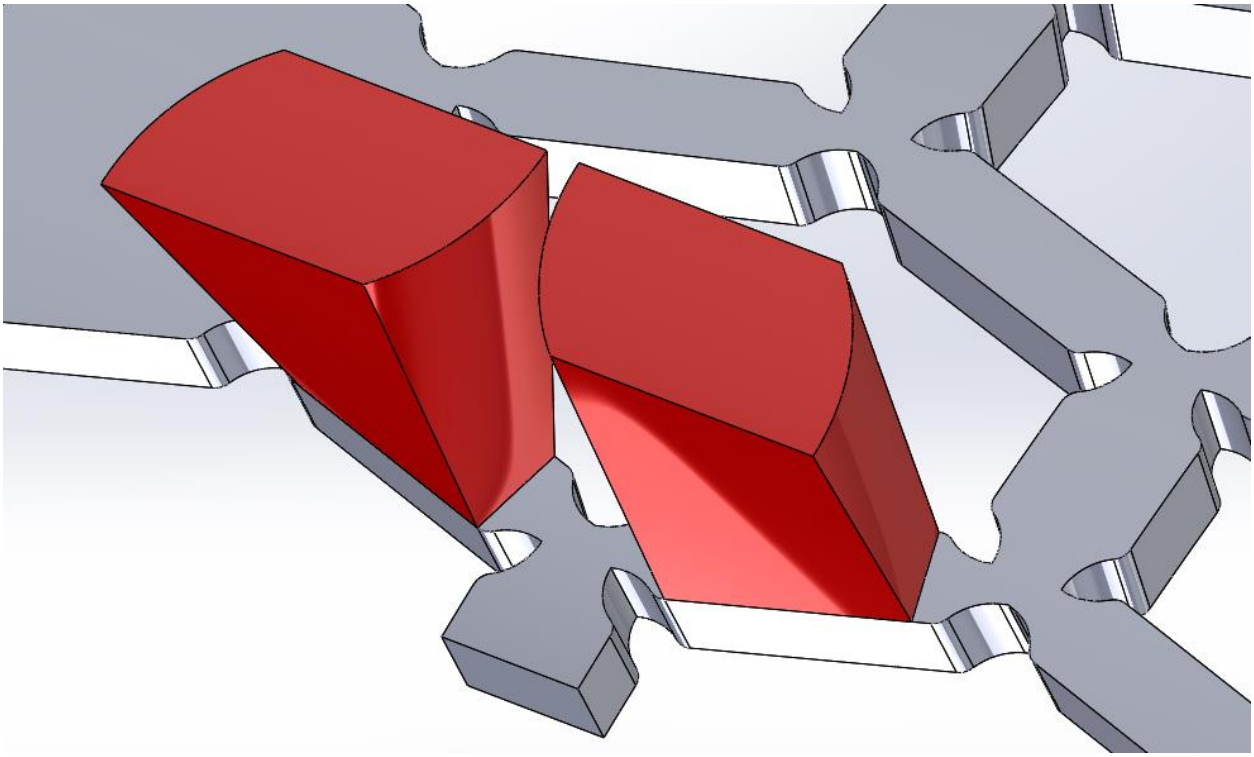

Figure 161: Only the teeth attached to the rotating beams are shown in this picture.

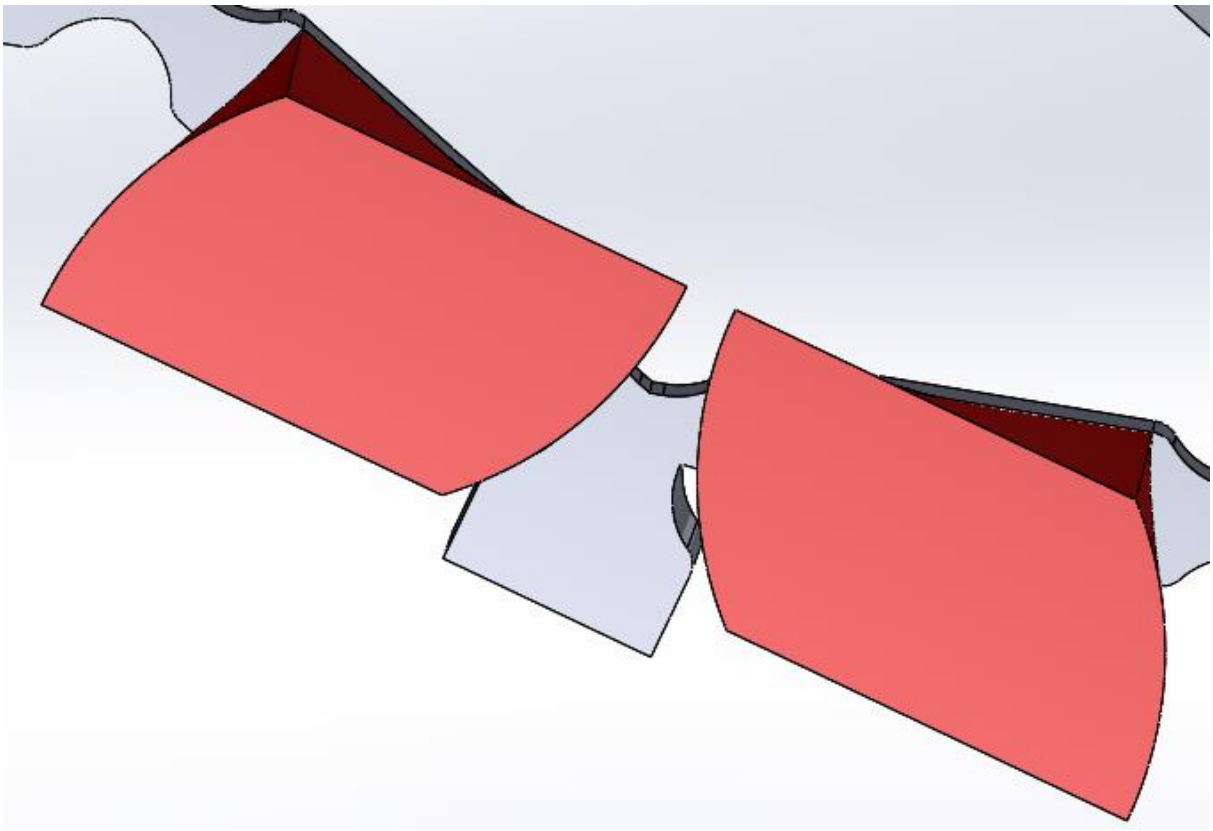

Figure 162: Alternative view of teeth attached to rotating beams, illustrating curvature for clearance.

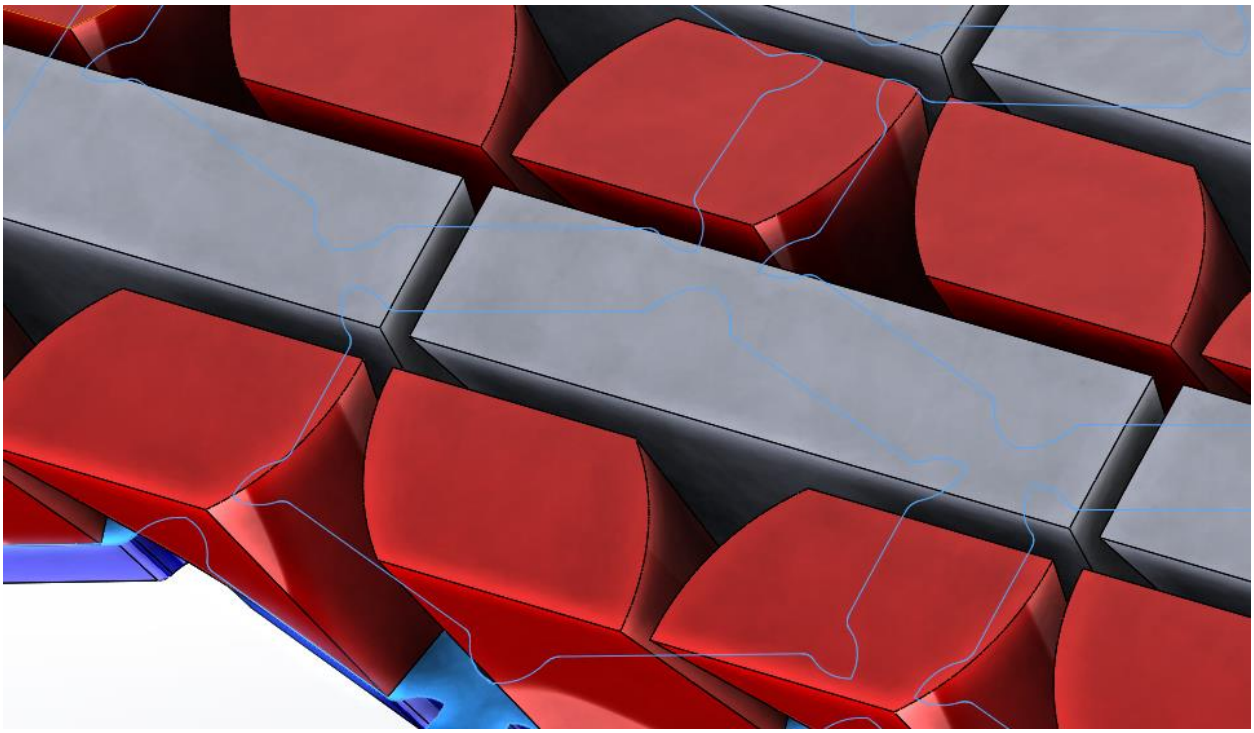

Figure 163: All teeth (red and grey) and backbone (blue, with the face to which the teeth are bonded highlighted), outside view.

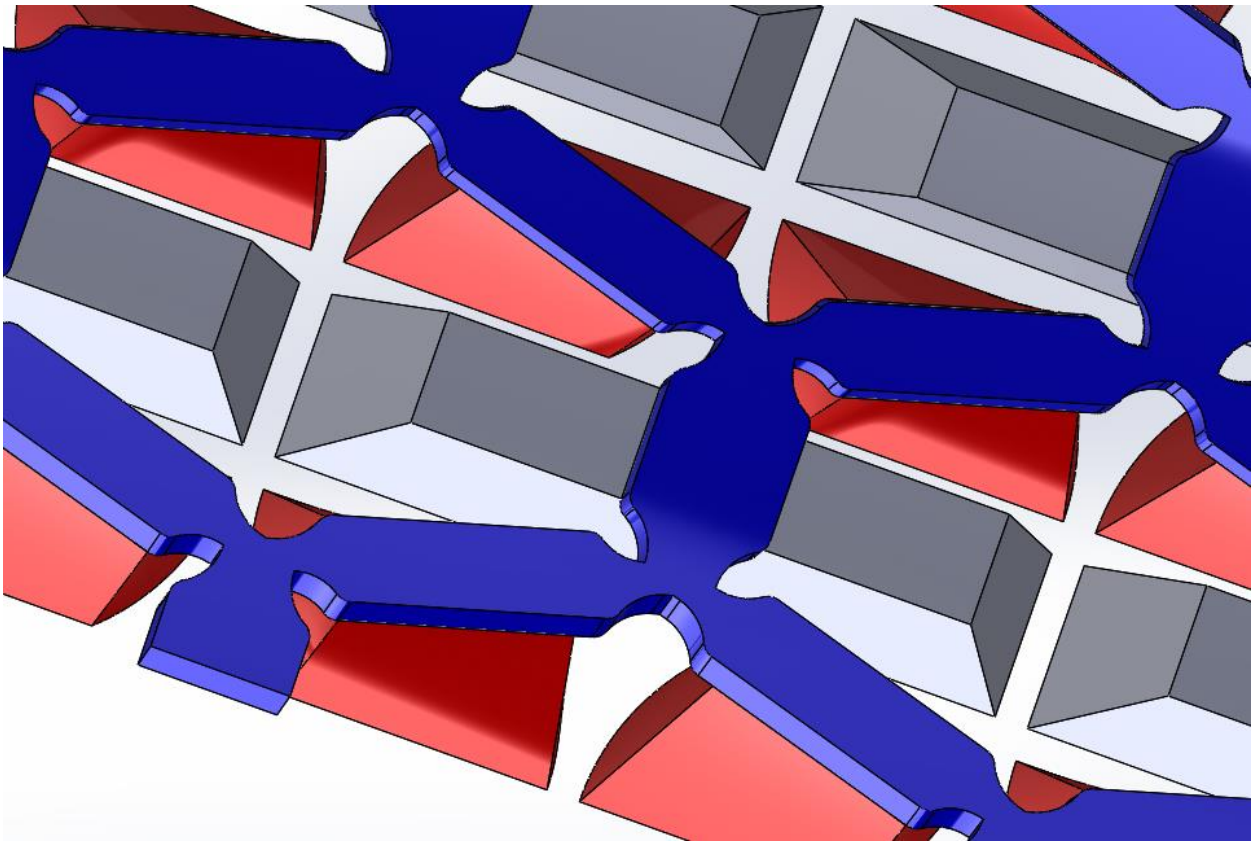

Figure 164: Inside view of mechanism annular comb with small teeth.

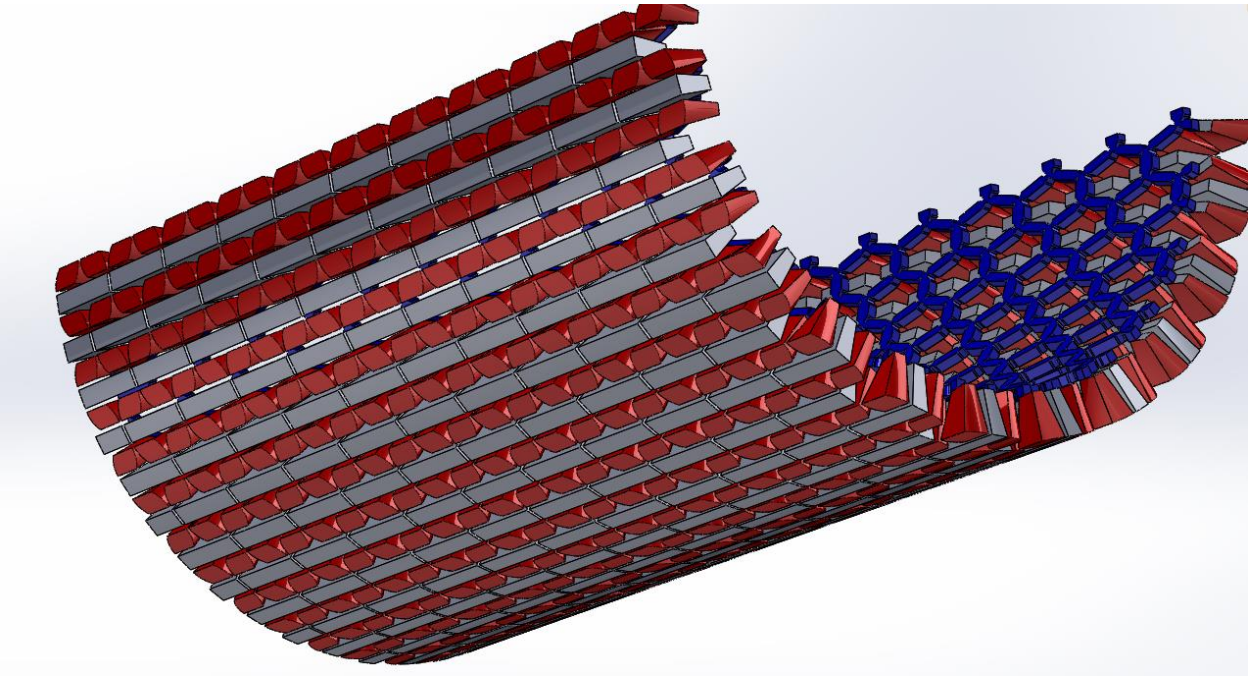

Figure 165: Overall view of mechanism annular comb with tiny teeth.

Tiny-Toothed Annular Comb, Free Sliding Contact with Leg.

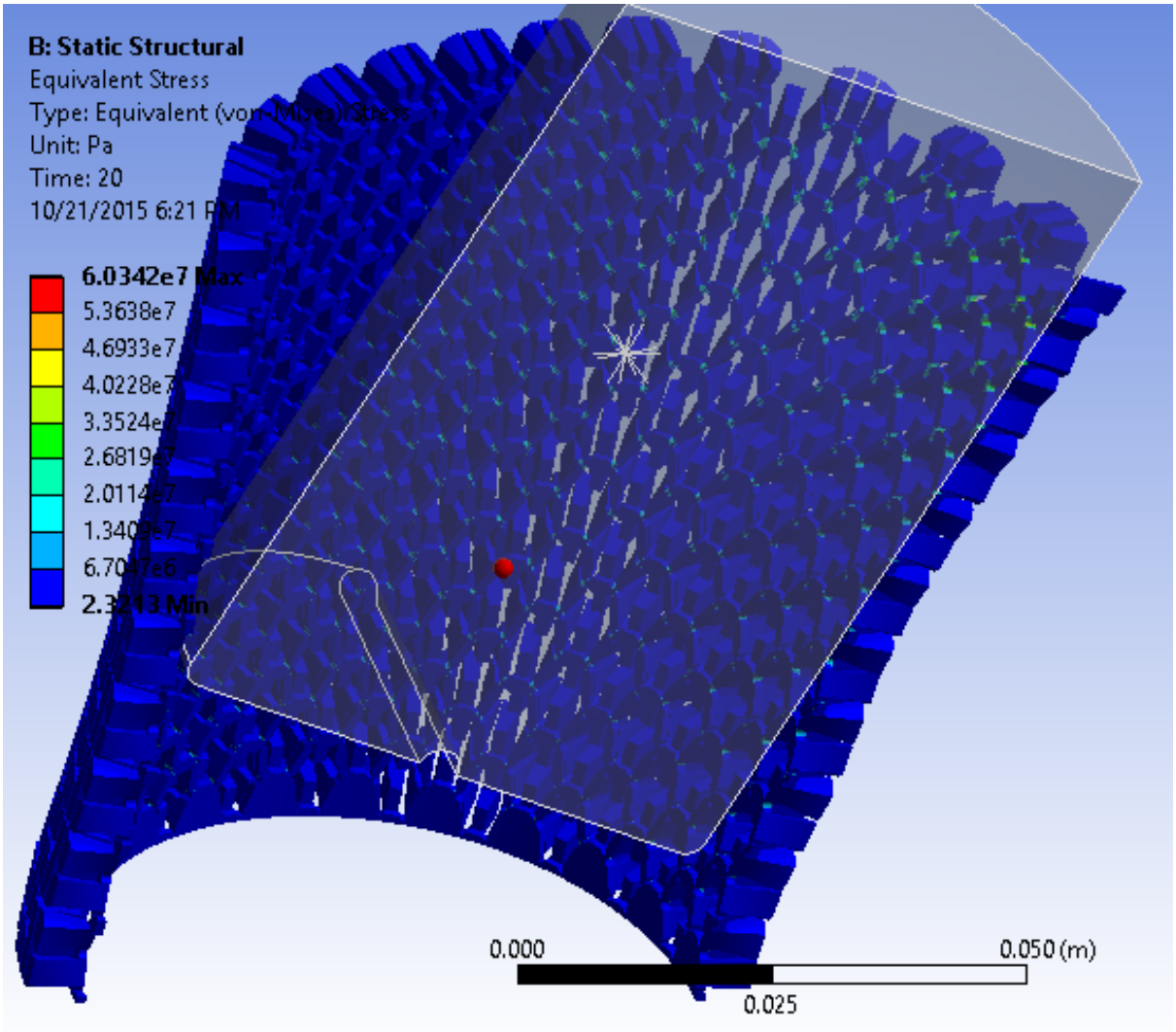
B: Static Structural
Equivalent Stress
Type: Equivalent (von-Mises) Stress
Unit: Pa
Time: 20
10/21/2015 6:21 PM
6.0342e7 Max
5.3638e7
4.6933e7
4.0228e7
3.3524e7
2.6819e7
2.0114e7
1.3409e7
6.7047e6
2.3213 Min
0.000
0.050 (m)
0.025

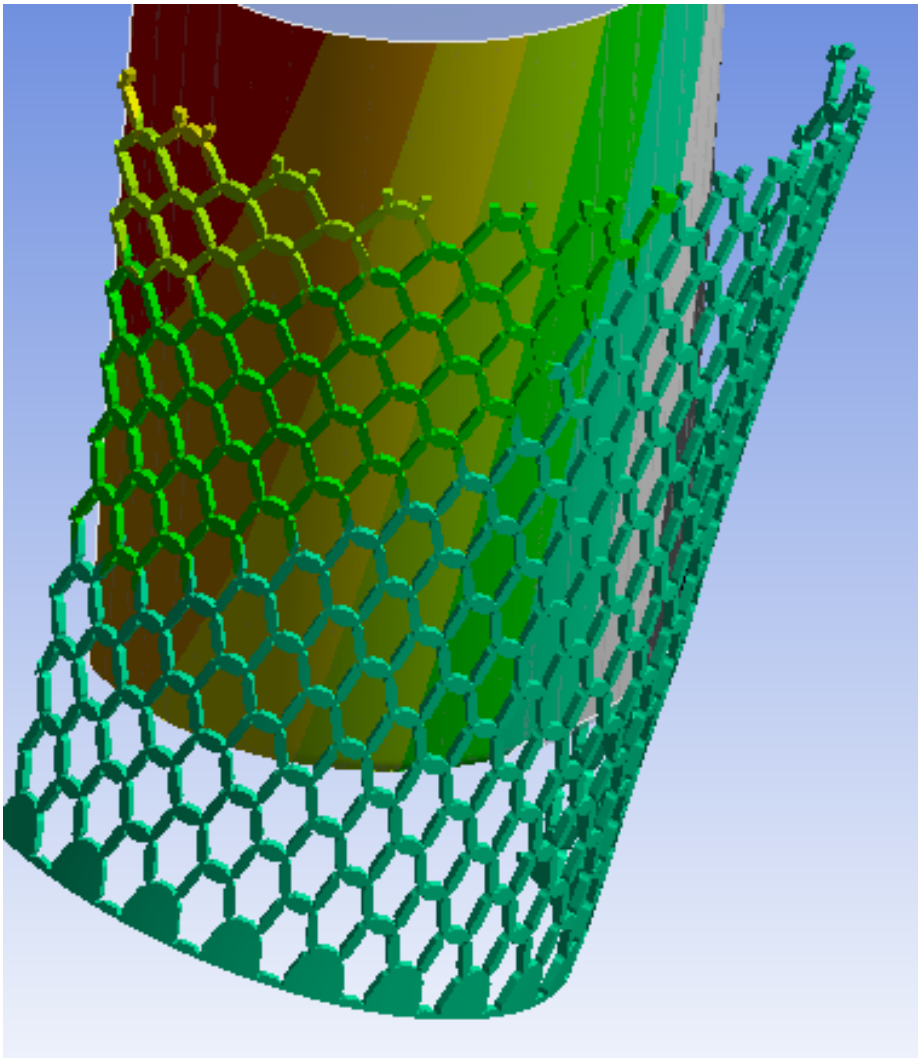

Figure 166: First view of sliding-contact tiny-toothed hex-backed annular comb (teeth hidden from view, but active in the simulation). No tensioning of cells is to be seen, but at least the teeth prevented shell buckling.

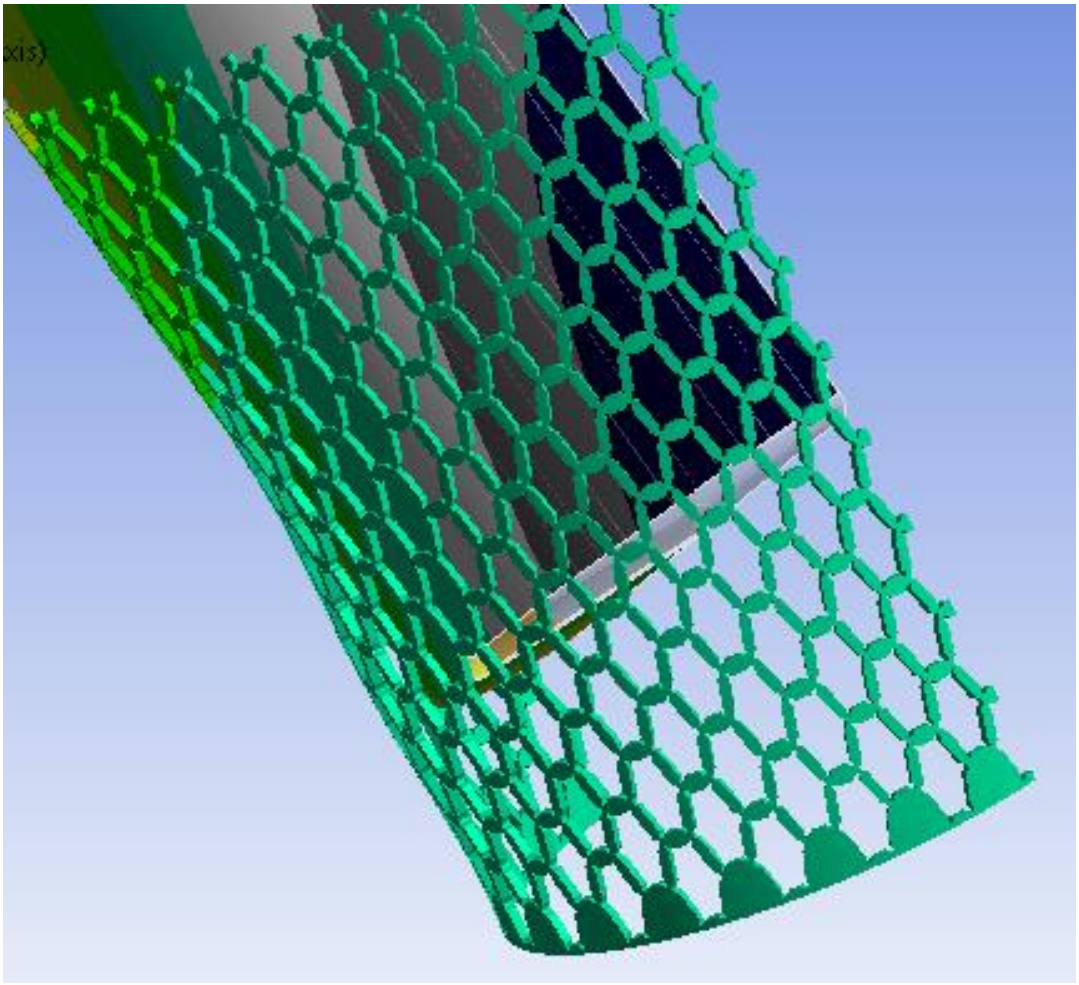

Figure 167: Second view of sliding-contact tiny-toothed hex-backed annular comb (teeth hidden from view, but active in the simulation). Little tensioning of cells is to be seen.

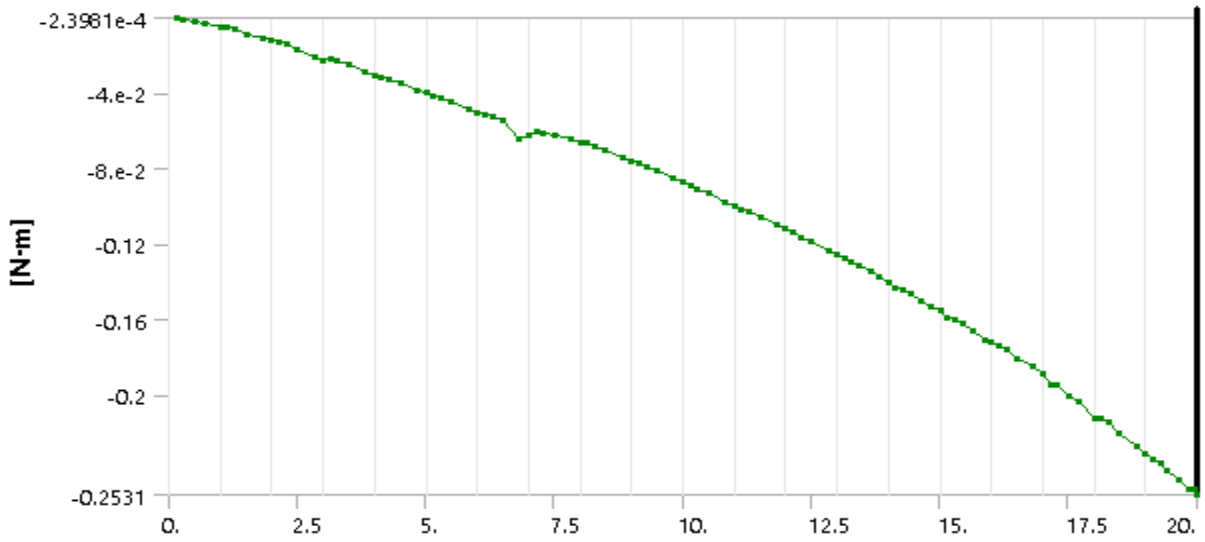

Graph 43: Moment reaction for the case of free, sliding contact between the leg and annular comb; note that the onset of stiffening was later than seen in any other annular comb simulation in this thesis.

Tiny Teeth, Top of Structure tied to Leg (Plus Sliding Contact).

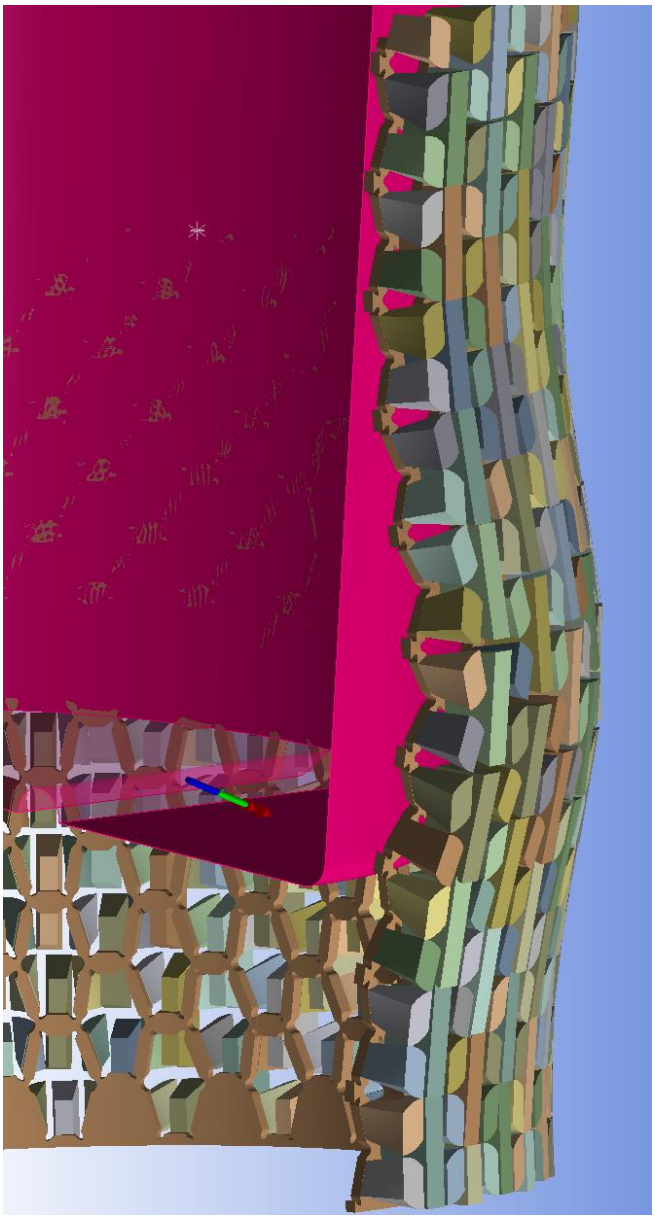

Figure 168: View, with teeth shown, of some buckling after 6.5° of leg rotation in the case of tied contact between annular comb and leg. Note that this buckling outwards defeated the teeth and eventually caused the simulation to fail.

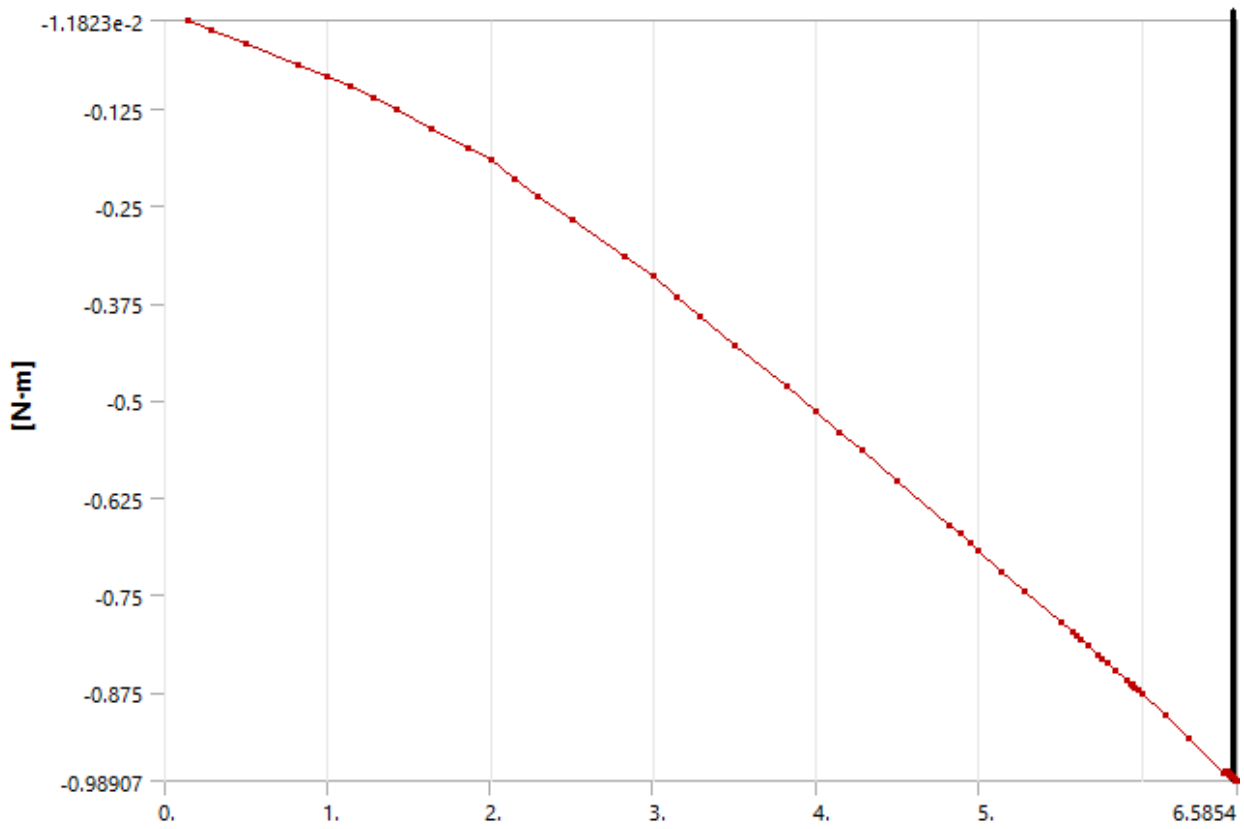

Graph 44: Moment reaction for the case of tied contact plus sliding contact. Note that this case was stiffer throughout the leg's motion range than was the previous case, which had the same geometry and material properties (and even mesh) but different boundary conditions.

Other Applications of Sculpted Compliant Joints in Annular Comb.

The annular combs studied in the previous chapter that featured wavy fiber bundles in the backbones might see better mechanical properties if the fiber bundles were also sculpted in the region in which bending is to be dominant for them when the overall backbone sees some tension. That said, as studies in this chapter have shown, only moderate fractions of the backbone will see tension (even when the top face of the annular comb is tied to the leg). The small teeth developed in this section might also be well-suited to the fiber bundles in such an annular comb as they should not inhibit fiber bending (ergo initial tensile compliance, followed

by subsequent tensile stiffening). That said, this domain no longer seems an attractive domain of research to this researcher.

Mechanism-Based Annular Comb.

A little-investigated concept from the chapter on the linear comb, a kinematically-decoupled mechanism-based comb featuring revolute joints with parallel axes instead of a compliant backbone, was adapted to form an annular comb. To this end, teeth with moderate gaps in the z and θ directions were patterned into a cylinder, and then joints were added in a pattern reflecting the cylindrical geometry and that seemed to give them complete freedom (which only the interrupted teeth should constrain when they began to touch). Initially, all joints were specified to be revolute joints, with vertical rows having parallel axes, and those in a given plane all intersecting in the center of the cylinder (certainly conforming to a geometry more complex than a cylinder would make joint axis placement for kinematic freedom more difficult). Figure 169 and Figure 170 show two pairs of links, each link connected to one other radially, and one other vertically, and Figure 171 shows half of a cylinder formed from these links. Note the interrupted teeth that should engage after rotation about either revolute axis.

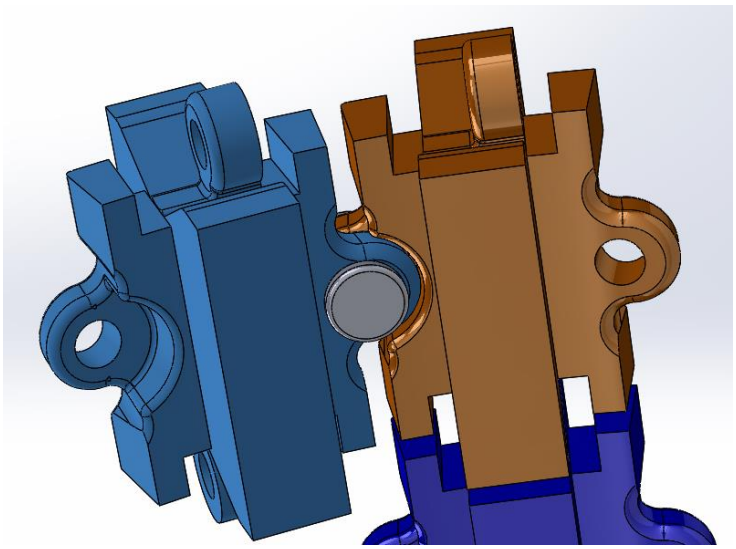

Figure 169: First tooth design for a mechanically-jointed annular comb with interrupted teeth and revolute joints between all links. First view.

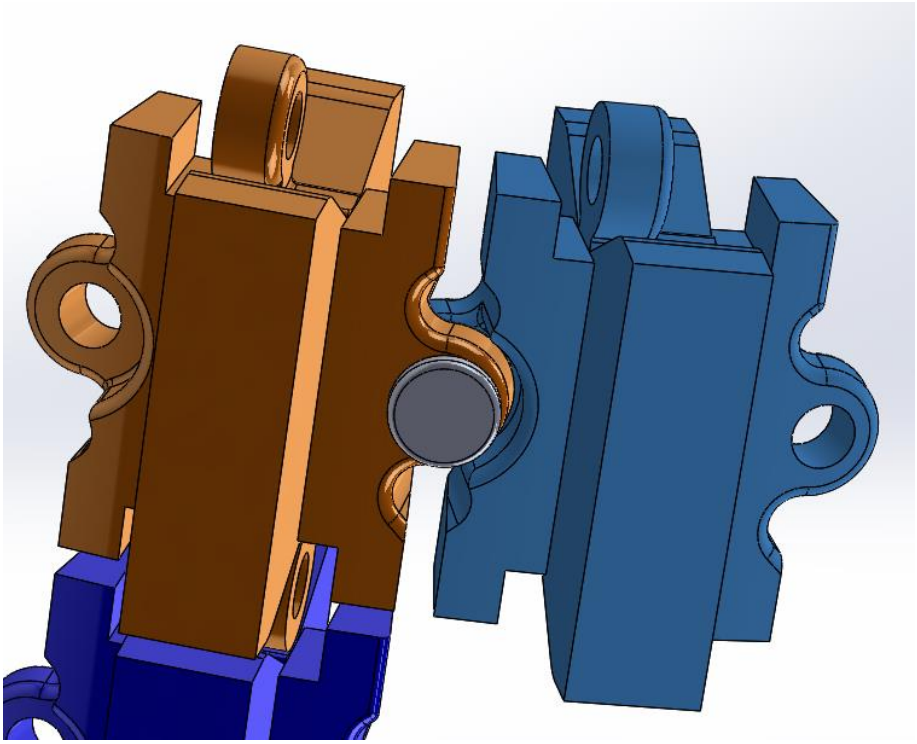

Figure 170: First tooth design for a mechanically-jointed annular comb with interrupted teeth and revolute joints between all links. Second view.

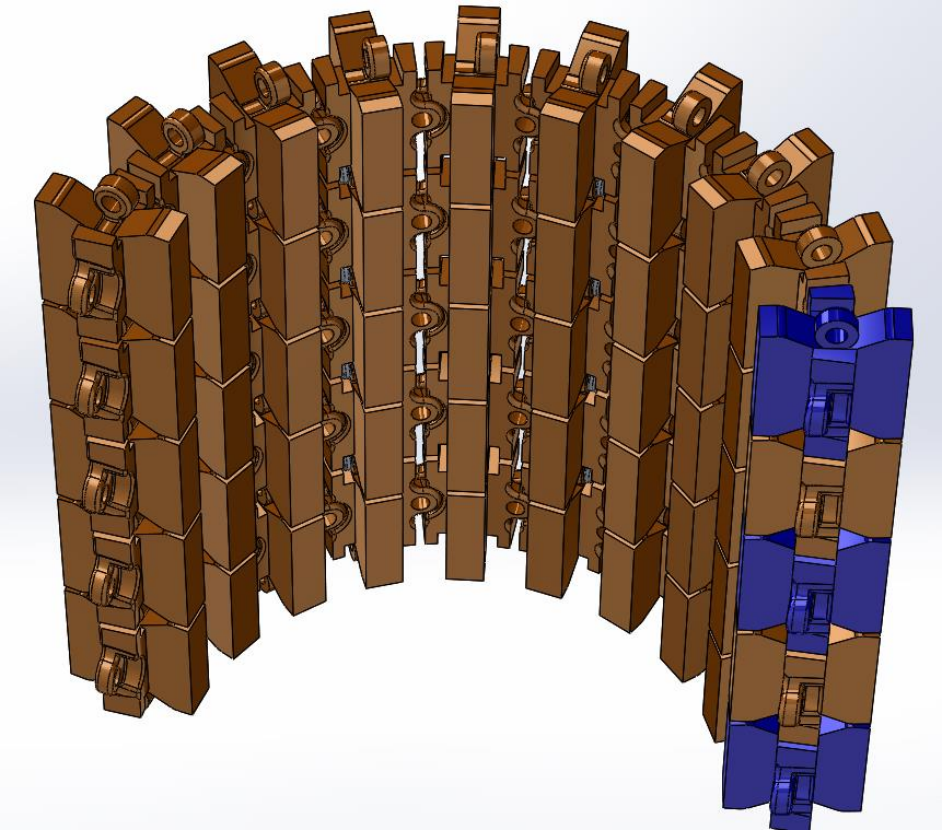

Figure 171: Half of a cylinder formed by joining the links developed above with pin joints.

Sadly, simple inspection showed this setup would not have any kinematic freedom (i.e. even before a single pair of teeth had contacted), so the radially-oriented revolute joints were replaced with spherical joints instead, in hopes that this arrangement would permit the "sock" to conform to the simulated leg as it rotated about the ankle. Figure 172 shows the modified link geometry. There are also clearances between joint features that may be appropriate for SLS 3D printing.

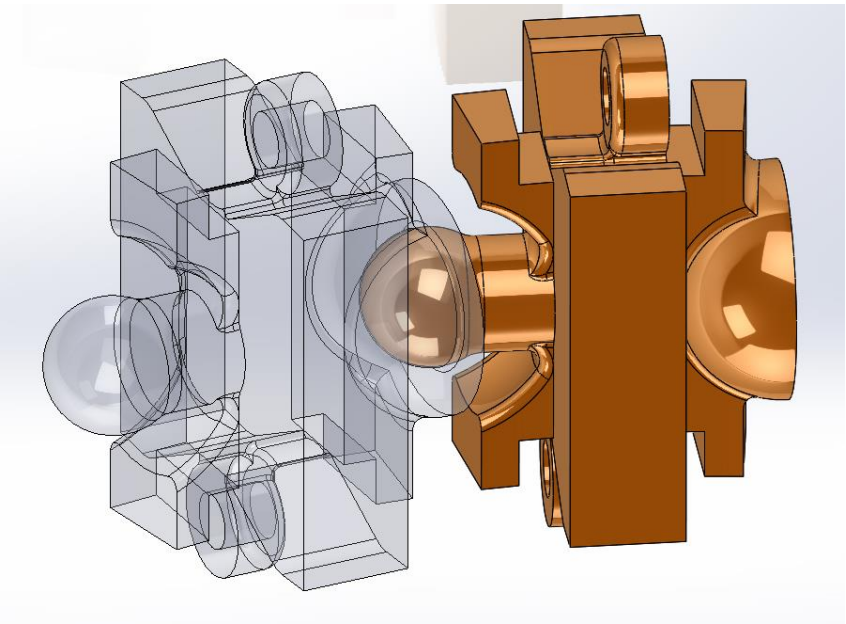

Figure 172: Two links with revolute joints for the connections to links above and below them and spherical joints for the links left and right. Note also the two sets of teeth that can lock up, one set in tangential contact, the other in vertical contact.

A cylinder was then generated from these links in preparation for a simulation of the behavior of the structure. The spherical joints had to be positioned such that the angle between them and the central axis of the cylinder would be evenly divisible into 360°. The resulting structure is shown in Figure 173.

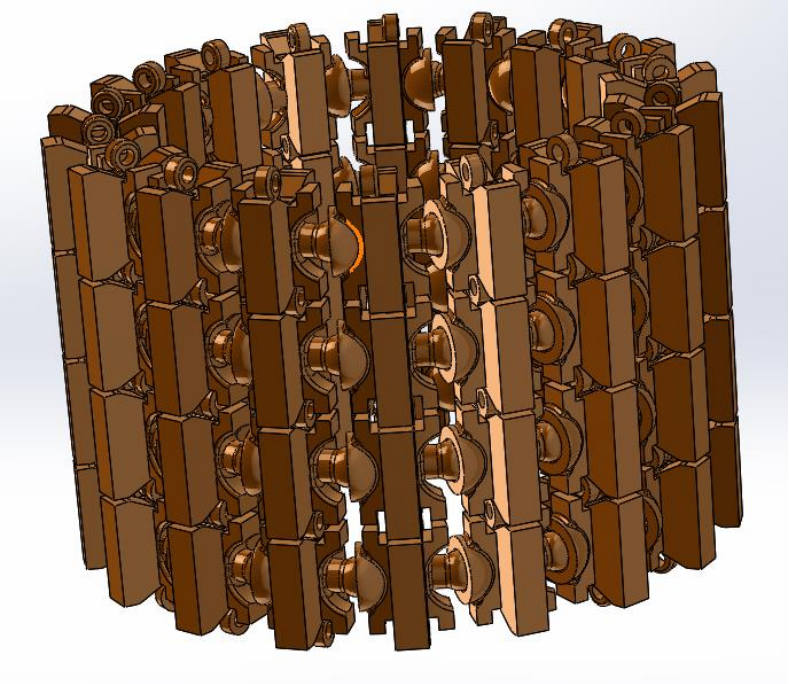

Figure 173: Overall structure of a basic, cylindrical structural-mechanism annular comb (CAD drawing).

In order to simulate the structure, a static rigid-body simulation was deemed unsuitable, for the structure is expected to have zero effective initial stiffness in the static case. Thus, a transient simulation of some sort had to be conducted, with an explicitly-integrated (according to the Runge-Kutta scheme) rigid-body simulation seeming preferable to a finite-element compliant, transient analysis since link deformation should be much smaller than displacement on average and the former would be much faster to compute. Note that the joints were not modelled with constraint equations (which would have been too tedious to set up, since ANSYS' rigid-body simulation program cannot automatically detect spherical joints, and there were nearly 750 total joints to establish), but with contact regions (which ANSYS' rigid-body program could detect automatically). While this was less computationally-efficient, it should if anything facilitate convergence, because the joints were already given tolerances. Figure 174 shows the setup of the first (and only) rigid-body simulation conducted of this idea.

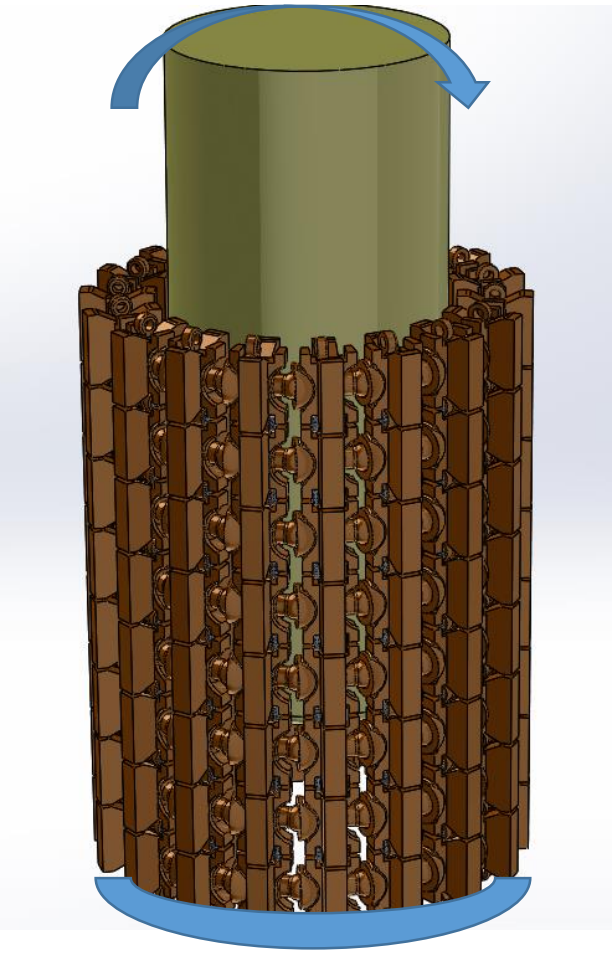

Figure 174: Boundary conditions for the rigid-body simulation of contact between the links and the rotating leg.

Unfortunately, this model also lacked the requisite kinematic freedom for leg movement—a rigid-body quasistatic simulation of leg rotation could not converge after a mere 0.3° of post-contact leg rotation. Of note, this simulation stoppage was not due to any tooth contacts at this amount of rotation; presumably, the structure is overconstrained, and perhaps even more revolute joints should be replaced with spherical joints – perhaps all, perhaps in some alternating pattern. (Replacing them with universal joints would entail even more complex geometry than what the model already features, although in principle they could also give the needed freedom.). The model might also (or instead) require some translational joints or complex cams to allow the side opposite the direction of leg rotation to lengthen as the model

develops overall curvature. It is even conceivable that very complex cams would need to be generated to permit the teeth the exact combination of rotation and translation required for some kinematic freedom (particularly along with good conformance to the leg) before lockup; clearly, such geometries become ever more impractical to generate and manufacture. Thus, given the lack of preliminary success with the idea, research into it was dropped.

Admittedly, even if the geometry had shown good mechanical performance in the rigid-body simulation (i.e. conforming to the simulated leg for many degrees of rotation, then locking up), there would still have been several potentially-fatal obstacles to overcome for this design to serve the application of this research. First, it might be computationally difficult to design teeth to conform to a geometry more complicated than a simple right cylinder while still maintaining. At the very least, if such geometry could be generated, it would probably be nearly impossible to mass-produce it, due to different link shapes throughout the geometry being needed, and the difficulty in assembling spherical joints out of plastic without snap-fits (which cannot take much load post-lockup); this in turn would relegate it to very wealthy customers, limiting potential profits. Finally, good rigid-body performance might not translate to good performance with real materials that are not infinitely stiff—in particular, the jointed nature of the structure would probably mean it would lack redundancy if one link failed. (In contrast, the toothed fabric arrays discussed later in this thesis enjoy a moderate degree of redundancy and can maintain most stiffness if one tooth shears off).

Strictly speaking, the idea of toothed links does not even have much in common with the previous idea of this chapter (using a backbone that stiffens in tension thanks to a compliant-mechanism pattern); however, the hexagonal-backed compliant-backbone comb might be altered with the principle of structural mechanisms underlying the mechanism-based annular comb by

tessellating a true mechanism of revolute joints whose axes converge on the central axis of the cylinder. (The revolute joints might need to be altered into complex cams to give them some freedom to let the leg bend the backbone forward, or the inherent compliance of the links and tolerances in the revolute joints might permit this); teeth could then be generated. However, this idea did not seem promising enough to generate a kinematic model. (Teeth could then be generated, perhaps small teeth attached each one to a single link, as in the latest compliant-backbone annular comb described in this chapter). However, time and resource constraints did not permit an investigation of this potential idea, so it will only be archived here.

Chapter 6. Two-Dimensional Teeth Arrays.

Abstract.

Two-dimensional arrays of teeth on flat fabric backbones (including fabrics of high-performance fibers) that give a stiffening-up effect in shell bending are studied, with fabric weave and material and tooth geometry and material varied in order to determine relative quantities to optimize stiffness increase at a reasonable radius of curvature for biological applications. A special tooth geometry that sees sympathetic deformation into a cylindrical shape is found to be especially promising. For maximum lockup effect, high tensile stiffness (at least in the direction in which lockup in bending is desired—the orthogonal direction can be compliant if lockup is not desired along it) combined with very low fabric thickness (giving low bending stiffness until the teeth are engaged) are both essential. Finally, a method of attaching and removing the fabric-plastic device securely to a test fixture simulating the human ankle is disclosed.

Introduction.

Textile fabrics generally combine moderate-to-high tensile stiffness with very low bending and in-plane compressive stiffnesses (which often leads to buckling and post-buckling deformation). In particular, the bending stiffness of a woven fabric is even lower than that of a solid sheet of the same material having the same thickness since fibers can slide past each other

to an extent, twist relative to each other, and even engage in microbuckling[51]. Also, some fabrics exhibit interesting anisotropies or nonlinearities that might be exploited for this application. Fabrics with rectangular weaves have significant amounts of "bias", that is, they have significant compliance in planar shear (even if they are stiff in biaxial and uniaxial tension); this might prove especially useful for an annular comb, since the backbone often experiences significant shear, regardless of whether the teeth are locked up or not (thereby producing unnecessary stiffness). By virtue of their interlocking chains (which become stiffer in large-displacement tension when tension of individual yarns straightens them out and thus removes bending of sections as a feasible mechanical mode), knits stiffen up after some tensile displacement. However, nonwoven (felted) fabrics tend to have low anistotropy or stiffening-up behavior, as do triaxial weaves.

The chainmail weaves considered in Chapter 2 might also prove an attractive substrate for teeth in this problem (given their kinematic freedom within a certain range), but their complexity of manufacture and design, both of which made them seem unattractive to the researchers of this thesis, combined with peculiar geometric compatibility requirements that would make tooth placement more difficult, rendered traditional fabrics more attractive to try first.

Preliminary Work—Solid-Backbone 2D Tooth Arrays.

Tooth arrays with solid backbones printed by 3D printing have uniformly-inferior mechanical properties for this application as compared with fabric-backed tooth arrays: the former have vastly higher initial stiffness (as they lack the low bending stiffness afforded by

[51] *Structure and Mechanics of Textile Fibre Assemblies*, ed. Schwartz, p.10

most fabric weaves) without any appreciable gain in post-lockup stiffness. Plus, they cost more to produce for the same tooth height and covered area than would most arrays (excepting those that use very expensive fabrics, which presumably confer some benefit that a solid nylon array would not). Thus, little effort was expended in researching them. Note that elastomeric materials might be successfully used to print a backbone with low bending stiffness (like that of most fabrics), but this material would also give the backbone low tensile stiffness and thus limited post-lockup stiffness. Figure 175 shows a basic planar array on a solid backbone.

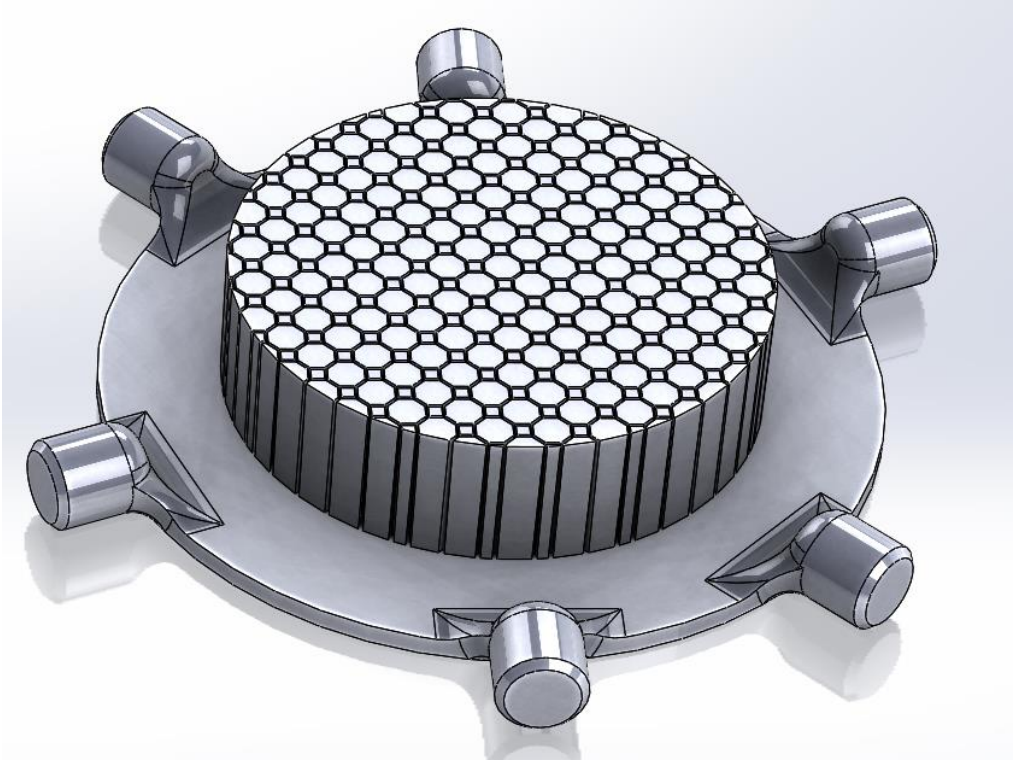

Figure 175: Planar tooth array on a solid backbone. Note that the backbone was quite thick (producing excessive initial stiffness, even for this discarded principle).

Mesomaterial-Backbone 2D Tooth Array.

As discussed in the chapter on the original annular comb concept, a 2D reentrant kite array has several interesting properties, including synclastic planar curvature, gross auxetic

behavior, and just a moderate amount of biaxial compliance (although it does not stiffen much in tension, unlike other arrays such as the hexagonal array). Early on into the research on 2D tooth arrays, a geometry that used a chiral, reentrant-kite-based backbone (with joints made into hollow cylinders for higher joint compliance) was developed, and then teeth were added on top of all joints (with the hope that they would not interfere with joint function and thus would not alter the auxetic and synclastic properties of the base). Figure 176 through Figure 178 show various images of the CAD of this array.

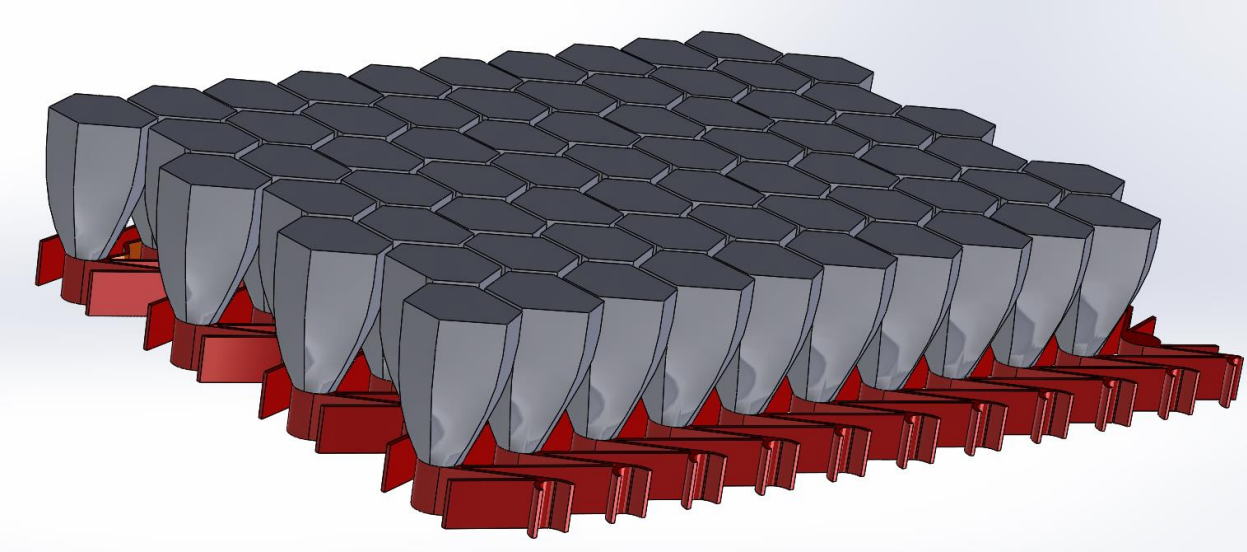

Figure 176: Overall view of 2D tooth array (shown in grey) on synclastic-curvature auxetic mesomaterial backbone (shown in red).

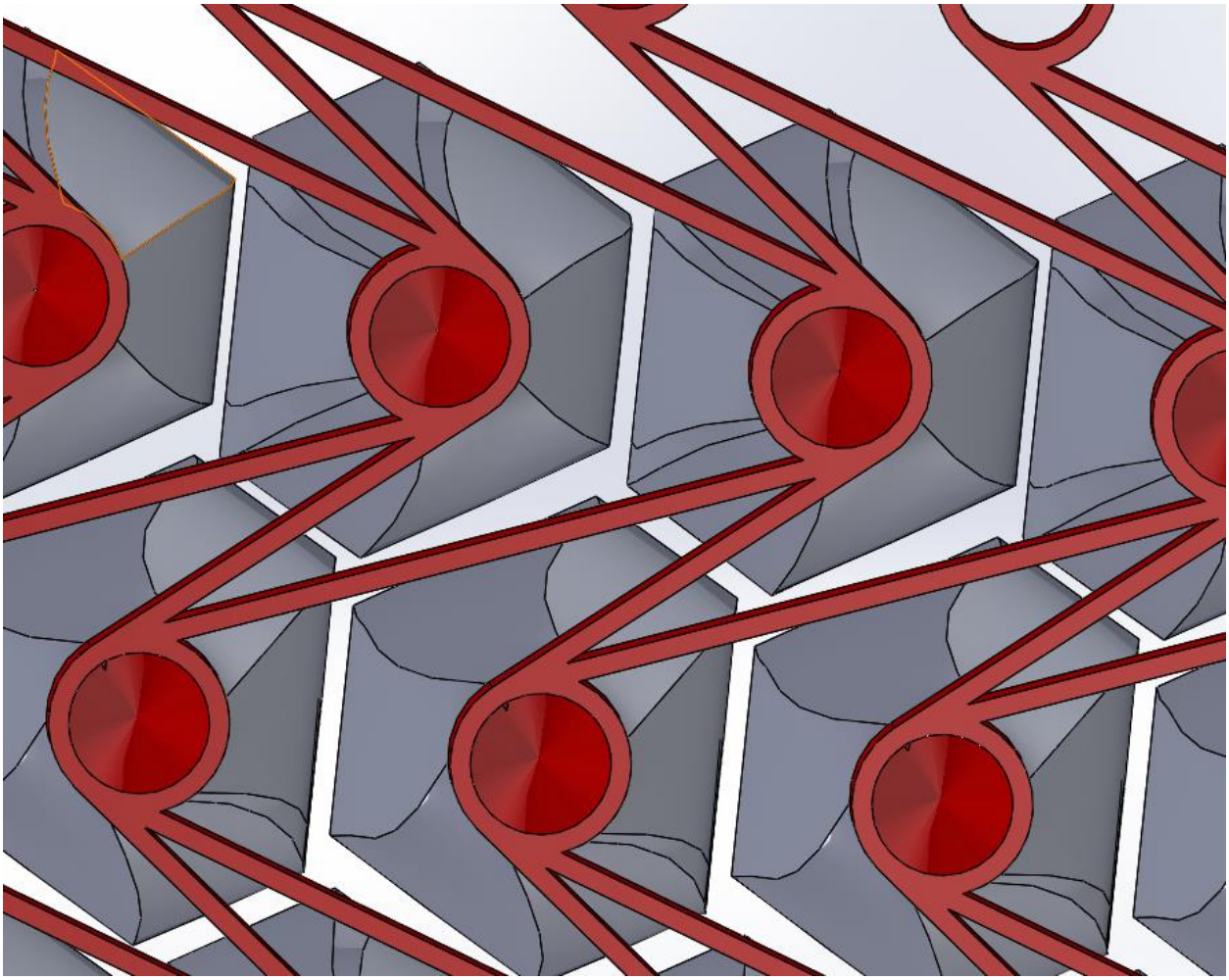

Figure 177: Underside view of 2D tooth array, showing backbone.

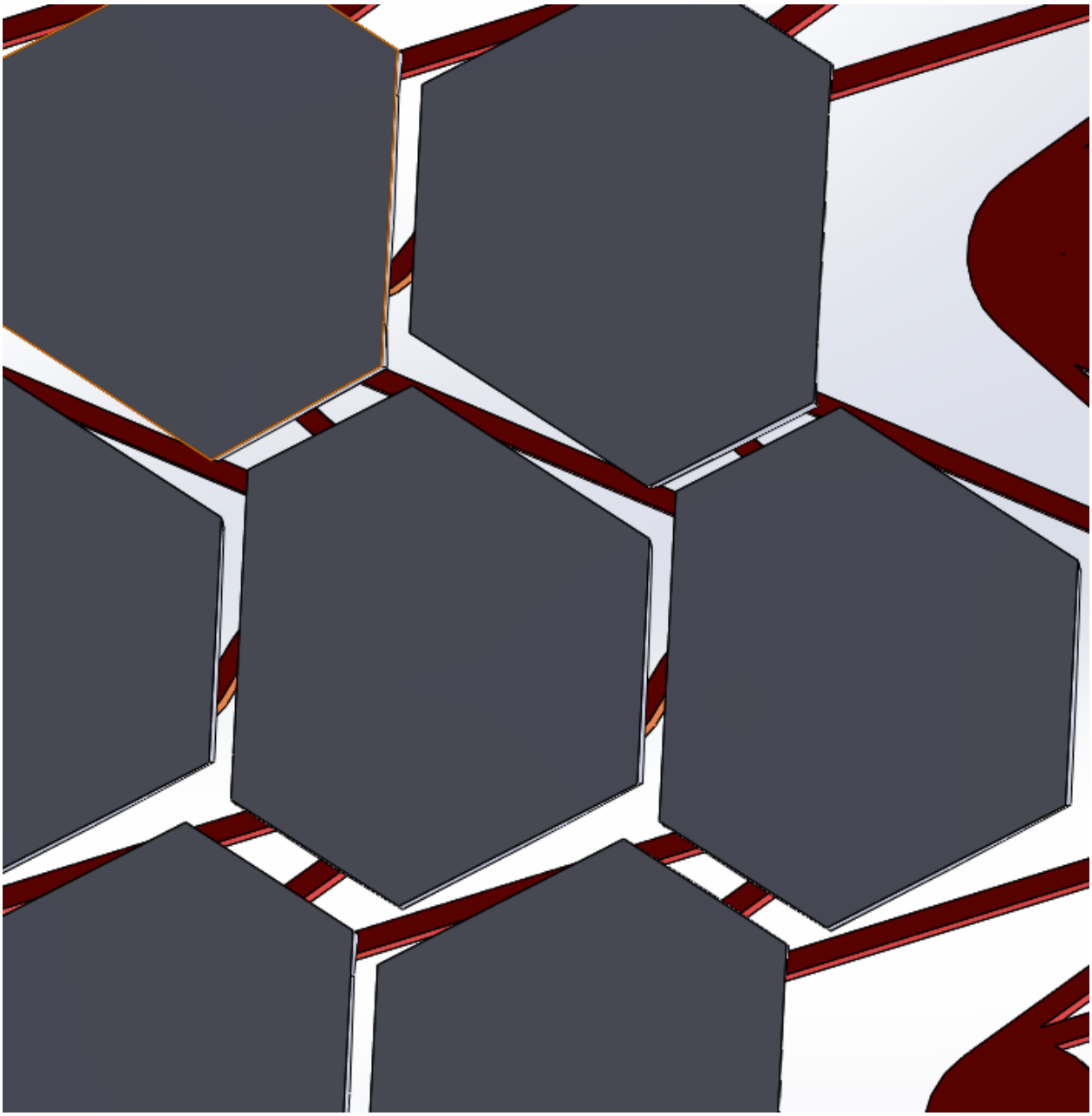

Figure 178: Top view of tooth array. Note the irregular hexagonal shape required to put teeth at the joints of the backbone and still obtain roughly the same gap distance everywhere.

Unfortunately, this array had enough compliance to the backbone that its post-tooth-contact behavior was far from satisfactory. In particular, the individual beams making up the backbone easily suffered shell buckling in local compression, while the cells could experience snap-through after some tension (preventing them from stiffening up; in fact, during snap

through behavior, tensile stiffness likely fell!). These modes are shown in Figure 179. On the other hand, pre-lockup stiffness was higher than ideal due to the backbone's overall thickness (even if that thickness was tempered by lower areal density, the individual beams contribute stiffness based on the cube of their height, whereas reduction in area reduces stiffness proportional only to the area reduced). The structure did indeed have synclastic curvature, as may be seen in Figure 180, though this novel curvature may only be a curiosity or may prove useful. Overall, the structure's mechanical behavior was completely unsatisfactory, but it apprised us of several important requirements of a toothed backbone.

Figure 179: Shell buckling of beams (with their long axes oriented to produce the highest second moment of area when the sheet is in bending) and snap-through of the kite shapes after bending, both of which inhibit post-lockup stiffness.

Figure 180: Overall view of the printed structure in bending. Note the synclastic curvature. Unfortunately, it was fairly compliant after "lockup".

Printing on Fabric Instead.

The failure of the above two ideas suggested that a very low bending stiffness is an essential property for a backbone in a successful toothed array (unlike the first array especially, although even the second one was suboptimal due to its high thickness). Such an array should thus be quite thin, but it may as well have high areal density. Additionally, tensile stiffness has no known drawbacks in a backbone; prior to tooth contact, it should not produce high pre-lockup stiffness if the backbone is thin enough, whereas after tooth contact, the neutral axis of bending should shift to put the backbone into tension. Given that fabrics of even high-strength fibers

(like carbon fiber, Vectran, *para*-aramids, fiberglass, boron fibers, etc.) can have very low bending stiffness despite massive tensile stiffnesses as long as they are sufficiently thin and use 2D weaves, it seems logical to transition to producing teeth on fabric instead of using solid backbones. Granted, there might be some benefit to a special backbone geometry that had built-in stiffening-up properties, special Poisson's ratio, etc. (for instance, the tension-stiffening backbones of the previous chapter), but simple fabrics should certainly be investigated first.

Basic Tooth Array on Fabric.

To be able to easily compare the mechanical effects of different fabric substrates, a simple array of "comb teeth" that could be printed on many different fabric samples was first designed. The array had a moderate tooth height (although the sponsor's intuition is that the final product's thickness should be below around 5mm, a tooth height of 1cm was employed because experiments showed that it was difficult with our existing 3D printer to achieve a proper gap for our preferred curvature radius at lockup with shorter teeth) and very small gaps between teeth to ensure lockup at relatively low backbone curvature; also, the ends of the teeth had flat sections of moderate length to ensure contact stability, for we discovered that small contact areas could lead teeth to slide along an axis normal to the initial base plane, thereby decreasing the distance between backbone and contact point for some teeth and thus reducing the post-lockup stiffness.

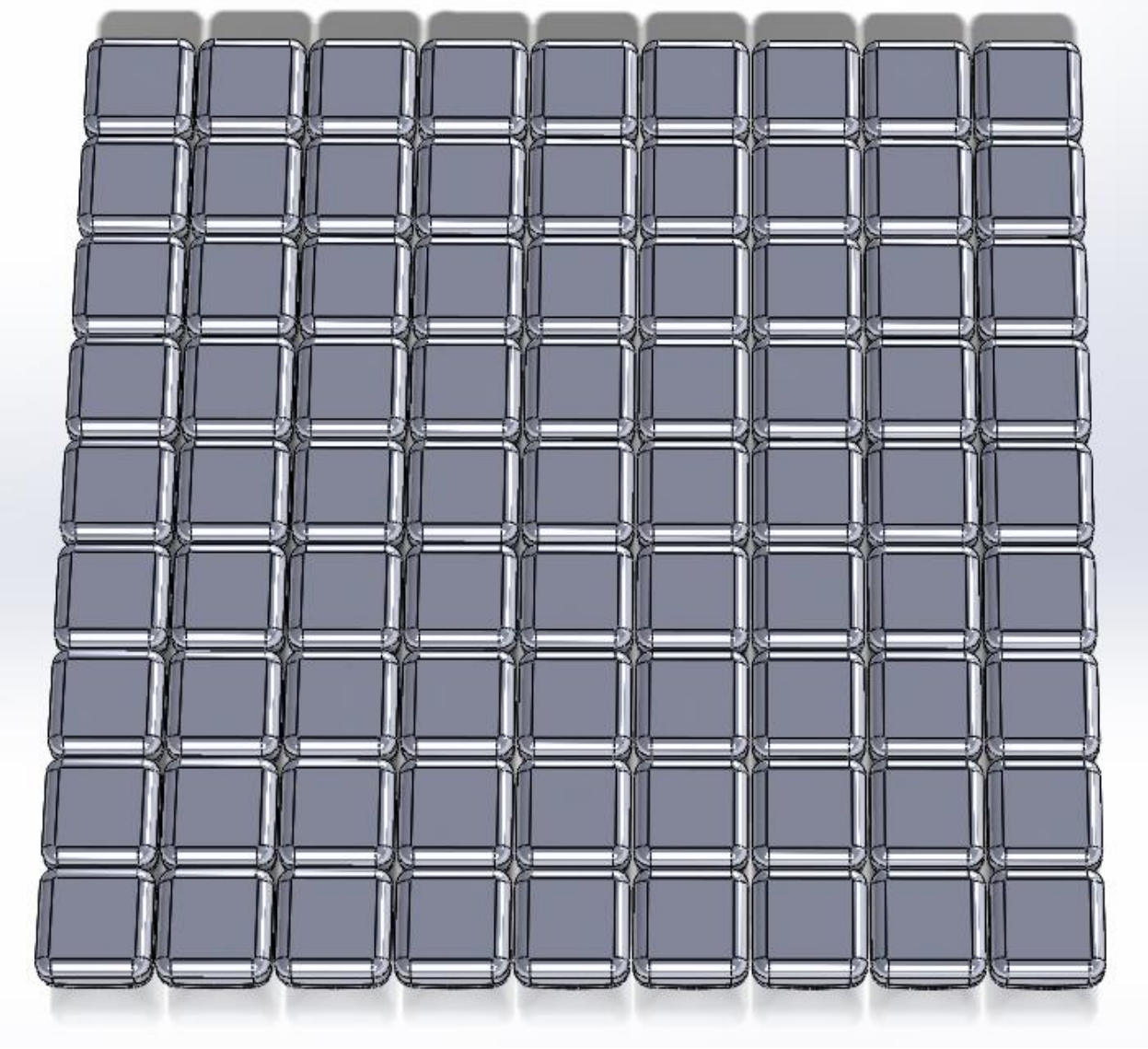

Figure 181: Square array of teeth with small gaps.

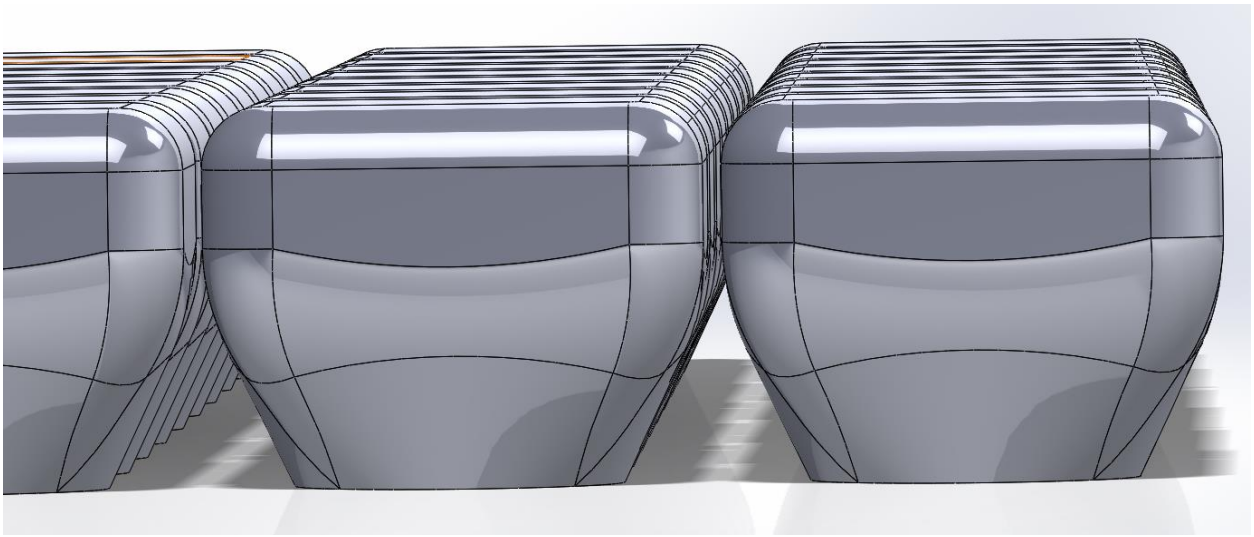

Figure 182: Large contact area ensures that teeth do not slide relative to each other once they do contact. (Another view of the teeth shown in previous figure).

This array was printed on a variety of fabrics. Nylon copolymer filaments were found to generally adhere to fabrics well; however, nylon is far from the stiffest of the thermoplastics that are commonly printed with FDM printers, and since the backbone itself (which is subjected to high strains and should also be compliant) is not printed, just the teeth (which should be as stiff as possible and experience low strains, especially when they are short), some mechanical benefit might be obtained from printing teeth with a stiffer filament. However, the Taulman nylon series exhibited excellent adhesion to most fabric substrates, whereas most other filaments tried exhibited poor to negligible adhesion (see Appendix _ for further details). A modified structural cyanoacrylate produced by Tech-Bond[52] capable of bonding to nylon and most other polymers was also added manually to the opposite side of fabrics after teeth were printed in the hopes that it would percolate through the fabric and contact the nylon; after application, an activator spray was employed to start the reaction. Of course, the efficacy of this bonding operation varied, with

[52] http://www.tech-bond.net/

some weaves being more readily penetrated by the adhesive, and some fabrics bonding better to it than others.

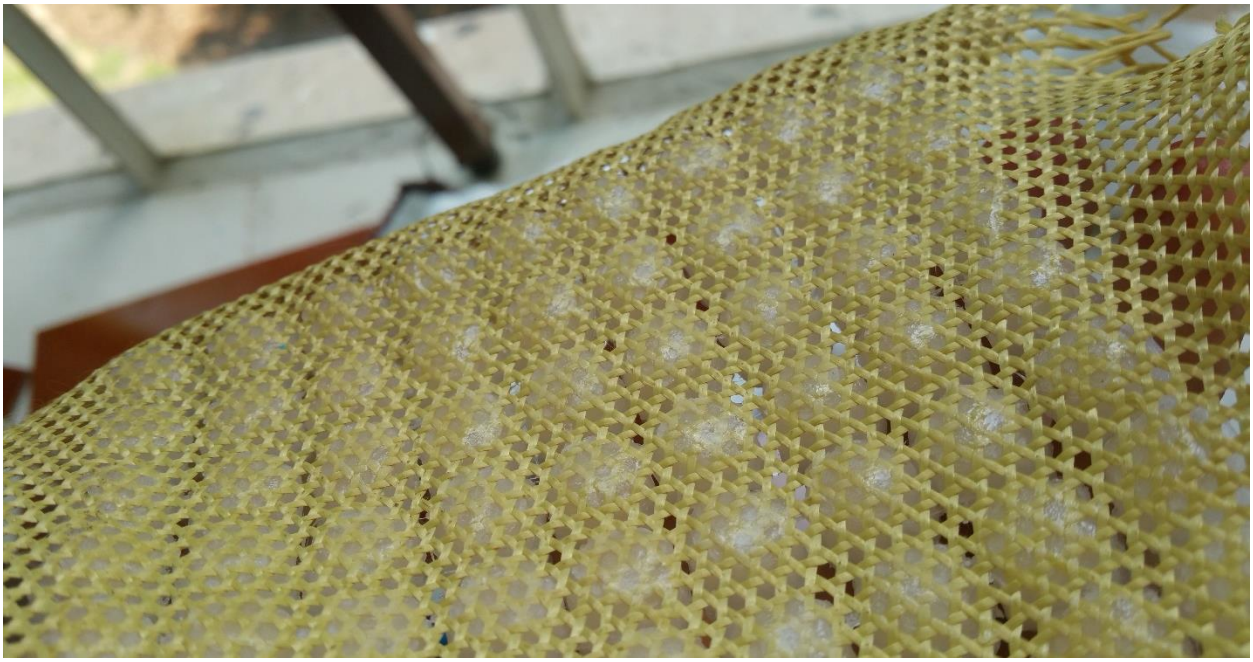

Figure 183: Tech-Bond structural cyanoacrylate (capable of bonding to nylons) was applied to the underside of this open weave at the bases of teeth, then activated for a more-secure bond than that offered by melting nylon to the fabric alone.

These preliminary results are summarized below.

Woven-Fiberglass Backbone.

While the use of fiberglass might raise some eyebrows, some weaves use such fine fibers that they absolutely do not splinter, even when pressed vigorously into sensitive areas of the body like the lips. That said, fiberglass is especially susceptible to abrasion (which might occur not only from external contact, but even from strands sliding over each other!), so it is not likely to be an ideal material. However, the rectangular fabric weaves in fiberglass available showed significant compliance along the "bias" (that is, in planar shear) along with significant uniaxial/biaxial tensile stiffness. Prior to lockup, where the bending properties of the pure fabric

dominated the mechanical behavior of the material, stiffness was extremely low, in fact, so low that any test fixture might need to be enclosed in a fluid with specific gravity similar to that of nylon or fiberglass so that buoyancy effects would cancel out those of gravity, for otherwise the fabric would have almost no bending resistance against gravity. After lockup, the high tensile strength of fibers and good adhesion between teeth and fibers (especially when augmented with structural cyanoacrylate) gave the fabric what felt like excellent stiffness.

Also, as a consequence of the rectangular weave and resulting ease of deformation on the bias, the nylon-fiberglass structure had some initial shear compliance that was later erased in lockup; Figure 186 shows the structure at the end of this initial compliance in this shearing mode. Note that initial shear compliance was orders of magnitude lower for the printed structure than for the plain fabric, presumably because those areas that are glued to teeth have very high stiffness in this mode.

Figure 184: Nylon tooth array on woven ultrafine fiberglass fabric--relaxed.

Figure 185: Showing bending lockup of fiberglass with tooth array.

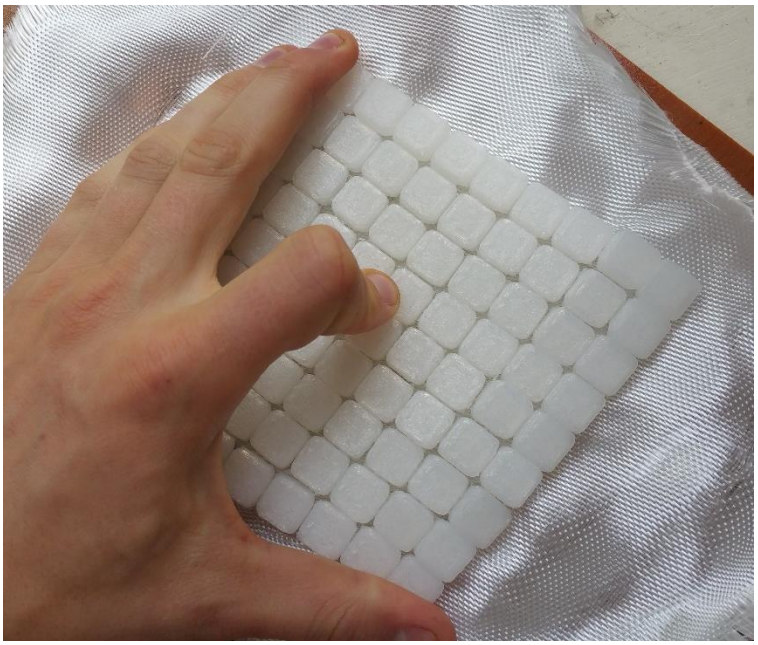

Figure 186: Showing lockup after some planar shear strain.

Triaxial Kevlar Fabric Backbone.

The triaxial weave of Kevlar had excellent tooth-fabric adhesion and felt even stiffer in lockup than the fiberglass weave of equivalent thickness (even though the Kevlar fabric had lower areal density, of fibers or mass). Although touted for its especial isotropy compared with rectangular weaves (since there are three, not just two, fiber directions), this property had no observable practically-beneficial effects, perhaps because the rectangular tooth array and corresponding angular gap differential added significant anisotropy. (Note that the weave completely eliminated the fabric's bias compliance, but bias compliance is thought to have a benefit for the leg-protection application). It might be interesting to try a hexagonal array with similar tooth gaps at the end on such fabric; then, differences between triaxial and rectangular weaves might emerge. Figure 187 shows the print in neutral, unbent position.

It might be interesting to investigate hexagonal or triangular arrays, especially on triaxial fabric, where tooth-tooth contact normals would be parallel to (or, if the teeth were sized properly, actually coincident with) fibers. (It was observed above that square-packed teeth have notably-different lockup properties at 45°; increasing the number of sides while maintaining tesselatability could reduce this angular differential). To this end, hexagonal and triangular arrays were generated with the same tooth-tooth gap and tooth height as those used for the square arrays. Figure 199 shows CAD geometry for a hexagonal array, and Figure 200 and Figure 201 show CAD geometry for a triangular array. Note the significant gaps at the corners of the triangles in the latter array; the hexagonal array may be preferable as it does not have such pronounced gaps (for these might contribute to lockup anisotropy).

Figure 187: Tooth array on triaxial-weave Kevlar fabric (neutral).

Tufted-Nylon Backbone Array.

Next, a scaled-down print on a fabric woven of highly-tufted carpet nylon (Robert Allen "Epic" fabric) was attempted. The pre-lockup bending stiffness of this fabric felt much higher

than that of the open, triaxial Kevlar weave investigated, likely the result of the much-greater thickness of this felt and the higher fiber density per unit volume. Also, despite the felted appearance and thickness of the threads making up the weave, the fabric had moderate bias compliance in planar shear, although its dissipative effects (mainly from friction between yarns) might be practically significant (unlike in the fiberglass weave). The print on this fabric was made with a nylon-elastomer alloy (more compliant than the nylon copolymer used for other prints) that apparently gave the teeth too much compliance, because the post-lockup stiffness of the structure was mediocre (and some contact-deformation of the edges of the teeth was visible after lockup). If nothing else, this shows that there is some need for stiff teeth, at least to a certain point (even though a FEA study from the previous chapter of an annular comb showed that replacing nylon teeth with perfectly-bonded steel teeth having 100x greater stiffness only increased total post-lockup stiffness by around 2x). Peel resistance was superb—the teeth could not be removed by hand. (This is especially fortunate for this particular fabric, as the thickness of the fabric would likely confound efforts to augment the bond with cyanoacrylate from the underside).

Figure 188: Tooth array on felted Nylon (at lockup point).

Silicone Rubber Backbone.

Next, an array was printed on a 1mm-thick sheet of silicone rubber coated with a sticky, non-curing adhesive, a picture of which is shown in Figure 189. Unfortunately, the very low tensile stiffness of the elastomer backbone produced an extremely-low post-lockup stiffness: after teeth contacted each other, the compliant backbone simply stretched to accommodate gross bending. The structure could be bent upon itself easily with one hand, as shown in Figure 190. Of note, the thickness of the rubber sheet even gave it higher bending stiffness than a thin Kevlar fabric like the triaxial weave used earlier, so the elastomer is inferior on both major criteria (high post-lockup stiffness and low pre-lockup stiffness), although its pre-lockup stiffness isn't high per se. Interestingly, standard Taulman nylon filaments (like Taulman 645 and 618) did not adhere to the silicone at all, but the Taulman nylon-elastomer alloy did adhere well enough to print without warping; indeed, the shear strength of the bond was high enough that the teeth did not come off when the overall structure was in bending, although this is hardly a testament to a high bond strength as its post-lockup stiffness was so low. Plus, resistance to peeling (a load that

would be encountered if the structure accidentally hit an obstacle) was quite poor, although it is conceivable that some curable adhesive could give the requisite peel strength.

Figure 189: Silicone-backbone comb array. At the subjective beginning of lockup (but the stiffening-up effect was so small as to make this difficult to detect).

Figure 190: Unsatisfactory post-lockup stiffness of the silicone-backbone tooth array.

All of these simple square-array prints enabled the researcher to draw several conclusions about the relationship between fabric mechanical properties and those of the overall printed structure. First, tensile stiffness in the fabric appears to be indispensable for high stiffness after lockup; fabrics with low tensile stiffness in one direction (for instance, the polyester-cotton-elastomer weave) experienced much lower post-lockup stiffness when part of the printed structure, and the elastomer structure barely stiffened at all thanks to its high backbone compliance. Fortunately, even very-high tensile stiffness does not necessarily lead to high pre-lockup bending stiffness, as seen in the Kevlar and fiberglass prints, which were quite compliant before lockup. Indeed, since a fabric's bending stiffness depends on the sheet's thickness as well

as the properties of its fibers and their orientations, high-strength fabrics should have a higher, more-favorable tensile-stiffness to bending-stiffness ratio since they can be thinner for the same tensile stiffness.

Cotton-Polyester-Elastomer Fabric Backbone.

This fabric had notable planar anisotropy as a consequence of the way the elastomer was woven in: it had significant compliance along one axis and the highest stiffness perpendicular to this axis; plus, it had significant shear compliance/bias (although it is unknown to this author whether this is due to the compliance in the less-stiff direction or the rectangular weave of the fabric). This anisotropy might prove extremely useful in this application because the stiff-backed annular combs experienced significant shear stress in the backbone throughout the deformation range, a mode illustrated in Figure 191 (contours of overall shear stress are shown in Figure 192). Note also that those annular combs that did not conform all around the leg bent inward at the area of the gap in a direction perpendicular to the main outward motion of bending, as shown in Figure 193. Granted, a fabric-backed comb should conform better, but if this mode of deformation occurred, it would be ideal if the backbone met it with compliance. That said, compliance in one direction may eliminate the possibility of tangential contacts between teeth contributing to a stiffening-up effect.

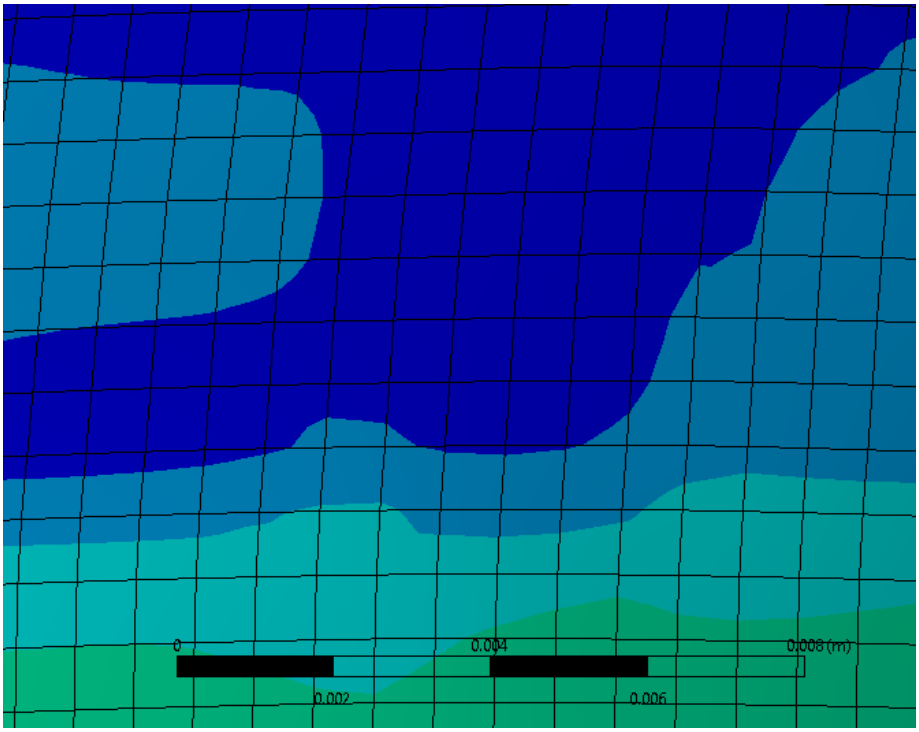

Figure 191: From an FEA study on the elastic-backbone annular comb, the shearing mode to which formerly-square-cross-section hexahedral elements were subjected.

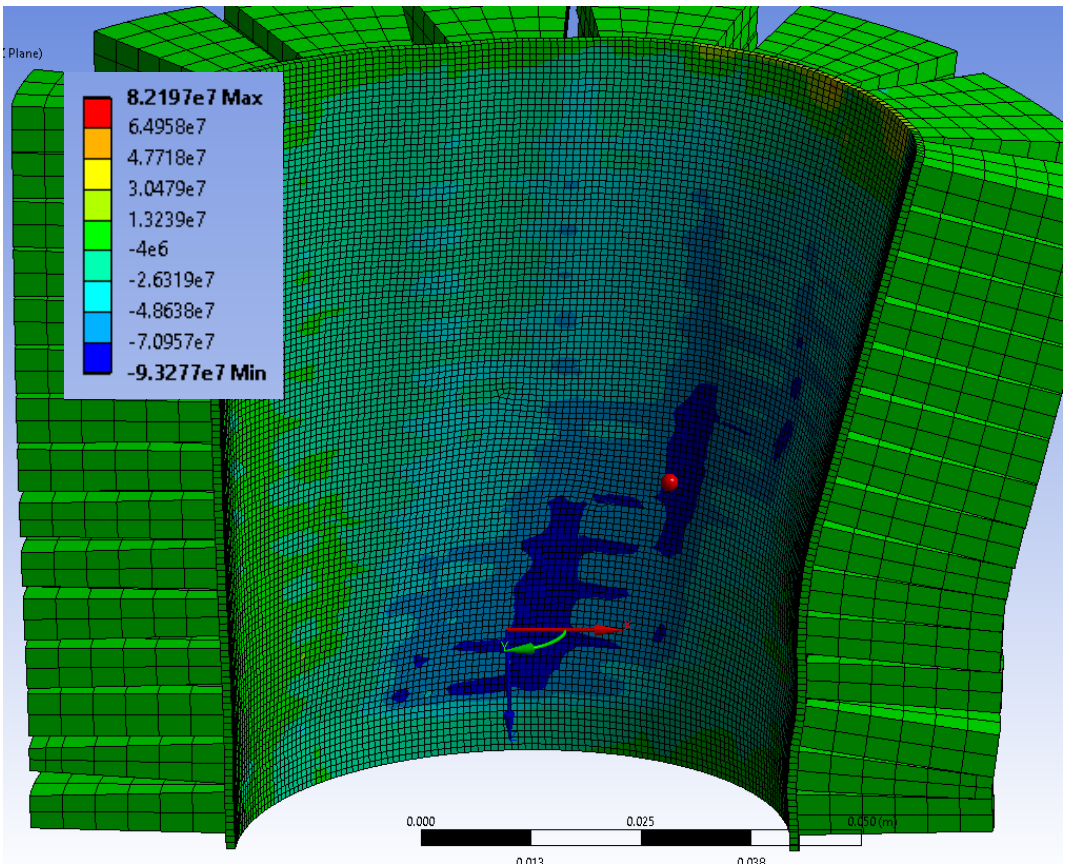

Figure 192: Some areas of the linear-comb backbone experienced high shear stress (resolved in the z-theta direction).

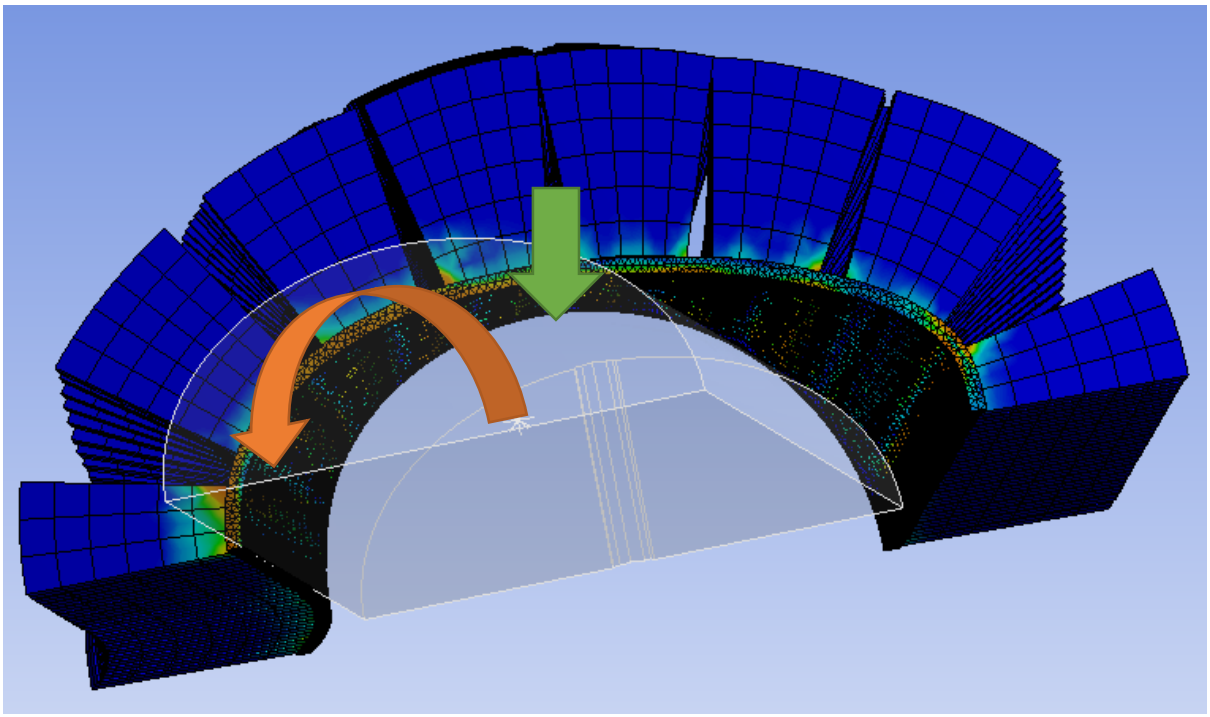

Figure 193: Leg rotation (shown with the orange arrow) results in inward contraction of part of the backbone (the part near the green arrow, which shows the direction of this deformation mode) because the backbone did not conform very closely here.

To this end, a square, 9x9 standard tooth array was printed on the fabric with Taulman 618 nylon filament; bonding between extruded filament and the fabric was quite good though later augmented with structural cyanoacrylate. Figure 194 shows the printed array in unbent position, with compliant and stiff directions drawn on fabric. Figure 195 shows post-lockup bending lockup in the more-compliant direction – note that it was quite soft in this direction even after lockup, and Figure 196 shows the post-lockup shape when bent in the stiffer direction, roughly at the very point of lockup (although it was difficult to strain the material much beyond this point). Despite the stiffness differential in the two directions, it felt as if the teeth closed up at the same radii of curvature in each direction. Of note, the weave is vulnerable to developing tears along the bases of teeth when the fabric is bent in the direction of higher compliance, as shown in Figure 198. While these tears appear to increase compliance in the softer direction

(and propagate when the structure is bent significantly), they do not appear to affect its properties in bending in the stiff direction as the cracks stay closed then. Finally, Figure 197 shows the array in planar shear roughly at the lockup point associated with this deformation mode. As expected, shearing had a fair amount of compliance thanks to the elastomeric content and nature of the weave.

Figure 194: Cotton-polyester-elastomer fabric with significant anisotropy (compliance in one axial direction much higher than in the other) with tooth array printed thereon. As shown by the drawings on the fabric, the single orthogonal compliant axis also renders the cloth compliant in shear, even though it does not have a weave that itself gives a lot of bias compliance.

Figure 195: Lockup curvature of the CPE-backbone array when bent along the compliant direction.

Figure 196: Lockup curvature of the CPE-backbone array when bent along the stiffest direction.

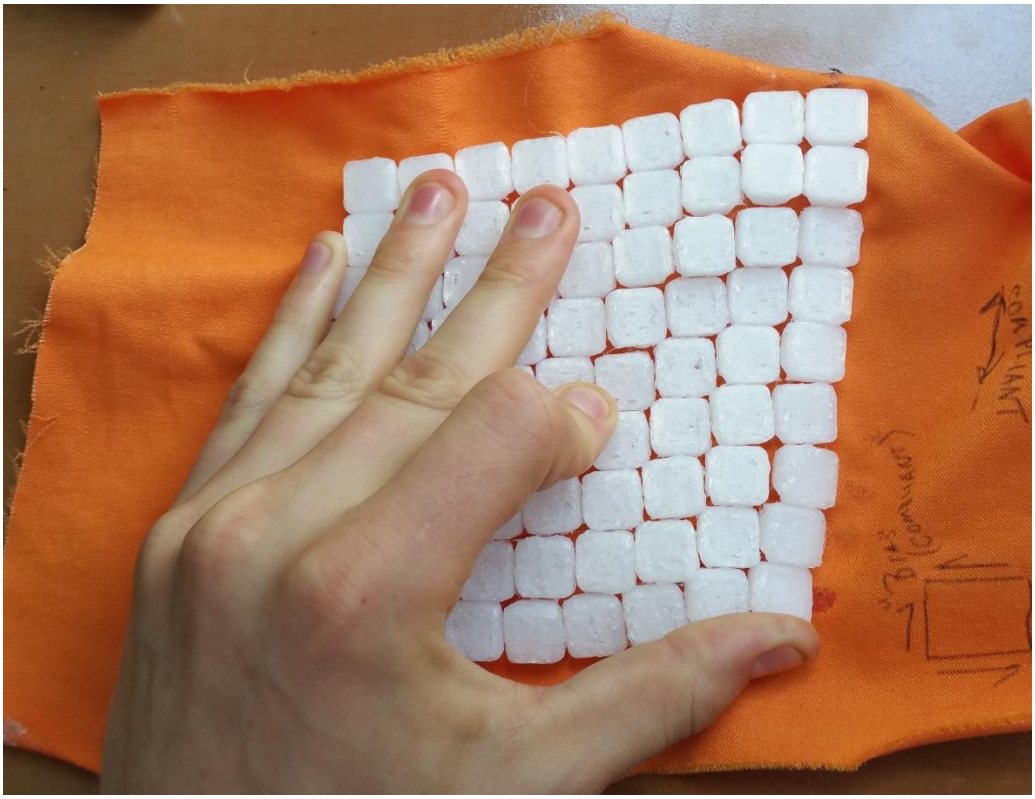

Figure 197: Lockup after some shear compliance of the CPE-backed tooth array.

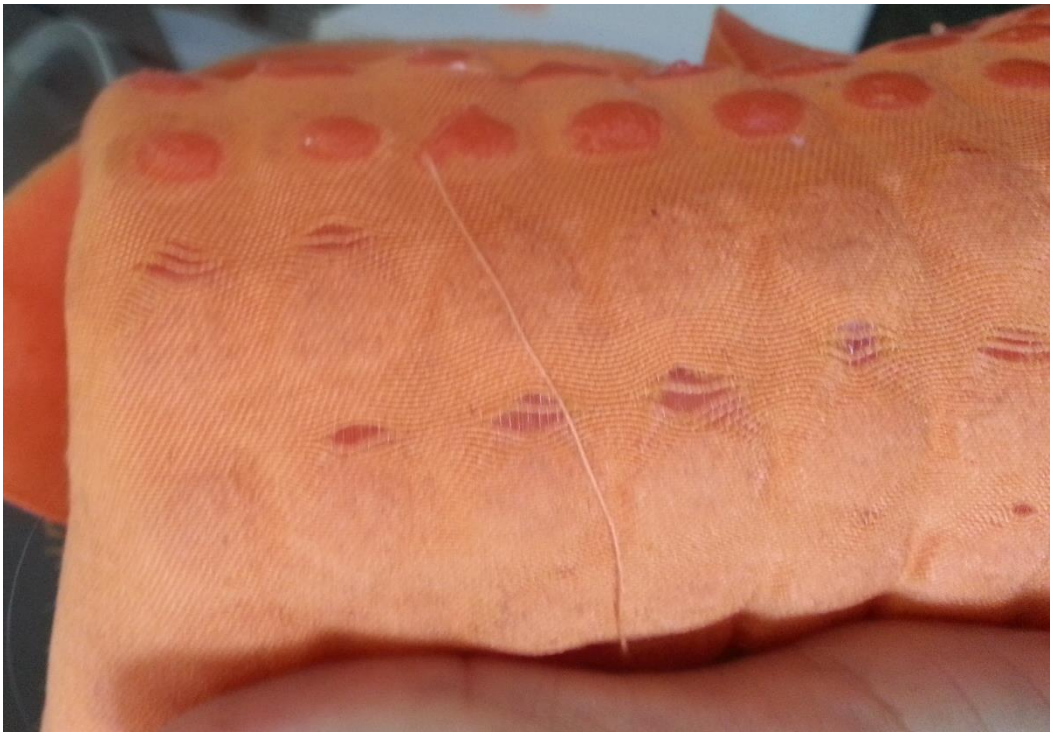

Figure 198: In bending in the more-compliant direction, the fabric reveals small tears near the bases of teeth. These presumably add to the backbone's compliance in this direction. It is not clear how they originated, whether simply from bending load that the low-strength elastomer fibers simply could not handle, heat damage from the printer extruder, etc.

Non-Square Arrays.

Several potential reasons to investigate non-square arrays were conceived of. First, hexagonal or triangular tessellations might be especially suited to triaxial weaves, because (depending on the angle of the pattern) contact normals between teeth could be made to be parallel (and, for the right tooth sizing relative to the weave, even coincident) with fibers, which might better exploit any residual anisotropy in the weave (although it is likely to be small). Also, hexagonal arrays should have less contact surface area than square arrays for the same base surface area by the Isoperimetric Theorem (whilst triangular arrays should have more than square arrays); thus, such arrays would permit an evaluation of the effects of contact surface area between teeth. Figure 199 shows a potential hexagonal array; note that the tooth initially flares

upwards to ensure that there is a limited tooth contact patch with the fabric, and then the flare ceases to afford a large area for tooth contact and reduce slipping between teeth. Figure 200 and Figure 201 show a potential triangular array.

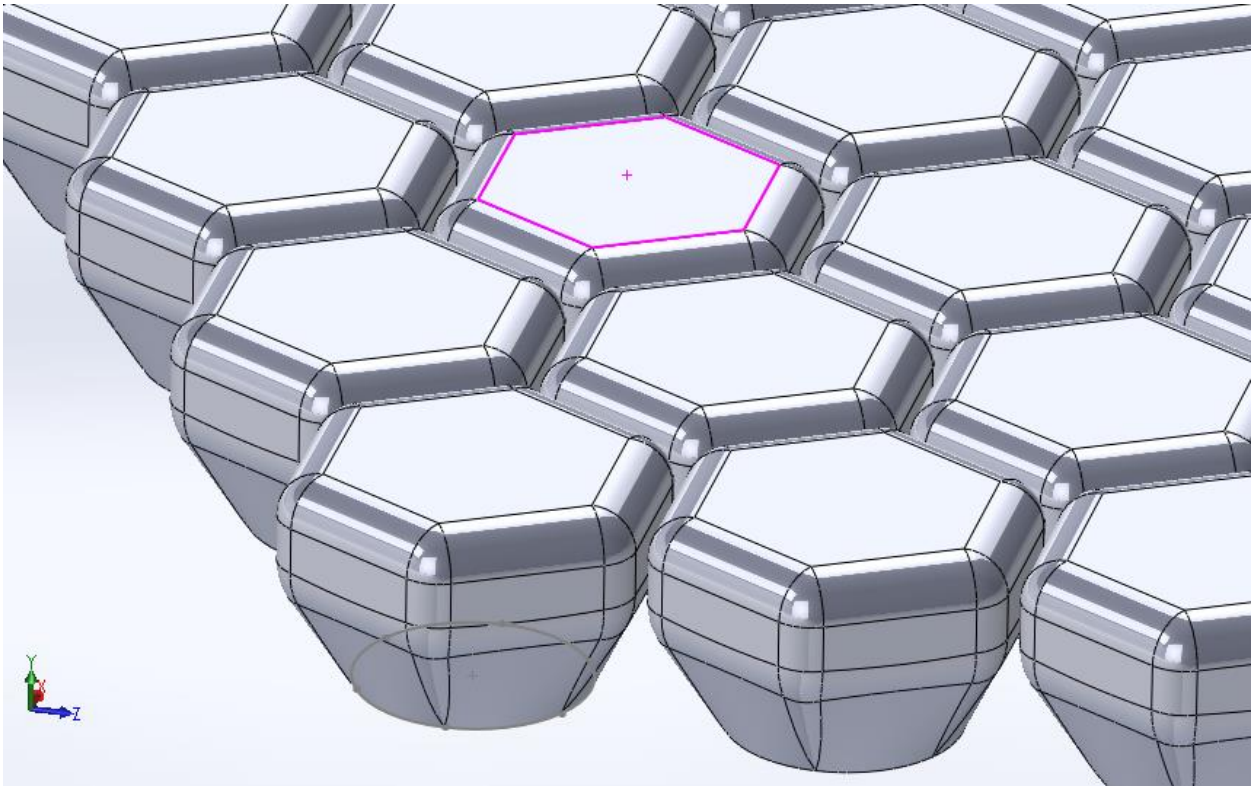

Figure 199: Potential hexagonal array to investigate the effects of teeth aligned with respect to triaxial weaves. Note that the gap distance and inscribing circles for the top cross-sections are the same as those of the rectangular array.

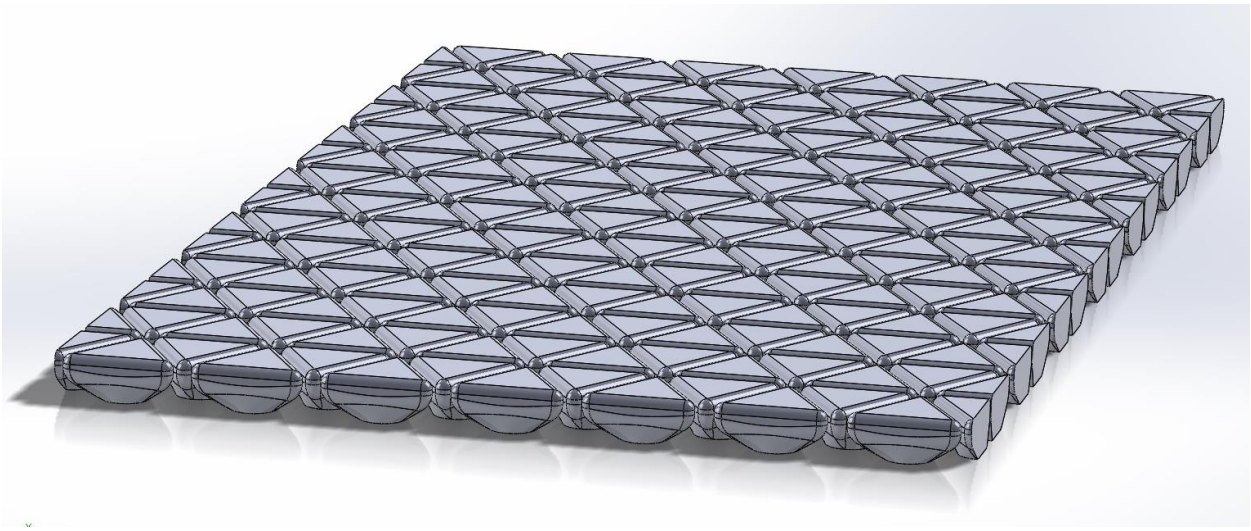

Figure 200: Triangular tooth array CAD geometry.

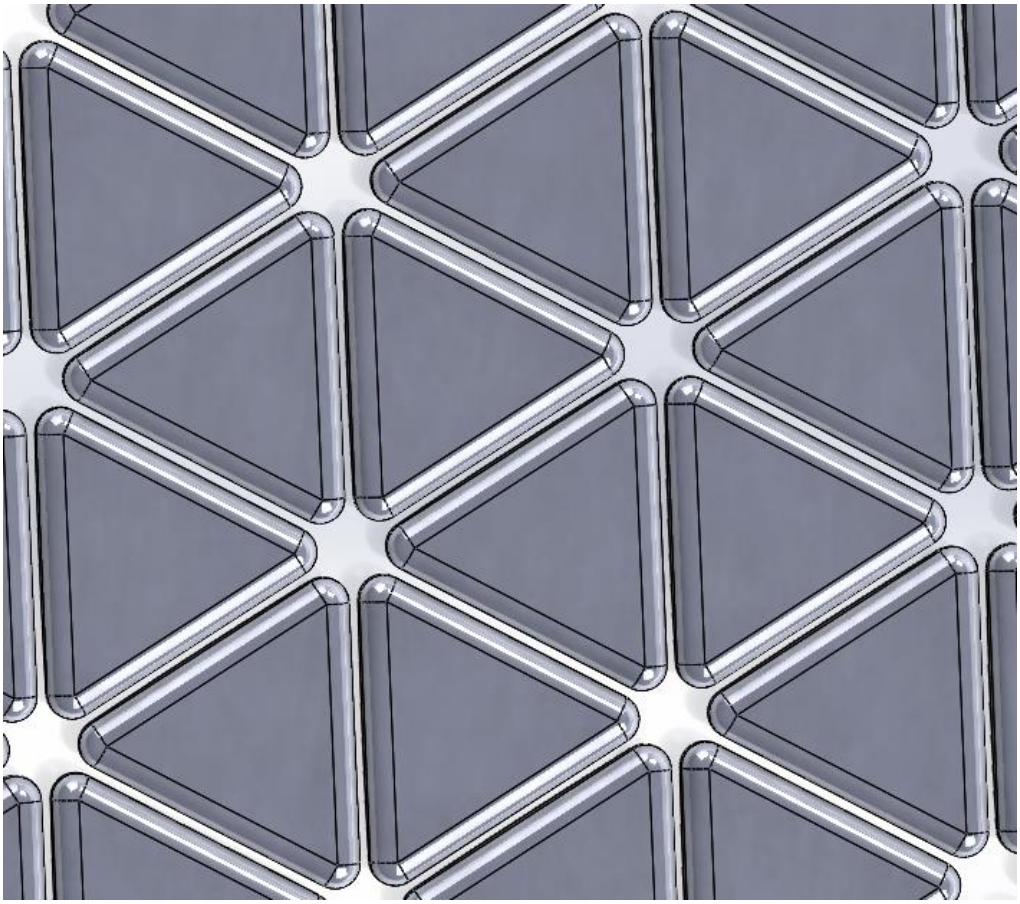

Figure 201: Top view of triangular tooth array CAD geometry.

Gross Behavior of Arrays and Behavior of Individual Teeth.

Several discrete gross deformation modes of initially-planar arrays are considered below. Perhaps the most important mode is when the array bends about an axis that both lies in the plane of the fabric and is parallel to a contact normal direction between teeth (for instance, in hexagonal arrays, angles at integer multiples of 60° fit this criterion, in square arrays, angles at integer multiples of 90°). Here, the array should assume the nearly-constant curvature that has generally been the object of study thus far. For instance, Figure 202 shows a hexagonal array, bent just until lockup along an axis parallel to one set of tooth contact normals.

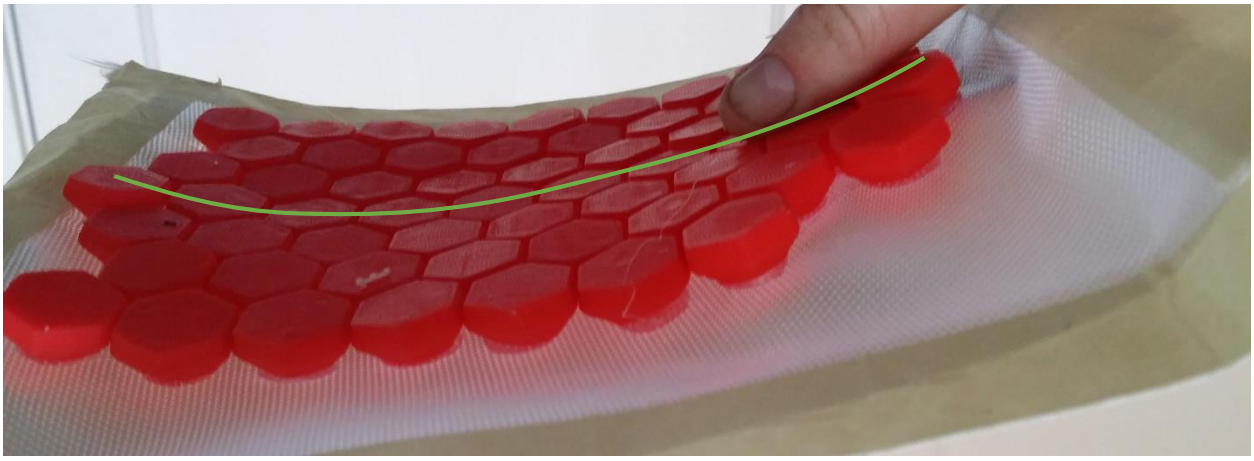

Figure 202: Basic hexagonal array, bent just until tooth contact. Given pure bending, the resulting backbone curvature should be nearly constant (traced in green above), producing a roughly cylindrical shape.

Once this constant curvature has been achieved from tooth contacts, however, teeth often begin to slide in a direction parallel to the normal of the fabric at the tooth's base's centroid. This is quite undesirable as many teeth come to contact each other at a low average distance from the fabric, and it is also rather unpredictable (it depends on how the local loads between teeth will produce static frictional loads). Figure 203 shows the hexagonal array used in the previous figure, subjected to further force that quickly results in vertical tooth sliding.

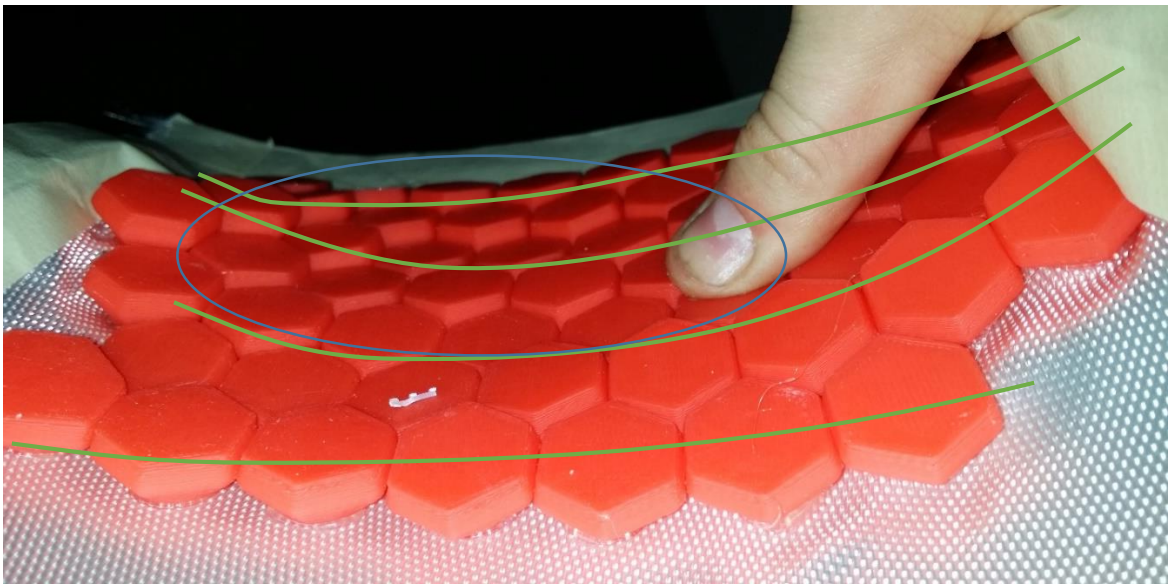

Figure 203: Further bending of the same array shown in the previous picture unfortunately results in vertical tooth sliding (strongest in the region circled in blue). This reduces post-lockup stiffness, and it produces uneven curvature; note that the same amount of bending force produces higher curvature at areas where tooth sliding is most significant (curvature along several areas of the array is traced in green).

To prevent this sliding, one might either coat the teeth with a substance that will increase the coefficient of static friction, or one might devise a geometry with concave features that could prevent this sliding by producing a contact in the direction of the normal of the fabric (i.e. "downward" from the point of view of the top of the tooth). The least-desirable tooth geometry from the standpoint of preventing vertical sliding would consist of teeth with sharp corners and angles with normals that point downwards; a sketch of such undesirable geometry is shown in Figure 204, and the subsequent tooth-sliding tendency is sketched in Figure 205 (with the fabric buckling that often results from this sliding also shown).

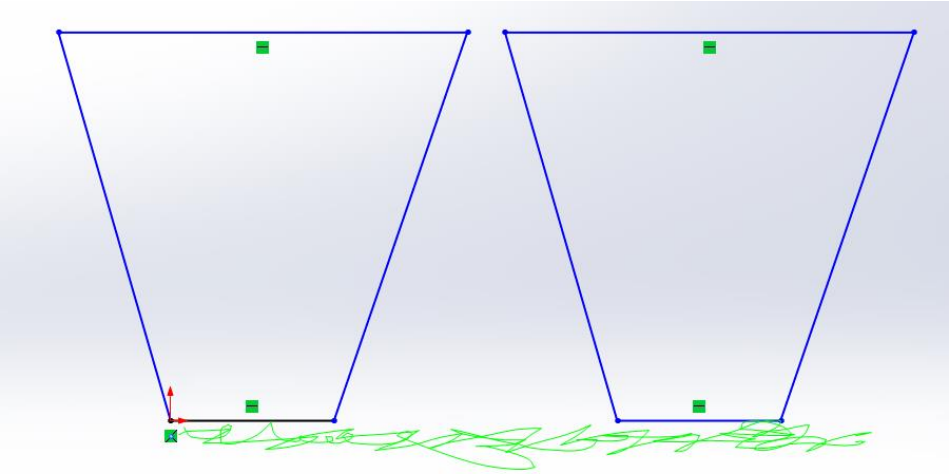

Figure 204: The above tooth geometry is likely to see significant vertical sliding between teeth when the overall structure is bent.

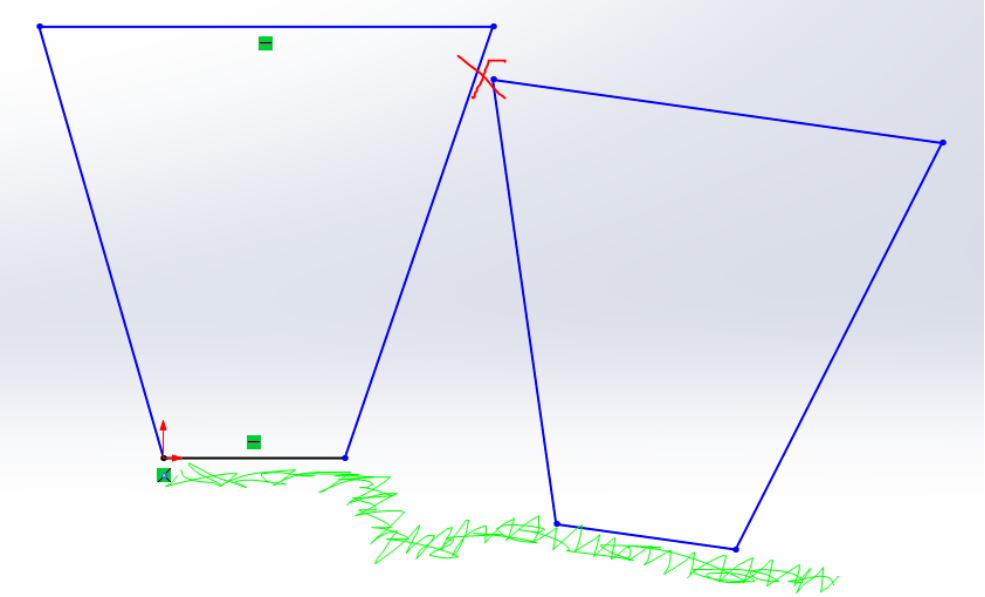

Figure 205: Bending of an array with teeth with sharp corners and edge normals facing downwards often causes the point of tooth contact (shown with the red x*) to move closer to the fabric, reducing the stiffening-up effect; the fabric often experiences buckling as well.*

If the teeth are purely convex in geometry, then bending about an axis in the *xy* plane but not perpendicular to any contact normal direction (i.e. at an angle other than a multiple of 60° for hexagonal arrays or other than 90° for rectangular arrays) results in different behavior, both

because the array assumes a saddle-shaped curvature, and because the array usually has moderately more freedom before it locks up. Both of these properties are due only in part to significant filleting at the corners of teeth (which leaves more clearance between teeth when the fabric bends parallel to normals between these fillets). It is also the result of teeth sliding along their edges. The property occurs even in arrays with non-woven backbones, so it does not rely on bias compliance. For instance, Figure 206 shows a square array of teeth on a non-woven nylon backbone being bent along an axis not parallel to the contact normals of its teeth, producing clear sliding. As shown in the comparison of Figure 207, the lockup curvature is much higher for bending about this direction than for bending at a 0° or 90° angle. It is expected that a tooth array wherein teeth had features to prevent this sliding would see roughly the same curvature at lockup during bending along axes not parallel to contact normal directions between teeth.

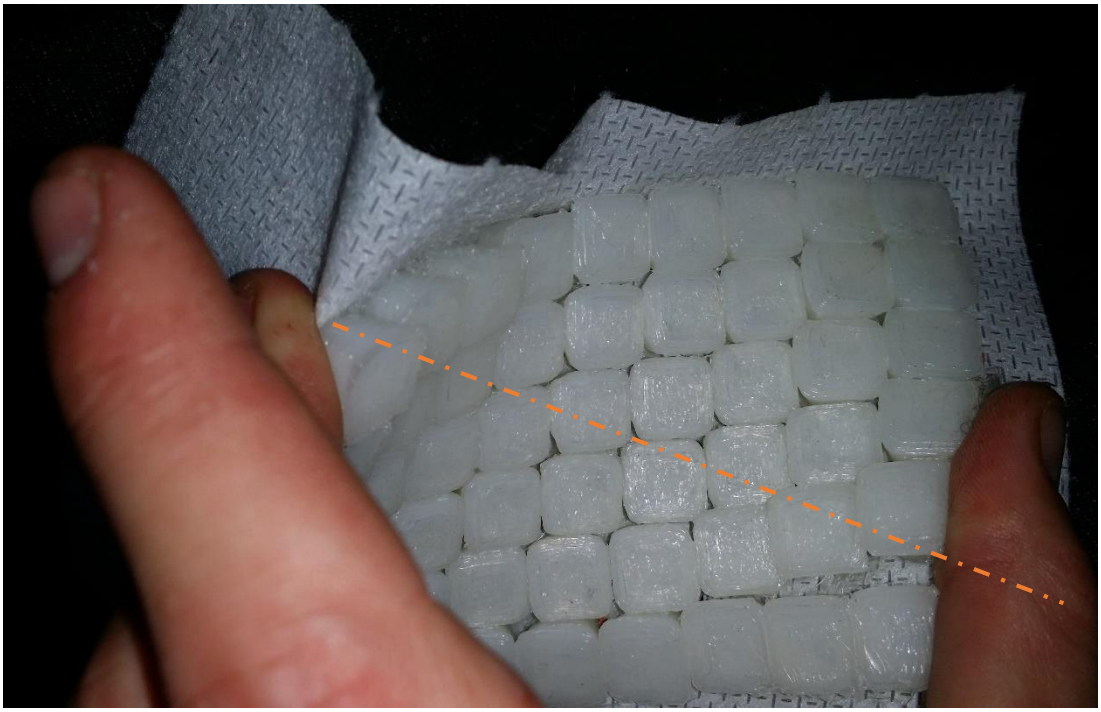

Figure 206: When a square array is bent along an axis not parallel to the contact normals between teeth (i.e. at an angle that is not an integer multiple of 90° for a square array), its teeth see sliding past each other, and much more curvature can be achieved before lockup than could be achieved when the array is bent along an angle that is a multiple of 90°.

Figure 207: Bending the square array about an angle that is an integer multiple of 90° (left) produces less curvature than bending about a different angle (right).

The in-plane shear behavior of fabrics is often as much a function of the amount of bias compliance possessed by the underlying fabric as of tooth-clearance effects. Arrays based on fabrics with square weaves can often shear freely (i.e. without their teeth touching) until the weave no longer permits it (i.e. due to gaps between yarns being closed up), as shown in Figure 208.

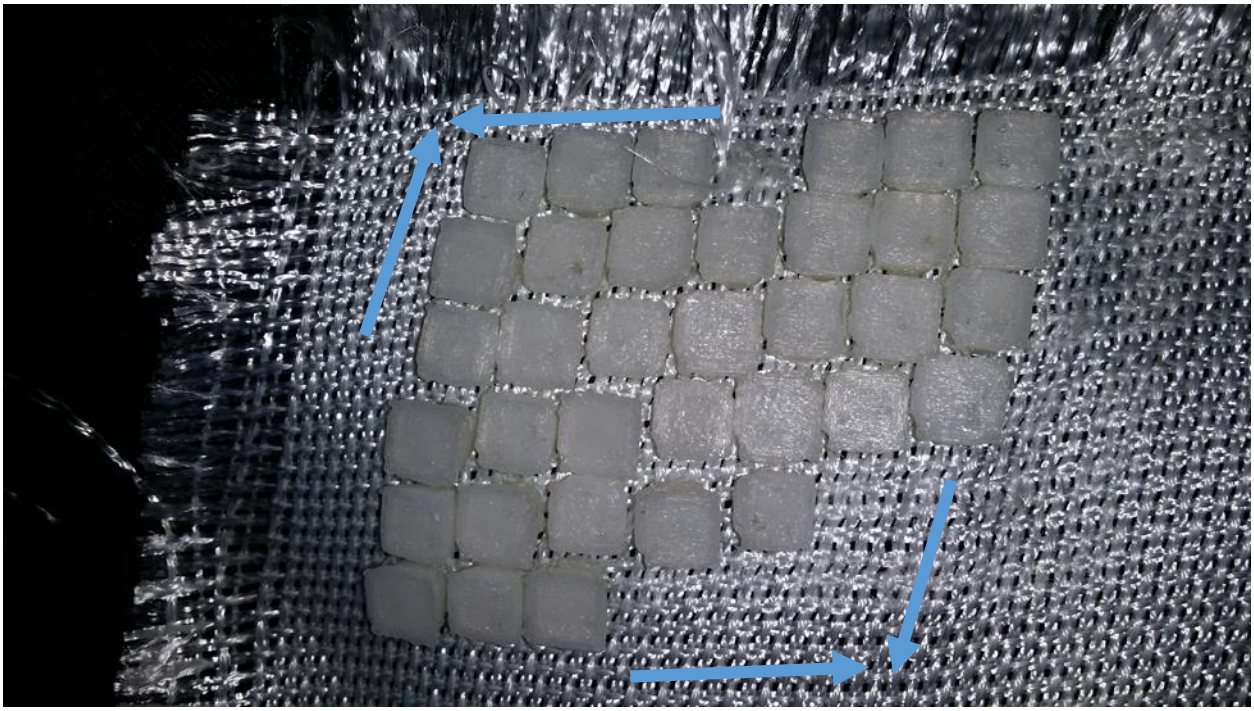

Figure 208: Simple in-plane shear of a square array. This array did not lock up in shear from tooth contacts, but rather from the radial stiffness of the individual yarns in the weave when the rhomboidal gaps between yarns closed up from shear. The mode of shearing is illustrated with blue arrows.

As discussed earlier, square weaves have local Poisson's ratios along the bias well in excess of 0.5. Thus, pulling in this direction has special effects on tooth arrays: it not only causes them to shear, but it also contracts the underlying fabric inward in a roughly-perpendicular direction. Sufficient contraction can actually bring teeth into contact with each other, as shown in Figure 209.

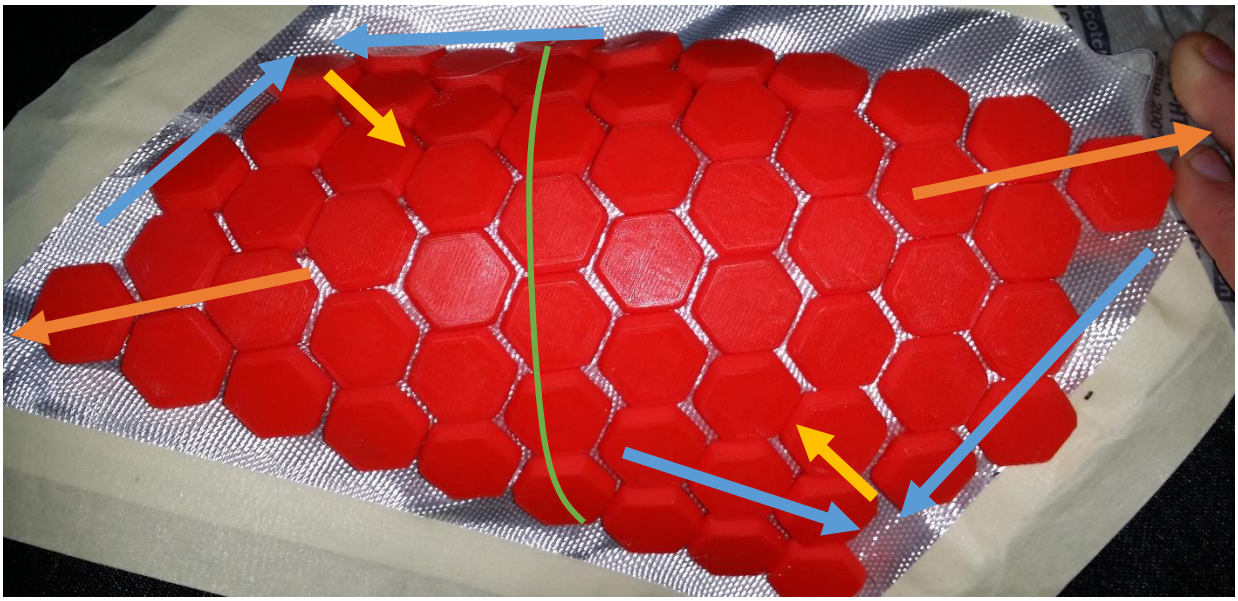

Figure 209: Pulling on an array based on a fabric with high bias compliance in the bias direction (shown with orange arrows) not only produces the expected in-plane shear (shown with blue arrows) but also results in strong inward contraction from Poisson effects (especially strong since the effective localized Poisson's ratio of a plain-weave fabric is well in excess of 0.5) shown with the yellow arrows. In turn, this brings teeth into contact along some faces, producing the roughly-uniaxial curvature that is highlighted with the green curve.

Bending about the axis normal to the fabric was a very stiff mode since it put much of the backbone into tension (in which it is quite stiff).

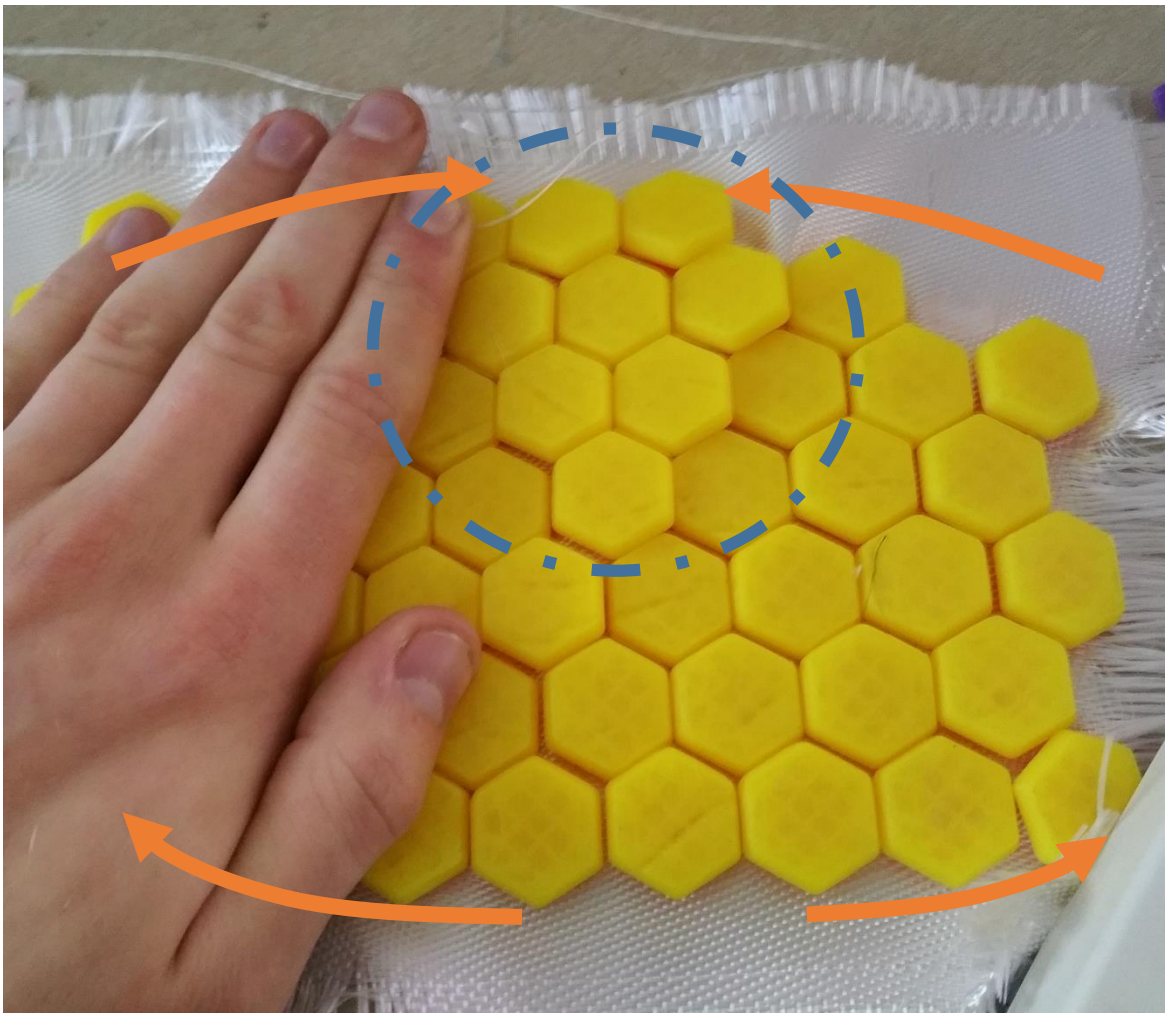

Figure 210: Bending of the fabric about the z axis (perpendicular to the fabric; the neutral axis of bending is in-plane), with areas of compression and tension exaggerated with orange arrows. Note that the areas of tooth compression often see the teeth slide past each other; hence, a triangle-shaped group of teeth has risen above others (circled).

So far, all of the arrays that stiffen up appreciably in gross bending have been made of fabrics with such high tensile stiffnesses that the arrays see little visible strain in uniaxial or biaxial tension. However, the behavior of an array in uniaxial or biaxial compression is quite complicated and usually results in buckling, which is thought to be crucial to producing an array that can conform to a complicated manifold and give it initial freedom of movement. However, this buckling can exacerbate tooth sliding problems absent features to constrain the teeth.

Adding Concave Features to Teeth.

In order to reduce tooth sliding in both in-plane and normal-to-plane directions, it was theorized that it would be necessary to create matching convex and concave features in teeth that would constrain sliding after an initial offset was overcome. To test this hypothesis, several types of teeth with convex features were studied. First, the square array (with an upward flare added to permit proper rolling contact) was modified to have a right-triangular cutout and protrusion; this shape tessellates, so a constant gap distance (in this case, 0.018", neglecting the effects of fillets) could be produced. Figure 211 shows a single tooth of this array, and Figure 212 shows CAD geometry of an entire undeformed array.

Convex-Concave Square Array.

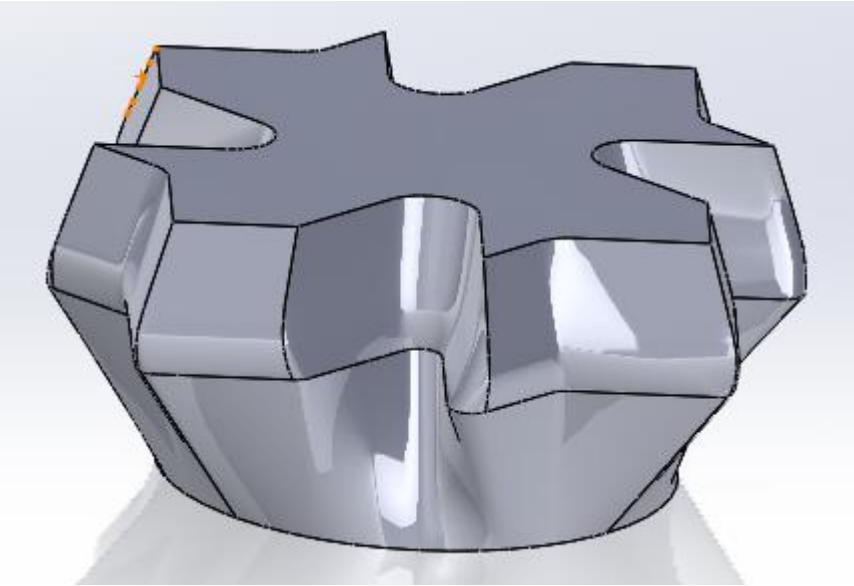

Figure 211: An alteration of a square tooth with convex and concave features.

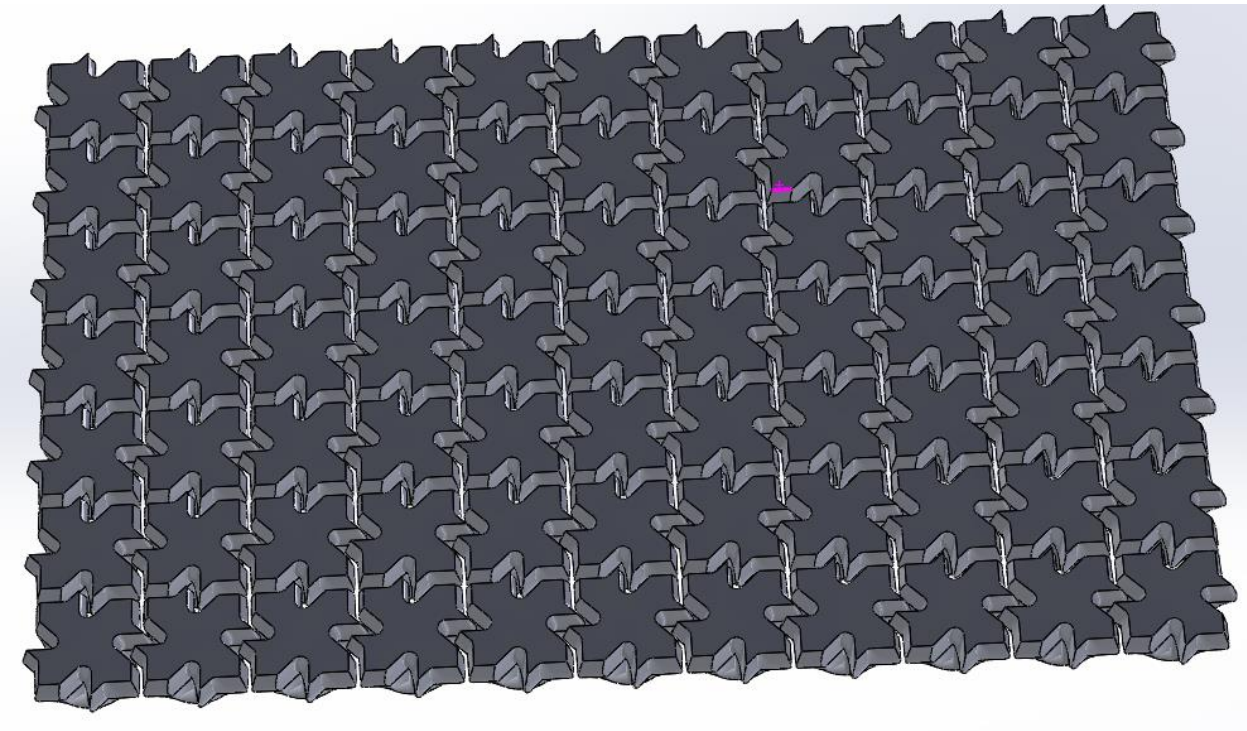

Figure 212: Full array of convex-concave square-like teeth.

While it was expected that the array's only remarkable properties would be in in-plane shear, the first thing that was observed was that it was strangely resistant to vertical sliding in ways that arrays with similar initial gaps and loft angles were not. It may be that, as an unintended consequence of the loft from a circular base up to the complex central cross-section, there are some regions with contact normal pointing in the positive *z* direction. Figure 213 shows the array in bending lockup.

Figure 214 shows the array locked up in one direction of in-plane shear (called "positive" for simplicity). Of the two directions, it is not surprising that the "positive" direction (which sees contact between the flat faces of the protrusions, whose normals are roughly parallel to the direction of tooth movement from shear) locks up effectively. However, in the opposite direction (as depicted in Figure 215) there is more shear freedom until lockup, and there is also a

clear tendency toward teeth camming each other apart thanks to the wedge angle created by the contacts (circled in the figure), producing less-stiff lockup.

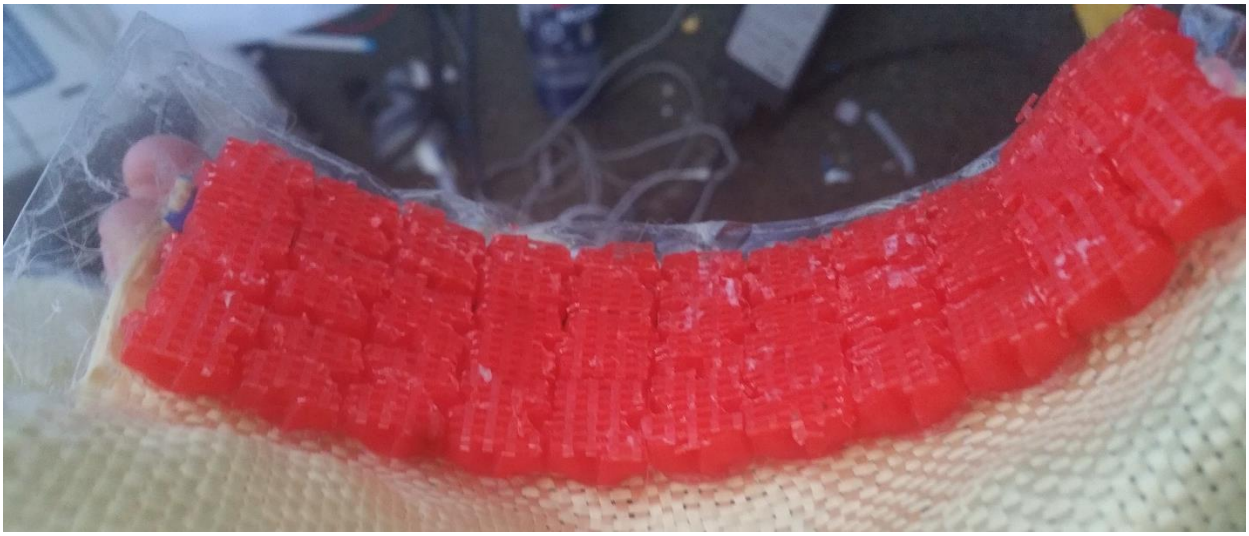

Figure 213: Array of convex-concave square-like teeth locked up in bending.

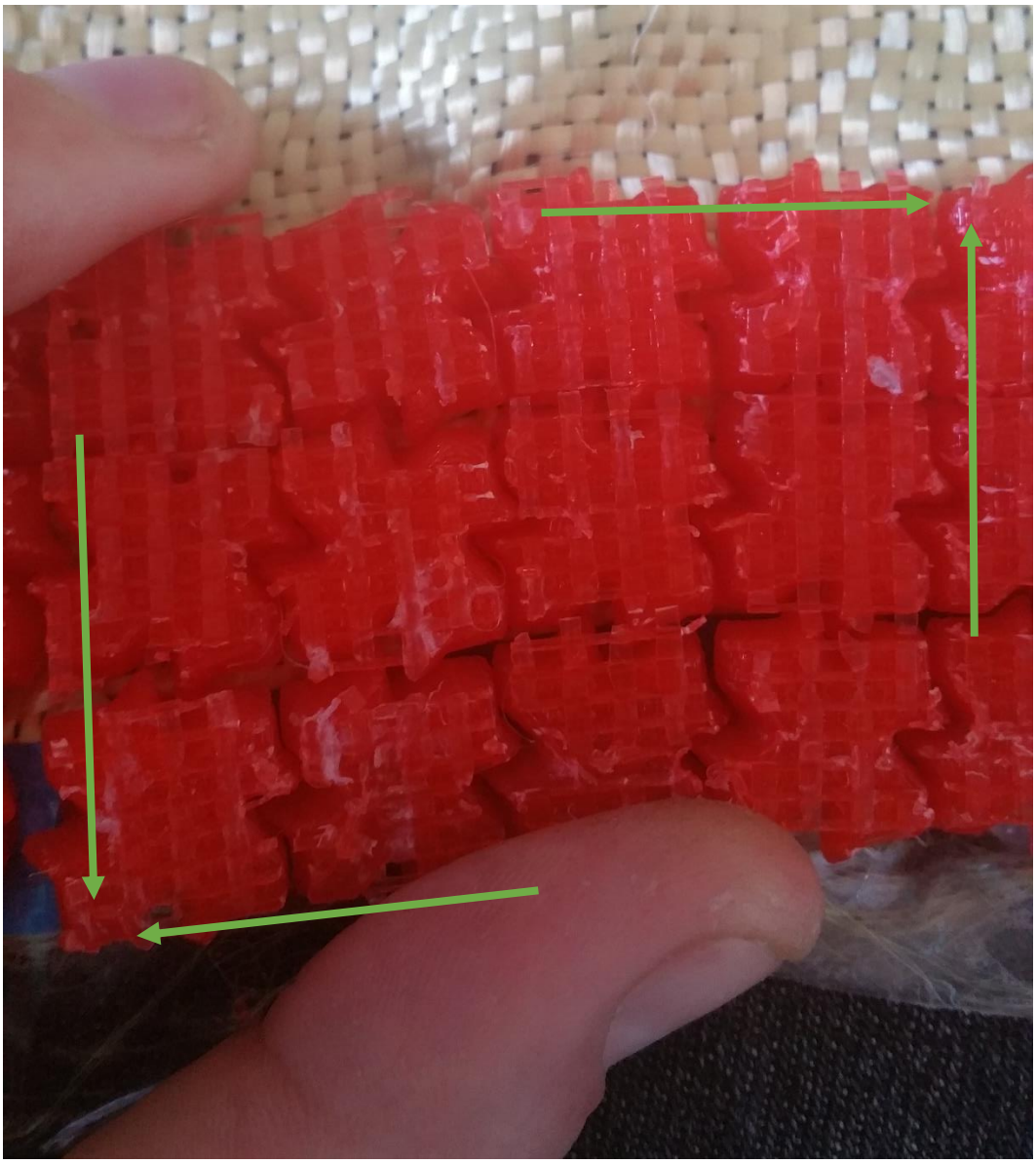

Figure 214: Array of convex-concave square-like teeth, effectively locked up after a relatively small amount of positive in-plane shear (shown with green arrows).

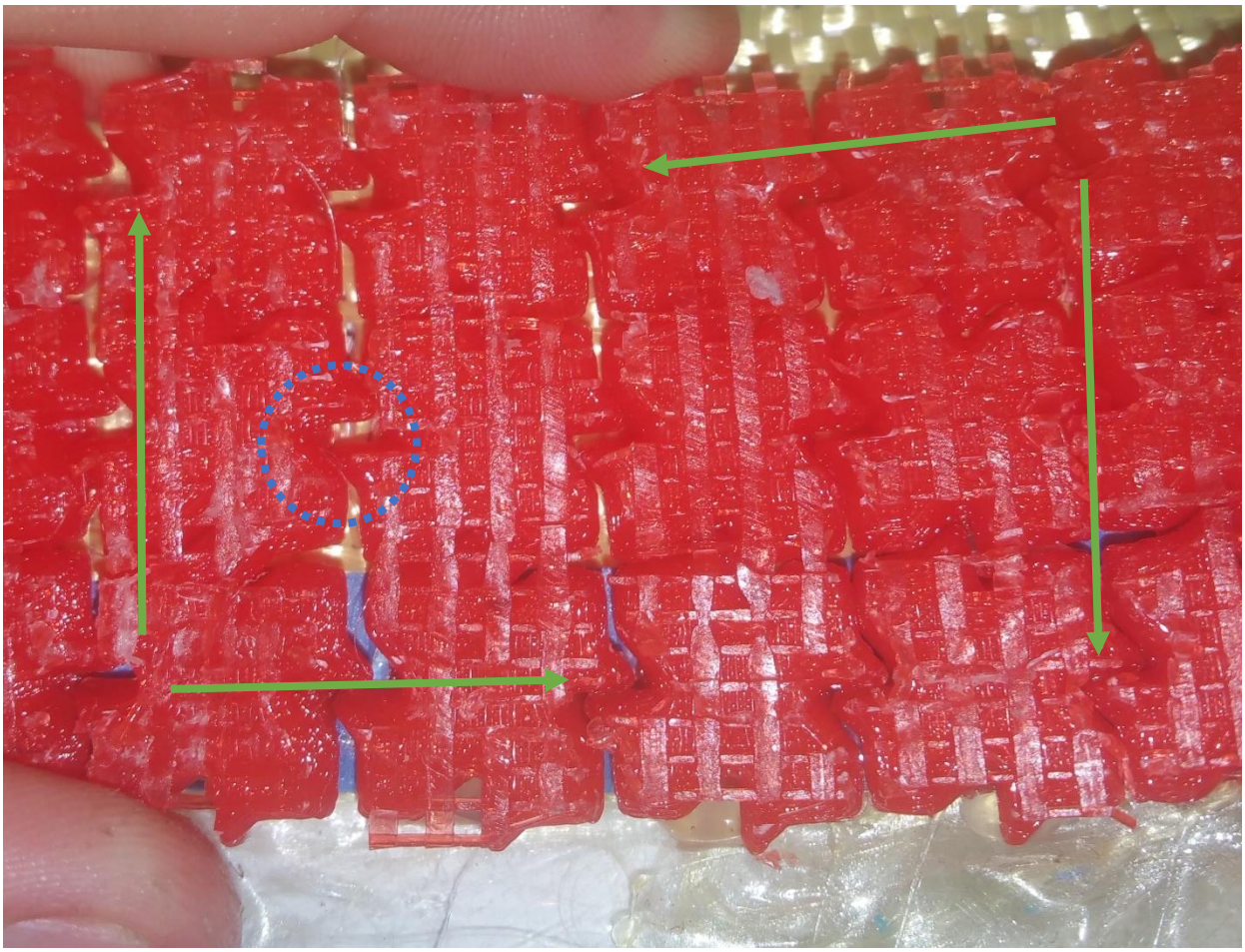

Figure 215: Array of convex-concave square-like teeth locked up in negative in-plane shear (i.e. the opposite direction from that shown in Figure 214), with direction of shear shown with green arrows. Note that the protrusions on the teeth tend to slide somewhat off of each other before finally locking up (less strongly than in the opposite direction); one especially clear view of this sliding is circled in blue.

Additionally, the protrusions and gaps acted to catch teeth that rotated away significantly from surrounding teeth, as might occur when the array tries to conform to a complicated surface manifold. Note that this is probably undesirable, because it makes it difficult for the array to return to its original shape and risks shearing teeth completely off the backbone; the wedges require the teeth to move further apart before they can get closer (which is their natural conformation). Figure 216shows an example of this behavior.

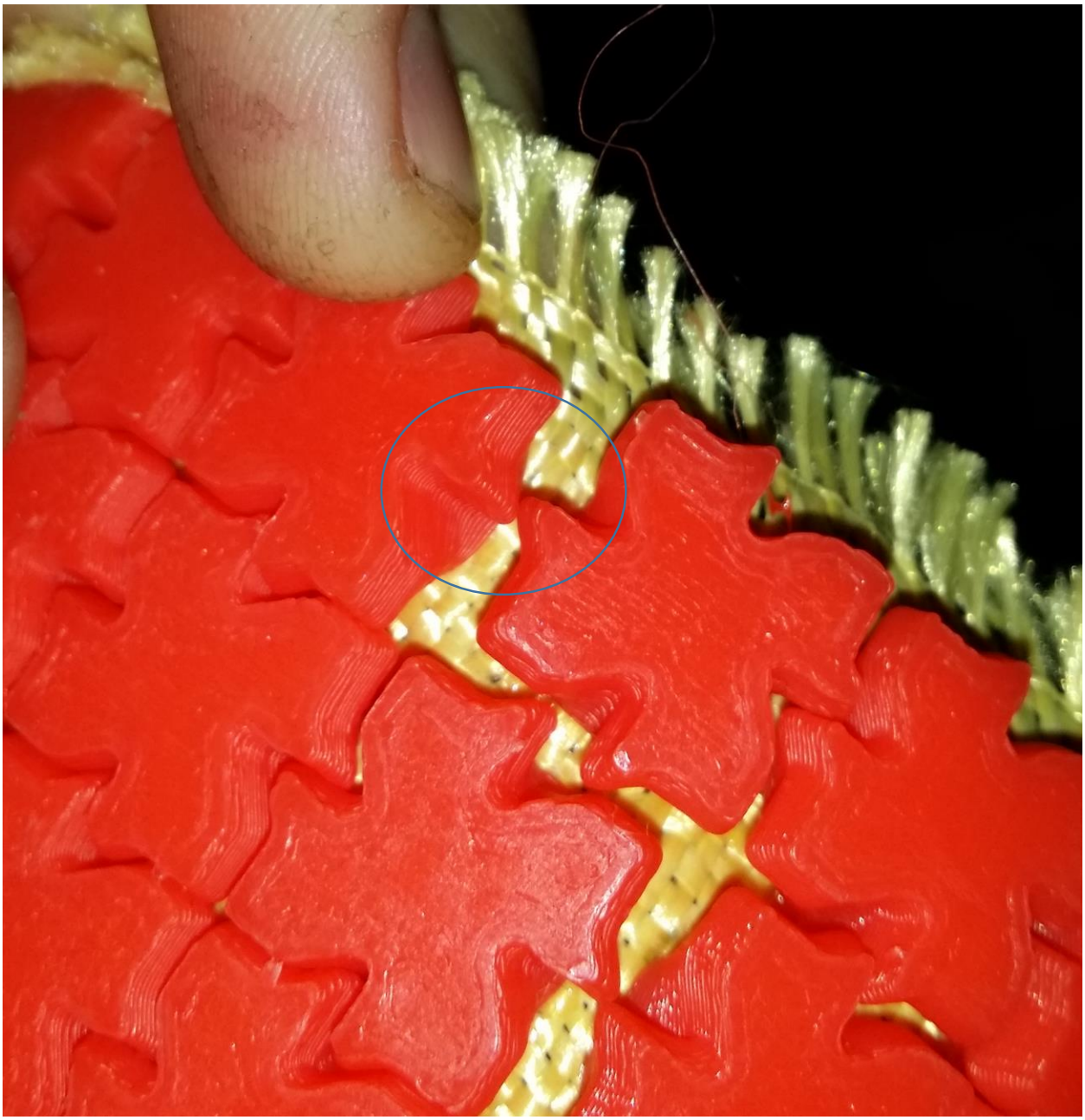

Figure 216: Tooth protrusions catching on each other as the array returns to standard shape after significant local shearing or bending (circled).

Teeth Based on Mercier's "Paradoxical Gear".

Finally, another way to handle tooth sliding (especially lateral sliding) is to try to take advantage of it by adding gearing-like cams on the teeth. In particular, there exists a sort of

"gear", the "paradoxical gear" of Mercier, that meshes in such a way that it rotates in the same direction as those gears with which it is meshing[53]. Although out-of-plane rotation is not a common known tooth deformation mode, even a perfect tooth-fabric bond would not prevent it, because the fabric not bonded to the tooth could bunch up to accommodate tooth rotation. Thus, a tooth array was created using a Mercier profile. Figure 217 shows a closeup of such a tooth, and Figure 218 shows CAD of the whole array in a "rectangular" pattern.

[53] http://www.jacquesmaurel.com/files/Explanations%20about%20the%20paradoxical%20gears.doc

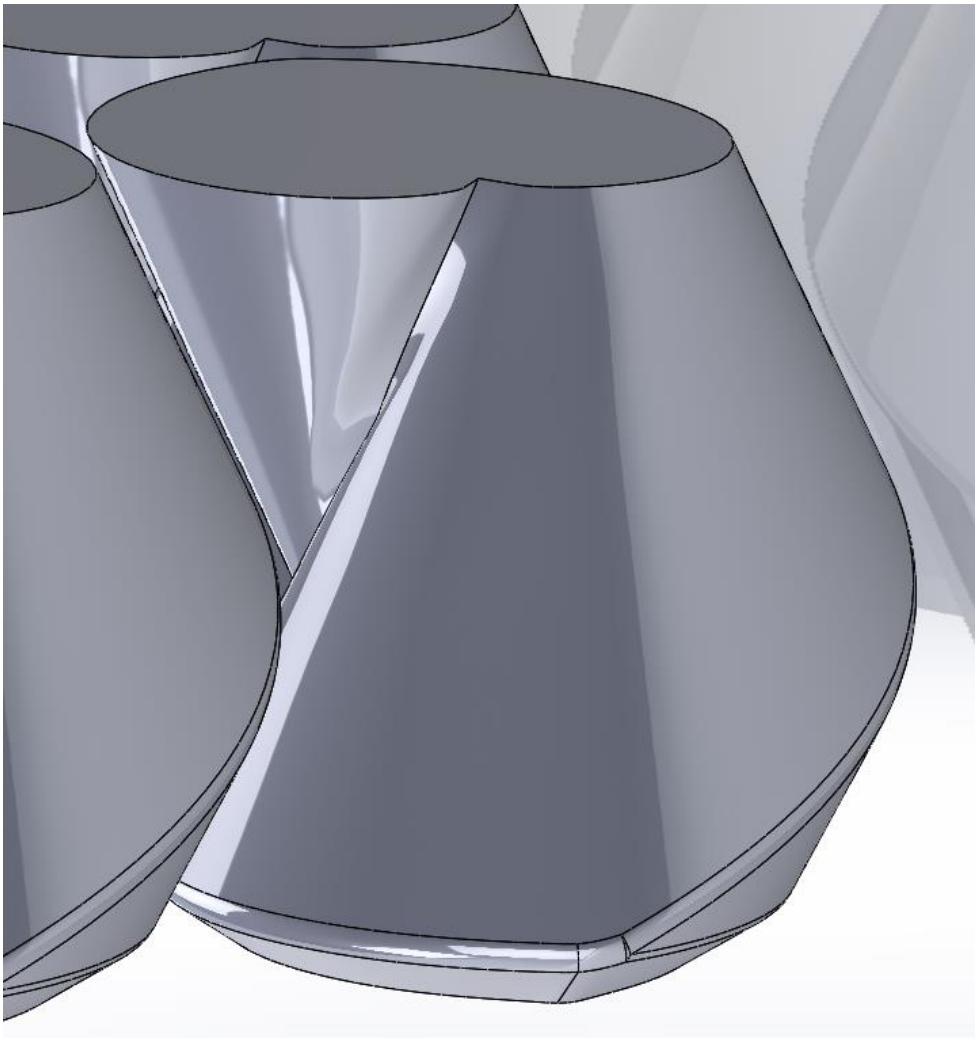

Figure 217: Single tooth based on the Mercier paradoxical gear (formed by sweep-rotating an involute of a circle). The teeth have an offset from each other of approximately 0.018", and should cam off each other to rotate in the same direction.

Figure 218: Array of teeth based on the Mercier paradoxical gear.

In retrospect, it seems laughable to attempt to use tooth rotation normal to the fabric—this is the stiffest of the rotational modes, and true paradoxical gears are usually generated from more than 180° of sweep rotation to ensure continuous positive camming, anyways (to reliably print this geometry without support material would then require either steep overhangs or very long teeth). However, the tooth array nonetheless had two interesting properties. First, the teeth were much less vulnerable to vertical sliding than teeth that lack the concave offset of these teeth; in essence, the cusp of the involute curve that was swept-rotated became like a gear tooth to engage other teeth and inhibit vertical sliding. Also, the array had noticeably higher curvature when bent 45° to the rectangular array than when bent at 0°. In contrast, the first rectangular array with added concavity had higher curvature when bent along the 0° axis than along the 45° axis. It is not immediately clear which curvature variation with angle (if either) would be preferable.

The Mercier tooth design was also modified to improve its planar behavior after the first 3D printing: first, the involute profile was given a full rotation (instead of half a rotation as in the first printing) when it was discovered that the printer could handle the attendant overhang without needing support material; the resulting geometry was expected to better resist tooth sliding thanks to each tooth now having one concave region and one convex region of contact with each of its neighbors in a square array. Also, the bottom of the tooth (once glued to the fabric, that is—not in the original print orientation) was tapered somewhat to reduce base contact area with the fabric. It is known that reduced base contact area gives more initial freedom (in gross bending and compression), and contact should not begin at the base because that will produce a lower stiffening-up ratio. The new tooth geometry is shown in Figure 219.

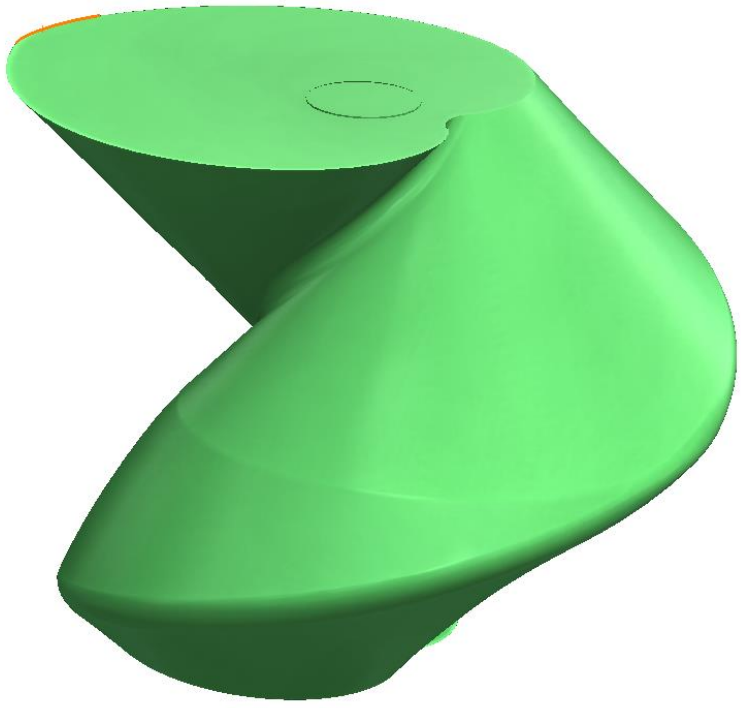

Figure 219: New Mercier-based tooth design, featuring the same height as the first tooth but double the revolution angle and a small taper near the base.

Basic interference analysis showed that the tooth could be packed in a regular hexagonal packing instead of the rectangular packing used in the first iteration of the array; Figure 220 shows a computer rendering of a hexagonal array with each tooth rendered transparent in order to highlight the roughly circular projected shape of each tooth. Note that what appears to be overlap between teeth is not overlapping but overhanging thanks to the spiral shape of the tooth (which ultimately is probably a good property since it should inhibit vertical sliding between teeth). Both packings were produced with the updated tooth design to see which had better properties.

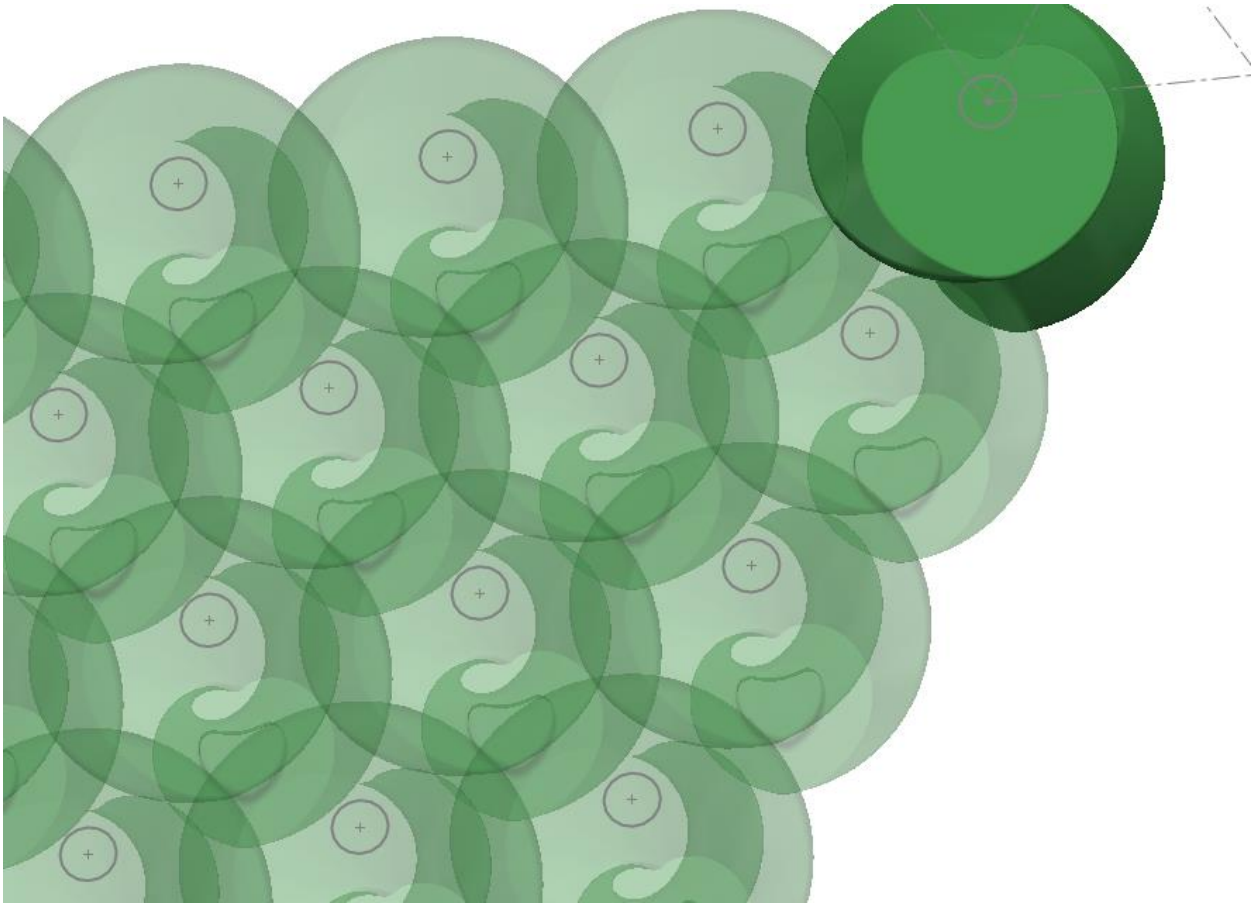

Figure 220: Hexagonal-close-packed arrangement of the Mercier-based tooth. Note how much larger the projected footprint of each tooth is versus its instantaneous cross-section.

Hexagonal-Close-Packed Paradoxical-Gear Teeth Arrays.

Although the initial clearance of 0.012” between teeth was far too small for any perceptible freedom before lockup (at least in the constrained direction), when the array was reprinted with a 0.026in clearance between every contact set, it had excellent lockup behavior, able to attain a moderate degree of curvature before locking up rapidly in single-axis bending. Figure 221 shows a picture of the array with 0.012” clearances bent until lockup.

Beyond this, the hexagonally-packed arrays with both 0.012” and 0.026” clearances had an unusual property: when subjected to a uniaxial compression load along one axis, they reoriented to have constant curvature perpendicular to this axis, in effect turning into semicylinders. The first version of the Mercier array did not have this property, probably because its base area was too great to allow much compressive freedom. Further compression tightened the cylindrical curvature of the array as well as shortening the cylinder somewhat. While this seems like a promising development since the shape of the manifold surrounding the joint to be protected is cylindrical, not planar or box-like, it should be noted that once compressed into a semi-cylinder, the array has little radial freedom (since the compression enforces tooth contacts). However, it might be possible to design an array with extra clearances in the direction that would become the vertical contact direction since the backbone is buckled after the structure is reoriented into the cylinder (as shown in Figure 224) and should thus be able to expand in tension freely, up to a point. Figure 222, Figure 223, Figure 224, and Figure 226 show different views of the two arrays with this sympathetic cylindrical deformation activated.

Figure 221: Lockup curvature in pure bending for paradoxical-gear-based array with .012" clearances (very small due to the small initial clearances).

Figure 222: Sympathetic cylindrical deformation of paradoxical-gear-based array with .012" clearances in compression along the axis shown in green (plus a small amount of bending).

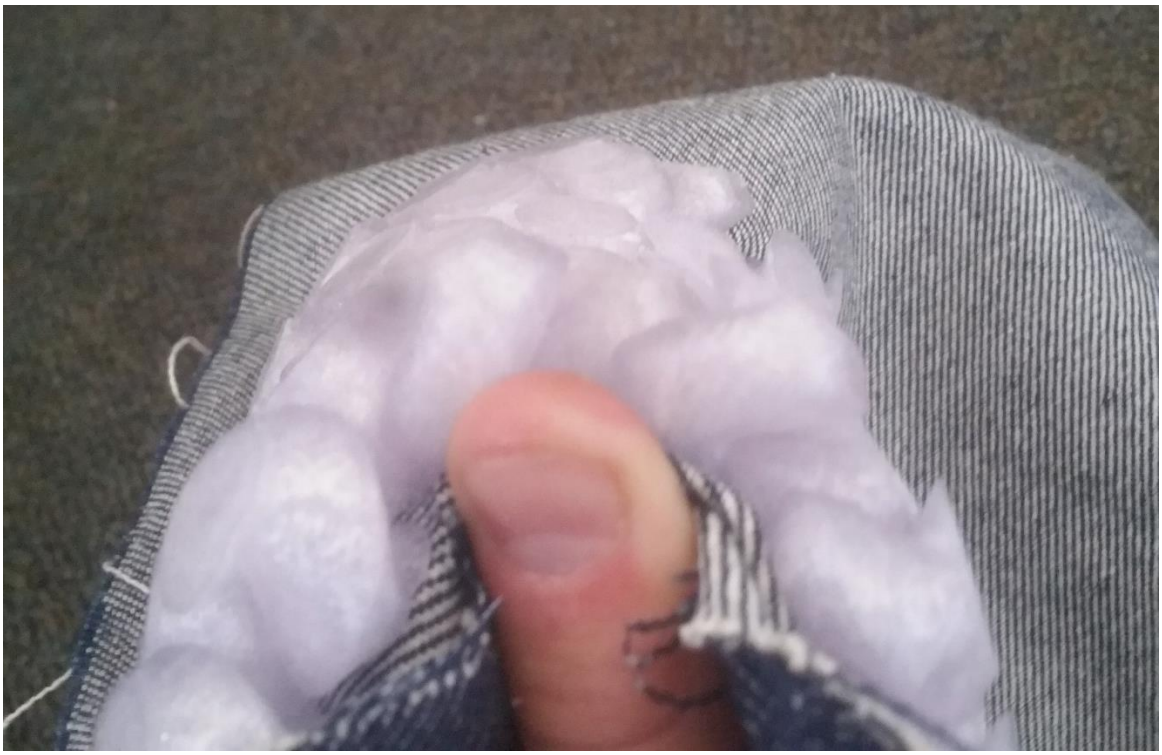

Figure 223: Another view of the paradoxical array with 0.012" initial clearances in compression with accompanying cylindrical sympathetic deformation

Figure 224: Underside view of the paradoxical array with 0.012" initial clearances in compression with accompanying cylindrical sympathetic deformation. Note the microbuckling the fabric experiences when the array is in compression

Figure 225: Lockup curvature in pure bending for paradoxical-gear-based array with .040" clearances (much higher than that seen with the 0.012"-clearance array).

Figure 226: Sympathetic cylindrical deformation of paradoxical-gear-based array with .040" clearances in compression along the axis shown in green (plus a small amount of bending).

Scaling the HCP Paradoxical-Gear Tooth Array.

Uniaxial shrinking and stretching operations were performed on the CAD of the paradoxical-gear-based HCP array, both along an axis perpendicular to the axis along which compression provoked sympathetic cylindrical deformation. The aim of these investigations was to see how sympathetic cylindrical curvature would change with the scaling: it was expected that positive scaling of the array perpendicular to the curvature normals would produce a larger radius of curvature, and that negative scaling would produce a smaller radius of curvature.

Figure 227 shows the negative-scaled array (width reduced by 20%, length constant) in a neutral position with the axis of shrinkage and axis of sympathetic cylindrical curvature indicated, and Figure 228 and Figure 229 show it in compression (producing sympathetic cylindrical curvature). Note that the curvature for this inwards-scaled array is stronger than that for the unscaled HCP paradoxical-gear array, exactly as expected.

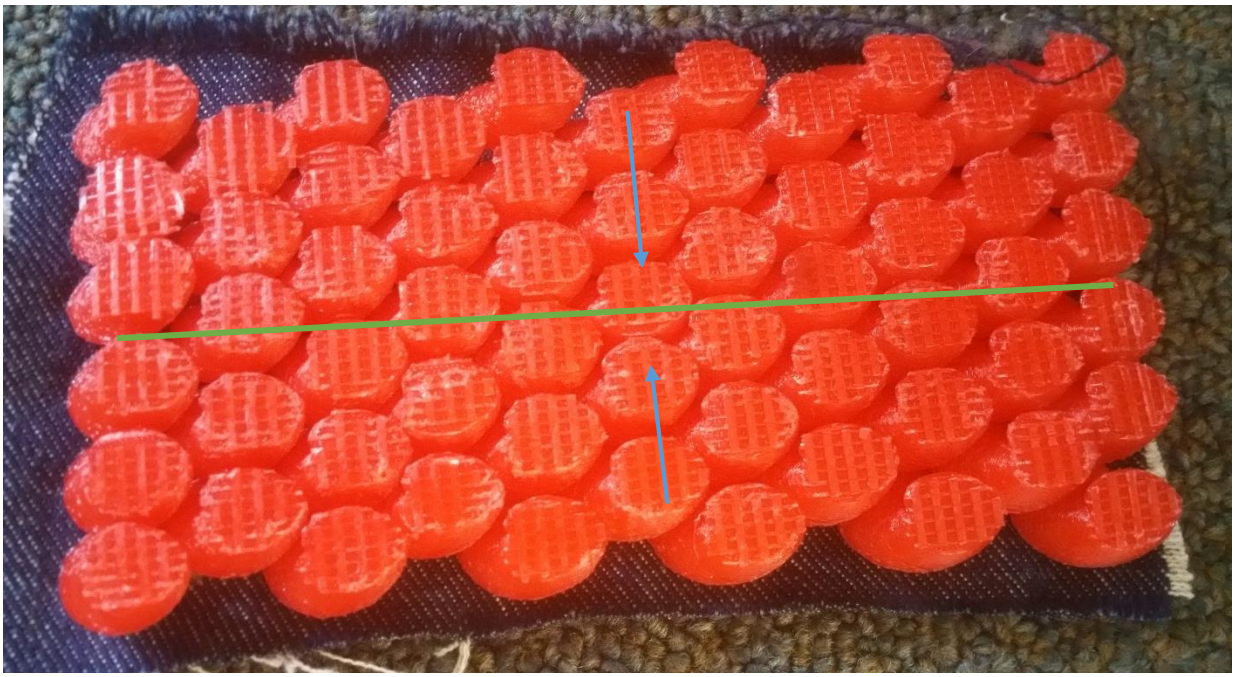

Figure 227: HCP paradoxical-gear tooth array, scaled inwards (along the blue arrows) to 80% of its original width. The axis along which compression results in coupled cylindrical deformation is shown in green.

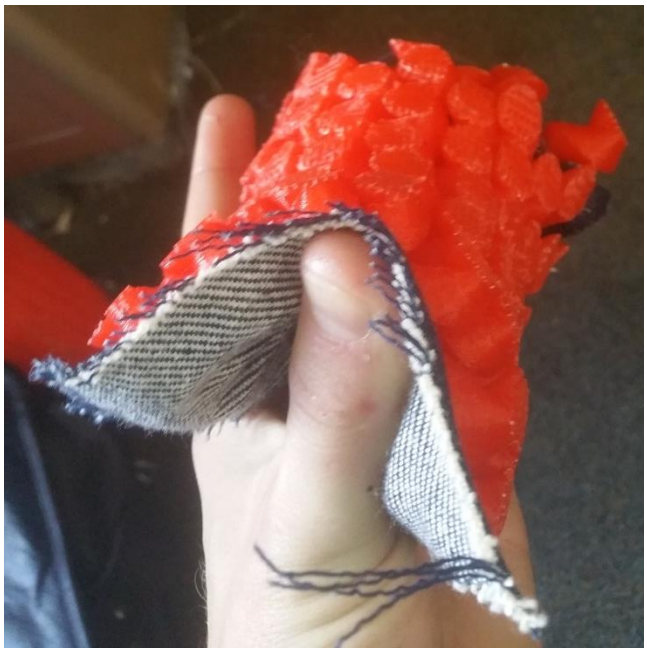

Figure 228: Top view of 80%-width-scaled HCP paradoxical-gear array in compression (with coupled cylindrical deformation). Note that this curvature is stronger than that for the unscaled HCP paradoxical-gear array.

Figure 229: Bottom view of 80%-width-scaled HCP paradoxical-gear array in compression (with coupled cylindrical deformation). Note that this curvature is stronger than that for the unscaled HCP paradoxical-gear array.

Figure 230: Post-lockup bending curvature of the array. Note that its curvature seems somewhat higher than that for the unscaled array (shown in bending in Figure 225), despite having the same nominal tolerances in the direction shown in green in Figure 227. This indicates that initial diagonal clearances between teeth also affect post-lockup position.

Likewise, shows the positive-scaled array (width increased by 25%, length constant) in a neutral position with the axis of shrinkage and axis of sympathetic cylindrical curvature indicated, and Figure 228 and Figure 229 show it in compression (producing sympathetic cylindrical curvature). Note that the curvature for this outwards-scaled array is smaller than that for the unscaled HCP paradoxical-gear array, exactly as expected.

Figure 231: HCP paradoxical-gear tooth array, scaled outwards (along the blue arrows) to 125% of its width. The axis along which compression results in coupled cylindrical deformation is shown in green.

Figure 232: Top view of 125%-width-scaled HCP paradoxical-gear array in compression (with coupled cylindrical deformation). Note that this curvature is smaller than that for the unscaled HCP paradoxical-gear array.

Figure 233: Underside view of 125%-width-scaled HCP paradoxical-gear array in compression along the axis drawn in green (with coupled cylindrical deformation). Note that this curvature is softer than that for the unscaled HCP paradoxical-gear array.

Square-Packed Paradoxical-Gear Array.

While the square packing (shown in neutral position in Figure 234) did not see cylindrical reorientation upon compression along any axis, compressing it along either of its diagonal axes produced a saddle-shaped/anti-clastic double-axis curvature, as shown in Figure 235. If anything, this behavior may be even more useful than the cylindrical deformation of the hexagonally-close-packed arrays. However, this array has very high compliance in bending along these diagonal axes (though excellent stiffness in bending along the square axes of tessellation) until a very high degree of anticlastic deformation has been achieved (at which point it becomes quite stiff); this is despite the very low theoretical clearances (0.012") between teeth along the rectangular axes of tessellation. (The axes are illustrated in Figure 234). It is likely due both to the high bias compliance of the plain weave of the fabric (illustrated in Figure 237) and to the high clearances between teeth on off axes, indicating that the hexagonal close packing is a more natural arrangement for this array. Indeed, the high bias compliance made it possible

to reorient the array in plane into a packing similar to true hexagonal close packing, whereupon compression in a specific direction produced sympathetic deformation that was closer to the cylindrical sympathetic deformation seen in the HCP arrays, as shown in Figure 236. Of note, it took compression along an axis perpendicular to the one required for the HCP arrays to see this quasi-cylindrical sympathetic deformation.

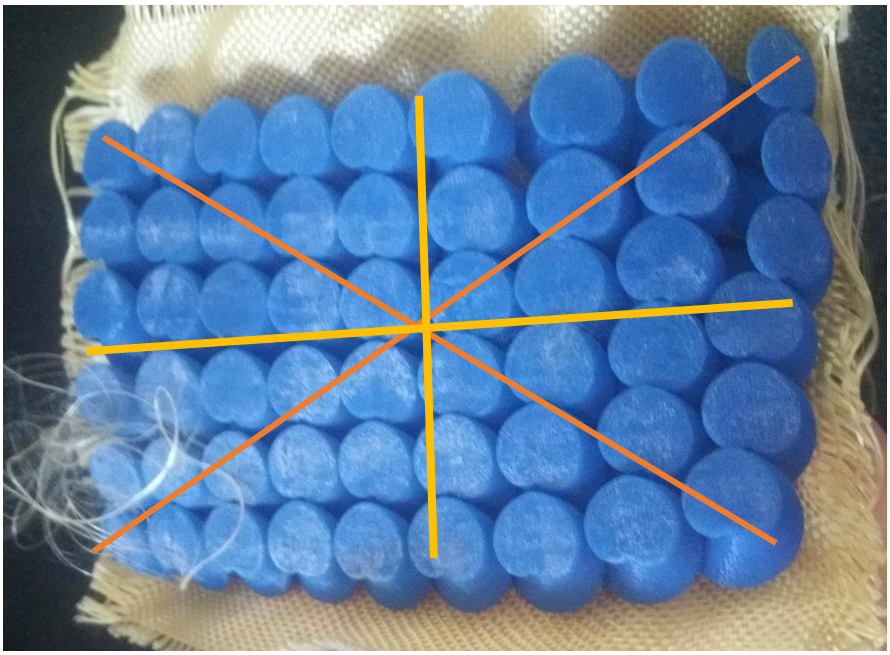

Figure 234: Square packing of paradoxical-gear-inspired teeth, roughly in neutral position. The axes in which the structure is quite stiff in bending are shown in gold color; these are the axes of tessellation. The axes in which it is very compliant in bending until a great deal of anticlastic curvature has been attained are shown in orange.

Figure 235: Compressing the square-packed array along either diagonal produces sympathetic deformation into a saddle shape (anti-clastic curvature).

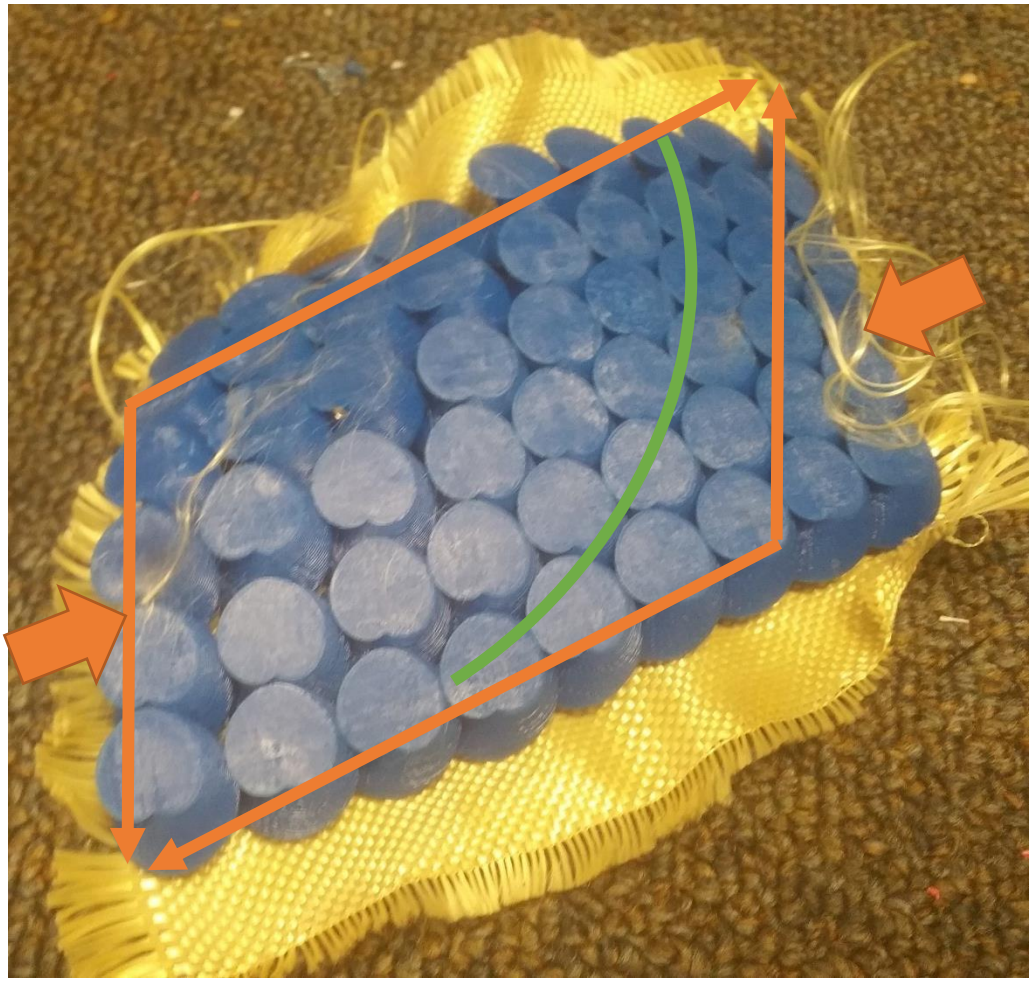

Figure 236: Shearing the array and *compressing it along the edges (as shown with orange arrows) gives the array mostly cylindrical curvature, much less anticlastic than in the previous picture. The resulting curvature is traced in green.*

Figure 237: Thanks to the plain weave of the fabric (which gives it high bias compliance) and the low contact area between tooth bases and fabric, the overall structure is quite compliant in shear, up to the point shown.

Of note, compression along the axis perpendicular to that which produces cylindrical deformation on the HCP arrays was governed by instability due to the non-conforming contacts between teeth. It could produce either anticlastic curvature or chevron-like double-anticlastic curvature; the latter mode is shown in Figure 238 (perhaps longer arrays would allow more than just these two modes).

Figure 238: "Double-chevron" instability mode with compression along the axis shown in green, 2 views.

Hexagonally-Packed Double-Rotated Tooth Array.

Paradoxical gears can consist of many sweep-revolutions of the base involute profile, or just one (although the number of revolutions versus the length of the gear will contribute to its pressure angle). Out of curiosity regarding the effects of multiple rotations on tooth lockup behavior, a paradoxical gear was generated with a total rotation of 540° instead of the 360° investigated above. As above, the base was tapered to increase unbonded fabric area for greater pre-lockup compliance; the geometry for an individual tooth is shown in Figure 239. As can be seen in the rendering of an entire array (shown in Figure 240), any given cross section of an

array in locked-up bending sees each tooth contacting at two distinct points thanks to the double rotation of the tooth geometry.

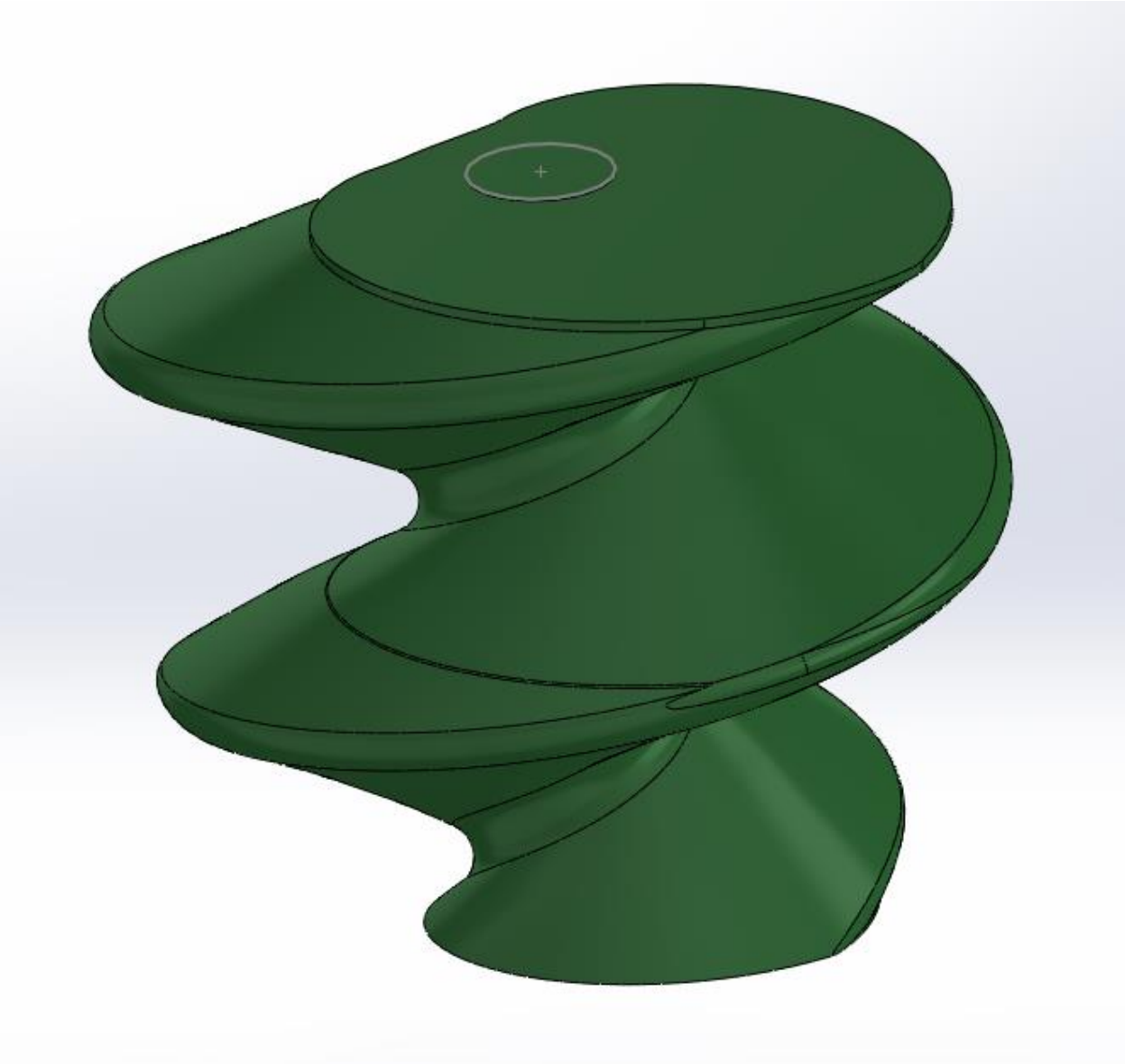

Figure 239: Geometry for double-rotated tooth.

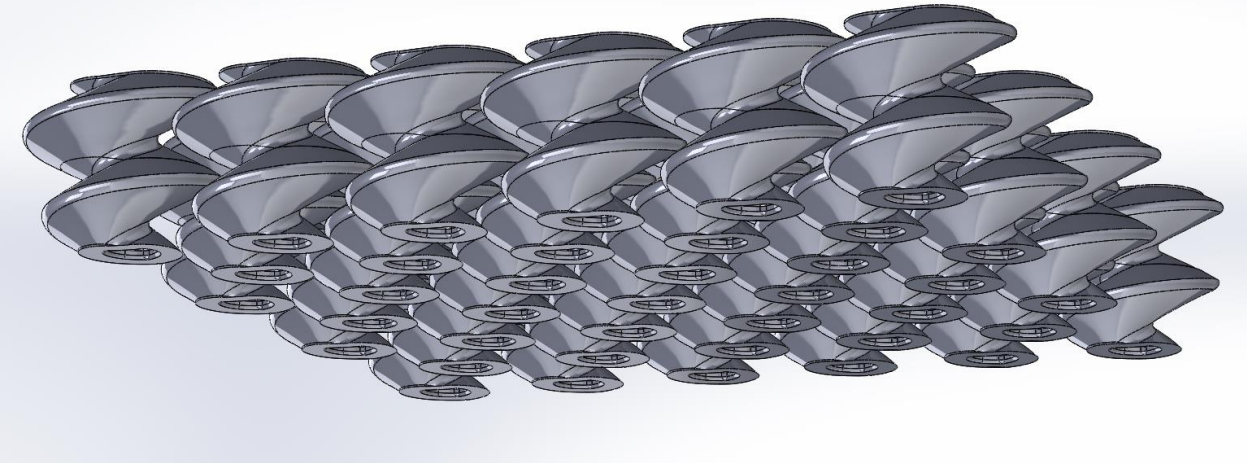

Figure 240: Rendering of hexagonally-close-packed array of double-rotated paradoxical-gear-inspired teeth (seen from the underside).

The printed array is shown in bending at lockup curvature in Figure 241. Although it used the same nominal CAD tolerances and same footprint size as an array that had a radius of curvature of around 12 inches at lockup, this array had a much higher radius of curvature at lockup, perhaps thanks to the poor quality of the print. (This poor quality was the result of steep, unsupported overhangs, thick print layers, and high printing speed to hasten production). This

poor quality is illustrated with a close-up view of several teeth in Figure 242.

Figure 241: Slight curvature of the double-rotated array at lockup.

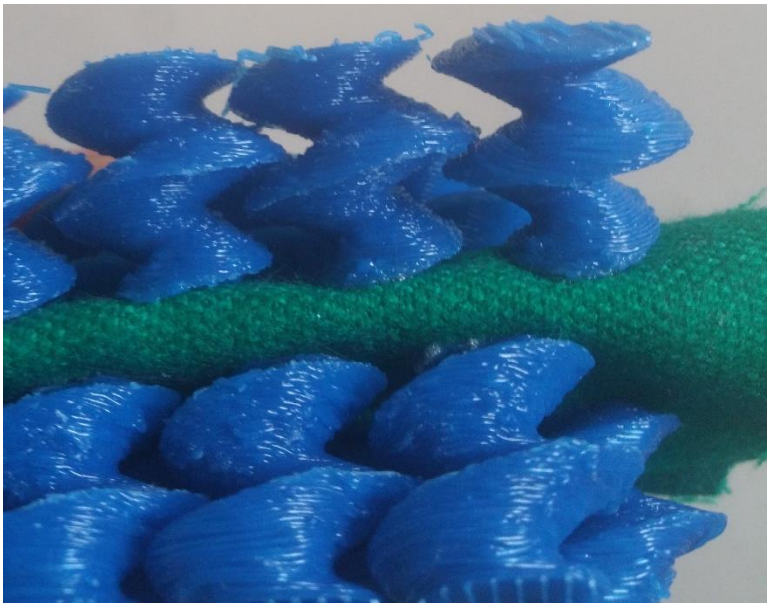

Figure 242: Closeup of several printed, double-rotated teeth showing fairly poor print quality.

However, this array possessed a property hitherto unseen in teeth arrays: synclastic sympathetic deformation following compression along a specific axis, as illustrated in Figure 243. While this special behavior is not likely to prove useful for the ankle protection problem (save perhaps to produce good conformation around the protruding ball of the ankle, and then only if the teeth are so small that their widths are a small fraction of the diameter of the ankle ball), it might be quite useful in conforming to the knee. Beyond this, compression along an axis (roughly 60° away from the axis that produces synclastic curvature) yielded sympathetic anticlastic curvature as in many other tooth arrays based on the paradoxical gear. This behavior is illustrated in Figure 244.

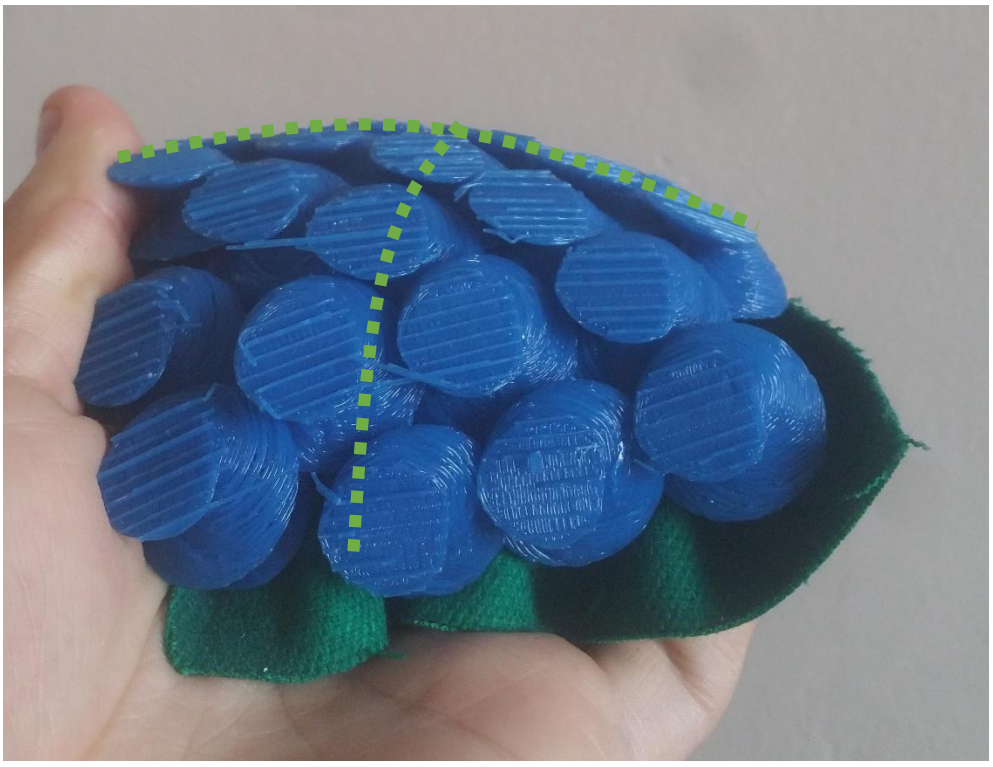

Figure 243: Compressing the array along a specific axis produces sympathetic curvature in two directions, yielding a synclastic or spherical double curvature. Compare this curvature to the merely cylindrical sympathetic deformation of the array based on the single-rotated paradoxical-gear tooth.

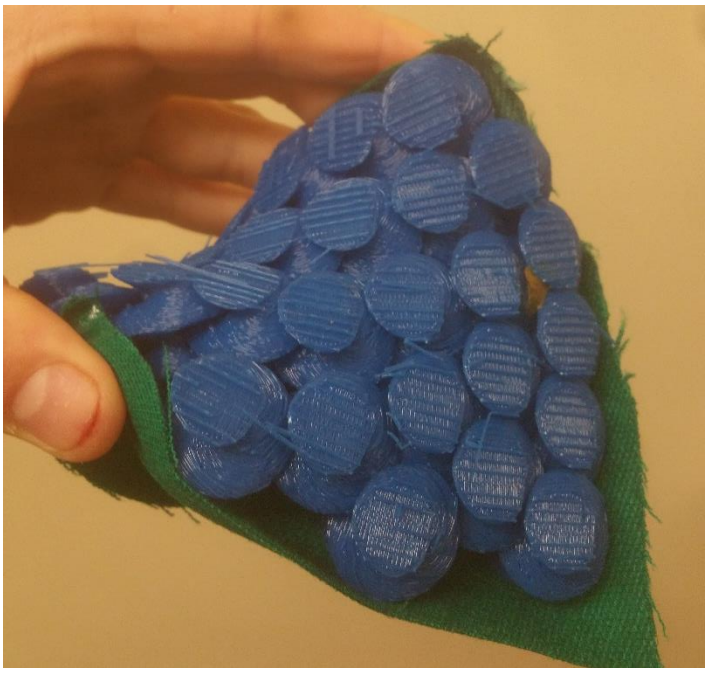

Figure 244: Compressing the array along a different axis from the one shown in the previous figure also produces sympathetic curvature in two directions, but this time the profile is anticlastic, as seen in most other paradoxical-gear arrays.

Arrays Based on Paradoxical Gears with More than One Tooth.

Paradoxical gears can be generated with more than one tooth by intersecting involutes of the base circle in much the same way that the teeth of traditional gears are generated. These gears can even mesh with paradoxical gears of different tooth numbers, provided the base circles of all gears are of the same diameter. Given the remarkable properties of the arrays based on single-toothed paradoxical gears, it was deemed interesting to experiment with arrays based on multiple-toothed paradoxical gears.

Three-Tooth Paradoxical Gear Array.

The geometry of a single tooth is shown in Figure 245. It was only possible to arrange this tooth in a hexagonal packing; an entire array is rendered in Figure 246. Of note, within a hexagonal packing, all gears had to be rotated at the same angle to pack closely, but there were

two different gap shapes between teeth (as shown in Figure 247 and Figure 248). One unique rotation will cause the gap shapes to converge and become the same (this orientation was used for the array shown in Figure 246 and is shown in detail in Figure 249 and Figure 250) and it seemed that this would be the choice less likely to produce anisotropy.

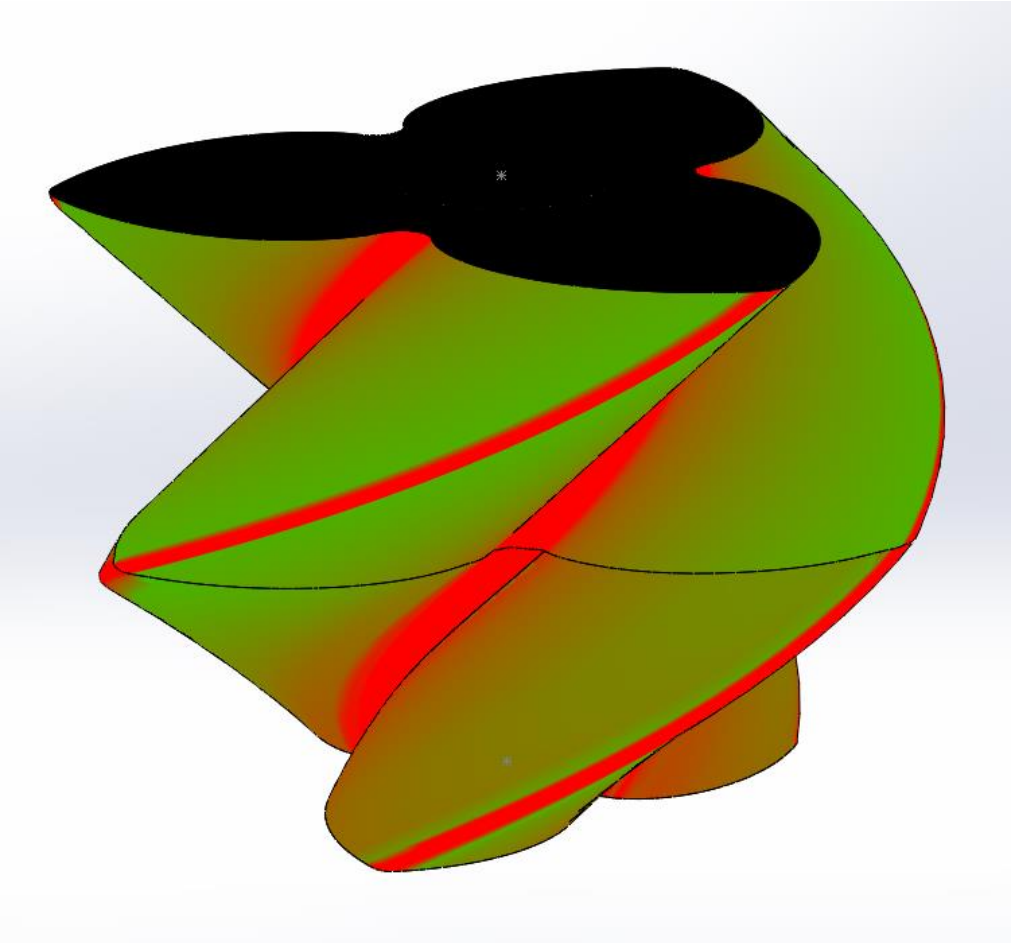

Figure 245: A single tooth based on a 3-toothed paradoxical gear, shaded by curvature.

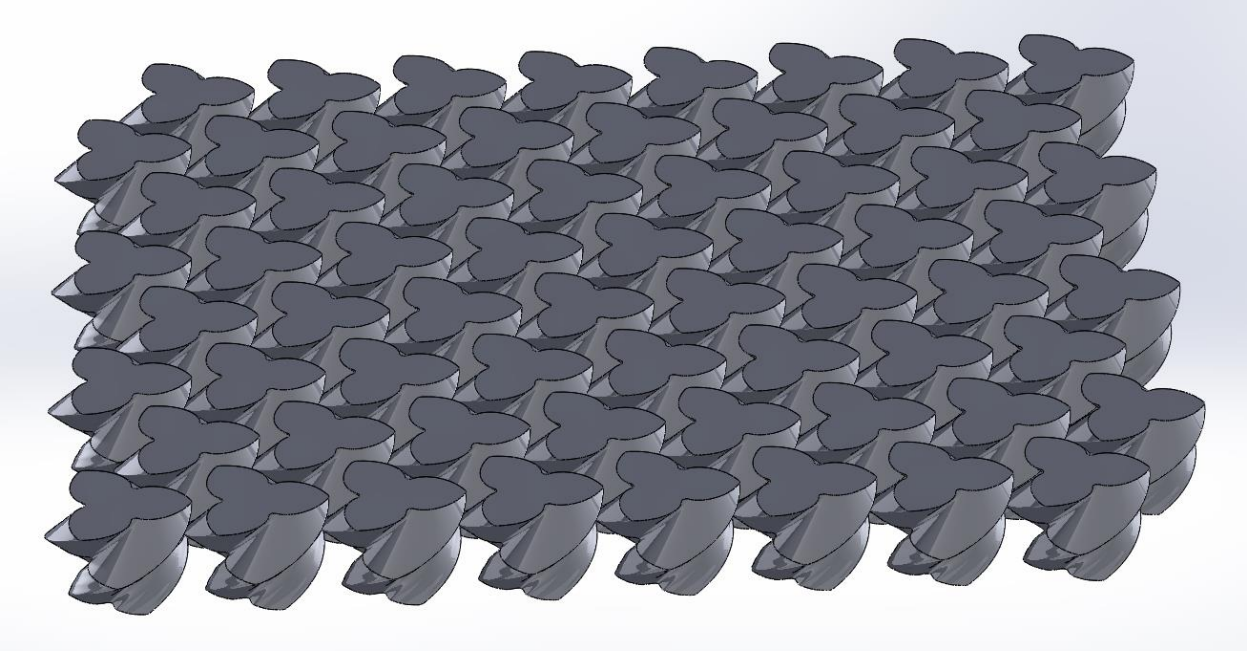

Figure 246: Hexagonally-close-packed array of teeth based on a 3-tooth paradoxical gear, arrangement 1 (teeth oriented such that contact occurs at the same height between all teeth).

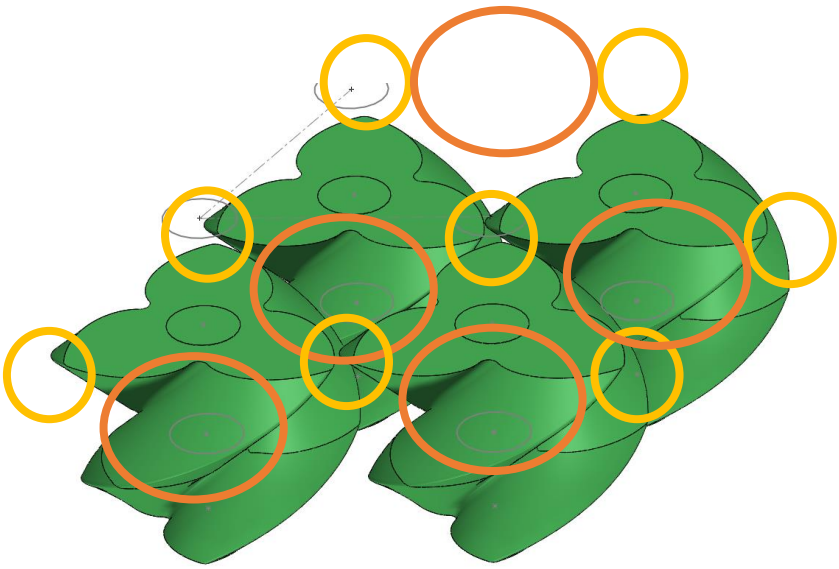

Figure 247: A rendering of three-toothed paradoxical-gear teeth with a rotation that causes there to be two different gap shapes between teeth (circled above in orange and yellow), isometric view.

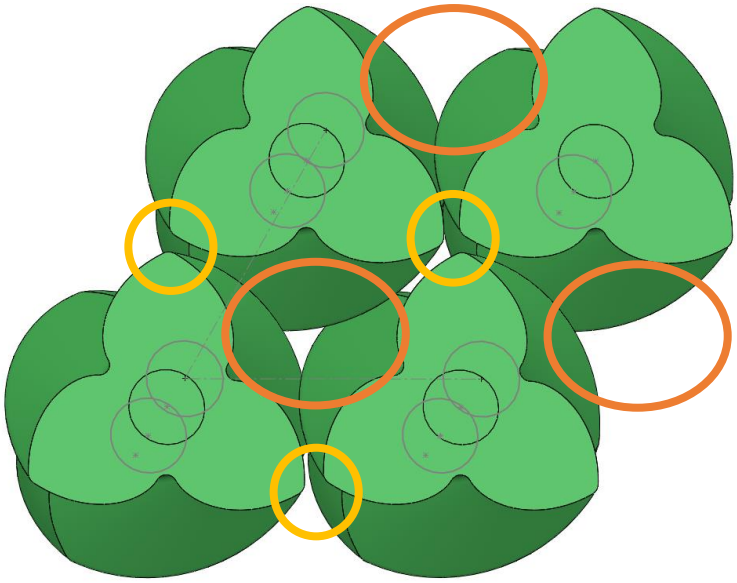

Figure 248: A rendering of three-toothed paradoxical-gear teeth with a rotation that causes there to be two different gap shapes between teeth (circled above in orange and yellow), top view.

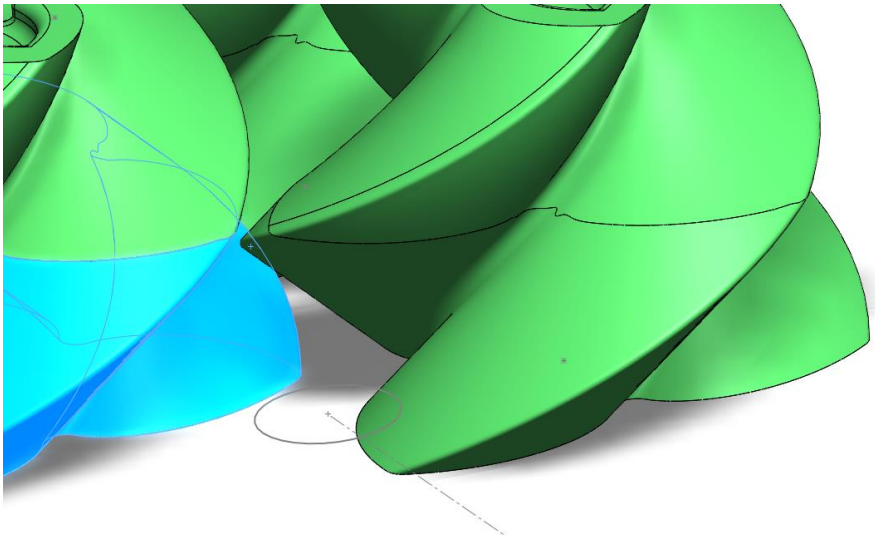

Figure 249: Side view of orientation that causes all gaps between teeth to be of the same shape.

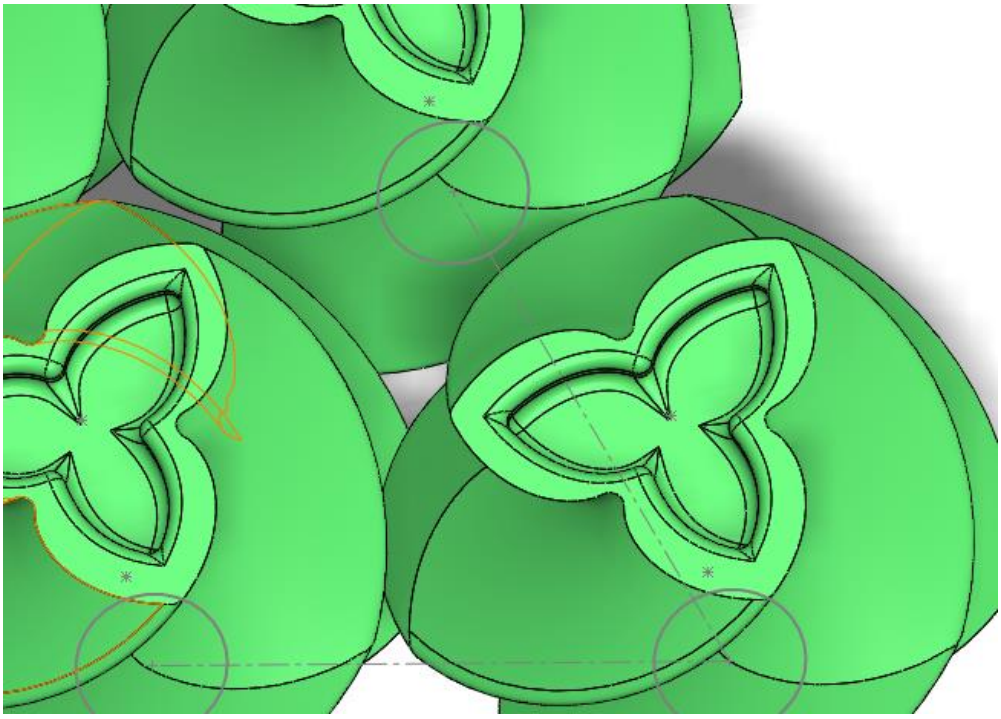

Figure 250: Bottom view of orientation that causes all gaps between teeth to be of the same shape.

The printed array is shown in Figure 251 at lockup in bending. The array had unusually poor stiffening-up behavior, largely due to the very small contact area between teeth; the teeth seemed to gouge into each other when the structure was in gross bending, as shown in Figure

252. (Poor print quality may even have helped to increase contact area here). Clearly, such a tooth design should be avoided as it gives unpredictable behavior and could even cause tooth failure.

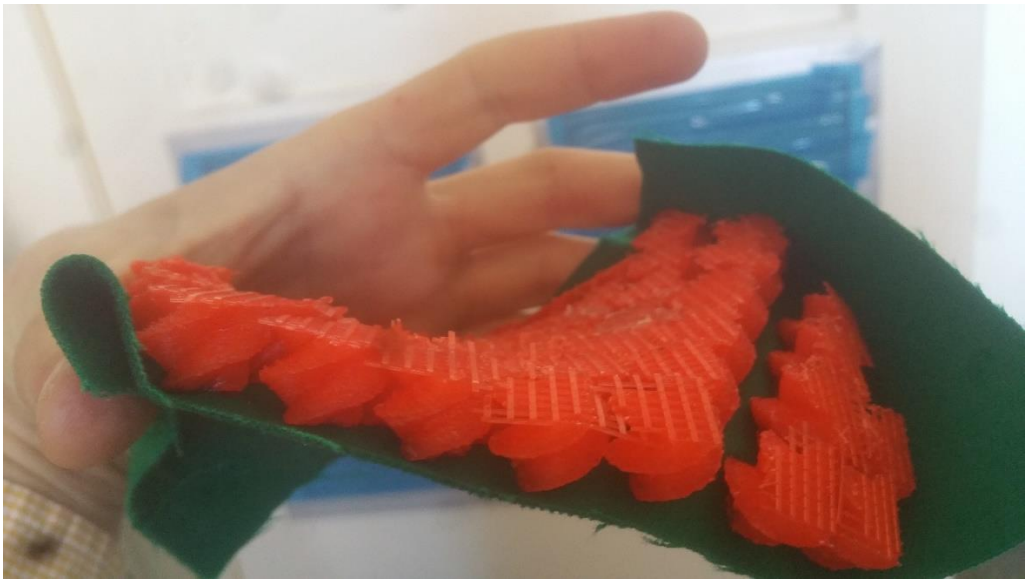

Figure 251: Three-toothed paradoxical-gear array at lockup in bending.

Figure 252: Close-up view of two teeth in contact over a very small area (circled) in bending.

Two-Tooth Paradoxical-Gear Arrays.

The final tooth geometry based on the paradoxical gear concept investigated in this thesis was based on a two-toothed involute paradoxical gear. Figure 253 shows a rendering of a single tooth in such an array. The tooth can be packed in a square packing while maintaining a constant offset between teeth, as shown in Figure 254; it should be noted that this packing can be achieved with any angle between the axis running between the tips of the two involute teeth on the element and one axis of the square tessellation; however, each gear needs to be rotated 90° from its horizontal and vertical nearest neighbors. Thus, for a given packing, there is still one independent variable: the rotation of half of the teeth in the array (with the orientation of the other half being 90° rotated from this orientation). The array shown in Figure 254 was produced

by orienting the teeth at a different angle than 0°/90°, and it is unknown if the angle of orientation affects lockup curvature or any coupled deformations.

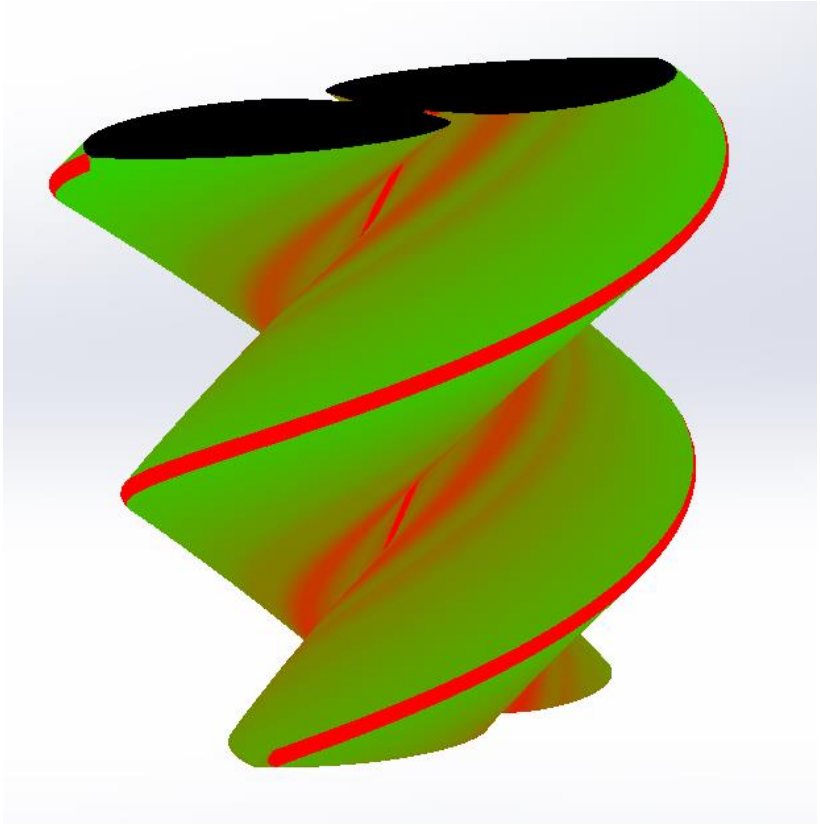

Figure 253: A single member of an array based on the two-toothed paradoxical gear, shaded by gradients of curvature.

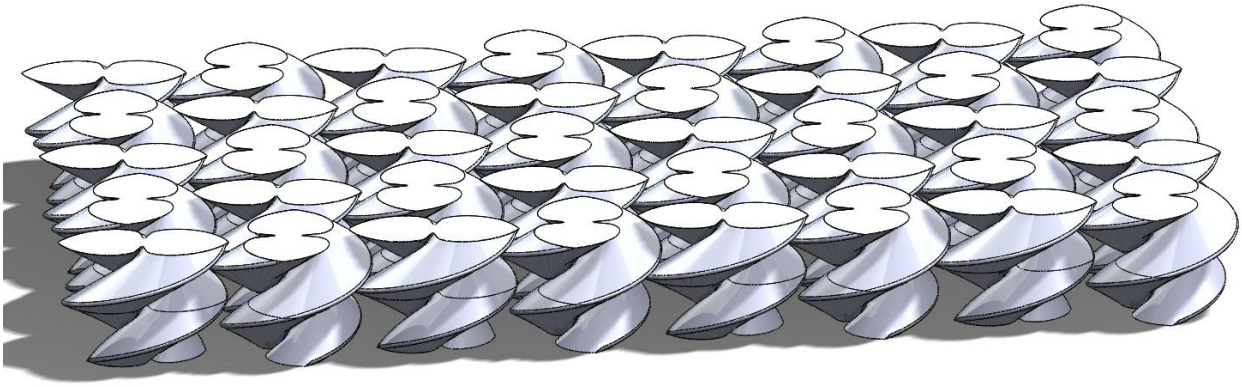

Figure 254: Square-packed array of two-tooth paradoxical gears.

When printed, the square-packed array had anti-clastic curvature when compressed diagonally and when bent along the same axis; compared with the square-packed array of paradoxical gears with one revolution, this array required less compressive force in bending to adopt the saddle-shaped curvature profile. Perhaps the higher twist rate of this tooth produced this effect, or perhaps it was simply the higher initial clearances between teeth. The anti-clastic sympathetic deformation of this array that limited axial compression produced is shown in Figure 255.

Figure 255: Two-toothed paradoxical-gear array in its anti-clastic deformation mode.

The two-toothed paradoxical gear can also be tiled hexagonally, but with one caveat: the center of each hexagon cannot consist of this tooth, and must either be empty or filled with some other body. It was speculated that it would be best to fill these gaps with some tooth to prevent excessive curvature and tooth sliding before lockup, and so a generic lofted shape was produced to fill these gaps while not interfering with the array's initial freedom, as shown in the rendering

in Figure 256. Beyond this, the teeth need to be at 60° angles to each other in order to tessellate properly with initial freedom, as shown in Figure 257. Fortunately, this arrangement does not involve knife-edge contacts, as did the tiling based on the three-toothed paradoxical gear.

Figure 256: Rendering of a large array based on the two-toothed paradoxical gear in hexagonal packing, but with the central element removed and replaced with a generic lofted shape.

Figure 257: Two-toothed paradoxical gears in triangular/hexagonal packing.

When printed, this array was fairly unremarkable, although it did have very low anisotropy in terms of curvature at lockup, as shown in Figure 258 and Figure 259. Diagonal compression (along the axis shown in Figure 260) produced anti-clastic sympathetic curvature, as shown in Figure 261, and compression along the axis shown in Figure 260 produced a cylindrical curvature profile, as can be seen in Figure 262. As usual, the sharp and unsupported overhangs produced a rough texture on the surfaces that faced downward during the print (these were later reoriented to face upward when the array was glued to fabric), and this roughness interferes with the tooth sliding that is required to engage the sympathetic saddle-shape curvature profile.

Figure 258: Lockup curvature for bending about a horizontal axis.

Figure 259: Lockup curvature for bending along a diagonal axis.

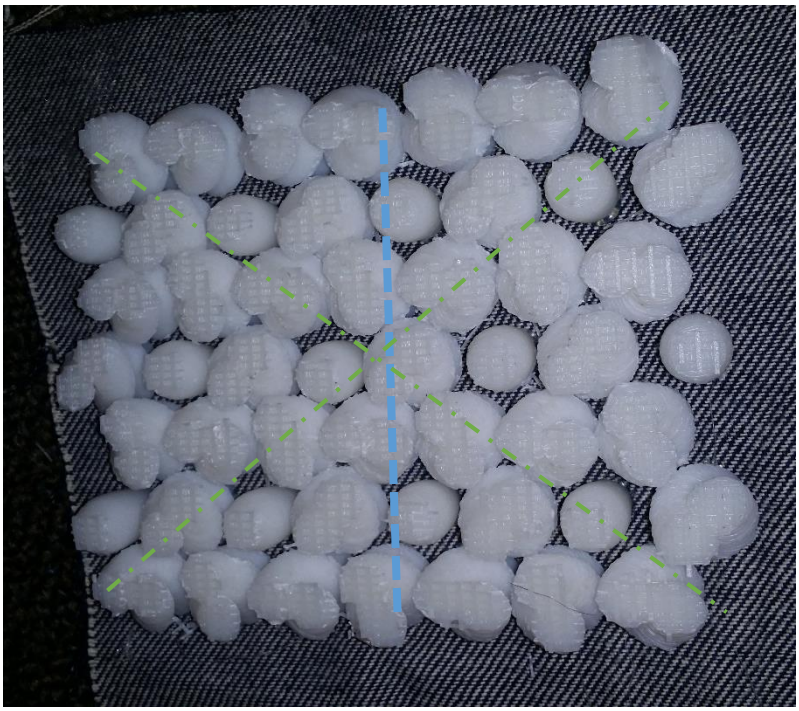

Figure 260: Compression along the axis shown in blue produces cylindrical conformation; compression along the green axes produces saddle-shaped conformation.

Figure 261: Sympathetic saddle-shaped curvature from compressing along a diagonal.

Figure 262: Sympathetic cylinder-shaped curvature from compressing along a vertical line.

Geared Teeth, Rotational Axis In-Plane.

Despite the interesting behavior of the paradoxical gear array, its behavior does not result from tooth rotations about their *z* axes, so interest in gear-based geometries with axes of rotations normal to the fabric plane may be misplaced. Perhaps a more logical application of the principles of gearing would be to make teeth that interface as the overall structure bends (i.e. with axes of rotation in plane). Granted, without special modifications they probably would not mesh if the initial shape were other than planar—i.e. if the fabric were wrapped around a cylindrical, etc. surface. Since rotation about the axis normal to the fabric is very difficult thanks to the glued interface between teeth and fabric (and since gears that rotate in opposite directions cannot be close-packed, all of the same size and shape, and still rotate), it does not seem logical to cut teeth with an extrusion normal to the plane. Rather, it makes more sense to revolve-cut

teeth around the normal axis (or extrude-cut parallel to the sides of the teeth), allowing the teeth to either simply stop frictional sliding, or enforce some rotation not in the *z* axis.

Specifically, if the centers of the gear circles are above the tooth bases, as the teeth mesh together, they will put the fabric into additional tension (which might be desirable to ensure that microbuckling of the fabric cannot reduce the structure's stiffness once stiffening-up is desired). Figure 263 shows a preliminary rendering of teeth based on this principle, although time did not allow full development and experimentation with them. It should be noted that these teeth require high tolerances in producing fine features (and, particularly relevant to production with desktop 3D printers, significant overhangs) to produce true rolling behavior, and this behavior might be difficult to adapt to cylindrical initial shapes (as the next chapter tries to do with simpler tooth shapes).

Figure 263: Illustration of the concept of teeth based on gear geometries. Strictly speaking, the teeth would not rotate the full 90° relative to each other that the geometry seems to allow (the fabric would have failed long before such strains would be achievable).

It should be noted that local fabric deformations could bring the gear-teeth features of the large teeth out of alignment and cause engagement at a different position than anticipated. This might require that a standard profile (such as the involute or cycloidal tooth shapes on specifically-circular profiles) be used so that the teeth can mesh at different initial positions. Note that most non-circular gears can only engage at a small number of positions when one's angle is fixed, often just one if the gears have no rotational symmetry (this also ignores the further constraint of the teeth themselves, which obviously limit the number of engagement angles of even circular gears, albeit not that much).

The most important tooth geometry that features convex and concave features to reduce both in-plane and out-of-plane sliding is developed in Chapter 8 (a chapter on fabric arrays that have initial cylindrical curvature). This geometry could easily be back-adapted to the planar array concept, but since the ultimate goal of this research is arrays that surround roughly-cylindrical geometry, the geometry is examined only in pre-curved cylindrical arrays.

Arrays with a Multiplicity of Normals.

A geometry having normals with numerous different orientations might have two interesting properties: first, it could arrest tooth sliding, and second, it might reduce the anisotropy that simple arrays feature, in which bending about an axis not normal to any contact normals tends to result in very different curvature at lockup from bending about an axis parallel to a pair of contact normals (this is illustrated in Figure 207 above). It is hoped that sliding would be negated if teeth could only slide a small distance along contacting normals before contacting a new tooth along a new normal direction (quite different from the original sliding direction). With even a moderate amount of friction, sliding should then hopefully cease. For instance, a tiling of regular octagons and squares gives four different normal orientations (as

opposed to three with a regular hexagonal array, three with a triangular array, two with a rectangular array, etc.).

P15 Pentagon Tessellation.

Another tiling was developed based on a recently-discovered convex pentagonal tiling[54] having numerous contact-normal directions. (Note that this tiling uses flipping in addition to rotation, so the teeth have chirality.) A toothed array based on this tessellation is shown in Figure 264, and two views of the individual tooth are to be found in Figure 265. A photo of the printed but undeformed array is shown in Figure 266.

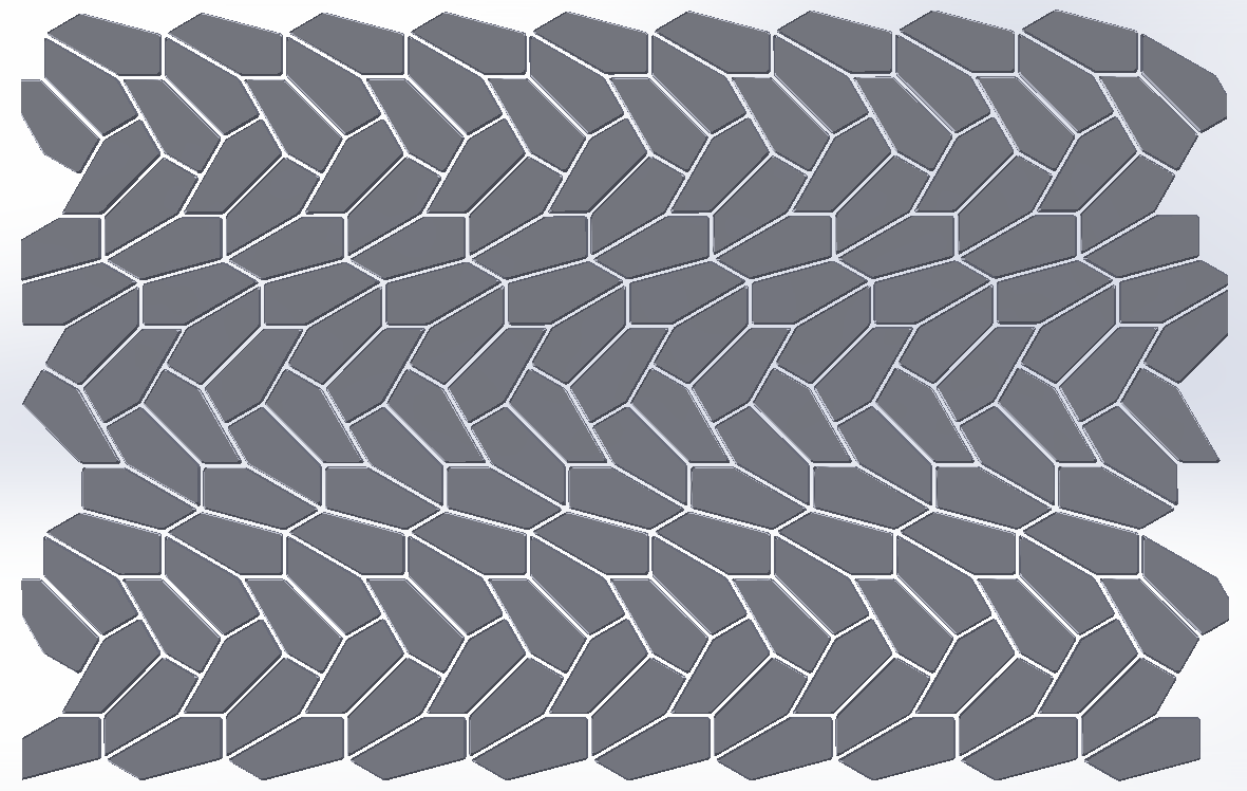

Figure 264: Convex pentagonal tiling made into an array. Note the multiplicity of normal angles.

[54] *Convex pentagons that admit* i*-block transitive tilings*, Casey Mann, Jennifer McLoud-Mann, David Von Derau

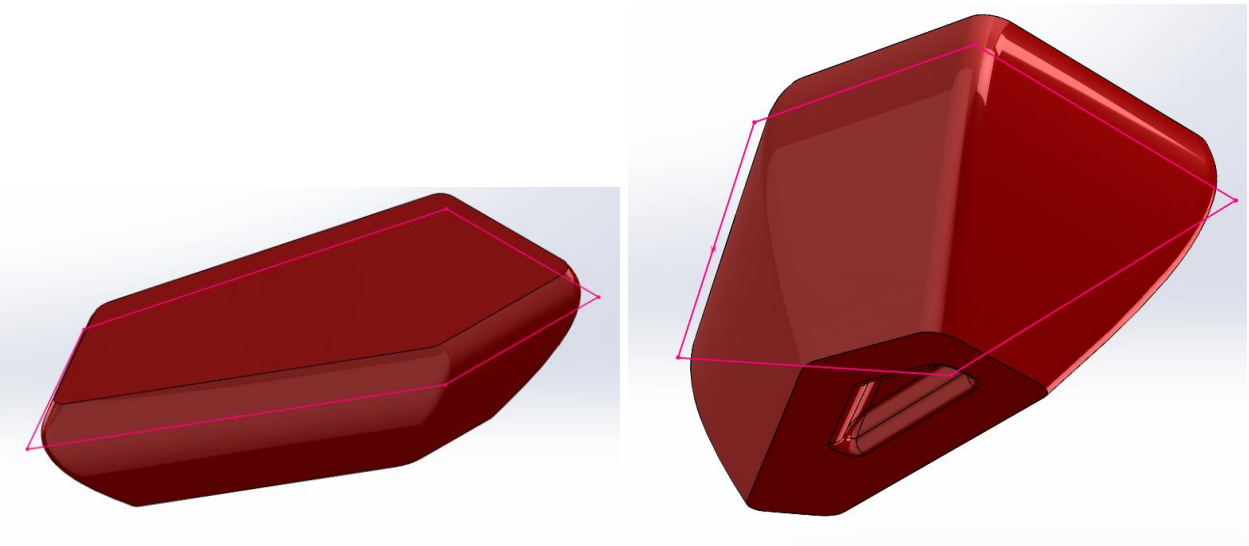

Figure 265: Two views of single pentagonal teeth for the above tiling.

Figure 266: P15 pentagon array as printed and glued to Kevlar fabric.

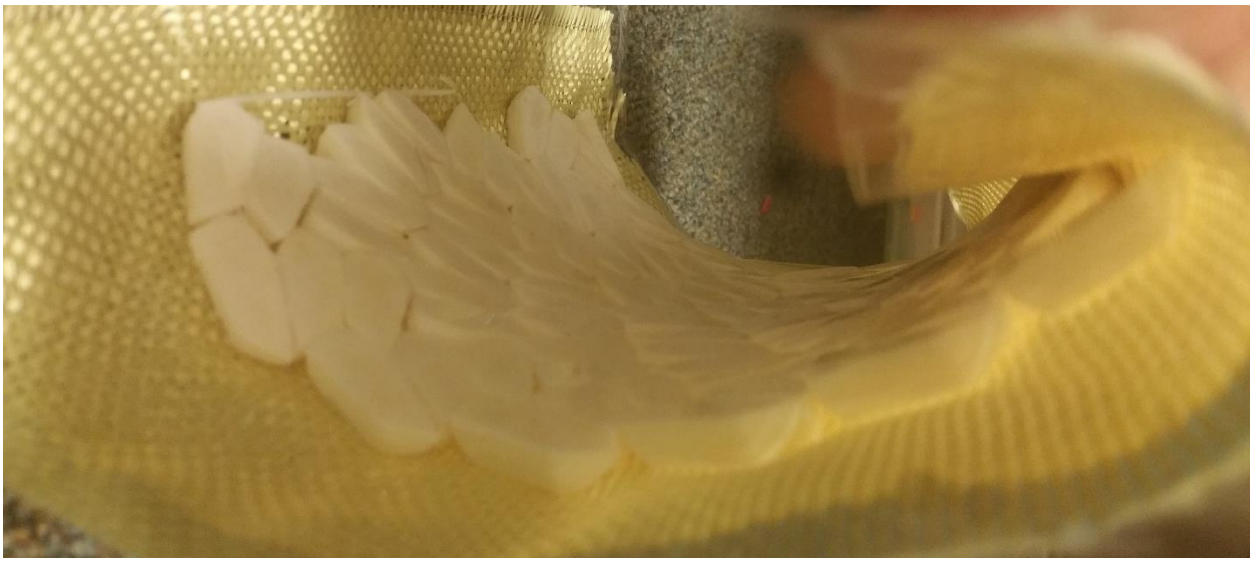

Figure 267: Post-lockup curvature of the P15 pentagon array, bent parallel to the warp direction of the fabric.

Figure 268: Post-lockup curvature of the P15 pentagon array at another angle.

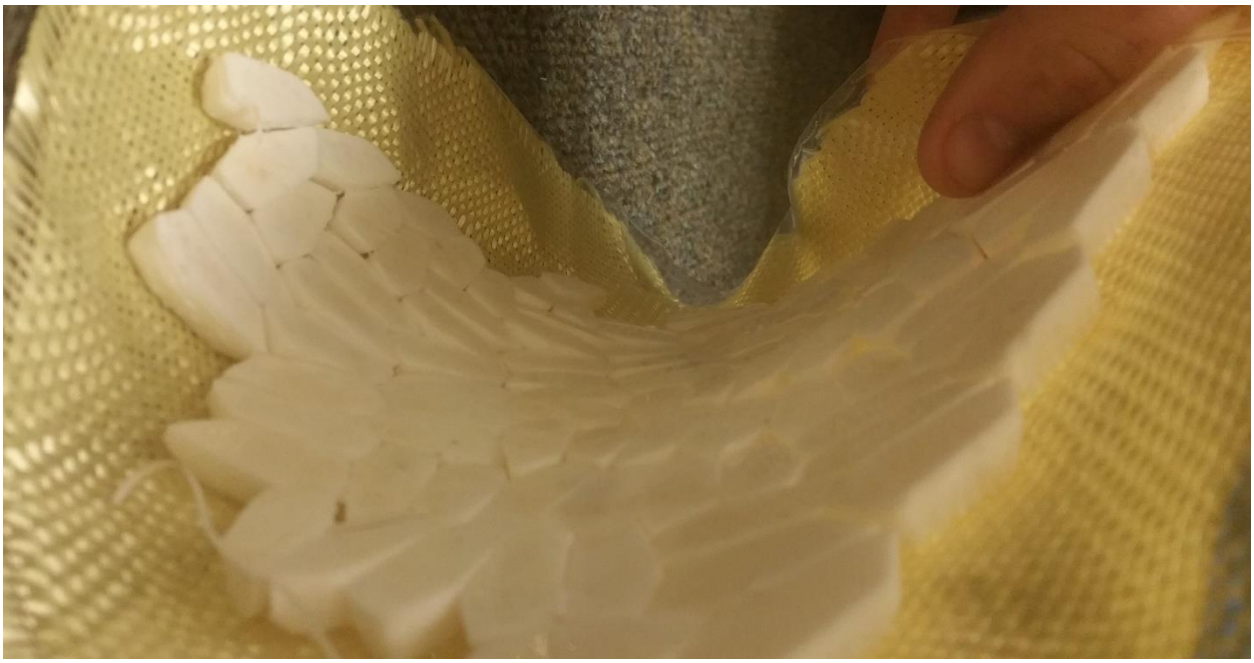

Figure 269: Post-lockup curvature of the P15 pentagon array at another angle.

Figure 270: Post-lockup curvature of the P15 pentagon array at another angle.

As concerns resistance to sliding normal to the fabric, the P15 array was much more resistant than the sliding-prone hexagonal array with an inward flare at the top (a feature

intended to combat vertical sliding) of Figure 203; this is despite the P15 array's complete lack of anti-sliding features, including significant inward flaring at the top, let alone concave features. Also, the magnitude of in-plane tooth sliding when rotating the axis of bending seemed greatly reduced as compared with the hexagonal array. Finally, the array seemed to have fairly low shearing freedom; while this might be due to the numerous potential normal directions that could impede shearing, it is more likely due to the high contact area between teeth and fabric, leaving little unbound fabric free to shear along the bias.

Arrays need not be limited to true tessellations: for instance, another set of potential tooth arrangements to investigate are the Penrose tilings. While not true tessellations, they have multiple-fold symmetry and are self-similar. For instance, the P1 tiling has five different normal directions and both convex and concave shapes; several generations are shown in Figure 271. However, as of this writing, no pressing need was seen to experiment with this tiling, given the difficulty of generating it. Ultimately, even self-similarity might prove unnecessary; the mathematics behind Voronoi patterns, for instance, might allow for better customization for the complex surface profile of an ankle.

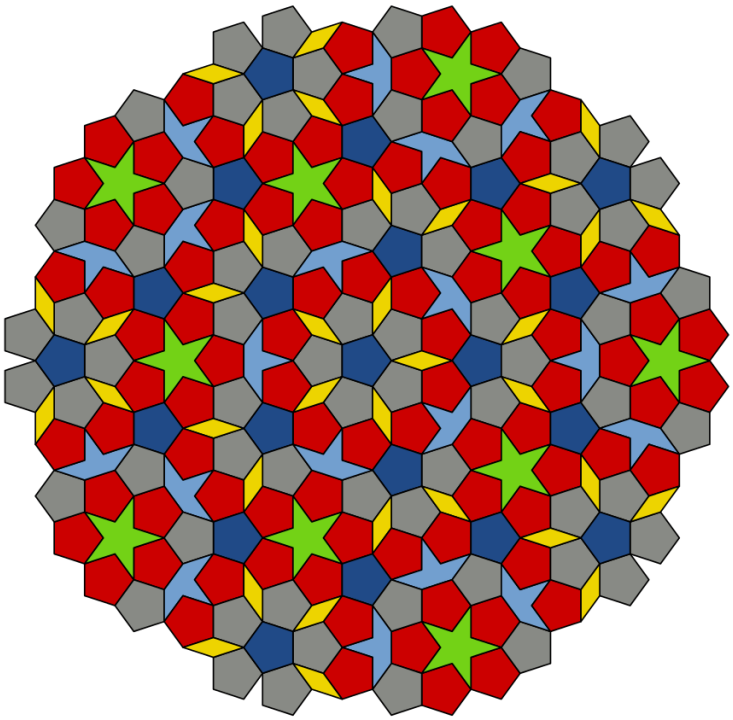

Figure 271: Several generations of the P1 Penrose tiling. (Public domain image)

Varying Gap Shape.

All of the previous tooth arrays have employed a fixed offset between the teeth at every point on the perimeters of their central cross-sections (even those based on the Mercier paradoxical gears), even though the offsets are higher at the very top (giving the teeth an inward angle that is intended to reduce vertical sliding) and at especially the very bottom (reducing contact area with the fabric). While this is likely a good property for the simplest 2D arrays that are not supposed to have any special deformation properties, merely lock up instantly and quasi-isotropically, it is conceivable that some beneficial coupled deformations could occur with special gap shapes (for instance, lockup in one bending direction might cause significant expansion or contraction in the perpendicular in-plane direction). To this end, several arrays with special gap shapes are considered below.

Array of Reuleaux "Triangles".

The first cross-sectional shape considered in this section is the Reuleaux "triangle", a union of arcs that has the special property of being able to roll between fixed parallel plates just like a circle. (Note that other Reuleaux figures, based on both regular and irregular polygons, also exist, and it is possible to create Reuleaux surfaces that can roll just like spheres). Figure 272 shows the tooth generated by lofting from a base circle to a Reuleaux "triangle" cross-section and then adding a taper at the top.

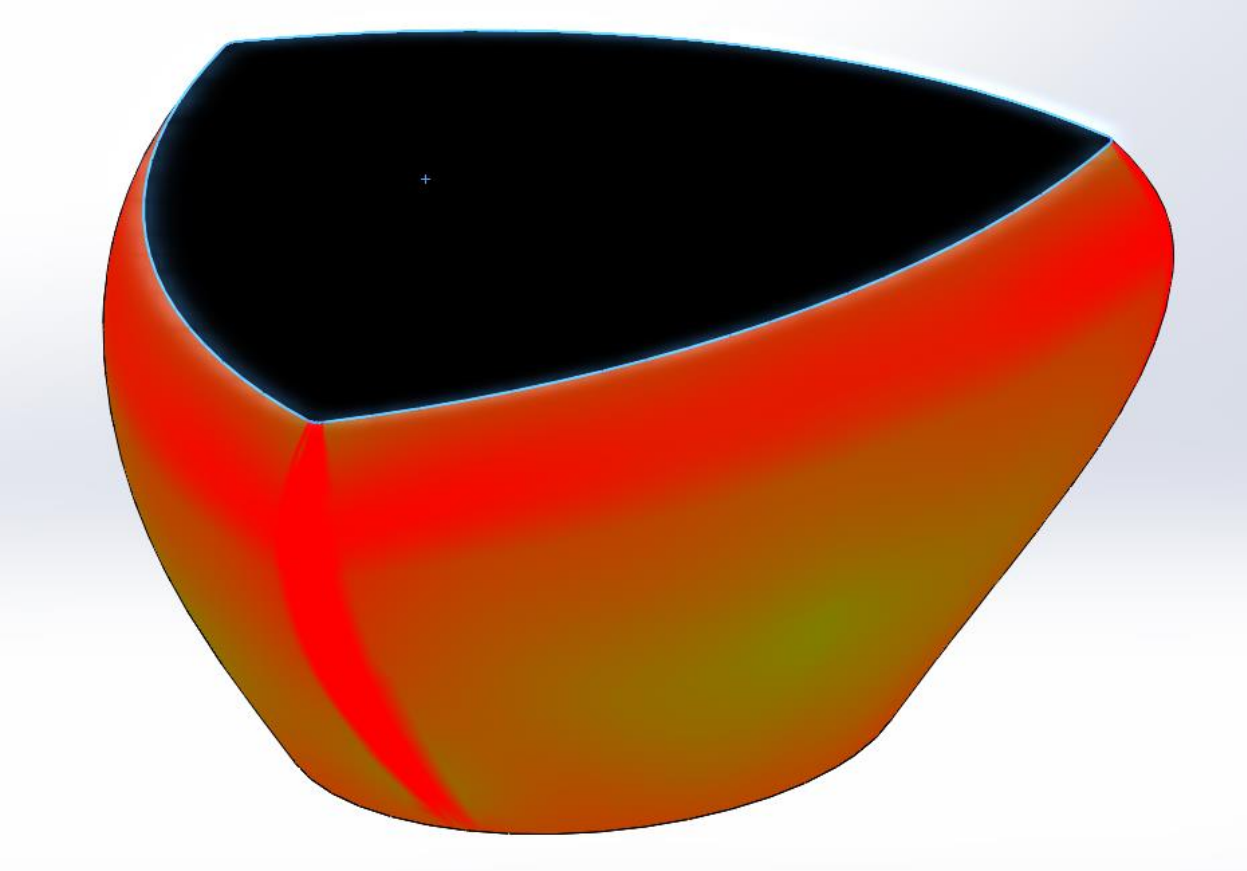

Figure 272: Individual tooth with cross-section based on Reuleaux "triangle". This rendering shows curvature gradients.

The array generated from arranging the inscribed triangles from which each Reuleaux "triangle" was offset is shown in Figure 273. The central cross-section and surrounding

inscribed triangle are shown in Figure 274. At the closest points between two teeth, there is a gap of 0.020"; however, this gap obviously widens rapidly along the perimeter towards the tips of the Reuleaux "triangles".

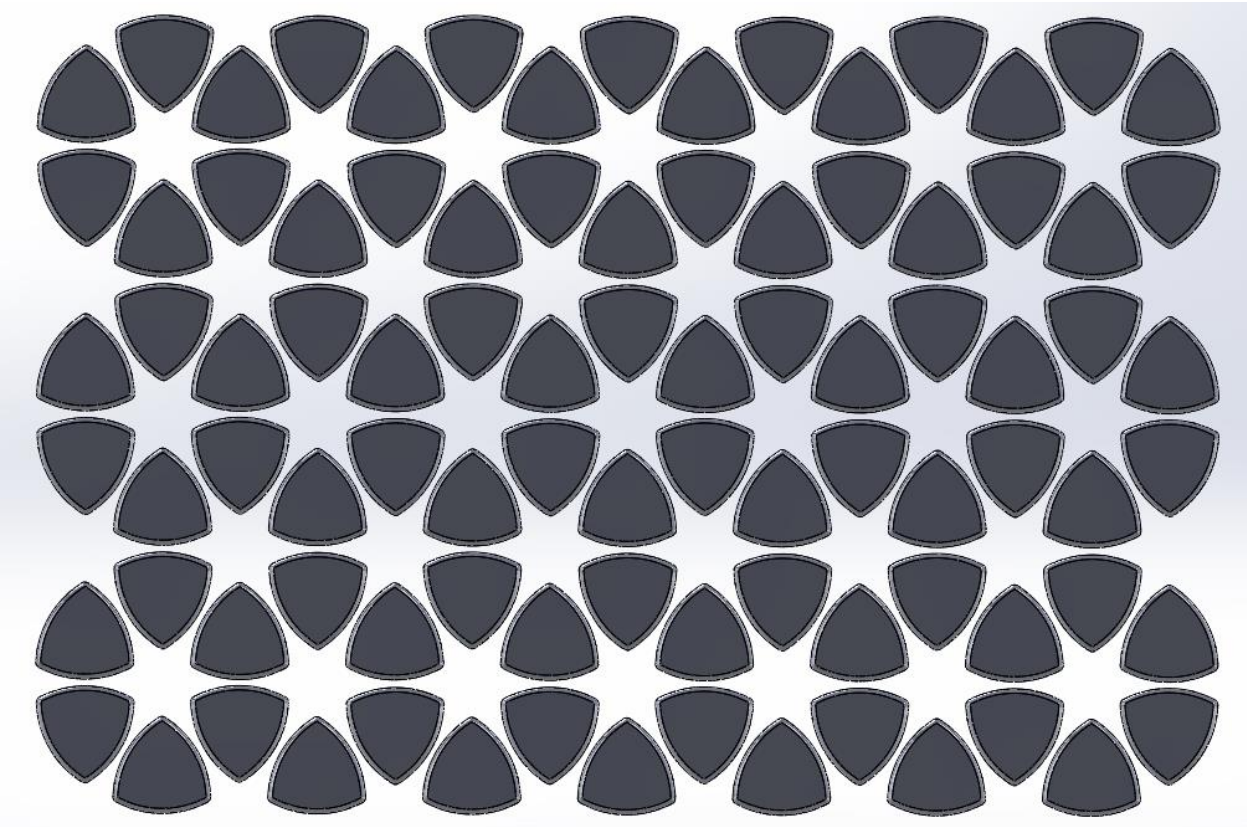

Figure 273: Array of "hexagonally-close-packed" Reuleaux teeth. Note the significant variation in distance between the teeth along the perimeters thereof, with a gap of 0.020" at the closest points.

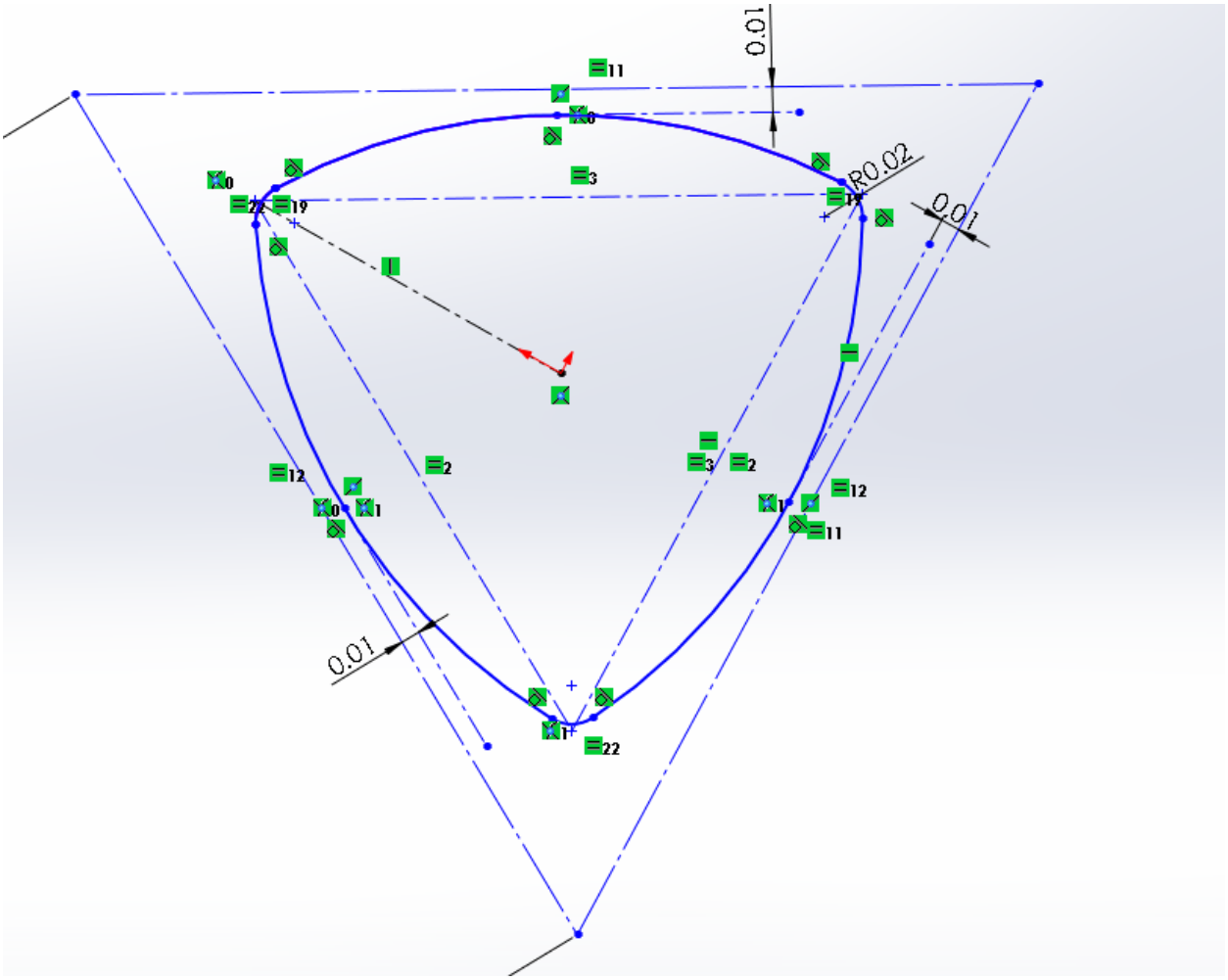

Figure 274: Detailed geometry of the central cross-section of an individual tooth, showing the large, inscribed triangle (which was the basis for the tessellation) in dashed lines, and the solid Reuleaux cross-section in solid arcs.

This array, when printed, did not lock up until very small radii of curvature were achieved thanks to the huge normal distances between the tips of the teeth; consequently, it failed in the basic function of all of these arrays (lockup in bending), and no other interesting properties were observed. (However, part of the reason for its failure to lock up was that teeth were prone to sliding along their *z* axes relative to each other). Figure 275 shows a picture of the array largely failing to lock up in bending. Perhaps the array would have more desirable behavior if the large gaps between teeth tips were replaced with cylinders.

Figure 275: The array based on Reuleaux triangles did not lock up effectively in bending.

Hexagonal Array with Concave and Convex Cylinder Faces.

Another array with curved faces was developed, but this time with concave as well as convex cylindrical faces. In contrast to the array based on the Reuleaux triangle, which had only convex cylindrical faces, this array should be able to capture teeth for pure rotation, whereas the former array saw unstable sliding.

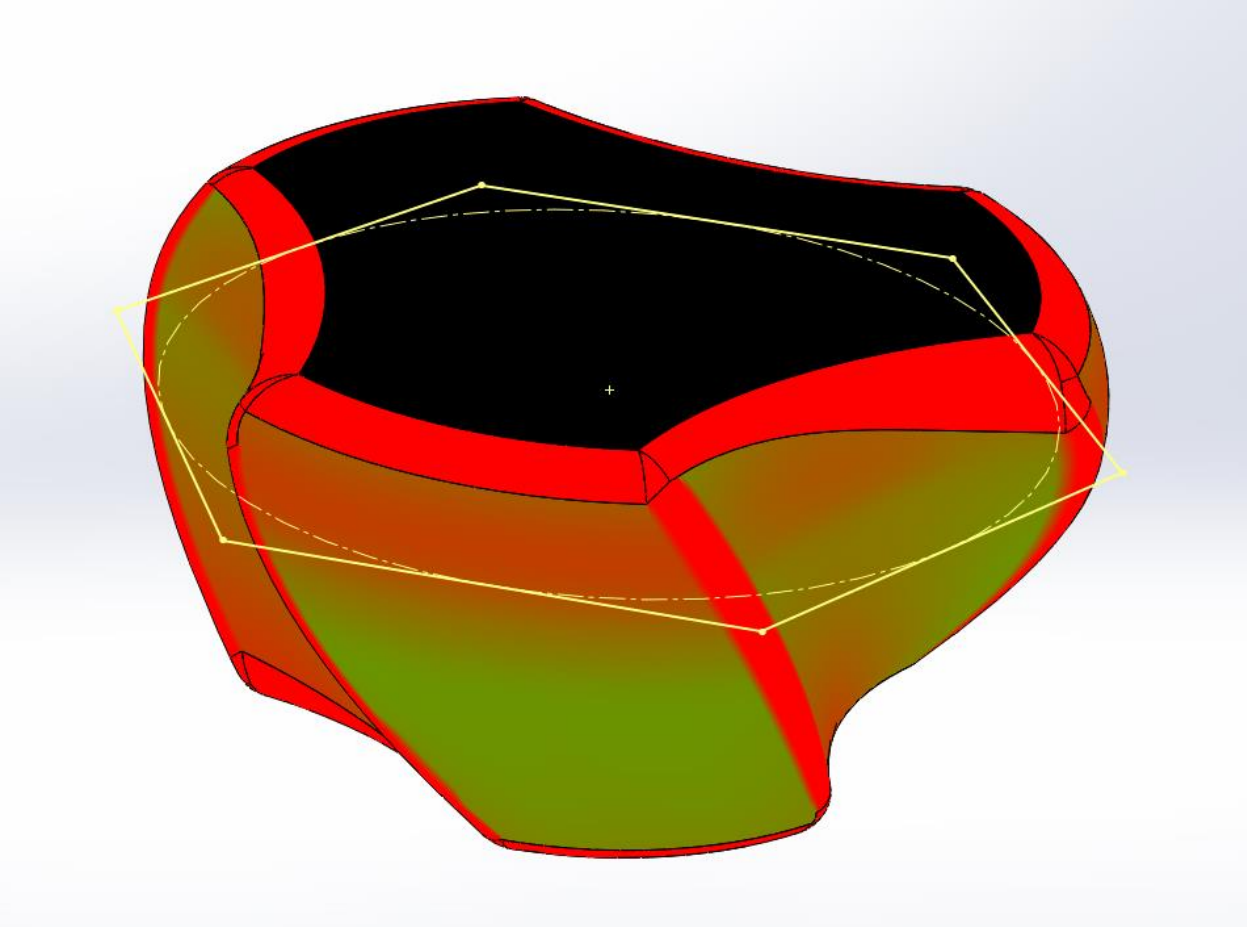

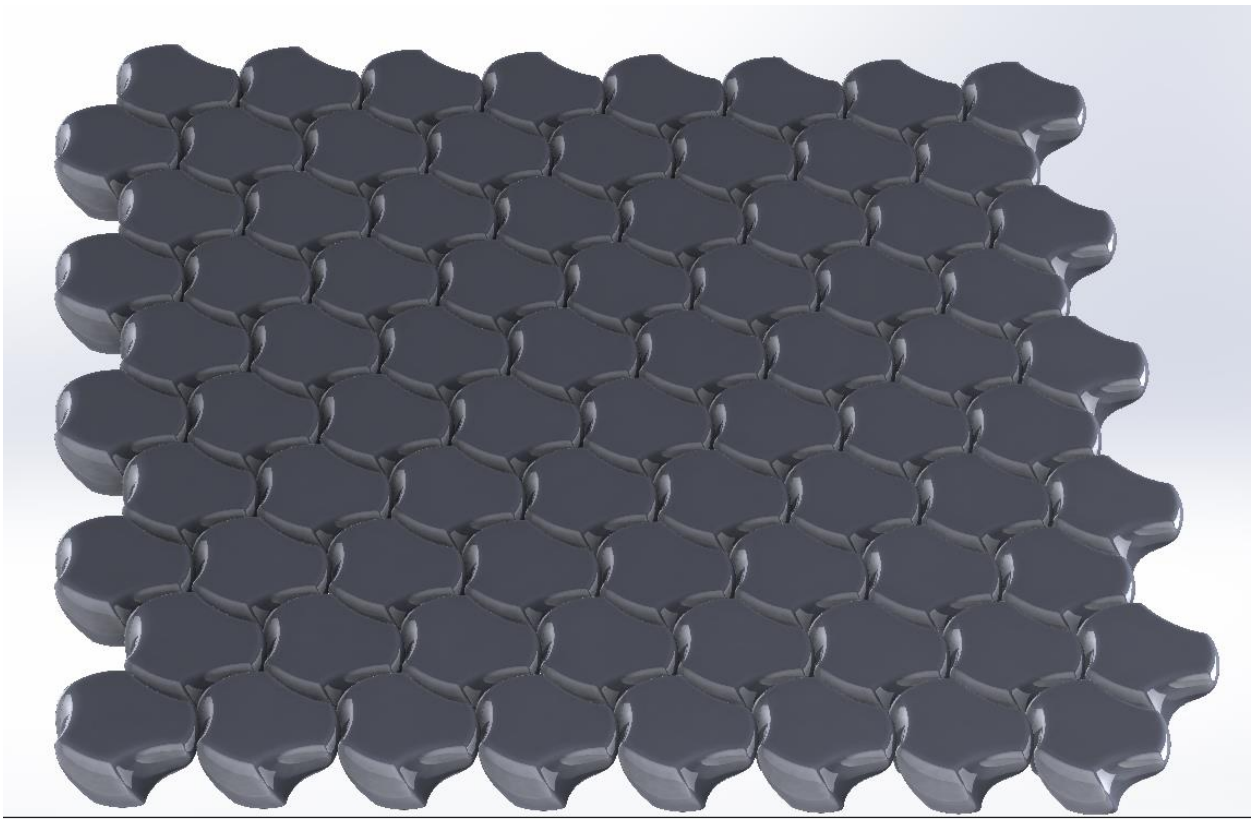

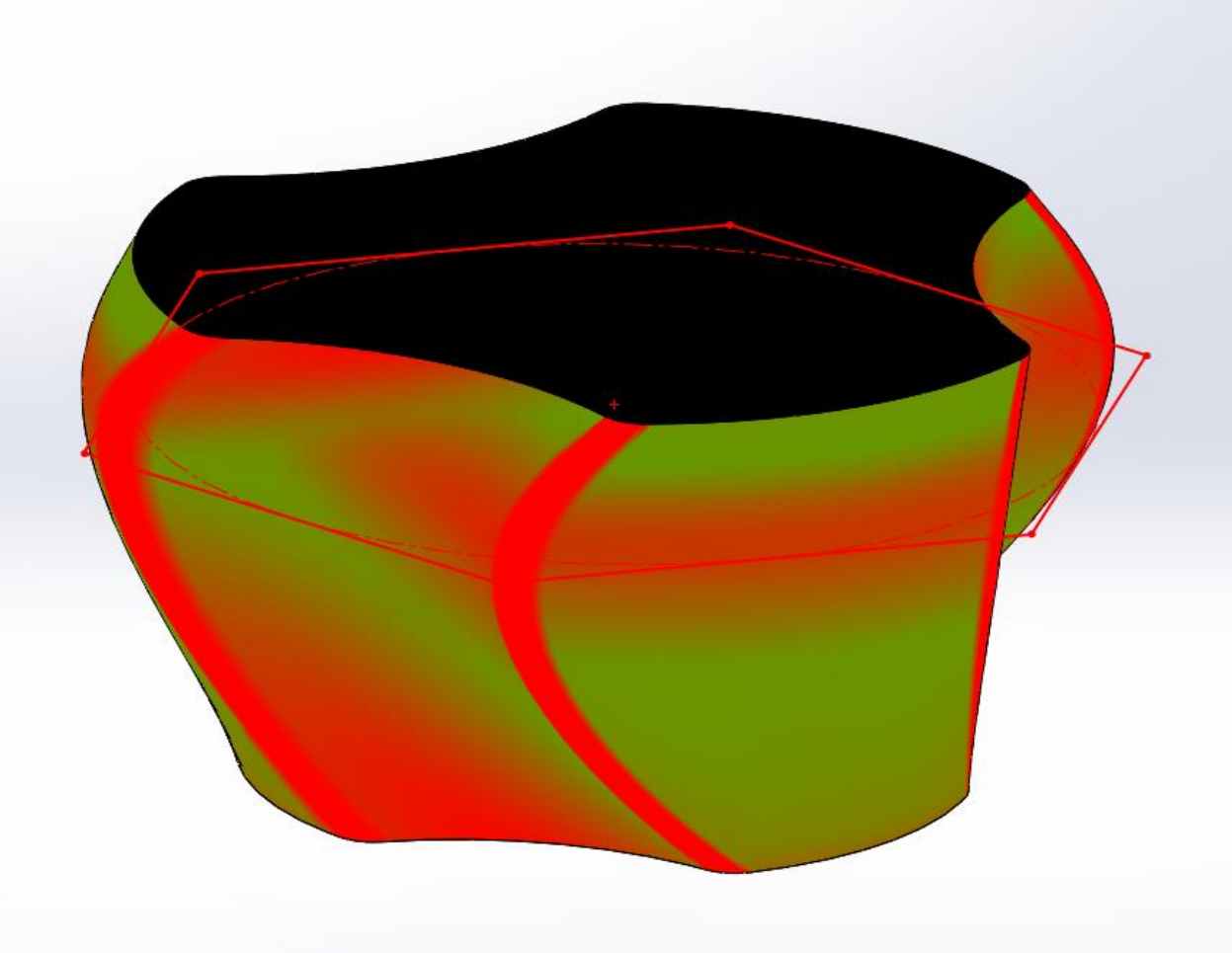

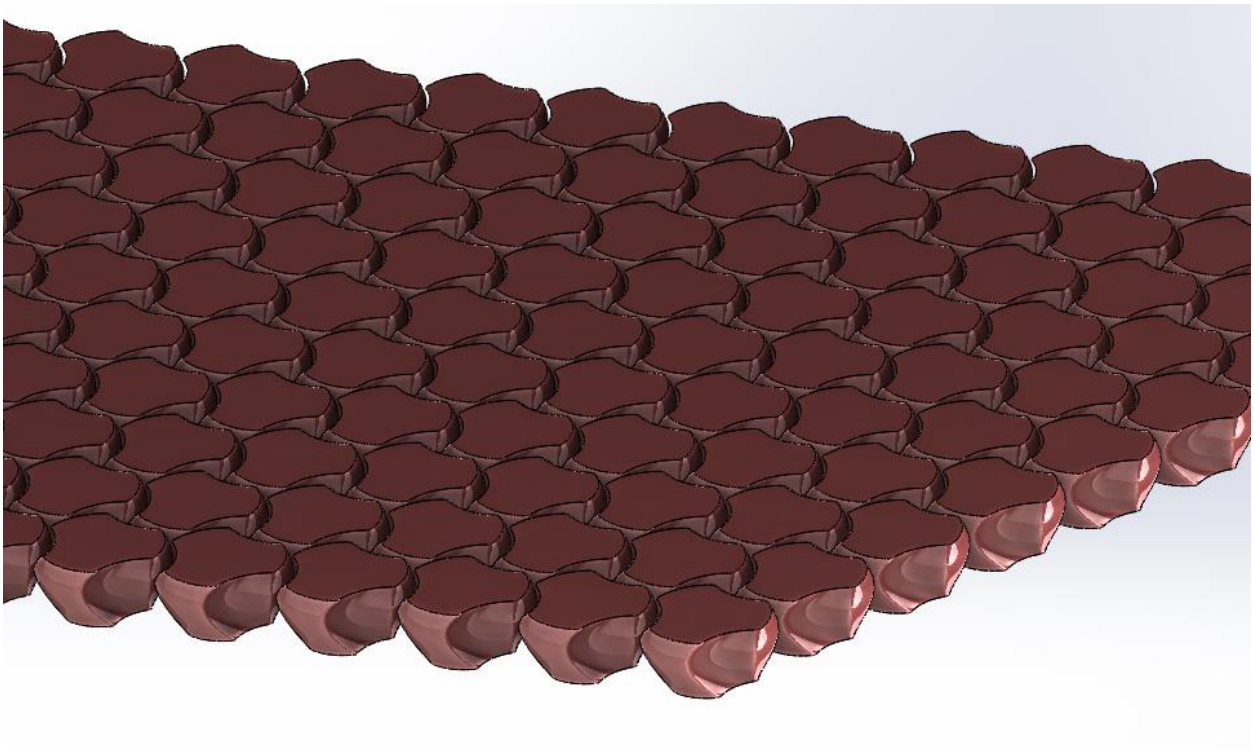

Auxetic-Inspired Rectangular Array.

It is well known that a linkage of rigid rectangles connected at their corners by revolute joints will expand and contract sympathetically in a perpendicular direction when expanded or contracted along another axis, as if it were an auxetic material, as shown in Figure 276. Absent

these revolute joints to constrain the rectangles in the array (and such revolute joints would not allow the backbone to curve at all, so they must be excluded; however, perhaps spherical joints would allow some initial freedom), the structure certainly would not be guaranteed to have auxetic behavior in gross bending, tension, or compression. However, it might have other interesting properties if the shapes of the gaps between the teeth change in some special way. Thus, an array was generated, with the sole tooth design shown in Figure 277 and a rendering of the overall array shown in Figure 294.

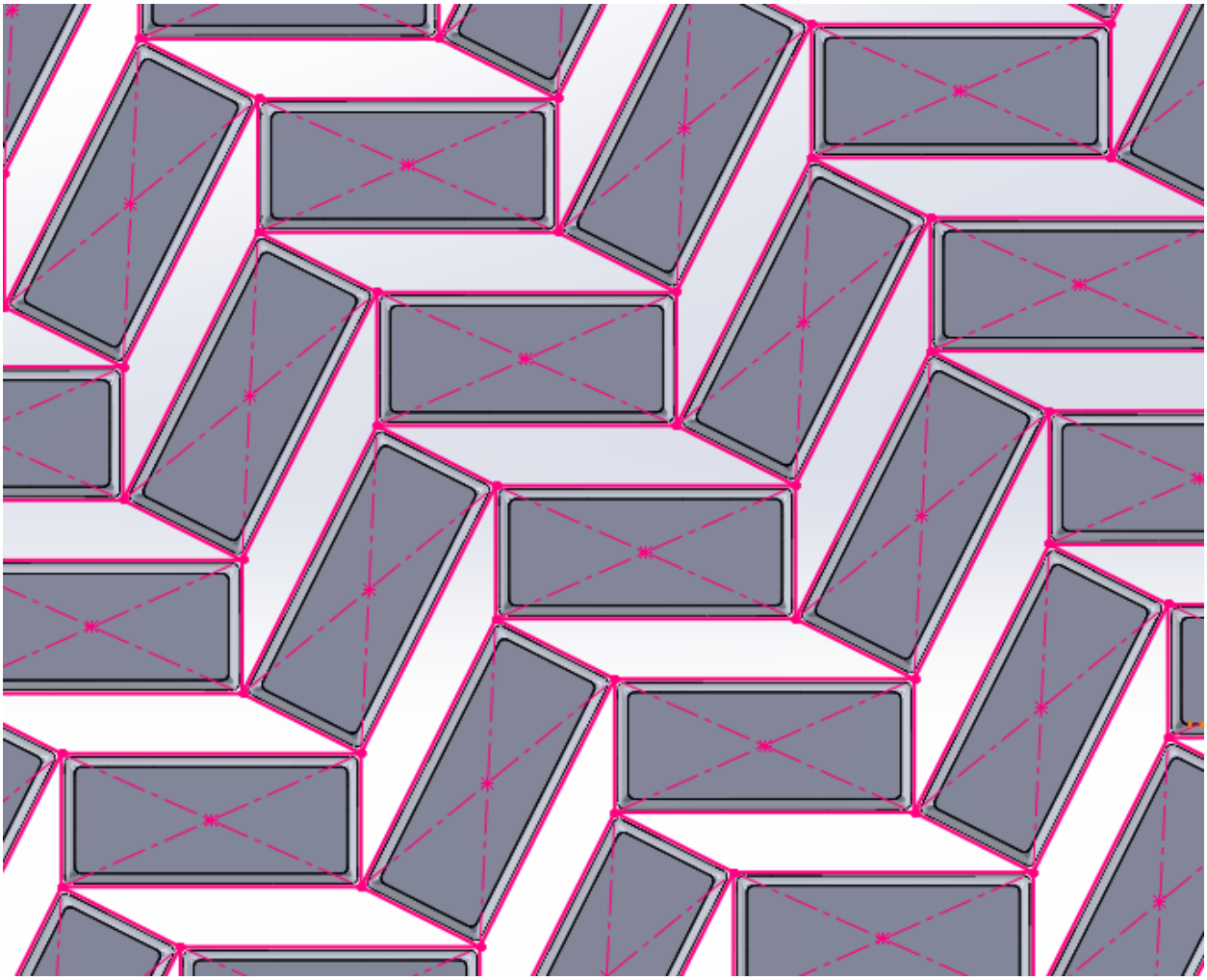

Figure 276: If the rectangles are rigid and linked at the pink dots by revolute joints normal to the plane, the structure will be perfectly auxetic.

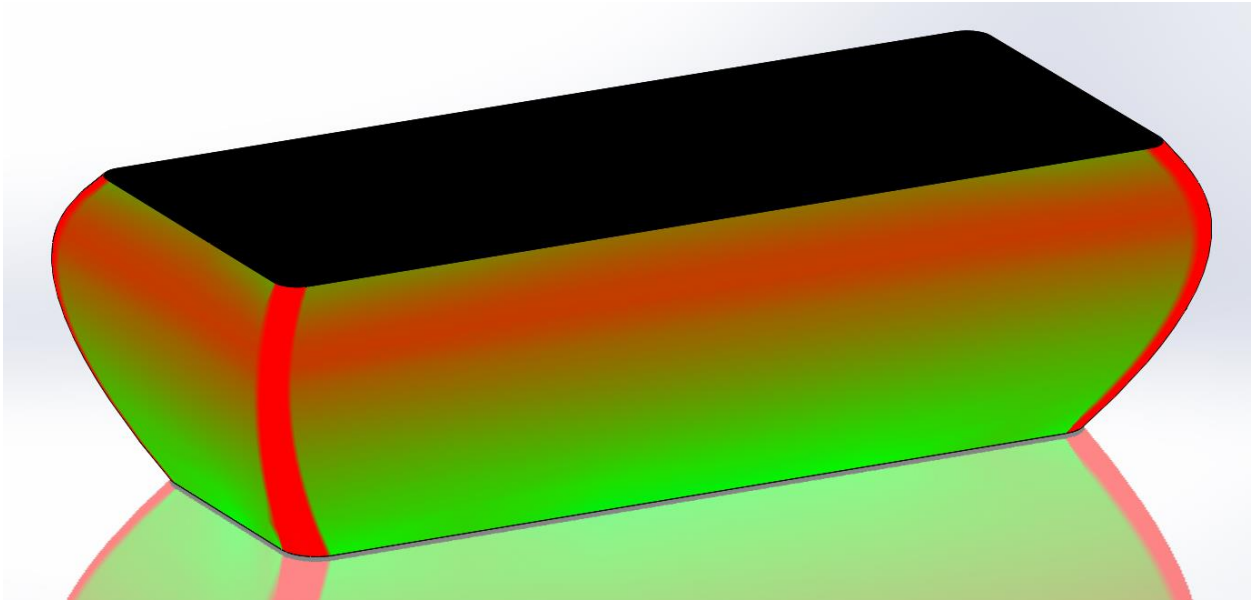

Figure 277: A single tooth in this array, with gradients of surface curvature.

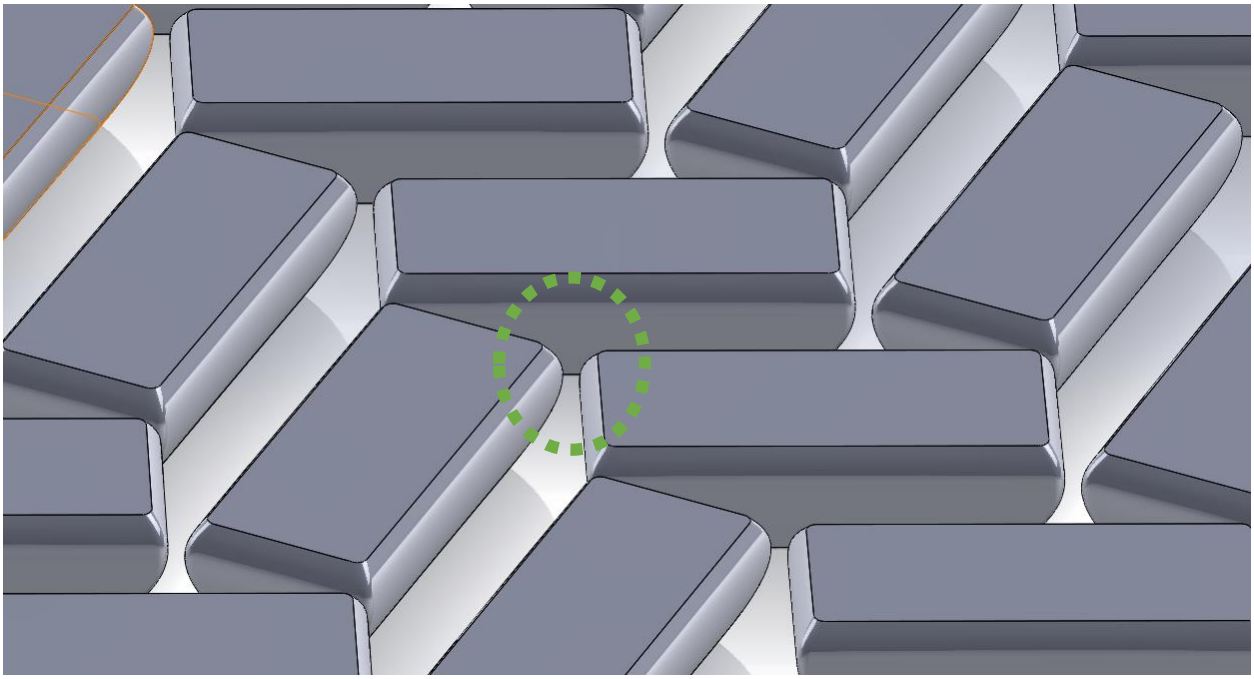

Figure 278: Rendering of auxetic-inspired tooth array. Note the gaps between tips of teeth (as well as the obvious parallelogram-shaped gaps between teeth sides that should give the array its auxetic properties). The performance of the printed array suggested that the tip gaps should be reduced to produce faster lockup.

Once printed, this auxetic-inspired array exhibited several interesting properties. First, it had an extreme degree of anisotropy in curvature at lockup depending upon the in-plane angle of orientation of the axis of bending. Figure 279 through Figure 282 show different radii of curvature at lockup, depending on the in-plane angle of the bending axis. This property could be tailored to allow the leg more freedom in one direction (e.g. dorsiflexion/plantarflexion) than in the orthogonal direction (i.e. inversion/eversion).

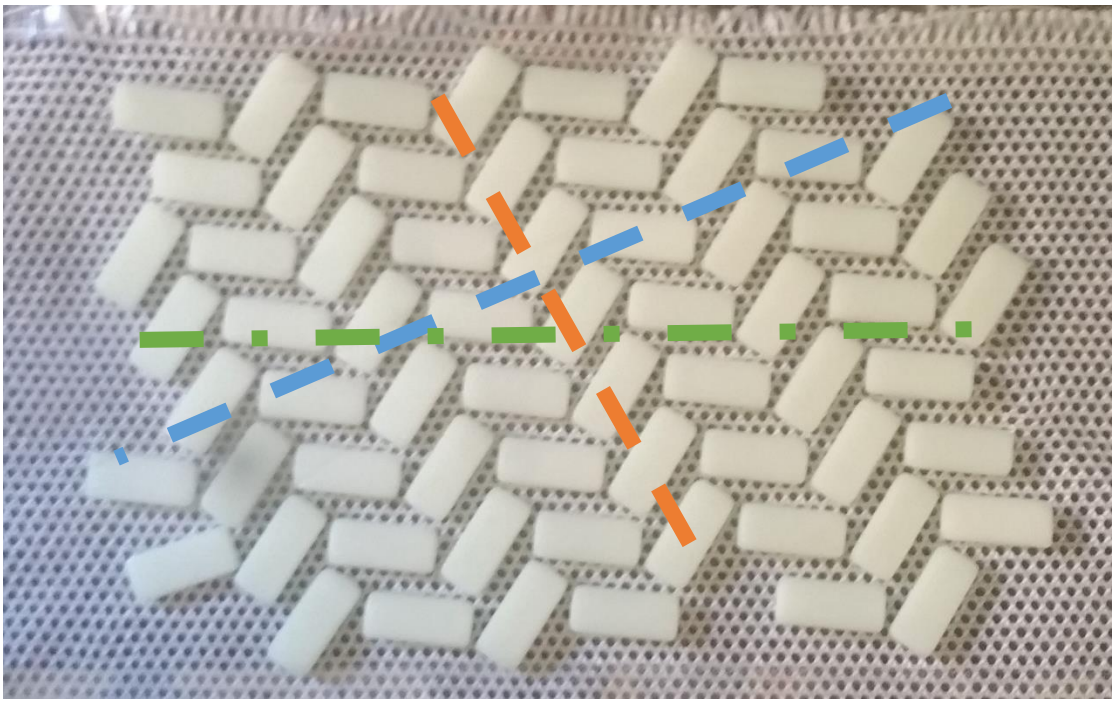

Figure 279: The auxetic-inspired array, laid flat, with the axes of bending superimposed. The following figures show the curvatures of the backbone when bent about the above axes. The blue axis corresponded to the highest curvature (see Figure 280), the green axis to a moderate curvature (see Figure 281), and the orange axis to the lowest curvature at lockup (see Figure 282). All of the associated pictures were taken immediately at lockup, without further bending, which would have rotated and/or elastically deformed teeth and possibly tensioned fabric.

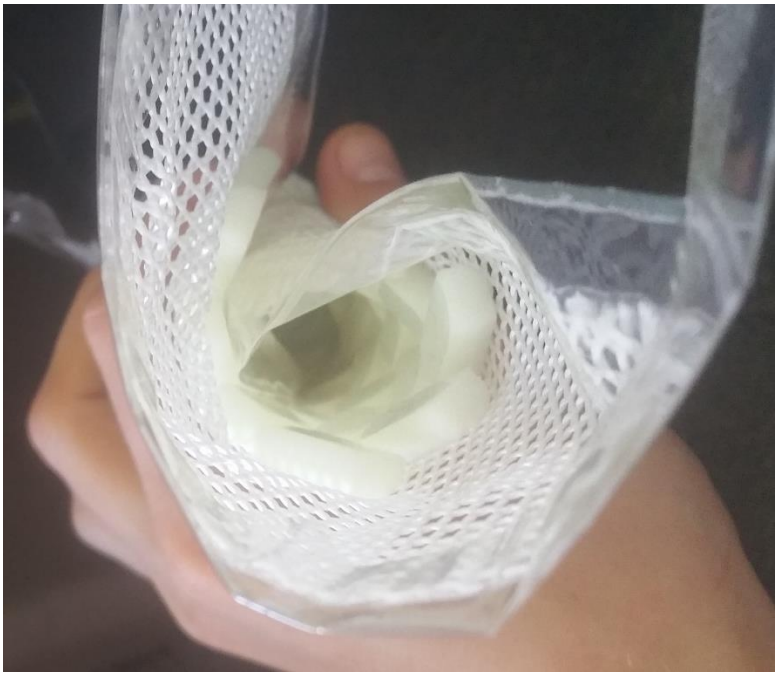

Figure 280: Curvature of the array at lockup after bending along the axis associated with highest curvature (shown in blue in Figure 279)

Figure 281: Lockup after bending about the axis associated with moderate curvature (the green axis in Figure 279).

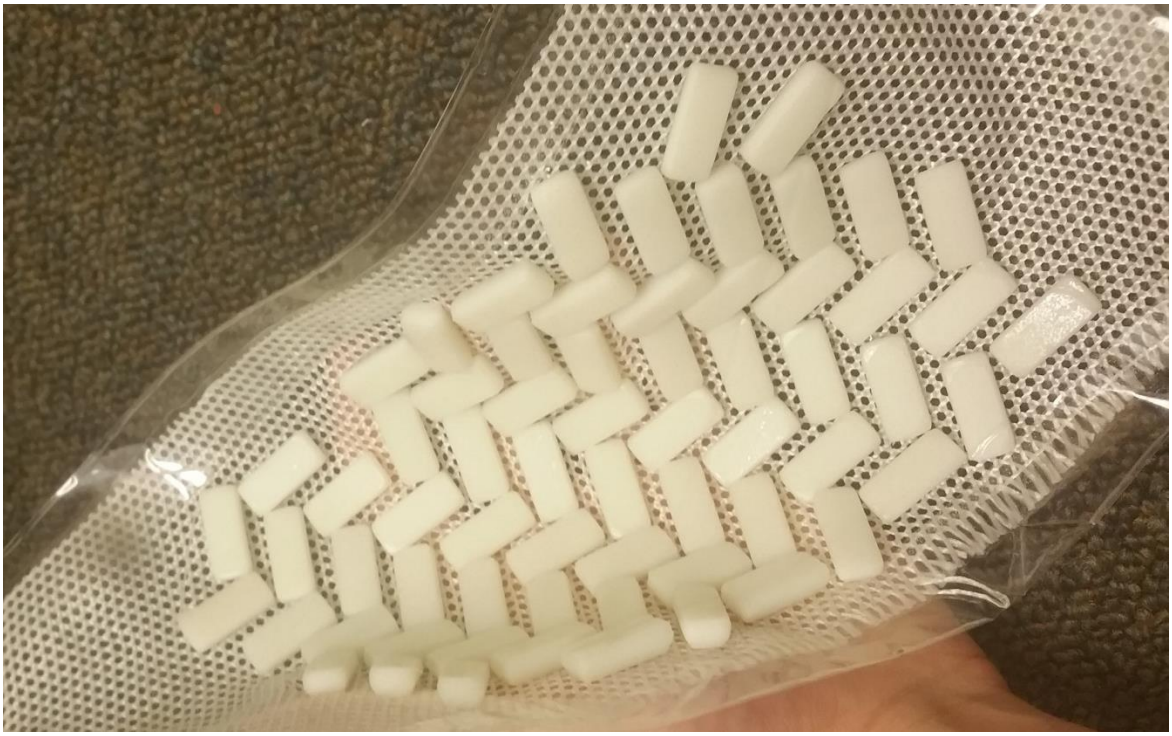

Figure 282: Auxetic-inspired tooth array, bent just until teeth touch (without any further deformation). The axis of bending here corresponds to the orange line in Figure 279.

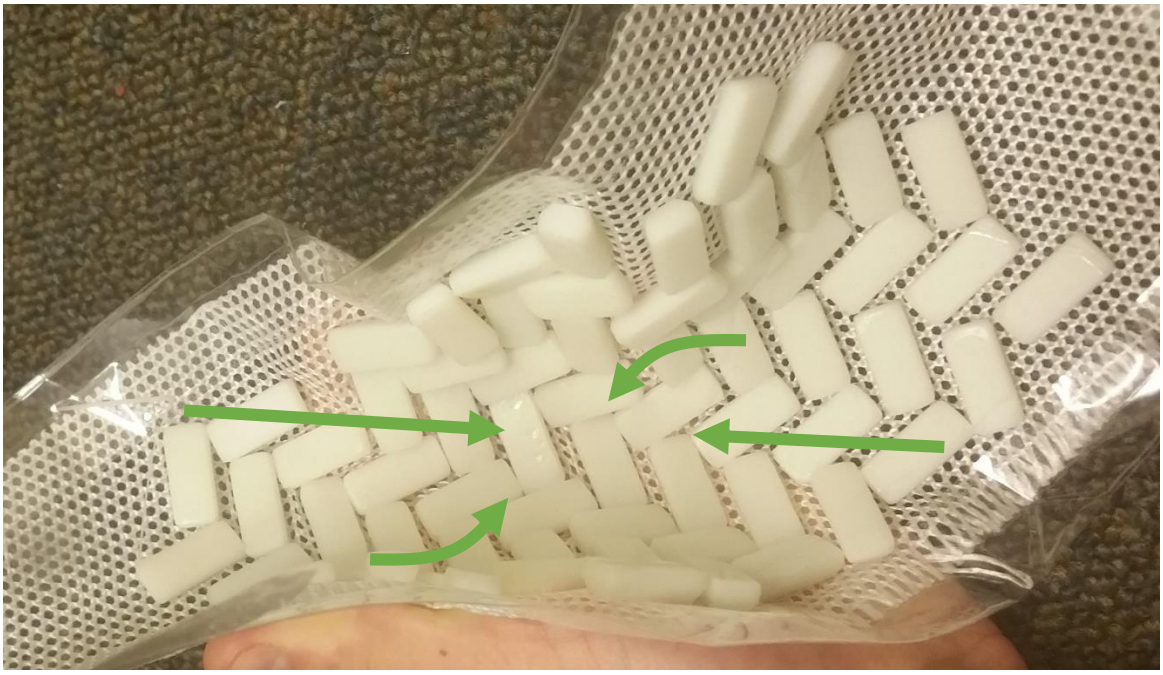

Figure 283: Further bending deformation along the axis of the previous figure. Note how the teeth rotated somewhat in order to close up the parallelogram-shaped gaps, producing biaxial contraction in the direction shown by green arrows.

Auxetic-Inspired Kite Array.

The researcher was also curious to establish whether traditional sources of auxeticity other than special gap shapes for planar beam networks would translate into auxetic-like behavior for tooth arrays in bending. As discussed in the chapter on annular combs, trusses composed of arrays of four beams connected to form a kite have strong Poisson effects, with Poisson's ratio approaching -7 for certain geometries. Although it was far from clear that making teeth with the same shape as the holes in these arrays would produce auxetic effects, it was attempted, with the tooth geometry used shown in Figure 284, the tessellation pattern in Figure 285, and the entire array in Figure 286.

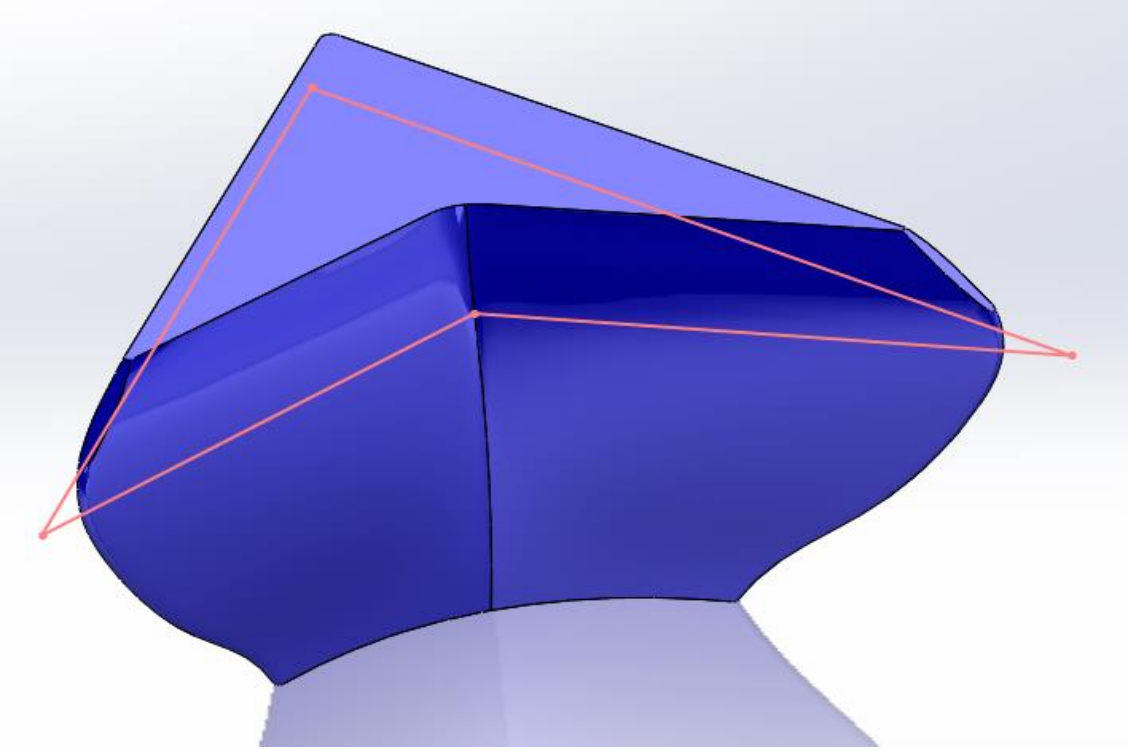

Figure 284: A single kite-shaped tooth.

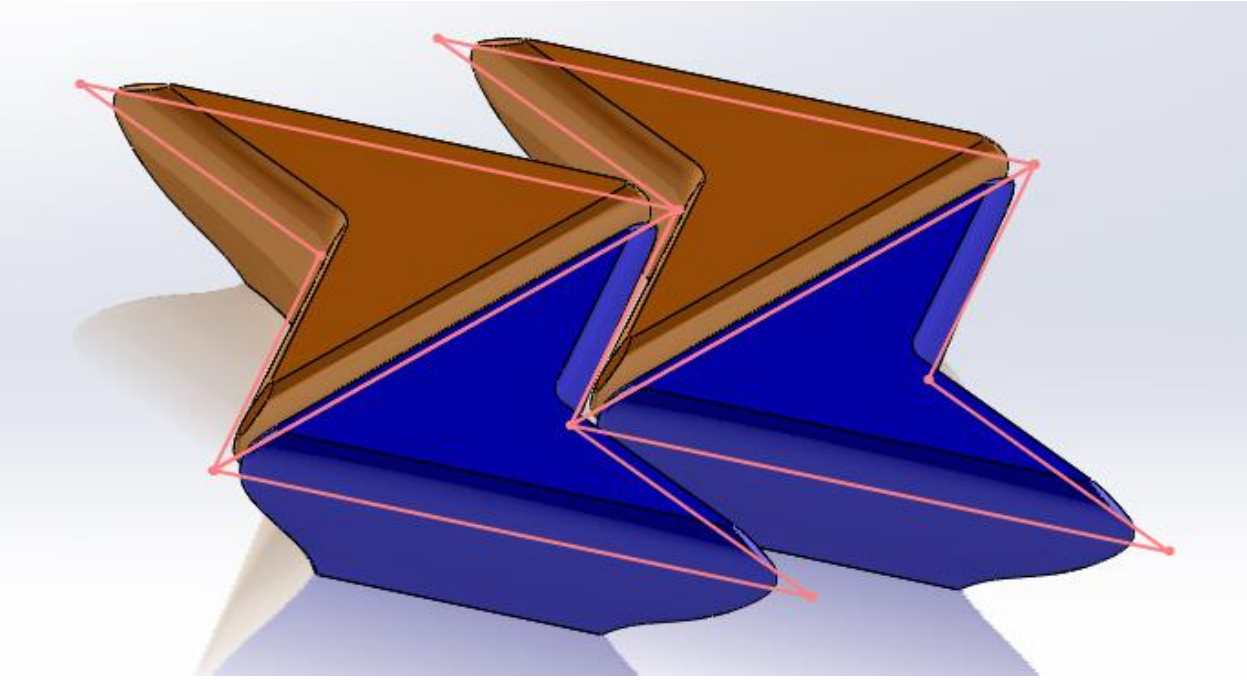

Figure 285: Four kite-shaped teeth in tessellation. The colors of the teeth do not indicate handedness as chirality is irrelevant in the tessellation of quadrilaterals.

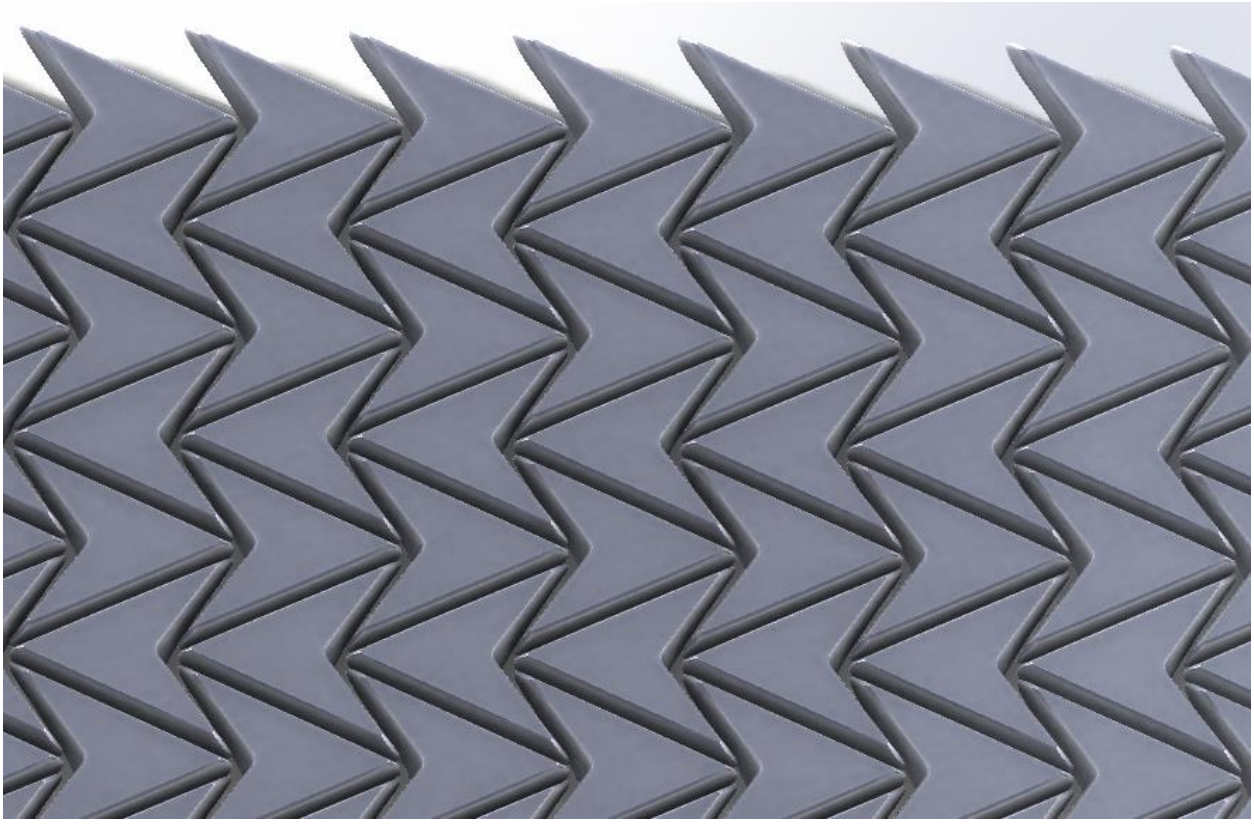

Figure 286: Computer rendering of an entire array of kite-shaped teeth.

Unfortunately, resulting array had no discernable properties of interest, aside from relative curvature isotropy (thanks probably to the four unique normal contact directions it possessed). Figure 287 and Figure 288 show curvatures at lockup in a couple different bending directions; they appear quite similar. The array did not have any observable auxetic effects, nor did it see any sympathetic deformation in uniaxial compression. It also did not have synclastic curvature of any kind: not only did it not see sympathetic bending about one axis with forced bending about an orthogonal axis, but (as with most arrays) bending about one axis reduced freedom to bend about the orthogonal axis. Finally, the tips of the teeth had such small radii that they saw significant plastic deformation and even crumbling when they contacted other teeth; such features should be avoided in production.

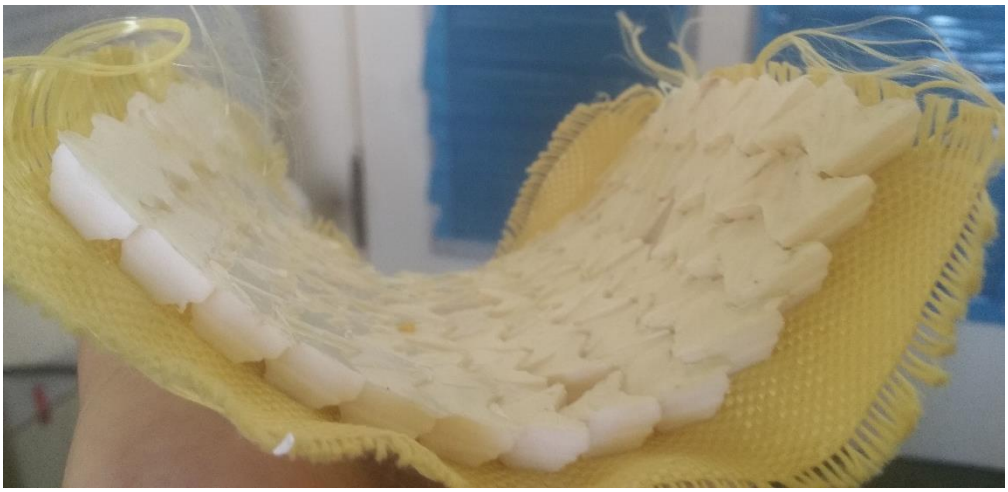

Figure 287: Lockup curvature in bending along an initially-horizontal neutral axis.

Figure 288: Lockup curvature in bending about a different axis from the one shown in Figure 287.

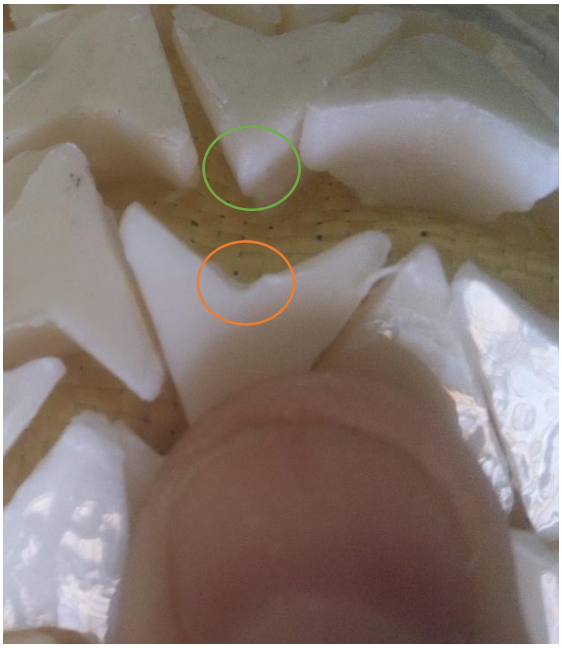

Figure 289: A deep gouge in one tooth (circled in orange) thanks to the indentation of the tip of another tooth (circled in green).

Hirschhorn Tiling.

The Hirschhorn tiling of chiral pentagons is not a true tessellation, but it has 6-fold symmetry[55]. The main reason it was deemed interesting for this application is its numerous normal directions it possesses might be expected to give the array near-perfect isotropy (ignoring any anisotropic effects added by the fabric). On the other hand, given the irregularity of the array, it could be quite difficult to generate teeth to conform to something more geometrically complicated than a plane. Figure 290 shows a rendering of the individual tooth geometry used, and Figure 291 a rendering of an entire array. Unfortunately, there was not enough time to manufacture this array, and anyways, the P15 tiling investigated above seems to have sufficient isotropy (if that is desired) in curvature at lockup.

[55] Michael D. Hirschhorn, D. C. Hunt: "Equilateral Convex Pentagons Which Tile the Plane." J. Comb. Theory, Ser. A 39(1): 1-18 (1985)

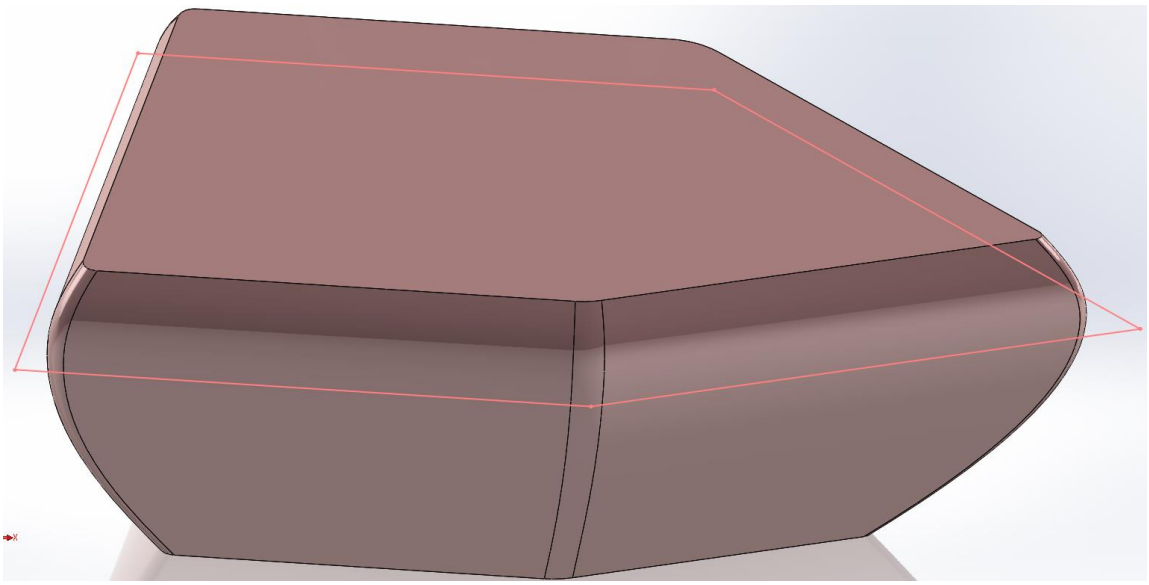

Figure 290: Tooth based on the pentagon used in the Hirschhorn tiling. The outlining pentagon is used for tessellation; the solid itself is somewhat offset from this pentagon, giving the initial clearance.

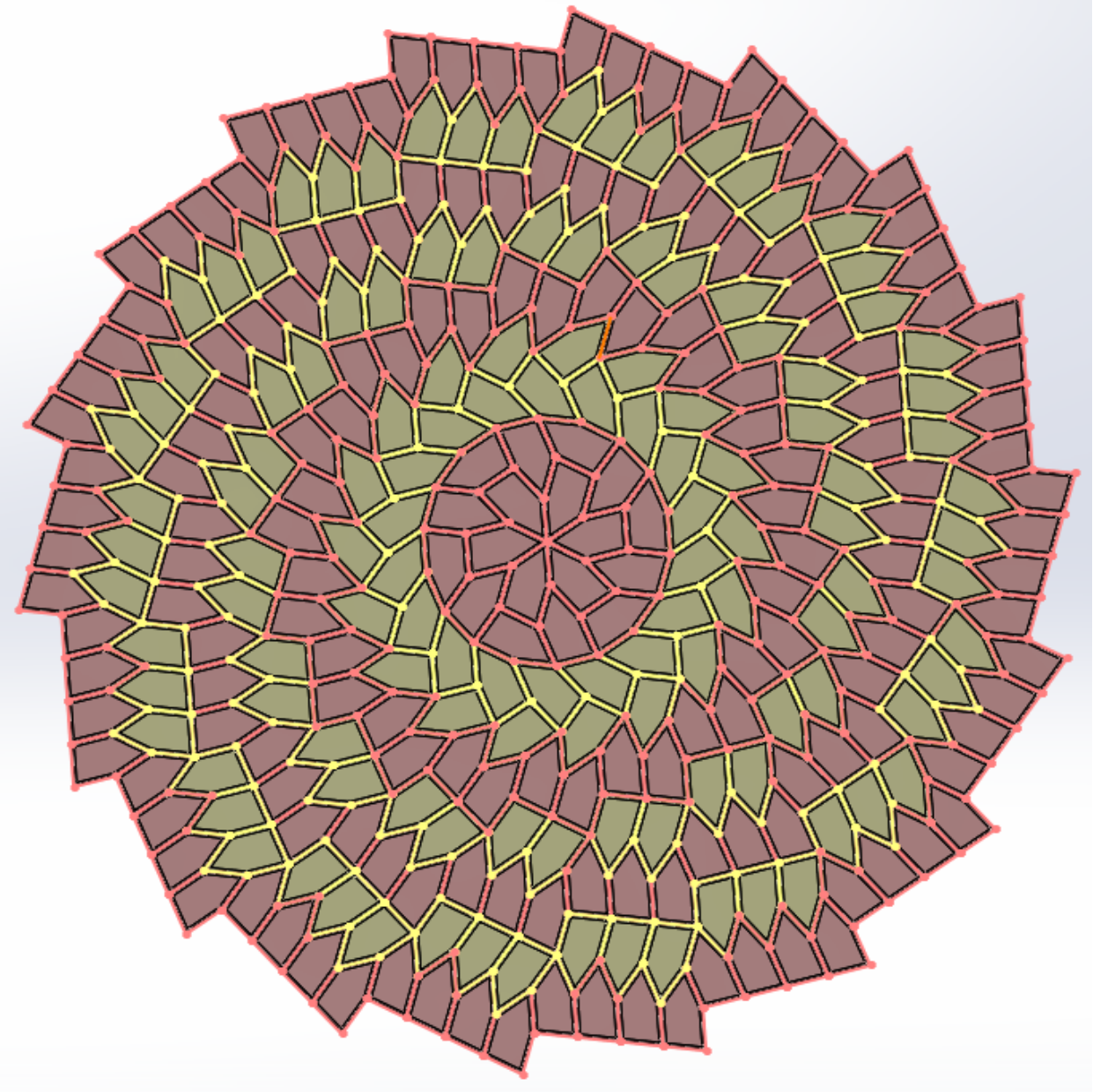

Figure 291: Rendering of tooth array based on the Hirschhorn tiling. The colors of the teeth indicate handedness of the pentagons.

Improving Mechanical Performance of Individual Teeth in Tooth Arrays.

The prime driver of lockup stiffness is using a fabric that has high tensile stiffness, and this is best obtained from high-stiffness fibers. Strictly speaking, a weave (for instance, a knit) that saw stiffening-up behavior in the fabric itself in tension might be an interesting backbone material (as it would give the material a more gradual stiffening-up profile, since it would initially be fairly compliant even after tooth contact), but the strain required to stiffen up would need to be fairly small to produce the high radius-of-curvature seen at the desired lockup geometry. Depending on the amount by which the fabric is stretched when wrapped around the ankle, the structure might need to experience a lot or just a little more tensile strain (which, once the structure is fully stretched, would be expected only after the teeth have locked up) to stiffen up.

Another way to increase post-lockup stress without affecting pre-lockup stress centers around stiffening the teeth: while using Taulman nylon filament for its good adhesion to fabrics, it was deemed advisable to print teeth hollow and then reinforce them with stiff materials, either composite or metal inserts that would be glued to the inside of the teeth. While this was indeed expected to increase post-lockup stiffness (by increasing tooth stiffness in both bending and lateral compression, the two main modes of tooth elastic deformation), it was unclear how significant the change would be. If nothing else, at least making the teeth completely solid (even if just filled with a stiff polymer like a thermoset, instead of a metal or ceramic) might prove a moderate improvement over using teeth printed with roughly 30% internal density (for it is customary when printing with FDM printers to make the perimeters of objects solid but to fill the interior only around 30% with polymer in order to save print time). For instance, Figure 292 shows a slice of a layer for a 3D print of comb teeth in which only the perimeters of the teeth are solid, and the interior is mostly hollow. Of course, it is physically possible to print at 100%

density (although sometimes this requires extra caution to avoid excessive heat retention and part distortion), but that greatly increases production times, which are already the main driver of costs. Figure 293 shows a proposed tooth array in which each tooth is cup-like and can be filled by casting with epoxy resin.

Weaves open enough to permit easy flow of adhesives might have their bonds with teeth strengthened by printing the teeth as inverted "cups"; while this would reduce the contact area between teeth and fabric during the initial print, once the print was completed, the structure could be turned upside-down, and each "cup" feature at the bottom of the teeth could be filled with an adhesive (strictly speaking, it would be desirable to use an adhesive with high enough surface tension that the cavity could be somewhat *over*filled for maximum adhesive-fabric interaction—but without the adhesive spreading to areas of the fabric that are to retain their flexibility). Alternatively, the teeth might be printed upside-down on a solid substrate, then adhesive poured into the cups, and finally the teeth glued to the fabric (and then removed from the hard print substrate), more on which later. Figure 294 shows a section view of a triangular tooth modified with such a cavity to be filled with adhesive.

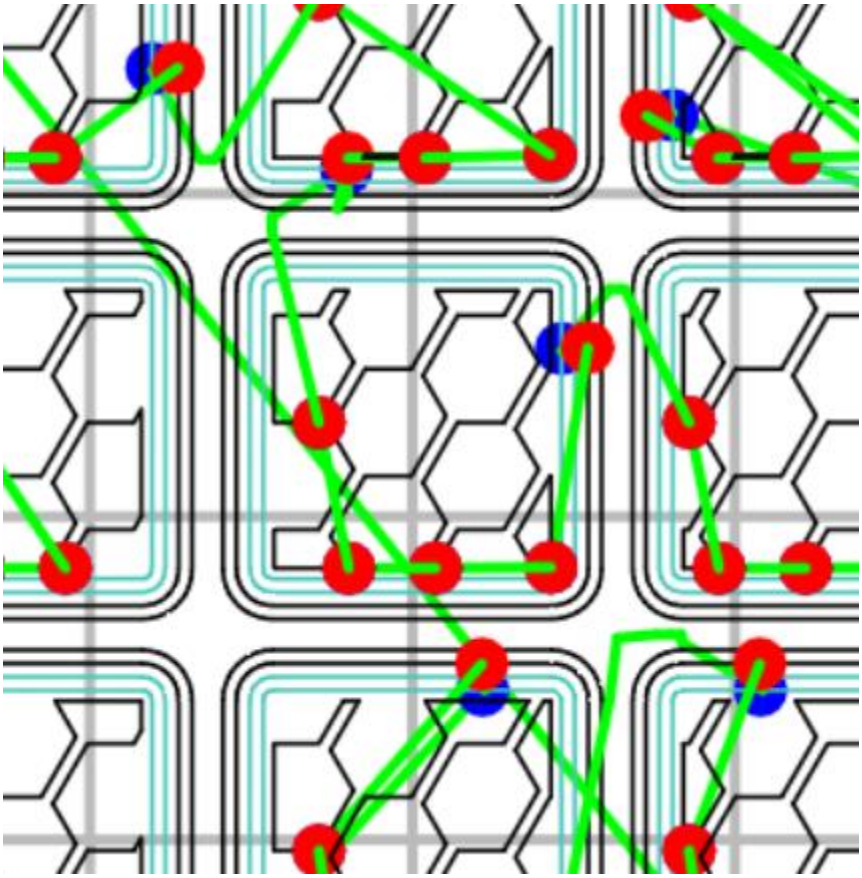

Figure 292: Hexagonal, low-density "infill" area inside solid perimeters to save print time. Taken from the G-code of the standard 9x9 square array. Black and cyan lines show paths along which filament is to be extruded from the 0.5mm nozzle. Green lines show travel without extruding.

Figure 293: Hollow tooth array to be printed on fabric and then reinforced with metal, composite material, or, at the very least, solid resin.

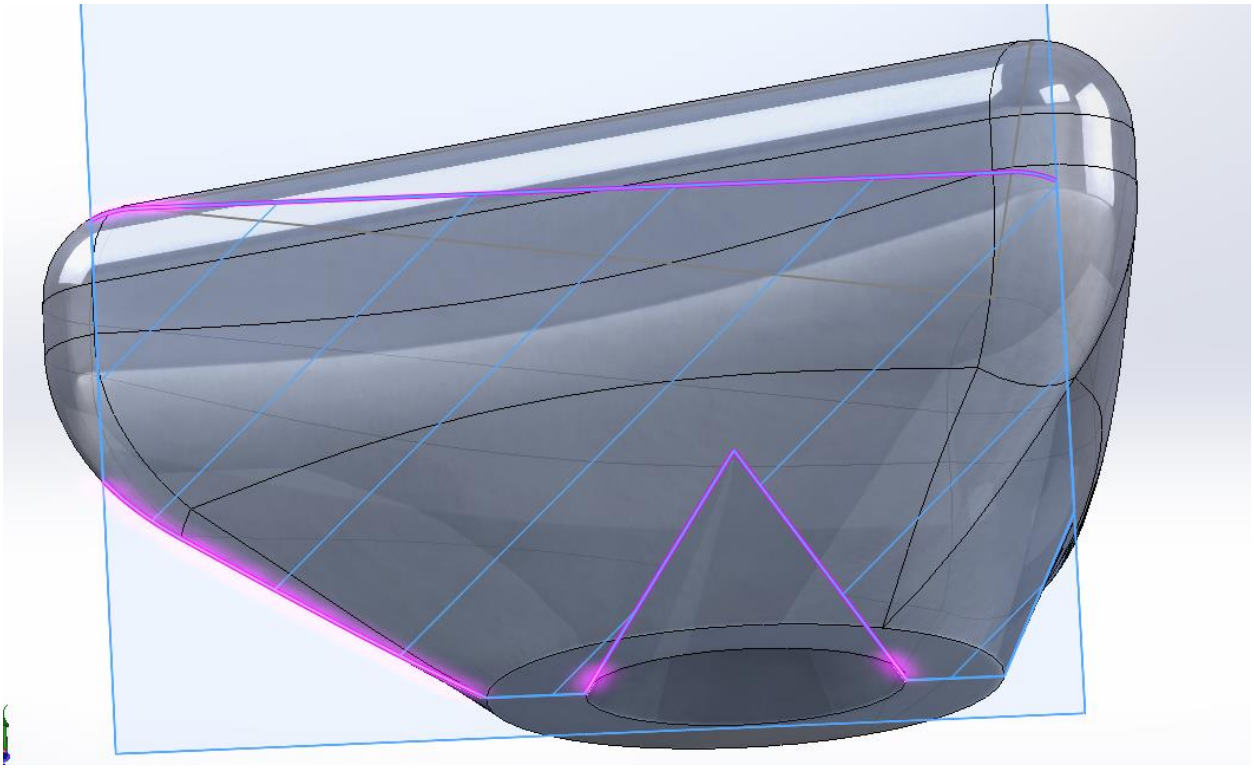

Figure 294: Triangular tooth modified with "cup" recess to be filled with an adhesive once the tooth is printed.

Improving Geometric Accuracy of Printed Tooth Arrays.

Gap Size vs. Tooth Parameters.

It was at first quite difficult to produce tooth arrays with even a relatively large gap of 0.040" between teeth at their closest points, partly because the teeth were being printed directly on fabric, leaving the print very warp-prone just from the compliance of the fabric and its imperfect attachment to the glass bed, and partly because the filament (nylon copolymer) selected for best adhesion to fabric is especially warp-prone. After switching to printing the teeth on glass (to be subsequently glued to the fabric in a separate operation) and using PLA, which is hardly prone to warping at all and is stiffer than nylon to boot, it was easy to obtain prints at drawn tolerances of 0.008" with very limited bridging between teeth that should be separate (and these bridges could easily be separated with a razor). That said, it was not feasible

to measure how consistent and precise the actual gap between teeth was, owing both to the small distances involved and the difficulty in holding the teeth steady.

Reversed Tooth Printing-Justification.

The original print orientation required overhangs of roughly 40° from vertical (in order to produce contact at the tip of the tooth, not at the base, and to ensure plenty of fabric is left unglued to the tooth to give initial bending compliance). Unfortunately, overhangs are not rendered very accurately with FFF 3D printing processes, because molten material does not cool instantly when it is deposited. Indeed, as discussed in the appendix on printing on fabric, overhangs can warp up (throwing the head off position and ruining the print) or bind together (requiring difficult separation of teeth with a razor blade, a process that often sees the fabric accidentally cut with the razor!). Of course, overhangs closer to vertical are more tolerable than those that are nearly horizontal, and the contact area could be increased to reduce the overhang angle, but it might be better to print the teeth separately, specifically inverted vertically so no overhangs are required. Then, the teeth would be glued to the fabric.

Not printing directly on fabric has both advantages and disadvantages. Among the advantages are the ability to do without overhang-induced distortion, developing a process that could eventually enter mass-production (no 3D printing required—teeth could be produced by injection molding or other high-volume, inexpensive processes), and the possibility that a glued tooth-fabric bond would be much stronger than a printed bond (or allow a wider array of tooth plastics and fabrics). Also, since printing on the fabric often sees the teeth "wobble" through interaction with the print head (when plastic has warped up) due to an imperfect bond between the double-sided tape and the fabric, printing the teeth separately on a hard surface would further increase tooth geometry precision. Finally, the double-sided tape employed to hold the fabric to

the glass print substrate (albeit imperfectly!) usually leaves a very viscous and sticky residue on the fabric once it has been heated; this would massively increase friction between a leg and the backbone, and given that test fixture and FEA experiments show the imperative of free sliding between leg and structure, this would be highly problematic.

However, dispensing with printing directly on fabric complicates precise tooth placement on the fabric. If the teeth are printed directly on a surface, and then their faces are painted with glue and a fabric is stretched taut and glued to the teeth, the print surface must not have too much adhesion to the teeth, or it might be difficult to remove them (even with a razor blade). On the other hand, a minimum amount of adhesion between print surface and teeth is required just to print properly. That said, the minimum adhesion is not great, so this may not prove much of a problem.

The teeth might also be printed on the surface, removed manually one by one, and then placed in a guide (also 3D printable) to hold them in the proper position to be glued. The guide would prevent *xy* motion but allow the manufacturer to lift the fabric straight up once the glue had cured. It would be particularly suited to fixing mass-produced teeth.

Regardless of the method of precisely positioning teeth, they might be welded to the fabric instead of glued (especially if the weave were relatively open to permit easy heating of the teeth, and if the fabric were made out of a material like fiberglass, Nomex, or Kevlar, that can tolerate the high temperatures at which the teeth might melt). However, gluing is likely to produce a stronger bond and be easier to implement, too.

Inverted Tooth Arrays—Implementation.

The manufacturing concept of printing the teeth face-down on a solid surface, gluing them to a taut piece of fabric, and then trying to remove the teeth seemed better-suited to low-volume manufacturing (i.e. prototype testing) and was thus preferred to the other means of manufacturing discussed above, at least if it would work.

A hexagonal array was modelled with several new features. First, small holes were produced in what would become the tooth bases once glued to the fabric in order to accommodate a fair quantity of adhesive. These depressions were to be slightly overfilled to ensure that adhesive would flow to cover the bottom of the teeth and ensure a full bond with the fabric. Next, as proposed earlier, the teeth were made hollow with an opening on the future top to allow filling with epoxy (and perhaps high-strength fibers); to print such geometry, however, a central pillar to support the bridged portion of the base had to be added. Finally, as proposed earlier, the teeth were made 50% wider (but no taller) than in the first iteration, with the tooth gap also increased correspondingly. The goal of this modification was to ensure that teeth did not blend together; however, it might be unnecessary for this mode of printing (since the tooth outer surface is no longer subject to the distortions occasioned by warping overhangs), which would allow a return to a smaller tooth gap (for faster lockup) and/or tooth footprint. Figure 295 and Figure 296 show CAD images of this proposed tooth array.

Note that this orientation *would* produce overhangs on the inside of the teeth (they would need to be made solid or infilled to prevent this), but since the inside does not need to be dimensionally precise to ensure precise lockup, this was not thought likely to be problematic. That said, if these overhangs warped up enough, they could throw the print head off in x or y and thereby ruin the print.

Figure 295: Print orientation for inverted teeth. Note the slight depressions in what will be the bottoms of the teeth (currently oriented upwards for the print) to be filled with glue that will attach the teeth to the fabric.

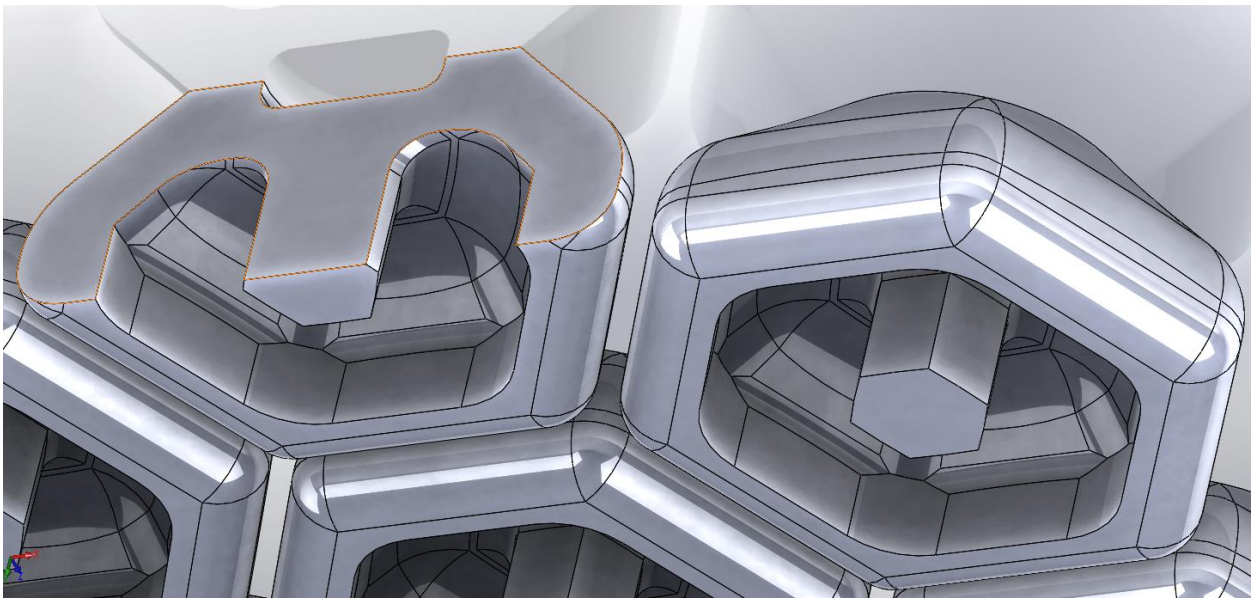

Figure 296: Underside view of the teeth. They will be hollow on the inside (and finally filled with epoxy for stiffness). The center "post" is only to facilitate printing.

Unfortunately, this design was surprisingly prone to warping, even with the most warp-resistant print settings (i.e. using PLA with a warmed chamber and bed); should one corner of a tooth would warp sufficiently, the print head will usually be thrown off course, thus shifting the position of one layer suddenly enough to ruin the print. Warping appears to occur because the "dome" shape of the inside of the inverted tooth has an overhang angle too close to horizontal: it could likely be reduced by making the base area of the printed (unfilled) tooth larger, though this

would reduce the volume available for reinforcement (certainly increasing print time, and perhaps reducing mechanical performance relative to what could be achieved with more of the volume consisting of high-strength reinforcement instead of printed filament). That said, filling the teeth with high-strength material is likely unnecessary: experimentation with teeth made of PLA (which is much stiffer than the nylon originally used) suggest that merely switching print material from compliant nylon, even at lower infill densities, makes the teeth stiff enough for tooth stiffness to no longer be the limiting parameter (rather, the bond between teeth and fabric is). Also, lower infill densities are desirable inasmuch as they keep down the overall weight and inertia of the structure.

Increasing Bond Strength between Teeth and Fabric.

While the question of how to make the bond between fabric and teeth strong enough that the teeth cannot be sheared or pulled off in service may be one that can be deferred until the tooth geometries are nearly finalized, some preliminary ideas for increasing the bond strength are disclosed here. First, the most obvious choice is to select a fabric for which there exist adhesives that bond well to it, and then employ one of those adhesives; a preliminary investigation into the bond strength between several high-strength fabrics and several commercial adhesives targeted at bonding plastics is to be found in Appendix III. (Of note, the bond strength between the adhesive and the printed part is rarely the limiting factor). Next, there appears to be some advantage in choosing a fabric weave that is somewhat open, allowing the bond with the tooth to be reinforced from the other side (either with more epoxy, or with an adhesive that bonds to cured epoxy as well as to fabric and 3D printed parts). The structural cyanoacrylate discussed earlier in this section was often used for this purpose, its low viscosity proving to be quite useful in allowing it to penetrate even denser fabric weaves.

However, if the above chemical modifications cannot produce a sufficiently strong bond, then it may prove necessary to add some mechanical features. While not simple, the threaded fastener system sketched in Figure 297 would likely prove quite strong. It consists of the tooth proper (now featuring a lengthwise hole, which need not be threaded), the fabric (which should have a hole pierced in it to allow the long fastener to go through it), a base plate that will abut the head of the fastener on the opposite side of the fabric from the tooth, and, at the very opposite end of the fastener, a threaded nut. Tightening this nut will pull the base plate into the fabric. Note that both the base plate and the tooth proper should be glued to the fabric as well. The long fastener and matching nut could be made of a high-strength plastic or a lightweight metal like aluminum. Admittedly, the improved bond strength of this system might be overshadowed by the annoyance of having objects on the side of the fabric contacting the leg; however, perhaps a soft cap over the fastener head would reduce the irritation this could cause.

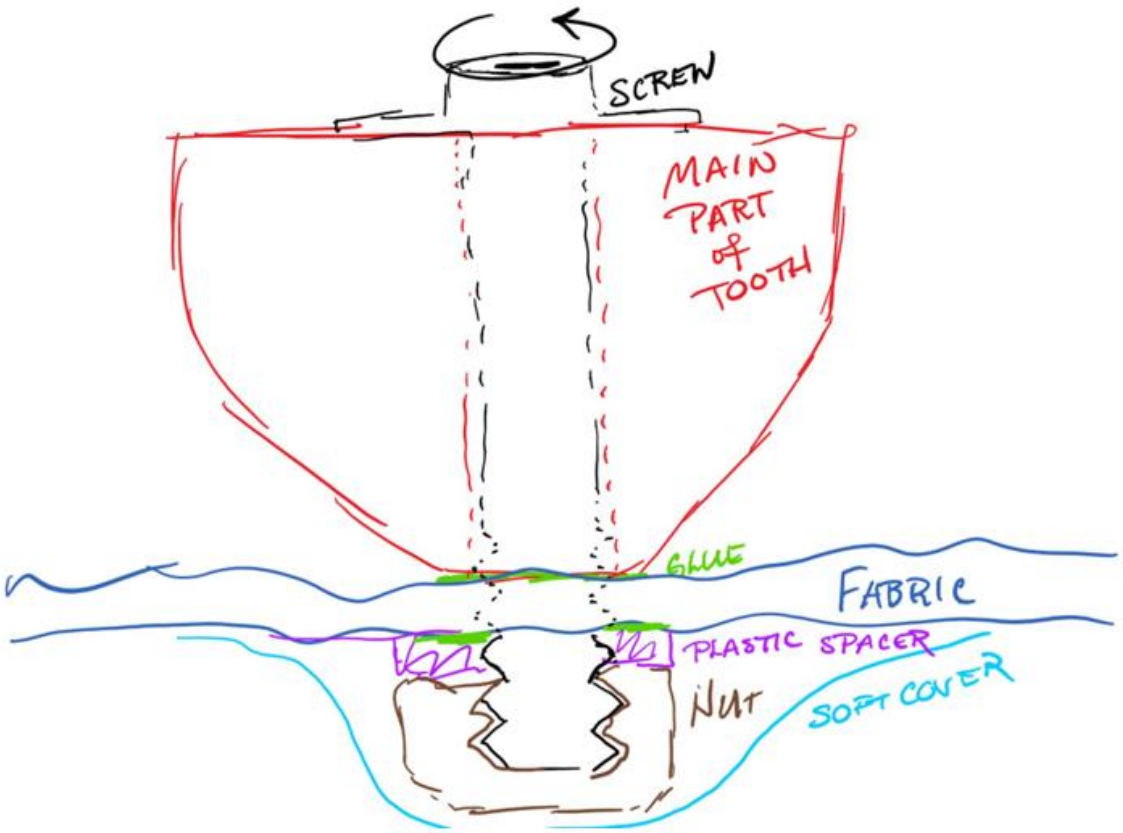

Figure 297: Sketch of proposed threaded fastener system for holding the teeth to the fabric. The threaded fastener should later be replaced with rivets, which are cheaper both to purchase and to assemble.

Another option might be to take advantage of the high bond strength between structural epoxies and high-strength fibers like Kevlar by 3D printing hollow shells for the teeth, placing these over the fabric sheet, placing a watertight non-stick sheet (for instance, one made of a fluoropolymer) underneath the fabric, and then pouring epoxy precursor into the hollow molds; some force would likely need to be applied to the nearly-filled molds to prevent uncured epoxy from leaking out from under them. Once the epoxy is cured, the fabric could be lifted off the non-stick sheet; the teeth should then consist both of the molds (which could be printed of a tougher material, such as nylon, to resist surface abrasion) and the cured epoxy inside; it would not be possible to reuse the molds. (Alternatively, the molds themselves could be printed of a

fluoropolymer and then removed and reused once the epoxy inside them was cured). If the non-stick sheet was somewhat compliant through its thickness, the pressure from the edge of the tooth mold would compress it enough that the fabric next to the base of the tooth would have an indented shape, allowing more adhesive to be filled in here if desired. The epoxy precursor could even be pressurized to reduce voids (although this would be useful mainly for reducing voids near the fabric, as the teeth themselves are not likely to fail before debonding from the fabric). While this setup would force the teeth to be solid (instead of having low-density infill as in 3D printed teeth, which gives the teeth low weight, albeit at the cost of strength and stiffness, which nonetheless does not appear to matter much), complicated molds could be devised to produce hollow centers for a lighter finished product. A sketch of this proposed process is shown in Figure 298: Sketch of tooth-filling process that should also see a strong bond between the filling epoxy and fabric. Admittedly, it is probably too complicated for implementation unless maximum tooth strength proves necessary (which thus far it hasn't).

Figure 298: Sketch of tooth-filling process that should also see a strong bond between the filling epoxy and fabric.

"Rivets" that Improve Bonding.

Fortunately, a much-simpler bonding strategy has been devised and appears to produce sufficient bond strength. It entails printing teeth bases with wells of significant volume (as in previous strategies), but in this case the purpose of the wells is two-fold: not only do they hold enough cyanoacrylate adhesive to coat the fabric, but they are also sized to accommodate a "rivet". The rivet is pressed in with some interference between the fabric and the cylindrical face of the tooth well and mating cylindrical face of the rivet. While the resulting press-fit is not nearly strong enough to hold the fabric to the tooth by itself, it can help orient the fabric before the adhesive has dried. However, its main purpose is to ensure that the adhesive thoroughly wets the fabric by forcing the fabric into the pool of adhesive; unriveted fabrics tend to arch slightly over the center of the tooth, scarcely being wetted by the adhesive. This bonding system has the

added benefit of increasing the surface area over which the fabric contacts the tooth (and over which bonding can take place when adhesive is applied) thanks to the flat face of the rivet, which compresses fabric against the flat base of the tooth.

Initially, the rivets used were solid (with a clearance of 0.015" printed for a 0.004" thick Kevlar weave) as rendered in Figure 299; they were sprayed with acetone-based activator spray just before being forced into the fabric laid on top of a tooth (whose well was already filled with cyanoacrylate adhesive). However, it was determined to modify the rivet shape with a central hole, as rendered in Figure 300. The corresponding manufacturing process thus entailed filling the tooth well with liquid adhesive, placing the fabric sheet over the tooth, pressing in the rivet with the central hole, pouring a little more adhesive down this hole if necessary to ensure it was full, and then adding a drop of activator from a PTFE needle. This process is illustrated with a sketch in Figure 301. The use of rivets with central holes allows for more consistent activation than could be achieved by spraying the rivet immediately before insertion (perhaps because the activator's carrying agent acetone evaporated away before the coated rivet encountered any adhesive that had penetrated the fabric) and also permitted the addition of extra adhesive through the central hole to ensure the fabric surface was wetted as well as possible.

The rivets were found to significantly improve bonding with both cyanoacrylate and basic hot melt adhesive. This is likely due nearly exclusively to the way in which they cause the fabric to be better wetted with adhesive, and not thanks to a strong press fit between the two plastic surfaces (as true rivets in jeans, for instance, work). If so, a modified version of the rivet that distorts the fabric less and just tries to force it to dip slightly into the pool of adhesive may be preferable; one such geometry is rendered in Figure 302. However, a picture of a real array bonded in the original fashion (i.e. in which the rivets pressed deeper into the fabric and

somewhat distorted it) is shown in Figure 303, and the distortion in the backbone seems mild and unlikely to worsen the mechanical properties of the array.

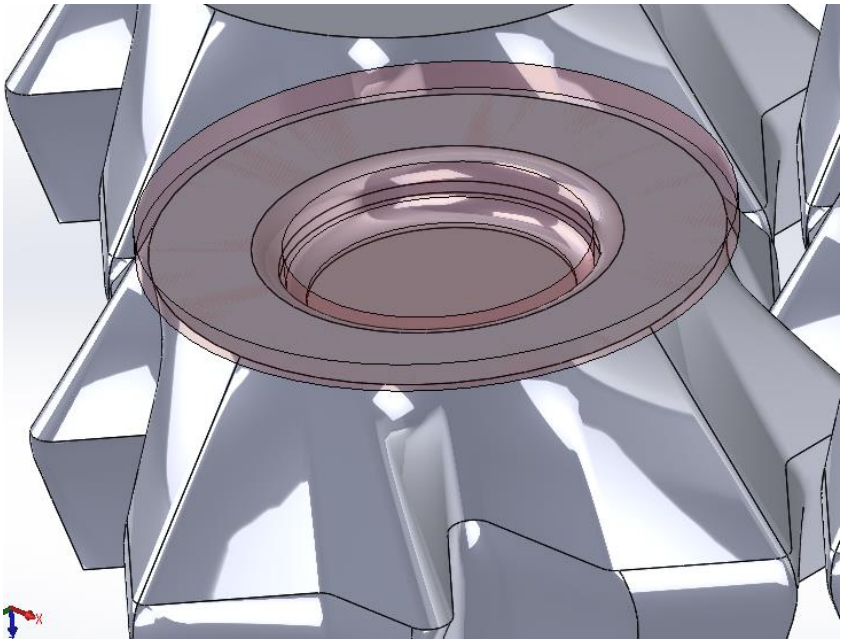

Figure 299: Simple, glue-aided rivet system (with tooth shown in grey and rivet transparent in red). Note the clearance between the projection of the rivet and the base of the tooth.

Figure 300: Rivet modified with hole in it to allow activating chemical to flow through and activate cyanoacrylate.

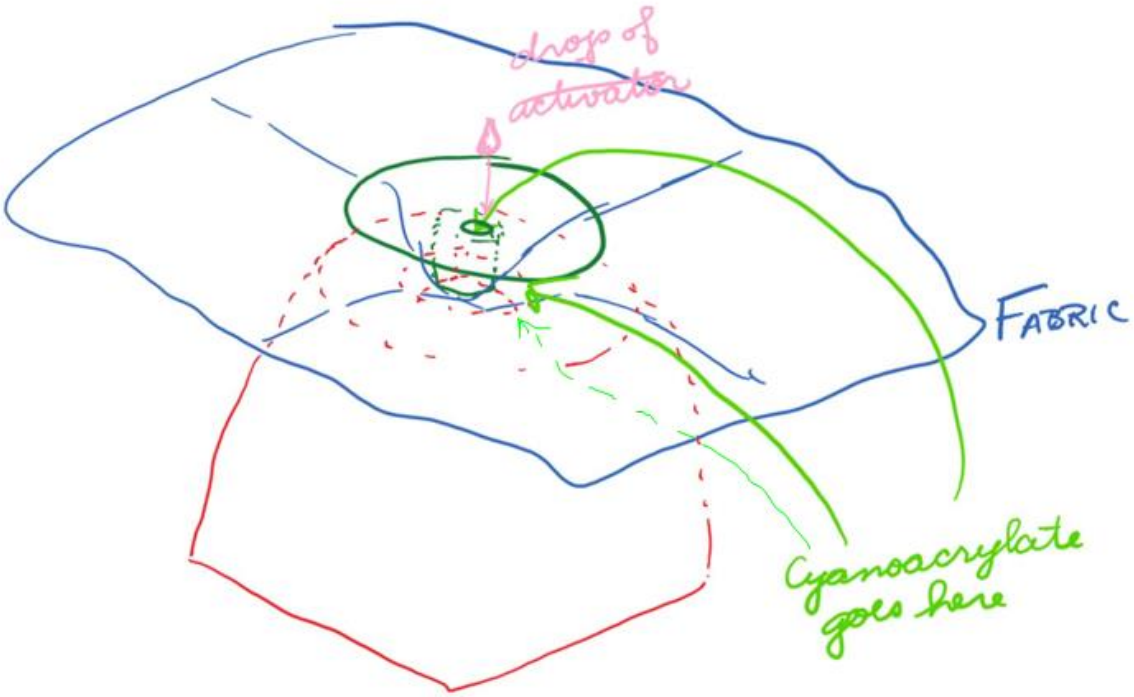

Figure 301: Sketch of "riveting"-gluing process. Tooth shown in red.

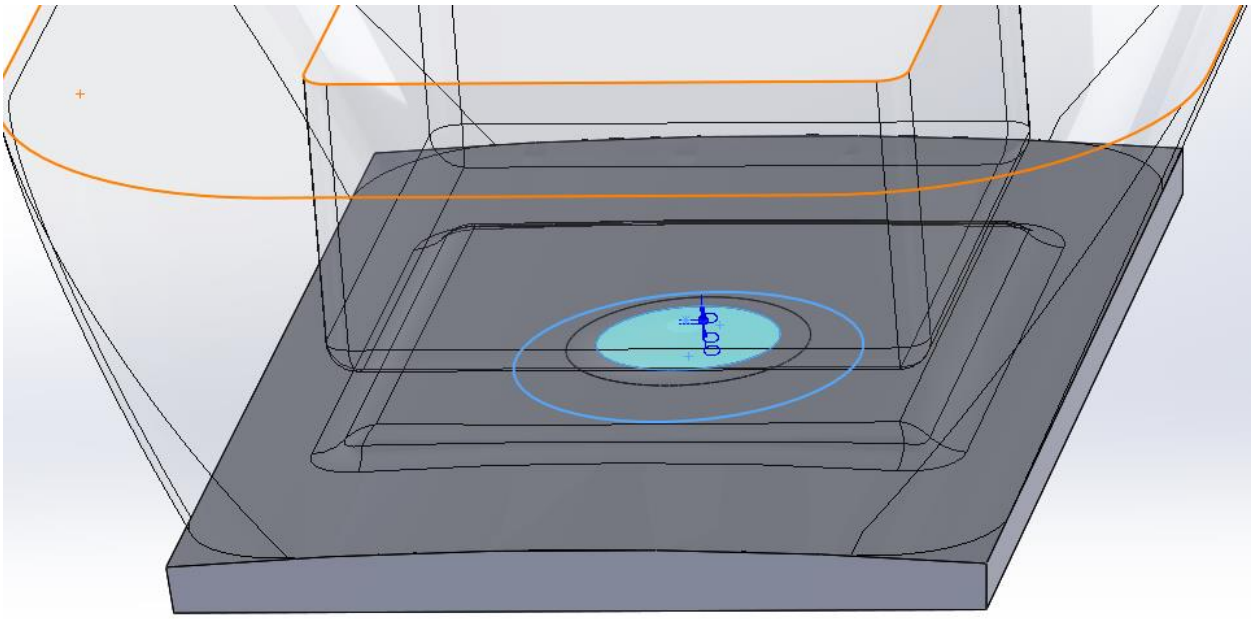

Figure 302: Another "riveting" option, in which the main function of the "rivet" is simply to introduce activator to the fabric and hold it in place, not relying on a press fit of any kind between a face on the rivet and a face on the base part. The conical feature highlighted in blue pierces the fabric slightly.

Figure 303: The underside of a fabric-backed array, showing rivets used to improve bonding between the teeth and the fabric.

Proposed UV-Activated Adhesive Strategy.

While this technique could certainly be used in mass production, future research should investigate the use of cyanoacrylates that cure only with UV light instead of chemical activation. Several potential benefits are envisaged from the use of UV-curing adhesives: most importantly, UV curing should ensure complete activation of the adhesive, which can be somewhat difficult to do with chemical activator while still coating the surfaces to be glued and yet avoiding premature activation. Also, there should be a near infinite work time with such adhesives, whereas the chemically-activated adhesive has a tendency to cure even without exposure to the activator spray (albeit slowly). Similarly, errant droplets from a spray targeted at another tooth can prematurely cure adhesive elsewhere. If this strategy were adopted, then the plastic components (teeth, rivets, etc.) would need to be produced in plastic transparent to the UV wavelengths required to cure the adhesive, and if the fabric used was itself opaque to UV light, light would need to be applied to both sides of the fabric.

Test Fixture with Fabric Arrays.

The test fixture developed in the previous chapter on the linear combs was retrofitted to test fabric arrays. First, an array to be tested had to be folded around the "leg" base and was attached thereto with a tensioned steel band (tightened around the base row of teeth). Next, the fabric needed to be attached to itself at the top to close it into a cylinder; this was most expediently accomplished by gluing (using structural cyanoacrylate and activator) for these tests. In basic tests, the glued area did not come apart, and gluing only above the protruding screw that gives one of the axes of the ball joint allowed non-destructive removal of fabric "socks". Of

note, neither of these mounting methods would be suitable for the final product: snaps, clips, and similar non-permanent mechanical attachments would be preferred for the top part of the product, and the base might be mounted securely into the shoe. Note that the "leg" consisted of a shaft wrapped with cardboard (for moderate contact stiffness approximating that of leg muscle) and coated with a low-friction Teflon-based tape.

Chapter 7. Planar Arrays Wrapped Cylindrically.

Introduction.

This chapter builds upon the research into planar fabric-backed arrays that stiffen up in bending by evaluating their properties when they are wrapped around a test fixture consisting of a cylindrical "leg", cylindrical "foot", and a ball joint between the two. Tested arrays included a square packing of square teeth (modified to prevent sliding) and multiple hexagonal packings of teeth based on the paradoxical gear (that have the added property of sympathetic cylindrical contraction in gross array compression); all were based on fabric backbones made of square weaves (giving the entire structures compliance along the bias). After experimenting with potential boundary conditions at the top of the wrapped array (namely where the leg is free to slide relative to the wrapped structure, versus fixed to the wrapped structure), it was determined that free sliding is essential to pre-lockup freedom. With this boundary condition, one array was found to produce real initial freedom and then substantial lockup thanks mainly to localized bending lockup of the array; shear lockup did not appear to occur, although a different tooth spacing might allow this.

Test Fixture.

The test fixture used for this study was largely developed previously for evaluation of the linear comb (see Figure 43 on page 69). However, for this application it had to be modified with a thicker "leg", since the contact behavior between the actual leg and wrapped "sock" is an

important mediator of force flow. Additionally, to accommodate a purely-cylindrical array without bunching the fabric, the base part (simulating the foot) had to have a ring fitted to give it a contact face of the same diameter as that of the leg. Figure 304 shows one of the parts used to increase the diameter of the part of the "leg" that would contact the protective "sock", and Figure 305 shows the entire assembly, minus a protective "sock". Note that these parts were produced in several different diameters, both to experiment with the effects of clearance distance between "leg" and "sock" on joint behavior, and to accommodate errors in "sock" diameter (since the "socks" were quite stiff in the tangential direction and could not be stretched over the "leg").

Figure 304: This part slid over the main arm of the "leg" (hence the oddly-shaped T-slot through the cylindrical axis) to properly contact the "sock".

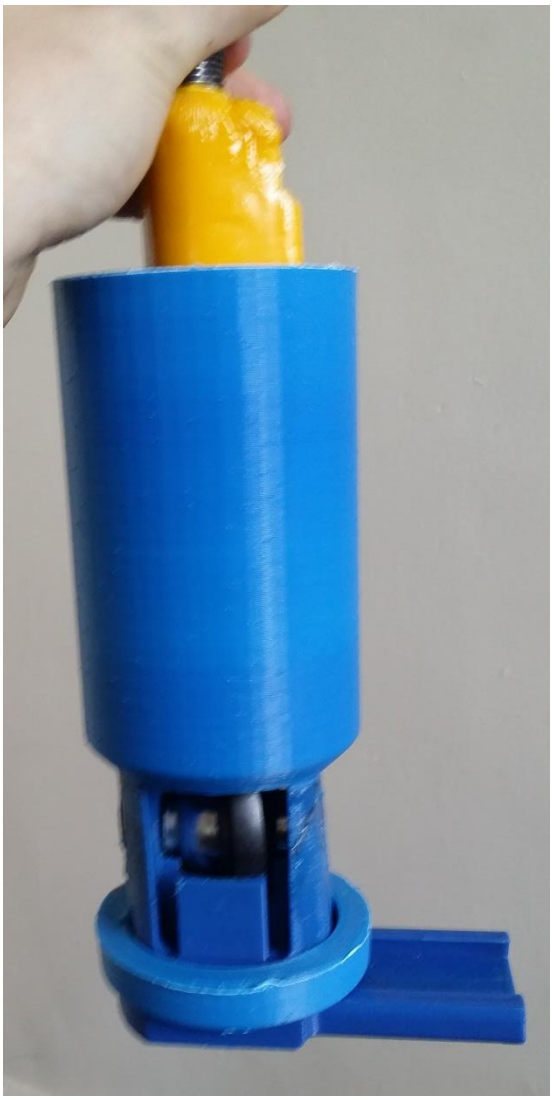

Figure 305: Ball-joint test fixture with surfaces for fabric in light blue. The top, light blue part is to slide relative to the "sock"; the bottom, ring-shaped part is to have the "sock" tightened against it with a metal band.

At first, it was unclear whether the fabric array should be free to slide relative to the leg, or whether the leg should be tied to the array. However, it soon became apparent that the latter boundary condition was unworkable since it would require the array to be put into tension after even a small amount of leg rotation (which might be well before lockup is desired), and the other side (which would see compression) might also be too stiff since the teeth on the array could help resist buckling. Strictly speaking, another conceivable boundary condition would be for the

angle of the array to be fixed at the top (by some cantilevering device) but still free to slide. While this might be better able to recruit the top-most teeth of the array, it would be difficult to establish a suitable joint without complicated geometries that would be prone to jamming.

Moderate clearances had to be established between the surface of the leg and the inner surface of the protective array. The clearances were necessary both for the leg to slide somewhat within the sock, and for the sock to be put on and removed in the first place. These were especially important because most arrays tested here used the "riveting" method of improving the bond between fabric and teeth discussed in the previous chapter, and these rivets were on the order of 0.05" thick (and had rough surfaces). In the final product, they should be smoothed (perhaps made of nylon, which would give both a low-friction contact with the leg if the surfaces were smooth, plus good bonding with cyanoacrylates) or even dropped if bonding can be improved sufficiently. Figure 306 shows a close-up view of some rivets on the side of the fabric facing the leg that illustrate the need for added sliding clearance between leg and "sock".

Figure 306: Plastic "rivets" (used to improve glue wetting of the Kevlar fabric) add some roughness to the back of the protective "sock".

The protective "socks" were produced by printing and gluing arrays onto Kevlar fabric, using the bonding techniques discussed in the previous chapter. Due to limitations on the maximum print size of the 3D printers used, the arrays had to be printed in multiple parts (usually 3 per sock); one of the three prints was then transferred whole to the gluing station (the print having been printed either on Kapton tape, with which the filament bonds securely enough that the array could be removed from the print bed without disturbing tooth alignment, or using a plastic "raft") and glued to the fabric. Next, another array was similarly transferred, and fitted by hand to mate with the final row of teeth of the first array with roughly the same clearances used within the arrays (admittedly, this part of the process was subject to some operator error, but most teeth had features to facilitate vertical alignment, leaving only horizontal distance subject to error, and since the teeth are separated tangentially once the array is curved into a cylinder and thus often cannot touch, precise tangential gaps between teeth probably do not matter much). Finally, this process was repeated until an array of the desired final length had been produced. Figure 307 shows an example of a long array produced by combining multiple printed arrays together on one piece of fabric.

Figure 307: Long array ready to be wrapped into a cylinder, consisting of three separate prints (conveniently produced in different colors).

After the arrays were glued onto the fabric, the whole structure was simply wrapped into a cylinder and extra fabric on one side simply glued behind the teeth on the other side. Figure 308 shows an array that has been glued into a cylinder.

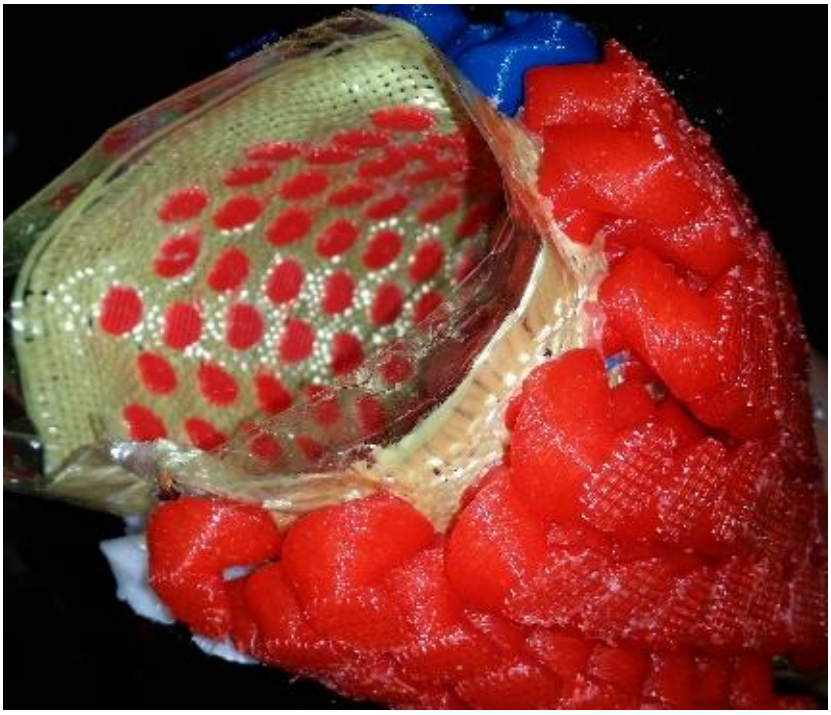

Figure 308: An initially-planar array that has been wrapped and glued into a cylinder.

Finally, the array was slid over both the “leg” and the ring on the “foot”, and then a steel band was placed over the bottom row of teeth, pressing the fabric onto the ring on the “foot”. Figure 309 shows the entire assembly with components labelled.

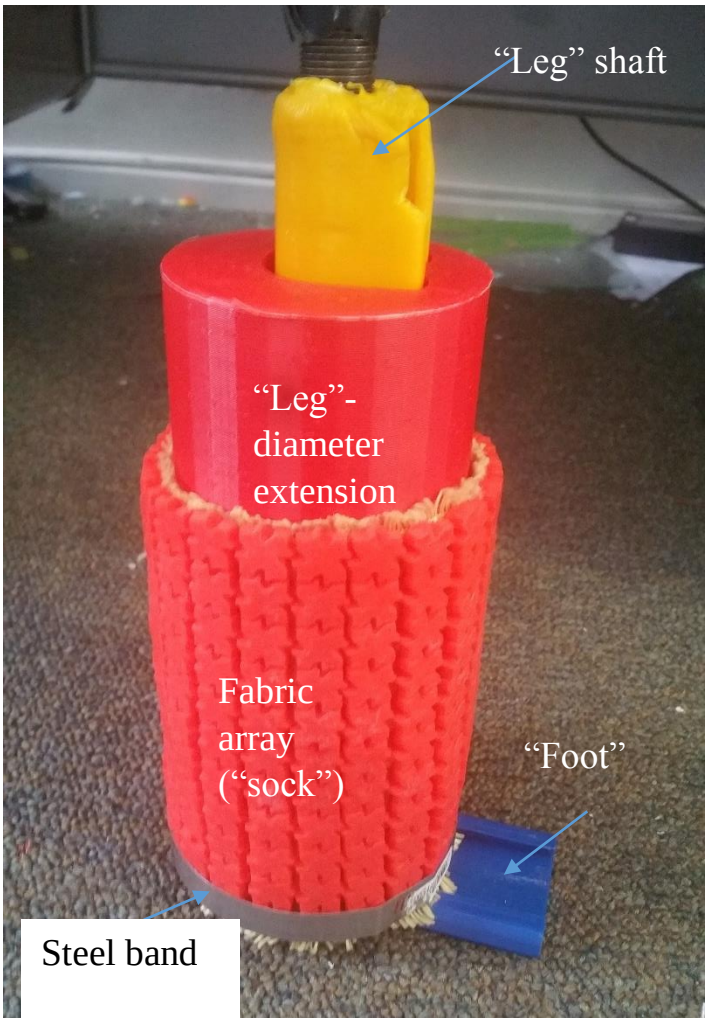

Figure 309: Test fixture with fabric array, leg-diameter extension, and ring (not visible) mounted.

Square-Packed Array of Square Teeth with Anti-Slide Features, 0.018” Vertical Gap.

The first planar array that was to be wrapped around the test-fixture “leg” was produced with a gap between teeth that would produce fairly small curvature at lockup in planar bending. Specifically, this curvature was selected based on what it was imagined a cross section of the array should look like for lockup to occur after some 15° of leg rotation. In other words, it was hoped that the same tooth gaps in the linear comb that would produce the desired backbone curvature of a linear comb could be used in a planar array that would be wrapped into a cylinder. The planar array constructed with this tooth gap is shown in Figure 310. Note that the tooth

profile used here was developed in the previous chapter to have features that inhibit sliding both normal to the fabric and parallel to it.

Figure 310: In planar bending, the structure had much more freedom before lockup than it did in cylindrical conformation.

Unfortunately, this array locked up nearly immediately; what little pre-lockup freedom the "leg" had appeared to be due mainly to initial clearances between the face of the "leg" and the backbone (or in the T-slot on which the diameter-extending part slides relative to the underlying rod). Figure 311 and Figure 312 show two side views of the array under moderate load (in opposite rotation directions). While one can see some curvature differences in the arrays under the two loadings (indicating that the structure is not perfectly locked up and completely unable to deform), there is much less curvature than the array could achieve when not wrapped, in the planar bending shown in Figure 310. Clearly, wrapping planar arrays into cylinders reduces their curvature at lockup (as viewed in side projections). Thus, a logical next step for the

investigation was to simply increase the vertical clearances between teeth to well in excess of what planar bending studies would suggest would be necessary.

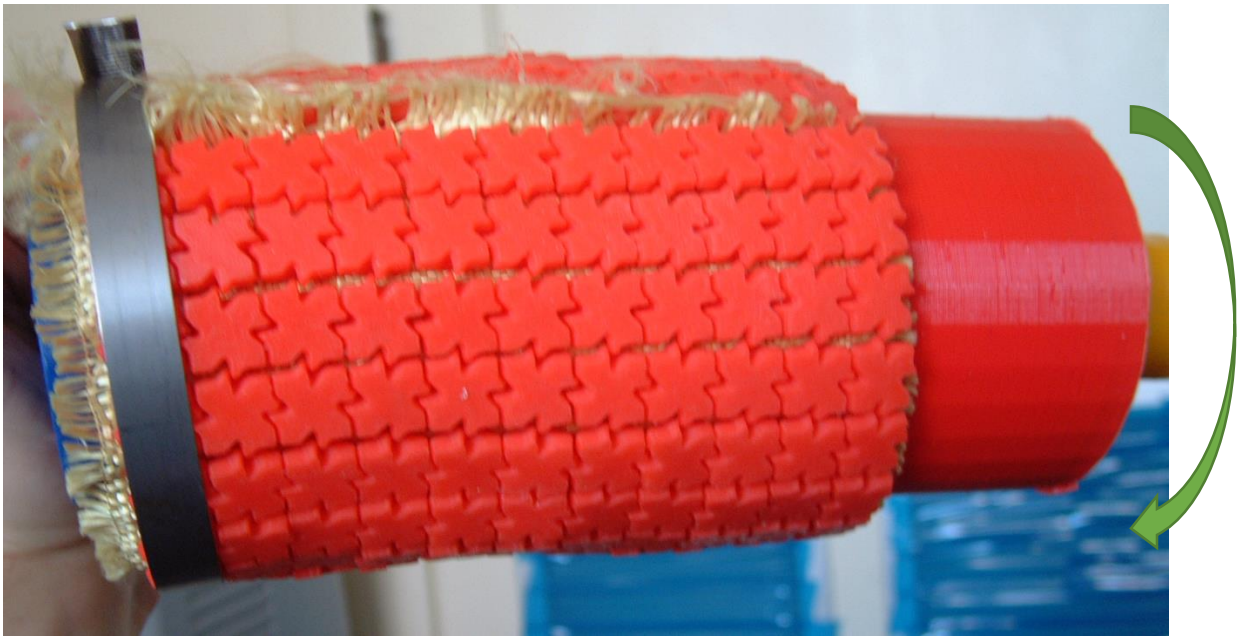

Figure 311: Side view of array mounted on test fixture; the direction of "leg" rotation is shown with the green arrow.

Figure 312: Side view of array mounted on test fixture; the direction of "leg" rotation is shown with the green arrow. (This is the same view but opposite direction of leg rotation from the previous figure).

Square-Packed Array of Square Teeth with Anti-Slide Features, 0.036" Vertical Gap (In Most Areas) and 0.018" Nominal Horizontal Gap (when Flat).

In order to give the joint sufficient freedom when the array was wrapped around it, the clearances in the as-wrapped vertical direction were significantly increased, predictably yielding a very high curvature at lockup. Unfortunately, time constraints required the researcher to use an already-printed section with lower clearances (0.024" instead of 0.036") in addition to the higher-clearance sections. It was decided to simply put this lower-clearance part of the array at 90° to the "leg" rotation in the hopes that it would be recruited only to a limited extent. Figure

313 shows the planar-bending-lockup curvature of the high-clearance portion of the array, and Figure 314 shows the planar-bending-lockup curvature of the low-clearance portion of the array.

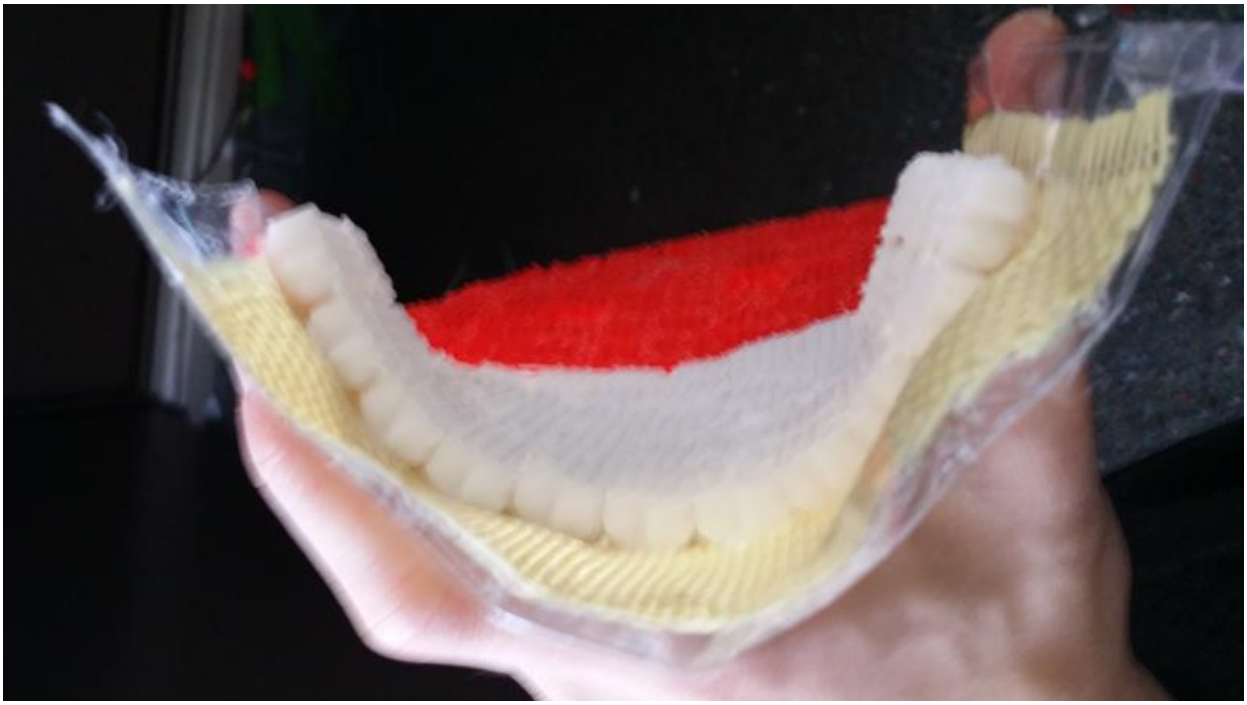

Figure 313: Curvature at planar-bending lockup of the high-clearance (0.036”) portion of the array.

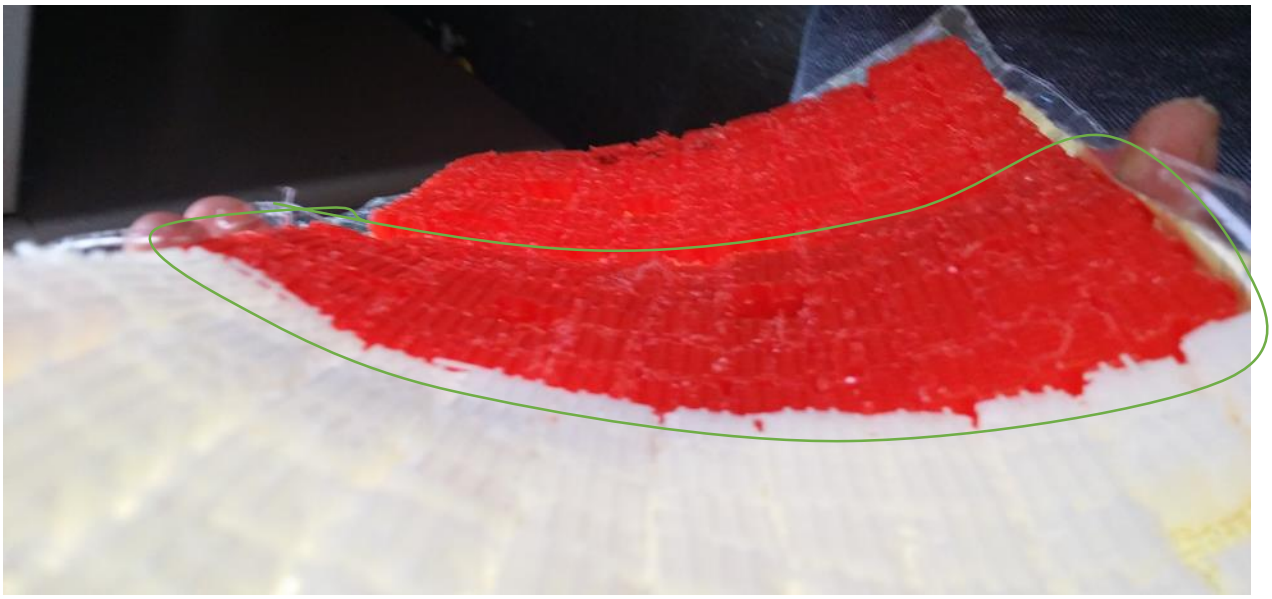

Figure 314: Lower lockup curvature in planar bending of the center part of the array since here (in the region circled in green) the initial vertical clearances between teeth were only 0.024" (compare with the higher curvature in the previous picture).

Gratifyingly, this configuration was basically successful, giving nearly zero initial resistance to joint rotation and then fairly rapid stiffening. Many of the teeth that are facing the direction in which the leg is displaced downwards see significant curvature, roughly that which the planar array with the same tolerances takes on in planar bending (see the circled part of Figure 315), and all of these teeth are nearly immobile to the touch, indicating that it is they that are taking the load. As expected, when the leg was rotated against the third of the sock with the lower clearance value between teeth, lockup occurred more rapidly than when rotation occurred 180° offset, facing the high-clearance portion of the sock. True to the tooth's heritage of being resistant to sliding normal to the plane, there was very limited slippage after initial tooth contact. Interestingly, the areas of fabric roughly 60° to 120° offset (in both rotational directions) from the leg saw significant in-shell shearing, no doubt in large part thanks to the high bias compliance the square-weave fabric possesses; this is readily evident in Figure 315, which shows the leg rotated against the high-clearance portion of the "sock". To a lesser extent, it is also

evident in Figure 318, in which the leg is rotated against the portion of the sock with the smaller vertical gaps; however, since the leg can rotate less from neutral against this direction, the sides of the sock see less shearing.

The success of the structure in locking up indicates that bias compliance does not hinder locking up (which was suspected since lockup seems to be dominated by uniaxial tensioning of the backbone, but not proven until this stage of the research). In fact, it suggests that bias-free triaxial fabrics would be a poor choice for the backbone, since yarns would locally be tensioned (a very stiff mode) when parts of the fabric are placed into in-shell shearing.

It is an open question how much the shear-locking features of the tooth were involved in lockup in this sample; the concave features intended to inhibit sliding in shear often appear close to touching in areas around 90° (in both directions) offset from the direction of leg rotation. However, after placing the structure under load, one can easily move these teeth with a finger, suggesting that they are not actually locked up. In contrast, teeth in the curved part of the sock (which is expected to be locked up in bending) are indeed immobile to the touch. Of note, he FEA modelling methodology proposed at the end of Chapter 8 would be quite useful to answer the question of which teeth are actually taking the load (and which can be eliminated or should be reshaped for additional stiffening up).

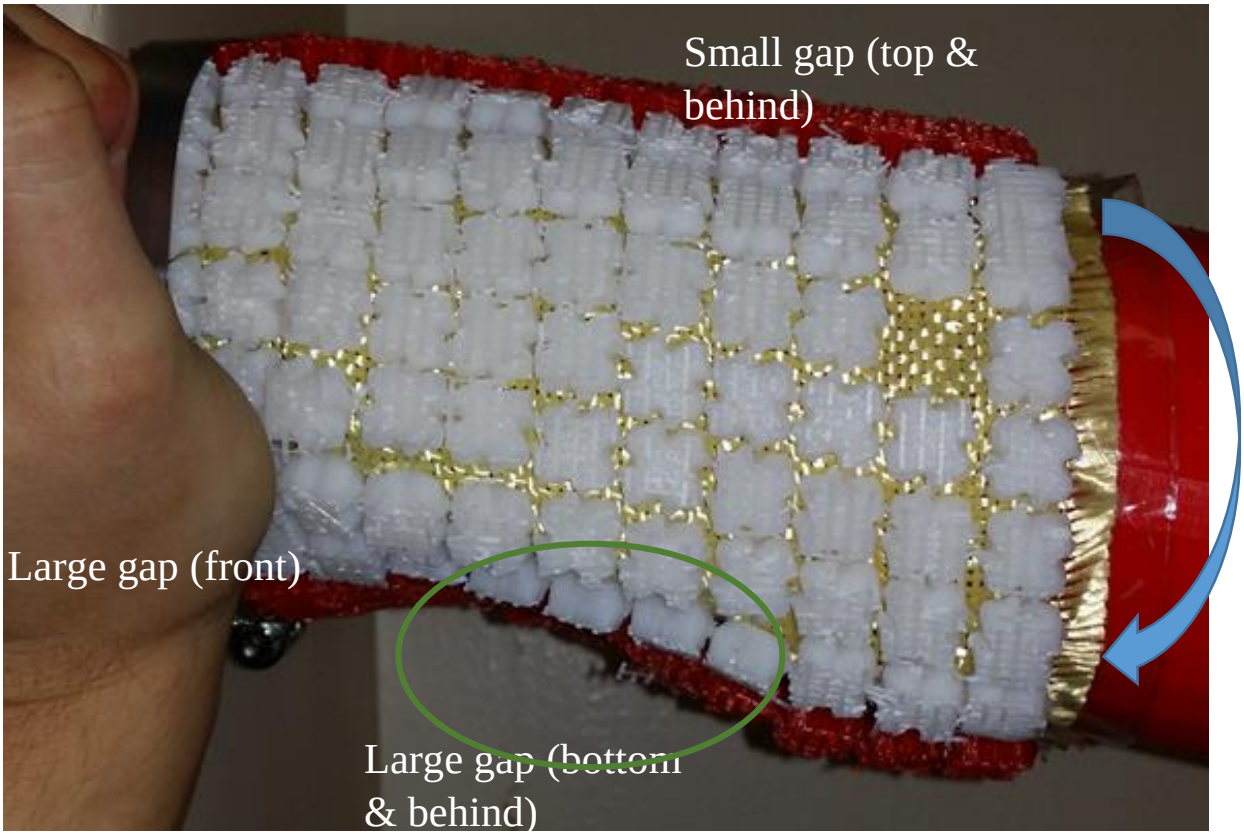

Figure 315: Structure in bending, with the rotation bringing the leg into contact with the portion of the array with large clearances. Note the shearing behavior of the white teeth. Bending direction shown in blue. Also note the inwards shell buckling (circled in green); this is where the lockup forces are concentrated, and the curvature here is roughly that at which the planar array locked up in planar bending, as shown in Figure 313.

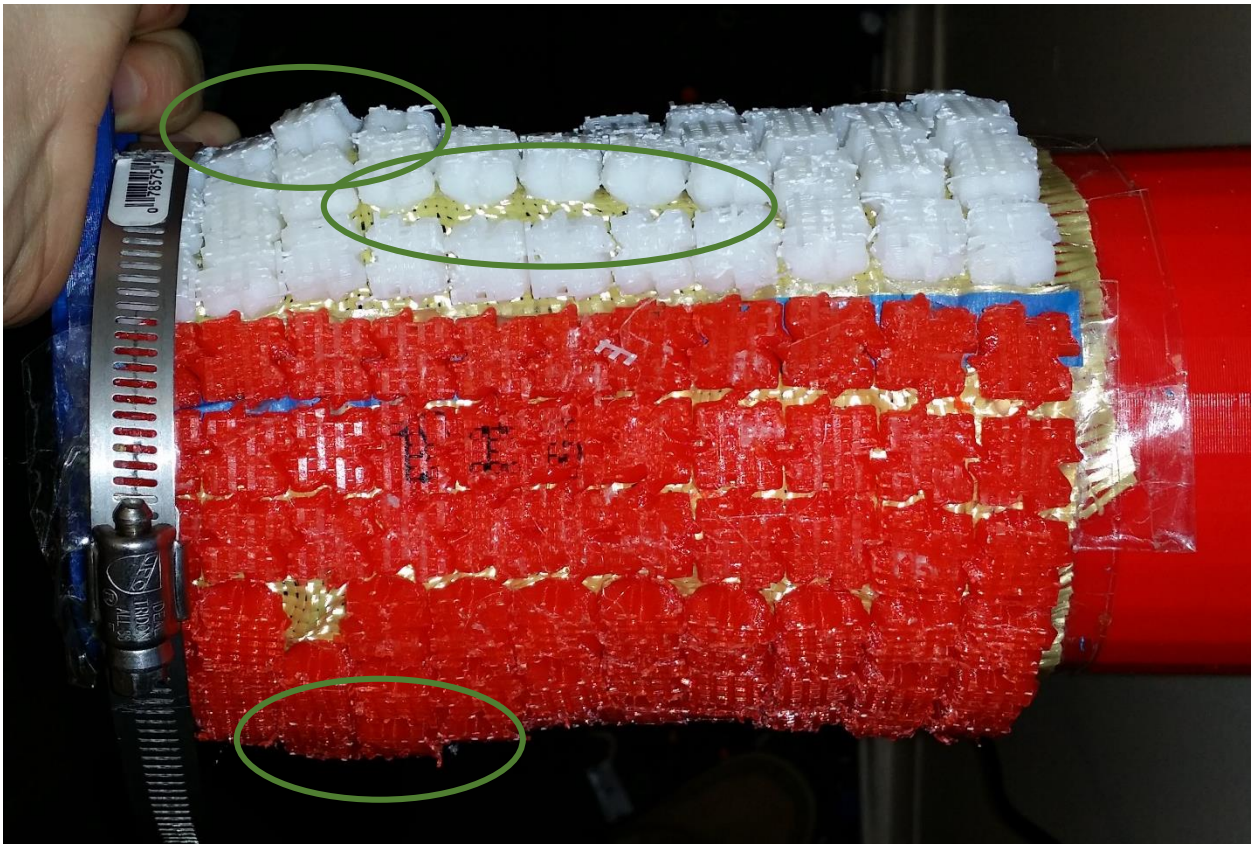

Figure 316: Different view of same load as in previous picture. Note shell buckling in a couple of places (circled in green).

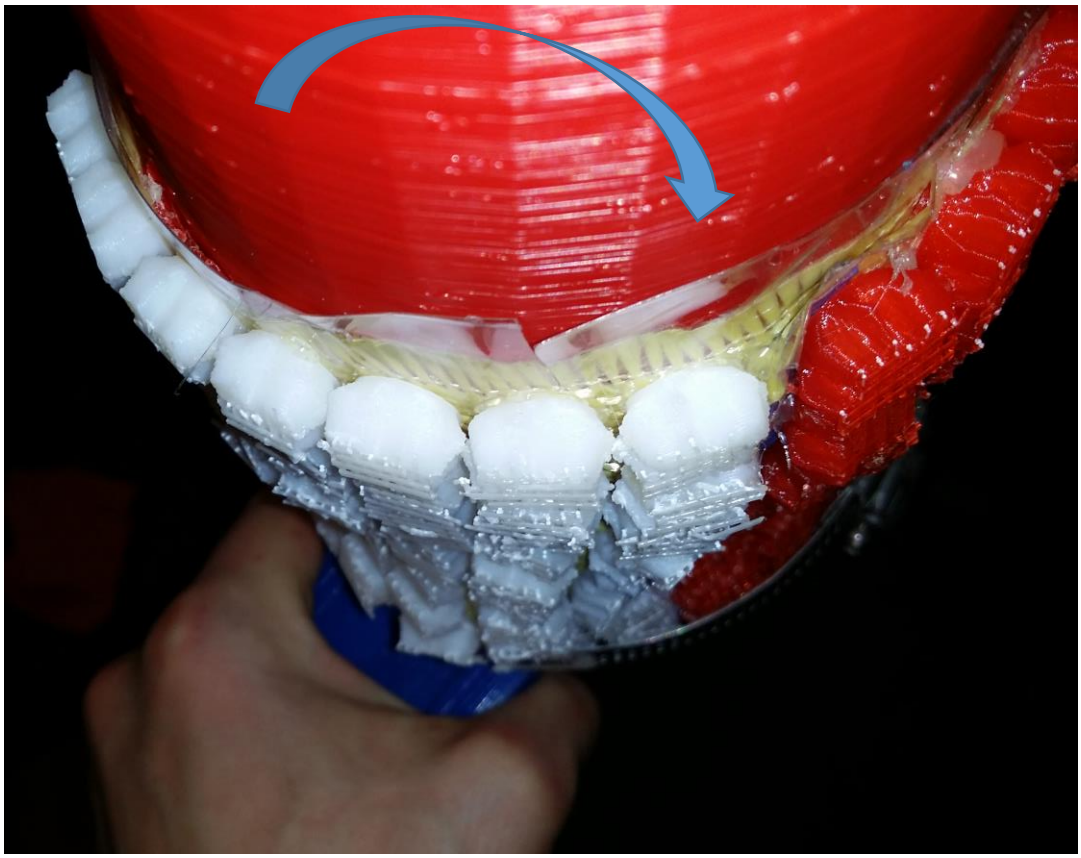

Figure 317: Another view of the setup (same direction of rotation as in the previous two pictures).

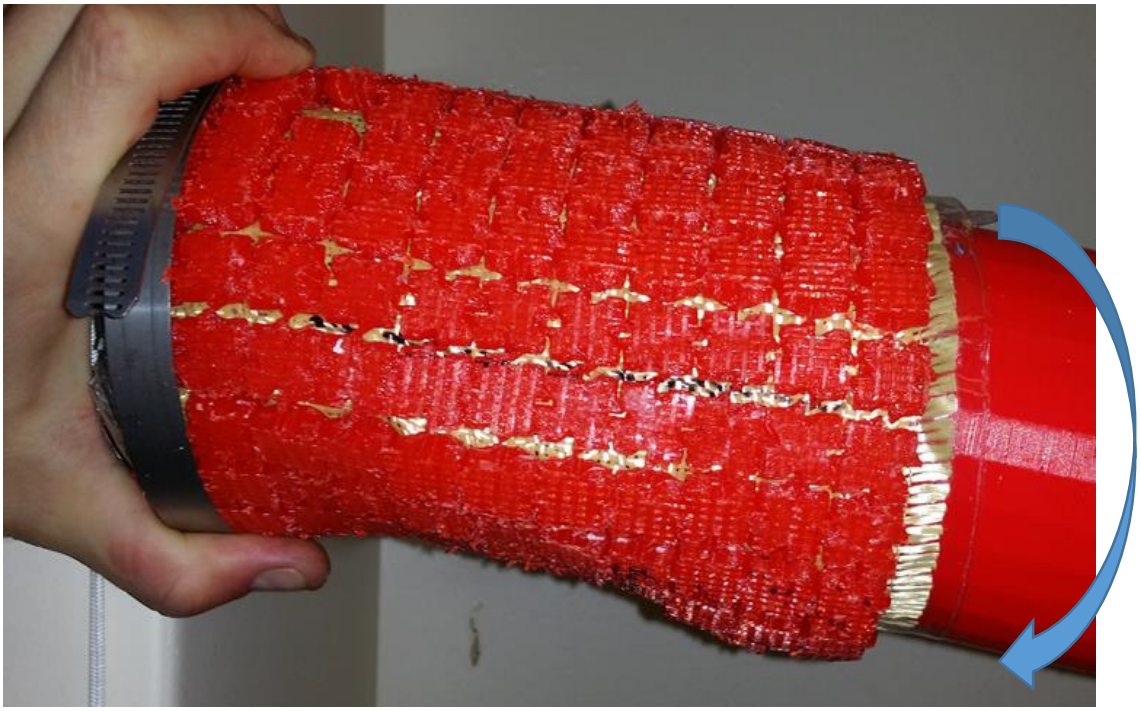

Figure 318: Bending in opposite direction as in the previous three pictures, against those teeth with the small (0.025" gap instead of 0.036"). View rotated 180° from Figure 315's. The base of the "foot" was perpendicular to the wall.

Finally, if the structure is tied to the leg (thus rendering the leg unable to slide inside it), there is very little forward and sideways rotation available to the leg, exactly as predicted (what little initial freedom comes from the backbone being slightly slack, and the freedom is lost when the backbone is appreciably tensioned). However, the leg has a modicum of initial rotational freedom about the axis of the leg thanks to the bias compliance of the fabric, but lockup occurs when teeth contact tangentially and when some anti-slide features of the teeth are engaged. Figure 319 and Figure 320 show lockup in transverse rotation in both directions.

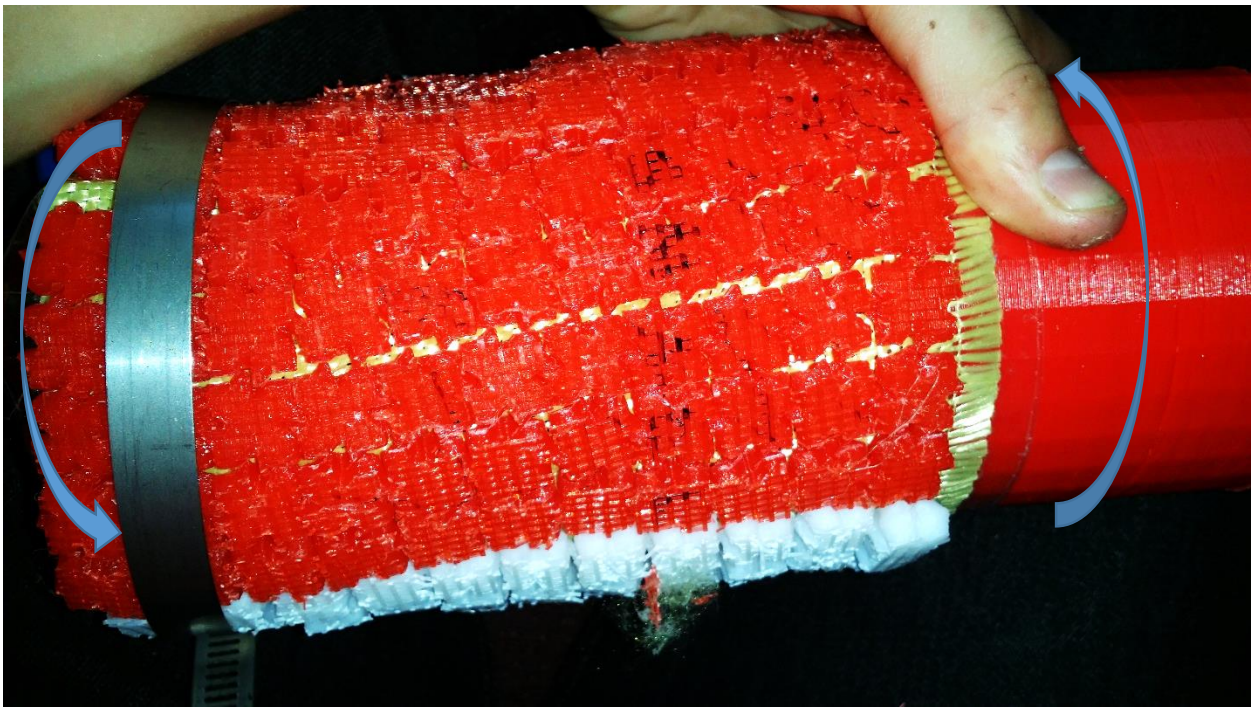

Figure 319: Torsional lockup of the array after being rotated clockwise (viewing from the top) thanks to tooth contacts. The direction of the torsion is also indicated with blue arrows.

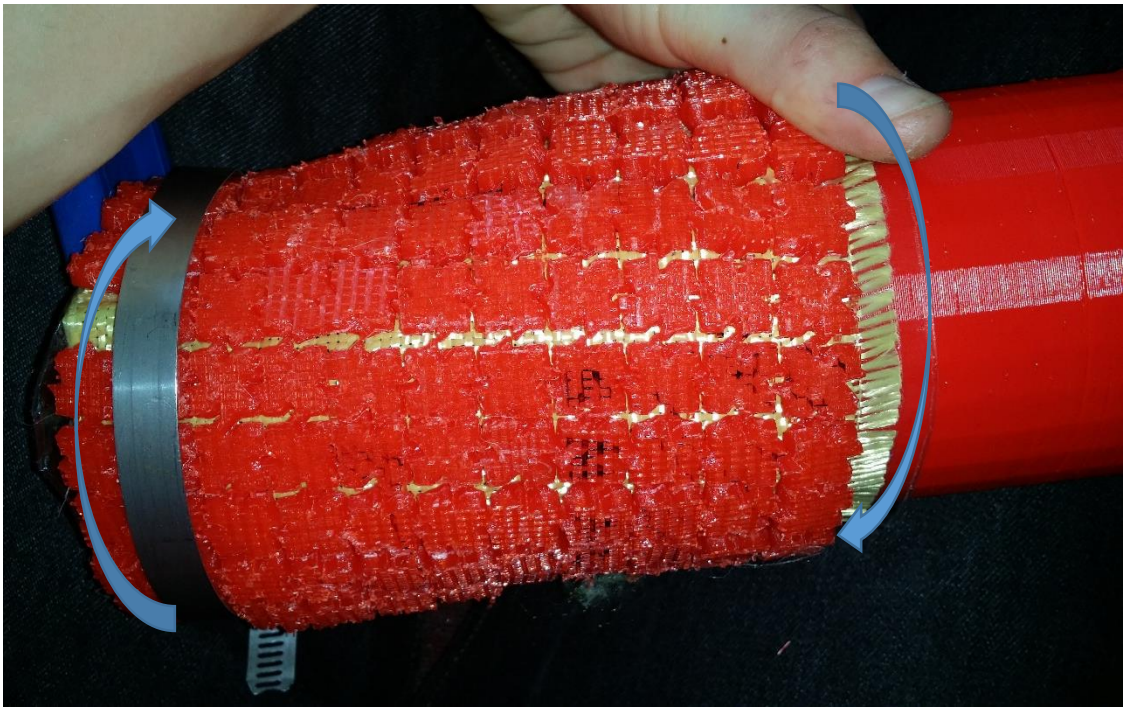

Figure 320: Torsional lockup of the array after being rotated counterclockwise (viewing from the top) thanks to tooth contacts. The direction of the torsion is also indicated with blue arrows. Note that this is the opposite direction of torsion from that of Figure 319.

While protecting against excessive transverse rotation might be quite desirable in a finished product (and this tooth configuration does this quite well), it must not come at the cost of immobilizing flexion and inversion/eversion; in fact, freedom in transverse rotation is probably much less important to athletic performance than freedom in flexion and inversion/eversion. Theoretically, a special device that allowed the leg to slide inside the sock but not rotate relative to it could take advantage of the structure's selective lockup in global transverse rotation, but this device would likely be complex and unreliable, requiring special T-slots to facilitate sliding.

Paradoxical Gear Array, 0.050" Gaps.

The next array to be wrapped into a cylinder was based on the hexagonal packing of the paradoxical gear (developed in the previous chapter). Knowing that cylindrically-wrapped arrays with a single tooth shape tend to require freedom to bend into higher curvature than the average curvature that the structure will see at lockup, generous gaps between teeth were created, and the lockup curvature in planar bending for this array can be seen in Figure 321. Confusingly, cylindrical sympathetic deformation occurred with compression along an axis perpendicular to the usual one, although compression along the usual axis resulted in some odd, instability-driven behavior, as may be seen in Figure 322.

Figure 321: Planar bending lockup curvature of the paradoxical-gear-based array with 0.050" offset between teeth.

Figure 322: Compressing the paradoxical array with 0.050" clearances between teeth does produce cylindrical conformation, but it seems to be governed by instability. What was once a straight "zig-zagged" row of teeth is traced in blue to illustrate the irregular behavior.

Chapter 8. Flared-Tooth Fabric-Backed Arrays.

Introduction.

The previous chapter's concept of attaching initially-flat arrays to fabric to cause the fabric to stiffen up after some bending deformation is extended to give a similar tooth array optimal stiffening-up after it has been bent (and then glued closed) into a cylinder or even a more-complex shape with non-zero curvature in multiple directions. The principal new property of these new arrays is unidirectional, cylindrical initial curvature thanks to teeth that are lofted outwards (forcing the array to have initial curvature to prevent tangential interpenetration between the lofted teeth); this principle could be extended to give initial curvature in multiple directions, producing an initial shape more complex than a simple cylinder. Due to the small tangential gap distances between teeth, lockup is controlled by both *z*-axis and tangential clearances between teeth, and special geometric features on the teeth prevent undesired tooth sliding (analogous to those developed for planar arrays in the previous chapter). A method of manufacturing such arrays was developed, entailing layout of the base parts precisely using 3D printing, followed by curving the fabric (over a mandrel if necessary) and manually installing the flared teeth. The method is employed to test the simplest-possible backbone and leg geometry, a right cylinder (with a very small offset between them) using a special test fixture.

Concept of Flared Tooth Arrays.

When the 2D arrays developed in the previous chapter were tested on the simple leg model, they did indeed stiffen up the joint rapidly. However, it seemed that relatively few teeth were recruited for stiffening (yielding a lower post-lockup stiffness for the structure's weight than could be obtained if more teeth were recruited), and this was attributed to two deficiencies: 1), the tendency of radial sections to buckle inwards until teeth touch tangentially, and 2), limited recruitment of the teeth roughly 90° away from the area of contact between the protective "sock" and the "leg". In order to better recruit teeth, it was theorized that an array that initially has a radius of curvature only slightly larger than that of the contacting cylinder would be able to recruit tangential tooth contacts as well as vertical tooth contacts for lockup. Admittedly, the superiority of such an array was far from certain: in particular, the ability of those portions of the sock 90° offset from the direction of leg rotation to shear freely may be an important driver of pre-lockup stiffness.

Figure 323 shows a rendering of two teeth oriented nearly in tangential contact on a circle whose radius is the desired initial radius of curvature of the undeformed array. In practice, it was not known at the beginning of this research even what order of magnitude of initial tangential gap would be desirable between the teeth, and later iterations of the concept featured much larger gaps than that shown, but in principle a full array based on this tooth will initially have a roughly-cylindrical shape.

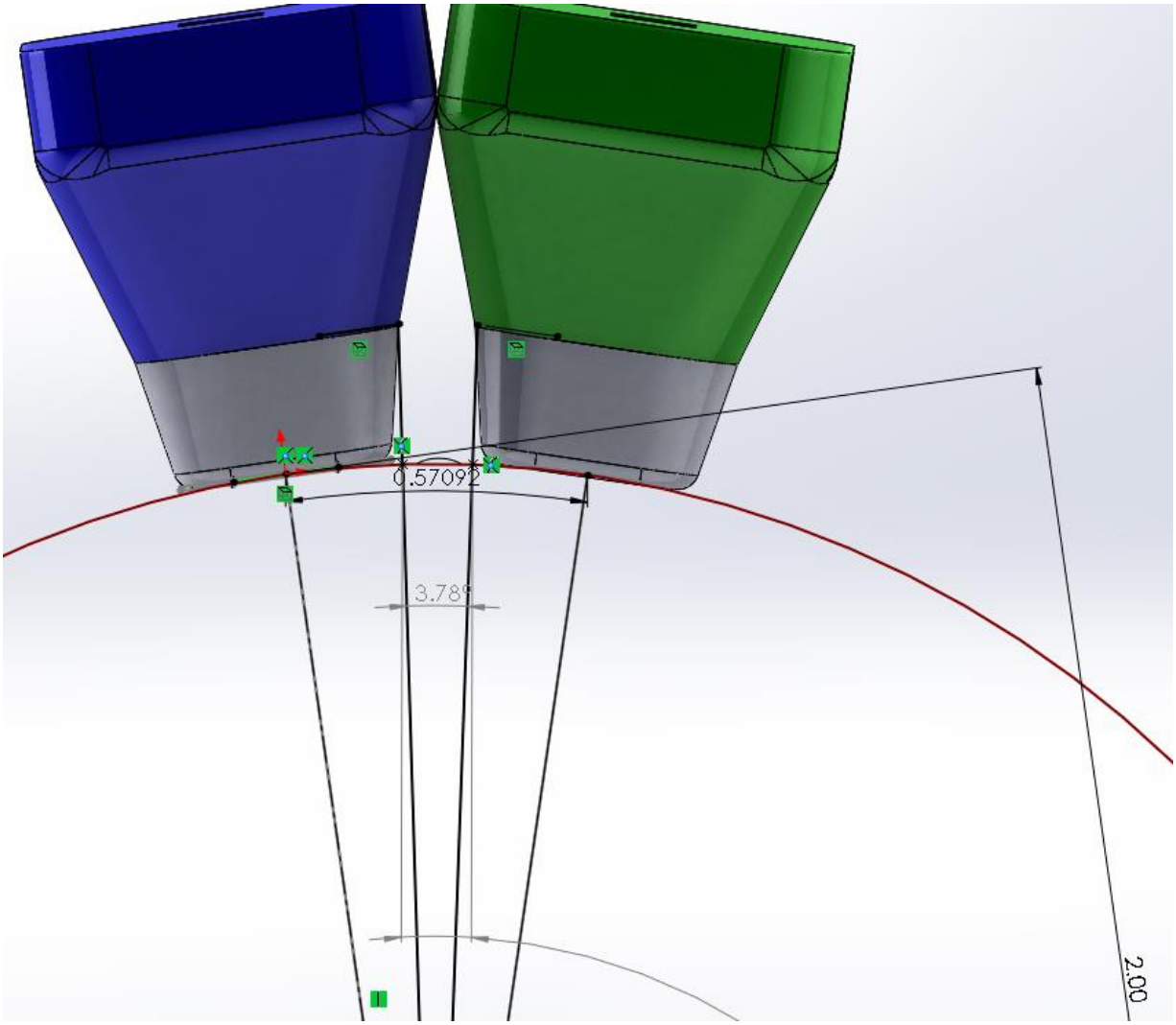

Figure 323: The distance between the centers of two base pieces (when printed flat) to leave the radial teeth barely touching tangentially around a "leg" of radius 2" is calculated as follows—the arc length between the centers of the base pieces. Note that this distance should be slightly increased to allow a bit less curvature before lockup.

Manufacturing the Pre-Curved Array.

It is not practical to print each tooth of a pre-curved array in one piece on a fabric over a cylindrical manifold, thanks to the width of the heater elements that protrude only a short distance above the extruder nozzle on most FDM printers, including those available to this

researcher. Also, it is unwise to print each tooth as a unitary body away from the fabric backbone and then attempt to accurately place each on the fabric by hand. Thus, a strategy of dividing the entire tooth part into two distinct parts, a "flared" part, and a "base" part, was devised. An array of the base parts was to be printed and glued to the fabric (or, alternatively, printed directly onto the fabric); then, the flared parts could be printed separately, and finally the flared parts would be fitted into the base parts. Figure 324 shows a sectioned view of a base part, featuring a small well into which glue to bond the base part to the fabric backbone may be poured, as well as a larger hole into which a corresponding feature on the flared part is to be fitted. Figure 325 shows a rendering of the flared part fitted into the base part.

The vertical distances between base part entities in the flat array would equal the *z*-distances between the base parts to produce the *z* gap desired of the teeth in the final, cylindrical conformation. However, the horizontal distances between base parts in the horizontal array would be the wrapped distance between base parts that would produce the desired tangential spacing in the cylindrical conformation, specifically as measured at the point of contact between the face of the base part that is to be glued to the fabric and the fabric itself. Thus, theoretically, for the flared parts to be inserted into an array of base parts constrained to remain flat, there would need to be penetration between the surfaces of the flared parts, as shown in Figure 326. However, as shown in Figure 327, there would need to be no such penetration in the vertical direction between the flared parts of the composite teeth.

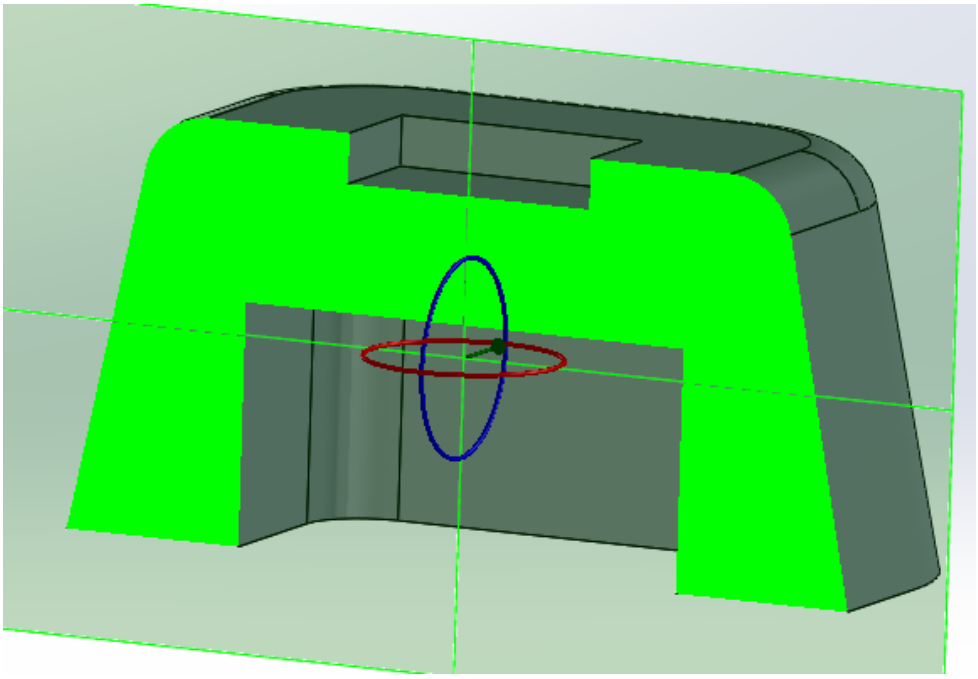

Figure 324: Section view of the base part, in print orientation. Note that the face currently on top is the one that will be glued to the fabric.

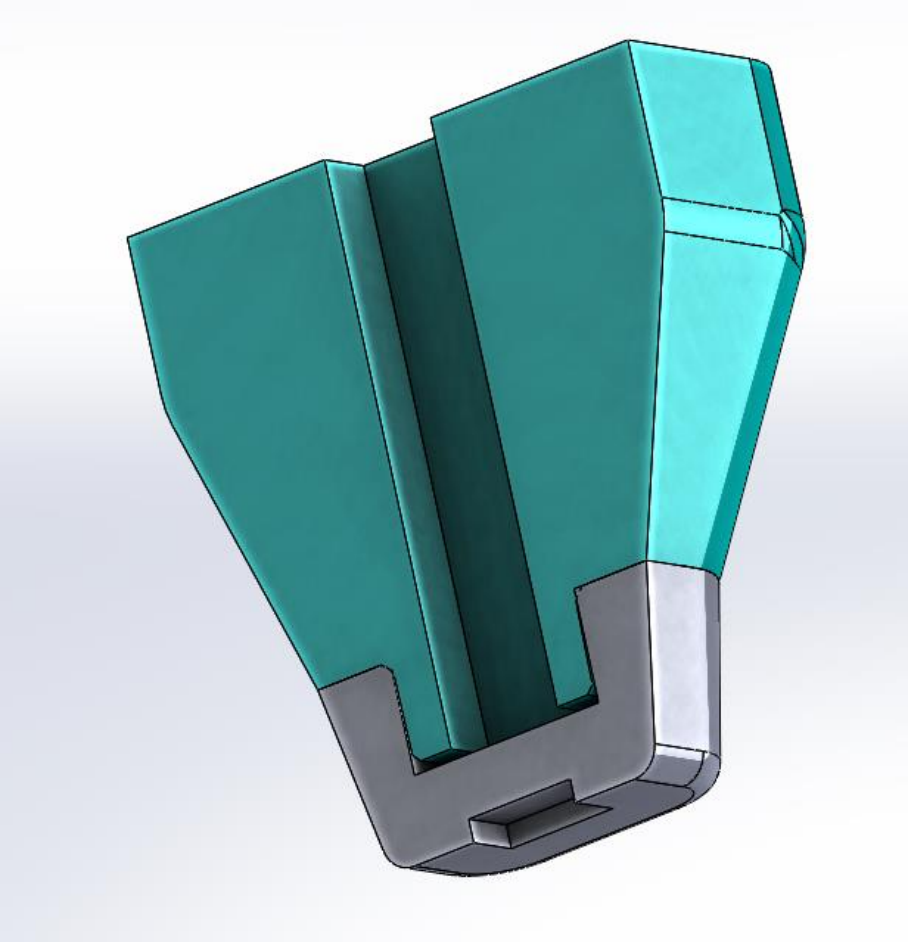

Figure 325: Sectioned view of base and wedge-shaped tip piece, latter press-fit into former. Note that the tooth part has a hole running its length to allow resin to be poured down it to better bond the two parts together; this was later abandoned as unnecessary.

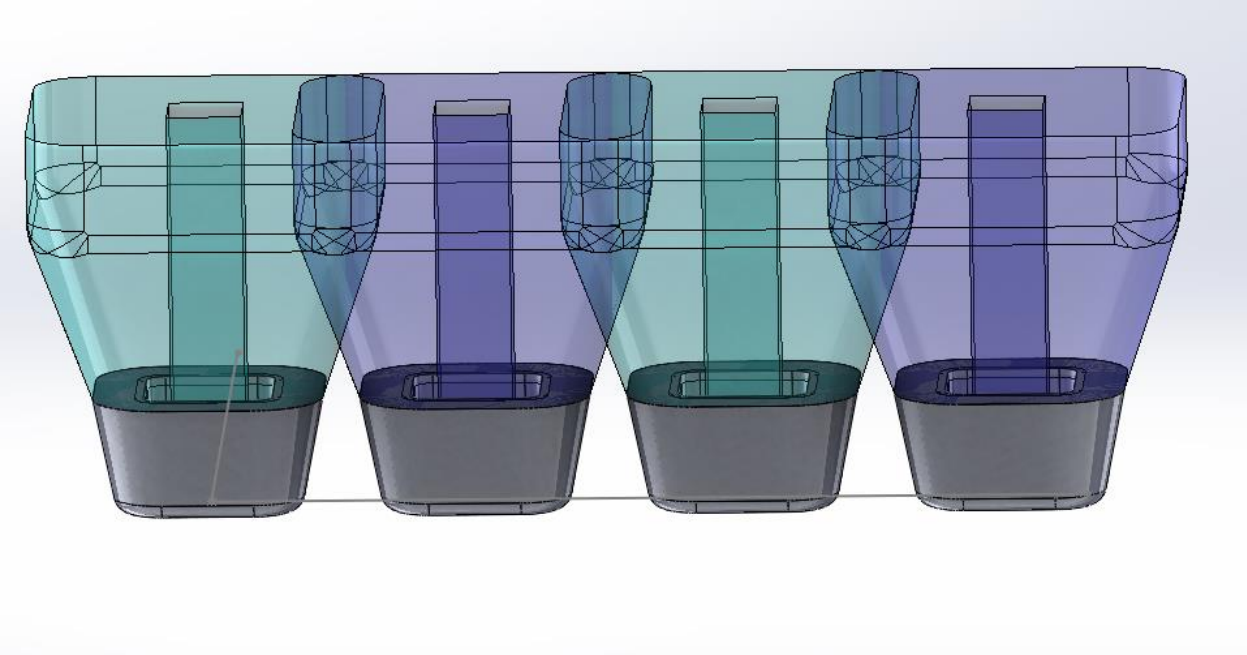

Figure 326: When bases are printed as follows, the fabric must then be curved, or the teeth will penetrate/touch as shown. (This is the radial direction, with a spacing as determined previously).

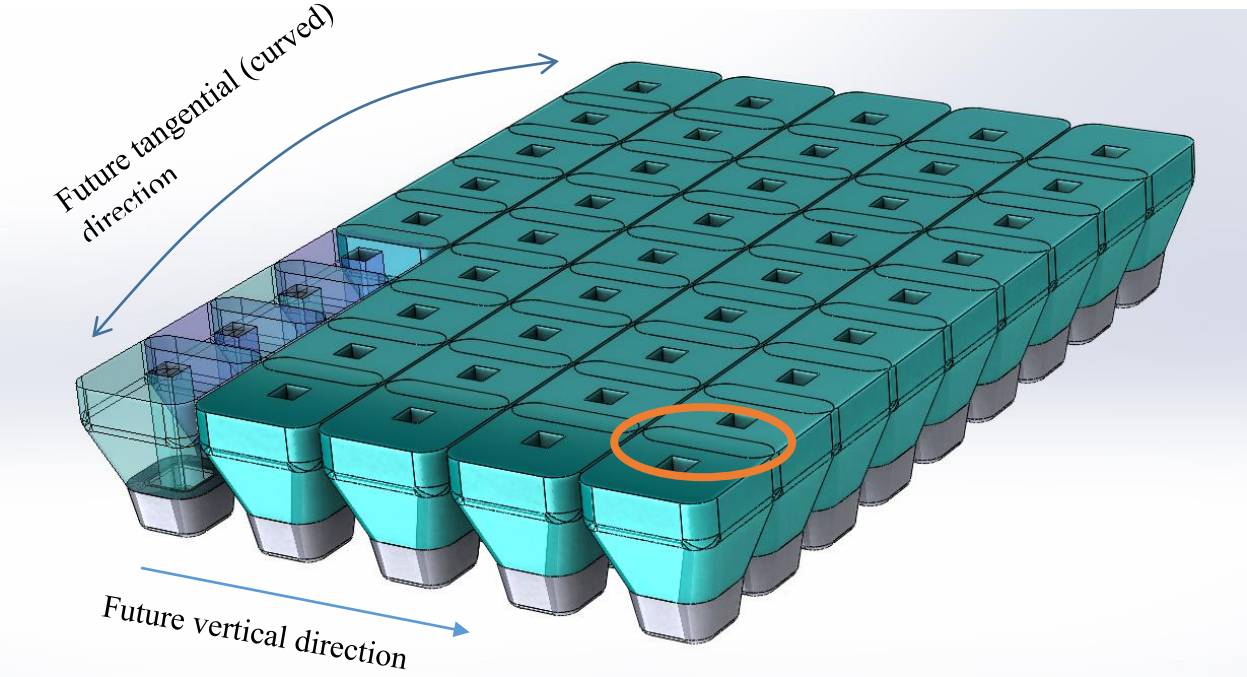

Figure 327: Positioning the grey, base parts. Since cylindrical conformation is desired, the bases are positioned such that the rows of teeth that will lock up vertically start off with 0.02" clearance. Obviously, the teeth cannot be assembled into this configuration without the backbone being curved; hence, in this drawing, the teeth are shown interpenetrating (e.g. as circled).

Soon after production started on this array, it became clear that the original tooth design had several defects. First, as in 2D arrays, flat contact surfaces are not ideal for the contacting faces of teeth as they allow sliding—either in the *x/y* directions, whereby the teeth can eventually slip out of contact or induce anticlastic curvature in the fabric, or in the *z* direction, whereby the locus of contact shifts closer to the fabric (reducing the stiffening-up ratio). In this particular case, it was easy for the teeth to slide in directions in the *xy* plane, and this was presumably due to the fact that the initial tooth design had a simple tooth geometry with no concave features that would allow one tooth to hold the other. As such, a single concave feature was added to the tooth, and a convex feature to mesh with another tooth's concave feature in tangential contact, as can be seen in Figure 328. While these teeth would likely benefit from cuts to prevent *z*-axis slippage as well, such features prove much harder to generate, and so they were neglected for the preliminary analysis of flared-tooth arrays.

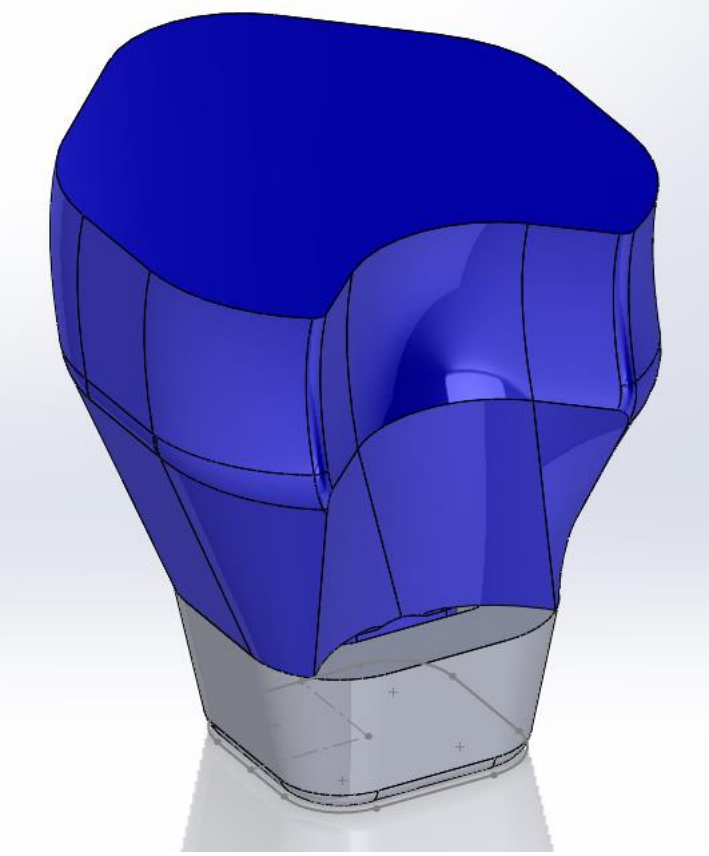

Figure 328: Altered geometry of flared tooth, featuring a cut to prevent teeth tangential to each other (i.e. sharing the same circle before deformation) from sliding much in the z relative to one another. This was simply a preliminary investigation; the final tooth design is likely to feature concave features between teeth that contact in the z, too.

As with the initial set of flared teeth, the redesigned tooth was given small clearances in both vertical and tangential contact with an initial radius of array curvature in order to cause tangential and z-axis lockup after a moderate amount of leg deformation. Two teeth in pre-contact position on a simulated backbone of the desired initial, unlocked curvature can be seen in Figure 329. This setup was also used in an attempt to ensure favorable contact normal angles once tangential contact began, although this phenomenon was not optimized by any means at this stage in design.

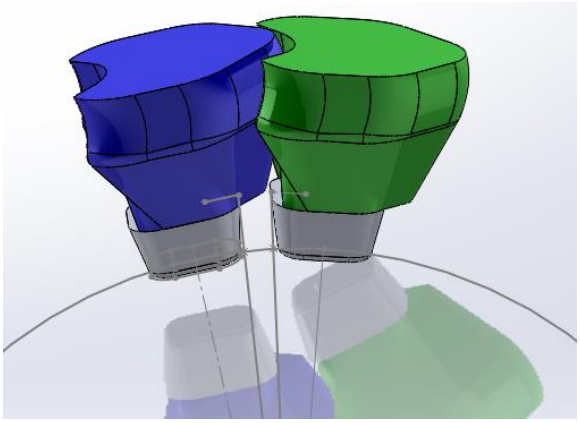

Figure 329: Two flared teeth, nearly in tangential contact. The normals of the bases of the teeth are perpendicular to the circle of curvature shown. This geometry gives the proper unrolled distance at which the base parts should be printed to produce a small tangential gap between the teeth when the structure is rolled into a cylinder having the curvature of the circle shown.

Once this array was completed, it was found to take up a roughly-cylindrical neutral shape, although, given the absence of internal teeth, this shape was unsurprisingly prone to shell-buckling inward. (The device must be tested with a simulated leg to determine whether internal teeth to reduce shell buckling inward are necessary, or whether the mere presence of the leg contacting the array is sufficient to prevent this.

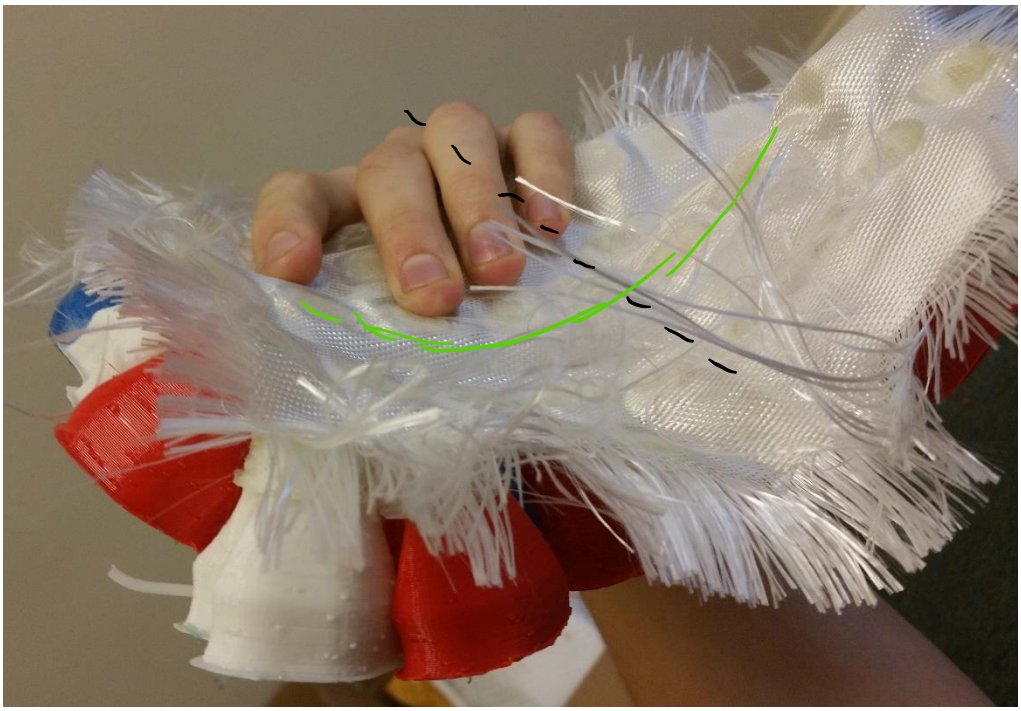

Figure 330: Precurved array in the undeformed position. Its cylindrical curvature is traced in green; the vertical axis of its cylindrical face is drawn with a black dashed line.

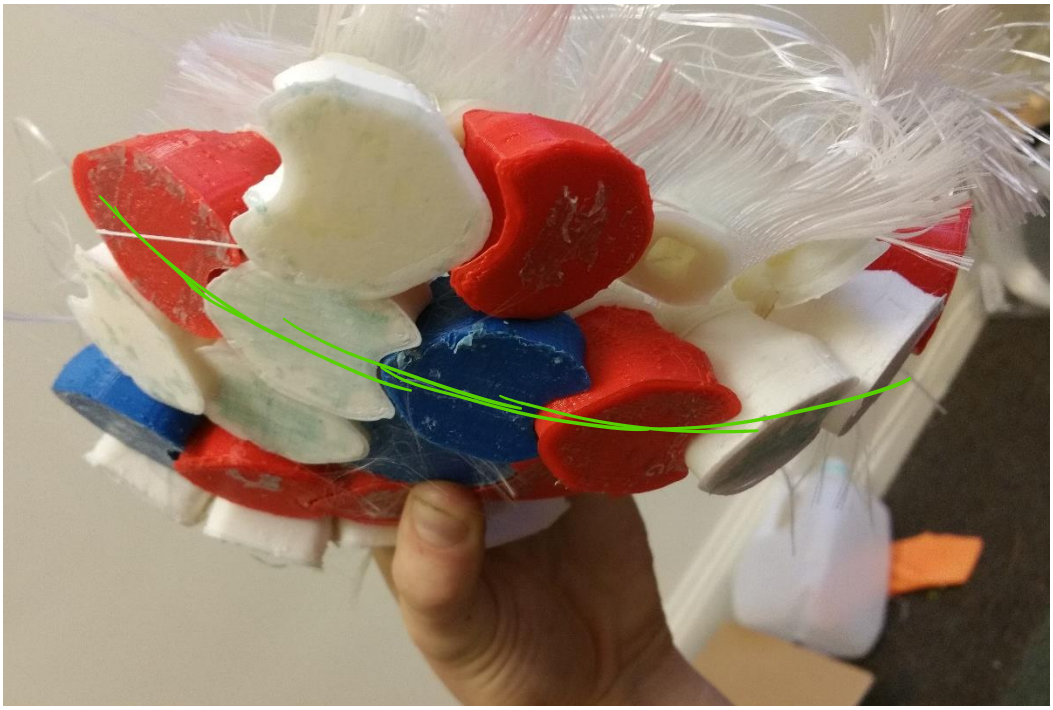

Figure 331: Another view of the undeformed array showing cylindrical curvature (traced in green).

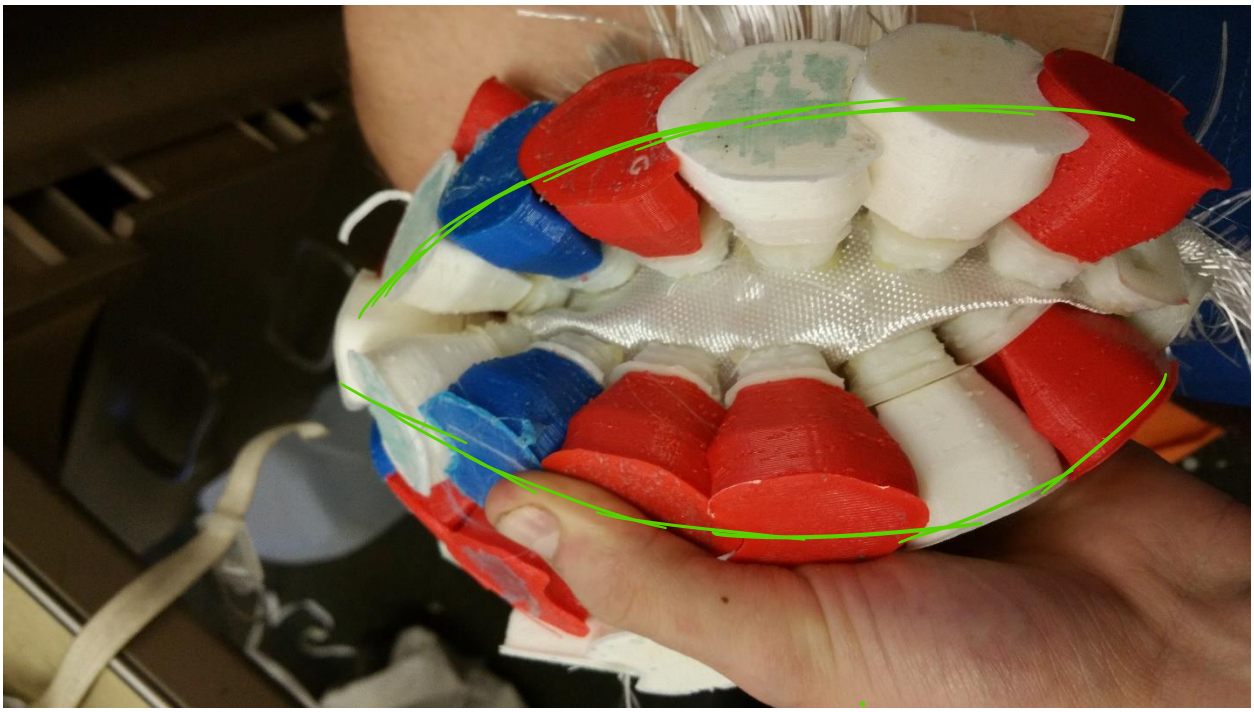

Figure 332: Bending the array backwards to highlight its curvature (note that interior teeth, as proposed above, would not allow this). The curvatures of the two rows of teeth are traced in green.

Another potential defect that was observed in the first set of flared teeth and not corrected in the next iteration was that the teeth tended to droop off the fabric backbone owing to their long length relative to contact area with the backbone and perhaps high density of infill as well (making the teeth quite heavy, and unnecessarily so). This problem is illustrated in Figure 333. As the shear strength of the bond between the tooth bases and the fabric was the main mechanical quantity limiting post-lockup stiffness (and not tooth contact stiffness), the infill density of the teeth could probably be reduced without any adverse mechanical results, at least for now. However, it will likely be advisable to make the teeth shorter for the same contact area with fabric to ensure better conformation of the array to the leg. There are also entirely different

reasons tooth length and weight should both be reduced (namely reducing the physical footprint and the weight and inertia of the device).

Figure 333: Drooping behavior of long and heavy teeth (note how their normals tend to be angled somewhat downwards from the average normal direction of the fabric). The direction of gravity is drawn in green.

For all these defects, the structure was fundamentally functional. When placed along the researcher's forearm, roughly centered over the wrist (and held there with light tension to make it conform to the wrist), it allowed some motion (despite the fact that several vertical rows of teeth were closely conforming to the wrist, as was much of the base fabric) until the teeth locked up in a pattern that did not permit sliding (prior to this, some tooth sliding occurred without producing either local or global lockup). There was even some tooth rotation about axes roughly normal to the fabric at the bond point, although this is a fairly stiff mode. Granted, the overall structure was laughably thick thanks to the massive teeth, and the post-lockup stiffness did not seem high

enough to prevent injury (thanks in large part to the fiberglass fabric used for the backbone, which was both too thin to give enough post-lockup stiffness and had poor bonding with cyanoacrylate; it was chosen for this sample only because no other fabric was then available to the researcher). However, it seems to demonstrate the importance of tangential as well as vertical contacts between teeth, given that all of the simple planar arrays (square and hexagonal arrays) did not perform well when wrapped into a cylinder; only those planar arrays whose teeth had special features (like the paradoxical-gear teeth, whose special shape enforced cylindrical sympathetic deformation, or teeth with concave features to prevent vertical sliding) could hope to perform acceptably in this configuration, but this cylindrical array lacks such features. Figure 334 shows a picture of the cylindrical array resting on a human wrist, undeformed (aside from being draped over a cylinder with a higher average curvature than what the array had been given) and compared with Note the complex motion of most teeth involved, and the resulting complex network of vertical and tangential contacts needed to prevent teeth from moving further. If the initial cylindrical curvature of the array had been higher (better conforming to the wrist), the behavior of the teeth probably would have been more predictable and efficient in terms of maximizing lockup stiffness versus tooth volume.

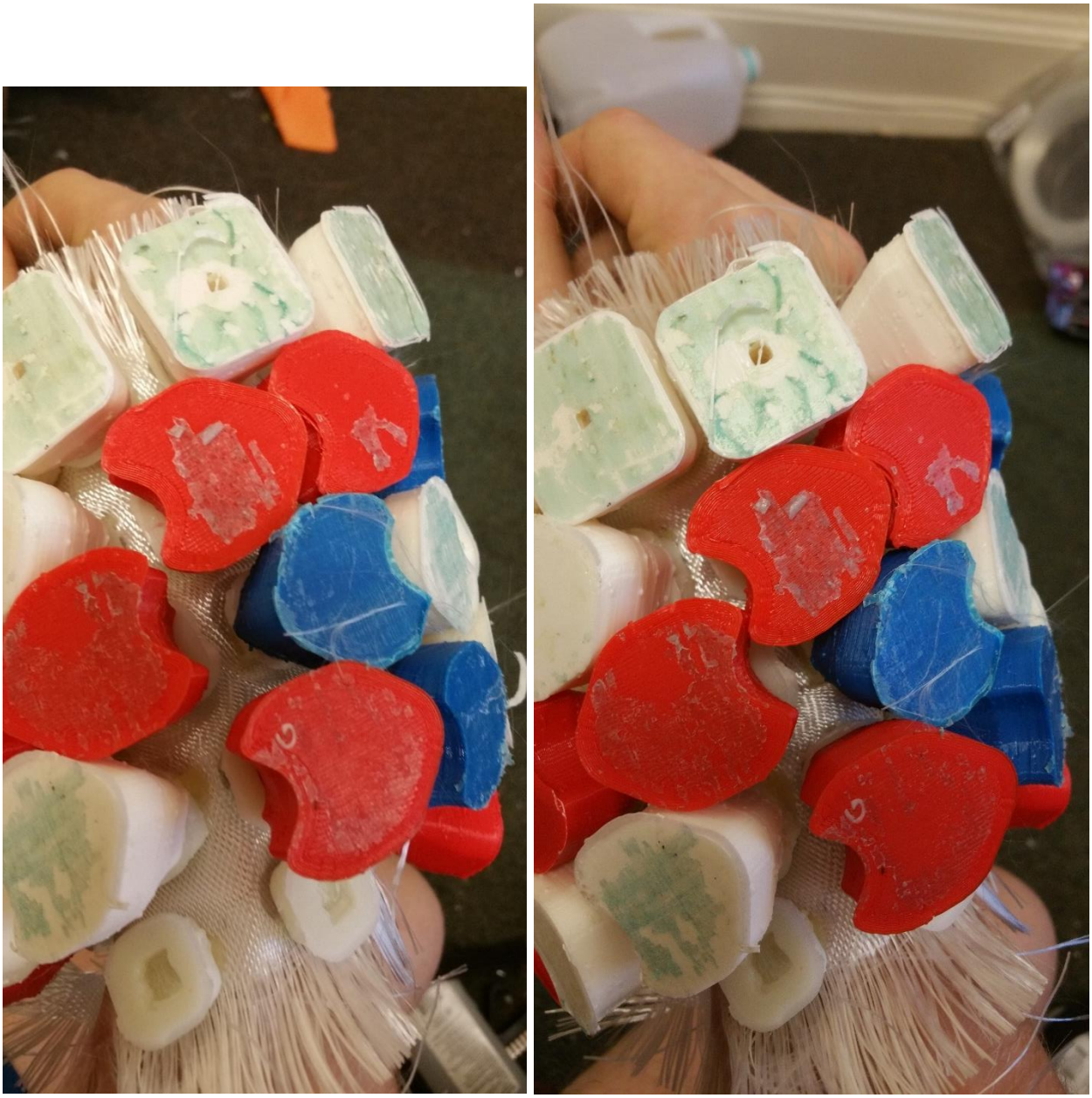

Figure 334: Cylindrical array tested on a human wrist. In the left picture, the wrist is in neutral position, with negligible bending along the netural axis of the cylindrical axis. A few teeth are touching lightly. In the right picture, many teeth have come to touch, both vertically and tangentially, and the structure is effectively locked up.

Second Iteration: Thinner Teeth with Anti-Slide Features.

While the above array appears to perform much better when wrapped around a wrist than did the initially-flat arrays, that preliminary sample was not sized to fit the test fixture we intend

to use; not only did it not wrap fully around the simulated leg, but its initial curvature was significantly lower than that of the leg, meaning that its teeth were far from tangential contact after the backbone was further curved to wrap around the leg. Thus, it was necessary to generate a new array for the test fixture. Beyond this, it seemed desirable to incorporate gear-like concave features to limit tooth sliding for reasons discussed above.

Pre-Curved Array on Arbitrary Manifold.

Given that the final product will need to conform closely to the leg and thus consist of a piece of fabric at least as dimensionally-complicated as a sock (likely more so, as socks have significant compliance in all directions, whereas this device needs high tensile stiffness at least in the vertical direction, and possibly also in the tangential direction. As such, it seemed a worthwhile experiment to put teeth on a manifold more complicated than a simple cylinder. A somewhat conical manifold, a loft between two circles of different diameters (corresponding to different circles on the test fixture developed for the linear comb and also used with planar arrays in the previous chapter) was designed, rendered on the test fixture in Figure 335. To produce this manifold out of fabric, one need only print out the template shown in Figure 375, trace it twice over the fabric, and glue the two halves together. However, the ease of producing the fabric belied the difficulty in tiling it with teeth.

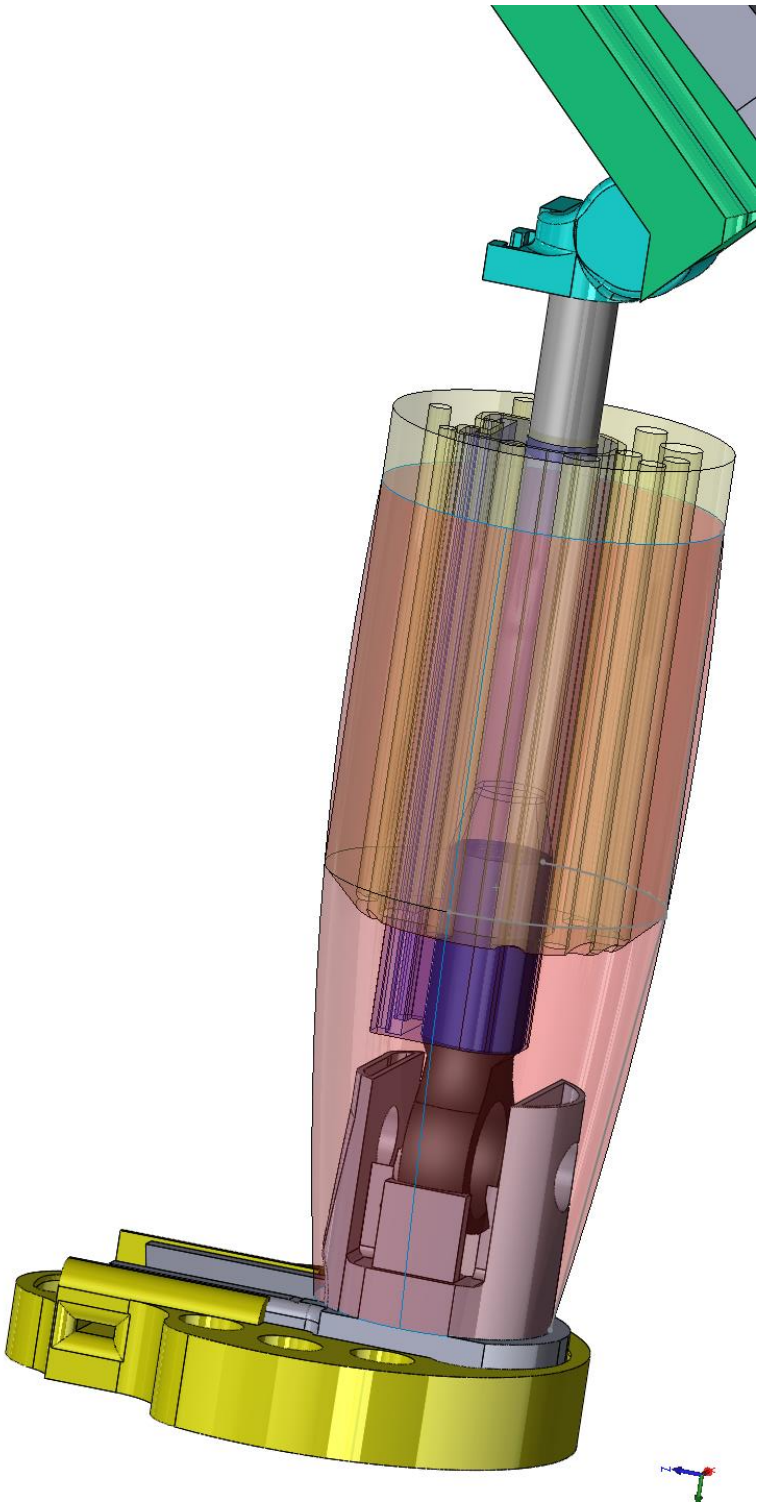

Figure 335: Test fixture with non-cylindrical manifold shown transparent in red. The teeth were to be spaced to allow the fabric to conform as closely as possible to this shape when undeformed, but it quickly became apparent that this would require highly irregular gaps between teeth in many places.

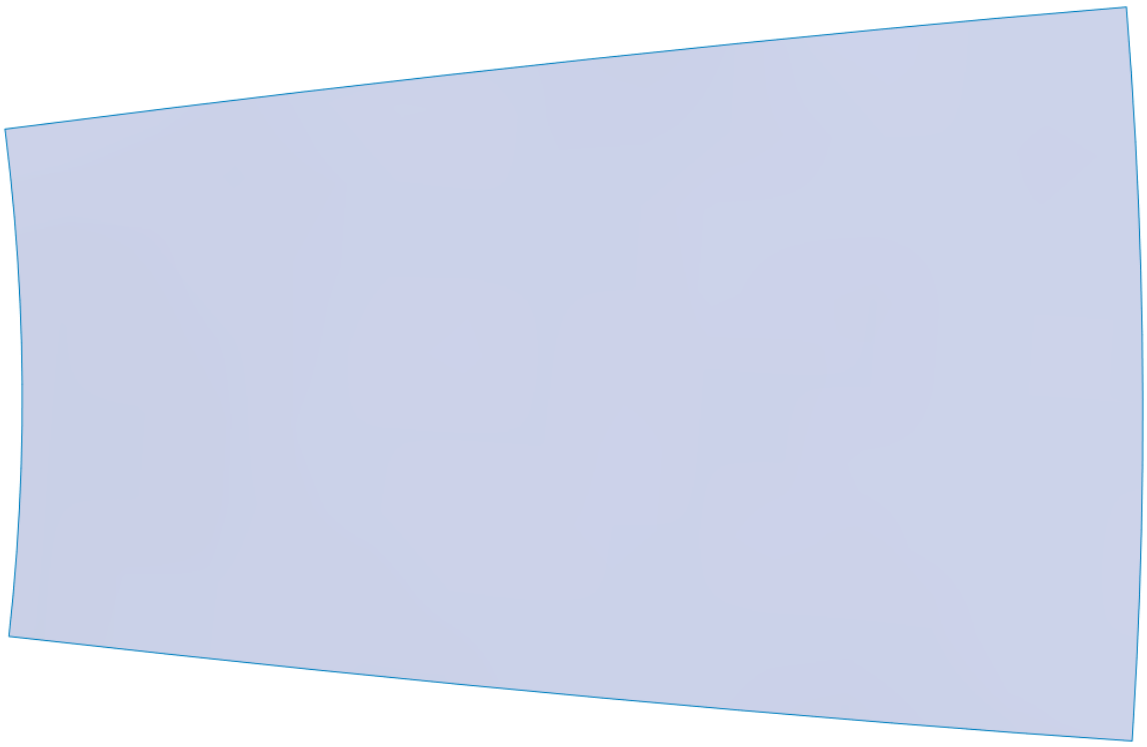

Figure 336: Flattened version of half of the manifold shown in the previous picture. This flat pattern was to be printed out on a paper printer after being scaled appropriately and then used to trace pieces of fabric.

Ambitious attempts at tessellating a single tooth design over this surface were quickly stymied. While it might indeed be possible to cover the surface with a single tooth that was separated from neighboring teeth by varying gaps (with the gaps varying merely from the constraint of tiling the tooth over the irregular shape and not from any mechanical considerations such as an attempt to optimize stiffening-up behavior), this was seen as far too great a challenge to attempt before proving the concept with a simple cylindrical manifold. In particular, while the final product will almost certainly have an irregular backbone like the one shown above, it will also likely consist of varying tooth shapes (as much to conform to this irregular backbone with even initial gaps as to produce the desired lockup characteristics), and this will likely require computer simulations to optimize both. Clearly, this step must wait, and the researcher's attention was thus returned to the simpler, cylindrical problem.

Flared Teeth with Anti-Slide Features ("FTASF Array").

A basic array for a regular, cylindrical manifold was developed by first creating a square-cross-section tooth with enough draft that there would be a 0.019" tangential gap between teeth 1cm in length on a cylindrical array with a radius of curvature of 1.688" (corresponding to the radius of the "upper leg" of the test fixture), then adding projections on one surface of the tooth (and corresponding faces to contact on the adjacent tooth) to prevent sliding in *x*, *y*, and *z*. A single ring of this cylinder (actually half

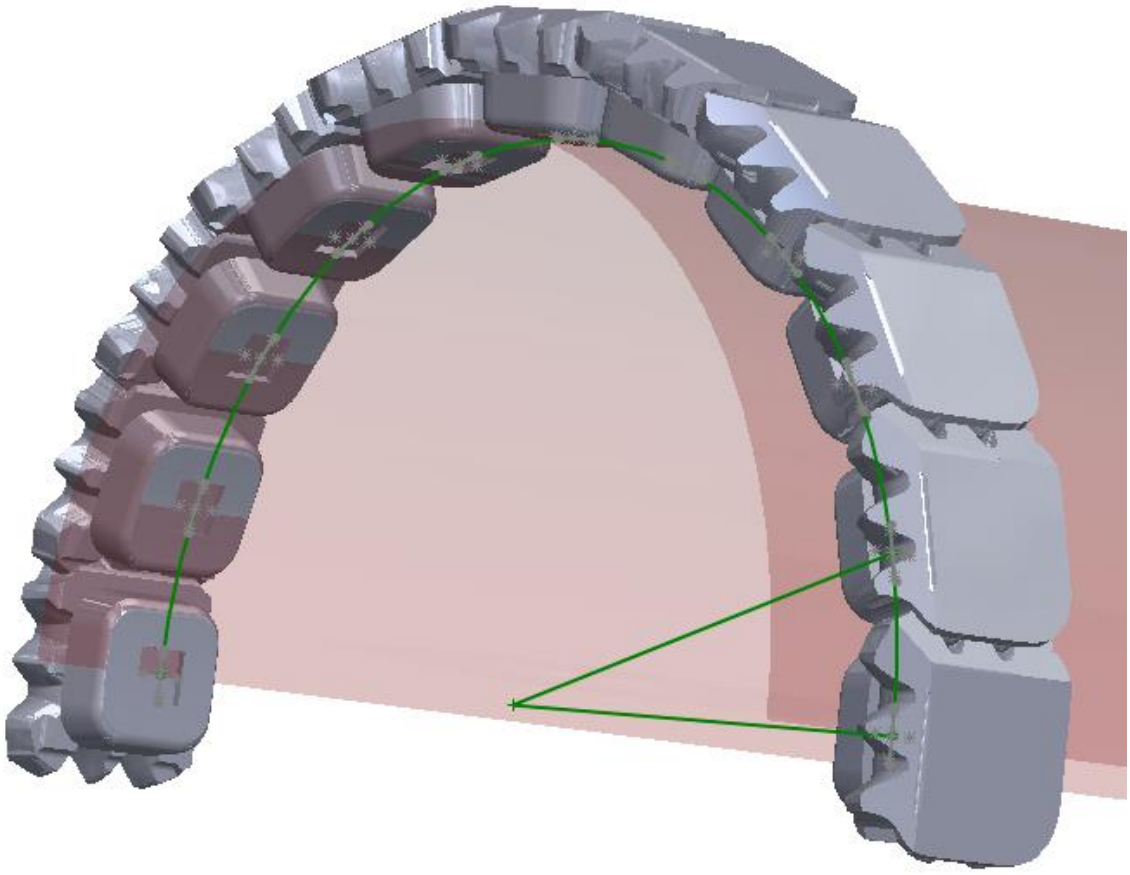

Figure 337: When using the only one size/shape of teeth, it is essential that the fabric can be covered with an integer number of teeth, otherwise there will be a significant gap between teeth that should be able to enter tangential contact. Fortunately, this 3.75" diameter cylindrical manifold and corresponding tooth geometry can be covered by exactly 20 teeth with a tangential clearance of 0.019".

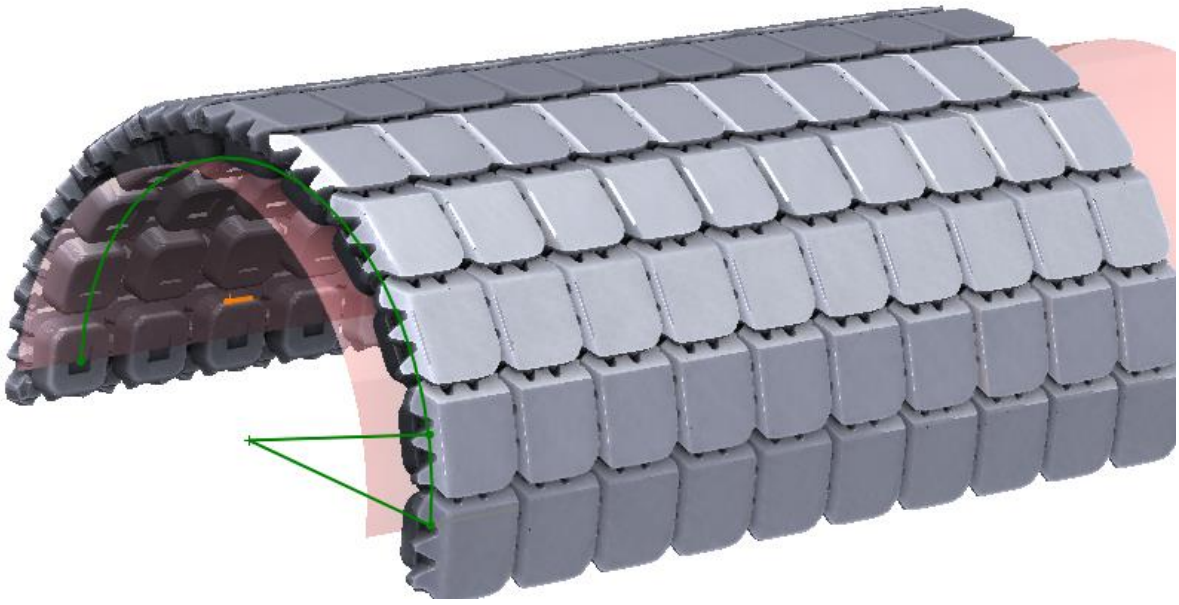

Figure 338: A computer rendering of full half-sheet of teeth with interpenetrating features. Clearly, the final product will need to be an entire cylinder, not a semi-cylinder.

For simplicity, the same gear-like geometry was used for faces that would contact tangentially as those that would contact vertically; strictly speaking, this might not be ideal, since the contacting surfaces were engineered to prevent rotation about an axis parallel to the cylindrical axis, not to prevent rotation about an axis parallel to the tangent to the circle of each row of teeth. These two axes are shown on a rendering of the tooth design in Figure 339. However, preventing tooth rotation along the latter of these two axes is likely far more important since vertical contact between teeth is probably more important to effective lockup.

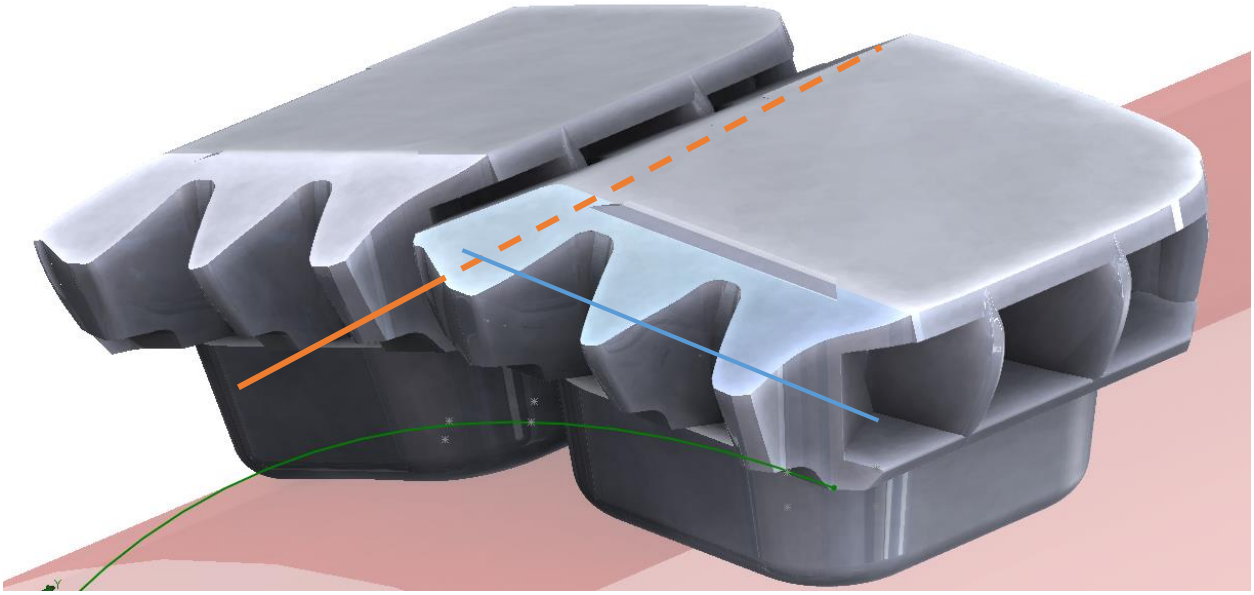

Figure 339: Rendering of two composite teeth (note their base parts as well as flared parts) with interpenetrating features, just before tangential contact (clearance:0.019"). The cuts in the teeth are shaped so as to prevent rotation about the axis shown in orange (i.e. the axis of tangential contact between teeth), and they may not be ideal for preventing rotation about the axis of vertical contact shown in blue (belonging to the right tooth and a hidden tooth below it).

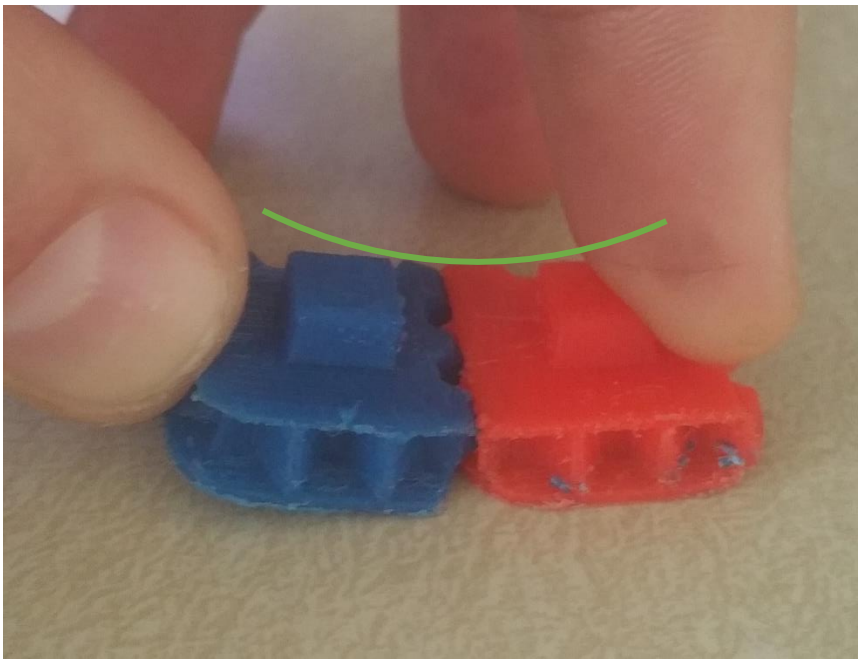

Figure 340: A picture of two teeth as printed in tangential contact (thus, their flat bottom and top faces are at an angle to each other). The circle of curvature to which they conform in this position is sketched in green. This mode is quite resistant to rotation.

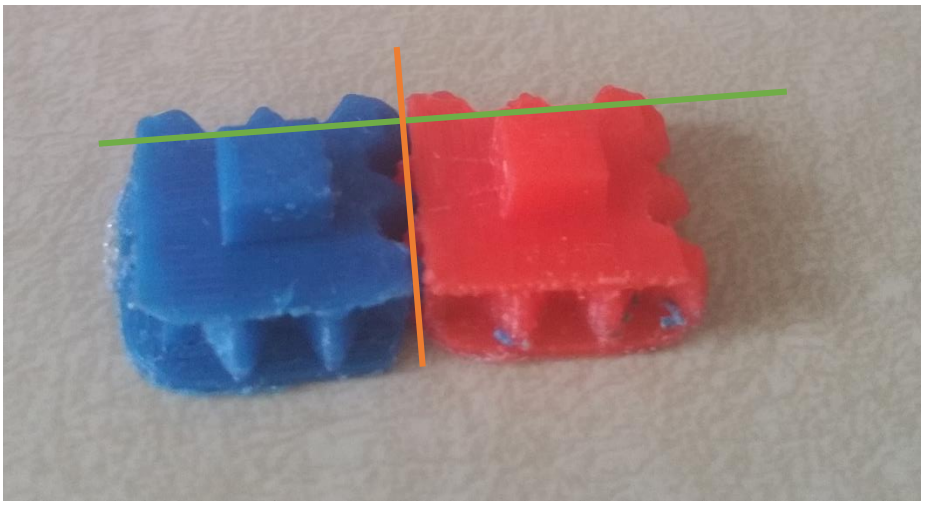

Figure 341: A picture of two teeth as printed in vertical contact (thus, their flat bottom and top faces are parallel to each other), the axis of which is shown in green. This mode is quite vulnerable to rotation about the orange axis, as shown in the next figure.

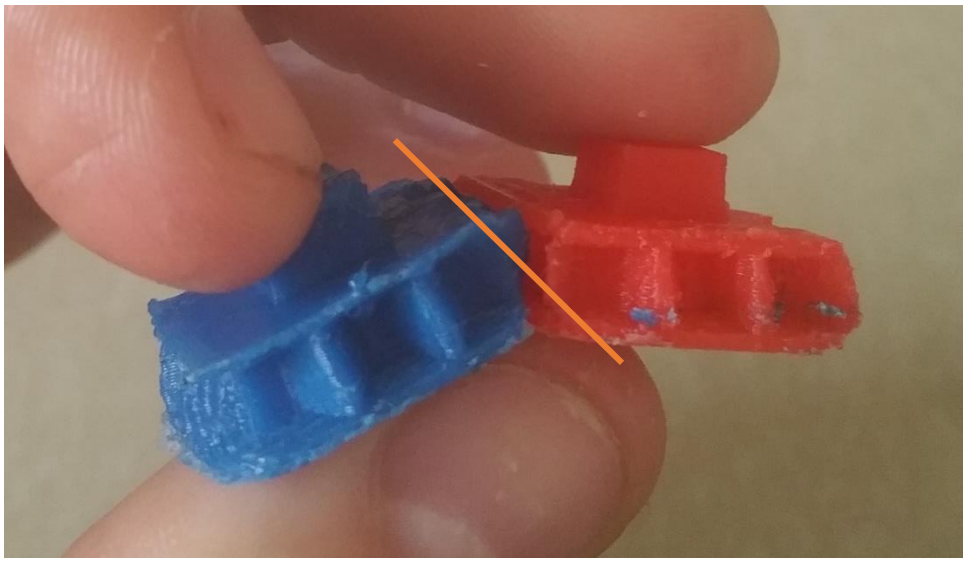

As an aside, a minor change to the base pieces was made in the hopes it would improve bonding with fabric: cylindrical cuts in one direction (parallel to the axis of the cylinder into which the overall structure is to be bent) were made in the base pieces, as shown in Figure 342. These cuts should conform to the initial curvature of the fabric when it is undeformed form its cylindrical shape. Without this feature (i.e. with the face that bonds to the fabric being flat), the fabric's curvature must transition sharply from the flat, bonded area to the area in between bonded base pieces. This sharp transition appeared to make the base pieces vulnerable to being pulled off. That said, the manufacturing method might need to be altered in order to take full advantage of this feature: currently, the base pieces are laid flat when the fabric is glued to them, which would require local distortions in the fabric to accommodate the new curvature on the bonding faces. Thus, creating a cylindrical scaffolding to hold the base parts in a cylindrical orientation (i.e. the orientation they will have once the teeth are installed in the bases) and then gluing the fabric to them might produce the best possible bond. That said, it is not necessary to optimize the fabric-base bond right now.

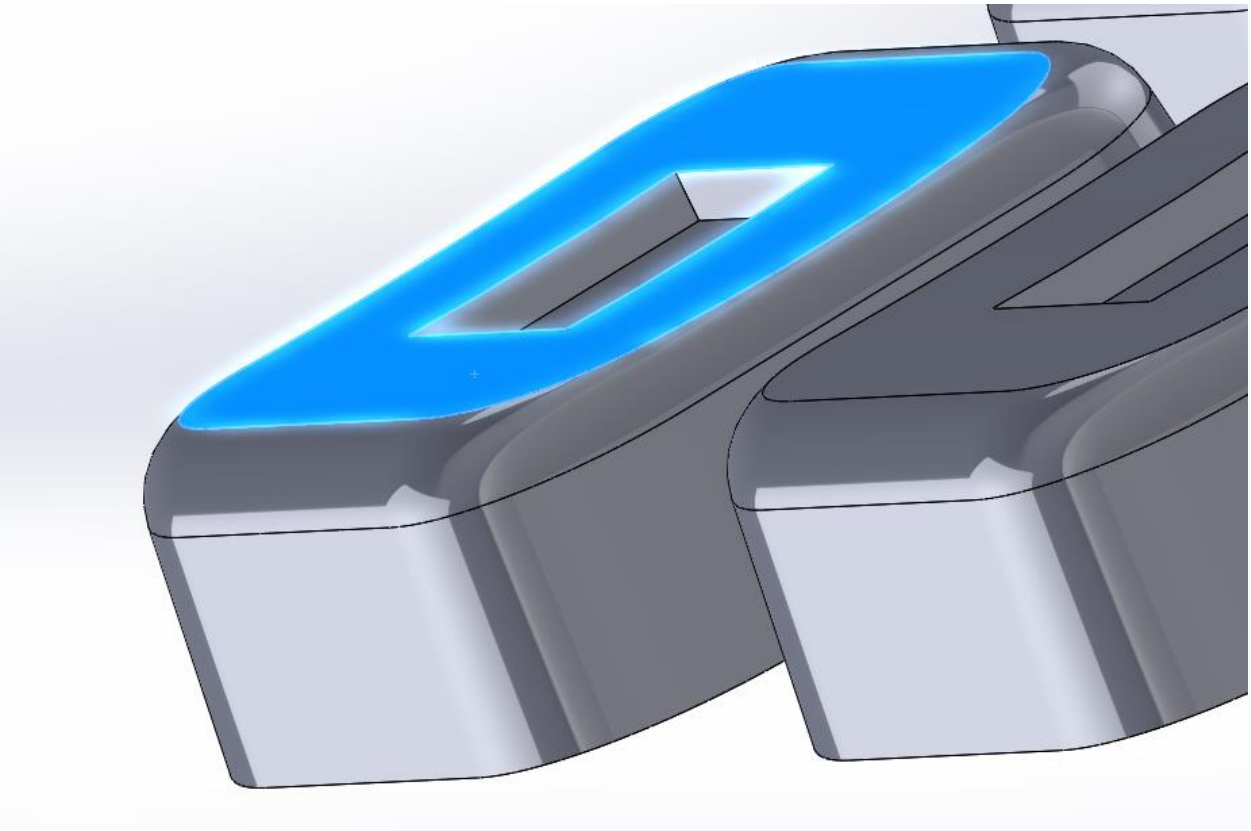

Figure 342: The face highlighted in blue was given some constant outward curvature with a cylindrical cut in an attempt to improve bonding to the fabric.

Testing Wedge-Shaped Segments of the FTASF Array.

Although it is perfectly conceivable that a full cylinder would behave differently from a radial section (say, 60 degrees' worth of the cylinder), just as planar arrays behave quite differently from arrays wrapped in a cylinder (as discussed in Chapter 7), it seems advisable to first test partial coupons of an entire cylinder, refining the gap between teeth as much as possible, before transitioning to experiments of full cylinders. After several iterations, a tooth spacing was discovered that gave the array an initial radius of curvature of around 2" (thus yielding a cylinder slightly wider than the test fixture's "leg" diameter of 3.5") and initial freedom in bending before lockup after around 25°. Strictly speaking, this segment of a cylinder has more bending freedom

than the entire cylinder should have, but just as the work of the previous chapter indicates that planar arrays have more curvature at lockup than do cylindrically-wrapped arrays, so to might partial-cylinder arrays have more freedom than full-cylinder arrays (for the same tooth spacings, etc.). Figure 343 shows a view of the undeformed segment, showing its initial cylindrical curvature. Figure 344 and Figure 345 show two views of the segment of the array subjected to a bending moment that locks it up.

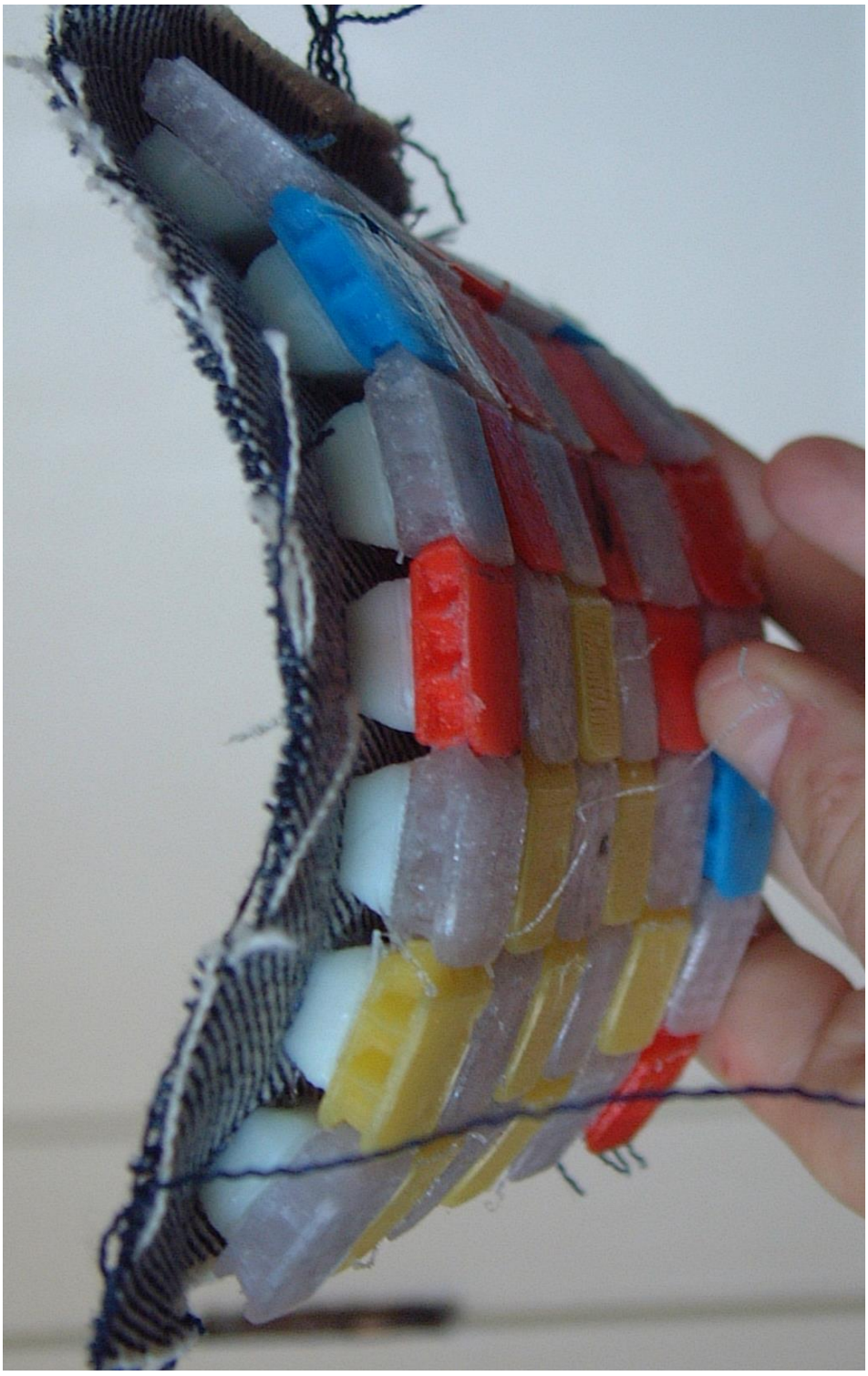

Figure 343: Undeformed pre-curved array, bottom view.

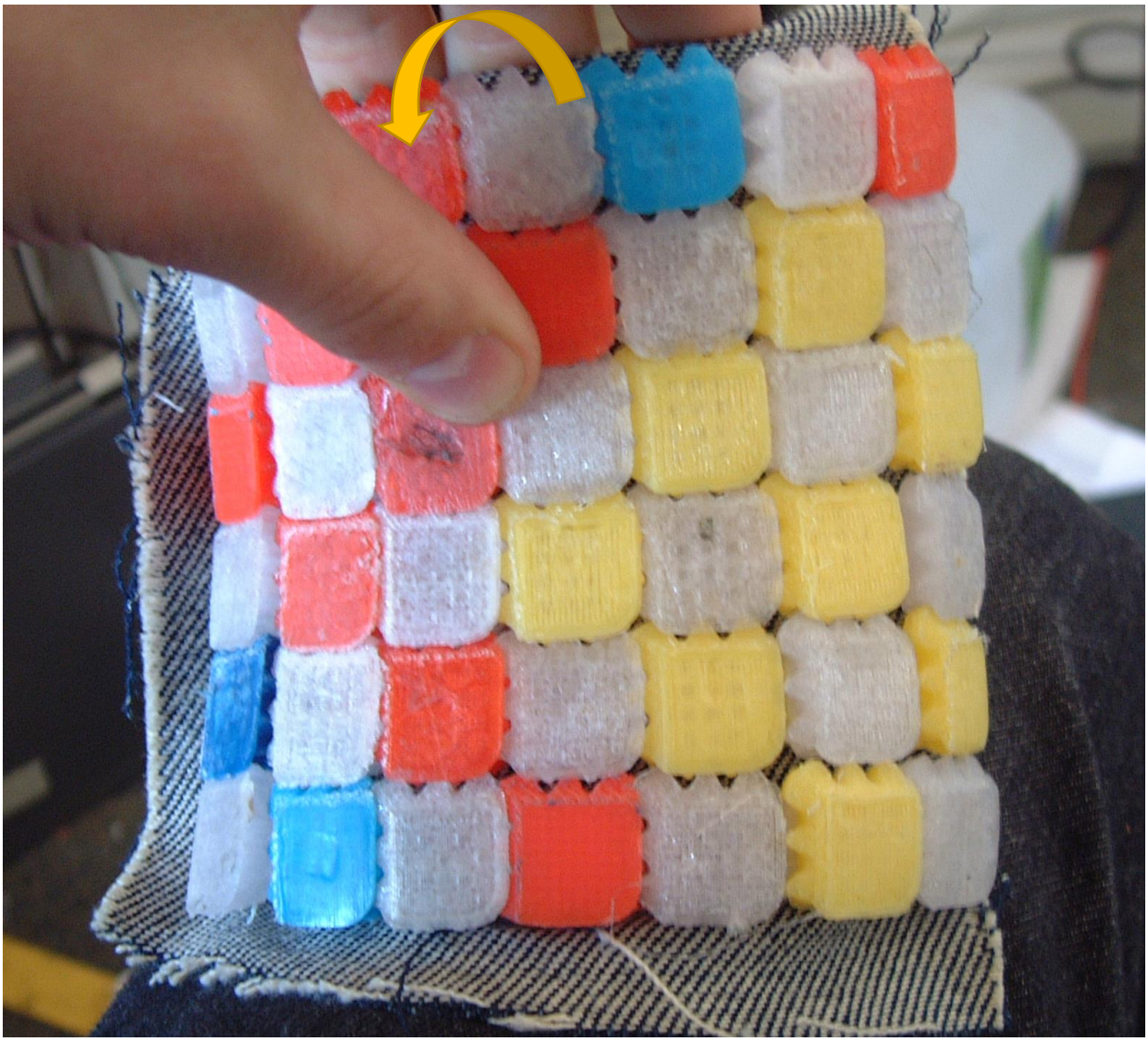

Figure 344: Pre-curved array in bending (the direction of which is shown by the yellow arrow), front view.

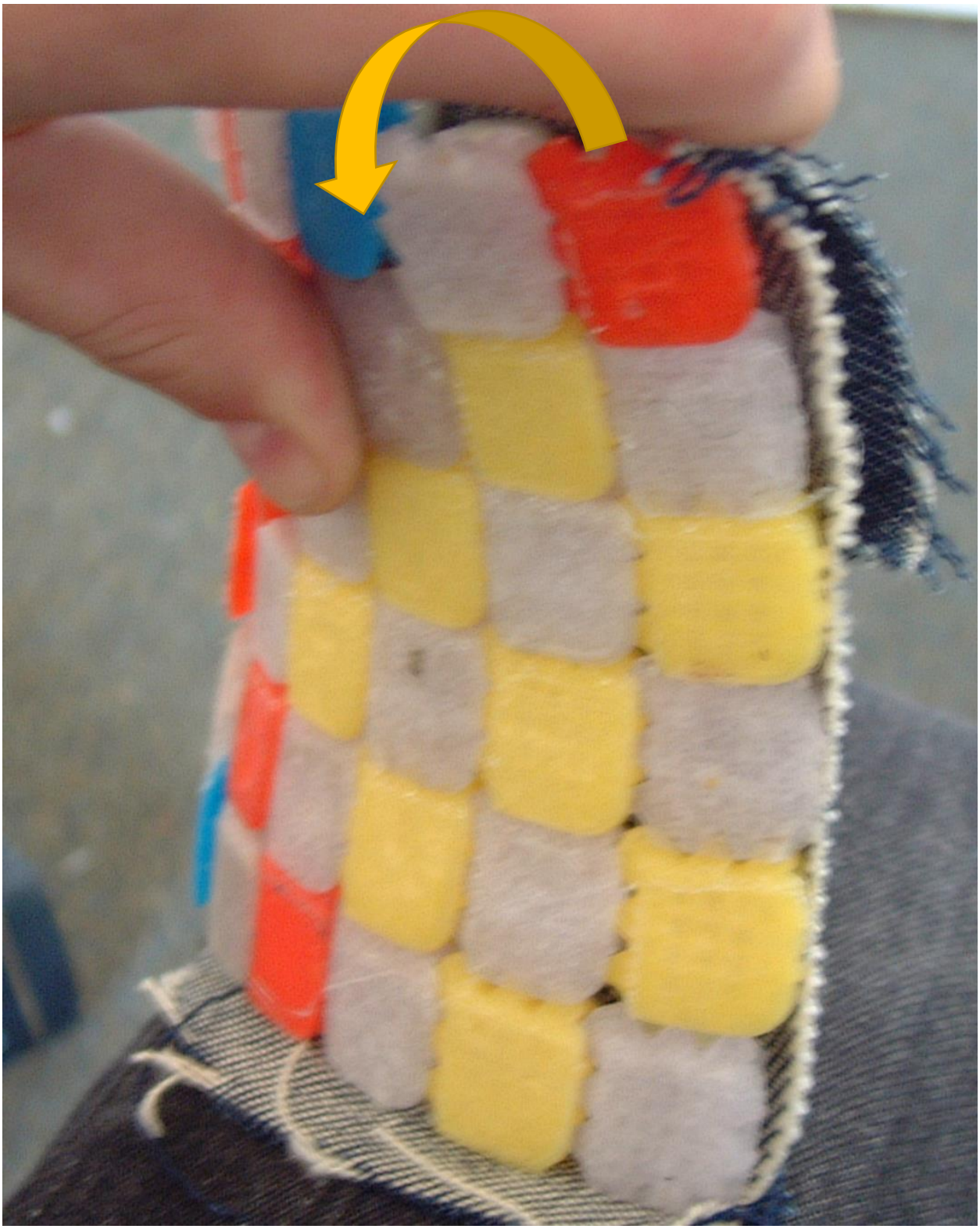

Figure 345: Pre-curved array in bending (the direction of which is shown by the yellow arrow), side view.

Of note, bending the portion of the cylindrical array in the direction opposite that in which it is supposed to stiffen is only free up to a certain point, as shown in Figure 346 (beyond this, some tooth contacts are inadvertently engaged, although they can slip past each other to an extent). This is likely undesirable, as, particularly in a full cylinder, it might reduce the structure's freedom when freedom is desired, and it might prove difficult to predict the onset of this contact as the teeth facing the direction of rotation are not engaged.

Figure 346: Bending the array in the opposite direction from that in which it is intended to stiffen up is free up to a point, but then some contacts are activated (as circled in orange).

Testing a Full-Cylinder FTASF Array.

The above experiments allowed the selection of vertical and tangential gap distances between teeth that provided the desired lockup curvature in wedge-shaped coupons; however, it

remained to be seen whether a full cylinder of the material would have comparable behavior. To this end, once the necessary gap distances for the desired lockup curvature had been achieved through trial and error, a full cylinder was constructed with the same gap distances. Figure 347 shows the cylinder mounted on the test fixture (after the ends were glued together). Strictly speaking, the cylindrical array had a slightly larger diameter than would have been ideal for the diameter of the simulated "leg" (leading to more sliding between leg and fabric and initial freedom not from the inherent initial freedom of the material in bending but from the "leg" not being in contact with the backbone initially). Also, the array was somewhat shorter than the length of the test fixture allowed, although it does not seem likely that there are many benefits to be gained from a significantly-longer protective structure.

Figure 347: Fabric array with FTASF teeth, mounted on the test fixture, with the joint in the neutral position.

Fortunately, it was possible to produce a full cylinder with an integer number of teeth in each circumferential ring (i.e. without having to use a fraction of one tooth for closure), although the gap between teeth along this seam is slightly out-of-spec, producing local curvature that is outwardly oriented (not inwardly oriented as at all other teeth), as may be seen in Figure 348: The region indicated with the green rectangle is the imperfect seam in the array. It did not seem to impair the overall function of the array, even though it saw teeth angled improperly thanks to improper spacing.. However, this minor arrangement imperfection did not hinder the array's performance. The array was produced on a woven fiberglass backing only because the woven

fiberglass fabric was the cheapest woven high-strength fabric available, not because it was thought to be a good candidate for the final product.

Figure 348: The region indicated with the green rectangle is the imperfect seam in the array. It did not seem to impair the overall function of the array, even though it saw teeth angled improperly thanks to improper spacing.

Ultimately, the array performed quite well in qualitative testing. When it was wrapped around the ankle simulator, the joint had initial freedom, but lockup occurred fairly rapidly. It appeared (to the naked eye) that the regions offset roughly ±90° from the direction of leg rotation saw lockup in shear first, causing the fabric in these regions to locally be tensioned (prior to this event, these regions should have had negligible shear stiffness thanks to the square weave of the fabric backbone, which has high bias compliance). Figure 349 shows an overall view of the

structure that focuses on the sheared regions of the array, and Figure 350 shows a close-up view of some teeth that have become locked up in shear. This second view shows that the convex and concave features on the teeth are essential to the structure's shear lockup (as might be expected from the wrapping of the 2D square array with similar features); of note, this particular array sees rather precarious contacts in shearing, since the wedged shape of the convex features cams the teeth apart vertically, leaving them further separated vertically than they were at the neutral position. Presumably, this vertical separation is halted by tensioning of the backbone, which might add to its stiffening effect (which would probably be beneficial). However, the small area of contact between the convex and concave features could see localized breakage.

However, locking up of some regions of the array in shear probably only stiffened the array moderately, and the main rise in stiffness probably did not occur until another degree of "leg" rotation, whereupon the region of the array facing the rotating leg would have seen teeth lock up in vertical contact, putting this area of the backbone strongly in tension and thus massively stiffening up the array. Figure 349 and Figure 351 through Figure 354 show regions of the array that see vertical compression of teeth after localized bending (leading to tensioning of the backbone and thus stiffening).

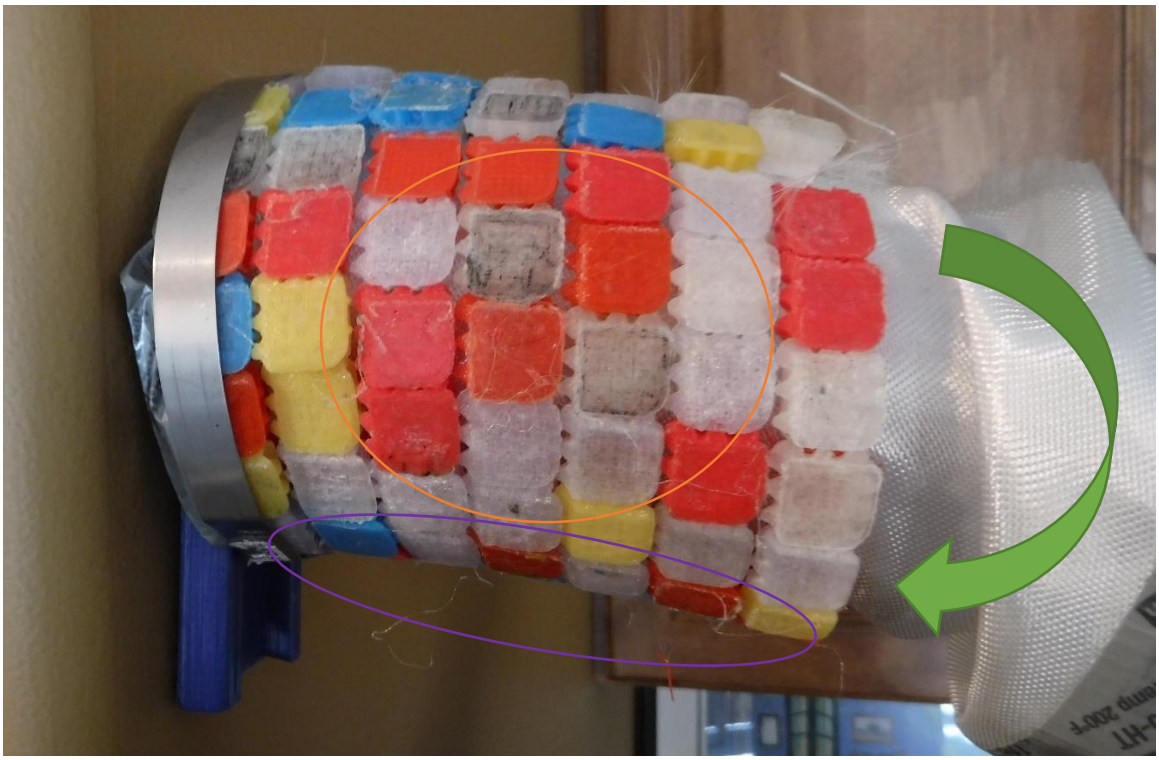

Figure 349: Fabric-backed array of FTASF teeth on test fixture, rotated until lockup, side view. The rotation direction is shown with a green arrow. Note the shearing of the array in the region circled in orange (this area saw lockup thanks to the anti-slide features of the teeth), and the bending of the array in the region circled in purple.

Figure 350: Close-up view of area offset 90° from the direction of leg rotation. The teeth in this portion of the array do not lock up in vertical contact from leg bending, but they do lock up in shear once they cannot slide past each other any further. In fact, the tooth design seems to cam the teeth apart vertically, leaving them further separated vertically than they were at the neutral position. This view most clearly shows the contact that produces shear lockup in the row that has been circled in green.

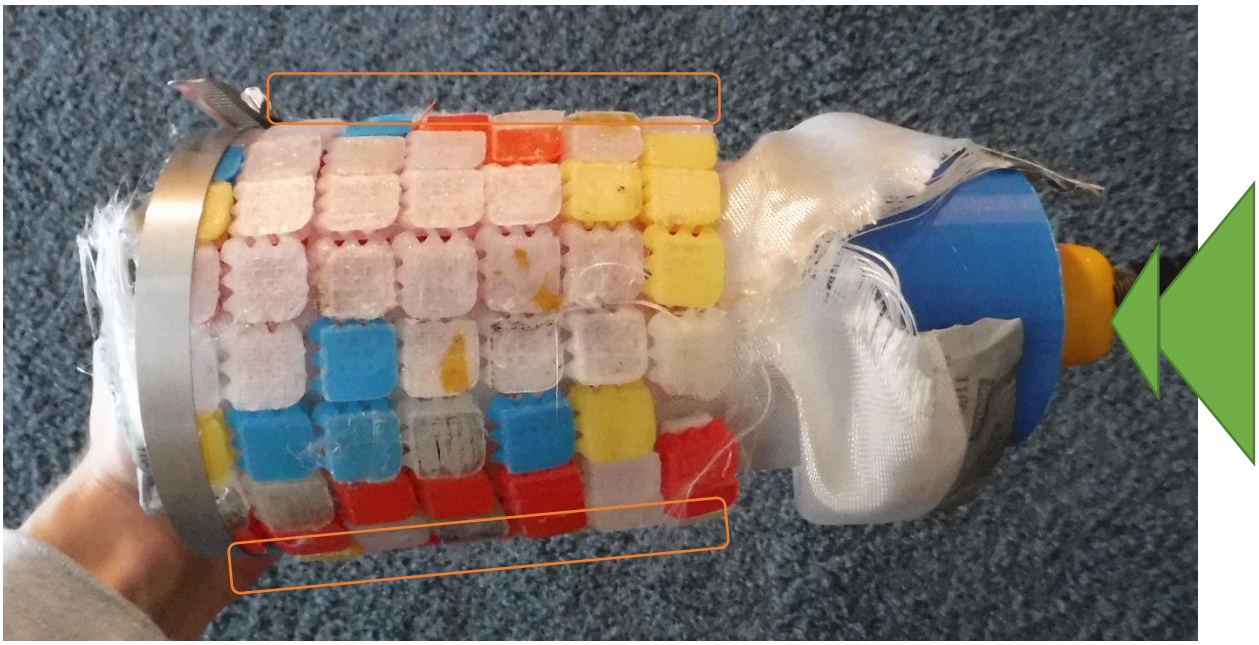

Figure 351: Fabric-backed array of FTASF teeth on test fixture, rotated until lockup, side view. The rotation direction is into the page, as shown with a green arrow. Shearing of the array occurs in the regions circled in orange (this area saw lockup thanks to the anti-slide features of the teeth).

Figure 352: Top-down view of array mounted on test fixture, with "leg" rotated in the direction shown by the green arrow.

Figure 353: Fabric-backed array of FTASF teeth on test fixture, rotated until lockup, side view. The rotation direction is out of the page, as shown with a green arrow. Shearing of the array occurs in the regions circled in orange (this area saw lockup thanks to the anti-slide features of the teeth), and bending lockup of the array occurs in the region circled in purple.

Although the ring of concave and convex features on each FTASF tooth does inhibit vertical sliding fairly well, should one tooth manage to slide vertically past one of its neighbors, it will usually find a new equilibrium in this undesirable position. A close-up picture of a tooth stuck in this position may be seen in Figure 354. Adding another ring of these features to each tooth might significantly improve control of vertical sliding, but at the cost of added

manufacturing complexity. Additionally, the next ring would need to be flared outward relative to the first one for positive engagement between both rings of concave/convex features.

Figure 354: The light blue tooth circled in orange has slid past its neighbors to the right and above it, preventing it from normal engagement with these two teeth.

Finally, the concave and convex features on the teeth that produce lockup after some shearing also cause the structure to lock up after a certain amount of torsional displacement. (Note that the cylindrical wrapping of the 2D square array with features to lock up the array after some shearing also had this property). Figure 355 and Figure 356 show the structure subjected to torsion up to lockup in opposite directions. While this might be useful for limiting transverse rotation of the ankle, the applying a boundary condition to let the leg that would let it slide

slightly up and down inside the sock but not rotate relative to the sock at all would require some complex joints that would be prone to reliability issues (these were discussed in greater detail in the previous chapter).

Figure 355: Maximum extent of torsional freedom at lockup, torsion in one direction (indicated with blue arrows).

Figure 356: Maximum extent of torsional freedom at lockup, torsion in opposite direction (indicated with blue arrows).

Next Steps for the FTASF Array.

Ultimately, the principles employed in this array seem fairly promising for constraining a joint by a constant bending angle when the structure is to lockup at the same bending angle when bent along any angle inside the plane of the foot. However, it is theoretically impossible to make the structure lock up at different angles depending on the direction of rotation (measured in the plane of the foot) while still using a constant tooth shape throughout the array, because those areas that are to have more freedom require larger vertical gaps, and a non-constant vertical gap is not compatible with a square tessellation. (Thus, the tooth shape might need to be changed to accommodate non-square tilings, or it might be necessary to use multiple tooth shapes throughout the array. Of the two options, the latter is less desirable as it would increase the complexity of assembly and require even more molds to manufacture). Beyond this, strictly speaking the structure might have different behavior if the vertical distances between teeth were increased to give the joint more bending freedom before lockup. It might turn out that small

tangential gaps between teeth are incompatible with large vertical gaps between teeth when the array is wrapped cylindrically (truncating the structure's freedom as shown in Figure 346 during the testing of wedge-shaped coupons of an entire cylinder.

Beyond these issues of the geometrical requirements for initial freedom, as with all arrays studied in this thesis, efforts should be undertaken to make the array thinner, lighter, and manufacturable without 3D printing.

Paradoxical Gear Flared Tooth Arrays.

Given the middling results of the FTASF tooth in a cylindrical array, it was determined to try another tooth shape for the cylindrical application, keeping in mind that ultimately it might not be possible to use just one tooth shape over the cylinder—it might prove necessary to vary tooth offset distances over the height and radial parameters of the cylinder, and, to cover the surface evenly, this might require different tooth shapes as well as different offset distances. Since flat arrays based on the paradoxical gear in a hexagonal packing were found in the previous chapter to have the special property of reconfiguring themselves into cylindrical curvatures when subjected to uniaxial compression along one axis (but not along axes at any other angle, including regular ones like integer multiples of 90° or 60°), they were thought to be especially well-suited to creating pre-curved cylindrical arrays: the only modification that should be necessary would be to flare the geometry of the tooth in the tangential direction of the final array. (However, simply using flat arrays after compressing them axially to sympathetically form them into cylinders seemed inadvisable as that seemed to reduce the initial gaps between teeth for both tangential and vertical contact).

Pre-Curved Cylindrical Array with Axis of Sympathetic Bending Perpendicular to Cylinder Axis.

In designing a cylindrical version of the paradoxical-gear array, the designer forgot that the sympathetic cylindrical contraction has only occured with compression along one particular axis (at least in unflared teeth in planar arrays) and accidentally oriented the teeth with their flared feature parallel to this axis (when logically, the flared feature for tangential contact should be perpendicular to the axis of compression that creates cylindrical contraction); this error is illustrated in Figure 357. Since the error was discovered well into production, it was deemed reasonable to at least test this array; after all, the flared features should give it initial curvature, and the complex behavior of the sympathetic cylindrical contraction might be unnecessary or even harmful, so testing the array principle without it could be useful. Figure 357 and Figure 358 show two computer-rendered views of this tooth array. Note that the differences between

this array and the 2D arrays utilizing paradoxical gear teeth are subtle.

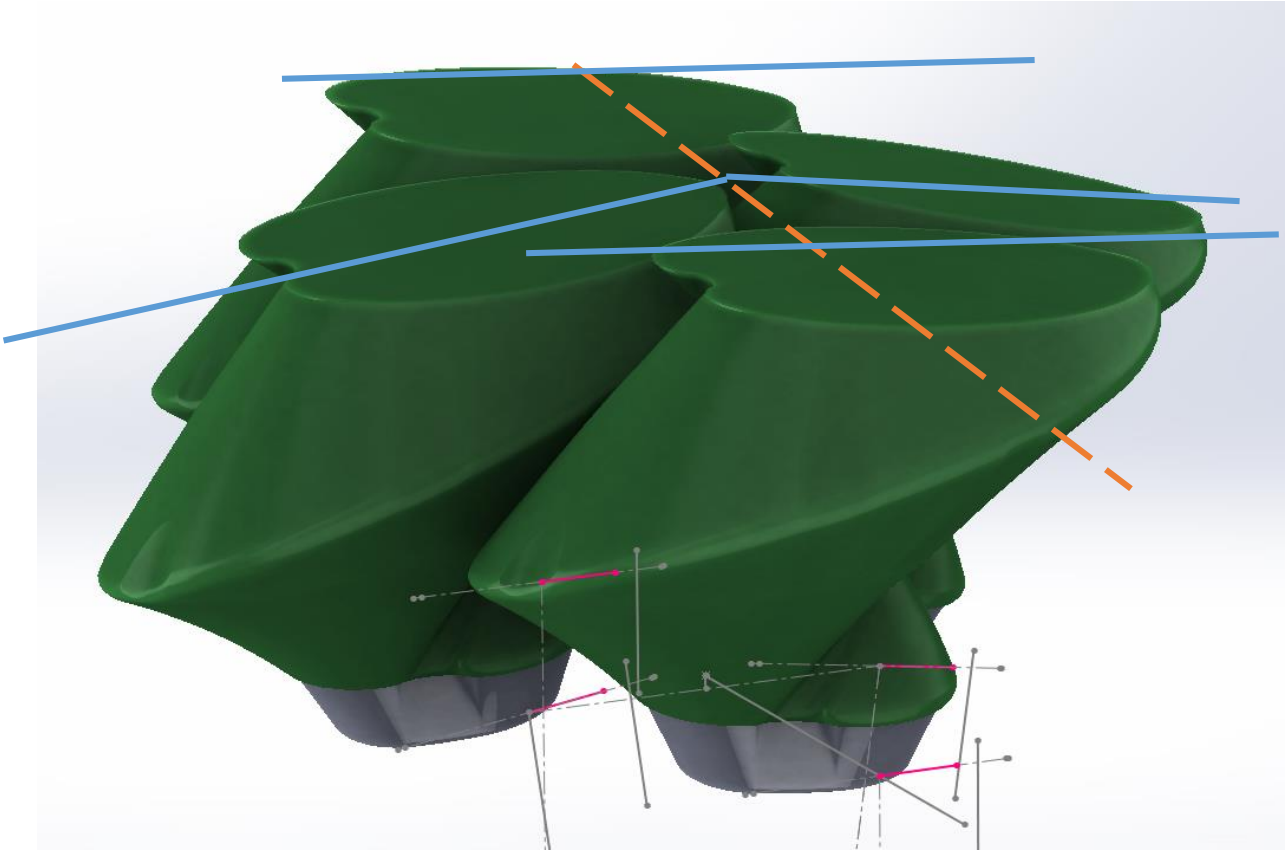

Figure 357: One view of computer rendering of teeth based on paradoxical array. Note flaring from the original shape to give tangential points of contact and initial curvature. The orange dashed line indicates the axis along which compression was hoped *to give sympathetic cylindrical deformation, and the blue lines indicate the axis (for each individual tooth) along which compression of a non-flared version of the tooth array would* actually *experience sympathetic cylindrical conformation.*

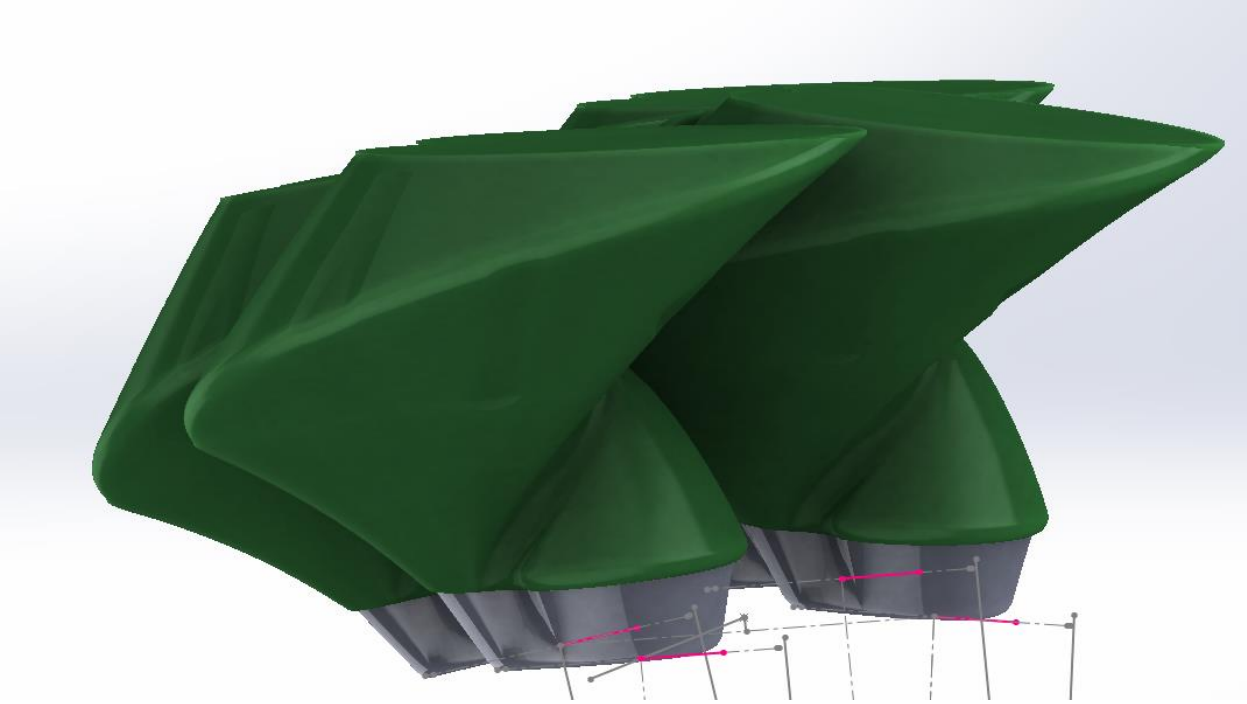

Figure 358: Another view of computer rendering of teeth based on paradoxical array.

It was determined to use an initial offset of 0.015" between teeth in both tangential and vertical directions, from which subsequent versions with more or less clearance in the two directions could be generated depending on the behavior of the first iteration. As usual, a 2D array of base parts that would be glued to the fabric and interface with the teeth was generated to provide these initial clearances. Initially, the designer accidentally generated a kite-based array of the base parts by tessellating along just two axes instead of the three required for a non-regular hexagonal packing, as shown in Figure 359. It was only after the base interfacing parts had been glued to fabric and teeth installed that the problematic effects of this additional mistake were discovered. Figure 360 and Figure 361 show a picture of the partially-finished array. Note the odd angles some teeth adopt even in the 'neutral' position (really, the closest approximation thereof with this irregular array). Not surprisingly, due to the irregularity of this array, most

teeth are initially touching, giving the array very little tangential and nearly zero vertical clearances and thus negligible initial freedom.

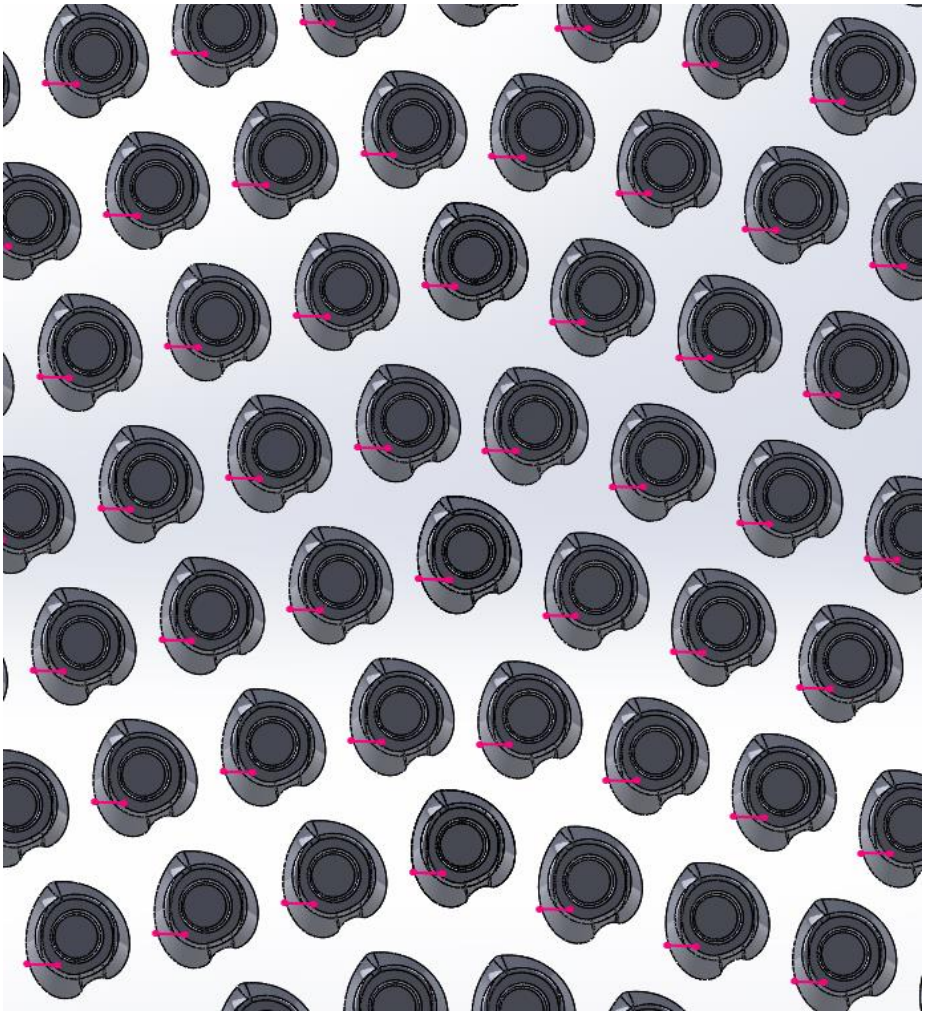

Figure 359: Spacing for base parts for flared version of paradoxical-gear array, derived from unrolling the cylindrical base-part array.

Figure 360: First iteration of flared paradoxical-gear array; note the strange tiling of base parts and corresponding (undesirable) initial synclastic curvature of the array. The array also had very little initial freedom.

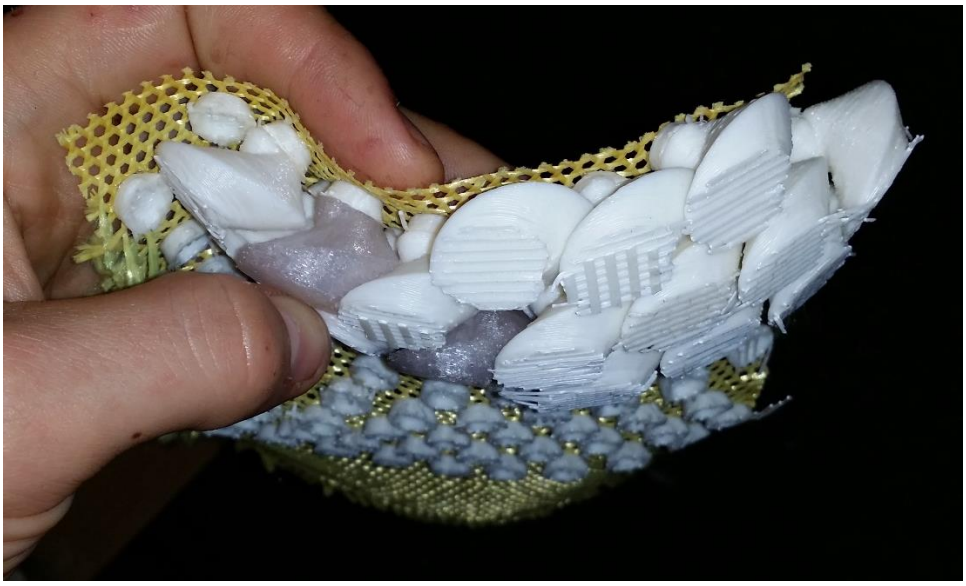

Figure 361: Another view of the same array in Figure 360.

The properly-generated base array with true hexagonal packing (albeit based on irregular hexagons) is shown in Figure 362. The first correct iteration of the array still had no initial freedom thanks to excessively-small gaps between teeth. Interestingly, it experienced cylindrical sympathetic deformation when compressed about an axis perpendicular to that expected (extrapolating from the behavior of planar arrays), as shown in Figure 363 and Figure 364.

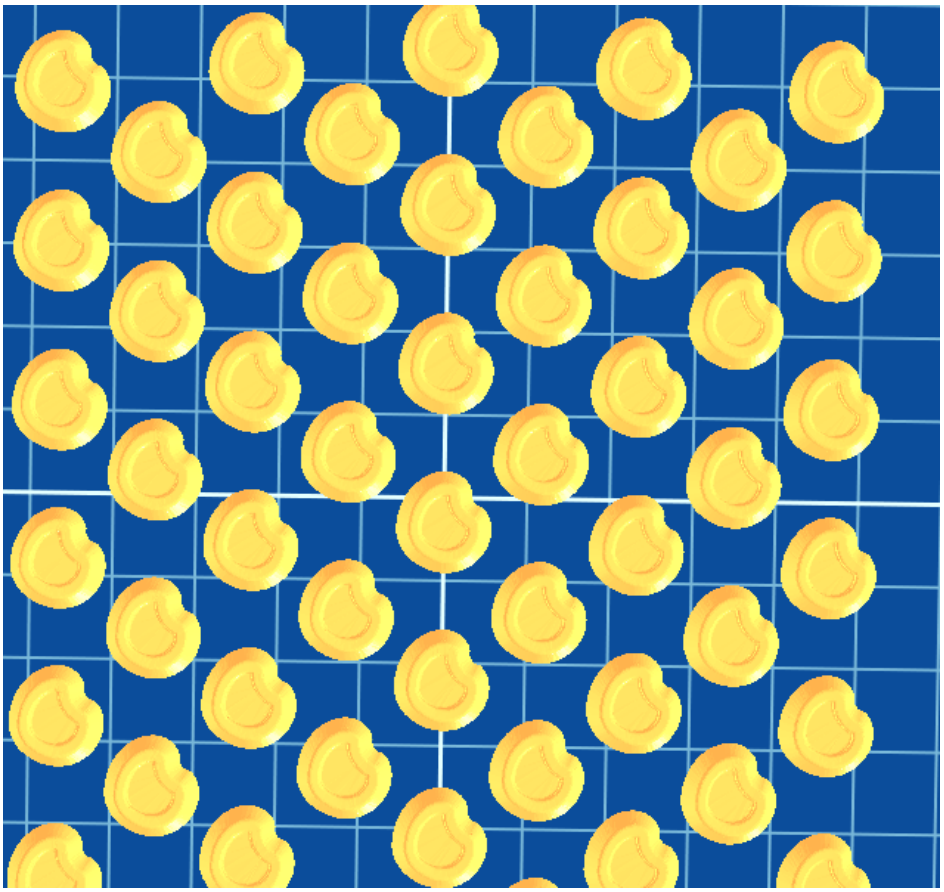

Figure 362: Proper hexagonal tiling of base elements for flared paradoxical-gear array.

Figure 363: Uncompressed flared paradoxical-gear array (note its undesirable lack of initial freedom and initial synclastic curvature).

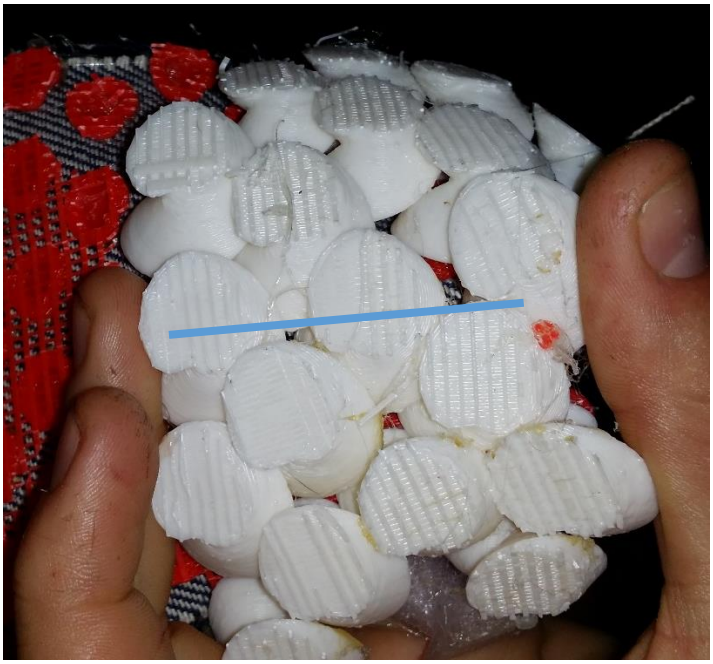

Figure 364: Compressing the array about the axis shown in blue produces sympathetic cylindrical deformation, though this axis is perpendicular to the one expected based on the behavior of planar arrays of unflared teeth.

The next iteration of this array was given much greater vertical freedom, with fairly promising results. As usual, a hexagonal array of base parts was first glued to the backbone; the array featured larger spacing between base parts than that used in previous iterations in order to give sufficient initial freedom to the final product. Then, the flared teeth were glued into the base parts. The completed array is shown in Figure 365; note its initial cylindrical curvature in the neutral position.

Figure 365: Pre-curved array (of the tooth configuration discussed above) in its neutral, cylindrical shape, with the cylindrical axis shown with a blue line.

Of note, the structure did not experience cylindrical conformation when compressed along the cylindrical axis (the blue axis shown in Figure 365)—this was mostly expected, but it was conceivable that the ability to conform cylindrically might also vary with gap distances between teeth, and, if so, the increased gap distances in this iteration might add it in a direction

that had hitherto not possessed it. In a related vein, the angular alignment between base parts and tooth inserts was somewhat variable, which would not be ideal for an array that relies on complex camming interactions between teeth to produce extra cylindrical curvature. However, since this array's orientation of the paradoxical gears does not produce this conformation, the inaccuracy in insert alignment likely will not matter much.

Interestingly, unbending the pre-curved array could be accomplished quite freely (when the ends of the array were not glued to each other, that is), but it produced a cylindrical curvature with its main axis perpendicular to the cylindrical axis of the original conformation; the second conformation is shown in Figure 366. Neglecting both frictional effects from teeth sliding relative to each other and the slight losses from bending the fabric backbone, this transition was nearly an equilibrium, zero-loss change (just as rotations of links in a mechanism with kinematic freedom should theoretically be). This transition is limited in freedom, since once the new cylindrical curvature has been achieved, further bending along the original axis will constitute vertical bending relative to the new cylindrical axis, and this will engage the backbone in tension after a bit more freedom. This property might allow for the constraint of a joint with much more complex motion than the ball joint under investigation in this thesis; however, for this assignment it is merely a curiosity. (Of note, the constraint of such a complex joint might benefit from adding teeth on the opposite side of the fabric from that on which teeth were added here, in order to prevent inward shell buckling.)

Figure 366: Bending the cylindrically pre-curved array to open up the initial curvature freely transforms the array into a cylindrically-curved array with the new cylindrical axis (shown in green) perpendicular to the original one (shown in blue). This transformation does not engage the backbone in tension and is thus very easy to accomplish.

Ultimately, this array successfully locked up after some initial freedom; different views of the lockup deformation profile can be seen in Figure 367 throughFigure 369. This array gave the joint more initial freedom before lockup than previously-tested wrappings (including the 2D square array shown in the previous chapter); it is hypothesized that the larger offset distance between tooth surfaces was not the only feature contributing to this increased freedom, and that the compressive freedom enjoyed by the array (thanks mainly to the relatively small areas of bonded contact between teeth and fabric, which inhibit fabric buckling in compression when they are large). Note also in Figure 367 that the portion of the array 180° offset from the direction of rotation conforms unusually well to the simulated "leg" (in contrast, for instance, with the

wrapped square array of the previous chapter, which saw the area around 180° away from leg rotation remain nearly vertical and thus separated from the leg)—this is certainly a desirable quality, and may result from the high initial compressive freedom enjoyed by the backbone, or may be a special property of the paradoxical gear teeth.

Figure 367: Side view of test fixture fitted with pre-curved array, bent until lockup. The green arrow shows the direction of bending, and the blue arrow shows the vertical direction (the plane of the base of the test fixture contains this vector).

Figure 368: Top view of test fixture fitted with pre-curved array, bent until lockup. The orange arrow shows the direction of bending.

Figure 369: Orthogonal view of test fixture fitted with pre-curved array, bent until lockup. The orange arrow shows the direction of bending.

Although this tooth design thus clearly appears effective, it is crucial to develop a modification of the tooth design that would produce much lower material thickness—the thickness of the material in this iteration was massive at nearly 0.75", giving the structure a correspondingly-undesirable weight. Beyond that, thus far there is no conclusive evidence that the additional manufacturing work required to produce a pre-curved array is compensated for by improved mechanical properties. Granted, this is largely the result of insufficient research into

the properties of wrapped 2D arrays (the obvious competitor to pre-curved arrays), specifically into differences in tooth recruitment between the two classes of arrays. In particular, it does appear that the pre-curved array sees more uniform deformation with joint rotation than did the wrapped 2D array of the previous chapter (which saw very localized deformation). However, it is difficult to quantify these differences by simple inspection; a computer model or motion camera approach (assigning a tracking particle to many if not all teeth) would probably be required for maximum precision in measuring tooth recruitments.

Ultimately, even if there are significant advantages to pre-curved arrays, that does not indicate that this specific paradoxical-gear tooth shape is of particular utility, particularly when it appears in the orientation shown above (i.e. the opposite orientation from the one that will produce sympathetic cylindrical conformation). The next section begins an examination of the flared paradoxical-gear tooth shape with the flaring and tangential orientation in the more-logical direction, although it was not possible to finish the investigation in the timeframe of this thesis.

Cylindrical Array with Axis of Sympathetic Deformation Collinear with Cylinder Axis.

In contrast to the above arrays based on the paradoxical gear, this one seems a more logical employment of the sympathetic-deformation properties of arrays based on the paradoxical gear. A CAD rendering of this geometry is shown in Figure 370. The small segment of the cylinder that was assembled is shown in Figure 371. This array had moderate initial cylindrical curvature (traced in the above-referenced figure) and a very small amount of initial bending freedom that ought to be increased in future iterations but was at least sufficient to demonstrate the ability of this structure to bend freely before lockup.

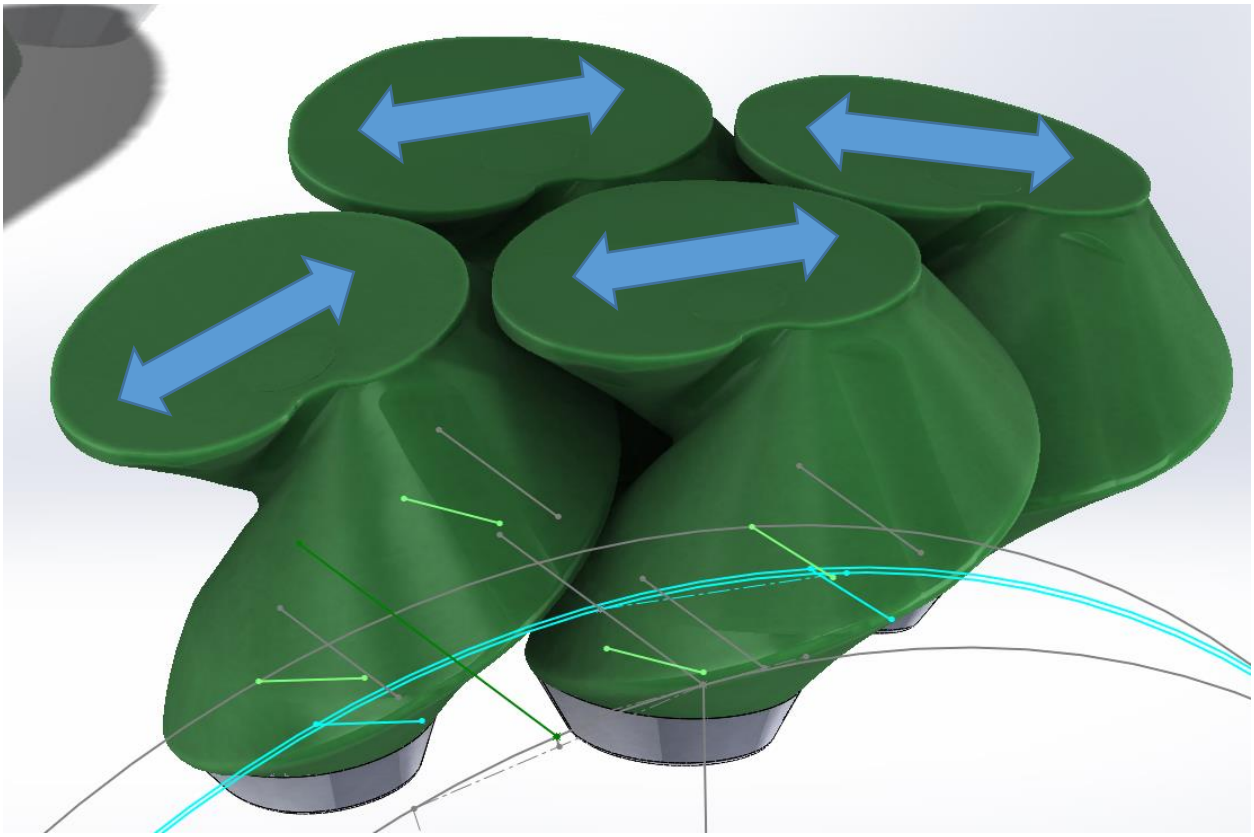

Figure 370: Array based on paradoxical gears with the alternate (or, rather, the more logical) orientation of flaring each tooth (the direction of this flaring is shown with the blue arrows). It is expected that compression along the grey axes will produce further cylindrical contraction.

Figure 371: Undeformed view of the array. Note the irregularity in the rotations of teeth; this is due to poor accuracy in assembly (likely the result of thin walls in the base feature that cannot exert a strong hold on the corresponding feature on the tooth inserts).

Confusingly, this orientation of the array experienced cylindrical sympathetic deformation about the opposite axis expected (as did the previous orientation), as can be seen in Figure 372. This frustrating behavior may indicate that the direction of cylindrical sympathetic conformation depends not just on the angle of rotation of the paradoxical-gear feature, but also on the offset distance between teeth and/or the flaring of the teeth required to produce initial cylindrical curvature. Future iterations of this array should be produced with an eye towards determining whether the improved spacing parameters recommended above happen to see the direction of cylindrical curvature conformation revert to the expected direction; if not, the tooth will likely need to be redesigned to produce further cylindrical conformation with compression while enforcing initial cylindrical curvature.

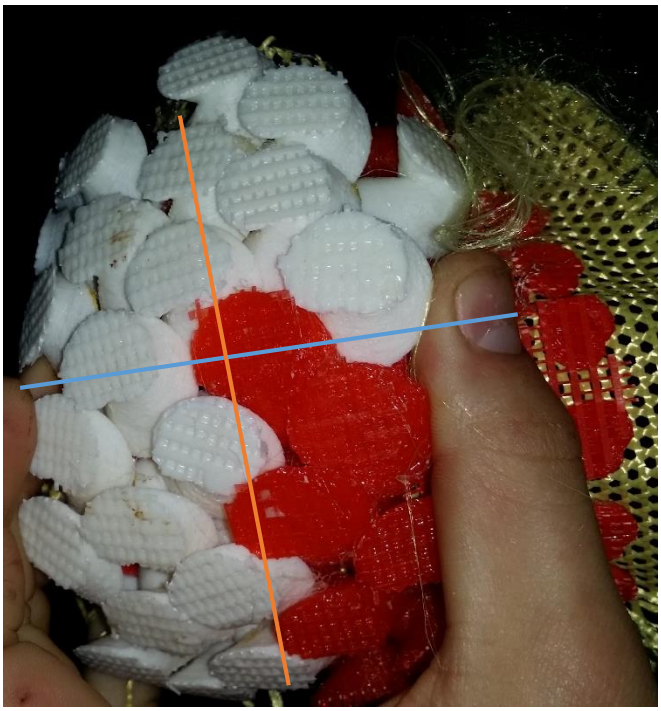

Figure 372: It is in compression along the blue axis, not the expected (orange) axis, that the array conforms cylindrically.

Proposal for Finite-Element Simulations of Fabric-Backed Precurved Arrays.

At first glance, it would seem nigh impossible to perform a meaningful FEA of the fabric-backed arrays shown in this chapter and the last. While the geometry could be easily-enough generated (ignoring the microscopic texture of the fabric), treating fabrics as simple solids of the same thickness would be as foolish as conflating carbon fiber fabric with the same thickness carbon-fiber-reinforced cured epoxy (based on a fabric of the same weave): the former has low bending stiffness (thanks to the abilities of fibers to slide and twist relative to each other and microbuckle in local compression) and negligible compressive stiffness along the fiber directions thanks to a near-instantaneous buckling onset, plus (if it is a square weave) bias freedom. That said, some solvers (including Abaqus, but not ANSYS) can model materials that have zero compressive stiffness, though such materials tend to require significant quasi-static

viscous stabilization even when the fabric has other loadings (e.g. a pressure loading that keeps the fabric moderately tensioned in most places).

One other potential approach would be to model the fabric backbone as a shell with much smaller thickness than the fabric's actual thickness, but to increase the material model's stiffness accordingly to give the overall structure the same tensile stiffness. It is hoped that this approach would reduce the structure's bending stiffness to a negligible quantity, especially post-buckling, while accurately capturing the high stiffness of fabric structures. However, arc-length and/or viscous stabilization methods would be needed to allow a quasi-static solution to converge after the onset of buckling; these methods can increase solution time, and artificial viscosity can add fictitious forces. That said, since predicting the structure's shape (and thus the needed shapes of individual teeth) would be the main concern in such simulations, not deciding whether post-lockup stiffness will be sufficiently high or the pre-lockup stiffness sufficiently low (these being easily testable and not likely to depend too much on tooth geometry if enough teeth are engaged in lockup and no teeth are touching before lockup), inaccuracies in force results should not matter too much here.

In either case, anisotropy from the limited fiber orientations should be easy to add, although, since the main task of FEA will be to find the optimum tooth shape at each point to produce lockup after a specific amount of rotation, this sort of anisotropy will not likely matter as tensile strains should be small relative to displacement from bending. However, the effects of fabric bias might me more difficult to model—a material model with high in-plane strain compliance would be a good start, but this alone would not capture the high effective Poisson's ratio along the bias.

In summary, it would likely be useful to learn computational or semi-computational techniques for modelling fabrics and adapt them to FEA techniques after local tooth contacts begin. Then, the effects of different clearances over the geometry of the protective structure on stiffening-up characteristics could be observed and optimized. Generating the arrays manually for testing on the test fixture is far too tedious.

Chapter 9. Conclusions and Future Research.

Clearly, some cylindrical wrappings of fabric-backed arrays developed in this thesis meet the most basic mechanical requirement of allowing a joint free motion within a certain range but then rapidly stiffening. This success contrasts sharply with the failure of the solid-backed "annular comb" arrays to lock up (even as they had excessive initial stiffness) in computer simulations. Additionally, the solid-backed linear combs investigated in this thesis proved to be difficult to integrate into a cylindrical context due to their inability to buckle or otherwise compress vertically, although their bending lockup behavior was acceptable.

The success of the fabric-backed arrays comes from two features: first, when teeth are not touching, the structures are quite compliant in bending, thanks to the fact that fabrics naturally have negligible bending stiffness, even if made of fibers that are extremely stiff in tension (e.g. Kevlar), as long as the fabrics are thin. Second, once the teeth touch, they put areas of the backbone into tension, giving very high stiffness-to-weight ratios. (In contrast, annular combs or even chainmail made of 3D printed plastic were limited in the maximum stiffness they could produce due to the low stiffness of unreinforced plastic). However, even the most successful arrays have so far performed well only with a highly-simplified simulator of the human ankle joint that neglects complexities in the manifold and rotational behavior of the human leg and ankle. Also, as yet there is no known way of computing a gap distance and tooth shape that will produce lockup at one specific angle—so far, these parameters have only been estimated with

simple trial and error (in contrast, planar arrays' curvature at lockup can easily be predicted; for some reason, wrapping such arrays into cylinders changes their lockup behavior).

As such, significant quantities of work remain to be done to bring a product to market. First, as far as mechanical and geometric considerations go, it remains to be seen what the maximum angle of freedom is that can be created for the underlying joint while still causing rapid lockup after that angle. (For instance, the studies in this thesis saw lockup at around 15°; however, lockup at plantarflexion or dorsiflexion should be much higher, perhaps 35°, and it is uncertain if this increased freedom can be achieved just by locally increasing tooth gap distances). It is this author's suspicion that significant amounts of compressive axial freedom in areas offset angularly from the contact patch will be needed to produce this. However, geometries that could produce this sort of freedom should only be investigated if high freedom cannot be achieved simply by increasing tooth gap distances (either everywhere in the array, or at least in regions offset from the contact patch).

Next, there is the problem of maximizing lockup efficiency by recruiting as many teeth as possible. Some of the cylindrical wrappings investigated in this thesis showed two regions of teeth that locked up: first, the teeth in the immediate "shadow" of the leg-contact area locked up in vertical contact with one another, and second, teeth offset roughly from 60° to 120° (clockwise and counter-clockwise) from the direction of leg rotation happened to lock up in shear at about the same time. It should be emphasized that this was the result of happy chance, and theoretically vertical lockup could take place so long before shear lockup that the latter would never contribute to overall stiffening (or vice versa). Thus, some relationship between shear and vertical gap distances to produce lockup in these two modes should be discovered. In a similar vein, if the manifold geometry is changed (as described below) to better conform to a

human leg, it may be necessary to optimize tooth shapes over the domain to ensure that all teeth inside a given vertical wedge in the cylinder lock up simultaneously in vertical contact, as currently happens with a cylinder.

As an aside, lockup efficiency could be further increased by networking threads of high-stiffness fiber with initial slack on the sides of the sleeve; only once the teeth had bent out enough to put the initially-slack fibers in tension would this region see stiffening. Admittedly, this idea has not yet been tested at all with cylindrical arrays, although it was briefly explored in this thesis in the context of the linear, plastic-backed comb; it should work as long as the teeth to which the fibers are attached have sufficient contact area with the fabric backbone, although it might be time-consuming to add these features.

Of note, for many joints, it is essential to be able to vary the lockup angle with respect to the direction of rotation. For instance, for the human ankle, lockup should happen much faster with inversion/eversion than for dorsiflexion/plantarflexion. Most of the cylindrically-wrapped fabric-backed arrays (both pre-curved and initially-2D) developed in this thesis use true tessellations of one or at most two shapes; in other words, both tooth shape and gap size are the same all over the rotational domain of the cylinders for these arrays. However, one array was developed with a sharp transition in vertical gap distance, and it indeed featured different lockup angles when the leg was rotated inside different planes. However, future research needs to demonstrate the feasibility of producing continuously-varying lockup rates at different cylindrical angles by varying tooth shape and/or gap distance over that cylindrical angle. As discussed above, other aspects of the array's performance may benefit from varying the tooth shape and gap sizes over the area of the array, so perhaps a unified process can be developed that produces an ideal lockup cross-sectional shape at every wedge comprising the cylinder.

Next, ways of accommodating the non-cylindrical geometry of the human leg and ankle complex must be considered, both to permit easy removal of the brace and to ensure problem-free interaction of the leg with the brace during movement. The most obvious solution, using a cylindrical or semi-conical manifold separated into two halves for easy removal, might not work due to the sharp inflection point in concavity at the end of the calf muscle; however, if either of these shapes does permit acceptable leg motion, it is clearly better to use such a simple shape than to investigate the alternative, namely using plain weaves of stiff fibers that are simply tailored to fit the leg closely (and perhaps split into two or more shells to allow removal and donning of the protective sleeve. To produce this geometry would vastly increase the complexity of manufacture, since the inelastic fabric would need to be cut and sewed in many places in order to conform to the leg. Another option would be to develop a fabric with stiff fibers (e.g. Kevlar) in the warp but elastomer fibers in the weft. The warp would then be oriented vertically, allowing stiffening when tooth lockup puts the backbone into tension, whereas the weft would not be involved in stiffening directly: its sole purpose would be to keep the sleeve on the leg while permitting the wearer to remove and apply it as necessary (much as a sock has elasticity that prevents it from falling down in the course of normal wear but still allows it to be removed). It is unclear if the fabric could lock up in shear with a low-stiffness fiber in the weft direction. Note that having a large offset distance between the leg and the protective structure is undesirable because it would take up too much space on the leg and risk catching on foreign objects, even though it would greatly simplify the question of how to put on and remove the brace.

Finally, a realistic biodynamic model of the human ankle joint should be used to produce realistic, coupled leg motions with a chosen method of securing the brace to the leg. The model

used in this thesis treats the ankle like a simple spherical joint, ignoring the complexities of coupled joint motions, but the actual behavior of the leg might see incorrect lockup patterns with a brace based on a spherical model. If necessary, tooth shapes and gaps should be varied over the domain to produce lockup with the more accurate leg motions.

It is anticipated that a FEA model of the fabric structure could allow easy optimization of all mechanical aspects of lockup, allowing the researchers to forgo the time-consuming manufacture of models with every new tooth or manifold shape. Such a computer model could consider the effects of a non-circular manifold, varying tooth shapes and gap distances over the domain, bias compliance, shearing regions, coupled motions in the ankle joint, and even special tooth geometries that give the structure extra initial compressive freedom. From the standpoint of computational efficiency, it would be wise to treat the teeth as rigid bodies and the backbone as a thin shell; however, it would be essential to use a material model that gives the fabric backbone both negligible compressive stiffness (ergo very low buckling resistance) and initial compliance in tension along the bias (although the radial stiffness of fibers means that the fabric will eventually stiffen along its bias).

Even once all requirements relating to lockup have been met, some other requirements must be taken into consideration to ensure the device is ready for athletics. For instance, the fabric sleeve must be breathable, the overall structure must be thin and light, the product must be able to withstand many wear cycles, etc. However, it is not anticipated that any of these requirements would prove insurmountable with the possible exception of the requirement of thinness: producing very thin tooth arrays might require more resolution than what the FFF printers used in this thesis are capable of, necessitating the use of stereolithography. That said, FFF printers might prove up to the task of generating sufficiently-thin arrays; as documented in

the final appendix to this thesis, the minimum tooth size that could be printed for the pre-curved cylindrical array with anti-slide features accurately enough for proper tooth interfacing had a total thickness of around 1cm, which may prove to be permissible for production.

Aside from manufacturing concerns about the minimum feasible tooth thickness, for a given tooth material (presumably unreinforced plastic), there might be a minimum tooth thickness required to produce the final stiffness needed to ensure safety of the wearer. As such, it is essential to determine the maximum acceptable thickness for athletic purposes and then investigate whether an array having this overall thickness can be made stiff enough for protective purposes. Specifically, this investigation should be concluded before significant amounts of time are invested into researches into tooth geometries.

Finally, although additive manufacturing techniques will likely be used heavily during the research phase, once ideal geometries are selected, it would be preferable to develop means of mass-producing the teeth (probably by injection molding) as well as automated ways of bonding them to the fabric. Perhaps several sizes of each brace should be designed so that the final product does not have to be tailored to fit each individual athlete (which would demand the use of digital manufacturing techniques). That said, if each tooth shape in a given manifold must be unique, or if extremely-complicated tooth shapes prove necessary, then it may not be possible to produce the teeth with injection molding, which would greatly increase the cost of the final product and correspondingly reduce sales volume and overall profits.

Appendix I. FDM 3D Printing Guidelines for Hyrel 3D Printer.

The fused-deposition modelling (FDM) 3D printing process is generally associated with hobbyist-grade products that serve only as decoration, devoid of mechanical functions; the use of FDM printers in actual industry is mostly limited to producing prototypes to gauge their look, feel and sizing—the hype about how additive manufacturing will supposedly enable a revolution by allowing printing of objects manifestly unsuited to it (e.g. cars and houses) notwithstanding.

Of course, additive manufacturing promises to allow creation of geometries that would be impossible or impractical to machine (e.g. highly-optimized truss structures that can possess better stiffness-to-weight ratios than solid or semi-hollow structures of the same base material.) The SLS process has thus far received the greatest attention for industrial purposes, as it can use materials that require high temperature processing (metals and ceramics). FDM processes, by contrast, cannot attain a temperature anywhere near that needed to melt steel, and even higher temperature plastics often give unsatisfactory print quality when printed at the elevated temperatures they require to flow.

Basic ABS Filament.

Average mechanical properties: 28.5MPa tensile strength, 1807MPa modulus as printed[56]. Large-scale surface roughness can easily be reduced with acetone vapor bath.

Hyrel print settings (through 0.5mm nozzle): 200 steps to prime, 225 to unprimed, .76 pulses/nL

[56] "Mechanical properties of components fabricated with open-source 3-D printers under realistic environmental conditions," Tymrak, Kreiger, and Pearce

Print temperature: 245°C first layer, 235°C remaining layers.

Recommended print substrates: Glass with layer of ABS applied (dissolve ABS in acetone, spread on glass, allow to evaporate. Don't inhale fumes!) ideal. Polyetherimide tape works reasonably well, too.

Print fan setting: Fan not recommended at all, except for bridges and possibly very small parts.

Cold-End Cooling? Not needed.

Heated bed? Yes.

Heated chamber? Yes.

Support material compatibility:

- HIPS—bonds well to ABS, but the D-limonene used to dissolve HIPS both embrittles and plasticizes ABS, too.
- PLA—bonds reasonably well to PLA. High strength NaOH (3 molar) recommended to dissolve PLA. ABS's resistance to NaOH is rated as excellent[57]

Other: Do not allow head to remain heated with ABS in the chamber (i.e. when not printing at all, or printing at such high vertical resolution that the mass flow rate through the head is low). It will degrade and become difficult to remove.

Graphite-Impregnated ABS Filament.

Average mechanical properties: significantly lower friction than standard ABS. Increased toughness and lower stiffness and strength (surprisingly).

[57] http://www.coleparmer.com/Chemical-Resistance

Hyrel print settings (through 0.5mm nozzle): 200 steps to prime, 220 to unprime

Print temperature: 245°C first layer, 235°C remaining layers.

Recommended print substrates: Glass with layer of ABS applied (dissolve ABS in acetone, spread on glass, allow to evaporate. Don't inhale fumes!) ideal. Polyetherimide tape works well, too.

Print fan setting: Fan not recommended at all, except for bridges.

Cold-End Cooling: Not needed.

Support material compatibility:

- HIPS—bonds well to ABS, even when graphite-infused, but the D-limonene used to dissolve HIPS both embrittles and plasticizes ABS, too.
- PLA—bonds reasonably well to PLA. High strength NaOH (3 molar) recommended to dissolve PLA. ABS's resistance to NaOH is rated as excellent[58]

Other: Do not allow head to remain heated with ABS in the chamber (i.e. when not printing at all, or printing at such high vertical resolution that the mass flow rate through the head is low). It will degrade and become difficult to remove.

Taulman Nylons.

Average mechanical properties:

Hyrel print settings (through 0.5mm nozzle): 200 steps to prime, 295 to unprime, .66 pulses/nL

Print temperature: 245°C first layer, 245°C remaining layers.

[58] http://www.coleparmer.com/Chemical-Resistance

Recommended print substrates: Prints pretty well on nylon-containing fabrics (these must be held down to a rigid surface with double-sided tape as well as tape around the edges). Sticks pretty well on PEI tape. Sticks too well to Garolite (better even than other nylons), such that removal is impossible.

Print fan setting: Perhaps for small details. However, nylon warps a lot.

Cold-End Cooling? Not needed.

Heated bed? Yes.

Heated chamber? Yes.

Support material compatibility:

- PVA—expected to bond very well to PVA, like other nylons. However, PVA is challenging to print.
- PLA—bonds reasonably well to PLA. High strength NaOH (3 molar) recommended to dissolve PLA. ABS's resistance to NaOH is rated as excellent[59]

Other:

PVA Filament.

Standard PLA Filament.

Average mechanical properties: 57MPa tensile strength, 3370MPa tensile modulus as printed[60]

Hyrel print settings (through 0.5mm nozzle): 200 steps to prime, 290 to unprime, .68 pulses/nL

[59] http://www.coleparmer.com/Chemical-Resistance
[60] http://www.appropedia.org/Mechanical_Properties_of_Components_Fabricated_with_Open-Source_3-D_Printers_Under_Realistic_Environmental_Conditions

Print temperature: 200°C first layer, 195°C remaining layers.

Recommended print substrates: glass (coat with PVA from a glue stick for best adhesion)

Print fan setting: Recommended for all layers.

Cold-End Cooling? NECESSITY with Hyrel head.

Heated bed? Not required but recommended at 40°C.

Heated chamber? Not required.

Support material compatibility:

- PVA.

Other:

Taulman in-PLA Filament.

Print temperature: 240°C first layer, 240°C remaining layers.

Recommended print substrates: glass (coat with PVA from a glue stick for best adhesion)

Print fan setting: Recommended for all layers.

Taulman-Eastman n-Vent Polyester Co-Polymer.

Print temperature: 255°C first layer, 250°C remaining layers.

Recommended print substrates: glass (coat with hairspray from a glue stick for best adhesion)

Print fan setting: Highly recommended for all layers.

Polyoxymethylene Co-Polymer.

Print temperature: 220°C first layer, 215°C remaining layers.

Recommended print substrates: very difficult to get the plastic to adhere to anything other than Delrin plastic. Doek cloth sometimes works.

Print fan setting: Highly recommended for all layers.

Hazards: This filament will release formaldehyde if heated above a certain temperature (which depends on the exact compounds used in the co-polymer)

High-Impact Polystyrene Filament.

Print temperature: 230°C first layer, 225°C remaining layers.

Recommended print substrates: glass (coat with hairspray)

Print fan setting: Not usually needed.

T-Glase Polyethylene Terephthalate Co-Polymer.

Print temperature: 235°C first layer, 225°C remaining layers.

Recommended print substrates: glass (coat with hairspray for best adhesion)

Print fan setting: Highly recommended for all layers.

Polycarbonate-ABS Alloy.

Print temperature: 275°C first layer, 265°C remaining layers.

Recommended print substrates: glass (coat with ABS dissolved in acetone for best adhesion)

Print fan setting: Unknown.

Appendix II. Special Considerations for Printing on Fabric with FDM Printer.

While there are other conceivable ways of attaching teeth to fabric (e.g. manufacturing them in two pieces with a rivet shape and then gluing the riveted parts to fabric), where feasible, printing directly on fabric is ideal for its ease and economy of manufacture (at least at a small production volume) and the precision with which the teeth can be laid out.

However, molten filament's adhesion to fabrics can be quite variable, depending not only on fabric, tooth material, heated print bed temperature, and tooth base geometry, but also on the means of holding the fabric to the bed, the contact pressure between extruder and fabric, and the tip geometry of the teeth. Improper operating conditions may not immediately result in a failed print; it may take until near the end of the print for it to warp enough that teeth merge together (rendering the print useless).

Fabric and Filament Combinations.

The following combinations of filament and fabric have been used with at least satisfactory bonding between filament and fabric—both as regards printability and mechanical strength:

- Cotton-polyester-elastomer weave and: Taulman 618, Taulman 910, Taulman PCTPE (nylons) – these cannot be peeled off without tearing the fabric.
- Kevlar weaves and: Taulman 618, Taulman 910 (note that these *can* be peeled off without tearing the weave, although it is not necessarily easy)

- Nylon fabrics (including non-wovens) and: Taulman 618, Taulman 910 (note that nonwovens bond more strongly to the Taulman-series nylons than do, say, the triaxial-weave nylon tested)
- Fine/soft fiberglass weaves and: Taulman 618, Taulman 910, Taulman PCTPE (nylons); n-Vent polyester copolymer filament;
- Cotton doek / "duck" cloth and: Taulman nylons,

The following combinations have moderate bonding strength – barely enough to print successfully (as determined by the subjective ease with which they could be peeled off—but they could possibly be strengthened with glue for mechanical applications):

- Cotton-polyester-elastomer weave and: n-Vent (polyester copolymer)
- Kevlar and: n-Vent (polyester copolymer), polycarbonate/ABS alloy (this was surprising as a Kevlar/PC-ABS composite has been developed[61])
- Silicone rubber (coated with adhesive) and: Taulman nylon copolymers
- Fine fiberglass fabrics and: PLA

The following combinations are known to be grossly deficient in bonding strength and do not even print successfully (if they did, a merely-weak bond could possibly be strengthened with glue):

[61] "Physical and Mechanical Characteristics of Kevlar Fiber-reinforced PC/ABS Composites", Sarawut Rimdusit, Parkpoom Lorjia, Kuljira Sujirote, and Sunan Tiptipakorn

- Carbon fiber and: PLA (including standard PLA and Taulman high-strength in-PLA)
- Kevlar fabric and: PLA (including standard PLA, PLA reinforced with 5% chopped carbon fiber, and Taulman high-strength in-PLA), HIPS, ABS
- Nylon fabric and: T-glase (a PET-copolymer), Taulman nylon copolymers

Securing Fabric.

Merely selecting compatible filament and fabric is only the beginning of the challenge of a successful on-fabric print. Printed plastic's tendency to warp up (due to temperature differentials between the print atmosphere and the latest layer—which heated bed and heated atmospheres can only somewhat mitigate) can usually be checked with sufficient bonding strength between the filament and the glass surface—when not printing on fabric. However, weaves that have significant tensile flexibility (if even in one direction) can easily have partly-printed teeth shifted in-plane (whenever the extruder catches, even slightly from minor warpage). To this end, it has proved necessary to coat the glass print surface with an adhesive that will hold the fabric. Obviously, a cross-linking glue or epoxy would be totally unsuitable since the fabric couldn't be removed subsequent to printing; however, double-sided tapes seemed promising for their constant layer thickness (thereby preserving levelness as much as possible) and impermanence.

Several double-sided tapes were experimented with, including Dritz tape targeted at fabrics, Duck-brand double-sided heavy-duty tape, and heavy-duty tapes used in composite layup. While the Duck-brand double-sided duct tape felt extremely sticky to a finger, it did not hold fabric quite as well as the Dritz-brand fabric tape, perhaps because the Duck adhesive gained some runniness at the high temperature (85°C) the bed was set at, or perhaps because of

the chemical composition of the adhesive. No type of tape lasted for more than one usage, and thus the glass had to have its tape removed after every printing.

The vertical softness added by the layer of tape also introduced new printing problems. Obviously, all but the thickest fabrics have significant bending compliance, which could easily translate into local rotation of the half-finished teeth during printing, although it may not produce significant inaccuracies in the shape of the finished product. It is also likely that the innate bending compliance of fabrics is exacerbated by the soft layer of tape now underneath the fabric. Perfect adhesion (i.e. rigid, without any possible lift-off) between fabric and plate would preclude this. However, the soft layer underneath the fabric also allows the print head to contact the fabric with a modicum of pressure, which is probably useful for producing a strong filament-fabric bond (as the plastic can be injected into the fibers to an extent). If the fabric were held against a hard surface (e.g. glass), any unevenness in the plate or fabric could cause the head to catch on the fabric and locally tear it up; not only would this contribute to local print defects, but if the fabric came to be raised sufficiently, it could derail the print (because the x and y positioning is accomplished with belts that can only bear a moderate amount of tension, perhaps not enough to move the head through the newly-created obstacle).

In printing on hard surfaces, it is customary to extrude an extra volume (often on the order of 50%) for the first layer to ensure the best-possible adhesion between print and surface (probably because this maximizes the contact area by flattening what would otherwise be cylindrical lines of filament). However, when printing on fabric, it may be harder for the filament to spread out, and it is recommended to use a much smaller extra print volume for the first layer (perhaps only 10%); otherwise, the first layer may have so much excess height that the

head will catch on cooled parts of the first layer even after the plate is lowered to the height of the second layer.

Finally, the fabric edges need to be constrained not to warp or slide; for some reason, double-stick tape alone is rarely sufficient to hold them, and the best practice is to fold the fabric under the plate and tape it to the plate there; then, the plate is taped to the heated bed (using both double-sided tape under the fabric and single-sided packing tape on top of it has proved best). Care must be taken to ensure that no folds exist on the underside of the glass plate, as these would angle the plate and nullify the levelness of the heated bed. Then, the print area should be surrounded with tape on top of the fabric to further guard against warping up. Clear packing tape has proved to adhere quite well to the fabric, better than masking tape, duct tape, and a special polyester-based tape used in composites. Figure 373 and Figure 374 shows pictures of the top and bottom of a glass plate with fabric securely attached.

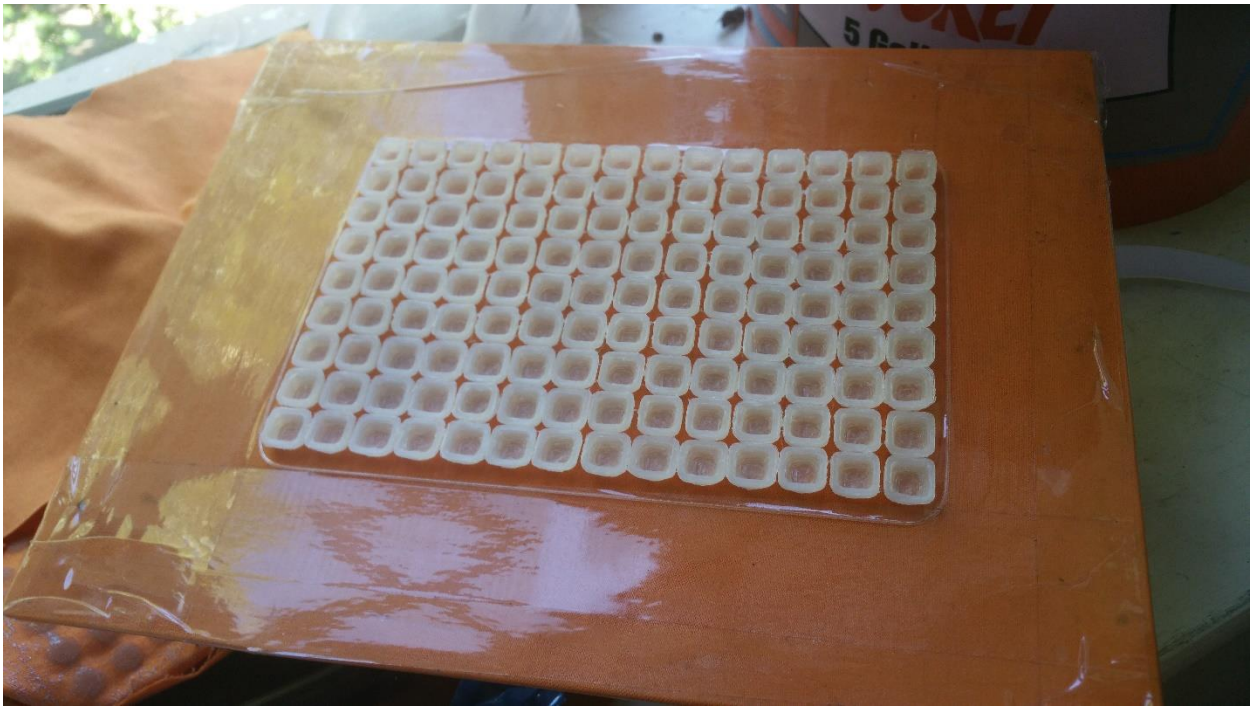

Figure 373: Top view of glass plate with fabric securely attached (note packing tape around print area to further protect against warping.

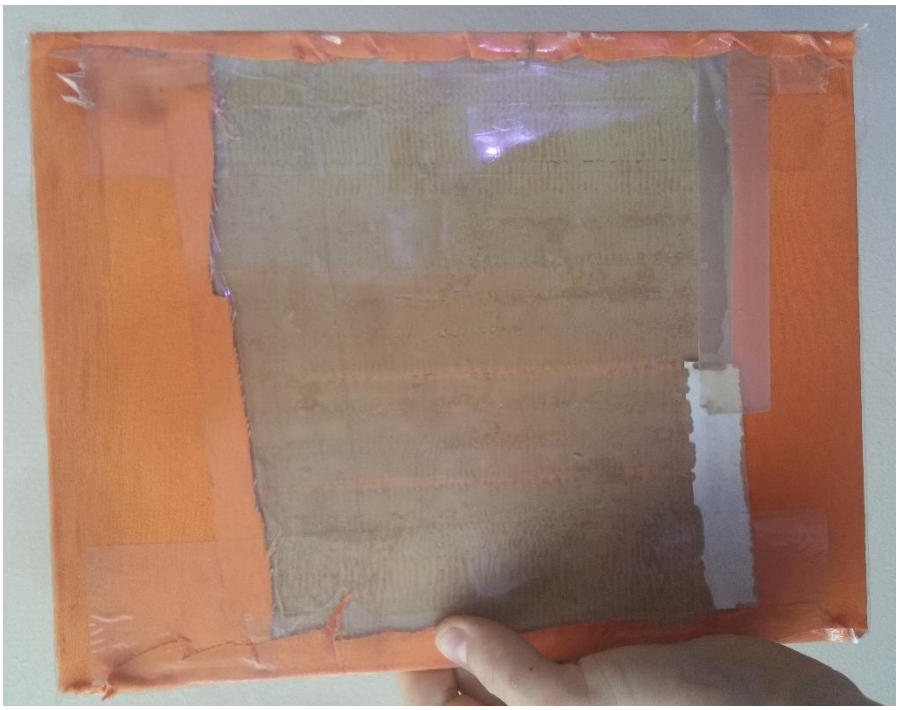

Figure 374: Underside of glass plate: the edges of the fabric have been secured with tape to the glass.

The tapes found to work best with each fabric type are as follows:

- Cotton doek cloth: duct tape and composite tape (fabric coated with double-sided adhesive)—even for applications only requiring one side to stick—work moderately well. Packing tape, polyester tape, and masking tape barely hold it.

Common Printing Faults.

Neglecting external sources of error (for instance, bugs in printer firmware, poor quality filament, etc.), there are still several sources of print errors unique to printing on fabric. This section will illustrate them with the aim of eliciting array redesign or a different fabric-holding strategy as needed.

Too-Small Tooth Gaps Result in Merging and Gross Warping Vicious Cycle.

This can be reduced by reducing warping (by heating the bed and print chamber), but mainly simply requires increasing the gap between teeth and improving the adhesion strength between the fabric and double-sided tape directly underneath it.

Too-Sharp Overhang Results in Localized Warping and Print Derailment.

This error is hardly unique to prints directly on fabric, and requires either using support material (perhaps breakaway support material) or reducing the overhang angle. The former solution may be more complicated when it comes to printing on fabric, however, because the support material itself must bond to the fabric strongly enough to allow the first layer to stick, but weakly enough that it can be removed from the fabric once the print is complete without tearing it.

Appendix III. Bonding Teeth to Fabrics with Adhesives.

Overview.

This appendix describes techniques for ensuring a good bond between plastic, 3D printed teeth that were printed on hard surfaces (instead of directly on fabrics, as in the previous section) and fabric backbones. The basic process is as follows:

1. Print teeth on a glass substrate (with whatever adhesive agents the filament requires, eg. PVA glue stick for Taulman nylon, ABS dissolved in acetone for ABS, hairspray for

PLA and n-Vent polyester, etc.), with the faces that will later be bonded to the fabric facing up. Tooth geometry should include shallow wells for holding adhesive.

2. Activate plastic-bonding epoxy as necessary, then fill teeth wells.
3. Press fabric into teeth, keeping it as flat as possible.
4. If the fabric weave is open enough, add some more epoxy on the opposite side of the fabric.

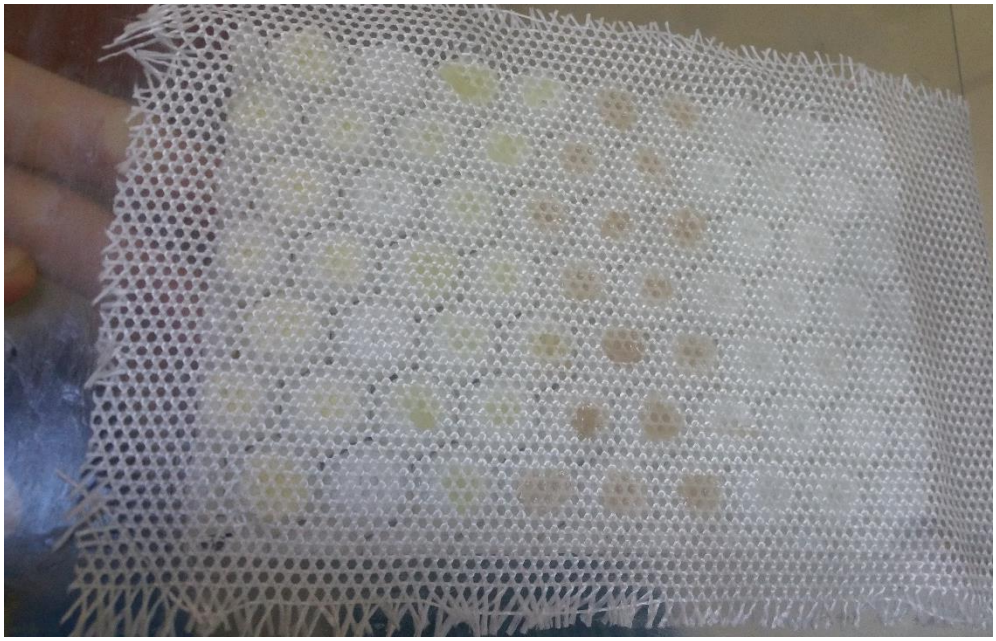

Figure 375: Showing an open weave with epoxy added to the outside of the fabric for improved bonding between the adhesive zone and the fabric.

5. Let the fabric and teeth bond to the epoxy (e.g. for over 24 hours).
6. Remove the teeth from the printing substrate.
7. Reinforce the inside of the teeth as necessary.

List of Compatible Fabrics and Adhesives.

The following table lists all the fabric-adhesive combinations attempted thus far, and whether it was easy to peel the fabric off from the adhesive patch by hand. It seems logical that

resistance to hand peeling is a necessary (if perhaps not sufficient) condition for employment of any given adhesive-fabric combination.

Fabric/Adhesive	**Super-Glue Plastic Fusion**	**Loctite Plastic Bonder**	**JB Weld Plastic Bonder**	**Structural Cyanoacrylate (with Activator)**	**Polyester Resin**	**Hot Melt Adhesive**
Polyester triaxial fabric	Fail	Good (provided bond on *both* sides of fabric)	Good	Good (but runny glue is hard to fill glue well completely with. Can add silica sand as filler)	?	?
Kevlar	Acceptable when both sides of fabric coated	Excellent	Good	Good when fabric thoroughly coated	?	Good
Doek (cotton), washed	Fail	Poor	Acceptable	Poor	Fail	?
Vectran	Fail	Fail	Poor	Fail	?	?
Fiberglass (fine weave)	(Untested)	Poor/acceptable	?	Poor/acceptable	Poor	Good

Nylon (green)	?	?		Poor/acceptable	Fail	?
Denim				Good		Good

3DP Filament/Adhesive	**Super-Glue Plastic Fusion**	**Loctite Plastic Bonder**	**JB Weld Plastic Bonder**	**Structural Cyanoacrylate (with Activator)**	**Polyester Resin**	**Hot Melt Adhesive**
PLA	Good	Good	Good	Good	Acceptable	Good
n-Vent (copolyester)	Good	Good	Good	Good	?	?
Taulman 618 (nylon)	Poor	Acceptable	Good	Good	?	?
ABS	Acceptable	Good	Acceptable/Good	Good	Good	Good

Appendix IV. Printing Fine Details with Support Materials.

Overview.

The precurved annular array with gear-like tooth features required the printing of parts with very fine detail and accurate tolerances (to ensure initial clearances as specified). Unfortunately, these parts required significant overhangs that need to be supported to maintain their dimensional integrity during the FDM process against the tendency to droop downwards; they also featured sharp corners that are prone to warping upwards (even with a cooling fan and heated chamber) unless held down sufficiently by material underneath. Since the only printers available to this researcher use FDM printing technology, not the SLS technique (which automatically provides support for overhang geometries), it was necessary to devise a support technique to ensure geometrical accuracy.

Hobbyists often find breakaway support material of the same material as that of the part itself to provide sufficient print quality. The slicing program that generates the G-code for the part computes a gap distance between the support structure and the overhang to be supported that minimizes the strength between the bond between the first overhanging part layer and the top support layer, while still remaining strong enough to catch the bottom extrusion layer. However, small pieces of the support material can still remain attached to the part even after most has been relatively-cleanly broken away, and if the gap distance is not large enough, the main part may

even be broken in the process of removing the support material (which would then be bonded too tightly to the part).

As such, hobbyists and professional users who need more accuracy than what single-material support schemes can provide use multiple-extruder setups, in which one extruder is to print the material used for the final part, and the other a different material that bonds neither too well nor too poorly to the main material. Thus, the choice of the second material is largely a function of the chemistry of the first material (though it is mainly determined in practice through trial and error); if the bond between the two materials is too strong, then attempts to break them apart will be more likely to damage the actual part, and if the bond is too weak, then the support material will not prevent upwards warpage and may not even allow the layer to extrude onto it (instead, the filament would curl up and probably stick to the extruding head until it was knocked off later in the print).

Granted, in the case of an excessively strong bond, it might be possible to dissolve away the support material with a selective solvent that does not dissolve the main material. Indeed, there are three combinations known to the 3D printing hobbyist community of main and support filament in which the support filament can be dissolved by a solvent that does not dissolve the main material to the same extent: ABS as main material and PLA as support dissolved in concentrated sodium hydroxide; PLA as main material and PVA as support dissolved in water; and ABS as main material and polystyrene as support dissolved in D-limonene. The third combination in practice proves to have poor performance as D-limonene also dissolves the styrene in ABS and seems to plasticize what ABS it does not dissolve. (Note that the dissolving action on the part of the solvent on the styrene in the ABS is strongest in an ultrasonic bath relative to the rate at which the bath sees the dissolution of the polystyrene support material, so if

one does wish to use an ABS/PS combination, one should under no circumstances employ an ultrasonic shaker to dissolve the PS afterwards.) The second combination is also fraught with issues, as PVA is difficult to extrude precisely (and thus strands of PVA filament often inadvertently become caught inside the perimeters of the PLA part, weakening it when they are subsequently dissolved out in water). Also note that a printer extruding PVA should be under constant supervision; if there is a jam during the print, it needs to be cleared quickly or the PVA will cross-link inside the teflon fusion chamber and ruin it. Because heads that have extruded PVA should immediately be purged after the end of the print with ABS or some other non-crosslinking filament, is also inadvisable to leave even the most reliable printer printing PVA overnight unless it will finish after the operator returns. These issues leave the ABS-PLA combination the most attractive from the standpoint of print quality and machine safety; however, a pressure-washing system is usually recommended to dissolve the PLA in concentrated NaOH solution, which represents a significant overhead and could have human safety concerns associated with it as well. Thus, it was desirable to find a support material combination that would produce better print quality than what can be obtained with single-material breakaway prints but that lacks the drawbacks associated with all known dissolvable support material combinations.

A Note on Warping of the Main Material.

While judicious use of support materials can inhibit warping of the main material (as can the use of a heated bed and heated chamber), the best way to avoid this is to use filaments that are less warp-prone, such as HIPS and PLA, rather than ABS and nylon. Also, if a flat section curls up at corners from warping (i.e. absent support material below, or given insufficient adhesion between the support material and main material), this can sometimes be corrected by

making the flat section thicker (perhaps on the order of 1mm thick); subsequent layers may be able to force the section to lie flat, since the underlying layers are softened by the addition of a new layer.

Filament Combinations for Breakaway Support.

The following combinations of filaments were found to have the ideal amount of adhesion during printing—not so much that the support could not be later broken away, but enough to allow the support material to adhere to the filament enough to prevent it from warping.

Of note, the bond between PLA and PVA is not terribly strong, and PVA can usually be broken away by hand, rarely requiring water to dissolve it. While breakaway support is indeed convenient, the weakness of this bond reduces the effectiveness of PVA as a support material in the first place, and since water is not problematic for PLA, not having to use it is of no mechanical benefit for the PLA part (in contrast to being able to avoid D-limonene submersion of ABS, which would be beneficial). Beyond that, the poor print quality of PLA and its potential to cross-link in the extruder still counterindicate the usage of PLA.

The bond between ABS and PLA is stronger, especially when high temperature PLA (printed at 240°C) is used instead of low-temperature PLA (printed at 200°C); however, it can still be broken fairly well with needle-nose pliers, and then any remaining PLA can be cleaned up with a NaOH bath if necessary.

Other combinations investigated:

- T-glase (PET/PTT) as main material, ABS as support: very strong bond, but ABS can be dissolved in D-limonene in an ultrasonic bath (leaving T-glase untouched).

- n-Vent polyester as main material, HIPS as support: poor sticking means HIPS support does little to prevent warpage upwards, but paradoxically fairly hard to break off, so it was necessary to dissolve HIPS in D-limonene. Anyways, n-Vent does not capture small details well, even with fan set to maximum speed.
- High-temperature PLA as main material, n-Vent as breakaway support: fairly good sticking, but less than ideal.
- High-temperature PLA as main material, HIPS as support: poor sticking means HIPS support does little to prevent warpage upwards but is paradoxically fairly hard to break off, so it was necessary to dissolve the HIPS in D-limonene. Fortunately, PLA seems very resistant to D-limonene.
- High-temperature PLA as main material, Taulman Bridge nylon as breakaway support: the adhesion between the two was good enough to prevent all warping when up to four parts were printed at a time (more on which below), and the toughness but low stiffness of nylon made it easy to break away since the support structures tended to stay in one piece. Nylon is fairly ooze prone, unfortunately.

Limiting Cooling Time for Proper Adhesion to Support.

Of note, warping increased significantly with multiple material combinations in transitioning from printing four teeth at a time to 40 (keeping all other potential variables, such as print speed, fan usage, etc. constant).

Print Quality with Ooze-Prone Support Materials.

Both nylon and PVA worked well as breakaway support materials (with PVA also being water-soluble, a quality beneficial for features that cannot be physically accessed to break away

the material, though it did not prove necessary for the tooth design manufactured here) for high-temperature PLA; unfortunately, despite their distinct chemical properties, they are both quite prone to oozing during printing, unlike PLA and ABS.

Appendix V. Reducing Tooth Size on FFF Printers.

To avoid inconvenience and adverse effects on athletic performance, it is essential to reduce the thickness of the tooth arrays as much as possible while retaining high post-lockup stiffness. Once fabric-backed arrays were developed that showed some basic success, efforts were made to reduce tooth size while retaining dimensional integrity, which was an especially-important concern for teeth that had special features intended to reduce sliding.

The first attempt to reduce tooth sizes centered around the flared rectangular teeth with anti-slide features (vertical and horizontal). Reductions to 70% and 50% of the original size were attempted; the 70% reduction had nearly flawless tolerances, whereas the teeth of the 50% reduction could not interface properly. However, detail capture was high enough even at 50% that teeth might still be produced that can indeed mesh if the nominal gap between teeth was increased or if filament flow were reduced in the outer perimeter. Figure 376 shows these prints. That said, further experimentation must be carried out to determine if lockup will be consistent over many prints.

Figure 376: Right to left: original teeth, teeth reduced to 70% of initial size, teeth scaled to 50% of initial size.

Bibliography.

"Whitepaper: Nonlinear Finite Element Analysis of Elastomers." MSC.Software. Web. 1 Nov. 2015. <http://www.mscsoftware.com/Submitted-Content/Resources/WP_Nonlinear_FEA-Elastomers.pdf>.

Bingham, Guy A., and Richard Hague. "Efficient Three Dimensional Modelling of Additive Manufactured Textiles." *Rapid Prototyping Journal* 19.4 (2013): 269-81. Web. 3 Nov. 2015.

Bückmann, Tiemo, Nicolas Stenger, Muamer Kadic, Johannes Kaschke, Andreas Frölich, Tobias Kennerknecht, Christoph Eberl, Michael Thiel, and Martin Wegener. "Tailored 3D Mechanical Metamaterials Made by Dip-in Direct-Laser-Writing Optical Lithography." *Adv. Mater. Advanced Materials* 24.20 (2012): 2710-714. Web.

"The New Frontier in Generative Orthotics." *CRP Technology 3D Printing and Additive Manufacturing Company RSS2*. CRP Technology, 16 July 2014. Web. 18 Aug. 2015.

Chen, Yan. "Design of Structural Mechanisms." Diss. U of Oxford, 2003. St Hugh's College. Web. 20 Apr. 2014. <http://www.eng.ox.ac.uk/civil/publications/theses/chen.pdf>.

Daggett, Susan, PhD. "Doing the Impossible with Poisson's Ratio : CompositesWorld." *High Performance Composites*. CompositesWorld, 31 Oct. 2012. Web. 14 Sept. 2015. <http://www.compositesworld.com/columns/doing-the-impossible-with-poissons-ratio>.

Gordon, J. E. *Structures: Or, Why Things Don't Fall Down*. Dacapo: Plenum, 1981. Print. p. 253

Gurley, Austin, David Beale, Royall Broughton, and David Branscomb. "The Design of Optimal Lattice Structures Manufactured by Maypole Braiding." *J. Mech. Des Journal of Mechanical Design* 137.10 (2015): 101401. Web.

Hafner, Brian, Walter Whatley, and Moreno White. "Development of an Advanced Biofidelic Lower Extremity Prosthesis." *Biomedical Engineering Foot and Ankle Motion Analysis Clinical Treatment and Technology* (2007): 613-37. Web.

Jutte, Christine V., Bret Stanford, Carol D. Wieseman, and James B. Moore. "Aeroelastic Tailoring of the NASA Common Research Model via Novel Material and Structural Configurations." *52nd Aerospace Sciences Meeting* (2014). Web.

Kadic, Muamer, Tiemo Bückmann, Nicolas Stenger, Michael Thiel, and Martin Wegener. "On the Practicability of Pentamode Mechanical Metamaterials." *Appl. Phys. Lett. Applied Physics Letters* 100.19 (2012): 191901. Web.

Larsen, U.d., O. Sigmund, and S. Bouwstra. "Design and Fabrication of Compliant Micromechanisms and Structures with Negative Poisson's Ratio." *Proceedings of Ninth International Workshop on Micro Electromechanical Systems*. Web.

Levangie, Pamela K., Cynthia C. Norkin, and Pamela K. Levangie. *Joint Structure and Function: A Comprehensive Analysis*. Philadelphia: F.A. Davis, 2011. Print.

Mann, Casey, Jennifer McLoud-Mann, and David Von Derau. "Convex Pentagons That Admit I-block Transitive Tilings." *Preprint*. Web. <arXiv:1510.01186 [math.MG]>.

Maurel, Jacques. "Explanations about the Paradoxical Gears." *Teaching Machine Design & Mechanics by Jacques Maurel*. Web. <http://www.jacquesmaurel.com/files/Explanations about the paradoxical gears.doc>.

Mckay, G. D. "Ankle Injuries in Basketball: Injury Rate and Risk Factors." *British Journal of Sports Medicine* 35.2 (2001): 103-08. Web.

Mitschke, Holger. *Deformations of Skeletal Structures: Finite Auxetic Mechanisms in Periodic Tessellations*. 2009. Print.

Jessica. "Kinematics Textile Swatches." *Nervous System Blog: Explorations in Generative Design and Natural Phenomena*. N-e-r-v-o-u-s, 2 Apr. 2015. Web. 21 Oct. 2015. <http://n-e-r-v-

Schwartz, Peter, ed. *Structure and Mechanics of Textile Fibre Assemblies*. Cambridge, England: Woodhead in Association with the Textile Institute, 2008. Print.

Shirk, M., T. Hertz, and T. Weisshaar. "Aeroelastic Tailoring - Theory, Practice, and Promise." *25th Structures, Structural Dynamics and Materials Conference* (1984). Web.

Smith, Jimmy. "The Ankle Paradox." *The Ankle Paradox*. T-Nation, 12 Feb. 2008. Web. 22 Feb. 2015.

"Rupture of the Joint-capsule at the Front of the Ankle Joint." *SportNetDoc.DK*. Web. 22 Aug. 2015. <http://www.sportnetdoc.com/foot-ankle/rupture-of-the-joint-capsule-at-the-front-of-the-ankle-joint>.

Sönnerlind, Henrik. "Obtaining Material Data for Structural Mechanics from Measurements." *COMSOL Blog Obtaining Material Data for Structural Mechanics from Measurements Comments*. COMSOL, 23 Feb. 2015. Web. 2 Nov. 2015.

"J-Shaped Curves." *TLP Library Elasticity in Biological Materials*. University of Cambridge. Web. 31 Oct. 2015.

"Tech-bond Solutions - Adhesive For All Materials, Adhesive For Plastics." *Tech-Bond Solutions*. Web.

"TheRingLord.com Chainmail Jump Rings Jumprings Scalemail Jewelry Supplies and Wire - Welders." *TheRingLord.com Chainmail Jump Rings Jumprings Scalemail Jewelry Supplies and Wire - Welders*. Web. 4 Apr. 2014.

Tummala, Yashwanth, Mary Frecker, Aimy Wissa, and James E. Hubbard. "Design Optimization of a Twist Compliant Mechanism With Nonlinear Stiffness." *Volume 2: Mechanics and Behavior of Active Materials; Structural Health Monitoring; Bioinspired Smart Materials and Systems; Energy Harvesting* 2.23 (2014). Web.

Virk, K., A. Monti, T. Trehard, M. Marsh, K. Hazra, K. Boba, C. D L Remillat, F. Scarpa, and I. R. Farrow. "SILICOMB PEEK Kirigami Cellular Structures: Mechanical Response and Energy Dissipation through Zero and Negative Stiffness." *Smart Mater. Struct. Smart Materials and Structures* 22.8 (2013): 084014. Web.

Bbanerje. "Stress-strain Curves for Various Hyperelastic Material Models." *Wikipedia*. Wikimedia Foundation. Web.

"PCTPE Features." *Taulman 3D*. Web. 4 June 2015.